Imperial College London

Computational and Experimental Characterisation of Water-Fuelled Hall Effect Thrusters

Jesús Manuel Muñoz Tejeda

Imperial College London

June 2024

Submitted in part fulfilment of the requirements for the degree of

Doctor of Aeronautics of Imperial College London

and the Diploma of Imperial College London

Declaration of Originality

I, Jesús Manuel Muñoz Tejeda, hereby declare that the contents of this thesis are original and have not been submitted in whole or in part for consideration for any other degree or qualification. This dissertation embodies my own investigation and credit is given when reference is made to the work of others.

Copyright Statement

The copyright of this thesis rests with the author. Unless otherwise indicated, its contents are licensed under a Creative Commons Attribution-Non Commercial 4.0 International Licence (CC BY-NC).

Under this licence, you may copy and redistribute the material in any medium or format. You may also create and distribute modified versions of the work. This is on the condition that: you credit the author and do not use it, or any derivative works, for a commercial purpose.

When reusing or sharing this work, ensure you make the licence terms clear to others by naming the licence and linking to the licence text. Where a work has been adapted, you should indicate that the work has been changed and describe those changes.

Please seek permission from the copyright holder for uses of this work that are not included in this licence or permitted under UK Copyright Law.

ABSTRACT

In this thesis, the use of water as a propellant for Hall Effect Thrusters (HETs) as an alternative to conventional xenon-fuelled HETs is explored. This is motivated by water's cost-effectiveness, multifunctionality, environmental benefits, and potential for In-Situ Resource Utilisation. Two propulsion methods are investigated: 1) water electrolysis propulsion, where oxygen and hydrogen are generated by a water electrolyser on board a spacecraft, and 2) a direct water vapour feed. A Particle-In-Cell computational model is developed to simulate water-based HET operation, incorporating all key propellant reactions and most-recent techniques to improve fidelity. The experimental tests progressed from oxygen-fuelled HETs with krypton cathodes to the first end-to-end water electrolysis system directly fuelled by a water electrolyser (i.e., an oxygen-fuelled HET in combination with a hydrogen-fuelled cathode). The first and second generation of water electrolysis HETs, referred to as *WET-HET* and *AQUAHET*, are tested and optimised to achieve the best possible performance; with *AQUAHET* showing a $\Delta\eta_{tr} = 20\%$ higher thrust efficiency for the same operating power. In the best-performing case, the *AQUAHET* produced a thrust of $T = 51.0 \pm 0.3$ mN, anode specific impulse of $I_{sp} = 3119 \pm 27$ s, and anode thrust efficiency of $\eta_{tr} = 24.4 \pm 0.3$ % at a discharge power of $P_d = 3200 \pm 1$ W, whereas for the *WET-HET* it was obtained a thrust of $T = 21.5 \pm 0.4$ mN, $I_{sp} = 3617 \pm 69$ s, and $\eta_{tr} = 17.1 \pm 0.7$ % at $P_d = 2232 \pm 1$ W. Tests using hydrogen as a cathode propellant yielded a $\Delta\eta_{tr} = 10\%$ efficiency drop compared to krypton. Water-vapour propulsion is also assessed, with water electrolysis showing a $\Delta\eta_{tr} = 20\%$ efficiency advantage. Additionally, radiofrequency excitation is investigated as a mechanism to improve the efficiency of these systems. This work presents the most up-to-date comprehensive assessment of water-fuelled HET propulsion, highlighting the potential of this technology for future space missions.

EXECUTIVE SUMMARY

This dissertation delves into the utilisation of water as a propellant for electric propulsion technologies, specifically Hall Effect Thrusters (HETs). Water, compared to the state-of-the-art of HETs which typically utilise xenon as a propellant, emerges as a viable alternative due to various factors, such as its cost-effectiveness, environmental sustainability, spacecraft multifunctionality and potential for In-Situ Resource Utilisation. Two approaches are examined: 1) water electrolysis propulsion, where a water electrolyser onboard the spacecraft separates water into oxygen (intended fuel for the thruster) and hydrogen (cathode's propellant), and 2) a direct water vapour feed.

A computational Particle-In-Cell code, encompassing a 0-dimensional and a 2-dimensional model, is developed to simulate the physics underlying water electrolysis and water vapour HETs. The principal reactions of oxygen (from water electrolysis), water vapour, and their dissociation products are incorporated to enhance the fidelity of the code in replicating these devices.

In the context of water electrolysis, an incremental testing timeline is established with the objective of achieving the first end-to-end experimental demonstration of a HET operating with the in-situ production of water electrolysis byproducts. Initially, oxygen-fuelled HETs are tested in conjunction with a krypton-fuelled cathode to further explore optimal operational conditions and deepen the understanding of the thruster's working principles. The first generation of a water electrolysis HET (the *WET-HET*) and its subsequent iteration (*AQUAHET*), built upon the lessons learned from the first generation, are tested using different geometrical configurations. The primary difference between the two thrusters lies in their channel mean diameter ($d_m = 25$ mm for the *WET-HET* and $d_m = 45$ mm for the *AQUAHET*). Moreover, the radial directionality of the magnetic field on the *AQUAHET* is enhanced to achieve higher anode thrust efficiency. An optimal channel length of $L = 13.1$ mm and channel width of $w = 5$ mm are determined for the *WET-HET* and *AQUAHET*, respectively. On average, under the most optimal conditions, the *AQUAHET* demonstrated a $\Delta\eta_{tr} \approx 20\%$ better anode thrust efficiency than the *WET-HET* for

the same discharge power. The best performing case for the *WET-HET* was achieved at a discharge power of $P_d = 2232 \pm 1$ W, corresponding to a thrust of $T = 21.5 \pm 0.4$ mN, anode specific impulse of $I_{sp} = 3617 \pm 69$ s, and anode thrust efficiency of $\eta_{tr} = 17.1 \pm 0.7$ %. The *AQUAHET* tests at $P_d = 3200 \pm 1$ W reported a thrust of $T = 51.0 \pm 0.3$ mN, anode specific impulse of $I_{sp} = 3119 \pm 27$ s, and anode thrust efficiency of $\eta_{tr} = 24.4 \pm 0.3$ %. Several campaigns were conducted at Stanford University, analysing the plasma properties and oxygen particles' composition of the discharge.

The subsequent tests involve the initial characterisation using the byproducts of water electrolysis (oxygen and hydrogen) from pressurised bottles. The results obtained indicate a slight yet discernible decrease in performance (around $\Delta\eta_{tr} \approx 10\%$) when hydrogen is employed as the cathode propellant instead of krypton. The results assess different hydrogen mass flow rates for a constant oxygen mass flow, thereby evaluating a variety of hydrogen-oxygen ratios (Φ) beyond stoichiometric conditions (Φ = 1:8). The results reveal no disparities in performance regardless of Φ.

Finally, the first end-to-end technological demonstration utilising oxygen and hydrogen directly produced by a water electrolyser was conducted at the European Space Agency facilities. The results successfully demonstrated the operability of the HET in conjunction with a water electrolyser.

The second branch of water propulsion (direct water vapour feed) is also explored and juxtaposed with water electrolysis. Under the same optimal conditions in both scenarios, findings suggest that water electrolysis outperforms water vapour propulsion by approximately $\Delta\eta_{tr} \approx 20\%$. Drawing upon the findings garnered throughout this thesis, an evaluation of the advantages and disadvantages of both technologies is conducted from a systems-level standpoint.

Radiofrequency (RF) excitation is also investigated using in-house software, and experimentally tested with the objectives of augmenting the HET total efficiency by increasing the energy of the electrons and promoting an ionisation event. The results indicate that, when utilising noble gases such as xenon or krypton, RF excitation yields a performance boost in the total thrust efficiency (up to $\Delta\eta_{tot} = 11\%$) when using the right combination of frequency ($f_{RF} = 470$ MHz), RF power ($P_{RF} = 12.3$ W) and peak magnetic flux density ($B = 0.0168$ T). With oxygen, the performance enhancement is negligible or too small to be detected using the thrust balance instrumentation.

NON-TECHNICAL SUMMARY

Similarly to the evolution of the automotive sector, which witnessed a significant shift from traditional fossil fuel-based engines towards alternative technologies, such as electric cars or hydrogen fuel cell vehicles, space vehicles are transitioning from the state-of-the-art propellants to other fuel types. This is particularly important not only in terms of reducing the production cost associated with developing and operating satellites, but also in fostering a more sustainable space sector.

This thesis experimentally demonstrates for the first time the feasibility of using water as a propellant in space vehicles, specifically within the context of electric propulsion. Electric propulsion differs from traditional chemical propulsion, which is utilised by entities like *NASA* and *SpaceX*, in that it does not rely on chemical energy. Instead, it harnesses the properties of the fourth state of matter, plasma: When a gas is heated to very high temperatures, neutral particles can lose electrons, acquiring a positive charge and forming ions. This ion-electron mixture constitutes plasma, which can be accelerated using electric and/or magnetic fields. Devices that use both electric and magnetic fields to accelerate plasma, arranged in a specific orientation, are known as "Hall Effect Thrusters". This thesis investigates Hall Effect Thrusters powered with water, identifying the most efficient operating and geometrical conditions for these devices. It also delves into the underlying physical phenomena that govern their operation, employing both experimental and computational methods to uncover the most pertinent insights.

The primary advantage of electric propulsion is its exceptional efficiency. However, the force it generates is really small, akin to the weight of a penny. This is why electric propulsion is not suitable for launching rockets into space; it does not produce enough force to do so. However, in space, where there is no friction to stop the satellite, a small continuous force over time can generate high velocities, which is useful to travel long distances.

Water is a promising alternative to current propellants due to its affordability, environmental friendliness, non-toxicity and ease of handling. Furthermore, water can serve multiple purposes

within the spacecraft. For example, in the medium to long term, as manned space missions become more common, a life-support system for astronauts, including water, will be necessary. Water is also present on Earth, the Moon, Mars, and other asteroids, suggesting it can be possible to fuel a spacecraft on another planet and reach further exploration of the cosmos.

Overall, the space industry could undergo a significant change by switching to water as propellant. If this happens, future spacecraft could take advantage of water's unique characteristics, promoting a more environmentally friendly space environment. To reach a stage where water can be used as a propellant for spacecraft, extensive research is required to determine the best materials for satellites to be compatible with water and their optimal operating conditions. This thesis validates the viability of water propulsion and provides valuable insights into the operational mechanics and physical principles underlying these systems.

ACKNOWLEDGMENTS

My first words of gratitude go to my PhD supervisor, Prof. Aaron Knoll. Over these four years of research, he has been an invaluable source of inspiration, support, and guidance. He is one of the people I have learned the most from in my entire life. I feel very fortunate to have shared these years of research with him. He is an excellent researcher, teacher, and most importantly, a wonderful person.

Prof. Mark Cappelli, PhD supervisor of Prof. Aaron Knoll, has also been a significant source of inspiration. During my time at Stanford University, he demonstrated a very pragmatic approach to conducting science, profound knowledge in the field, and a dedication that was evident in every conversation we had.

My laboratory colleagues and friends have been crucial in creating a dynamic and friendly environment over these years. I would like to especially thank Dr. Alexander Schwertheim who, together with Prof. Aaron Knoll, taught me everything I needed to succeed in my experiments. Dr. Schwertheim is, without a doubt, the most brilliant PhD student I have worked with, endowed with immense gratitude, humour, and knowledge about the field.

I am also very grateful to the European Space Agency and all the people I have worked with there, who contracted me to conduct this research and believe in this technology as much as I do. *ALIENA Pte Ltd* and *URA Thrusters Ltd* greatly supported my thesis by sharing hardware and knowledge, which I could use to build upon my research and strengthen my abilities to conduct science.

Last but not least, I would like to thank my family. They gave me the opportunity to start my studies in science and engineering and have always believed in me. For all their support, kindness, gratitude, and generosity, this thesis is dedicated to all of you.

CONTENTS

ABSTRACT i

EXECUTIVE SUMMARY ii

NON-TECHNICAL SUMMARY iv

LIST OF PUBLICATIONS, CONFERENCES AND OTHER CONTRIBUTIONS xv

LIST OF ACRONYMS, SYMBOLS AND SUBSCRIPTS xvii

1 *BACKGROUND* 1

1.1 **Space Propulsion** 1

1.1.1 Chemical Propulsion (CP) 2

1.1.1.1 Solid Propellant Systems 3

1.1.1.2 Liquid Propellant Systems 3

1.1.1.3 Cold Gas Systems 4

1.1.2 Electric Propulsion (EP) 4

1.1.2.1 Electrothermal Propulsion Systems 4

1.1.2.2 Electrostatic Propulsion Systems 5

1.1.2.3 Electromagnetic Propulsion Systems 6

1.1.3 Nuclear Propulsion (NP) 7

1.1.3.1 Nuclear Thermal Propulsion (NTP) 7

1.1.3.2 Nuclear Electric Propulsion (NEP) . . . 7
1.2 **Hall Effect Thrusters (HETs)** . . . 8
1.2.1 Technology . . . 8
1.2.1.1 Thruster Overview . . . 8
1.2.1.2 Cathode Overview . . . 10
1.2.1.3 Alternative Propellants . . . 13
1.2.2 Physics . . . 17
1.2.2.1 Particles Motion . . . 18
1.2.2.2 Plasma Waves and Radiofrequency (RF) Excitation . . . 20
1.2.3 Simulation Tools . . . 24
1.2.3.1 Fully-Kinetic Models . . . 24
1.2.3.2 Full Particle-In-Cell Models . . . 25
1.2.3.3 Multi-Fluid Models . . . 25
1.2.3.4 Hybrid Models . . . 25

2 *MOTIVATION AND OBJECTIVES* **27**

2.1 **Two Distinct Ideas: Water Electrolysis and Water Vapour** . . . 27
2.1.1 Water Electrolysis . . . 27
2.1.2 Water Vapour . . . 28
2.2 **Benefits and Prospects of Water Propulsion Technologies** . . . 28
2.2.1 Space Propulsion Environmental Studies . . . 29
2.2.2 Multi-Mode Water Propulsion System . . . 31
2.2.2.1 Water Electrolysis Multi-Mode . . . 31
2.2.2.2 Water Vapour Multi-Mode . . . 35
2.2.3 Links to the United Nations Sustainable Development Goals (SDGs) . . . 38
2.2.4 In-Situ Resource Utilisation (ISRU) . . . 38
2.2.5 Cost Savings . . . 39

2.3 **Technological Challenges** . . . 40
2.3.1 Computational Simulations . . . 40
2.3.2 Material Compatibility . . . 41
2.3.3 Performance . . . 41
2.3.3.1 Thruster Geometrical Optimisation . . . 42
2.3.3.2 Magnetic Field . . . 43
2.3.3.3 Discharge Power . . . 43
2.3.3.4 Radiofrequency (RF) Excitation . . . 43
2.3.4 End-To-End Technology Demonstration . . . 44
2.4 **List of Objectives for this Thesis** . . . 45

3 *COMPUTATIONAL CHARACTERISATION* **47**

3.1 **Baseline and Previous Codes** . . . 47
3.1.1 PlasmaSim 2-Dimensional (2D) Code . . . 48
3.1.1.1 Main Loop . . . 48
3.1.1.2 Particle Tracking and Electrostatic Computational Domains . . . 49
3.1.1.3 Simulation Inputs . . . 50
3.1.1.4 Particle Initialisation . . . 51
3.1.1.5 Collisional and Ionisation Model . . . 51
3.1.1.6 Simulation Constraints and Spatial Discretisation . . . 53
3.1.1.7 Electric Potential . . . 54
3.1.1.8 Particles' Motion . . . 57
3.1.1.9 Boundary Conditions . . . 58
3.1.1.10 Computational Time . . . 58
3.1.1.11 Performance Estimation . . . 59
3.1.2 PlasmaSim 0-Dimensional (0D) Code . . . 61
3.1.2.1 Reduction in Dimensionality . . . 61

3.1.2.2 Simulation Inputs . . . 61
3.1.2.3 Boundary Conditions . . . 62
3.2 **Numerical Modelling** . . . 64
3.2.1 Methodology . . . 64
3.2.1.1 Combining the 0D and 2D Particle-In-Cell Codes . . . 65
3.2.1.2 A Double-Stage Reactive Model . . . 67
3.2.1.3 Energy-Fixed Versus Energy-Conserved Models . . . 72
3.2.1.4 Resolving Poisson's Equation . . . 73
3.2.1.5 Turbulent Collisionality . . . 74
3.2.1.6 Simulation Inputs . . . 75
3.2.1.7 Boundary Conditions . . . 76
3.2.1.8 Radiofrequency (RF) Excitation . . . 78
3.2.2 Results and Discussion . . . 82
3.2.2.1 Water Electrolysis-Fuelled Hall Effect Thrusters . . . 82
3.2.2.2 Water Vapour-Fuelled Hall Effect Thrusters . . . 92
3.2.2.3 Radiofrequency (RF) Excitation . . . 101

4 *EXPERIMENTAL CHARACTERISATION* **114**

4.1 **Overview of Experiments** . . . 114
4.1.1 Technology timeline . . . 114
4.1.2 Laboratory Hardware . . . 117
4.1.2.1 Hall Effect Thrusters . . . 117
4.1.2.2 Cathodes . . . 123
4.1.2.3 Thrust Balance . . . 128
4.1.3 Performance parameters . . . 130
4.1.4 Electric Circuit and Ignition Process . . . 132
4.1.5 Laboratories and Facilities . . . 134

4.2 **Campaigns A - Oxygen-Fuelled Hall Effect Thrusters with a Xenon/Krypton-Fuelled Cathode: Performance Characterisation** . . . 135
4.2.1 Methodology . . . 135
4.2.1.1 Experimental Set-Up and Vacuum Chamber Facilities . . . 135
4.2.1.2 Electronics . . . 136
4.2.1.3 Fluidics . . . 138
4.2.1.4 Working Procedures . . . 138
4.2.1.5 Thruster's Geometrical Configuration and Material Selection . . . 139
4.2.2 Results and Discussion . . . 139
4.2.2.1 Influence of Cathode Selection . . . 139
4.2.2.2 The Grade of the Ceramics Walls . . . 142
4.2.2.3 Anode Plate Compatibility Analyses . . . 144
4.2.2.4 Magnetic Field . . . 147
4.2.2.5 Mass Flow . . . 151
4.2.2.6 Channel Length Dependence . . . 155
4.2.2.7 Channel Width Dependence . . . 162
4.2.2.8 Comparison Between the First (*WET-HET*) and Second (*AQUAHET*) Water Electrolysis Hall Effect Thruster Generation . . . 164
4.2.2.9 Numerical Model and Experiments . . . 166
4.3 **Campaigns B - Oxygen-Fuelled Hall Effect Thrusters with a Xenon/Krypton-Fuelled Cathode: Physics Characterisation** . . . 168
4.3.1 Methodology . . . 168
4.3.1.1 Experimental Set-Up and Vacuum Chamber Facilities . . . 168
4.3.1.2 Electronics . . . 170
4.3.1.3 Fluidics . . . 171
4.3.1.4 Working Procedures . . . 172
4.3.1.5 Thrusters Set-Up . . . 172

4.3.1.6 ExB Probe . . . 173
4.3.1.7 Langmuir Probes . . . 181
4.3.1.8 Spectrometer . . . 184
4.3.2 Results and Discussion . . . 185
4.3.2.1 Plasma Particles' Composition . . . 185
4.3.2.2 Acceleration Voltages . . . 189
4.3.2.3 Plasma Properties at Different Locations . . . 191
4.3.2.4 Oxygen Plasma Spectrum . . . 194
4.3.2.5 Numerical Model and Experiments . . . 195
4.4 **Campaigns C - Water Electrolysis-Fuelled Hall Effect Thrusters: Oxygen and Hydrogen from Pressurised Cylinders** . . . 196
4.4.1 Methodology . . . 196
4.4.1.1 Experimental Set-Up and Vacuum Chamber Facilities . . . 196
4.4.1.2 Electronics, Fluidics and Working Procedures . . . 196
4.4.1.3 Thrusters' Geometrical and Material Configuration . . . 200
4.4.2 Results and Discussion . . . 201
4.4.2.1 Hydrogen-To-Oxygen Ratios (Φ) . . . 201
4.4.2.2 Water Electrolysis (Oxygen/Hydrogen) vs Oxygen/Krypton . . . 207
4.4.2.3 Oxidation of the Hardware Using Oxygen and Hydrogen . . . 212
4.4.2.4 Performance Comparison . . . 215
4.5 **Campaigns D - Water Electrolysis-Fuelled Hall Effect Thrusters: End-to-End Testing with a Water Electrolyser** . . . 217
4.5.1 Methodology . . . 217
4.5.1.1 Experimental Set-Up and Vacuum Chamber Facilities . . . 217
4.5.1.2 Electronics, Fluidics and Working Procedures . . . 221
4.5.1.3 Thrusters' Geometrical and Material Configuration . . . 222
4.5.1.4 Water Electrolyser Hardware . . . 222

4.5.2 Results and Discussion . . . 225
4.5.2.1 Water Electrolyser Validation . . . 225
4.5.2.2 Hydrogen Cathode Validation . . . 227
4.5.2.3 End-to-End Water Electrolysis Hall Effect Thruster Validation . . . 228
4.6 **Campaigns E - Water Vapour-Fuelled Hall Effect Thrusters: Performance Characterisation** . . . 234
4.6.1 Methodology . . . 234
4.6.1.1 Experimental Set-Up and Vacuum Chamber Facilities . . . 234
4.6.1.2 Electronics, Fluidics and Working Procedures . . . 234
4.6.1.3 Thrusters' Geometrical and Material Configuration . . . 235
4.6.1.4 Water Vapour Feed System . . . 236
4.6.1.5 Water Condensation Control System . . . 239
4.6.2 Results and Discussion . . . 243
4.6.2.1 Mass Flow Dependence . . . 243
4.6.2.2 Magnetic Field Strength Dependence . . . 245
4.6.2.3 Water Electrolysis vs Water Vapour-Fuelled Hall Effect Thrusters 247
4.6.2.4 Numerical Model and Experiments . . . 255
4.7 **Campaigns F - Radiofrequency (RF) Excitation** . . . 256
4.7.1 Methodology . . . 256
4.7.1.1 Experimental Set-Up and Vacuum Chamber Facilities . . . 256
4.7.1.2 Electronics, Fluidics and Working Procedures . . . 256
4.7.1.3 Thrusters' Geometrical and Material Configuration . . . 256
4.7.1.4 Radiofrequency (RF) Hardware . . . 261
4.7.2 Results and Discussion . . . 269
4.7.2.1 Noble Gases-fuelled HETs: Xenon and Krypton . . . 269
4.7.2.2 Oxygen-Fuelled HETs . . . 275
4.7.2.3 Numerical Model and Experiments . . . 277

5 *CONCLUSIONS* **278**

5.1 **Computational Characterisation** . . . 278

5.2 **Experimental Characterisation** . . . 280

6 *FUTURE WORK* **288**

6.1 **Computational Characterisation** . . . 288

6.2 **Experimental Characterisation** . . . 290

A APPENDIX **I**

A.1 Analysis of Strengths, Weaknesses, Opportunities and Threats (SWOT) . . . I

A.1.1 Strengths . . . II

A.1.2 Weaknesses . . . II

A.1.3 Opportunities . . . III

A.1.4 Threats . . . III

A.2 Verification Studies of *PlasmaSim* . . . IV

A.2.1 Benchmark of Axial-Radial Particle-In-Cell Codes . . . IV

A.2.1.1 Simulation Inputs . . . V

A.2.1.2 Verification Results . . . VI

A.2.2 Reactive Model Against an Analytical Solution . . . VII

A.2.2.1 Analytical Diatomic Model . . . VIII

A.2.2.2 Analytical Solutions for the Dissociative Reaction . . . IX

A.2.2.3 Analytical Solutions for the Ionising Reaction . . . IX

A.2.2.4 Analytical Solutions for the Dissociative-Ionising Reaction . . . XI

A.3 Validation Studies of *PlasmaSim* . . . XIV

A.3.1 Simulation Inputs . . . XV

A.3.2 Validation Results . . . XV

A.3.3 Error Accumulation . . . XVIII

LIST OF PUBLICATIONS AND OTHER CONTRIBUTIONS [1]

Journal Papers (1^{st} author):

[1] JM. Tejeda, M. Reza, F. Faraji and A. Knoll. Performance enhancement of hall effect thrusters using radiofrequency excitation. Acta Astronautica, 194:145–161, 2022.

[2] JM. Tejeda, A. Schwertheim and A. Knoll. Water as an environmentally friendly propellant for a multi-functional spacecraft architecture. International Journal of Energetic Materials and Chemical Propulsion, 22(2), 2023

[3] JM. Tejeda and A. Knoll. An oxygen-fuelled hall effect thruster: Channel length, ceramic walls and anode material experimental analyses. Acta Astronautica, 203:2, 2022.

[4] JM. Tejeda and A. Knoll. A water vapour fuelled hall effect thruster: Characterization and comparison with oxygen. Acta Astronautica, 211:702–715, 2023.

[5] JM. Tejeda et al. Experimental demonstration of a water electrolysis hall effect thruster operating with a hydrogen cathode. Acta Astronautica, 2019:542–554, 2023.

Conference Papers (1^{st} author):

[6] JM. Tejeda and A.Knoll. A water electrolysis hall effect thruster computational model with radiofrequency excitation. In 37th International Electric Propulsion Conference, IEPC-2022-313, Massachusetts Institute of Technology, Cambridge, MA (USA).

[7] JM. Tejeda, A. Knoll, F. Marchioni and M. Cappelli. Plasma properties characterization of oxygen-fuelled hall effect thrusters for water electrolysis propulsion. In 9th Space Propulsion Conference, number 0015, 05-2024, Glasgow, Scotland.

[1] Notice that the content of these publications is shared within this thesis with permission from the journal and conference organisers.

[8] JM. Tejeda et al. First end-to-end technological demonstration of a water electrolysis hall effect thruster operating with a water electrolyser. In 38th International Electric Propulsion Conference, IEPC 2024-175, Toulouse, France.

Conference Papers (co-author):

[9] E. Rosati et al. Sizing and preliminary design of a 2-kw water propelled hall effect thruster. In 37th International Electric Propulsion Conference, IEPC-2022-317, Massachusetts Institute of Technology, Cambridge, MA (USA).

[10] M. Abbi et al. Investigation on the wall interactions of a hall effect thruster using water vapor as a propellant. In 37th International Electric Propulsion Conference, IEPC-2022-346, Massachusetts Institute of Technology, Cambridge, MA, USA, 2022.

Awards and Other Contributions:

2020-2021. European Space Agency – Fly Your Thesis! programme selection (team leader and founder of DZH Dynamics, testing and Attitude Control and Determination System (ADCS) based on the Dzhanibekov effect in microgravity conditions (link).

2020-2021. Top 10 Business Ideas (DZH Dynamics), granted by ACTUA-UPM (Universidad Politécnica de Madrid, link).

2021. British Spanish Scholarship, granted by the British Spanish Society (link).

2021. 1^{st} Position in NanoStar European challenge (link).

2021. Finalist of PhD Student of the year, granted by 'FindAPhD.com' (link).

2022. Finalist of STEM for Britain, invited to the UK Parliament to show my research (link).

2024. Postgraduate Travel Award by the 'Old Centralians' Trust' (link).

2024. Best PhD Paper Award, granted by 'Association Aéronautique et Astronautique de France', at the Space Propulsion Conference for the paper Ref. [7] (link).

2024. 1^{st} position at the Imperial Zero Pollution Pioneer Awards for the development of green-technologies in the mobility sector (link).

LIST OF ACRONYMS, SYMBOLS AND SUBSCRIPTS

Acronyms

- 1D: One dimensional
- 2D: Two dimensional
- 3D: Three dimensional
- a.u.: Adimensional Units
- ABEP: Air-Breathing Electric Propulsion
- BN: Boron Nitride
- CP: Chemical Propulsion
- CVF: Cathode Vapour Feed
- DC: Direct Current
- DZH: Dzhanibekov
- ECR: Electron Cyclotron Resonance
- EP: Electric Propulsion
- FEEP: Field Emission Electric Propulsion
- GIE: Gridded Ion Engine
- HEMPT: High Efficiency Multistage Plasma Thruster
- HER: Hydrogen Evolution Reaction
- HET: Hall Effect Thruster
- HPC: High-Performance Computing
- IOD: In-Orbit-Demonstration
- IR: Infrared
- ISRU: In-Situ Resource Utilisation
- IV: Current-Voltage
- LAF: Liquid-Anode-Feed
- LANDMARK: Low Temperature Magnetized Plasma Benchmarks
- MMH: MonoMethylHydrazine
- MON: Mixed Oxides of Nitrogen
- MPD: MagnetoPlasmaDynamic
- NASA: National Aeronautics and Space Administration
- NEP: Nuclear Electric Propulsion

- NP: Nuclear Propulsion
- NPT: Nuclear Thermal Propulsion
- NWC: Near Wall Conductivity
- OER: Oxygen Evolution Reaction
- PEEK: Polyetheretherketone
- PEM: Proton Exchange Membrane
- PFA: Perfluoroalkoxy
- PGM: Platinum Group Metal
- PIC: Particle-In-Cell
- PKC: Primary Krypton Concentrate
- PMAD: Power Management and Distribution
- PPT: Pulsed Plasma Thruster
- QLP: Quadrupole Langmuir Probes
- REACH: Registration, Evaluation, Authorisation and Restriction of Chemicals
- RF: Radiofrequency
- RFC: Reversible Fuel Cell
- SDG: Sustainable Development Goals
- SEE: Secondary Electron Emission
- SPF: Small Plasma Facility
- SWOT: Strengths, Weaknesses, Opportunities and Threats
- TEM: Transverse Electric Magnetic
- TFE: Tetrafluoroethylene
- TM: Transverse Magnetic
- TRL: Technology Readiness Level
- UHF: Ultra-High Frequency
- VCA: Voice Coil Actuator
- VDF: Velocity Distribution Function
- VHF: Very-High Frequency
- WET-HET: Water ElecTrolysis Hall Effect Thruster
- WFB: Water Feed Barrier
- ZGV: Zero-Group-Velocity

Symbols

- α: Propellant utilisation efficiency
- δ: Discharge efficiency
- Δp: Pressure losses in a pipe
- Δt: Time step
- ΔV: Potential difference of the ExB plates
- ΔV_a: Potential of an ion on the ExB probe
- ΔV_c: Potential of an ion at the cathode's plane
- Δx: Spatial step
- ϵ: Force to displacement constant
- ϵ_0: Vacuum permittivity constant ($\epsilon_0 = 8.85 \times 10^{-12}$ F/m)
- η_P: Efficiency from RF power utilisation
- η_T: Total efficiency (computational)
- η_{tot}: Total efficiency (experimental)
- η_{tr}: Anode thrust efficiency
- γ: Factor
- λ_D: Debye length
- μ: Electron mobility
- μ_v: Dynamic viscosity
- ν: Collision frequency
- $\bar{\nu}$: Non-dimensional parameter
- ν_t: Turbulent collision frequency
- Φ: Oxygen-to-hydrogen ratio
- ϕ: Plasma potential
- ϕ_f: Floating potential
- ϕ_m: Channel mean diameter
- ϕ_p: Experimentally measured plasma potential at a certain location
- ϕ_x: Computationally calculated plasma potential at cell x
- π: Ionisation fraction
- ρ: Charge density
- σ_x: Cross section of the species x or process x
- A^i: Area (cross sectional) in $\vec{i}$ direction
- $\vec{B}$: Magnetic field (vector)
- B: Magnetic field (magnitude)
- C_1: Constant

- C_2: Constant
- c_1: Non-dimensional parameter
- c_2: Non-dimensional parameter
- c_n: Average velocity of the species x within a cell
- d_1: ExB probe: collimator diameter
- d_2: ExB probe: collimator exit diameter
- d_3: ExB probe: drift tube input diameter
- d_e: ExB probe: electric field plates distance
- d_m: ExB probe: magnets distance
- $\vec{E}$: Electric field
- d_4: ExB probe: drift tube exit diameter
- E_{ion}: Ion energy
- E_x: Energy of the process x
- F: Lorentz's force
- f_{AMU}: Antenna matching unit frequency range
- f_{Ny}: Nyquist frequency
- f_{PA1}: Power amplifier 1 frequency range
- f_{PA2}: Power amplifier 2 frequency range
- f_{RF}: Radiofrequency frequency
- f_{sg}: Signal generator frequency
- g_0: Earth's gravitational constant ($g_0 = 9.81\ m/s^2$)
- i: Imaginary number
- I: Current
- $I_{\dot{m}}$: Equivalent current for injected mass flow
- I_e: Electron current
- I_h: Heater current
- I_k: Keeper current
- I_m: Magnet current
- I_n: Bessel's function of second kind
- I_{si}: Ion saturation current
- I_d: Anode discharge current
- I_i: Ion current
- I_{sp}: Anode specific impulse
- J_i: Current density of species i
- J_n: Bessel's function of first kind
- K: Constant
- k: Wave's number
- k_t: Turbulent constant

- k_B: Boltzmann constant ($k_B = 1.38 \times 10^{-23}\ m^2kg/s^2K$)
- L: Channel length
- L_c: ExB probe: collimator tube length
- L_d: ExB probe: drift tube length
- L_f: ExB probe: ExB length
- L_p: Pipe length
- M: Mass of propellant
- $\dot{m}_a$: Anode mass flow rate
- $\dot{m}_c$: Cathode mass flow rate
- m_e: Electron mass constant ($m_e = 9.11 \times 10^{-31}$ kg)
- m_n: Neutral mass
- N: Number of super-particles
- n: Integer number
- n_x^0: Initial number density of the species x
- $N_{cells,i}$: Number of cells in the direction i
- n_x: Number density of the species x
- P_t: Turbulent collision probability
- P_d: Discharge power
- P_{fil}: Plasma filament cathode power
- P_h: Heater power
- P_{hydro}: *Hydrocat* power
- P_k: Keeper power
- P_m: Magnet power
- P_{PA1}: Power amplifier 1 output power
- P_{PA2}: Power amplifier 2 output power
- P_{RF}: Radiofrequency power
- P_{sg}: Signal generator output power
- P_c: Cathode power
- q: Elementary charge constant ($q = 1.602 \times 10^{-19}$ C)
- Q: Volumetric mass flow rate
- r: Radius of collision
- R: Resistance
- R^2: Coefficient of determination
- R_{in}: Resistance of inner electromagnetic coils
- R_{out}: Resistance of outer electromagnetic coils
- $\dot{R}_x$: Loss rate of process x
- S: Size of superparticle

- S_F: Safety factor
- T: Thrust
- $TTPR$: Thrust-To-Power-Ratio
- T_x: Temperature of the species x
- u_n: Speed of neutral drift
- v^*: Velocity of an ion on the ExB probe
- V^-: Negative voltage
- V^+: Positive voltage
- $V_{a,RF}$: Anode radiofrequency discharge voltage
- V_{acc}: Acceleration voltages
- V_{axis}: Voltage at the ExB axis
- $V_{c,RF}$: Cathode radiofrequency discharge voltage
- V_d: Discharge voltage
- V_h: Heater voltage
- $v_{i,x}$: Velocity of the species i (axial, x)
- v_{ion}: Corrected ion velocity
- V_{ol}: Volume of the computational domain
- V_{RF}: Radiofrequency voltage
- V_g: Ground voltage
- V_k: Keeper voltage
- V_m: Magnets voltage
- v_w: Wein velocity
- w: Wave's angular frequency
- W: Channel width
- w_{ce}: ECR angular frequency
- w_{pe}: Plasma frequency
- w_{RF}: Radiofrequency angular frequency
- X_C: Cathode's location
- Z: Charge number

Chapter 1

BACKGROUND

This chapter aims to provide a brief overview of space propulsion and the different technologies existing within this field. For that purpose, the predominant types of propulsion systems (chemical, electrical, and nuclear) are delineated. A particular focus is placed on Electric Propulsion (EP), specifically Hall Effect Thrusters (HETs), as being the subject of investigation in this thesis. An exploration of their operational principles, physics, principal propellants, and existing computational models is undertaken.

1.1 Space Propulsion

Space propulsion is referred to as the utilisation of momentum transfer and Newton's third law of motion to propel spacecraft through outer space [11, 12]. By expelling mass at high velocities, momentum is transferred in the opposite direction, facilitating the movement of spacecraft for space missions and exploration.

The journey of space propulsion began with the earliest attempts to achieve spaceflight, which dates back to the late 19th century [11]. The initial concept of space propulsion was rooted in the idea of using rocket engines to overcome the Earth's gravitational pull and reach space. The development of rocket technology, particularly the design and construction of liquid-fuelled rockets, was a monumental step forward in the history of space propulsion [11]. The first liquid-fuelled

rocket, the Goddard liquid-propellant rocket, was designed by Robert H. Goddard in the 1920s, marking a significant milestone in the field [13].

Following the success of liquid-fuelled rockets, the space race in the mid-20th century saw the development of more powerful rockets capable of carrying payloads to orbit [14]. The era of space exploration was characterised by the launch of numerous spacecraft, including satellites and manned missions, which relied heavily on chemical propulsion (CP) systems [15]. The Apollo missions to the Moon and the first manned spaceflights were pivotal moments in space propulsion history, showcasing the capabilities of chemical rockets to transport humans and payloads into space [16].

As space exploration advanced, the need for more efficient and versatile propulsion systems became apparent. In this context, the introduction of EP began to emerge as a promising alternative to CP [12]. This concept dates back to 1906 when Robert Goddard considered the possibility in his personal notebook, and it was later published by Konstantin Tsiolkovsky in 1911 [17].

The concept of nuclear propulsion (NP) began to gain serious consideration in the mid-20th century, especially in the context of space exploration [18]. The Cold War era saw the United States and the Soviet Union exploring the potential of NP for aircraft and missiles, aiming to maintain nuclear bombers in the air for extended periods as a deterrence measure [19]. NP remains a promising area of research and development, with ongoing efforts to overcome the technical challenges associated with radiation shielding and the safe management of nuclear materials [20].

The distinction between CP, EP, and NP systems became more pronounced as advancements in technology allowed for the exploration of different propulsion mechanisms. The following subsections further explore these topics.

1.1.1 Chemical Propulsion (CP)

CP systems are fundamentally based on the use of chemical reactions to release energy, which is then converted into kinetic energy to propel a spacecraft [21]. They are designed to satisfy high-

thrust impulsive maneuvers, offering lower specific impulse compared to their EP counterparts [12] but significantly higher thrust-to-power ratios [1].

They can be mainly divided into solid and liquid CP systems, although cold gas systems are also considered CP devices which do not fall into the previous two categories.

1.1.1.1 Solid Propellant Systems

Solid propellants are composed of a fuel and an oxidiser combined into a single solid mixture. Stored in solid form, they are ignited directly upon firing [22]. Known for their simplicity and reliability, solid propellants do not require a separate oxidiser to be stored and transported. However, they offer lower specific impulse compared to liquid propellants, resulting in a higher propellant mass needed to achieve a given manoeuver.

1.1.1.2 Liquid Propellant Systems

Liquid propellants consist of two separate liquids: a fuel and an oxidiser. These liquids are stored in separate tanks and mixed together in the chamber at the time of firing [23]. Offering a higher specific impulse than solid propellants [21], liquid propellants are suitable for applications requiring high efficiency, such as upper stages of rockets that operate in space. Although more complex, liquid propellants are easier to throttle and restart compared to solid propellants. Within liquid propellants, two categories can be identified. The first one is mono-propellant systems. Here, a single liquid propellant decomposes at the catalyst bed of the combustion chamber. An example of a mono-propellant fuel is hydrazine (N_2H_4) [24]. The second one is bi-propellant systems. Here, two separate liquids (a fuel and an oxidiser) are mixed together in the combustion chamber at the time of firing. Examples of bi-propellants include Mixed Oxides of Nitrogen (MON) and MonoMethylHydrazine (MMH) [25].

[1] Power is defined in CP as the the energy released during chemical reactions, whereas in EP it is the electrical power supplied to the system.

1.1.1.3 Cold Gas Systems

Cold gas systems utilise the expansion of pressurised gas to generate thrust, without involving any combustion. Unlike solid or liquid rockets where a combustion process is necessary, cold gas systems operate solely on pressurised gas. In these systems, the propellant can be stored in solid, liquid, or gaseous form, but it must exit the nozzle in gaseous form for the system to function [26].

1.1.2 Electric Propulsion (EP)

EP can be defined as the use of energy from a source not stored in the chemical bonds of the propellants with the purpose of providing or augmenting the exhaust velocity of the propulsion device [27]. EP exhibits notable fuel efficiency, albeit with significantly lower thrust levels attainable compared to CP [28]. Depending on the process used to accelerate the propellant, EP thrusters are categorised into: electrothermal, electrostatic and electromagnetic propulsion systems.

1.1.2.1 Electrothermal Propulsion Systems

Electrothermal propulsion entails the utilisation of electrical energy to impart heat to a propellant. This can be accomplished by directly heating the propellant or by heating a catalyst bed to facilitate propellant decomposition. Resistojets and arcjets are examples of electrothermal propulsion systems [12, 29].

Resistojets involve heating the propellant by passing it through a resistively heated chamber or over a resistively heated element before entering a downstream nozzle. The augmentation in exhaust velocity arises from thermal heating of the propellant, which constrains the specific impulse to modest levels (500 s). Notice that this method of propulsion is classified under EP because it relies on electrical energy to generate force, rather than chemical reactions [30].

Conversely, in Arcjet thrusters, an electrical discharge is induced within the flow between a cathode and an anode. This imparts additional energy to the propellant flow, consequently allowing for higher specific impulse compared to resistojets [31].

1.1.2.2 Electrostatic Propulsion Systems

Electrostatic thrusters are propulsion systems that generate thrust by accelerating charged particles through electric fields. Electrostatic propulsion systems encompass two principal concepts: Gridded Ion Engines (GIEs), also known as Ion Thrusters, and Field Emission Electric Propulsion (FEEP) thrusters, also referred to as electrospray thrusters [32].

GIEs comprise a series of closely spaced grids, typically fabricated from conductive materials such as tungsten or molybdenum. These grids serve as electrodes which are charged to high voltages. Various methods are used to ionise the gas, generally xenon, including the use of internal hollow cathodes within the discharge chamber which provide the primary electrons for that purpose. The ions are accelerated by the electric field between the grids, with the potential difference between the grids dictating the velocity of the ions. From the initial grid, the ions are accelerated by the acceleration grids. Subsequently, the ions exit the thruster through an exhaust aperture, generating thrust in the opposite direction [33]. By regulating the voltage applied to the grids, grid ion engines can finely adjust thrust level and direction with precision. Ion thrusters exhibit the highest efficiency (from 60% to $>$ 80%) and very high specific impulse (from 2000 s to over 10,000 s) compared to other thruster types [12].

FEEP thrusters produce thrust by emitting tiny droplets of a conductive liquid, typically a metal like indium or cesium, using an electric field [34]. These droplets are emitted from a sharp needle-like emitter, driven by an extremely high power (around 10 kV) applied between the emitter and an extractor electrode. FEEP thrusters are renowned for their precise thrust control, high efficiency, and minimal levels of electromagnetic interference, rendering them suitable for missions necessitating fine attitude control, precise orbit adjustments, and station-keeping maintenance [12].

1.1.2.3 Electromagnetic Propulsion Systems

Electromagnetic thrusters are propulsion systems that generate thrust by utilising electromagnetic forces. Unlike electrostatic thrusters, which primarily depend on electric fields, electromagnetic thrusters utilise both electric and magnetic fields to accelerate charged particles, typically ions, thereby producing thrust [35].

Various types of electromagnetic propulsion systems exist, with several concepts still undergoing investigation.

The most famous ones are Hall Effect Thrusters (HETs), also known as Hall Thrusters. They function by establishing a magnetic field to confine electrons and an electric field, to accelerate the ions (therefore, creating thrust) [36]. Notice though that some people classify HETs as electrostatic devices because the strength of the magnetic field is too weak to have any major influence in the ions (just the electrons), as it will be explained in Section 1.2.2. HETs constitute the focal point of this thesis and a comprehensive evaluation of this engine type is described in the following sections.

Pulsed Plasma Thrusters (PPTs) represent another variant of electromagnetic thruster. They employ pulsed discharges to ionise a fraction of a solid propellant ablated into a plasma arc, utilising electromagnetic effects in the pulse to accelerate ions to high exit velocities. The pulse repetition rate governs the thrust level [12, 37].

MagnetoPlasmaDynamic (MPD) Thrusters also belong to the electromagnetic category. In this instance, a very high current arc ionises a significant portion of the propellant, which is accelerated by the electromagnetic forces in the plasma discharge. As both the current and the magnetic field are typically generated by the plasma discharge, MPD thrusters tend to operate at exceedingly high powers (1-10 MWs) to generate adequate force for high specific impulse operation, thereby yielding high thrust compared to the aforementioned technologies [38].

1.1.3 Nuclear Propulsion (NP)

Unlike conventional CP systems that rely on the combustion of propellants or EP devices that uses the energy not stored in the chemical bonds to propel a spacecraft, NP harnesses the energy released by nuclear reactions to generate thrust, offering unparalleled efficiency and potential for deep space exploration missions.

NP encompasses various concepts, including Nuclear Thermal Propulsion (NTP) [39] and Nuclear Electric Propulsion (NEP) [40].

1.1.3.1 Nuclear Thermal Propulsion (NTP)

NTP harnesses the energy generated by nuclear reactions to heat a propellant, typically hydrogen, to extreme temperatures (2000-3000 $^{\circ}C$). This superheated propellant is then expelled through a rocket nozzle, generating thrust. One of the primary challenges in NTP development is the design of a robust reactor capable of withstanding the harsh conditions of space while ensuring safety and reliability. Additionally, efficient heat transfer mechanisms and advanced materials are required to prevent overheating and maintain optimal performance [39, 41].

1.1.3.2 Nuclear Electric Propulsion (NEP)

The fundamental prerequisite of a NEP system lies in the conversion of thermal energy generated by the nuclear reactor into directed kinetic energy of the propellant. The successful execution of this objective in the context of space necessitates the implementation of systems capable of managing both the harnessed energy and its residual waste. The core components integral to NEP include the reactor, power conversion system, heat rejection system, and the Power Management and Distribution (PMAD) system [40].

Notice that, despite its immense potential, both NTP and NEP for spacecraft pose technical, regulatory, and safety challenges. Designing compact, lightweight nuclear reactors capable of withstanding the harsh conditions of space while ensuring safe operation remains a significant engineering hurdle. Moreover, concerns regarding the environmental impact and potential risks

associated with launching nuclear-powered spacecraft into orbit necessitate stringent safety protocols and international regulations. Nevertheless, ongoing research and development efforts, coupled with advancements in materials science, reactor technology, and space exploration objectives, continue to drive progress in the field of NP for spacecraft.

Finally, it should be noted that the categorisation of space systems into CP, EP, and NP represents merely one approach for classifying these systems. For instance, NTP and CP can be integrated into thermal propulsion systems, alongside solar thermal propulsion [40]. The classification outlined herein serves solely to acquaint the reader with the intricate and expansive realm of space propulsion. For a more thorough comprehension, numerous references within the literature offer comprehensive coverage of this subject [11, 12, 15, 39, 40].

1.2 Hall Effect Thrusters (HETs)

The principal focus of this thesis investigation is rooted in the exploration of HETs propelled by water. The subsequent sections aim to elucidate the operational principles of HETs in general, delve into their most relevant physics phenomena, and outline the computational tools available for the simulation of these complex devices.

1.2.1 Technology

1.2.1.1 Thruster Overview

A schematic illustration of a HET with its main components is presented in Figure 1.1.

HETs generally consist of an annular channel formed by insulating walls, typically ceramics, terminating in a conductive plate known as the anode [12]. The magnetic field is induced by either electromagnets or permanent magnets depending on the specifications of the space mission [42] (more information in Section 4.1.4).

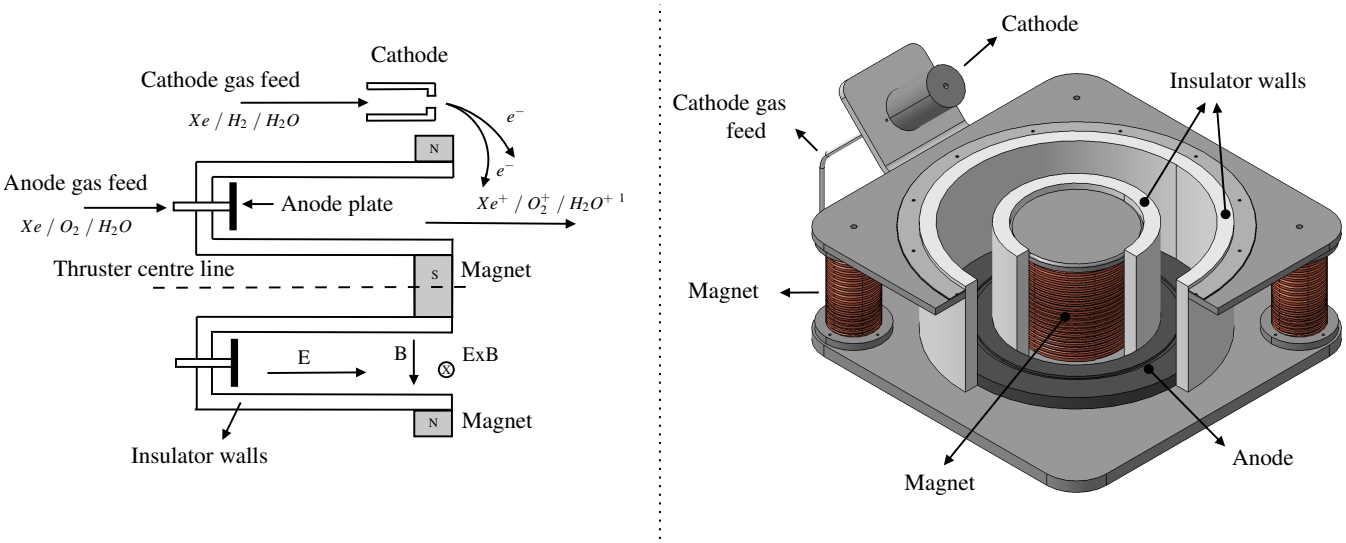


Figure 1.1: Schematic illustration of the cross section of a Hall Effect Thruster showing its most relevant components. Diagram based on the thruster *SPT-100* [12]. Notice that other ion species can be created due to different dissociation, ion dissociation, and attachment processes of diatomic propellants, such as oxygen or water vapour.

The magnetic field configuration typically follows a Gaussian distribution, reaching its peak adjacent to the end of the channel and exhibiting radial orientation across the channel. The specific parameters of the thruster's geometry, including channel diameter, width, and length, along with the magnetic field characteristics, govern the overall performance, efficiency, and operational lifespan of the thruster.

Propellant injection occurs at the anode plate, with various methods discussed in the literature. A prevalent approach involves the utilisation of small apertures in the anode plate, typically measuring 1 mm or less in diameter, which are connected to a feedline. In this way, when the propellant is supplied, it traverses the small apertures, eventually entering the thruster chamber.

The cathode (see Section 1.2.1.2), located externally to the thruster or centrally mounted within it, emits electrons that are attracted towards the anode plate due to the voltage differential between the anode and the cathode, known as the discharge voltage (see Section 4.1.4). Under these conditions, electron-neutral particle collisions may occur, leading to ionisation events of the form:

$$A + e^- \rightarrow A^+ + 2e^- \tag{1.1}$$

The resultant ion experiences acceleration in the direction opposite to that of the electrons due to the discharge voltage between the anode and cathode. This acceleration of ions outside the thruster generates an impulsive force, propelling the thruster in the opposite direction, thereby creating thrust.

It is noteworthy that the ionisation reaction represents merely one of several reactions plausible within a HET. Particularly for propellants such as O_2 or H_2O, other phenomena such as dissociation, ion dissociation, or attachment processes may occur. These phenomena constitute the reactive model, which is specific to each propellant and will be comprehensively discussed in Section 3.2.1.2.

Due to the radial orientation of the magnetic field within the thruster, electrons do not travel directly towards the anode. Instead, they undergo gyromotion along the magnetic field lines, thereby prolonging their residence time and enhancing the likelihood of encountering neutral particles prior to reaching the anode. Although described in simplistic terms, the electron motion is considerably complex. Further elucidation on particle dynamics within a HET is provided in Section 1.2.2.1.

1.2.1.2 Cathode Overview

The cathode, alternatively termed the electron gun, electron emitter, or neutraliser, constitutes a vital component within a HET. During the startup phase, it is needed to provide electrons to the discharge chamber, thus catalysing the ionisation reactions within the thruster. Throughout steady-state operation, the cathode serves to neutralise the discharge beam, thereby facilitating a continuous output of plasma from the system.

Various types of cathodes have been conceived, developed, and evaluated within the domain of HETs. Among these, hollow cathodes stand out as the most prevalent, owing to their capability to yield high electron current densities at relatively modest powers, sustaining operation for extended durations [43]. A schematic illustration of a hollow cathode with its main components is presented in Figure 1.2.

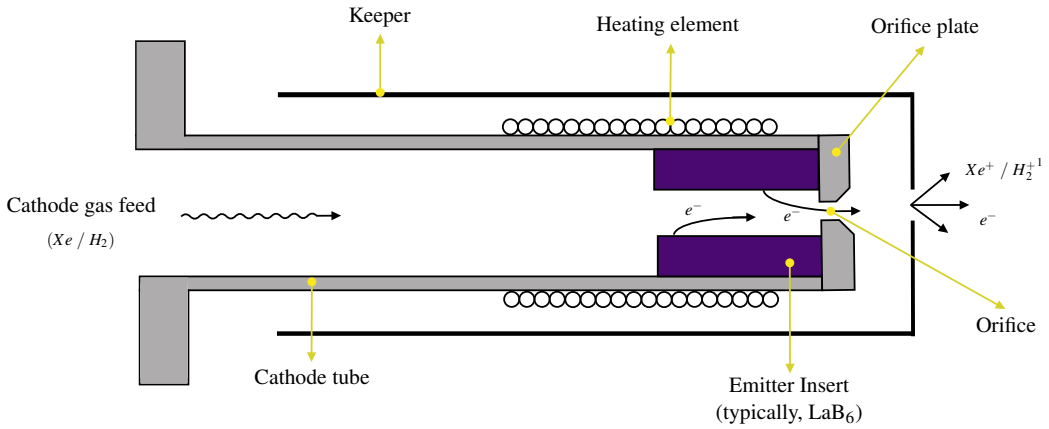


Figure 1.2: Schematic illustration of a hollow cathode. Diagram based on the references [12, 43]. [1]Notice that other ion species can be created due to the different dissociation, ion dissociation and attachment processes of diatomic propellants, such as hydrogen.

These cathodes comprise a hollow tube made of a refractory metal and sealed at one end by a plate featuring an orifice. A hollow cylindrical insert, crafted from a low work function material (typically Lanthanum hexaboride, LaB_6 or Barium oxide, BaO, impregnated with tungsten [44]), is positioned within the tube, making contact with the end plate. As the work function of a material refers to the energy required to liberate an electron from its surface, a low work function facilitates electron emission. Together with BaO, LaB_6 possesses one of the lowest known work functions among materials suitable for cathode inserts, making it highly efficient at emitting electrons when subjected to the appropriate conditions of temperature and electric fields.

Furthermore, LaB_6 exhibits good thermal stability and resistance to degradation under the high-temperature conditions prevalent in cathode operation. Its robustness allows for prolonged usage without significant deterioration in performance, making it an ideal choice for the demanding operational requirements of cathodes in EP systems.

Encircling the exterior of the tube is a resistive heating element, designed to elevate the temperature of the emitter insert (typically, LaB_6 or BaO), thereby augmenting thermionic emission. Subsequently, a gas, typically xenon, is introduced into the tube, traversing over the insert and constricted by the orifice. An electrode, termed a keeper, is situated just beyond the orifice, set to a high positive potential. With adequate heating, mass flow rate, and keeper potential, electrons are extracted from the emitter surface and drawn towards the keeper. These

electrons interact with the gas provided through the feedline, creating a plasma inside of the device which exists throughout the top aperture of the cathode (see Figure 1.2).

Different types of cathodes are documented within the literature. For instance, plasma bridge neutralisers, also referred to as filament cathodes, are utilised for laboratory experimentation. In this context, electrons are not emitted by a LaB_6 insert but by a thin tungsten filament, (approximately 0.5 mm in diameter), heated using very high currents, (around 20 A). The drawbacks of plasma bridge neutralisers are their power requirements (which are higher than those of hollow cathodes) and their limited lifespan (the tungsten filament does not last longer than a few hours of testing at these current levels). Consequently, plasma bridge neutralisers are unsuitable for space applications but offer an affordable alternative for laboratory testing.

In this thesis, both hollow cathodes and plasma bridge neutralisers were employed to test a HET. The details of these two cathodes are discussed in Section 4.1.2.2.

It is noteworthy that cathodes are not solely employed within the context of HETs. Other thrusters, such as GIE and Magnetoplasmadynamic Thrusters (MPDTs), also require a neutraliser for the aforementioned purposes. Moreover, other cathode concepts have been developed, with a special mention to radiofrequency (RF) or microwave cathodes. These cathodes, mostly used in the context of GIEs although also employed in the context of HETs, consist of a waveguide structure containing a static magnetic field and an antenna. Neutralising electrons are generated through two methods [45]. First, the antenna introduces waves into this structure at a frequency that matches the Electron Cyclotron Resonance (ECR), effectively heating the electrons. The heated electrons then break down the feed gas within the waveguide, generating a plasma that serves as an electron source. Second, these types of cathodes operate on the principle of Direct Current (DC) discharge. The potential difference propels electrostatic acceleration of electrons from the cathode plasma to the ion beam. This acceleration is sufficient to drive electron impact ionisation of neutrals, producing electrons for the ion beam neutralisation [45]. In both scenarios, these electrons exit the cathode through a downstream aperture. While RF or microwave cathodes produce low currents for a set power (approximately 100 mA and up to around 10 W), hollow cathodes can produce

high currents for the same set power (up to approximately 100 A and often up to around 5 kW) [12, 45]. However, microwave cathodes do not utilise any insert, such as LaB_6, and are therefore not subjected to oxidation. This characteristic is particularly crucial for water propulsion, as any oxygen present within a hollow cathode can limit its lifespan. Further information regarding the compatibility of cathodes is provided in the next Section 1.2.1.3. [2]

1.2.1.3 Alternative Propellants

This section aims to provide a comprehensive overview of the current advancements in alternative propellants for HETs. The analysis is structured to evaluate the compatibility of propellants with both the thruster and the cathode. This dual focus is crucial for the development of in-space hardware that is suitable for space missions, specifically HETs.

Thruster

Certain authors categorise alternative propellants into three distinct groups: gaseous propellants, condensable propellants, and molecular propellants [44]. Gaseous propellants encompass monoatomic noble gases, such as xenon (Xe) and krypton (Kr). Condensable propellants include those that are either solid or liquid at or near room temperature, such as iodine (I), magnesium (Mg), zinc (Zn), and bismuth (Bi). The third group comprises molecular propellants such as water (including water vapour, H_2O and the products of water electrolysis, namely oxygen O_2 for the thruster and hydrogen H_2 for the cathode, see Section 2.1), and others such as air, which is important in the context of Air-Breathing Electric Propulsion (ABEP). ABEP pertains to the utilisation of atmospheric gases present in the low Earth's atmosphere as propellant for spacecraft. This technology represents a significant departure from traditional propulsion methods that depend on on-board fuel, offering the potential for more advanced and cost-effective space missions. Although ABEP falls outside the scope of this thesis, it is a promising field in the context of EP, and interested readers are encouraged to delve deeper into the available literature research [46, 47, 48].

[2] Note that not all RF cathodes operate at the ECR frequencies, some of them work at much lower frequency (tens of MHz) or in the GHz range but without magnetic field.

Table 1.1: Compilation of 1) physical properties (data taken from [49]), 2) ideal performance metrics of Hall Effect Thrusters at $P_d = 3$ kW of discharge power ($V_d = 300$ V and $I_d = 10$ A) using different propellants (following the guidelines of [12, 44]) and 3) other implications which can be considered when evaluating different propellants.

	State-Of-The-Art	**Water Propulsion**		**Other Alternative Propellants**				
	Xe	**O_2**	**H_2O**	**Kr**	**I**	**Mg**	**Zn**	**Bi**
Mass [u]	131	32	18	84	127	24	65	209
First Ionisation Energy [eV]	12.1	13.6	13.5	14.0	10.5	7.6	9.4	7.3
Melting Point [°C]	-112	-219	0	-157	114	650	420	271
Boiling Point [°C]	-108	-183	100	-152	182	1090	910	1559
Density [g/cm^3]	5.9	1.4	1.0	3.7	4.9	1.7	7.1	9.8
Ideal Thrust [mN]	286	141	106	228	281	123	202	360
Ideal Isp [s]	2141	4336	5781	2679	2177	4975	3033	1697
Propellant Cost Per Kg [$]	≈ 9322	<1	<1	≈ 934	≈ 32	≈ 9	≈ 3	≈ 8
Toxicity	None	None	None	None	Medium	Medium	Low	Low
ISRU Potential	No	Yes	Yes	No	No	Yes	Yes	No
Multi-Mode Propulsion	No	Yes	Yes	No	No	No	No	No
Subsystems Synergies	No	Yes	Yes	No	No	No	No	No

Table 1.1 summarises the main physical properties (mass, first ionisation energy, state transition points at atmospheric conditions -1 atm-, density), the ideal performance in terms of thrust and specific impulse (I_{sp}) and other traits which can be considered when selecting the propellant (more information in Chapter 2).

The principal physical properties are obtained from the literature [49]. The propellant mass is of high importance, given its direct correlation with thrust production potential, albeit at the expense of reduced specific impulse (I_{sp}). The first ionisation energy delineates the minimum energy required for an ionisation event to occur. The lower first ionisation energy, the lower energy threshold for plasma generation. The melting and boiling points hold particular significance concerning propellant injection methodology. Conventionally, the propellant supplied into the thruster necessitates being either in liquid or gaseous state to induce indirect or direct plasma formation, respectively. For propellants inherently not conforming to these states, a bespoke feed mechanism is required to either liquefy or vaporise the propellant, ensuring it continuously remains above its melting point to avert deposition. For instance, in the case of bismuth, the feed system elevates its temperature to 280 °C (exceeding its melting point of 271 °C), subsequently delivering it to a porous heated anode for subsequent evaporation. Alternative approaches, such as utilising a

heated anode composed of the propellant material itself, facilitating direct sublimation within the discharge chamber during thruster operation, are a possibility [44]. In the context of water vapour propulsion investigated within this thesis, a dedicated feed system was devised and evaluated to transition water from liquid to gaseous state (more information in Section 4.63). Nonetheless, the requisite feed system, while indispensable for certain propellants, typically entails drawbacks by augmenting system mass, cost and complexity. Finally, the mass density is important for determining not only the thrust and specific impulse the system can provide but also the size of the propellant tanks: the higher this value, the more propellant can be stored in a fixed volume.

The ideal thrust and I_{sp} presented are very simplistic figures of merit calculated based on the following formulas taken from Ref. [44]:

$$T = \sqrt{\frac{2M}{q}} I_d \sqrt{V_d} \tag{1.2}$$

$$I_{sp} = \frac{1}{g_0} \sqrt{\frac{2qV_d}{M}} \tag{1.3}$$

where g_0 is the Earth's gravitational constant ($g_0 = 9.81\ m/s^2$), q is the elementary charge ($q = 1.602 \times 10^{-19}$ C), M is the mass of the propellant expressed in kg and I_d and V_d are the anode discharge current and voltage, respectively. In this study, $V_d = 300$ V and $I_d = 10$ A were used to characterise the performance of each propellant.

It should be noted, as previously highlighted, that evaluating a thruster's performance solely based on propellant mass and operating parameters is not reflective of reality. Indeed, plasma generation and the various reaction processes significantly influence the efficiency and losses present of HETs. Chapter 3 delves into a computational model which can actually aim to replicate the physics of these devices. Nonetheless, this initial approach can serve as a valuable tool for swiftly comparing the feasibility of different propellants and their potential integration into the system.

The findings presented in Table 1.1 indicate that water propulsion (whether through water electrolysis or water vapour), compared with the state-of-the-art of HETs which use xenon as

a propellant, yields a high specific impulse at the expense of low thrust. Additionally, water propulsion offers cost-effectiveness, non-toxicity, potential for In-Situ Resource Utilisation (ISRU), multimode propulsion capabilities, and synergies with other subsystems. Given the centrality of water propulsion in this thesis, an in-depth analysis of this technology is presented in Chapter 2.

Other alternative propellants, while promising, lack the cost-effectiveness and additional advantages that water could offer when used onboard spacecraft. However, of particular significance is the utilisation of krypton as a short-term substitute for xenon-fuelled HETs. Krypton, being ten times less expensive than xenon, offers comparable, albeit slightly inferior, performance. *SpaceX* has employed krypton for their HETs within the *Starlink* constellation [50], together with other research groups [51, 52, 53]. Furthermore, a significant advancement emerged in 2023 with *SpaceX*'s development of a $P_d = 4.2$ kW argon-fuelled HET. They reported a thrust of $T = 170$ mN, specific impulse of $I_{sp} = 2500$ s, and an anode efficiency of $\eta_{tr} = 50\%$ [54]. Note nevertheless that the conditions under which this performance was achieved, as well as whether the thruster was fuelled solely by argon or a combination of argon and xenon, remain undisclosed.

In 2020, the first in-orbit demonstration of an iodine-fuelled HET was successfully executed by the company *ThrustMe* [55]. Iodine, due to its substantial mass, can achieve performance levels akin to those of xenon. Moreover, it possesses the advantage of being stored as a solid, with a density of 4.9 g/cm^3 [43]. However, its boiling point of 182 $°C$ necessitates the integration of a feed system to supply the propellant in gaseous form, ensuring no deposition on the thruster surfaces.

Bismuth [56, 57], magnesium [58] and zinc [59, 60] share a similar drawback: high melting and boiling points necessitating a feed system for propulsion system fuelling, as previously described. Nonetheless, current research endeavours are focused on optimising the feed system and overall performance of these propellants to enhance their competitiveness.

Other alternative propellants, including adamantane [61], buckminsterfullerene (C60) [62], caesium [63] and mercury [63] are still under exploration. The development of HETs and the selection of alternative propellants represent a rapidly advancing research area aiming to identify affordable, high-performing, and environmentally friendly fuels to improve the cost, operational

lifespan and performance of these devices.

Cathode

In general, the range of propellants suitable for the cathode is more constrained than for the thruster. Hollow cathodes represent the preferred choice in HETs, incorporating a low work function insert, such as LaB_6 or BaO, to generate electrons (see Section 1.2.1.2). The involvement of chemistry in the formation of the low work function surface renders cathodes susceptible to poisoning, which can substantially augment the work function and thereby limit its operational lifespan [12]. In this context, oxygen and water, along with carbon dioxide and air at elevated partial pressures, are recognised as the most potent poisoners of hollow cathodes [12]. Noble gases are ideal candidates for hollow cathode propellants as they do not interact with the insert. Hydrogen however, a byproduct of water electrolysis, is also known not to interact with the insert and is thought to even mitigate poisoning. [64, 65]. Notice however that its actual practical application in the context of HETs at the start of the thesis was yet to be confirmed.

RF or microwave cathodes offer the advantage of not necessitating an insert for electron generation, thereby enabling the use of nearly any propellant. This attribute is particularly significant in the context of water vapour propulsion (refer to Section 2.2.2.1). Nonetheless, these cathodes are confined to operate within the μA to mA range [45, 66] [3]. For achieving several amps of current, hollow cathodes are the preferred option.

1.2.2 Physics

This section seeks to introduce some of the most fundamental physical phenomena within HETs. It is important to note that these devices are extraordinarily complex, and their underlying physics are yet not entirely comprehended. For a more detailed exploration of the physics involved and their operational principles, readers are directed to the existing literature [12, 67, 68].

[3] Notice that this is because of the high power to current production, and not a fundamental limitation of the technology

1.2.2.1 Particles Motion

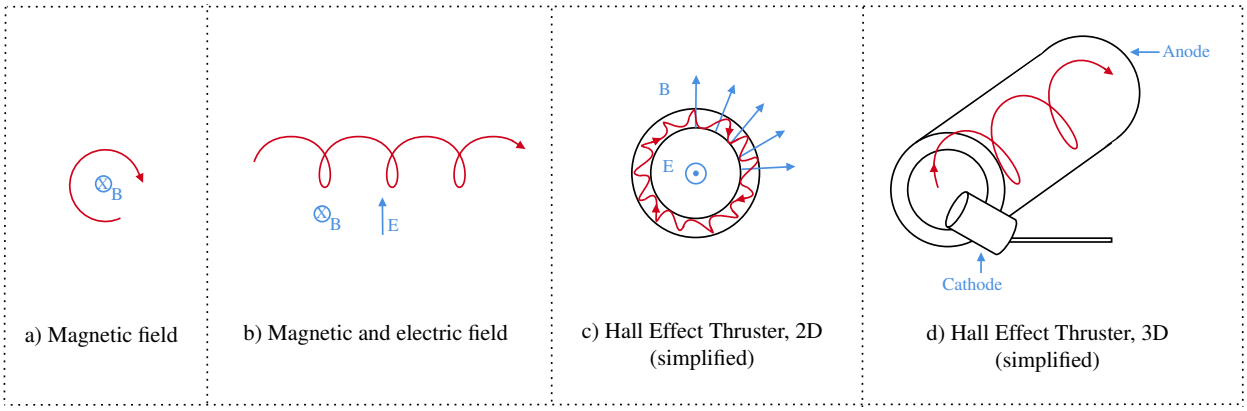


Figure 1.3: A very simplified schematic illustration of electron motion in a magnetic and an electric field acting in the context of a Hall Effect Thruster.

The accelerated plasma within a HET exhibits distinct movements due to its interactions with nearby particles and the existing electric and magnetic fields. Depending on the type of species (neutral, electron, or ions), these movements are different. Possibly, the electrons are the particles which exhibit a more intricate movement in the channel, as being affected by both, the superimposed electric and magnetic fields. Figure 1.3 illustrates a very simplified schematic of the electron movement in a magnetic and electric field, in particular within the channel of a HET.

Electrons

To start with, the superimposed electric field existing in HETs attracts the electrons to the anode. The magnetic field, typically on the order of 10^{-2} T, is strong enough to influence the electrons' motion but too weak to have any major effect on the ions. The electrons, just because of the magnetic field, experience a gyromotion around the magnetic field lines (see Figure 1.3a). However, the combination of a radial gyromotion and a push force coming from the superimposed electric field makes the electrons drift instead of going in a perfect circular motion (Figure 1.3b). This drift motion occurs around the annular circumference of the channel. However, it is important to note that the gyroradius (also referred to as the Larmor radius [67]) of the electrons is very small (less than a millimetre [67]). Therefore, it can be simplified that the electrons go around the channel

in 2-dimensional (2D) circular drift motion (Figure 1.3c). Notice that the electrons do not go into a perfect circular motion, but they irregularly bounce between the inner and outer channel along the magnetic field lines [69].

The superimposed electric field not only makes the electrons drift around the channel but also attracts the electrons to the anode, so the final simplified picture of the 3-dimensional (3D) electrons' motion in a HET could be represented by Figure 1.3d. It is noteworthy that this simplified schematic does not consider any collisions or electron-ion interactions that could influence their trajectory, nor does it account for the irregular bouncing of electrons between the inner and outer walls as depicted in Figure 1.3c [4].

Ions

The ions, in an opposite manner to the electrons, are mainly attracted to the cathode plane due to the discharge voltage difference between the anode and cathode. However, the ions are not significantly affected by such a weak magnetic field and are primarily accelerated in a straight line, thereby creating thrust. Notice that, in practice, this acceleration is not perfectly straight, leading to the so-called "plume divergence losses".

A special case occurs near the anode region, where the acceleration of the electrons also drags the ions with them. Consequently, the ions adjacent to the anode region are accelerated in the opposite direction, towards the anode, similar to the electrons. This phenomenon will be further explored in Chapter 3.

Neutrals

The neutrals are injected at the anode plane and traverse and exit the channel, undergoing collision, ionisation and other events; not being affected by the magnetic and/or electric field.

It is important to note that, in reality, the movement of these particles (electrons, ions and neutrals) is exceedingly complex, necessitating a high-fidelity computational model to accurately

[4] Notice that plasma oscillations account for the observed axial motion of the electrons, as they would not be able to move in the axial direction without electron-neutral scattering collisions or through wall interactions.

track their trajectories. Chapter 3 delves into the computational model developed in this thesis to simulate the movement of particles within a HET.

1.2.2.2 Plasma Waves and Radiofrequency (RF) Excitation

The previously described particle movements can induce specific types of waves, contingent upon the plasma conditions. In this thesis, the exploration of how a particular type of electron wave (X-Waves) could influence the performance of a single-stage HET is undertaken, both computationally and experimentally. As a general overview, this section delves into the examination of the different electron plasma waves that could be investigated. For that matter, Figure 1.4 summarises the principal electron waves that might exist, contingent upon the wave's nature and the configuration of external electric and magnetic fields. For more specific information about HET excitation with other types of waves, readers are referred to the available literature [70, 71, 72, 73, 74, 75, 76, 77, 78].

Types of electron plasma waves

Before starting, it is important to note that for the description presented here (electron plasma waves), it is assumed that the ions are too massive to move at the frequencies involved, forming a fixed and uniform background of positive charge [67]. For a description of ion waves, the readers are directed to the literature overview of these waves [67, 68].

A plasma wave is classified as "parallel" or "perpendicular" based on the direction of the wave (represented by the wave vector, $\vec{k}$) relative to the superimposed (and undisturbed) magnetic field ($\vec{B}$). The terms "longitudinal" and "transverse" refer to the direction of $\vec{k}$ relative to the oscillating electric field of the wave ($\vec{E}$). If the oscillating magnetic field associated with the wave is considered zero, the wave is electrostatic; otherwise it is electromagnetic [67].

Within electrostatic waves, one can distinguish between A) Langmuir waves (also known as plasma oscillations) or B) upper hybrid excitation. In Langmuir waves, there is either no superimposed magnetic field, or that magnetic field is parallel to the direction of the wave. In the upper hybrid excitation, the superimposed magnetic field is perpendicular to the wave's direction.

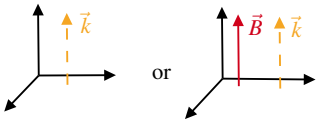
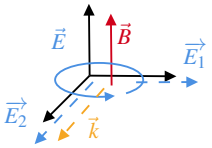
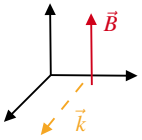
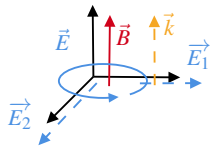
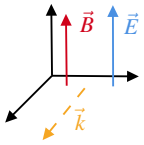
Name	Directionality	Name	Directionality
Langmuir Wave (Plasma Oscillation) [Electrostatic]		Extraordinary Wave (X-Wave) [Electromagnetic]	
Upper Hybrid Excitation [Electrostatic]		Right-Hand Polarised Wave (R-Wave) [Electromagnetic]	
Ordinary Wave (O-Wave) [Electromagnetic]		Left-Hand Polarised Wave (L-Wave) [Electromagnetic]	

Figure 1.4: Simplified illustration of the different types of electron waves as predicted using cold plasma theory.

Within electromagnetic waves (i.e., radio waves travelling through a plasma), those where the oscillating electric field of the wave and the superimposed magnetic field are parallel to each other and perpendicular to the direction of the wave are called Ordinary Waves (O-Waves). Since these waves have no component of either the electric or the magnetic field along the propagation direction of the wave, they are also referred to as Transverse Electric Magnetic (TEM mode) [68].

Conversely, if the direction of the wave is in the same plane as the oscillating electric field and perpendicular to the superimposed magnetic field, they are referred to as Extraordinary Waves (X-Waves, Transverse Magnetic -TM- mode). These waves are typically elliptically polarised instead of plane polarised, as the O-Waves. That is, as the wave propagates into a plasma, it develops (E_x) and (E_y) components along $\vec{k}$, thus becoming partly longitudinal and partly transverse. It can also be demonstrated that for finite values of E_x and E_y, the magnetic component of the wave field becomes insignificant, while the electric component aligns predominantly with the direction of propagation. For this reason, these waves are considered "quasistatic", and an electrostatic formulation is suitable for their modelling [68].

Finally, Right-Hand (R-Wave) and Left-Hand elliptically polarised waves (L-Wave) can be studied if the direction of the wave is perpendicular to the superimposed magnetic field.

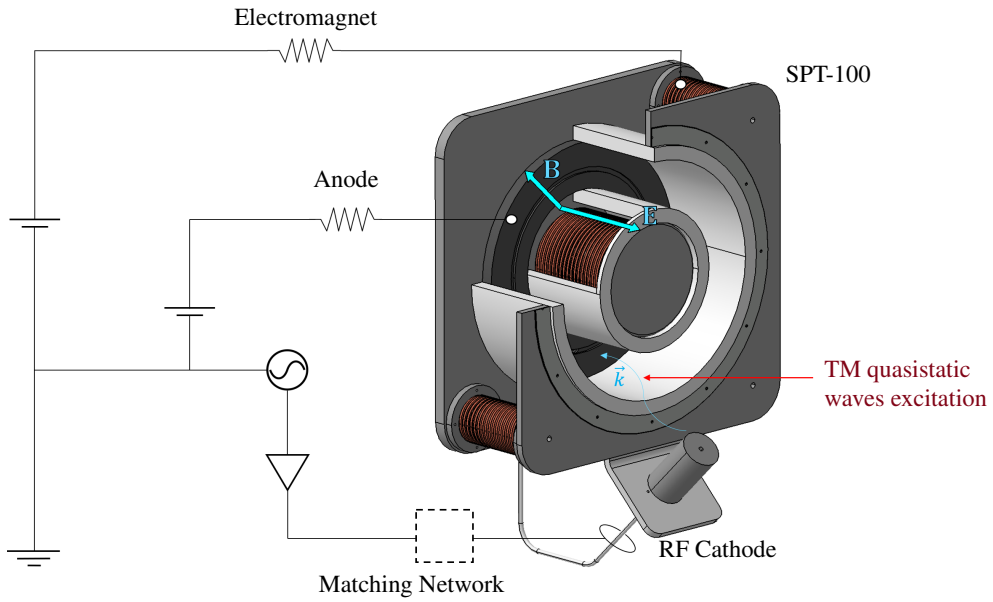


Figure 1.5: Graphical representation of the X-Waves (TM quasistatic waves) excitation in a Hall Effect Thruster, specifically the *SPT-100*. A high level schematic of the electronics involved is also described. Diagram published in [1].

Given the disposition of electric and magnetic fields of HETs (see Figure 4.13) and the longitudinal direction of the wave when being excited from anode-cathode (or cathode-anode), X-Waves could be excited within HETs (see Figure 1.5). This type of excitation will be studied within this thesis, aiming to better understand the physics of the wave from a computational perspective (Section 3.2.2.3) and also from an experimental point of view (Section 4.7).

Absorption and Accessibility of X-Waves using Hot Plasma's Theory

The absorption and accessibility of plasma waves can be examined through cold plasma theory or hot (or warm) plasma theory. Cold plasma theory operates under the assumption of a zero plasma temperature, whereas hot plasma theory does not; offering a more complex yet high-fidelity description of the real scenario where plasma waves propagate [67, 68].

Generally, the absorption of plasma waves predominantly occurs at the resonance condition, where the frequency of the RF wave aligns with a fundamental frequency of the plasma motion and the wave number (k): $k \to \infty$. The dispersion relation of the TM quasistatic waves near a resonance condition is investigated here (Equation 1.4) to establish fundamental knowledge about their absorption and resonance before analysing the results obtained (see Section 3.2.2.3).

$$\bar{\nu}\frac{w_{ce}^2(\vec{x})}{w_{pe}^2(\vec{x})} = e^{-\bar{\nu}} \sum_{n=-\infty}^{+\infty} \frac{n\ I_n(\bar{\nu})}{(w/w_{ce}(\vec{x}) - n)} \tag{1.4}$$

$$\bar{\nu} = \frac{k_B T_e(\vec{x})}{m_e} \frac{k^2}{w_{ce}^2(\vec{x})} \tag{1.5}$$

This equation is derived using hot plasma theory as in Refs. [79, 68], showing how the wave's speed depends on its wavelength or frequency. In Equation 1.4, $\bar{\nu}$ is an non-dimensional parameter defined as shown in Equation 1.5, n is an integer number and w is the frequency of the wave excited. I_n is the Bessel's function of second kind, which is related to the Bessel's function of first kind (J_n) with imaginary argument by $I_n(x) = (-i)^n J_n(ix)$ [80]. k_B is the Boltzmann's constant ($k_B = 1.380 \times 10^{-23}\ m^2 kg/s^2 K$) and T_e is the electron temperature at a specific location ($\vec{x}$).

w_{ce} and w_{pe} are, respectively, the ECR frequency and plasma frequency expressed as:

$$w_{ce}(\vec{x}) = qB(\vec{x})/m_e \tag{1.6}$$

$$\omega_{\mathrm{pe}}(\vec{x}) = \sqrt{\frac{n_{\mathrm{e}}(\vec{x})q^2}{m_e \varepsilon_0}} \tag{1.7}$$

where m_e refers to the electron mass ($m_e = 9.11 \times 10^{-31}$ kg), ϵ_0 is the permittivity of vacuum ($\epsilon_0 = 8.85 \times 10^{-12}$ F/m), n_e stands for electron density (m^{-3}) at location $\vec{x}$ and B is the magnitude of the superimposed magnetic field at location $\vec{x}$.

Ira Borah Bernstein [79] conducted extensive investigations into these waves, leading to these solutions often being referred to as 'Bernstein modes'. He demonstrated that Equation 1.4 has only real solutions of w [79]. In practical terms, this implies the absence of temporal damping or instabilities in these waves, which is highly beneficial for plasma energy absorption.

Equation 1.4, apart from predicting w_h: $w_h^2 = w_{ce}^2 + w_{pe}^2$ (the upper hybrid resonance frequency which also appears in the cold plasma approximation), establishes the existence of other resonance frequencies depending on the parameter $\bar{\nu}$. Table 1.2 summarises the different conditions and

Table 1.2: Resonance points of quasistatic waves (TM mode) depending on $\bar{\nu}$ parameter.

Condition	**Approximation**	**Resonance**
$\bar{\nu} < 1$	Low Temperature Limit	$w = n\ w_{ce} \rightarrow \quad n \geq 2$
$\bar{\nu} \approx 1$	No approximation possible	Numerical calculation from Equation 1.4
$\bar{\nu} > 1$	High Temperature Limit	$w = n\ w_{ce} \rightarrow \quad n \geq 1$

approximation limits (low, high, or none) to be used depending on the value of $\bar{\nu}$ obtained.

Section 3.2.2.3 provides an overview of these equations within the context of a HET, aiming to determine which approximation is applicable in this scenario and to better understand the implications of the dispersion relationship of these waves and their propagation.

1.2.3 Simulation Tools

As previously discussed, although HETs may appear straightforward in their design, they involve intricate physical processes. Accurately simulating HETs is crucial as it aids in determining the most effective geometric configuration and operating parameters prior to fabrication. Given the inherent experimental testing complexity, coupled with its associated cost and time required, computational simulations have gained significant importance over the past two decades [81]. If properly implemented, these tools can provide preliminary insights into the HET performance under diverse conditions before being developed and tested. This section offers an introductory overview of the state-of-the-art computational methodologies employed for this purpose. An extensive description of the functionalities and trade-offs between them can be found in the literature [81, 82, 83].

1.2.3.1 Fully-Kinetic Models

In fully-kinetic models [84, 85], Boltzmann-Vlasov equation is numerically integrated and discretised in a domain of 6 dimensions [81]. However, these models are only viable for low-dimensional analyses due to the high dimensionality of phase space (6 dimensions for a 3D problem) and the challenges associated with modelling certain terms within the Boltzmann-Vlasov equation [81].

1.2.3.2 Full Particle-In-Cell Models

Full Particle-In-Cell (PIC) models [86, 87, 88] also integrate Boltzmann-Vlasov equation but they adopt an alternative Lagrangian-Eulerian approach compared to fully kinetic models: they follow the particle trajectory and the distribution function is sampled from a known initial state and propagated using Lorentz's force. Moreover, in PIC simulations, particle populations are represented as macro-particles and are self-consistently advanced along with the electric and magnetic fields, which are known at designated mesh nodes. Presently, these models offer high fidelity at the expense of extensive computational time. Therefore, there is a concerted effort within the scientific community to develop new simulation methodologies aimed at accelerating these codes [89, 90, 91, 92]. In this study, a PIC model is devised to simulate water-fuelled HETs using state-of-the-art techniques described in the literature to accelerate these simulations.

1.2.3.3 Multi-Fluid Models

In multi-fluid models [93, 94], the plasma is treated as a fluid rather than individually resolving the physics of each particle (or macro-particle). This approach offers the advantage of significantly reducing the computational time required for the simulation to converge. However, these simulations are limited by the fact that the detailed structure of the velocity distribution function is not captured (an assumption of a Maxwellian distribution is typical). Therefore, wave-particle interactions cannot be captured by these models self consistently. Consequently, while multi-fluid codes facilitate rapid convergence, they generally offer lower fidelity compared to PIC codes.

1.2.3.4 Hybrid Models

A hybrid model [95, 96, 97] employs a PIC approach for a specific group of species (typically the heavy particles, neutrals, and ions) while utilising a fluid representation for others (generally, the electrons). These models provide a compromise between computational time and fidelity compared to PIC codes and multi-fluid models. However, when prioritising simulation fidelity, PIC codes are nowadays the preferred option.

Having reviewed the state-of-the-art in EP and the various techniques, tools, software, and hardware currently employed, the following chapter explores why water propulsion stands out as a promising option for medium to long-term space missions. Beyond its immediate advantages in cost-effectiveness and environmental sustainability, water propulsion offers the potential for enhanced spacecraft multifunctionality and, critically, supports the concept of In-Situ Resource Utilization (ISRU). This potential makes it not only a viable alternative but a transformative one, enabling spacecraft to leverage resources found on lunar or planetary bodies to refuel, thereby reducing dependency on Earth-based supply chains. These combined benefits underscore the motivation behind this thesis's focused investigation into water propulsion as a pathway to achieving more sustainable, flexible, and autonomous space exploration.

Chapter 2

MOTIVATION AND OBJECTIVES

This chapter deliberates on the motivation and objectives of the thesis by A) analysing the advantages and potentialities of water propulsion technologies and B) addressing the technological challenges that this work endeavors to tackle. Additionally, in Appendix A.1, the strengths, weaknesses, opportunities and threats of this technology are discussed.

Part of the work presented here is based on the work presented in Lisbon, Portugal at the Space Propulsion Conference in 2022 [2].

2.1 Two Distinct Ideas: Water Electrolysis and Water Vapour

First of all, it is important to distinguish between the two concepts envisaged for the utilisation of water onboard a spacecraft: 1) water electrolysis and 2) a direct water vapour feed. The distinction between these two concepts is fundamental, as this thesis evaluates, characterises, and compares both concepts throughout. A brief overview of these two is provided here, which is further extended along the thesis using the research conducted on both ideas.

2.1.1 Water Electrolysis

In the context of water electrolysis for HET propulsion, it is proposed that an electrolyser onboard the spacecraft could separate water into oxygen (the propellant used for the thruster -anode-)

and hydrogen (for the cathode). The exploration of thruster operation with oxygen was the initial research point of the Imperial Plasma Propulsion Laboratory. Throughout this thesis, when oxygen is employed as a propellant for the thruster (anode), but a noble gas or any other gas (excluding hydrogen) is utilised for the cathode, the configuration is referred to as an "oxygen-fuelled HET". The term "water electrolysis-fuelled HET" is reserved for instances where oxygen and hydrogen are used simultaneously for the thruster and cathode, respectively.

This investigation aims to continue the initial exploration of this concept by A. Schwertheim and A. Knoll [43] by fulfilling the objectives outlined in Section 2.4.

2.1.2 Water Vapour

In water vapour-fuelled HETs, water in its gaseous phase would be directly fed into the thruster. Consequently, water vapour technologies do not require an electrolyser onboard the spacecraft, which signifies a reduction in mass, volume, and complexity. Water vapour has been investigated for other types of EP systems, such as Helicon Thrusters [98], Electrodeless ECR thrusters [99, 100], and GIEs [101, 102]; however, fewer comprehensive studies had been conducted in the context of HETs at the start of this thesis.

This research aims to initiate the exploration of water vapour at the Imperial Plasma Propulsion Laboratory as an alternative to water electrolysis (Section 4.6), and also evaluate and compare these two strategies to identify which one could be more advantageous to implement (Section 4.6.2.3). The objectives related to this idea are also detailed in Section 2.4.

2.2 Benefits and Prospects of Water Propulsion Technologies

This section delves into the advantages and potential of water propulsion technologies. First of all, the environmental benefits of transitioning from conventional propellants to water propulsion are examined. Subsequently, the synergies of water within a spacecraft and the various multi-modes available when employing water are reviewed. This analysis encompasses both branches of water propulsion technologies: water electrolysis and water vapour. The relevance of these technologies

to the United Nations Sustainable Development Goals (SDGs) is also discussed.

Beyond sustainability and hybrid architectures, water emerges as a highly promising candidate for In-Situ-Resource-Utilisation (ISRU). This is attributable to the widespread presence of water not only on Earth but throughout the Solar System. The potential of water as a material to be harvested on other planets is also explored.

From a financial standpoint, water is advantageous due to its abundance compared to the state-of-the-art propellants utilised in these technologies and other alternative solutions currently being investigated. A cost analysis of water against the most traditional propellants currently in use is presented.

Lastly, the performance and efficiencies of these systems are assessed and discussed.

2.2.1 Space Propulsion Environmental Studies

Water is environmentally friendly, and its use does not compromise the Earth, favouring the sustainability of the space sector. This is particularly important in light of the environmental implications arising from the production and use of state-of-the-art propellants in CP and EP.

On the one hand, for CP systems, hydrazine and its derivatives are predominantly employed as propellants. Despite their utility, hydrazine presents significant risks, including being corrosive, explosive, carcinogenic, and highly toxic to both humans and the environment [103]. The severity of these risks led the European Chemicals Agency to classify hydrazine as a 'very high concern' candidate in 2011, prompting propulsion engineers to explore less toxic alternatives [104].

On the other hand, the majority of EP devices utilise the noble gas xenon as the propellant [12]. Xenon is easily ionised and its low chemical reactivity allows it to be safely stored and handled. Although not toxic, xenon's environmental friendliness is compromised by its scarcity on Earth, with concentrations of less than 0.01 parts per million in the Earth's atmosphere, approximately 1 part per million in seawater, and about 2 parts per million in the Earth's crust [105]. This scarcity necessitates an energy-intensive and challenging extraction and purification process. Studies have estimated that the extraction of xenon from a Primary Krypton Concentrate (PKC) can require

up to 4353 kilowatt-hour (kWh) per kg of xenon produced [106]. This process contributes to the emission of over 1000 kg of CO_2, based on greenhouse gas reports [107]. In space, satellites consume hundreds of kilograms of xenon during missions, such as the spacecraft BepiColombo, which had approximately 581 kg of xenon on board [2]. Assuming the average CO_2 production per kWh of power generated in Europe in 2016 [108], the production of this quantity of xenon would equate to approximately 750 tons of CO_2. This figure exceeds the carbon footprint of an average UK citizen for their entire lifetime. Other missions, like the Asteroid Redirect Robotic Mission, are expected to use 5300 kg of xenon [109]. Not only during the space mission but also during the extensive testing phase, which can exceed 1000 hours [109], hundreds of kilograms of xenon are consumed. This massive energy requirement results in a substantial emission of greenhouse gases.

Conversely, the energy cost associated with using water as a propellant is negligible compared to other alternatives. For space applications, water undergoes filtration processes (negligible energy cost), deionisation or demineralisation (ranging between 0.1 to 0.5 kWh per litre [110, 111]), distillation or reverse osmosis (with an energy cost of 2-5 kWh per litre [112, 113]), and sterilisation (between 0.01-0.1 kWh [114, 115]).

Assuming an average of these energy costs, the total to produce 1 litre of water could be 2.1 kWh (210 kWh for 100 litres).

Figure 2.1 illustrates the energy cost of 1 kg of xenon versus 100 kg of water and several other products, such as aluminium [116], titanium [117], beef [118], milk [119] or even bitcoin [120].

It is important to note, however, that the energy cost and associated carbon emissions of a propellant form only a part of the total manufacturing lifecycle of a satellite. To maintain a sustainable and environmentally responsible production process, compromises must also be made in other areas, including the design and production of the satellite itself, launch, deployment, in-orbit operations, and disposal.

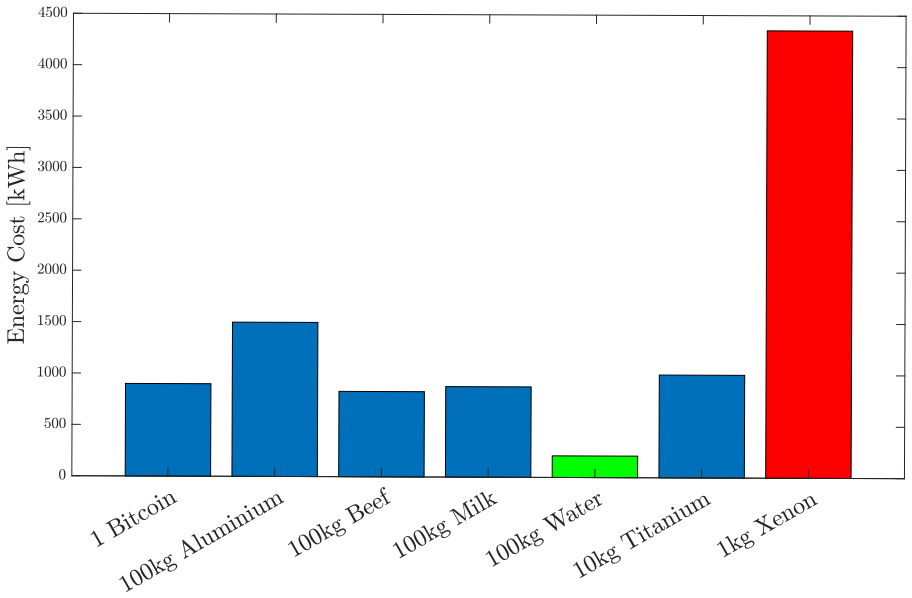


Figure 2.1: Energy cost of water and xenon in comparison with other standard products.

2.2.2 Multi-Mode Water Propulsion System

The different spacecraft architectures that could be implemented thanks to the unique multifunctional traits of water are discussed here, both for water electrolysis and for water vapour.

2.2.2.1 Water Electrolysis Multi-Mode

The water electrolysis multi-mode architecture is graphically described in Figure 2.2.

In the most simple scenario, water electrolysis propulsion necessitates a water propellant tank, an energy source derived from the spacecraft bus, and heaters utilised by an electrolyser to separate water into diatomic oxygen and hydrogen: $H_2O + Energy \rightarrow 1/2\ O_2 + H_2$. These two propellants are subsequently employed to fuel the thruster (anode) and the cathode of the propulsion system. Nevertheless, this represents merely the commencement of the potential applications of this propellant.

A Reversible Fuel Cell (RFC), which comprises a fuel cell and water electrolyser, can be employed instead of just a water electrolyser. This approach allows for the production of diatomic oxygen and diatomic hydrogen when energy is supplied to the system (charge mode), as well as the reserve process (discharge mode): $1/2\ O_2 + H_2 \rightarrow H_2O + Energy$.

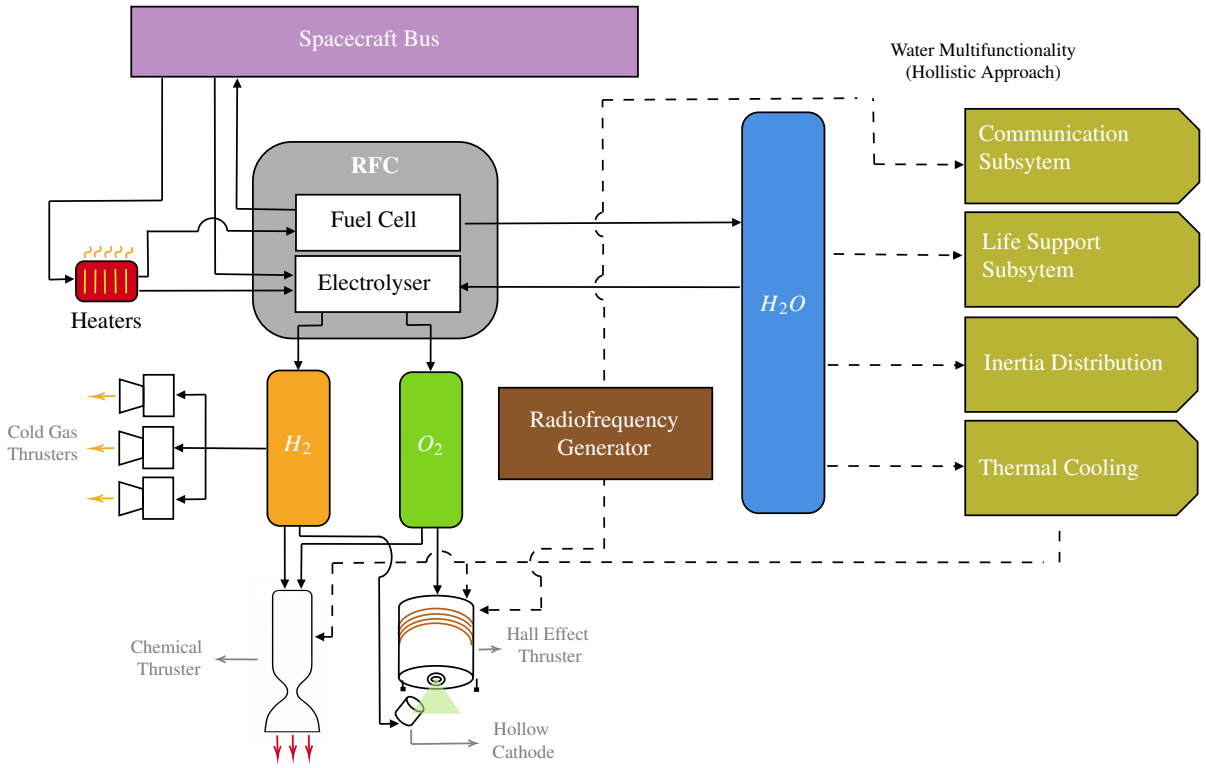


Figure 2.2: Water electrolysis propulsion multi-mode. The dashed arrows refer to additional elements which can be used in combination of the others or not, depending on the needs of the customer.

By dividing water into diatomic oxygen and hydrogen, a CP thruster can also be utilised in conjunction with the EP system. Research into a CP system employing these propellants was undertaken by C. Muir and A. Knoll [121, 122]. This arrangement allows the operator to execute high thrust chemical manoeuvres or high specific impulse electrical manoeuvres, leading to a considerable reduction in overall mass by sharing a single propellant storage and management system. Moreover, should there be an excess of hydrogen, which signifies that the thrusters are operating below the stoichiometric ratio of hydrogen-oxygen (Φ) = 1:8, cold gas thrusters using diatomic hydrogen as a propellant can be employed. This thesis will also delve into the implications of operating in ratios that deviate from the stoichiometric ratio (Section 4.4.2.1).

Consequently, this system offers exceptional flexibility for trajectory planning, enabling the spacecraft operator to remain highly adaptable to mission changes. Even mid-mission, the capability to seamlessly redistribute propellant to either the CP, EP or cold gas system allows for drastic

trajectory changes, crucial for manned missions where an emergency might necessitate a mission alteration.

For instance, an exploration mission to Jupiter's moon Io would greatly benefit from a multi-mode chemical/electrical propulsion architecture:

1. The spacecraft is released from the launcher and detumbles using a hydrogen cold gas system.
2. A kilo-newton class CP water-fuelled thruster is fired at perigee, placing the spacecraft on a hyperbolic trajectory escaping Earth.
3. An EP water-fuelled thruster is utilised to adjust the course on a deep-space cruise.
4. An orbit insertion burn is performed by the CP water-fuelled thruster to be captured by Jupiter.
5. The EP water-fuelled thruster provides drag compensation to perform very low orbit trace-gas sampling of Io's atmosphere.
6. Depending on the results obtained, electric orbit raising can be employed to study other Jovian moons, or chemical plane changes can be employed to sample atmospheres in the polar region.

Missions to Mars and the Moon may similarly benefit from this type of multi-mode architecture, where the added ISRU potential becomes an additional benefit. In fact, water extracted from the lunar or Martian regolith could also be used as fuel for the return journey to Earth.

Another concept explored in this study is the utilisation of a RF generator to enhance the performance of a HETs. The frequency band of the communication subsystem depends on the mission type conducted. For certain applications, the Ultra-High Frequency (UHF) band (300 MHz to 3 GHz) and Very-High Frequency (VHF) band (30 MHz to 300 MHz) are utilised. This suggests that an RF generator could be employed to improve the performance of a HET and for the communication systems of a satellite (Sections 3.2.2.3 and 4.7).

Furthermore, the water tank onboard the spacecraft can serve additional functions beyond serving as propellant for the thrusters. In the medium term, as manned space missions become more prevalent, water can be employed for the life support system of astronauts. Additionally, when not in use, water can be utilised for thermal cooling: the thrusters could benefit from a water recirculation system to reduce their temperature during operation.

The utilisation of water (or any moving mass) to redistribute the inertia of a satellite has been one of the main complementary lines of work during this PhD. In summary, by controlling the inertia of a satellite, spacecraft can access novel phenomena that traditional spacecraft do not have access to. These spacecraft, named as "Transformable Spacecraft," possess the ability to alter their inertia distribution and/or shape. One of the phenomena triggered by this transformable spacecraft is the Dzhanibekov effect (DZH effect, in short). The DZH effect is a 180° flip exhibited by rigid bodies when spinning around their intermediate axis of inertia. This research demonstrated, for the first time, that the DZH effect can be manipulated (activated or deactivated) by employing a system (moving masses or liquids) that alters the axis of rotation of the satellite (intermediate axis when the DZH effect is active and the major/minor axis when the effect is not active). The controlability of this effect, combined with the use of current technology such as reaction wheels, can create an Attitude Determination and Control System (ADCS) which is faster and more energy-efficient than the state of the art (using solely reaction wheels).

This research was tested through a microgravity flight campaign in Bordeaux (France) in collaboration with the European Space Agency and Novespace during the 37th Parabolic Flight Campaign. The team responsible for this investigation included this thesis' author (also, research director of the group, from *Imperial College London*), Guillermo Reales Gutiérrez (from the *European Organization for Nuclear Research*), Iván Castro Fernández, Miguel Segovia Mora, Carmen García Cabetas, and Alberto Rodríguez Amor (from *Universidad Carlos III de Madrid*).

The technology investigated was registered through an international patent (reference: P202330613, titled: "A system, method and computer program product for enhanced attitude control of a vehicle in torque-free conditions") and presented at the UK parliament in the event *STEM for Britain*.



Figure 2.3: Microgravity testing of a tranformable spacecraft during the 37^{th} Parabolic Flight Campaign. The multifunctionality of water or moving masses was successfully tested by controlling for the first time the Dzhanibekov effect in microgravity conditions.

As this line of research is complementary, readers are directed to works published as part of this investigation for more information about it [123, 124, 125, 126, 127, 128].

Figure 2.3 illustrates the research conducted under microgravity conditions aboard the Airbus A310 Zero-G aircraft, operated by *Novespace* [129].

2.2.2.2 Water Vapour Multi-Mode

The water vapour multi-mode architecture is shown in Figure 2.2. Part of synergies explored with water electrolysis still apply in this multi functional system, such as the RF generator for the communication subsystem, the life support subsystem for the astronauts, thermal cooling and inertia distribution.

However, one of the most distinct differences is that the water electrolyser is not needed onboard. Instead, a water feed system is in place. This system is in charge of the phase transition from liquid to vapour water and controlling and monitoring the pressure and temperature.

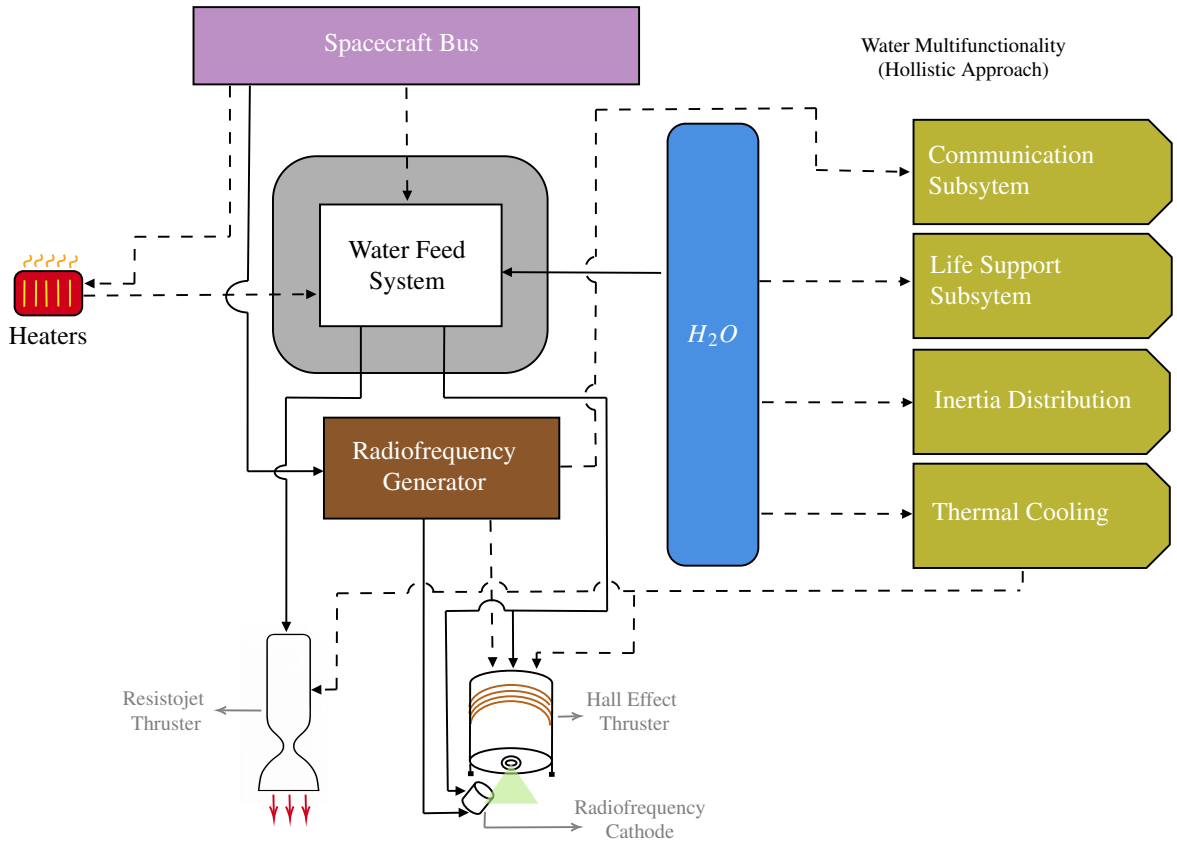


Figure 2.4: Water vapour propulsion multi-mode. The dashed arrows refer to additional elements which can be used in combination of the others or not, depending on the needs of the customer.

A heater can be used to help with the phase transition, although some systems may use of other techniques, such as capillary tubes to maintain the water in gaseous phase at all times [102, 130].

For the HET, direct water vapour is used as a propellant for the thruster (anode). For the cathode, two different options can be envisaged. One of them is the use of a noble gas or any other source of propellant which would need to be onboard of the spacecraft. This is because thermionic emitter cathodes (such as LaB_6 cathodes) would be poisoned if directly exposed to water vapour or oxygen [12, 131]. The second option would be the use of a RF cathode also running with water vapour [132]. Notice however that these cathodes operate in the μA to mA range due to the large power requirements needed to operate at higher currents [66]. For achieving several amps of current at an optimised power level, LaB_6 cathodes are the selected option [66]. A trade-off between these options would need to be asserted to come up with the right cathode selection.

Table 2.1: United Nations Sustainability Development Goals (SDGs) addressed in this PhD thesis.

SDG Number	**Topic**	**Current technology situation**	**Water muti-functionality contribution**
7	Affordable and Clean Energy	Xenon prices have skyrocketed in recent years, reaching several thousands of euros per kg [133]. This price is also volatile as it strongly depends on its use of other applications such as medicine [134].	Water is cheap, which reduces the total cost of the mission, opening new horizons for small stakeholders willing to contribute to the space science and economy. A water spacecraft architecture reduces the cost of the mission, easing global space accessibility.
9	Industry Innovation and Infrastructure	Polluting EP and CP propellants are still used nowadays, without a clear substitution which can better respect the environment [135].	Water propulsion is an emerging technology, and the multi-functionality approach of water in space is a novel concept with advantages at subsystem and system level.
12	Responsible Consumption and Production	The production of xenon for space propulsion is not sustainable, as the demand of EP systems has exponentially increased during the last decades. Xenon content in the air is 87 parts per billion, with a very slow regeneration rate [134].	Water production does not compromise the environment, being reusable in Earth for testing purposes. It is abundant in the Solar System, which can be useful for ISRU, helping to develop a responsible propellant alternative.
13	Climate Action	The environmental carbon footprint of xenon jeopardises the environment (see Figure 2.1). Hydrazine is toxic, and its released during ground tests is contributing to green-house effects [104].	Water does not have an environmental carbon footprint associated with it, and its use in development, storage and testing does not affect the environment.

For a systems' perspective, the most attractive idea is to use water vapour for both, the thruster (anode) and the cathode, as included in Figure 2.4. The use of a RF cathode running with water vapour has been successfully tested in a GIE by the company *Pale Blue* [102, 130].

Pale Blue also offered the possibility of combining their ion thruster with a resistojet, both water vapour fuelled [102, 130]. In this research, it is envisaged that a similar combination could be constructed by using a HET in combination with a resistojet, according to Figure 2.4.

2.2.3 Links to the United Nations Sustainable Development Goals (SDGs)

The adoption of water as a propellant for a multi-mode chemical-electrical propulsion system improves performance while reducing the impact on the environment. As a result, the development of this technology directly aligns with several of the United Nations SDGs, as seen in Table 2.1.

In fact, the explosive growth of the space sector is analogous to the widespread adoption of the automobile market back in the early 20th century, where the protection of the Earth was not taken as a primary concern [136]. The result of a non-sustainable market implementation can be seen today, where a flawed system struggles to reinvent itself for the good of the environment. By investing in water-propelled systems and sustainable spacecraft development, an environmentally friendly propulsion market can be created, benefiting future generations.

2.2.4 In-Situ Resource Utilisation (ISRU)

Generally speaking, ISRU refers to the practice of collecting, processing, storing, and using materials found or manufactured on other astronomical objects, such as the Moon, Mars, and asteroids. This is done in order to replace materials that would otherwise need to be transported from Earth [137]. This approach aims to enhance the capabilities of human exploration by reducing the mass and cost of space missions, making it more affordable and sustainable to establish extraterrestrial exploration and operations [138].

Water is a critical resource for ISRU, being essential for life support, propellants, and construction materials. The Moon, Mars, and asteroids are potential sources of water and other volatile resources; although the exact location, form, concentration, and distribution of these resources remain areas of ongoing research [139].

Specifically for water harvesting, the Moon has abundant raw materials that could support a variety of applications. The lunar highland material anorthite, for example, can be used as aluminum ore, and lunar regolith can be processed into glass and ceramic products. Over twenty methods have been proposed for oxygen extraction from lunar regolith, which could also be used

for life support [139].

The exploration of Mars and asteroids for water and other resources is also underway. These planets also possess significant reserves of water ice and other volatiles. The advancement of water as a propellant for spacecraft, in conjunction with ISRU research, would facilitate the extension of space missions into deeper regions of the universe.

2.2.5 Cost Savings

The economic advantages of employing water as a propellant represent a compelling incentive to mitigate the expenses associated with the current state-of-the-art propellants. In the context of EP, xenon stands out as a very expensive gas, mainly due to its intricate production methodologies, as previously discussed in Section 2.2.1 [133, 140].

To illustrate the cost implications of xenon, numerous quotations and purchase orders were conducted throughout this PhD thesis for xenon bottles. Manufacturers reported that a small bottle containing 50 litres of xenon is approximately equivalent to £2000 (approximately €2350). That means, every litre is approximately £47 (approximately €55). Notice that approximately 169.5 litres of xenon is equal to 1 kg [141].

The elevated cost of xenon is closely linked to its inherent volatility (refer to SDG Number 7). Xenon's utilisation in EP accounts for a mere fraction of its overall application, given its widespread use in other areas such as medicine (e.g., photon emission computed tomography -SPECT- and magnetic resonance imaging -MRI-), light-emitting devices (e.g., flash lamps, arc lamps), calorimeters and microelectromechanical systems, among other applications. Any fluctuations in its usage across these areas can significantly impact its price [134].

In contrast, water serves as a very affordable propellant. The primary expense associated with water is the energy required to prepare it for space applications. Based on the estimates in Section 2.2.1, the preparation of one litre of water requires approximately 2.1 kWh. Given the current (2024) electricity prices in the UK, where 1 kWh is valued at £0.29 [142], the cost for one litre of water would be £0.61 (0.70 €). This makes water approximately 77 times cheaper than xenon in

terms of cost.

As a conclusion, the prohibitive cost and associated volatility of xenon [133, 140] present a substantial economic hurdle for both large and small EP companies [143]. Transitioning to water as a propellant not only offers substantial cost savings but also aligns with environmental considerations and leverages the synergistic potential of water with other onboard subsystems.

2.3 Technological Challenges

In this section, the technological challenges associated with the utilisation of water as a propellant in EP are discussed. Water, being a novel propellant, necessitates further research to prepare it for space applications. Throughout this thesis, an extensive effort has been made to enhance the understanding, address, resolve, or alleviate these challenges in order to facilitate the advancement of water in the EP market.

2.3.1 Computational Simulations

One of the most potent instruments for gaining a deeper comprehension of HETs is the employment of computational models. An overview of the current methodologies for simulating HET technology was presented in Section 1.2.3.

The predominant set of existing tools is oriented towards simulating xenon-fuelled HETs, given that the majority of thrusters currently utilise this propellant. The transition from xenon to water as a propellant (in its two branches: water electrolysis, where oxygen is supplied to the thruster -anode-, and water vapour, where water in its gaseous state is used to fuel the thruster -anode-) necessitates a novel computational model that accurately incorporates the fundamental shifts from employing a noble gas to a diatomic reactive propellant. This is not merely a matter of adjusting the mass and Van der Waals radius of the species to be modelled; instead, a new reactive model is needed. This model must encompass the ionisation, dissociation, ion dissociation, attachment, and excitation reactions not only of the principal species (O_2 for water electrolysis or H_2O for water vapour), but also for its products (O in the case of water electrolysis and O, OH, H_2 and H in

the case of water vapour). This innovative model must also be capable of predicting the physical phenomena of these devices on a realistic timescale. The incorporation of new species into the model, along with their associated reactions, significantly increases the total computational time. Consequently, the new model must be designed to converge more rapidly without altering the physics of the problem.

Throughout this thesis, a novel computational model was developed with the goal of modelling oxygen and water vapour-fuelled HETs, aiming to predict the plasma physics of these new devices. Section 3 details this model and the outcomes achieved with it.

2.3.2 Material Compatibility

Xenon, as a noble gas, is recognised for its non-reactive nature with the HET device. This characteristic is crucial for space applications, where the thruster operates continuously for extended periods of time (for example, 20,000 hours in the case of the *BepiColombo* mission). The use of water introduces oxygen, which can contaminate and oxidise the thruster surfaces. Beyond performance implications, oxygen's presence can undermine the technology's functionality, unless materials are carefully selected. This thesis investigates a material analysis of the hardware components in contact with the oxygen plasma, specifically the anode plate and thruster walls. The findings from this analysis are detailed in Sections 4.2.2.2 and 4.2.2.3.

2.3.3 Performance

One of the main reasons for the current lack of water utilisation as a propellant is its lower efficiency compared to xenon-fuelled HETs. This is not unexpected. Xenon possesses a much higher mass ($m_{Xe} \approx 131$ u) than oxygen ($m_{O_2} \approx 32$ u) or water vapour ($m_{H2O} = 18$ u). In practice, this translates to a higher expected thrust at a given power when using xenon; although the particles' expelled velocity is lower compared to oxygen or water vapour. Although this scenario could represent a trade-off between thrust and exit velocity, the inherent losses of diatomic propellants arising from dissociation events that do not contribute to thrust (since they

do not produce ions) ultimately diminish the thrust efficiency of water. Even in the best case scenario, the thrust efficiency of water is expected to never reach the levels of efficiency of xenon. Nonetheless, attributes such as its lower cost, synergies with other subsystems, environmental benefits, access to multi-mode propulsion, or ISRU potential can offset its lower efficiency, making it the preferred option in some space missions. Nonetheless, a significant portion of this thesis is dedicated to identifying methods to enhance the performance of water-fuelled devices, aiming to render them market-competitive. Various strategies for performance improvement are detailed in the subsequent subsections.

2.3.3.1 Thruster Geometrical Optimisation

Throughout all the years dedicated to research on HETs, the thruster geometry has been optimised for the use of xenon as a propellant. Nonetheless, the physics and phenomena involved in water-fuelled HETs exhibit distinct characteristics, suggesting that a distinct geometry, in terms of channel length, width, or diameter, could further benefit these devices when propelled by water. The investigation into the effects of channel length on oxygen-fuelled HETs was initiated by A. Schwertheim and A. Knoll [43]. In this thesis, this research is extended by examining a broader range of channel lengths to gain a comprehensive understanding of the implications from utilising very short (5.5 mm) to large (59.8 mm) channels, as detailed in Section 4.2.2.7. Additionally, the impact of altering channel width (from 4 mm to 5 mm) is also explored (Section 4.2.2.7). Changing the channel diameter however, presents a more complex challenge. This complexity stems from the fact that a larger channel necessitates the development of a new thruster, unlike adjustments to channel length or width, which can be accommodated within the same thruster. Consequently, performance changes associated with altering the channel diameter (from 25 mm to 44 mm) must also consider the associated changes in other factors such as the magnetic field topology, inherent to the design of a thruster. With this consideration in mind, the effects of these changes in channel diameter are also investigated (Section 4.2.2.8).

2.3.3.2 Magnetic Field

The investigation into the influence of magnetic field topology and strength on the performance of oxygen-fuelled HETs was pioneered by A. Schwertheim and A. Knoll [43]. These studies concluded that a Gaussian geometry, akin to that of xenon-fuelled HETs, was optimal for maximising anode thrust efficiency. Additionally, it was found that magnetic fields significantly stronger than those typically used in xenon-fuelled HETs were advantageous for oxygen-fuelled HETs.

Similarly, this thesis extends the exploration of the impact of magnetic field strength on oxygen-fuelled HETs, not only from a performance perspective but also by delving into the underlying physics (Section 4.3). Further analyses on water vapour-fuelled HETs across a variety of magnetic field strengths are also conducted (Section 4.6).

2.3.3.3 Discharge Power

From the initial research, it was observed how the discharge power affected the performance of oxygen-fuelled HETs [144, 143]: the higher the discharge power, the higher the thrust efficiency. This dissertation aims to explore the underlying physics of these devices and provide insights into the phenomena observed with water-fuelled HETs with an increase discharge power. Additionally, the plasma characteristics at varying discharge powers are quantified, offering valuable correlations for computational models (Section 4.3).

2.3.3.4 Radiofrequency (RF) Excitation

One of the theories that are tested in this thesis is the potential use of RF excitation as a method to boost the performance of HETs. This methodology, intended for any propellant used, could be of particular interest to achieve a multi-mode architecture as the ones presented in Sections 2.2.2.1 and 2.2.2.2. This thesis initiates a numerical investigation into this idea (Section 3.2.2.3) to be tested with experiments using the lessons learnt from the computational model (Section 4.7).

2.3.4 End-To-End Technology Demonstration

The journey towards a comprehensive technological demonstration holds significant importance, specifically within the domain of water electrolysis propulsion. This is primarily due to the uncertainty surrounding the compatibility of a hydrogen-fuelled cathode with an oxygen-fuelled HET at the commencement of this PhD study. Despite the successful ignition and testing of an oxygen-fuelled HET under a variety of conditions in previous research [144, 143], it remained uncertain whether a hydrogen-fuelled cathode could effectively function in conjunction with the oxygen-fuelled HET. Moreover, it was unclear whether the thruster and cathode could successfully work using directly the products of water electrolysis generated by an electrolyser. Such a demonstration is pivotal for the research, as it would render the entire concept unfeasible if proven impossible. To address this, a strategic roadmap was devised to systematically test a range of components in increasingly complex scenarios, culminating in a complete end-to-end technological demonstration (Section 4.5). The main timeline of the research is described in Section 4.1.1.

Oxygen-Fuelled Hall Effect Thruster

The technological demonstration commenced with the oxygen-fuelled thruster, as detailed in Section 4.2. In there, the optimal operating conditions, geometric characteristics, and material compatibility of the thruster were explored. The physics underlying oxygen-fuelled HETs were also examined by measuring key plasma physics properties relevant to these devices (see Section 4.3). These tests were conducted at the Stanford Propulsion Laboratory, which is part of Stanford University, in a collaboration established with the Imperial Plasma Propulsion Laboratory.

It is important to note that these tests utilised noble gases as the cathode propellant, ensuring that the thruster's performance, using oxygen, was solely evaluated. This approach simplified the investigation by isolating the thruster from any changes in the cathode, thereby allowing for a clearer understanding of the thruster's performance characteristics. Additionally, these experiments eased the testing safety constraints, as utilising oxygen and hydrogen in stoichiometric

ratios within the same environment poses the risk of ignition unless appropriate precautions are taken. Once a comprehensive understanding of the operational principles of oxygen-fuelled HETs was achieved, subsequent advancements in the technological development pathway were pursued, as seen below.

Hydrogen Cathode

Upon characterising the oxygen-fuelled HET, the system incorporated a custom-made cathode design capable of using hydrogen as a propellant. These tests facilitated the evaluation of the system utilising the by-products of water electrolysis, (oxygen and hydrogen). Section 4.4 outlines the tests conducted and the insights gleaned from them. It is important to note that, for this experimentation, oxygen and hydrogen were provided by pressurised cylinders rather than through the in-situ production of a water electrolyser. These tests were scheduled to be conducted last, concluding the end-to-end technological demonstration.

Water Electrolyser

The final test incorporated a water electrolyser, which supplied in-situ produced oxygen and hydrogen to the thruster (anode) and cathode, respectively. Section 4.5 outlines the various experiments conducted under these conditions. This investigation took place at the European Space Agency Propulsion Laboratory, located at the European Space Agency facilities in the Netherlands (ESTEC), in a collaboration with the Imperial Plasma Propulsion Laboratory.

2.4 List of Objectives for this Thesis

This section outlines the main objectives of this thesis, aiming to give a complete overview of the research conducted to achieve these goals.

- Evaluation of the benefits of water propulsion (water electrolysis and water vapour) compared to current propellants. This encompasses analyse the environmental advantages, formulation

of multi-mode architectures, alignment with the United Nations SDGs, potential for ISRU, and cost savings (Section 2.2).

- Development of a computational code capable of simulating the physics of water propulsion HETs (water electrolysis and water vapour, Section 3).
- Provision of novel insights into the performance of oxygen-fuelled HETs, including an assessment of material compatibility, the impact of channel length, channel width, and potentially channel diameter, through a comparative analysis between the first and second generations of water electrolysis HETs (Section 4.2).
- Investigation of the physics of oxygen-fuelled HETs by examining the species present in the plasma as a function of the operational parameters, and measurements of the most important plasma properties using Langmuir probes (Section 4.3).
- Experimental demonstration of the capability of a HET to operate using the products of water electrolysis (oxygen for thruster and hydrogen for cathode), followed by performance evaluation under various metrics and comparison with a HET employing oxygen for thruster and a noble gas for cathode (Section 4.4).
- Experimental validation of a HET's ability to operate in tandem with a water electrolyser, supplying in-situ generated oxygen and hydrogen to the thruster and cathode, respectively (Section 4.5).
- Design, development and testing of a water feed system for characterising a water vapour HET (Section 4.6).
- Establishment of a trade-off between water electrolysis and water vapour technologies based on these findings (Section 4.6.2.3).
- Design, testing and characterisation, both computationally and experimentally, of the performance implications of utilising a HET excited with RF waves (Sections 3.2.2.3 and 4.7).

Chapter 3

COMPUTATIONAL CHARACTERISATION

This section provides an overview of the computational code developed within the scope of this thesis (referred to as *PlasmaSim*) to simulate water-fuelled HETs in two distinct branches: water electrolysis (oxygen) and water vapour. Part of this work was published in [1] and also presented at the 37^{th} International Electric Propulsion Conference in Boston, United States [6]. *PlasmaSim*'s development involved a collaborative effort with Universidad Carlos III de Madrid and the researcher Jesús Perales-Díaz [145].

3.1 Baseline and Previous Codes

At the start of this thesis, the 2-dimensional (2D) version of *PlasmaSim* developed by A. Knoll, was provided. This code was intended to establish a baseline for replicating the behaviour of xenon-fuelled HETs, albeit necessitating verification and validation. Simultaneously, A. Schwertheim developed the 0-dimensional version (0D) of *PlasmaSim*, utilising a simplified formulation derived from the 2D model [43].

This section offers an overview of the functionality of these codes prior to presenting the latest version of *PlasmaSim* developed within the framework of this thesis. The ultimate goal was to

develop a code capable of replicating the behaviour of water-fuelled HETs with the added possibility of incorporating RF excitation.

3.1.1 PlasmaSim 2-Dimensional (2D) Code

PlasmaSim is a fully kinetic electrostatic axial-radial PIC simulation, written in C++ and Unreal Engine [146], developed in-house within the Imperial Plasma Propulsion Laboratory. Three particle species were modeled: neutrals, ions and electrons.

3.1.1.1 Main Loop

All the processes that will be explained throughout this section are combined within a loop process, as depicted in Figure 3.1. This process goes as follows:

At the start of the simulation, the 3-dimensional (3D) volume of the HET is filled with particles (see "Particle Tracking and Electrostatic Computational Domains", Section 3.1.1.2). The initial conditions of the particles and the domain volume are taken from the simulation inputs of the user (see "Simulation Inputs", Section 3.1.1.3) and initiated as seen in "Particle Initialisation" (refer to Section 3.1.1.4). Then, the code initiates macroparticle collisions (see "Collisional and Ionisation model", Section 3.1.1.5) during each iteration of the simulation. Subsequently, the attributes of these macroparticles are interpolated onto a grid. Then, Δt and Δx are adjusted (see "Simulation Constraints and Spatial Discretisation", Section 3.1.1.6), and Poisson's equation is resolved to derive the electric potential, ϕ (see "Electric Potential", Section 3.1.1.7). [1]

Following the computation of $\vec{E}$ from ϕ, the vector field is interpolated, incorporating the input magnetic field, $\vec{B}$, at the position of each macroparticle. Finally, the macroparticles are moved and accelerated by the action of the fields (see "Particles' Motion"), and the boundary conditions are applied to the particles that cross the domain limits (see "Boundary Conditions"). Subsequently, this iterative process recommences within the loop.

[1] Note that adjusting Δt is not needed to resolve Poisson's equation but is necessary for advancing the simulation in time. Therefore, it needs to be updated before advancing the position of the particles ("Pusher", in Figure 3.1). However, Δx needs to be adjusted before calculating Poisson's equation to ensure adequate accuracy of the solution.

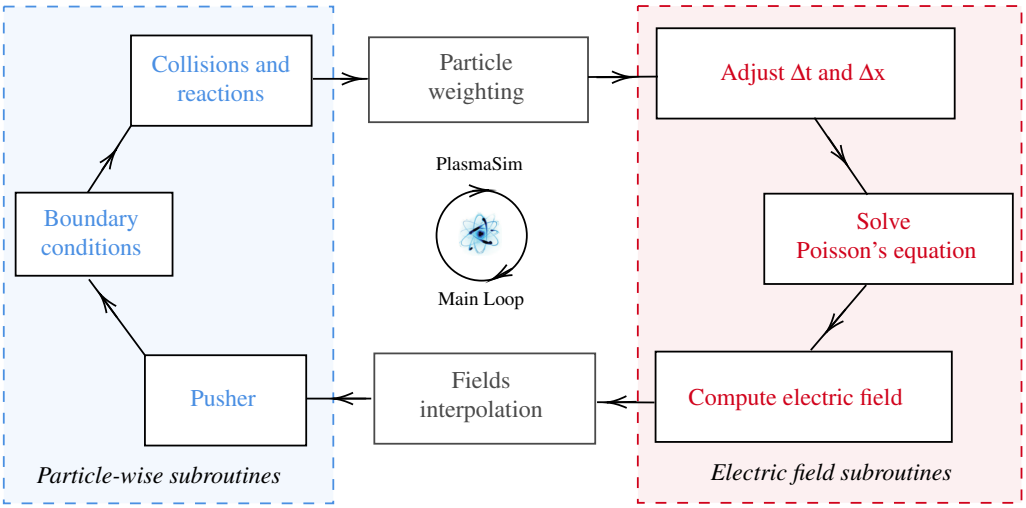
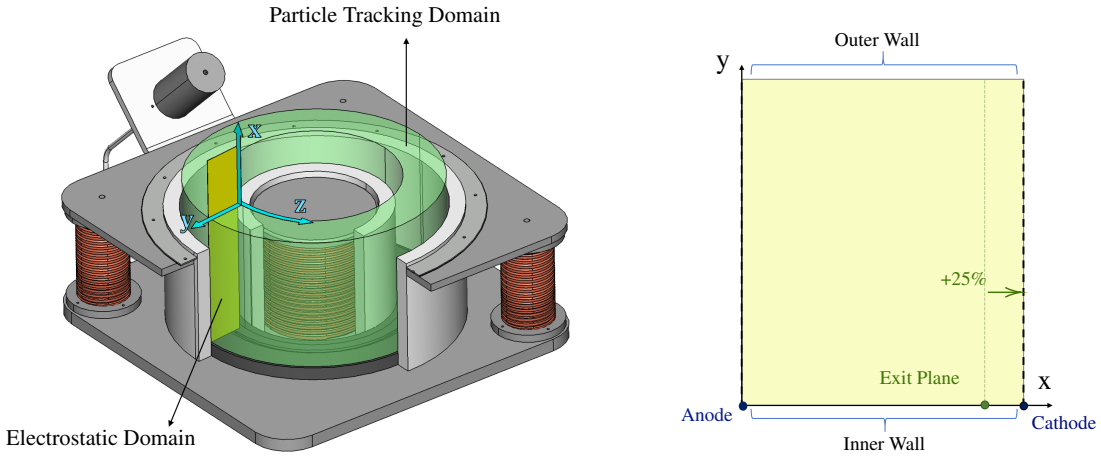


Figure 3.1: Main loop of *PlasmaSim*.



(a) *PlasmaSim* domains' representation in SPT-100

(b) Electrostatic domain used for solving Poisson's equation

Figure 3.2: *PlasmaSim* particle tracking domain (green) and electrostatic domain (yellow) used to solve Poisson's equation. The $\vec{x}$ axis is along the channel length and $\vec{y}$ throughout the channel width. Diagrams published in [1].

3.1.1.2 Particle Tracking and Electrostatic Computational Domains

The particle tracking domain, electrostatic computational domain and axis system used in *PlasmaSim* for the representation of the results are presented in Figure 3.2a for a standard xenon-fuelled HET (the *SPT-100* [147, 148]). This volume is extended 25% from the exit plane to take into account the free space exhaust and the cathode location (see Figure 3.2b). While the particles are tracked in the 3D volume inside the thruster, the resolution of Poisson's equation is 2D (in the axial-radial domain). As will be explained, a particular formulation termed "pseudo-2D" is employed instead

of the traditional 2D discretisation of Poisson's equation to accelerate the simulations.

3.1.1.3 Simulation Inputs

Table 3.3 provides the list of inputs that the user can define in order to adapt the simulation.

Note that the electron, ion and neutral temperatures, as well as the plasma number density, neutral number density and the number of super particles vary throughout the simulation. The values reported in Table 3.3 just correspond to the initial conditions used for starting the simulation. Notice that, in the case of the neutral density, not only the constant initial value can be provided but also a 1D axial profile, as will be explained further in Section 3.1.1.4. The number of super-particles per cell is recommended to be greater than 25 to ensure proper random statistics per cell. The magnetic field can be input by means of a text file that shows the exact axial shape and strength of the field throughout the axial length of the domain. The permittivity of free space is held constant to $\epsilon_0 = 8.85 \times 10^{-12}\ Fm^{-1}$, and no adjustments are made to this parameter to maintain the integrity of the physics involved [2].

Table 3.1: Simulation inputs for *PlasmaSim* 2D in its initial formulation.

Input	**Units**
Propellant	[-]
Channel length (L)	[mm]
Channel width (W)	[mm]
Channel mean diameter (ϕ_m)	[mm]
Cathode location (X_C)	[mm]
Anode mass flow rate ($\dot{m}_a$)	[mg/s]
Discharge voltage (V_d)	[V]
Magnetic field (B)	[T]
Initial number density of each species i (n_i)	[m^{-3}]
Injected electron temperature ($T_{e,in}$)	[eV]
Injected ion temperature ($T_{i,in}$)	[eV]
Injected neutral temperature ($T_{n,in}$)	[K]
Number of cells	[-]
Minimum number of super-particles per cell	[-]

[2] Although this parameter is sometimes increased in PIC methods to accelerate the simulations, the physical processes could be impacted in unexpected ways using this approach.

3.1.1.4 Particle Initialisation

For the initialisation of particles, the Box-Muller transformation was employed to ensure that the initial velocity distribution of each particle conforms to a Maxwellian distribution, contingent upon their initial temperature [149].

Concerning their spatial distribution throughout the channel, electrons, ions, and neutrals are organised into super-particles of size S, where $S = \frac{V_{ol}\ n_x}{N}$, with V_{ol} denoting the computational domain volume, n_x representing the particle number density of the species x, and N indicating the number of super-particles in the simulation.

In the case of electrons and ions, they are uniformly distributed throughout the channel at their specific initial conditions, from which the distribution evolves over time. However, for the neutral population, a distinct spatial distribution can be employed as an input to expedite the convergence of the solution. These distributions are derived from the final state conditions of previous simulations running for several tens of microseconds. Once this initial neutral distribution throughout the channel is established, various methods can be employed to obtain a random distribution of super-particles that adhere to this trend. Moss [150] and Walter [151] proposed different algorithms requiring $\mathcal{O}(n \ln n)$ time for initialising a set of n values. In *PlasmaSim*, Vose's Alias algorithm [152], initially proposed by Michael Vose in 1991, has been implemented, reducing the initialisation time to $\mathcal{O}(n)$. The rationale behind using a tailored initial neutral number density distribution is to achieve a balance between the ionisation and plasma loss rates, ensuring that the plasma number density closely approximates to the quasi-steady-state conditions.

3.1.1.5 Collisional and Ionisation Model

Within *PlasmaSim*, three types of elastic particle collisions were modelled: electron-neutral, ion-neutral, and neutral-neutral collisions. The Monte Carlo Collisions (MCC) approach [153] was employed in all cases, as depicted in Figure 3.3.

Initially, the collision cross-section and the collision frequency are computed. The collision

frequency (ν) is defined as in Equation 3.1:

$$\nu = n_n \sigma_x \sqrt{|v_x|^2 + c_n^2} \tag{3.1}$$

Here, n_n is the neutral number density, $|v_x|$ is the modulus of the particle's x speed, c_n is the average speed of the neutral particles within the cell and σ_x is the particle's x cross section. σ is modelled as a hard sphere $\sigma = \pi r^2$, where r is the radius of the collision, being the sum of the Van Der Walls radius of the collision particles.

Subsequently, it is statistically determined whether the collision shall occur. If so, a representative collision target is randomly generated based on the local properties within the cell [153]. The neutrals are assumed to follow a Maxwellian distribution. Then, the two-body interaction is resolved. Marsaglia's recipe [154] is then utilised to determine the direction of the relative velocity vector between the particles after collision. Conservation of momentum and kinetic energy of the colliding particle pair are employed to derive the velocity of the particle after collision.

The ionisation model follows a similar scheme as depicted in Figure 3.3. However, in this instance, an energy-dependent electron impact ionisation cross-section is employed. In the case of xenon ionisation, these cross-sections are sourced from prior literature studies [155]. Notice that this initial formulation of *PlasmaSim* was aimed to model xenon-fuelled HETs, and the different ionisation events of xenon were modelled to account for this propellant. This formulation was further enhanced when modelling the complex reactive model of water (Section 3.2).

Upon completion of the collision, an ion and an electron are created with random Maxwellian distributions at a fixed temperature (the injected temperature defined by the user initial conditions, T_{in}, see Table 3.3). This value also coincides with the temperature at which the particles are being released from a collision with one of the dielectric walls. By doing so, it is possible to thermalise the plasma at a set condition and help the model to reach steady-state in a shorter time duration.

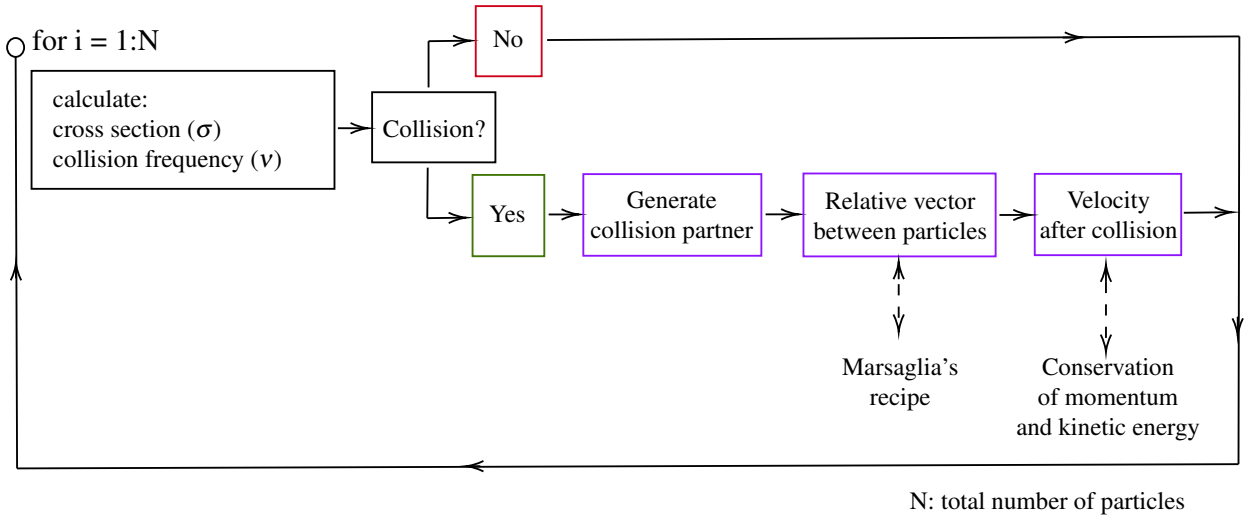


Figure 3.3: *PlasmaSim* collision model flow chart. Diagram published in [1].

Notice that, in this initial formulation, the energy lost in the reaction is not considered and therefore the energy of the reactants and products is fixed. This methodology will be improved to a global energy-conserved model in the final version of *PlasmaSim* (Section 3.2.1.3).

3.1.1.6 Simulation Constraints and Spatial Discretisation

PlasmaSim, like other computational codes that advance in time and space, is inherently limited by its maximum temporal and spatial resolution. Indeed, a significant limitation of PIC codes lies in the need to resolve the governing physics' phenomena at very small temporal and spatial scales to achieve self-consistency [82] (refer to Section 1.2.3.2). Despite the computational burden it implies, full PIC simulations offer unparalleled fidelity compared to other simulation methodologies.

PlasmaSim employs an adaptive time-stepping scheme to progress through the simulation. At each step, the chosen time increment must satisfy constraints imposed by the plasma frequency time step (Δt_{pe}, Equation 3.2), the electron gyrofrequency time step (Δt_{ce}, Equation 3.3), and the Courant-Friedrichs-Lewy condition (Δt_{CFL}, Equation 3.4):

$$\Delta t_{pe} < \frac{2\pi}{w_{pe}} = 2\pi\sqrt{\frac{m_e\epsilon_0}{n_e q^2}} \tag{3.2}$$

$$\Delta t_{ce} < \frac{2\pi}{w_{ce}} = 2\pi\frac{m_e}{qB} \tag{3.3}$$

$$\Delta t_{CFL} < \frac{\Delta x}{|v_e|} \tag{3.4}$$

For the spatial increment, it is ensured to always be smaller than the Debye length (λ_D, Equation 3.5):

$$\Delta x < \lambda_D = \sqrt{\frac{\epsilon_0 k_B T_e}{n_e q^2}} \tag{3.5}$$

In practice, a Safety Factor (S_F) of 6 ($S_F = 6$) is applied.

The Debye length is used for the grid generation, needed to solve Poisson's equation. The required number of cells in each direction is computed as in Equation 3.6:

$$N_{cells,x} = S_F \frac{L}{\lambda_D}; \qquad N_{cells,y} = S_F \frac{W}{\lambda_D} \tag{3.6}$$

The most conservative (highest) number of cells between these two is used to have an uniform grid of N_{cells} (i.e., $N_{cells} = \max(N_{cells,x}; N_{cells,y})$), which is used to solve the Poisson's equation in each direction (Section 3.1.1.7). Different simulations using a smaller and larger safety factor have proven the grid convergence with these conditions.

Because of the finite spatial step, an error's accumulation occurs when using numerical solvers, which can be particularly problematic when the number of time steps is very high. The error of numerical schemes is estimated in Section A.3.3.

3.1.1.7 Electric Potential

A novel computational approach, termed as a "pseudo-2D" method, is employed to calculate the 2D electric field along the radial-axial coordinates of the thruster. Unlike the conventional full 2D PIC approach, which represents the computational domain with a two-dimensional array of cells, this method discretises the domain into two sets of 1D cells along the axial ($\vec{x}$) and radial ($\vec{y}$) directions of the thruster. A prescribed solution form splits the Poisson's equation into two parts, allowing for separate solution along the $\vec{x}$ and $\vec{y}$ axes. This pseudo-2D strategy confers notable

computational advantages for two primary reasons. Firstly, it entails solving the field using two 1D arrays of order N elements, which is notably faster compared to solving a 2D array of order N^2 elements. Secondly, it enables a significant reduction in the number of particles within the simulation, while ensuring a minimum number of particles per cell (defined by the user), owing to the considerably larger cell volume inherent to the pseudo-2D method.

Starting with the Poisson's equation [3], the overall plasma potential ($\phi(x, y)$) is calculated as the sum of two terms, $\phi_1(x)$ and $\phi_2(y)$, dependent solely on the $\vec{x}$ axis and $\vec{y}$ axis respectively, yielding Equation 3.7. Due to the independence of ϕ_1 on y and ϕ_2 on x, the formulation is split into two parts (Equations 3.8 and 3.9):

$$\nabla^2\phi(x,y) = \frac{\partial^2\phi_1}{\partial x^2} + \frac{\partial^2\phi_2}{\partial y^2} = \frac{-\delta}{\epsilon_0} \tag{3.7}$$

$$\frac{\partial^2\phi_1}{\partial x^2} = c_1\left(\frac{-\delta}{\epsilon_0}\right) \tag{3.8}$$

$$\frac{\partial^2\phi_2}{\partial y^2} = c_2\left(\frac{-\delta}{\epsilon_0}\right) \tag{3.9}$$

In these equations, δ represents the charge density, computed as $\delta = q(n_i - n_e)$, while c_1 and c_2 are two non-dimensional parameters. The values of c_1 and c_2 are arbitrary as long as they sum up to 1. In *PlasmaSim*, they are defined as $c_1 = \frac{dx}{dx+dy}$ and $c_2 = \frac{dy}{dx+dy}$. Equations 3.8 and 3.9 are then discretised into a tri-diagonal system to obtain the potential at each grid point (Equations 3.10 and 3.11 respectively):

$$-\left(\frac{A^x i - 1}{\Delta x i - 1}\right)\phi(x)i - 1 + \left(\frac{A^x i - 1}{\Delta x_{i-1}} + \frac{A^x i}{\Delta x i}\right)\phi(x)i - \ -\left(\frac{A^x i}{\Delta x_i}\right)\phi(x)i + 1 = \frac{\Delta y i}{\Delta x_i + \Delta y_i}\left(\frac{\delta_i}{\epsilon_0}\right) \tag{3.10}$$

[3] Notice that Poisson's equation is derived from Maxwell's equations; specifically, Gauss's law for electricity and the definition of the electric field as the gradient of the electric potential.

$$-\left(\frac{A^y j-1}{\Delta y j-1}\right)\phi(y)j-1+\left(\frac{A^y j-1}{\Delta y_{j-1}}+\frac{A^y j}{\Delta y j}\right)\phi(y)j-\ -\left(\frac{A^y j}{\Delta y_j}\right)\phi(y)j+1=\frac{\Delta x j}{\Delta x_j+\Delta y_j}\left(\frac{\delta_j}{\epsilon_0}\right) \tag{3.11}$$

These equations necessitate closure with the boundary conditions described in Table 3.2. Here, $A^x = Y\ Z$ and $A^y = X\ Z$ denote the cross-sectional areas in the $\vec{x}$ and $\vec{y}$ directions respectively, with $X = L$, $Y = W$, and $Z = \pi\phi_m$: representing each one of the simulation domain dimensions. Notice that, for the simulations, the annular domain represented in Figure 3.2a (green) is unwrapped to a cubic domain as displayed in Figure 3.4. Although using Cartesian coordinates simplifies the representation of the problem, one of the next steps in the code development process involves transitioning to cylindrical coordinates (see Chapter 6). This transition will allow for a more comprehensive representation of the system.

As previously highlighted, this pseudo-2D methodology notably reduces the requisite number of particles and enhances the computational efficiency of the field solver. Consequently, it facilitates full-scale modelling of a HET at realistic plasma densities over considerably extended timescales. Such simulations employing a full 2D PIC model would approach the computational thresholds of currently available high-performance computing clusters. By adopting this technique, an approximate solution capable of capturing the "average" radial direction's effect on the plasma parameter evolution is obtained. Thereby, the overall impacts of particle and energy loss to the wall are captured, constituting a more substantial contribution to enhancing the accuracy of the obtained integral performance parameters compared to the axial distribution of energy loss addressed by full 2D models. The pursued approach thus diverges from the prevalent practice in 1D axial PIC codes, where wall losses are introduced through ad-hoc means involving artificial coefficients and/or collisions. Consequently, while this methodology possesses limitations, it further enhances the self-consistency of the simulation in capturing wall loss effects while reducing computational time relative to a full 2D PIC model.

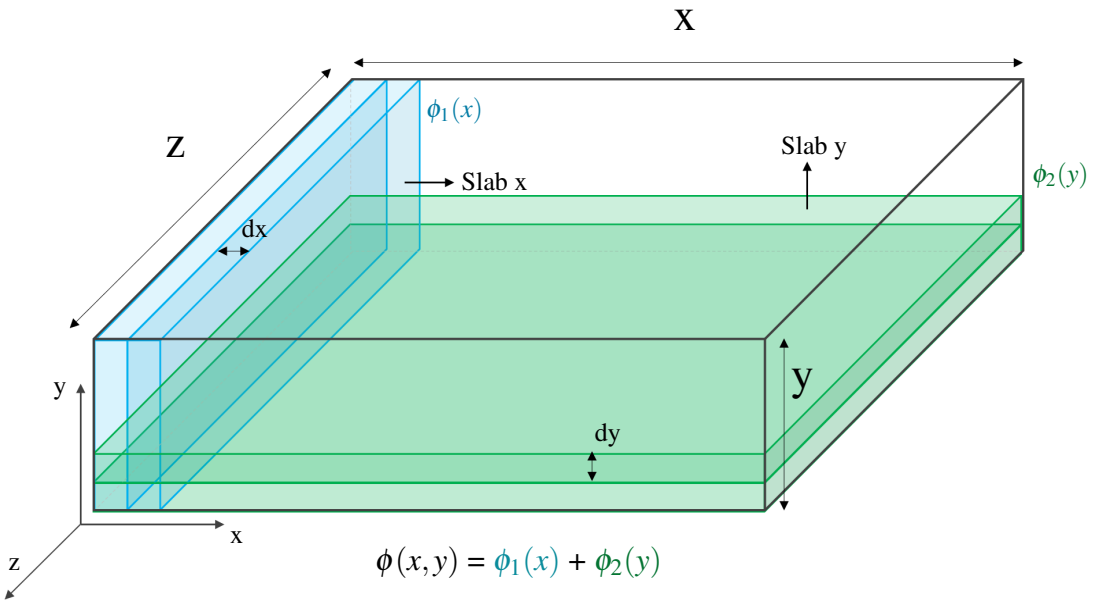


Figure 3.4: *PlasmaSim* pseudo-2-dimensional approach to solve the Poisson's equation. The 3-dimensional particle tracking domain of the HET (Figure 3.2a) is unwrapped to a cubic domain for the simulations. Diagram published in [1].

Finally, it is worth noting that, as will be detailed in Section 3.2, the pseudo-2D electric potential formulation underwent further refinement for the ultimate iteration of *PlasmaSim* tailored for modelling water-fuelled HETs.

3.1.1.8 Particles' Motion

The trajectories of charged particles are determined by applying the Lorentz force (Equation 3.12) to each particle i:

$$m_i \frac{d\vec{v_i}}{dt} = q\left(\vec{E_i}(x,y) + \vec{v_i} \times B(x_i)\right) \tag{3.12}$$

where $\vec{E_i}$ its electric field computed as

$$\vec{E_i} = (\phi_i - \phi_{i+1})/\Delta x_i \ \vec{i} + (\phi_j - \phi_{j+1})/\Delta y_j \ \vec{j} \tag{3.13}$$

The Boris pusher method was employed to advance the particles' position at each time step. For an in-depth understanding of this technique, readers are referred to the literature [82, 156, 157].

3.1.1.9 Boundary Conditions

Table 3.2: Boundary conditions for *PlasmaSim* 2D in its initial formulation. Table published in [1].

Location	Electrons	Ions	Neutrals
Anode ($x = 0$ m)	Recirculating condition	Removed	Reflected
Cathode ($x = X_C$ m)	Reflected	Removed	Reflected
Free loss	Removed	Removed	Removed
Dielectric walls ($\vec{y}$ axis)	Removed	Recombined	Reflected
Azimuthal direction ($\vec{z}$ axis)	Periodic	Periodic	Periodic

The different boundary conditions introduced in the initial formulation of *PlasmaSim* aiming to replicate the behaviour of xenon-fuelled HETs are summarised in Table 3.2.

The anode is located at the very start of the computational domain ($x = 0$ m), whereas the cathode is assumed to be placed at the end: $x = X_C$ m (extended, as seen in Figure 3.2b, 25% extra to account for the position of the cathode). The recirculation condition governing electrons at the anode entails their reintroduction at the cathode plane with a randomised Maxwellian distribution at the initial electron temperature specified by the simulation. This condition facilitates the continuous flow of electron current from cathode to anode, emulating the operation of a closed circuit comprising the thruster and power supply. Upon reintroduction, ions assume neutrality at the temperature assigned in the simulation parameters. The reflection of electrons at the cathode's boundary serves not only a physical function but also acts as a strategy to prevent the formation of a sheath at that juncture.

Notice that these boundary conditions were further improved in the ultimate version of *PlasmaSim* when modelling water-fuelled HETs, as will be explained in Section 3.2.

3.1.1.10 Computational Time

Throughout this section, various strategies aiming to accelerate the computational time of the simulations have been outlined, such as the pseudo-2D Poisson's equation or the algorithms of the collision model (Section 3.1.1.5). The alteration of the value of the vacuum permittivity ϵ_0 was also

evaluated as an approach to enhance computational speed. This methodology, initially introduced by Szabo [158] and also known as 'artificial permittivity', involves increasing the constant value of the vacuum permittivity or dielectric constant by a factor γ ($\epsilon' = \epsilon_0\ \gamma^2$). Different values of γ have been proposed in the literature to achieve a suitable trade-off between computational speed and accurate results. Zhao [159] suggested using values of $\gamma^2 < 1600$, whereas Szabo proposed a more moderate value of $\gamma^2 \approx 100$. Through exploration of the different solutions obtained with these values, it was deduced that altering the dielectric constant, even by a factor of 10, significantly modifies the physics of the problem and, consequently, the results obtained. For instance, a higher vacuum permittivity with $\gamma^2 = 10$ diminishes the plasma density distribution (ultimately leading to plasma quenching), affecting the physics and thrust performance, despite reducing the computational time by approximately 15 times. Based on these conclusions, which are also coherent with the research of other groups and the plasma community, no artificial permittivity was used to maintain the integrity of the problem's physics untouched.

In general, the computational time required for each simulation varies considerably depending on the initial conditions, particularly the initial neutral and plasma density, along with the physical volume of the computational domain. For instance, for the results outlined in Section A.3.2, the simulation took approximately 1000 hours (approximately 40 days) to reach $\approx 15\mu s$ on a standard simulation computer (HP Z1 G5 model [160]). For that reason, the simulations presented in Section 3.2 were conducted at the Imperial College London High-Performance-Computer (HPC).

The 2D version of *PlasmaSim* underwent several verification studies to ensure its capabilities compared to state-of-the-art PIC codes. These studies are included in Appendix A.2.

3.1.1.11 Performance Estimation

Using *PlasmaSim*, it is possible to estimate the performance of a HET and correlate it when sufficient data is available from the literature.

For this purpose, specific impulse (I_{sp}) and thrust (T) are computed at the exit of the channel, utilising the average ion axial velocity at that location ($v_{i,x}$), the gravitational acceleration at the

Earth's surface, g_0 and the anode discharge voltage and current (V_d and I_d):

$$T = \dot{m}_a \; v_{i,x} \tag{3.14}$$

$$P_d = V_d \; I_d \tag{3.15}$$

$$I_{sp} = \frac{v_{i,x}}{g_0} \tag{3.16}$$

$$\eta_a = \frac{T \; v_{i,x}}{2P_d} \tag{3.17}$$

V_d is an input from the user (Table 3.3) whereas I_d is obtained as an average value across the entire axial ($\vec{x}$ axis) extent of the domain (Equation 3.18). From the simulation results, it is observed that the current remains stable throughout the domain. This averaging approach is employed to avoid oscillations at specific positions, such as at the cathode plane, where sheath effects might lead to non-physical results.

$$I_d = A\left(\overline{|J_i|} + \overline{|J_e|}\right) = A\left(\sum_{n=1}^{N_{cells,x}} q \; n_i \; |v_{i,x}| + \sum_{n=1}^{N_{cells,x}} q \; n_e \; |v_{e,x}|\right) / N_{cells,x} \tag{3.18}$$

In Equation 3.18, J_i refers to the current density of the species i.

The electron mobility (μ) is calculated as the ratio between the average electron axial velocity ($\hat{V_{e,x}}$) and the average axial electric field ($\hat{E_x}$): $\mu = \hat{V_{e,x}}/\hat{E_x}$.

Thrust-To-Power-Ratio ($TTPR$) is calculated as $TTPR = T/P_d$, expressed in mN/kW.

Making use of these equations, the performance predictions coming from *PlasmaSim* were validated against the *SPT-100* thruster (see Appendix A.3).

3.1.2 PlasmaSim 0-Dimensional (0D) Code

A simplified version of *PlasmaSim*, based on its 2D counterpart, was developed as part of A. Schwertheim's thesis [43]. The aim of this code was to explore potential optimisations for the geometry of a HET utilising oxygen from water electrolysis, prior to developing a thruster compatible with this propellant (see Section 4.1.2.1). A detailed description of this software can be found in A. Schwertheim's thesis [43]. Here, just the main differences from the 2D version are highlighted.

3.1.2.1 Reduction in Dimensionality

The most significant change in the 0D model, compared to the 2D version, is its reduced dimensionality. While particle tracking remains 3D, Poisson's equation is solved for a single cell, hence the term "0D model". This assumes a linear electric field, using the discharge voltage at the anode potential defined by the user and the grounded cathode potential at the simulation length's exit plane ($x = X_C = 0$ V) [43].

Furthermore, the magnetic field is not considered in the 0D formulation. Practically, this implies the absence of azimuthal Hall current and precludes electron cyclotron motion [43]. This simplification, while facilitating computational efficiency, imposes constraints on the 0D model's ability to accurately replicate the complex phenomena existing within a HET.

3.1.2.2 Simulation Inputs

The simulation inputs for *PlasmaSim* 0D closely resemble those employed in its 2D counterpart, albeit with some adjustments (see Table 3.3).

Due to the absence of a magnetic field, the electrons are unable to attain the typical temperatures observed in a HET. Consequently, the electron temperature, rather than being self-determined through collisions and prolonged residence time facilitated by the magnetic field, remains constant in this 0D simulation based on the user input. For consistency, the temperature of the ions and neutrals are also kept constant to the value set by the user.

Table 3.3: Simulation inputs for *PlasmaSim* 0D in its initial formulation.

Input	**Units**
Propellant	[-]
Channel length (L)	[mm]
Channel width (W)	[mm]
Channel mean diameter (ϕ_m)	[mm]
Cathode location (X_C)	[mm]
Anode mass flow rate ($\dot{m}_a$)	[mg/s]
Discharge voltage (V_d)	[V]
Initial number density of each species i (n_i)	[m^{-3}]
Electron temperature (T_e)	[eV]
Ion temperature (T_i)	[eV]
Neutral temperature (T_n)	[K]
Number of super-particles	[-]
Time step	[s]

An additional requisite for this simplified model, not pertinent to the 2D formulation, is the specification of the simulation time step. In the former case, Equations 3.2, 3.3, and 3.4 dynamically computed this parameter during each iteration. However, the absence of multiple cells and a magnetic field renders Equations 3.3 and 3.4 inapplicable. Hence, a conservative and fixed time step is implemented to advance the simulation temporally. Based on a sensitivity analysis conducted on this model, a time step of $\Delta t = 10^{-7}$ s is commonly utilised [43].

Lastly, the specification of cell count becomes redundant as OD codes inherently operate with a singular cell, as explained earlier.

3.1.2.3 Boundary Conditions

The boundary conditions implemented within *PlasmaSim* 0D are outlined in Table 3.4.

The boundary conditions governing neutrals remain consistent with those employed in *PlasmaSim* 2D. Conversely, for ions, the approach diverges from the 2D model wherein recombination occurs at the walls. Instead, ions are subjected to simple reflection, mirroring the treatment of electrons.

Table 3.4: Boundary conditions of *PlasmaSim* 0D in its initial formulation.

Location	**Electrons**	**Ions**	**Neutrals**
Anode ($x = 0$ m)	Recirculating condition	Reflected	Reflected
Cathode ($x = X_C$ m)	Reflected	Removed	Reflected
Free loss	Removed	Removed	Removed
Dielectric walls ($\vec{y}$ axis)	Reflected	Reflected	Reflected
Azimuthal direction ($\vec{z}$ axis)	Periodic	Periodic	Periodic

This modification contributes to expediting these computational processes while effectively confining the plasma within the computational domain. It is worth noting, as previously emphasised, that the 0D formulation is tailored towards achieving rapid convergence with reduced fidelity; in contrast to the high-fidelity albeit slower convergence characteristic of the 2D model.

The different verification and validation methods of this code can be found in A. Schwertheim thesis 43.

Notice that small modifications to the initial and boundary conditions also distinguish the final versions of the 0D and 2D models. These modifications aim to enhance the overall fidelity of these codes and provide a more accurate representation of water-fuelled HETs, as will be discussed in the following Section 3.2.

3.2 Numerical Modelling

3.2.1 Methodology

This section provides an overview of the final version of *PlasmaSim* developed within this thesis, aimed at modelling water-fuelled HETs in its two branches: water electrolysis (oxygen) and water vapour. This version is titled: '***PlasmaSim*: a Double-Stage 0-Dimensional and 2-Dimensional Particle-In-Cell code**'.

The ultimate model incorporates both the 0D and 2D formulations. Specifically, the low-fidelity 0D model is utilised to refine the initial conditions of the 2D, enabling faster time progression in the high-fidelity 2D simulation. Further elaboration on this strategy is provided in Section 3.2.1.1.

To simulate the physics of water-fuelled HETs comprehensively, a "double-stage reactive model" was introduced. This model encompasses not only the reactions of the propellants (O_2 and H_2O, referred to as "1st stage") but also considers reactions involving all the dissociation products (O, OH, H_2, and H, named as "2nd stage"). Section 3.2.1.2 provides detailed insights into this novel reactive model employed.

The fidelity of the code was further augmented by adopting an energy-conserved model (Section 3.2.1.3), wherein energy losses from each reaction are accounted for to ensure global energy conservation.

Improvements were also made to the resolution of Poisson's equation using the pseudo-2D method, building upon the work of F. Farbod , M. Reza and A. Knoll [89, 90, 91, 92]. These enhancements are elucidated in Section 3.2.1.4. It is important to note that the 2D formulation remains axial-radial, without resolving the azimuthal direction. To address this limitation, turbulent collisionality was introduced into the code. This is important in order to capture the azimuthal-wise electron fluctuations of the HET, which are important for the electron transport throughout the channel (more information in Section 3.2.1.5).

Finally, the combined set of initial and boundary conditions needed for this combined code to

run is provided in Sections 3.2.1.6 and 3.2.1.7.

3.2.1.1 Combining the 0D and 2D Particle-In-Cell Codes

Throughout A. Schwertheim thesis and also highlighted in the previous Section 3.1.2, the limitations of the 0D formulation were discussed. Primarily, not resolving the electric field and not accounting for the magnetic field in a HET is a too simplistic approach for any PIC aiming to model a HET. However, the 0D code can still provide valuable insights that can be used as the starting point for a higher fidelity 2D code to work.

In practice, by using the 0D model, it is possible to determine important factors which can reduce the computational time of the 2D model and/or give a preliminary intuition of the physics behind these thrusters, including:

1. Whether if the 1st stage reactive model can, by itself, produce realistic results or if the 2nd stage is necessary, at the expense of a larger computational burden.

2. Whether if any of the reactions (see Section 3.2.1.2) can be neglected or not, due to the fact that the species' production is negligible compared to other species.

3. A preliminary understanding of the species' fraction produced by the thruster.

Notice that the computational speed-up of the 0D model is approximately 10^6 times faster than the 2D model. Consequently, incorporating the 0D model does not impose a significant time burden compared to the 2D model.

The communication scheme between the two implementations of *PlasmaSim* is illustrated in Figure 3.5. In this depiction, the 0D implementation is initiated using the conditions outlined in Table 3.7. Subsequently, the convergence of *PlasmaSim 0D* is assessed. If convergence is not achieved, the user must initiate the simulation again with a different set of initial conditions. Conversely, if the simulation converges, the steady-state number density is examined for each species. If a species's density is deemed irrelevant (approximately two orders of magnitude lower than others), it is not tracked in *PlasmaSim 2D*, and the associated reactions are disregarded.

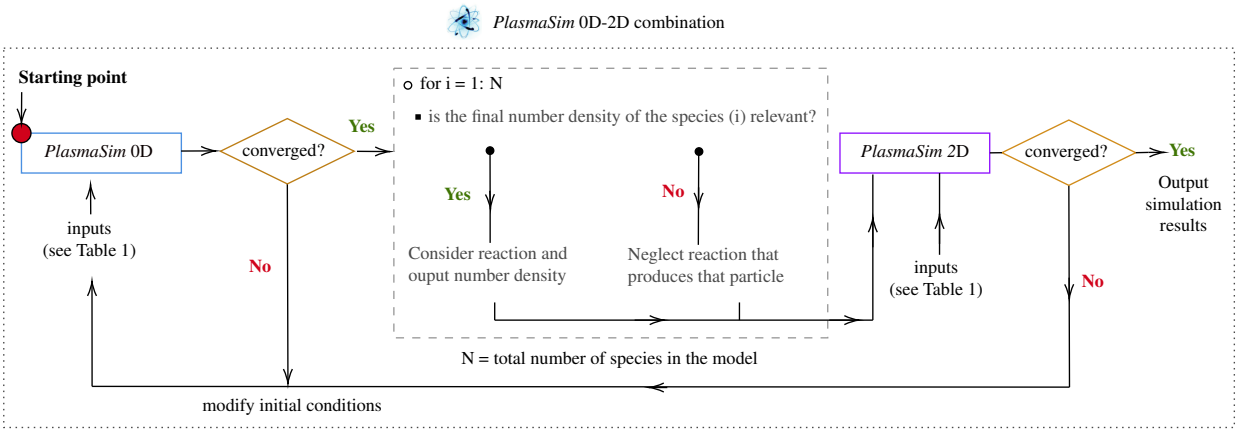


Figure 3.5: Main diagram of the combined 0-dimensional 2-dimensional *PlasmaSim* model.

This significantly expedites the computational time required for the 2D model to reach a steady solution. Conversely, if a species's density is significant, it serves as the initial density for *PlasmaSim 2D*. Presumably, as this initial density is close to the steady-state value, the final convergence is achieved more rapidly compared to providing an initial guess. If convergence is not attained with *PlasmaSim 2D*, the user is directed back to the initial conditions from *PlasmaSim 0D*, and the simulation recommences. Upon achieving a stable simulation, the outputs are analysed.

It is worth noting that despite *PlasmaSim* employing memory-shared parallelisation and being executed on a High-Performance Computing (HPC) system, a single simulation may still require several weeks to cover a time span of 10 μs. The computational bottleneck in this context primarily arises from the reactive model (Section 3.2.1.2). This is partly due to the multitude of individual reactions and the computational resources required for their execution. Overall, the reactive model consumes approximately 34% of the total computational time (equally split between the 1st and 2nd stages). Notice that the `C++` subroutines are parallelised using the OpenMP library [161]. Within Unreal Engine, owing to its incompatibility with OpenMP, the *ParallelFor* function is utilised for multithreading [162].

3.2.1.2 A Double-Stage Reactive Model

As briefly highlighted before, the reactive model employed in *PlasmaSim* (applicable to both the 0D and 2D formulations) encompasses two sequential stages in the overall reaction process: (a) the 1st stage executes the various reactions undergone by neutral particles of the initial propellant species, while (b) the 2nd stage handles the pertinent reactions of species derived from the 1st stage. Section 3.2.2.1 underscores the distinctions between utilising either a 1-stage or 2-stage model. Additionally, other types of reactions, such as excitation or rotational and vibrational modes, which can coexist alongside ionisation and dissociation reactions [163], are incorporated in both stages to enhance the fidelity of the code.

Water Electrolysis (Oxygen)

The oxygen reactive model comprises a total of 18 reactions distributed between the 1st and 2nd stages. Table 3.5 presents these reactions along with their corresponding energy losses for each stage. Notice that, during an attachment process, the energy lost corresponds to the kinetic energy of the electron (K_e). Regarding the ion dissociation double reaction of O_2, its energy loss (53.7 eV) is computed as the summation of the dissociation reaction of O_2 (5.1 eV) and the double ionisation of O (48.6 eV). Additionally, Table 3.5 enumerates the excitation collisions considered for the water electrolysis discharge. These include all electronic excitations, with vibrational and rotational modes of O_2 not included due to their negligible impact on this type of discharge [163]. It is assumed that the frequency of de-excitation for all excited states is much higher than the electron-neutral collision frequency; hence metastable states are not simulated. Nevertheless, the influence of metastable states on both oxygen and H_2O discharges can be assessed in future studies.

Table 3.5: Reactive model of water electrolysis (oxygen): 1st stage (blue) and 2nd stage (green).

Reaction	**Energy Loss**
1st stage	
O_2-Elastic: $O_2 + e \rightarrow O_2 + e$	-
O_2-Dissociation: $O_2 + e \rightarrow O + O + e$	5.1 eV [Ref. 164]
O_2-Ionisation: $O_2 + e \rightarrow O_2^+ + 2e$	12.1 eV [Ref. 165]
O_2-Ion dissociation (+): $O_2 + e \rightarrow O^+ + O + 2e$	18.8 eV [Ref. 165]
O_2-Ion dissociation (++): $O_2 + e \rightarrow O^{++} + O + 3e$	53.7 eV
O_2-Attachment: $O_2 + e \rightarrow O^- + O$	K_e
O_2-Elec. exc.: $O_2 + e \rightarrow O_2^*(a^1\Delta_g) + e$	0.98 eV [Ref. 166]
O_2-Elec. exc.: $O_2 + e \rightarrow O_2^*(b^1\Sigma_g^+) + e$	1.66 eV [Ref. 166]
O_2-Elec. exc.: $O_2 + e \rightarrow O_2^*(A^3\Sigma_u^+, A'^3\Delta_u, c^1\ \Sigma_u^-) + e$	4.05 eV [Ref. 166]
O_2-Elec. exc.: $O_2 + e \rightarrow O_2^*(B^3\Sigma_u^-) + e$	6.12 eV [Ref. 166]
2nd stage	
O-Elastic: $O + e \rightarrow O + e$	-
O-Ionisation: $O + e \rightarrow O^+ + 2e$	13.6 eV [Ref. 165]
O-Double ionisation: $O + e \rightarrow O^{++} + 3e$	48.6 eV [Ref. 167]
O-Attachment: $O + e \rightarrow O^-$	K_e
O-Elec. exc.: $O + e \rightarrow O^*(^1D) + e$	1.96 eV [Ref. 168]
O-Elec. exc.: $O + e \rightarrow O^*(^1S) + e$	4.18 eV [Ref. 168]
O-Elec. exc.: $O + e \rightarrow O^*(^3P^0) + e$	9.20 eV [Ref. 168]
O-Elec. exc.: $O + e \rightarrow O^*(^5S^0, {}^3S^0, {}^5P, {}^3P, {}^5D^0, {}^3D^0) + e$	> 12.0 eV [Ref. 168]

Water Vapour

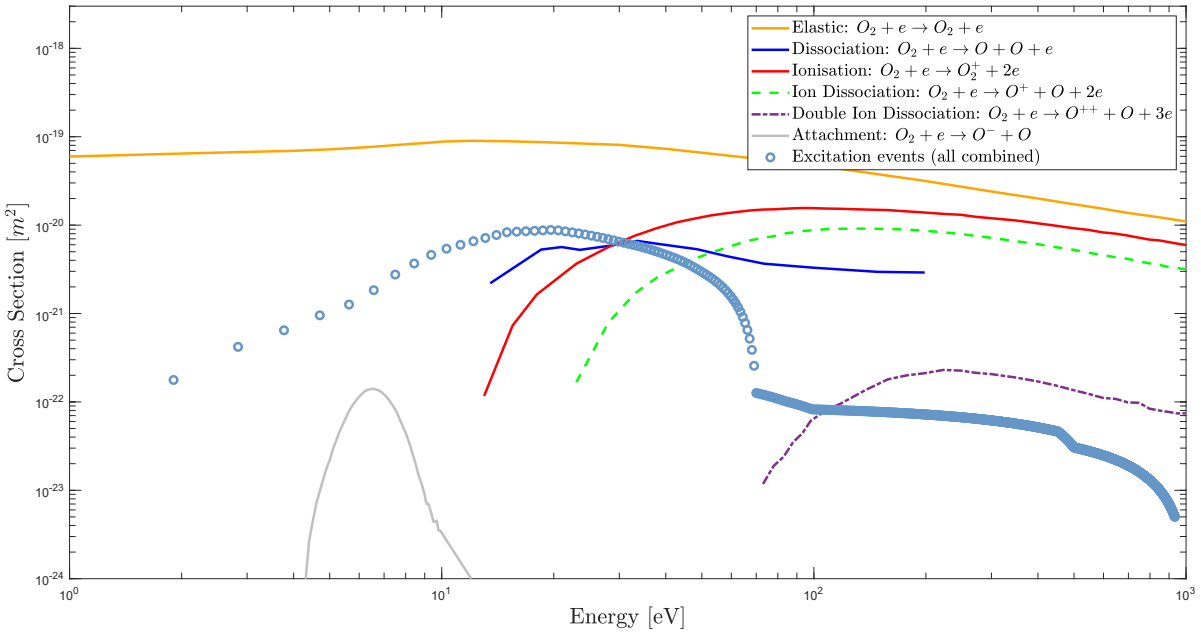
The water reaction model incorporates a total of 45 reactions, 25 of which are assigned to the first stage and 20 to the second stage, as seen in Table 3.6.

Once again, for every attachment process, the energy loss corresponds to the kinetic energy of the incident electron (K_e). The double energy loss during the ion dissociation reaction from H_2O to O^{++} (55.7 eV) is calculated as the sum of dissociation reaction II (7.1 eV) and the double ionisation of monoatomic O (48.6 eV). Table 3.6 also includes the excitation collisions considered for the H_2O discharge. These include: (i) H_2O stretching and bending modes, its first four rotational modes [169], and its first six electronic transitions [170, 171]; (ii) OH three lowest-energy electron transitions [172] and its first vibrational mode [173]; (iii) H electronic transitions up to n = 4 [174]; and (iv) H_2 most relevant electronic transitions [175]. It is important to highlight that the reactions regarding H_2 could be neglected due to the low fraction density of this species, as will be detailed in Section 3.2.2.2. Lastly, notice that that the reactions for monoatomic oxygen are the same as those used in water electrolysis (refer to Table 3.5).

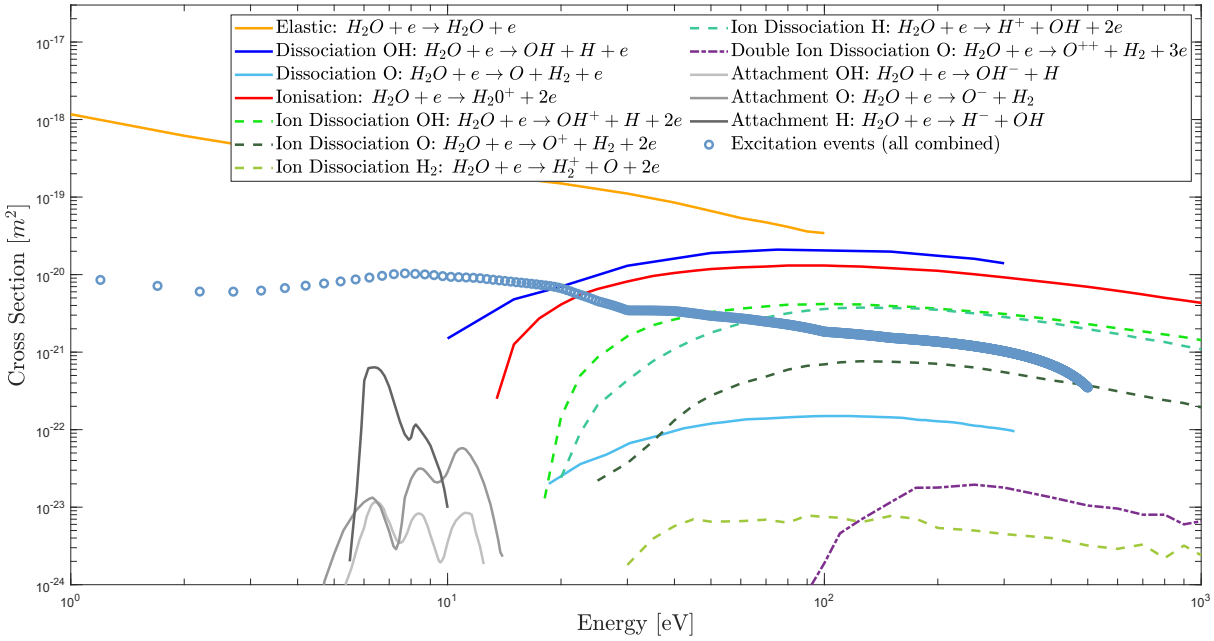
Table 3.6: Reactive model of water vapour: 1st stage (blue) and 2nd stage (green).

Reaction	**Energy Loss**
1st stage	
H_2O-Elastic: $H_2O + e \rightarrow H_2O + e$	-
H_2O-Dissociation I: $H_2O + e \rightarrow OH + H + e$	5.1 eV [Ref. 164]
H_2O-Dissociation II: $H_2O + e \rightarrow O + H_2 + e$	7.1 eV [Ref. 176]
H_2O-Ionisation: $H_2O + e \rightarrow H_2O^+ + 2e$	12.6 eV [Ref. 165]
H_2O-Ion dissociation I: $H_2O + e \rightarrow OH^+ + H + 2e$	18.1 eV [Ref. 165]
H_2O-Ion dissociation II: $H_2O + e \rightarrow OH + H^+ + 2e$	18.3 eV [Ref. 165]
H_2O-Ion dissociation III: $H_2O + e \rightarrow O^+ + H_2 + 2e$	19.0 eV [Ref. 165]
H_2O-Ion dissociation IV: $H_2O + e \rightarrow O + H_2^+ + 2e$	20.7 eV [Ref. 165]
H_2O-Double ion dissociation: $H_2O + e \rightarrow O^{++} + H_2 + 3e$	55.7 eV
H_2O-Stretching: $H_2O + e \rightarrow H_2O^*(101{+}001) + e$	0.53 eV [Ref. 169]
H_2O-Bending: $H_2O + e \rightarrow H_2O^*(010) + e$	0.3 eV [Ref. 169]
H_2O-Elec. exc.: $H_2O + e \rightarrow H_2O^*(\overline{a}^3B_1) + e$	7.1 eV [Ref. 171]
H_2O-Elec. exc.: $H_2O + e \rightarrow H_2O^*(\overline{A}^1B_1) + e$	7.5 eV [Ref. 171]
H_2O-Elec. exc.: $H_2O + e \rightarrow H_2O^*(^3A_2) + e$	8.9 eV [Ref. 171]
H_2O-Elec. exc.: $H_2O + e \rightarrow H_2O^*(^1A_2) + e$	9.2 eV [Ref. 171]
H_2O-Elec. exc.: $H_2O + e \rightarrow H_2O^*(\overline{b}^3A_1) + e$	9.5 eV [Ref. 171]
H_2O-Elec. exc.: $H_2O + e \rightarrow H_2O^*(\overline{B}^1A_1) + e$	9.7 eV [Ref. 171]
2nd stage	
OH-Elastic: $OH + e \rightarrow OH + e$	-
OH-Ionisation: $OH + e \rightarrow OH^+ + 2e$	13.0 eV [Ref. 165]
OH-Dissociation: $OH + e \rightarrow O + H + e$	4.4 eV [Ref. 164]
OH-Attachment: $OH + e \rightarrow OH^-$	K_e
H-Elastic: $H + e \rightarrow H + e$	-
H-Ionisation: $H + e \rightarrow H^+ + 2e$	13.6 eV [Ref. 165]
H-Attachment: $H + e \rightarrow H^-$	K_e
O-Elastic: $O + e \rightarrow O + e$	-
O-Ionisation: $O + e \rightarrow O^+ + 2e$	13.6 eV [Ref. 165]
O-Double ionisation: $O + e \rightarrow O^{++} + 3e$	48.6 eV [Ref. 167]
O-Attachment: $O + e \rightarrow O^-$	K_e
H2-Elastic: $H_2 + e \rightarrow H_2 + e$	-
H_2-Ionisation: $H_2 + e \rightarrow H_2^+ + 2e$	15.4 eV [Ref. 165]
H_2-Dissociation: $H_2 + e \rightarrow H + H + e$	4.5 eV [Ref. 164]
H_2-Ion dissociation: $H_2 + e \rightarrow H^+ + H + 2e$	18.0 eV [Ref. 165]
H_2-Attachment: $H_2 + e \rightarrow H_2^-$	K_e
OH-Vibrational: $OH + e \rightarrow OH^*(\nu = 1) + e$	0.43 eV [Ref. 173]
OH-Elec. exc.: $OH + e \rightarrow OH^*(A^2\Sigma^+) + e$	4.0 eV [Ref. 172]
OH-Elec. exc.: $OH + e \rightarrow OH^*(a^4\Sigma^-) + e$	7.4 eV [Ref. 172]
OH-Elec. exc.: $OH + e \rightarrow OH^*(1^2\Sigma^-) + e$	7.9 eV [Ref. 172]
H_2-Rotational: $H_2 + e \rightarrow H_2^*(J = 02) + e$	0.05 eV [Ref. 175]
H_2-Elec. exc: $H_2 + e \rightarrow H_2^*(a^3\Sigma_g^+) + e$	9.2 eV [Ref. 175]
H_2-Elec. exc: $H_2 + e \rightarrow H_2^*(B^1\Sigma_u^+ \text{and } C^1\Pi_u) + e$	12.0 eV [Ref. 175]
H-Elec. exc.: $H + e \rightarrow H^*(n = 2, 3, 4) + e$	[10.2-12.8] [Ref. 174]
O-Elec. exc.: → see Table 3.5	-

The cross-sections corresponding to each of these reactions are outlined in Figures 3.6 and 3.7. For a better visualisation, the cross-sections of the excitation events for both oxygen (Table 3.5) and water (Table 3.6) are all combined.



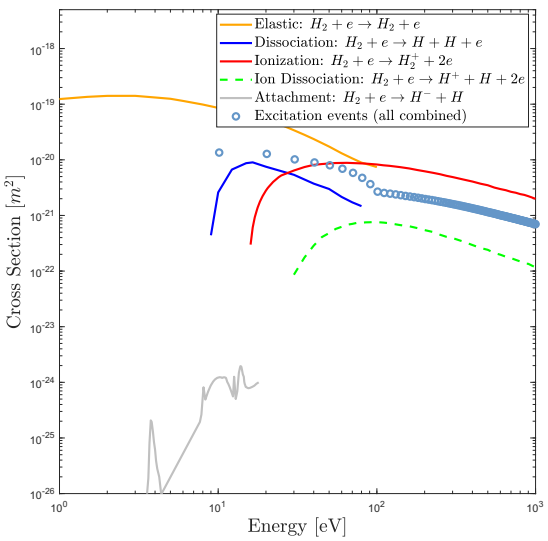
(a) Cross Sections of diatomic O_2



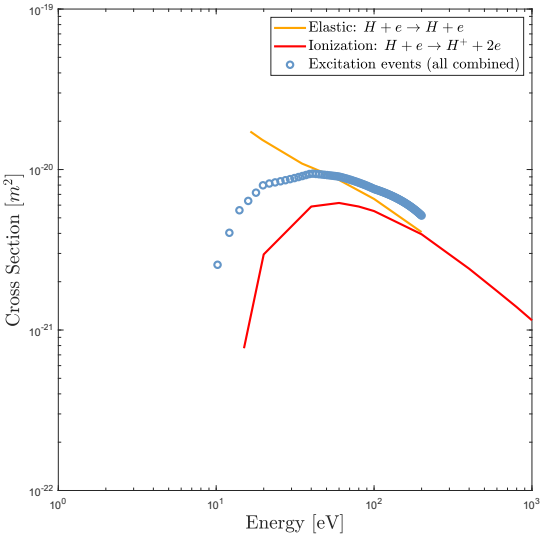
(b) Cross Sections of water H_2O

Figure 3.6: Cross sections of the most relevant processes for the first stage particles: diatomic oxygen O_2 (Figure 3.6a) and water H_2O (Figure 3.6b; as a function of the electron energy (i.e., electron temperature). Data taken from [166, 169].

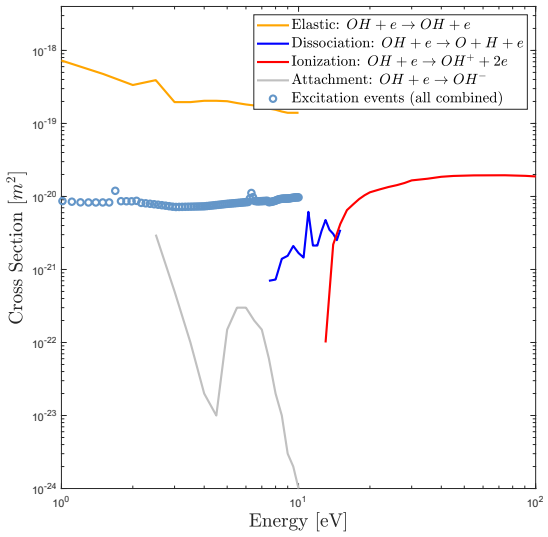
A thorough understanding of the cross-sections of a specific propellant and their dependence on electron energy is essential for comprehending what could be the optimal operating conditions of a thruster (which is closely related to the in-channel electron temperature) and for gaining preliminary insights into the impact of the energy losses during discharge.



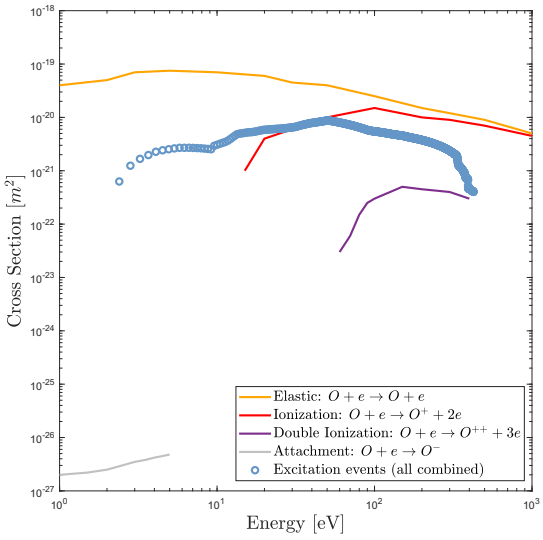
(a) Cross sections of molecular H_2



(b) Cross sections of monoatomic H



(c) Cross sections of Hydroxyl radical OH



(d) Cross sections of Monoatomic O

Figure 3.7: Cross sections of the most relevant processes for the second stage particles: molecular H_2 (Figure 3.7a), monoatomic H (Figure 3.7b), hydroxyl radical OH (Figure 3.7c) and monoatomic O (Figure 3.7d); as a function of the electron energy (i.e., electron temperature). Data taken from [170, 171, 172, 173, 174, 175].

It is remembered that, in order to enhance the propellant utilisation efficiency as much as possible, the ionisation cross-section should be maximised, while other reactions that do not directly produce ions should be minimised.

To verify the successful implementation of the reactive model, the results obtained from the model are compared to an analytical solution specific to this problem. The details of this analysis are provided in Appendix A.2.2.

3.2.1.3 Energy-Fixed Versus Energy-Conserved Models

The initial formulation of *PlasmaSim* used an energy-fixed model where the energy lost from the reactions was not considered (see Section 3.1). However, in this new formulation, due to the existence of multiple reactions for different species, it was necessary to implement a global energy-conserving model.

Although these two approaches differ on how the energy of the reaction is distributed, both start from the same methodology explained in Section 3.1: For each particle, the cross section of a reaction (σ) and the collision frequency (ν) is calculated (refer to the previous Figure 3.3). The cross section for each species is the one obtained from the literature (see Figures 3.6 and 3.7). Then, it is statistically checked if the collision will occur or not. If this is the case, the local properties within the cell are taken to generate a representative collision target [153]. Once this is done, the product species are generated depending if the energy-fixed or the energy-conserved approach is selected.

The energy-conserved methodology applies energy conservation to every reaction as follows:

$$E_{prod} = E_{reac} - E_{lost} \tag{3.19}$$

Here, E_{reac} represents the energy of the reactants, and E_{lost} denotes the energy lost during the reaction and E_{prod} is the energy of the products modified by subtracting E_{lost}. E_{lost} depends on the type of reaction and the reactants involved (refer to Tables 3.5 and 3.6). It is considered that the energy of the products and reactants is their actual kinetic energy ($E_{prod} = K_{prod}$, $E_{reac} = K_{reac}$).

Simultaneously, it is assumed that heavy species (ions, denoted by subindex i, and neutrals, denoted by subindex n) have the same velocity as the reactants, thereby conserving energy ($K_{prod,n} = K_{reac,n}$ and $K_{prod,i} = K_{reac,i}$). However, electrons (subindex e) absorb the entirety of the energy lost during the reaction following this procedure:

1. First, initial the kinetic energy of the electrons is computed ($K_{reac,e} = 1/2 m_e v_e$).

2. Next, the kinetic energy $K_{reac,e}$ is adjusted by subtracting the energy lost (using data from Tables 3.5 and 3.6) according to Equation 3.19, yielding the modified electron energy (products): $K_{prod,e} = K_{reac,e} - E_{lost}$).

3. $K_{prod,e}$ is evenly distributed among the number of electrons generated by the reaction. For instance, in a double ionisation reaction producing 3 electrons, each output electron receives 1/3 of the total $K_{prod,e}$.

4. Utilising Marsaglia's recipe [154], the velocities of the output electrons are randomised.

3.2.1.4 Resolving Poisson's Equation

For *PlasmaSim* 2D, the "pseudo-2D" approach used to resolve Poisson's equation was previously overviewed in Section 3.1. This method was used to reduce the computational cost of full 2D simulations while capturing the effect of the radial direction of the discharge using a fully decoupled plasma potential . This method was further improved with a novel formulation described by F. Farbod, M. Reza and A. Knoll [89, 90, 91, 92] aiming to increase the fidelity of the solution while supposing a great advantage in terms of computational time.

In this new method, although the starting point remains the sum of two terms: $\phi(x, y) = \phi_1(x) + \phi_2(y)$, which leads to Equation 3.7, these two parts are now partially (and not fully) decoupled. This is achieved by integrating once along each of the directions, resulting in the two following 1D ordinary differential equations:

$$\frac{d^2\phi_1(x)}{dx^2}W + \left.\frac{d\phi_2(y)}{dy}\right|_W - \left.\frac{d\phi_2(y)}{dy}\right|_0 = -\frac{1}{\varepsilon_0}\rho^x(x) \tag{3.20}$$

$$\frac{d^2\phi_2(y)}{dy^2}L + \left.\frac{d\phi_1(x)}{dx}\right|_L - \left.\frac{d\phi_1(x)}{dx}\right|_0 = -\frac{1}{\varepsilon_0}\rho^y(y) \tag{3.21}$$

where

$$\rho^{\mathrm{x}}(x) = \frac{1}{W}\int_0^{\mathrm{W}} \rho(x,y)dy \quad \rho^{\mathrm{y}}(y) = \frac{1}{L}\int_0^{\mathrm{L}} \rho(x,y)dx; \tag{3.22}$$

Here, ρ represents the charge density and ε_0 denotes the permittivity of free space.

Despite the enhancement in fidelity compared to the baseline resolution explained in Section 3.1, the computational time exhibits only a relatively modest increment. This is due to the presence of $N + N$ equations within the current model, in contrast to the former formulation, which featured only N equations. Both are significantly faster than a full 2D case, which necessitates $N \times N$ equations.

The boundary conditions for Equations 3.20 and 3.21 are as follows: at the cathode and anode boundaries, ϕ_1 is set to 0 and V_d, respectively; in the radial direction, $\phi_2(y_\mathrm{inner}) = \phi_2(y_\mathrm{outer}) = \mathcal{C}$, where $\mathcal{C}$ is an arbitrary value [4] . The system of differential equations formed by Equations 3.20 and 3.21 is discretised with a centred finite differences scheme for the second partial derivatives, and forward and backward schemes for the first-order derivatives at the boundaries.

The electric field, $\vec{E}(x, y)$, is updated every time step. This is obtained from the gradient of ϕ ($\vec{E}(x, y) = -\nabla\phi(x, y)$). The gradient of ϕ is numerically computed using a centred finite difference scheme.

3.2.1.5 Turbulent Collisionality

A turbulent collisionality was also introduced in the latest version of *PlasmaSim* 2D in order to capture the azimuthal-wise fluctuations of the plasma properties. This was motivated by literature research, which indicates that this addition is necessary to capture the full functionality of a HET using any 2D radial-axial plasma simulation code [177, 178]. This affects only electron macroparticles. The turbulent collision frequency (ν_t) is defined, following Ref. [163], as:

$$\nu_\mathrm{t} = k_t \frac{\omega_\mathrm{ce}}{16} \tag{3.23}$$

where k_t is a parameter quantifying the average turbulence level. The collision probability is then calculated as $P_\mathrm{t} = \nu_\mathrm{t}\Delta t$. For every electron in the simulation, P_t is then compared to a random

[4] Remember that it is the derivative of the potential which is calculated (the electric field). Therefore, particularly when using a method like the "pseudo 2D", which decouples the axial and radial directionality, the selection of this constant is not relevant and can be set to any value.

number to check if the collision shall occur or not. Through the sensitivity analysis conducted on the turbulent parameter k_t, it was concluded that a minor collisionality ($k_t = 0.01$) proved sufficient to maintain the plasma. This selected value aligns with those reported in the literature [83, 179]. Furthermore, the sensitivity analysis indicated that values of this magnitude yielded consistent outcomes, whereas values an order of magnitude higher led to plasma extinction. This occurrence is attributable to the excessive demagnetisation of electrons when k_t is too large, resulting in an inadequate plasma containment. The turbulent collision is represented as an elastic isotropic scattering process, ensuring conservation of electron energy before and after the collision [163].

3.2.1.6 Simulation Inputs

The initial conditions of the combined *PlasmaSim* 0D/2D model are summarised in Table 3.7.

With the modifications detailed throughout this section, the propellant can now be either O_2 for water electrolysis simulations or H_2O for water vapour simulations.

It is worth noting that, as mentioned in Section 3.1, the temperature of electrons, ions, and neutrals remains constant for the 0D model but just serves as the initial condition for the 2D formulation. The constant electron temperature for the 0D model ranged from $T_e = 13 - 35$ eV. The impact of selecting the electron temperature is discussed in Section 3.2.2.2. For the 2D model, the electron injection temperature is adopted from the literature ($T_e = 5$ eV, [180]). Neutrals are assigned a temperature of $T_n = 300$ K and ions $T_i = 0.1$ eV, for both the 0D (constant temperature) and the 2D model (injected temperature).

Regarding densities, the 0D model outputs steady-state predictions based on the initial user guesses, which then serve as initial conditions for the 2D model (see Section 3.2.1.1).

In the 2D model, a drift velocity is applied to the neutrals, corresponding to an anode wall temperature of 750 K [181].

Additionally, two new parameters, the Secondary Electron Emission (SEE) temperature and the electron reflection yield coefficient, are introduced to model the electron boundary condition on the dielectric walls for the 2D model, as explained in Section 3.2.1.7.

Table 3.7: Simulation inputs for the combined version of *PlasmaSim* 0D-2D aimed to model water-fuelled HETs (water electrolysis, oxygen, and water vapour).

Model	**Parameter**	**Input**	**Units**
0D/2D	Propellant	O_2, H_2O	-
0D/2D	Channel length (L)	35	mm
0D/2D	Channel width (W)	5	mm
0D/2D	Channel mean diameter (ϕ_m)	20	mm
0D/2D	Cathode location (X_c)	44	mm
0D/2D	Anode mass flow rate ($\dot{m}_A$)	1.0	mg/s
0D/2D	Discharge voltage (V_d)	300	V
2D	Magnetic field (B)	Figure 3.12a	T
0D	Initial number density of each species (n_i)	2.0×10^{20}	m^{-3}
0D/2D	Constant/Injected electron temperature (T_e)	13-35 (0D) / 5 (2D)	eV
0D/2D	Constant/Injected ion temperature (T_i)	0.1	eV
0D/2D	Constant/Injected neutral temperature (T_n)	300	K
2D	Initial neutral drift ($u_{n,in}$)	750 [181]	m/s
2D	SEE temperature	1.0 [180]	eV
2D	Electron reflection yield	0.5 [182]	-
2D	Number of cells	$\approx$ 40000	-
2D	Minimum number of super-particles per cell per species	$>$ 50	-

The geometrical parameters and the B axial profile correspond to the Imperial Plasma Propulsion Laboratory thruster named *WET-HET* [43] (see Section 4.1.2.1), where the software results will be evaluated. The selected operating point, defined by a pair ($\dot{m}_A, V_d$), falls within the nominal operational range of the thruster. No scaling is applied to the value of the permittivity of free space.

3.2.1.7 Boundary Conditions

The boundary conditions selected for the combined version of *PlasmaSim* 0D-2D model can be found in Table 3.8. An effort was made to align the boundary conditions of the 0D and 2D codes to ensure a more consistent formulation across both models. Nevertheless, two primary distinctions arise between these versions:

Table 3.8: Boundary conditions for the combined version of *PlasmaSim* 0D-2D aimed to model water-fuelled HETs (water electrolysis -oxygen-, and water vapour). The conditions highlighted in dark red exclusively belong to the 2D code, while those in dark green solely affect the 0D model. All other conditions are applicable to both the 0D and 2D formulations.

Location	**Electrons**	**Ions**	**Neutrals**
Anode ($x = 0$ m)	Removed	Recombined	Reflected
Cathode ($x = X_C$ m)	Quasineutrality & removed / Removed	Removed	Removed
Free loss	Removed	Removed	Removed
Dielectric walls ($\vec{y}$ axis)	Secondary Electron Emission / Reflected	Recombined	Reflected
Azimuthal direction ($\vec{z}$ axis)	Periodic	Periodic	Periodic

1. Boundary condition for electrons at the cathode: In the 2D version, a quasineutrality condition is employed. This condition evaluates the adjacent cell to the cathode boundary and injects electrons as necessary to establish a quasineutral plasma at that location. Subsequently, any electrons crossing the boundary are eliminated. This approach aims to eliminate any sheath at the cathode boundary and has demonstrated superior performance compared to the recirculating condition implemented in the model baseline [92] (refer to Section 3.1). However, implementing this condition within the confines of the 0D model, which comprises only one cell, remains unfeasible. Therefore, the electrons are simply removed in the 0D formulation.

2. Boundary condition for electrons at the dielectric walls: The fidelity of the 2D model was enhanced by adopting a linear SEE model, as detailed in Ref. [182]. Electrons emitted from SEE follow a Maxwellian distribution function for their velocities, with a user-defined temperature (set at $T_e = 1.0$ eV in these simulations; see Table 3.7), and subjected to another user-defined coefficient, known as the electron reflection yield (set to 0.5 eV following recommendations from the literature [182]; see Table 3.7). The 0D model, inherently being a low fidelity model, did not integrate the SEE formulation to uphold its characteristic fast convergence. Consequently, electrons in this model are simply reflected.

Ion recombination was also incorporated into the 0D model, employing the anode as an additional site for recombination in both formulations. Additionally, thanks to the added drift

velocity of the neutrals, they could replenish the channel much faster and those crossing the cathode boundary could be directly removed instead of being reflected as in the previous version. The validity of these conditions was verified by other researchers [183] and progressively implemented in PlasmaSim, assessing the discrepancies in profiles resulting from different conditions.

3.2.1.8 Radiofrequency (RF) Excitation

Excitation and Generation

To implement the excitation of RF waves into *PlasmaSim*, first of all, the optimal excitation strategy needs to be evaluated. Based on the theoretical framework described in Section 4.7, several methods for exciting these waves under the mentioned conditions were considered:

- Option 1: AC+DC voltage superposition at the anode. Equation 3.24 shows the generated RF discharge voltage at the anode ($V_{a,RF}$) in this case:

$$V_{a,RF} = V_d + V_{RF}\cos(w_{RF}t) \tag{3.24}$$

  where $V_{RF}\ cos(w_{RF}t)$ represents the AC oscillating voltage with amplitude V_{RF} and angular frequency w_{RF}, corresponding to the one of the excited electromagnetic wave.

- Option 2: AC voltage in the cathode. As the cathode is normally biased at zero potential, this AC voltage will be oscillating around this zero voltage condition, obtaining a RF cathode voltage ($V_{c,RF}$) of:

$$V_{c,RF} = V_{RF}\cos(w_{RF}t) \tag{3.25}$$

- Option 3: Antenna at the exit plane. By doing that, it is possible to induce longitudinal waves into the channel with the same directionality as in the two previous approaches.

Performing a trade-off between all above-mentioned options, it was concluded that Option 2 (applying AC voltage at the cathode) might be the most practical in terms of simplicity and

efficiency. The presence of RF cathodes is not something new, as several models have been successfully tested in EP devices as an alternative of hollow cathodes [184]. Indeed, microwave cathodes have been used in space missions for EP applications already, such as in the Ion Thrusters of Hayabusa and Hayabusa2 [131, 185], while they are currently being studied in the context of single-stage HETs as well [186]. In this case however, instead of containing the electromagnetic waves inside the RF cathode setting the cathode ground potential constant, the cathode ground potential can oscillate and in consequence can excite the thruster and possibly augment its performance. This approach is much easier to incorporate than Option 1, as it requires no modification in the thruster itself; therefore reducing the number of components needed. From a systems' perspective, this is much attractive than incorporating an extra antenna as in Option 3.

Code Modifications

By implementing minor modifications to *PlasmaSim*, it is possible to analyse the impact of RF electrostatic waves on HET simulations, which can then be further post-processed and analysed. The X-waves are considered quasistatic (see Section 1.2.2.2), so *PlasmaSim*, being an electrostatic PIC model, fits the purpose of this study. However, for a full treatment of plasma-wave interactions, electromagnetic codes are more appropriate, and interested readers are directed to the work by Álvaro Sánchez et al. [187, 188, 189].

For these simulations, the selected time step of *PlasmaSim* needs to be further constrained, being smaller than the excited RF wave time step (Δt_{RF}, Equation 3.26):

$$\Delta t_{RF} < \frac{2\pi}{w_{RF}} \tag{3.26}$$

The imposition of the RF wave time step aims to accurately capture the temporal evolution of the wave across the computational domain. In practical implementation, a safety factor of $S_F = 25$ is employed to ensure adherence to the aforementioned temporal constraints.

The boundary conditions for the HET discharge potential also need adjustment. To implement

the selected strategy (making the cathode potential oscillate at the right frequency and voltage), the boundary condition at the cathode's plane is modified by using an alternating potential centered at $\phi = 0$ V of amplitude V_{RF} and frequency f_{RF} (see Equation 3.25). The specific selection of V_{RF} and f_{RF} depends on the specific wave being studied.

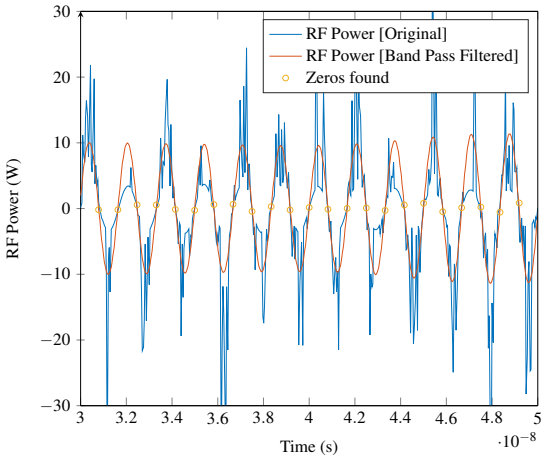
RF Power

In order to make a fair comparison between all simulation cases, both the RF excitation power and the DC discharge power need to be considered when computing the performance efficiency of the thruster. The DC discharge power and the performance parameters in terms of specific impulse (I_{sp}) and thrust (T) are calculated as presented in Section 3.1.1.11. The RF power (P_{RF}) is computed as stated in Equation 3.27:

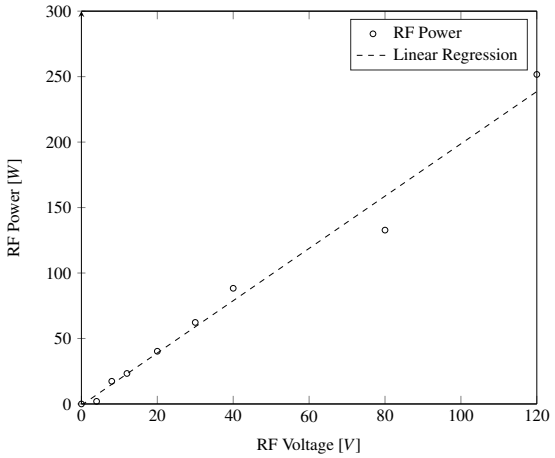
$$P_{RF} = V_c(t) \cdot J(t) \cdot A \tag{3.27}$$

where $V_c(t)$ represents the oscillatory voltage at the cathode location, and $J(t)$ denotes the current density, calculated as the aggregated contribution of the ions ($J_i(t)$) and the electrons (see Section 3.1.1.11). This oscillating signal is filtered using a band-pass filter, with the frequency band selection resulting from a 5% offset from the main signal frequency of P_{RF}. Figure 3.8a presents an example of the original and filtered RF power signals for the case of $f_{RF} = 600$ MHz and $V_{RF} = 10$ V. Once the time dependence of the AC signal is obtained, its semi-amplitude is computed by calculating the difference between the zeros of the function and the maximum/minimum found between zeros. This is averaged over the simulation time and multiplied by 2 to obtain the final signal amplitude. For instance, in Figure 3.8a, the RF power obtained using this procedure is $P_{RF} = 19.8$ W (approximated to $P_{RF} = 20$ W).

Figure 3.8b illustrates the relationship between RF voltage and RF power. It is apparent that both parameters seem to follow a linear relationship between them over the range of excitation voltages investigated.



(a) RF power signal (t) at a frequency of $f_{RF} = 600$ MHz and RF voltage of $V_{RF} = 10$ V



(b) RF power computation at different RF voltages, and its associated linear regression plot

Figure 3.8: Characteristics of the RF power expressed as a function of time and RF voltage.

It has also been observed that changing the RF frequency while keeping the RF voltage has little effect on the RF power, indicating that RF power is mostly independent of the selected RF frequency.

Additionally, due to this RF excitation, a new parameter, denoted as the 'computational total efficiency' (η_T, Equation 3.29), needs to be calculated. It is computed as the product of the combined power coming from the DC power to the HET (η_a, Equation 3.17) and the total power utilisation taking into account the RF excitation power coming from the cathode (η_P, Equation 3.28).

$$\eta_P = \frac{V_d \cdot I_d}{V_d \cdot I_d + P_{RF}} \tag{3.28}$$

$$\eta_T = \eta_a \cdot \eta_P \tag{3.29}$$

Notice that *PlasmaSim* does not account for the power consumed by the cathode. Therefore, this is the closest parameter resembling the total efficiency which is experimentally calculated, η_{tot} (Section 4.1.3, Equation 4.4).

The next sections present the results obtained with this software when modelling water-fuelled HETs and also RF-excited HETs.

3.2.2 Results and Discussion

3.2.2.1 Water Electrolysis-Fuelled Hall Effect Thrusters

This section provides an overview of the outcomes obtained from the ultimate version of *PlasmaSim* employing oxygen (derived from water electrolysis) as the anode propellant. Initially, the results obtained from the 0D model are outlined. Subsequently, the findings of the 2D model, supported by the 0D outputs, as explained in Section 3.2.1.1, are presented.

0-Dimensional (0D) Model

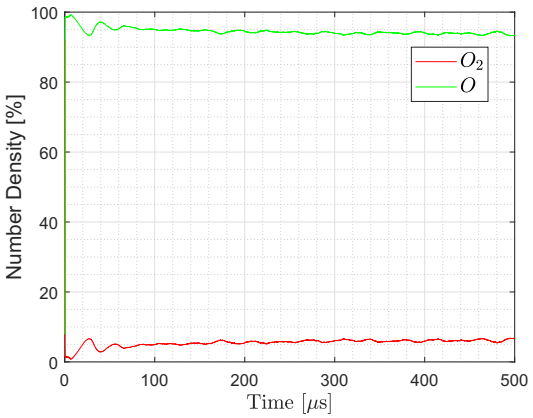
1st Stage Reactive Model Versus 1st & 2nd Stages Reactive Model

This initial analysis focuses on evaluating the discharge characteristics when solely employing the 1st stage reactive model in contrast with the utilisation of both the 1st and 2nd stage reactive model. By conducting this comparison, the significance of having a complete reactive model can be analysed.

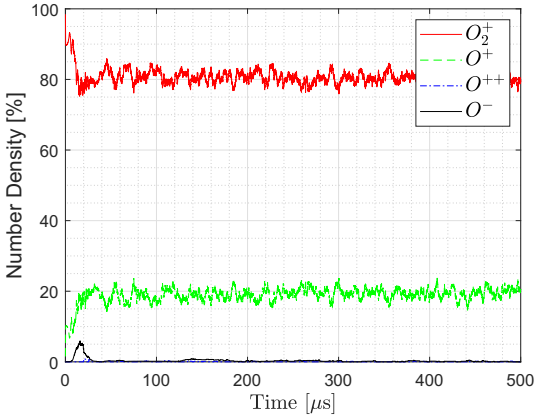
The results are presented in Figure 3.9. The relative number density (in %) for the neutrals and ions population is shown. Figures 3.9c and 3.9d depict how, with only the 1st stage, monoatomic O dominates the neutral population. This dominance arises because the reactions involving monoatomic O are not considered, leaving these species without other possible reactions. Regarding ions, O_2^+ accounts for 80% of the total population, as additional reactions that could generate O^+ or other ions are not included, resulting in an unbalanced plasma plume.

In contrast, when employing the 1st and 2nd stage reactive model, the monoatomic O species can now react and become O^+ ions.

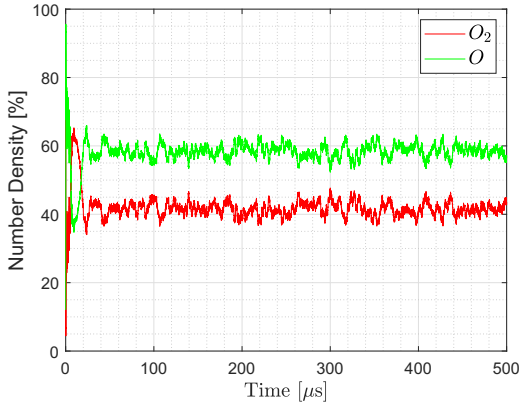
Based on the differences obtained, it becomes evident that incorporating the 2nd stage is needed for establishing a comprehensive and realistic formulation capable of simulating the behaviour of oxygen-fuelled thrusters accurately. For that reason, the subsequent sections will present the results obtained using both, the 1st and 2nd stages. These conclusions are parallel to those obtained with water vapour, as will be seen in Section 3.2.2.2.



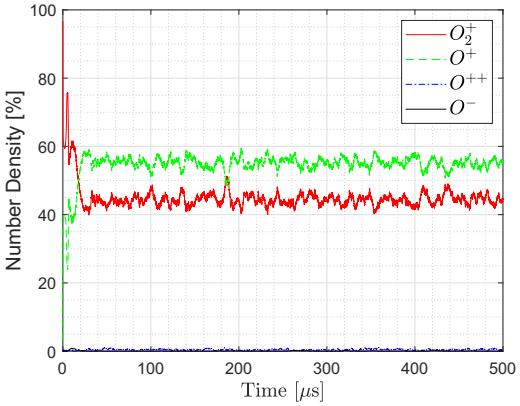
(a) 1st stage - neutrals relative density



(b) 1st stage - ions relative density



(c) 1st & 2nd stage - neutrals relative density

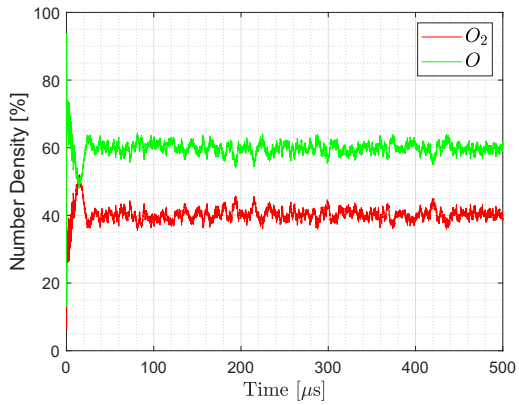


(d) 1st & 2nd stage - ions relative density

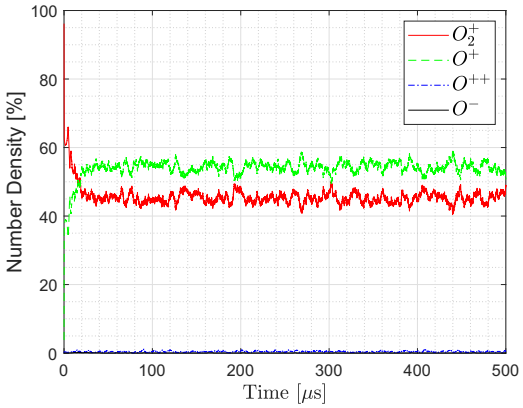
Figure 3.9: Comparison of results obtained from *PlasmaSim* 0-dimensional simulations, considering solely the 1st stage reactive model versus utilising both the 1st and 2nd stage reactive model, using oxygen as the propellant. The simulations employ an electron temperature of $T_e = 20$ eV, maintaining the energy-conserved approach.

Effects of the Energy-Conserved Versus Energy-Fixed Approaches

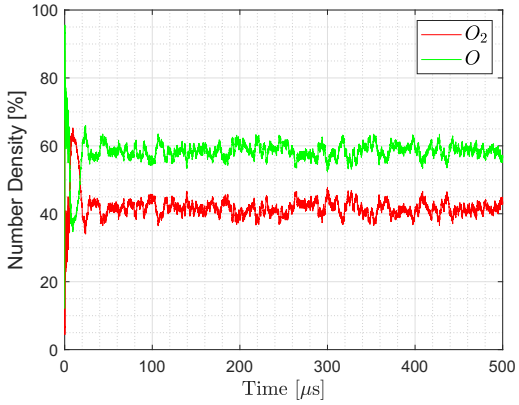
The results obtained with *PlasmaSim 0D*, using either the energy-fixed or energy-conserved approaches, are presented in Figure 3.10. An electron temperature of $T_e = 35$ eV is chosen to exemplify the results. Both, the final number densities of neutrals and ions and their ratio, show minimal differences between the two methods. This is thought to be due to the fact that electrons are highly mobile, so the rate at which they hit the wall and/or reach out of the boundaries of the domain is much greater than the reaction collision rate. As the electrons get thermalised as part of the boundary conditions to the electron temperature selected by the user, this phenomenon ultimately dictates the final temperature of the electrons and not the temperature at which these particles are created after a collision.



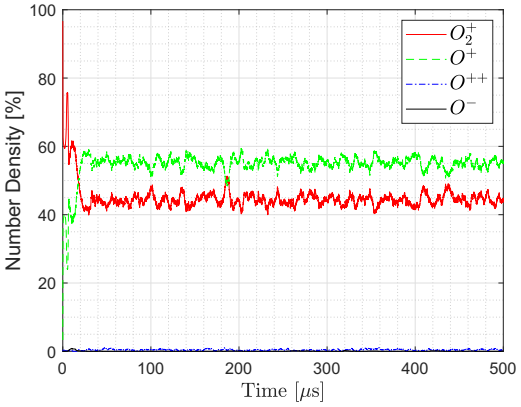
(a) Energy-fixed - neutrals relative density



(b) Energy-fixed - ions relative density



(c) Energy-conserved - neutrals relative density



(d) Energy-conserved - ions relative density

Figure 3.10: Species relative density values of a water electrolysis (oxygen-fuelled) Hall Effect Thruster as predicted by *PlasmaSim* 0-dimensional code. Simulation obtained using the energy-fixed (Figures 3.10a and 3.10b) and the energy-conserved (Figures 3.10c and 3.10d) approaches, with an injected electron temperature of $T_{e,in} = 35$ eV.

In any case, as the energy-conserved approach is a more realistic scenario and there are no differences in computational time using either of the two approaches, the results presented hereafter will include the energy-conserved method unless otherwise specified.

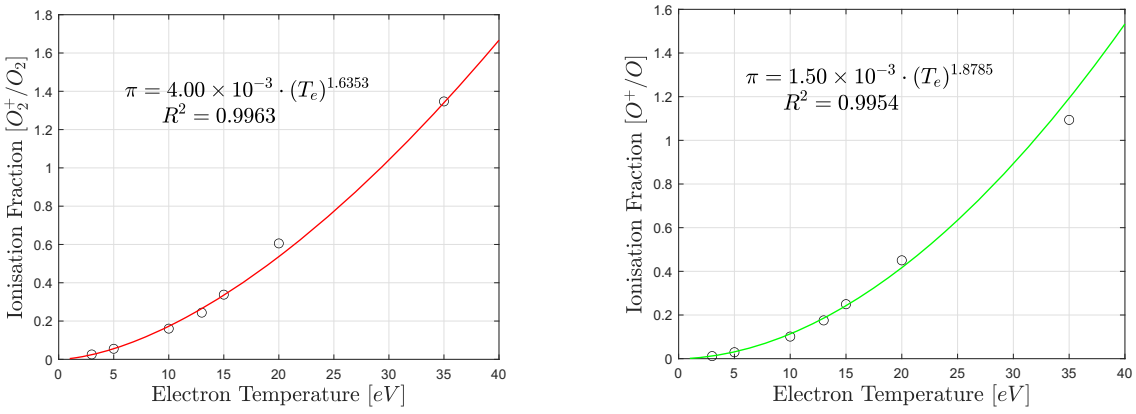
Notice that, although the results are shown for oxygen as an example, the same conclusions apply to the case of water vapour.

Lastly, it is important to note that, as illustrated in Figures 3.9 and 3.10, the ion population predominantly consists of O_2^+ and O^+ particles. Negative and double-charged ions appear to be negligible under these discharge conditions. These findings will be experimentally validated and compared with these results coming from the numerical model in Sections 4.3.2.1 and 4.3.2.5, respectively.

Effects of the electron temperature (T_e)

Table 3.9: Ratios of the main oxygen ion species (O_2^+/O^+) as a function of the user-input electron temperature T_e as suggested by the *PlasmaSim* 0-dimensional formulation.

Electron Temperature [eV]	**13**	**15**	**20**	**35**
O_2^+/O^+	69/100	70/100	76/100	83/100



(a) O_2 (b) O

Figure 3.11: Ionisation fraction of the different species in the oxygen discharge as a function of the user-input electron temperature (T_e) selected in the *PlasmaSim* 0-dimensional formulation.

In *PlasmaSim* 0D, the user input of T_e is quite relevant, not only because it sets the initial electron temperature but also because electrons are released from the walls at this specific temperature (see Section 3.1.1.5). By selecting a different T_e, different conditions within the thruster can be simulated, which in practice are influenced by the discharge power of the thruster.

Beginning with an investigation into the impact on ions, particularly focusing on their interrelation, Table 3.9 demonstrates the consequences of varying T_e for oxygen within the 0D model. Double ion ratios have been omitted, given their insignificant contribution to the overall species population in the plasma (refer to Figure 3.10). These findings elucidate that an elevated T_e leads to an increase in the O_2^+/O^+ ratio. This can be attributed to the evolution of molecular oxygen cross-section as a function of the electron temperature: the empirical cross-sectional data presented in Figure 3.6a shows that raising the electron temperature (T_e) augments the ionisation cross-section of molecular oxygen, while the dissociation cross-section remains constant. The 0D model effectively captures these phenomena, as depicted in Table 3.9. These conclusions will be experimentally validated in

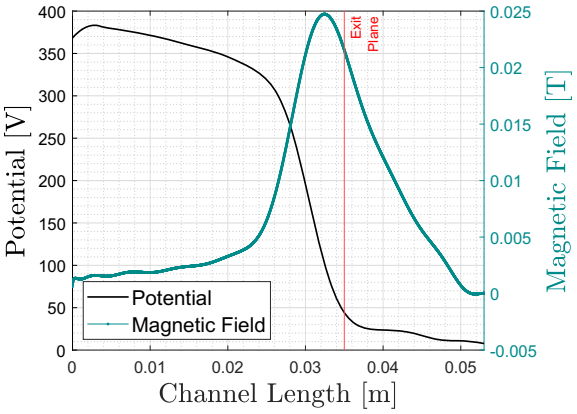
Section 4.3.1.6.

Regarding the ionisation fraction (π) of the species in the oxygen discharge, they all seem to follow an exponential fitting between π and T_e. As observed in Figure 3.11, a fitting of the type: $\pi = AT_e^{-B}$ for T_e in the range of $T_e = 3 - 35$ eV seems to correlate very well with these variables, with most Coefficients of Determination (R^2) being close to 1. Notice that, in a logarithmic scale, the power-law relationship described here will appear as a straight line. Similarly, the effects of T_e on the water vapour simulations will be demonstrated in Section 3.2.2.2.

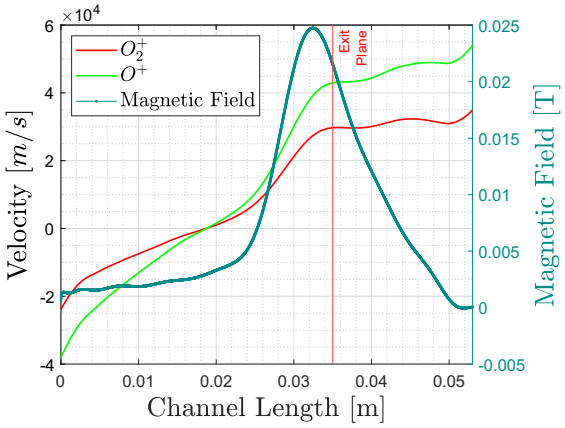
2-Dimensional (2D) Model

The results of the 2D model (combined with the 0D model as described in Section 3.2.1.1) are presented here using oxygen (water electrolysis) as a propellant. Figure 3.12 shows the 1D time-averaged axial profiles of the most relevant plasma properties, which are radially and time-averaged. Artificial sheath affects at the anode are not included.

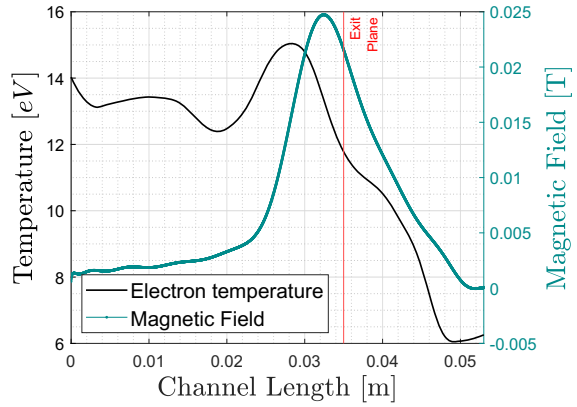
To start with, Figure 3.12 illustrates the axial profiles of the electric potential, ϕ (Figure 3.12a); the fluid velocities of ion species, $v_{\mathrm{i,O_2^+}}$ and $v_{\mathrm{i,O^+}}$ (Figure 3.12b); and the electron temperature, T_e (Figure 3.12c). Specifically, Figure 3.12a shows a sharp drop in ϕ just upstream of the thruster chamber exit, corresponding to the peak of E_x. This aligns with the position of the magnetic field peak, typical in HET discharges. The occurrence of the electric potential drop mainly inside the thruster chamber is characteristic of conventional HETs fuelled by noble propellants, owing to the upstream position of the B peak relative to the channel exit. An anode sheath is also evident, with a ϕ drop of around 60 V, approximately 3-4 times the local T_e, as depicted in Figure 3.12c. The relatively minor decay of T_e from its maximum value toward the anode can be linked to the low cross-section of electron-O_2 ionisation collisions compared to typical HET propellants [163]. This same rationale has been used to explain why experimentally observed Te profiles are wider in krypton discharges than in xenon ones [190]. This outcome also suggests the importance of including excitation collisions in simulations, which can significantly influence the power balance [163].



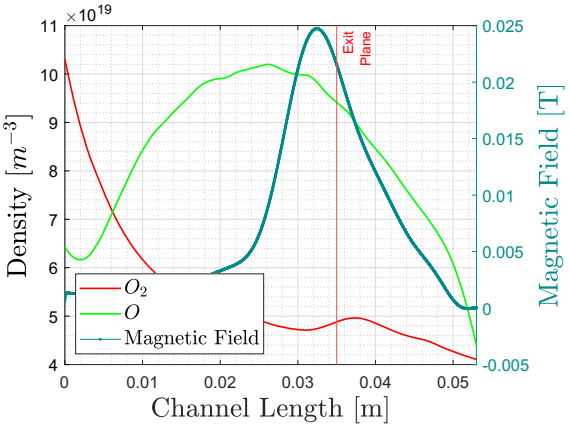
(a) Potential: ϕ



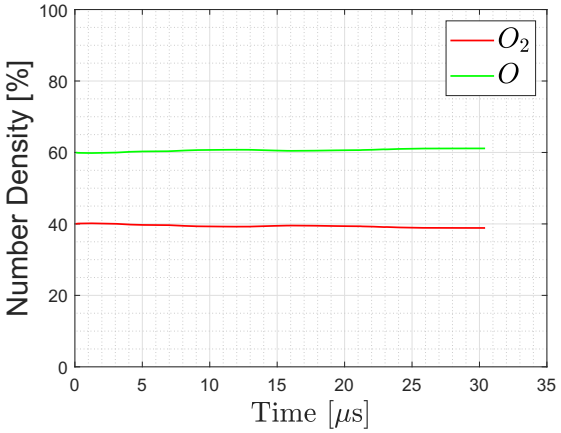
(b) Ion velocities: ui_x



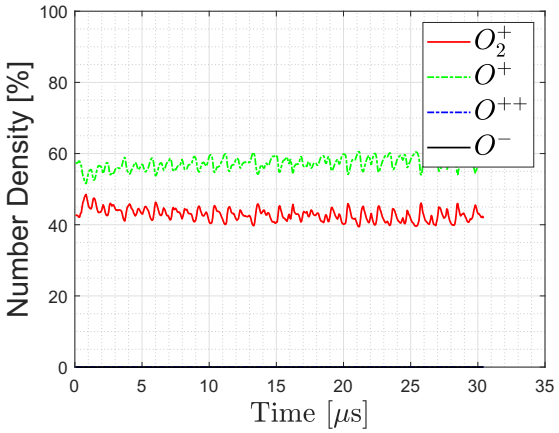
(c) Electron temperature: T_e



(d) Neutral densities: n_n



(e) Neutral relative density



(f) Ions relative density

Figure 3.12: 1-dimensional time-averaged axial profiles of the most relevant radially-averaged plasma magnitudes using oxygen (from water electrolysis propulsion) as propellant.

In Figure 3.12b, the downstream-most velocity of O_2^+ ions is approximately 35 km/s, while that of O^+ ions is 50 km/s, both with a turning point at around $x = 0.02$ m. The velocity range found at the anode is considered too high to be physical and will be further studied in future work.

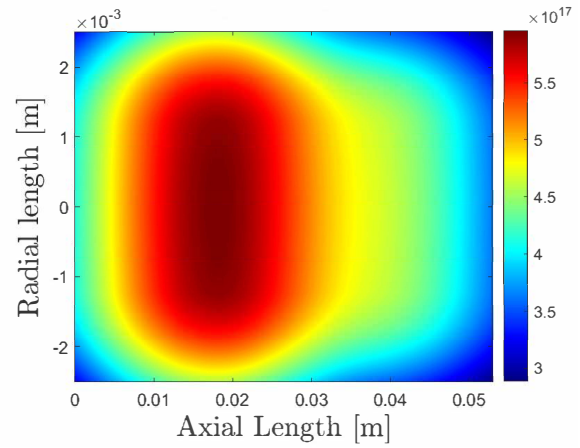
Figure 3.12d show the profiles of neutral density for the species O_2 and O. Distinct trends

for O_2 and O appear in these plots: while O_2 originates from the anode and exhibits a declining density profile along the channel due to diverse ionisation and dissociation events, the neutral density profile of O peaks mid-channel. This peculiarity arises from the source of particle creation: O is generated from a dissociation or ion dissociation event that occurs within the channel, whereas O_2 is injected at the anode plane.

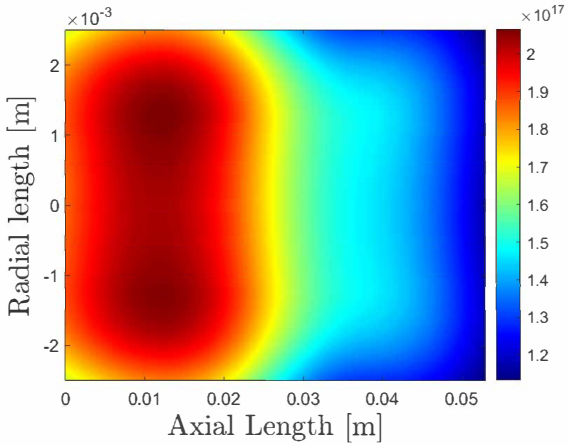
Similarly to the results presented with the 0D model (Figure 3.10), Figures 3.12e and 3.12f show the relative densities of neutrals and ions. Both the 0D and 2D models yield comparable outcomes regarding species distribution within the discharge, as evident in Figures 3.12e and 3.12f. This consistency in results significantly enhances their credibility. Under the operating conditions outlined in Table 3.7, the neutral species O_2 and O are present in a 40-60% proportion (as depicted in Figure 3.12e), mirrored by the ion species O_2^+ and O^+ (40-60%, as presented in Figure 3.19f).

Figure 3.13 presents the 2D profiles of the plasma density (electron density, Figure 3.13a, O_2^+ ion density, Figure 3.13b, and O^+ ion density, Figure 3.13c). The bulk of the plasma is located in the middle of the channel, as shown in Figure 3.13a. However, the contribution of the O_2^+ and O^+ ions appears different: while O^+ ions are strictly located in the middle of the channel (peaking around $x = 0.020$ m), O_2^+ ions seem to be created closer to the anode (peaking around $x = 0.013$ m). This is a consequence of the neutral density profiles of O_2 and O (Figure 3.12d). Also, the number density of O^+ ions seems to be confined within the core of the channel width, whereas the number density of O_2^+ ions is not as contained within the radial length. Consequently, there is still a relatively large number density of O_2^+ ions near the walls. This is thought to be due to the ion recombination processes with the wall, which increases the number density of O_2 neutrals at these locations.

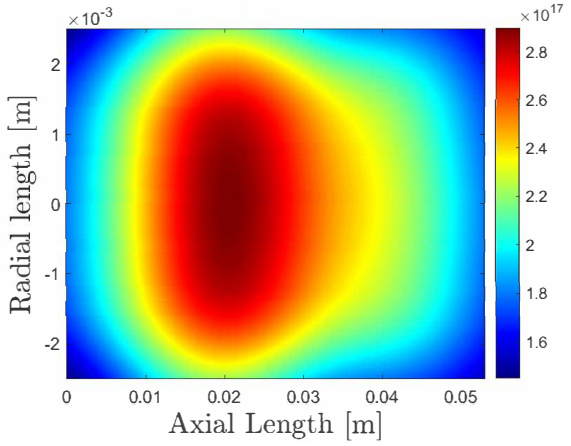
To complement the ion velocity profile (Figure 3.12b), the Velocity Distribution Function (VDF) of O_2^+ and O^+ is depicted in Figure 3.14. Here, the Z-axis represents the number density of each species as a function of the axial length (X-axis), while the Y-axis denotes the axial velocity. It is observable from this plot that the velocity directionality changes at the location $x = 0.025$ m, corresponding to where the magnetic field begins to increase (Figure 3.12a).



(a) Electron density: n_e

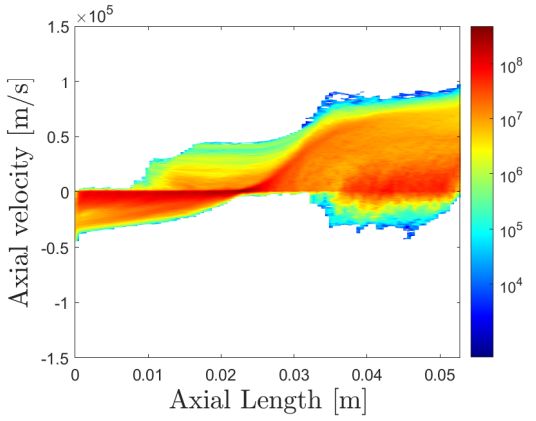


(b) Ion density O_2^+: n_i, O_2^+

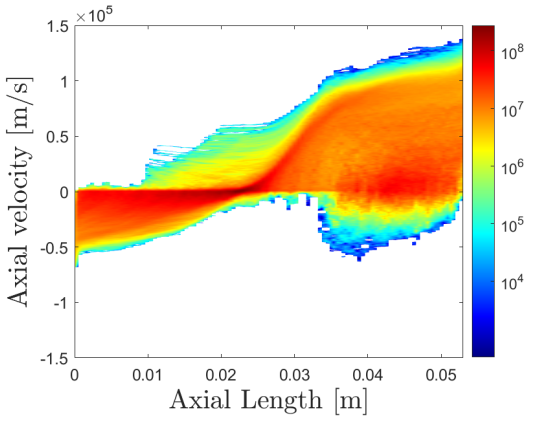


(c) Ion density O^+: n_i, O^+

Figure 3.13: 2-dimensional time-averaged axial profiles of the radially-averaged plasma densities using oxygen (from water electrolysis propulsion) as propellant.



(a) O_2^+



(b) O^+

Figure 3.14: Velocity Distribution Function (VDF) of the oxygen plasma plume (O_2^+ and O^+). The Z axis represents the number density of the species as a function of the axial length (X-axis), while the Y axis shows the axial velocity of the species.

The ions exhibit stronger acceleration toward the cathode compared to the anode, as expected,

although there is a distinct population of particles that undergo further acceleration in both directions. This phenomenon is attributed to fluctuations in plasma properties during the thruster's breathing mode oscillation.

A comment on the breathing mode of the thruster should also be included. In these simulations, the characteristic breathing mode oscillation (typically observed as a low-frequency discharge current oscillation in HETs) was not discernible. Instead, a higher-frequency oscillation, identified as the Ion Transit Time mode, was observed. Note that the breathing mode represents the periodic depletion and refilling of neutral gas in the ionisation region, and some thrusters exhibit a 'soft' breathing mode oscillation that can be challenging to detect. Experimental data is essential to further evaluate both the breathing mode and the Ion Transit Time mode oscillations, as these phenomena affect the overall stability and efficiency of thruster operation.

Figure 3.15 displays the fraction of total power losses associated with the different reactions existing in the discharge. An important distinction should be made: in reality, a dissociation event represents an inherent loss in the system, as it does not generate ions and therefore does not contribute to thrust. This loss is additional to the associated energy loss of the reaction itself. For that, it should be noted when analysing this study that solely the energy losses presented in Table 3.5, irrespective of whether if the reaction leads to ionisation or not, are being considered.

Finally, notice that the ionisation energy loss comes from the ionisation reaction and the ion-dissociation reaction, which is equally distributed into the ionisation loss and dissociation loss in the results shown in Figure 3.15.

In these conditions, the dissociation losses amount to more than 10% of the total amount. The largest fraction of power is spent on the ionisation of monoatomic oxygen, as also observed in Ref. [163]. For diatomic oxygen, the excitation collision with the largest cross-section is $O_2 + e \rightarrow O_2^*(B^3\Sigma_u^-) + e$, resulting in an energy loss of 6.12 eV. This value is approximately half of the energy loss associated with ionisation (12.1 eV) and one-third of the energy loss from ion dissociation (18.8 eV). Hence, the results from Figure 3.15, which indicate that the excitation losses of O_2 are one-third of the power losses from ionisation, appear consistent.

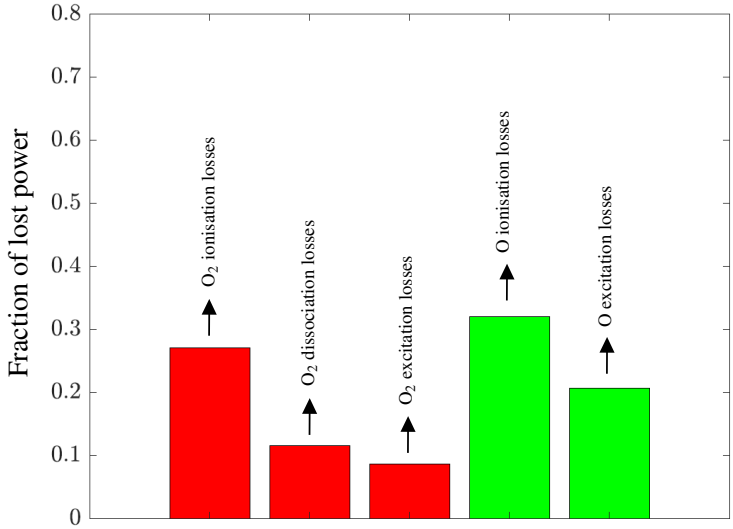


Figure 3.15: Fraction of total power losses associated with inelastic collision events, for the case of oxygen (propellant of water electrolysis propulsion).

Overall, the power losses from the reactive model, along with the different reactions that do not contribute to thrust, are among the main efficiency penalties associated with the usage of molecular propellants [44]. Excitation losses are significant, with atomic excitation collisions being predominant, as observed in Ref. [163]. The combined cost of excitation collisions amounts to 30% of the total energy losses from all the inelastic collisions.

A direct comparison between these simulations and the experiments conducted in oxygen-fuelled HETs (see Chapter 4.2) is performed in Sections 4.2.2.9 and 4.3.2.5. More specifically, the performance (in terms of thrust, anode specific impulse, and anode thrust efficiency) and the plasma plume composition of the thruster *WET-HET* fuelled by oxygen are compared between the predictions from the numerical model and the experimental part of this activity, thus validating the results obtained here. Note that an analytical verification of the reactive model is also available in Appendix A.2.2.

3.2.2.2 Water Vapour-Fuelled Hall Effect Thrusters

In a similar fashion as with water electrolysis (previous Section 3.2.2.1), this section provides an overview of the outcomes obtained from the ultimate version of *PlasmaSim*, this time employing water vapour as the anode propellant. Initially, the results obtained from the 0D model are shown. Then, the findings of the 2D model, supported by the 0D outputs (see Section 3.2.1.1), are presented.

0-Dimensional (0D) Model

1st Stage Reactive Model Versus 1st & 2nd Stages Reactive Model

Section 3.2.2.1 highlighted the necessity of incorporating the 2nd stage reactive model of oxygen to ensure a consistent formulation for the distribution of plume particles.

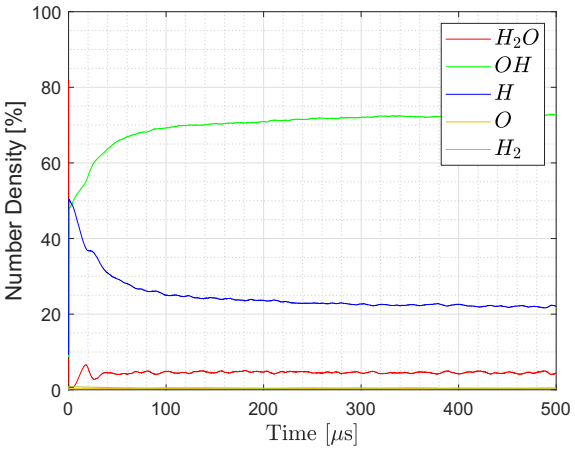
A similar conclusion arises when analysing the results obtained with water vapour (Figure 3.16). Utilising only the 1st stage results in a neutral population dominated by OH and H, originating from the dissociating reaction of H_2O. Since there are no further ionisation reactions from these neutrals, the ion population mainly consists of H_2O^+.

However, including both the 1st and 2nd stages leads to a different relative distribution of neutrals and ions in the plume. In this scenario, the majority of neutrals are H particles, while the ion population is distributed among OH^+, H_2O^+ and O^+.

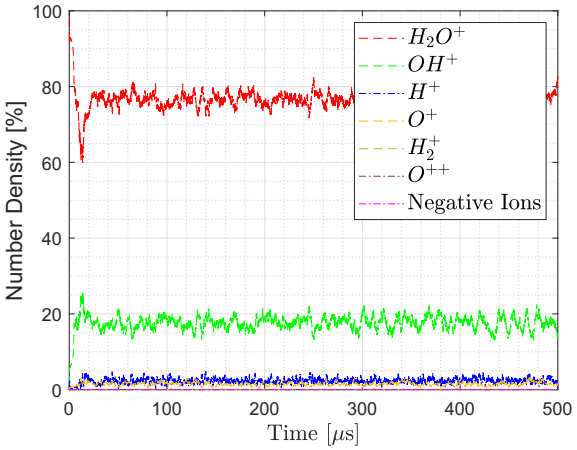
These differences underscore the necessity of incorporating the 2nd stage for water vapour as well, to ensure a consistent representation of the species present in the plasma plume of the thruster.

Effects of the Electron Temperature (T_e)

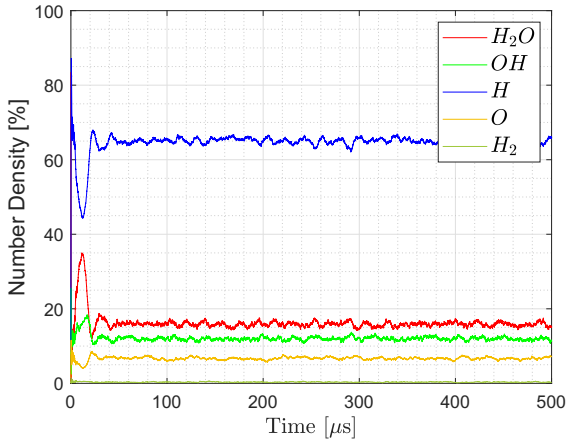
To complement the results obtained on the effects of the electron temperature in the oxygen discharge shown in Section 3.2.2.1, the same analysis is presented when choosing water vapour as the propellant.



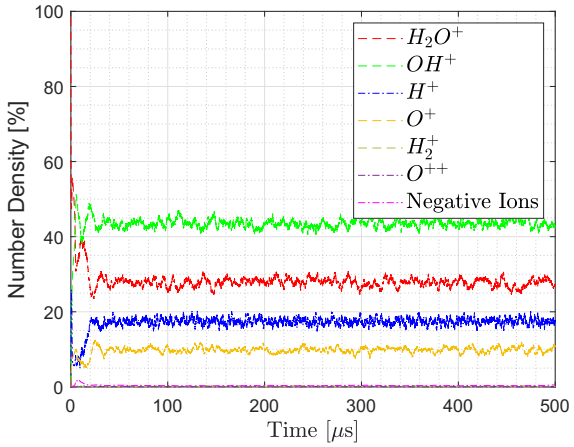
(a) 1st stage - neutrals relative density



(b) 1st stage - ions relative density



(c) 1st & 2nd stages - neutrals relative density

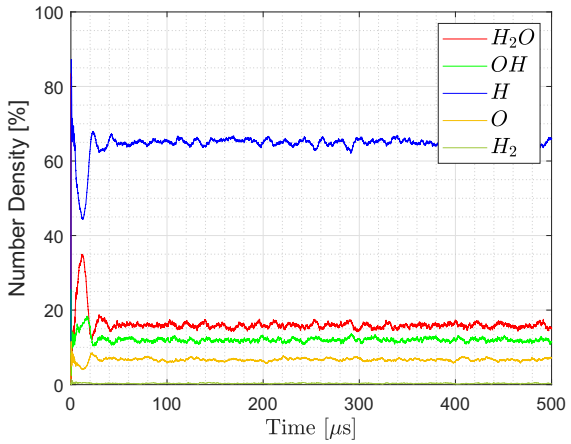


(d) 1st & 2nd stages - ions relative density

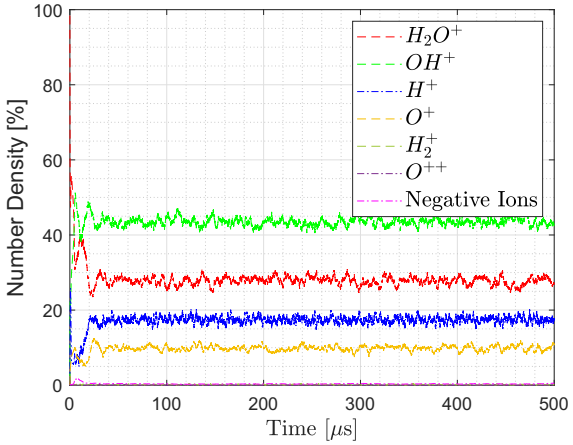
Figure 3.16: Comparison of results obtained from *PlasmaSim* 0-dimensional simulations, considering solely the 1st stage reactive model versus utilising both the 1st and 2nd stages reactive model, using water vapour as the propellant. The simulations employ an electron temperature of $T_e = 20$ eV, maintaining the energy-conserved approach.

To start with, Figure 3.17 visually compares the results obtained from the 0D model for two electron temperatures ($T_e = 20$ eV and $T_e = 35$ eV). Complementing this analysis, Table 3.10 shows the tabulated ratios of the ion species with respect to the electron temperature.

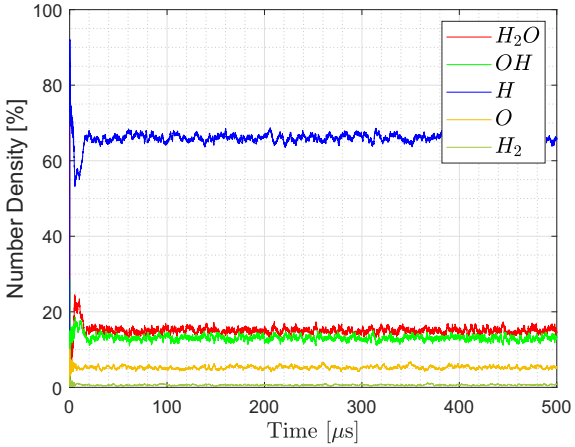
At first glance, the impact of changing the electron temperature is not very noticeable in Figure 3.17. However, the ratios do change depending on the electron temperature, as presented in Table 3.10. This is due to the cross-sectional area of the water vapour molecule varying with the electron temperature (Figure 3.6b). This graph reveals a steeper increase in the dissociation reactions of water vapour compared to the increase in the ionisation cross-section within the range of $T_e = 20 - 40$ eV.



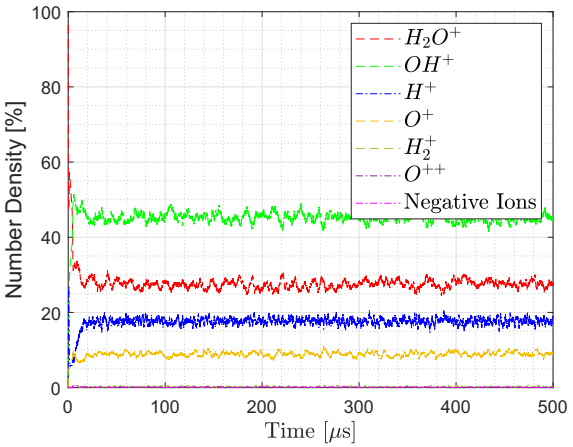
(a) $T_e = 20$ eV - neutrals relative density



(b) $T_e = 20$ eV - ions relative density



(c) $T_e = 35$ eV - neutrals relative density



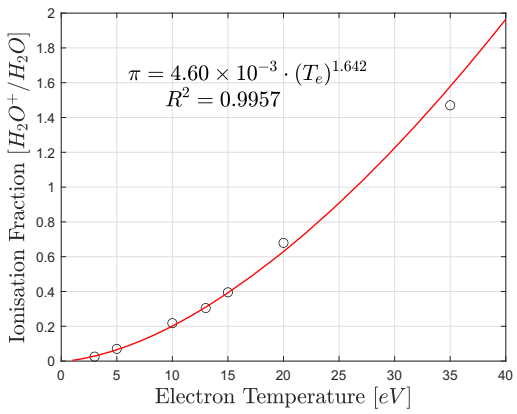
(d) $T_e = 35$ eV - ions relative density

Figure 3.17: Relative density values of a water vapour species in a Hall Effect Thruster discharge as predicted by the 0-dimensional model. Simulation obtained using the energy-conserved approach and an user-input electron temperature of $T_e = 20$ eV for Figures 3.17a and 3.17b and $T_e = 35$ eV for Figures 3.17c and 3.17d.

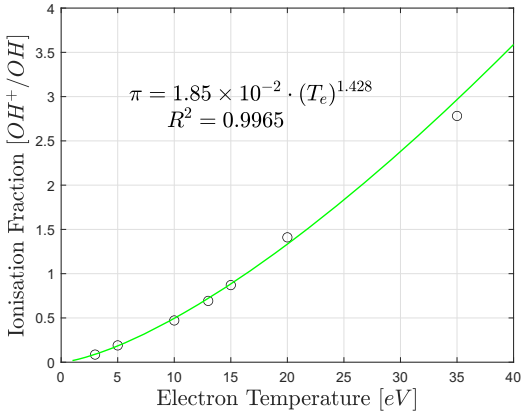
Table 3.10: Ratios of the main water vapour ion species as a function of the user-input electron temperature T_e.

Electron Temperature [eV]	**13**	**15**	**20**	**35**
H_2O^+/OH^+	66/100	66/100	64/100	60/100
H_2O^+/H^+	271/100	168/100	161/100	154/100
H_2O^+/O^+	248/100	268/100	285/100	307/100

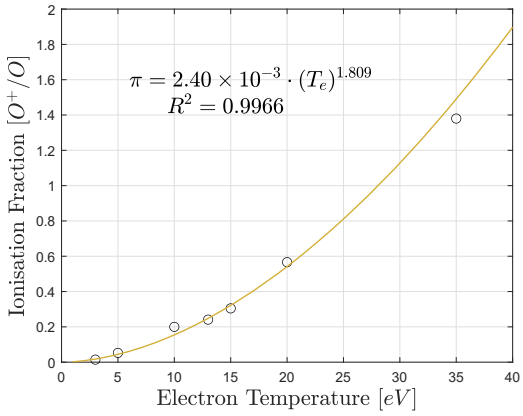
This trend applies to all the species except for O^+, whose cross-section starts with a slower slope in that range. The results of the ratios shown in Table 3.10 as a function of the electron temperature correlate this behaviour of the plasma with the experimental cross-sectional data for the water molecule.



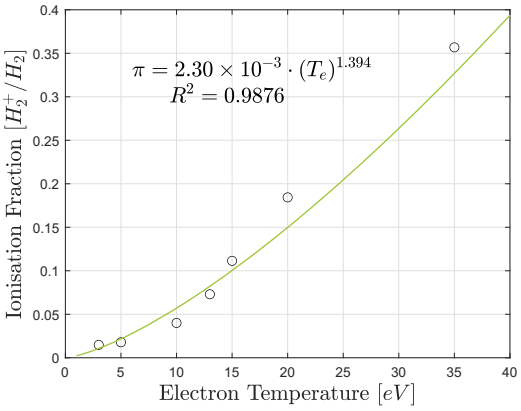
(a) H_2O



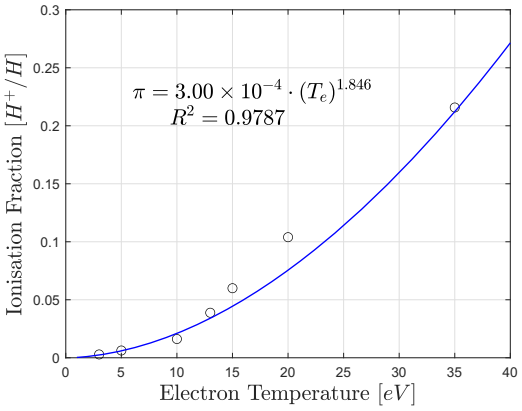
(b) OH



(c) O



(d) H_2

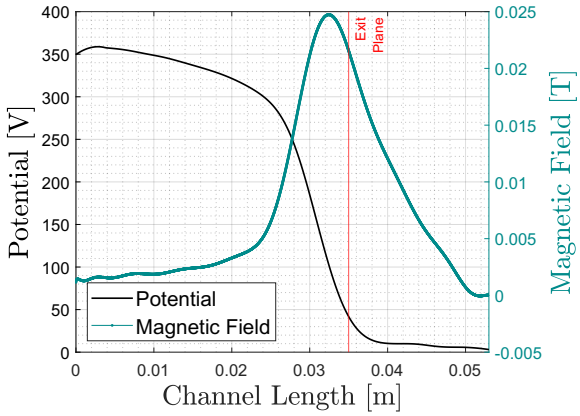


(e) H

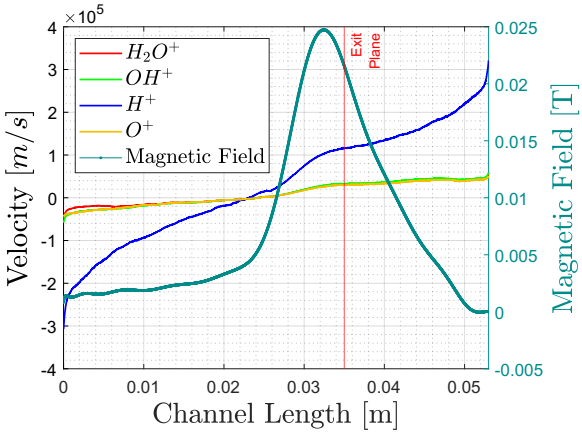
Figure 3.18: Ionisation fraction (π) of the different species in the water vapour discharge as a function of the user-input electron temperature (T_e) selected in *PlasmaSim 0D*.

Lastly, Figure 3.18 presents the ionisation fraction π as a function of the electron temperature T_e. Similarly to the case observed with the oxygen simulations, π fits an exponential function of the type: $\pi = AT_e^{-B}$ ($R^2 \approx 1$).

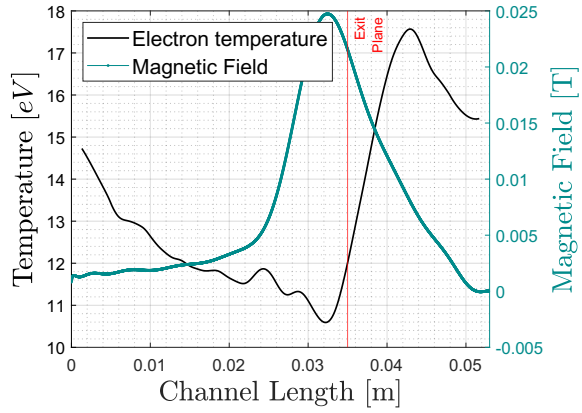
2-Dimensional (2D) Model



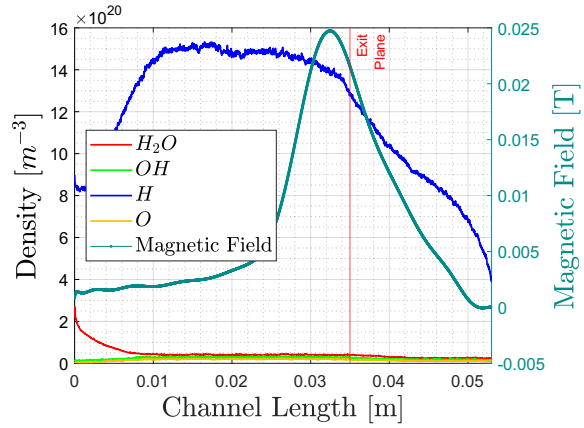
(a) Potential: ϕ



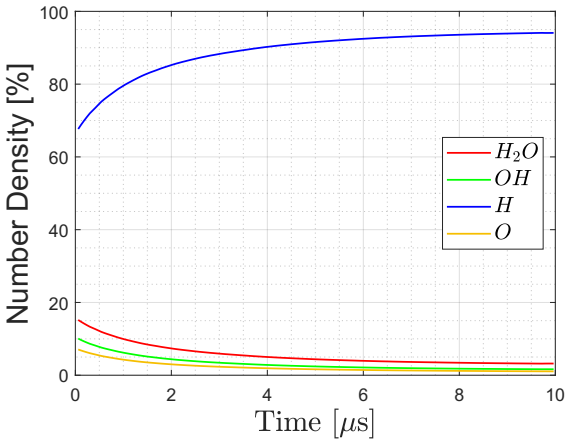
(b) Ion velocities: ui_x



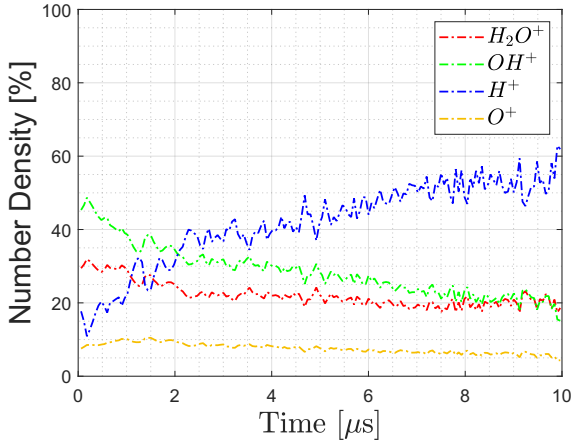
(c) Electron temperature: T_e



(d) Neutral densities: n_n



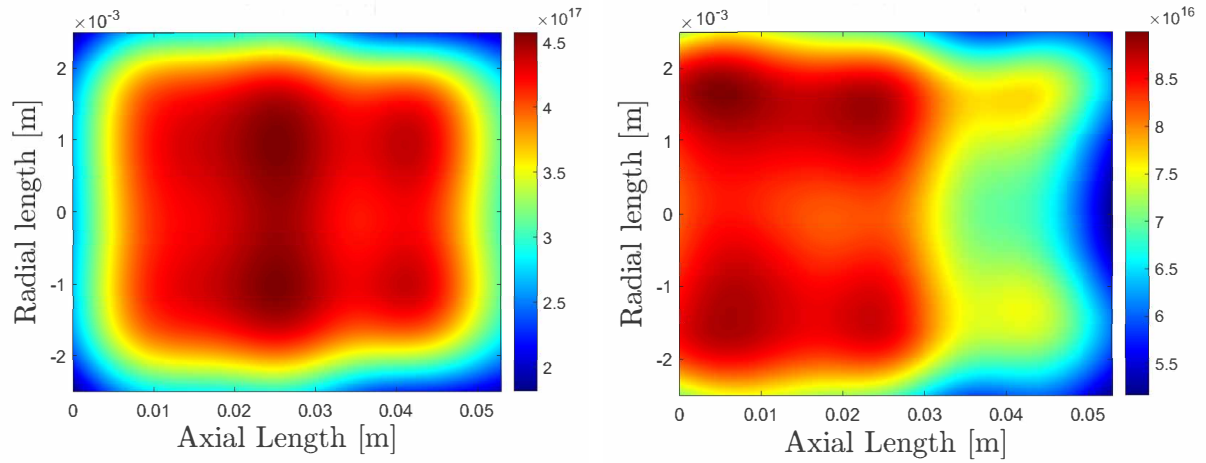
(e) Neutral relative density



(f) Ions relative density

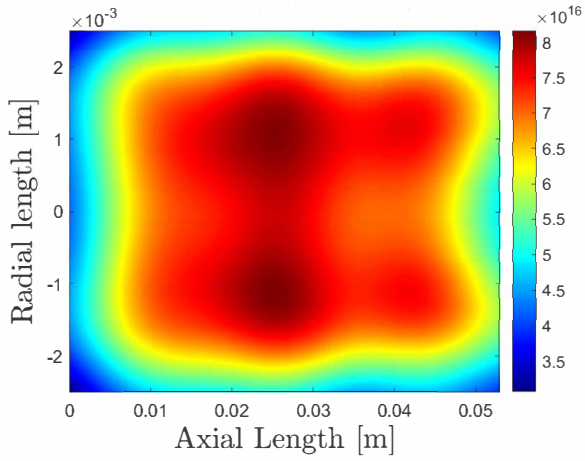
Figure 3.19: Time-averaged axial profiles of relevant radially-averaged plasma magnitudes from the pseudo-2-dimensional model of the discharge with water (for water vapour propulsion).

Similarly to the results obtained with oxygen, the 2D water vapour simulations are presented in Figures 3.19 and 3.20.



(a) Electron density: n_e

(b) Ion density H_2O^+: n_i, H_2O^+



(c) Ion density OH^+: n_i, OH^+

Figure 3.20: 2-dimensional time-averaged axial profiles of the radially-averaged plasma densities using water vapour as propellant.

Figure 3.19a displays the electric potential ϕ, while Figure 3.19b showcases the ion velocity profiles for various species within the discharge. Figure 3.19c illustrates the electron temperature. Similar to the oxygen scenario, there is a potential drop along the channel, sharply declining where the magnetic field begins to intensify. However, in contrast to oxygen, the plasma predominantly comprises more ion species with varied relative masses (H_2O^+, OH^+, H^+, O^+). Notably, H^+ particles, being lighter, experience faster acceleration within the domain compared to heavier particles like H_2O^+, OH^+, and O^+. The average velocity of H^+ species at the exit of the channel is 300 km/s, whereas H_2O^+ and OH^+ species have an exit velocity of around 40 km/s.

Regarding the neutral density profiles, depicted in Figure 3.19d, akin to oxygen simulations, the propellant density (H_2O) declines within the domain, peaking at the anode plane upon injection.

Other neutral species originate from dissociation or ion dissociation events, peaking within the channel.

The relative species density of neutrals and ions alongside the profiles of neutral densities are showcased in Figures 3.19e and 3.19f. Predominantly, the neutral density consists of H species, similar to findings from the 0D model (Figure 3.17). The distribution of ion species, starting from the results of the 0D model, shows that H^+ ions are more predominant, with a similar distribution of species for the rest of the ions.

Figure 3.20 depicts the 2D profiles of electron density and two ion species (H_2O^+ and OH^+). The electron density peaks near the end of the channel, a consequence of the relative plasma density of the different species. H_2O^+ ions exhibit peaks within the channel, with two prominent peaks in the upper and lower radial domains. In contrast, the ion density of OH^+ and other ion species peaks near the end of the channel, where the ionisation rate is the highest (due to the strong magnetic field intensity in that location).

Similarly to Figure 3.14, Figure 3.21 illustrates the VDF of the most relevant water vapour ions present in the plume (H_2O^+, OH^+, and H^+). The velocity of H^+ ions, notably higher than that of other species, exhibits two directionalities with a turning point at $x = 0.025$ m, similar to the behaviour observed with oxygen. Once again, the presence of particles undergoing further acceleration compared to the bulk of the plasma is attributed to fluctuations in plasma properties resulting from the thruster's breathing mode oscillation.

Finally, Figure 3.22 shows the fraction of power losses from inelastic collisions in the discharge with water vapour as propellant. The largest fraction of power is spent on the ionisation and electronic excitation of atomic hydrogen. In particular, electronic excitation losses of H amount to more than 40% of the total inelastic power losses, indicating highly inefficient operation. The large fraction of H-excitation losses can be partly attributed to the relatively high density of atomic hydrogen neutrals.

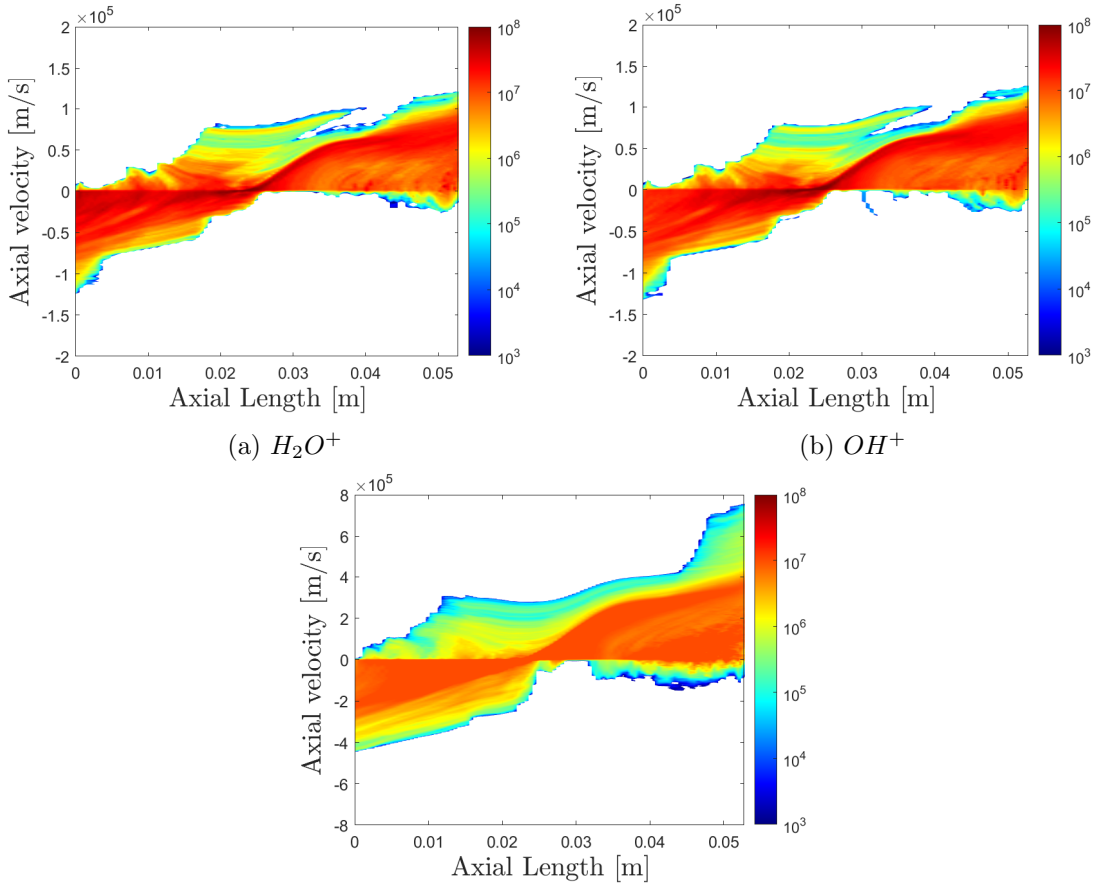


Figure 3.21: Velocity Distribution Function (VDF) of the water plasma plume (H_2O^+, OH^+ and H^+). The Z-axis represents the number density of the species as a function of the axial length (X-axis), while the Y-axis shows the axial velocity of the species.

For H_2O, the ionisation losses are the highest, closely followed by dissociation losses, with excitation losses being less significant. Regarding OH, power losses are primarily driven by the ionisation reactions, with dissociation and excitation losses playing minor roles. For monoatomic O, power losses are evenly distributed between ionisation and excitation losses. Note that, as depicted in Figure 3.17, the neutral and ion population of H_2 is orders of magnitude lower than other species, hence it is not included in the analysis.

The same conclusion regarding the breathing mode and Ion Transit Time mode observed with water electrolysis was also reached when using water vapor as a propellant (see Section 3.2.2.1).

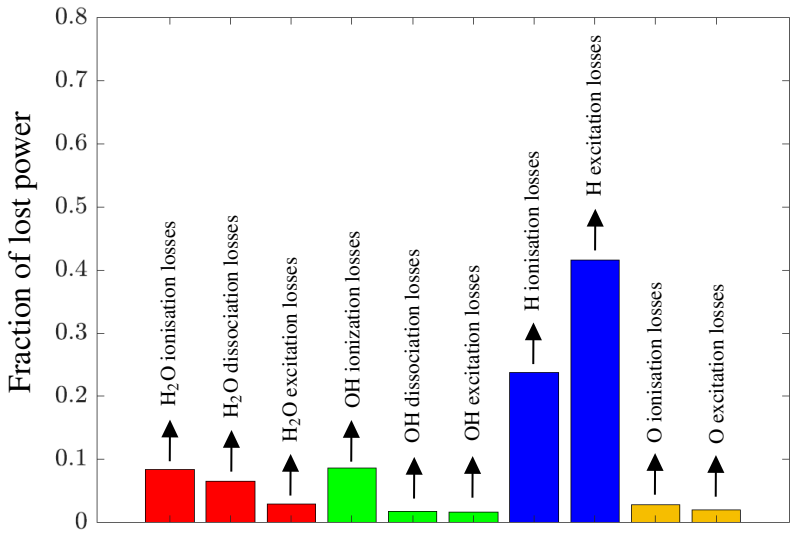


Figure 3.22: Fraction of total power losses associated with inelastic collision events, for water vapour propulsion.

Finally, note that performance predictions from these simulations and the experiments conducted in water vapour-fuelled HETs (see Section 4.6) are analysed in Section 4.6.2.4. More specifically, the results from the numerical model in terms of thrust, anode specific impulse, and anode thrust efficiency are compared with experiments, thereby validating the results presented in this section.

3.2.2.3 Radiofrequency (RF) Excitation

This section summarises the results on the computational analysis of RF excitation in HETs using the PIC code earlier described. The main goal is to establish a strong baseline to support the experimental part of this activity, which will be presented in Section 4.7. Note that the results presented here rely on the original version of *PlasmaSim* 2D code (Section 3.1.1), incorporating only the modifications to add RF excitation (Section 3.2.1.8) and the oxygen reactive model (Section 3.2.1.2) when this propellant is used.

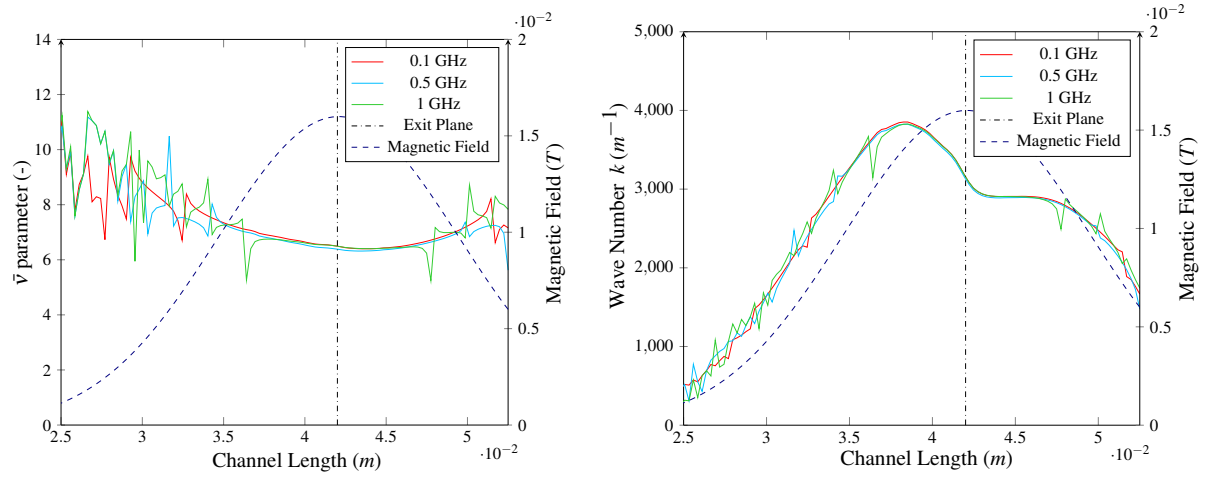
Low and High Temperature Limits

Section 1.2.2.2 concluded that the resonance condition of X-Waves depended on whether the low or high-temperature limits were applicable in the study case (see Table 1.2), based on the parameter $\bar{\nu}$ (Equation 1.5).

To understand which one is applicable in HETs, $\bar{\nu}$ was computed throughout the channel of a standard xenon-fuelled HET, the *SPT-100*, by numerically resolving Equation 1.4. The results are presented in Figure 3.23a. The magnetic field topology shown in Figure 3.23a and the axial plasma properties computed from the validation case (Figure A.6) were used to obtain $\bar{\nu}$.

Once $\bar{\nu}$ is known, the wave number k can be calculated using Equation 1.5 (Figure 3.23b). $\bar{\nu}$ and k are both shown in the region of interest of the *SPT-100*, which is where the magnetic field is present ($x = 0.025 - 0.053$ m). For other regions, Equation 1.4 shows singularities as $w/w_{ce} \to \infty$, and the dispersion relation does not apply. Fluctuations in Figure 3.23a and Figure 3.23b appear when a main resonance condition $w_{RF} = n\ w_{ce}(B(x))$ is achieved. In reality, singularities are present there where $k \to \infty$ and $\bar{\nu} \to \infty$.

As seen in Figure 3.23a, $\bar{\nu}$ remains practically constant within the magnetic field region, showing values of $\bar{\nu} > 1$ for the whole domain, with low dependence on the RF frequency. As explained in Table 1.2, for these values, it is expected to achieve resonances at w_{ce} and higher harmonics. This condition was also checked when numerically resolving Equation 1.4.



(a) $\bar{\nu}$ distribution

(b) Wave number k distribution

Figure 3.23: Hot plasmas' theory $\bar{\nu}$ and wave number k distribution throughout the *SPT-100* channel. Results published in [1].

Notice that, due to the typical Gaussian shape of the magnetic field in HETs, the resonance condition of $w_{RF} = nw_{ce}(B(x))$ can be achieved at different locations of the channel by tuning the RF frequency and therefore changing where the ECR frequency and the RF frequency match. In practice, this provides a method to control the location of the resonance condition, allowing the power to be deposited, for instance, upstream of the ion acceleration region.

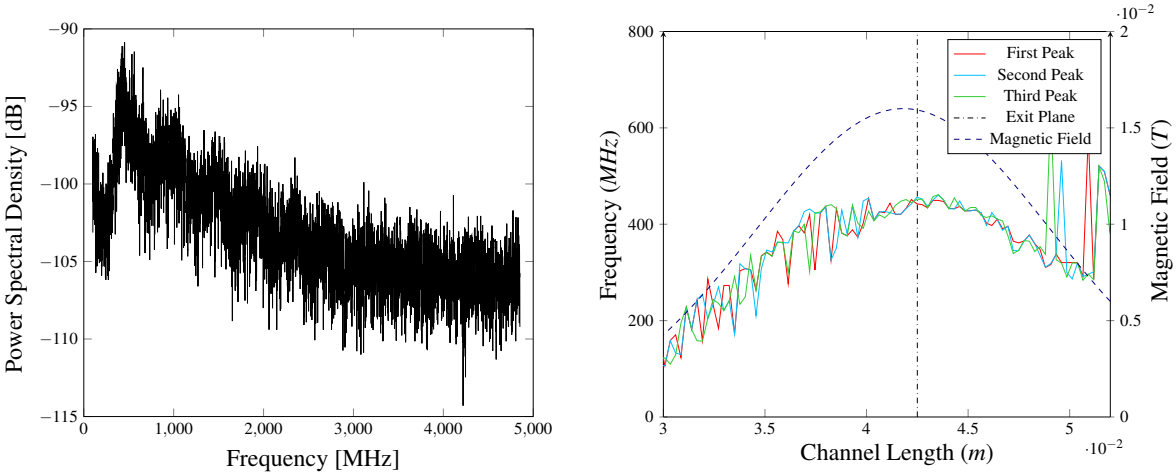
Using the relationship $w_{ce} = qB(x)/me$, the frequency range of the ECR condition is expected to approximately vary from $f_{RF} \approx 0 - 450$ MHz, between $x = 0 - 0.0425$ m. Higher harmonics of these frequency ranges might also benefit the thruster performance as remarked in Table 1.2, so the results presented account for higher frequencies as well to look for these harmonic resonances. In fact, any axial location in the magnetic field region can in principle be a resonance point ($k \to \infty$) where an accumulation of ECR harmonics takes place, and the TM quasistatic waves propagate according to Equation 1.4.

Spectral Analyses

Multiple sets of spectral analyses over the entire domain of the *SPT-100* have been performed in both unexcited and excited simulations. Due to the small and adaptable time and spatial step and the tracking of plasma properties at the superparticle level, *PlasmaSim* can detect any

possible intrinsic resonance behaviour in the plasma. In practice, the recording time step of the simulations is around $t_r = 10^{-10}$ s, which theoretically permits the identification of any peak in the power spectral density up to the Nyquist frequency ($f_{Ny} = \frac{1}{2t_r} = 5$ GHz). Data collected from simulations lasting a few tens of microseconds quickly becomes unmanageable at these recording time steps. For this reason, data is only collected within a specific time range, typically after the simulations have passed through the initial transient behaviour. In the presented results, data is recorded from $t = 2.0 - 2.5\ \mu s$. Different analyses over a larger time frame have led to the same conclusions, which gives confidence in the appropriateness of the selected recording window. In this context, electric field, potential, plasma density, ion and electron velocity, electron temperature, and other plasma properties have been analysed. Welch's approach [191] has been used to estimate the spectral density of plasma variables. To crosscheck the results and conclusions, Periodogram signal estimation [192] has also been applied. Both techniques have led to the same conclusions.

On the one hand, Figure 3.24 shows the spectrum analysis results of the **unexcited** *SPT-100* thruster, specifically for the electron temperature. On the other hand, the power spectral density at a particular location of the domain ($x = 0.043$ m) is shown in Figure 3.24a. This location is chosen to illustrate the identification of resonances in the plasma. Then, at every spatial location such as in Figure 3.24a, a spectrum analysis for the electron temperature is obtained. There, the maximum values of power spectral density are identified ("First Peak", "Second Peak", and "Third Peak"). Three maximums are collected to avoid uncertainty in identifying the maximum value and its associated frequency. Subsequently, these results are compiled in Figure 3.24b. It can be observed how the peaks in the power spectral density evolve according to the Gaussian magnetic field topology. More importantly, these peaks correspond to the ECR frequency, which is a function of the local value of the magnetic field at that particular location.



(a) Power Spectral Density at $x = 0.043$ m

(b) Power Spectral density peaks at different locations of the domain

Figure 3.24: Spectrum analysis of electron temperature for the unexcited *SPT-100*. Results published in [1].

On the other hand, Figure 3.25 shows the results obtained with a RF **excited** *SPT-100*, using a frequency of $f_{RF} = 450$ MHz and a cathode oscillating voltage of $V_{RF} = 10$ V. This specific case is shown due to the conclusions that will be later presented. The spectrum analysis over the magnetic field region shows a particular phenomenon where the resonances are locked into the excited frequency.

This frequency-locking phenomenon maintains the resonance condition throughout a larger section of axial locations, close to the vicinities where the magnetic field strength initially matched the ECR frequency (Figure 3.24b). Plasma benefits from this behaviour as the spatial location of the resonance increases, not limited to a discrete axial location where theoretically the magnetic field topology matches the RF wave at the ECR frequency. As the electron temperature indicates the electron energy, Figures 3.24b and 3.25 anticipate that by exciting the electrons at the local ECR frequency, their temperature (and hence, their energy) can increase as they absorb the energy deposited by the RF wave. This can potentially result in an improvement in thruster performance. These conclusions are further explored within the following sections.

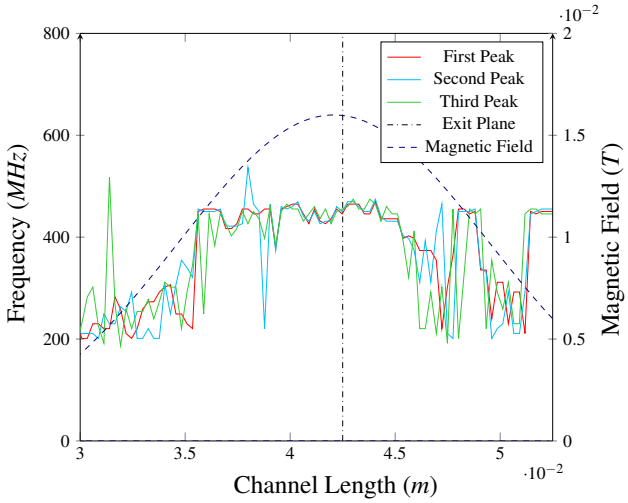


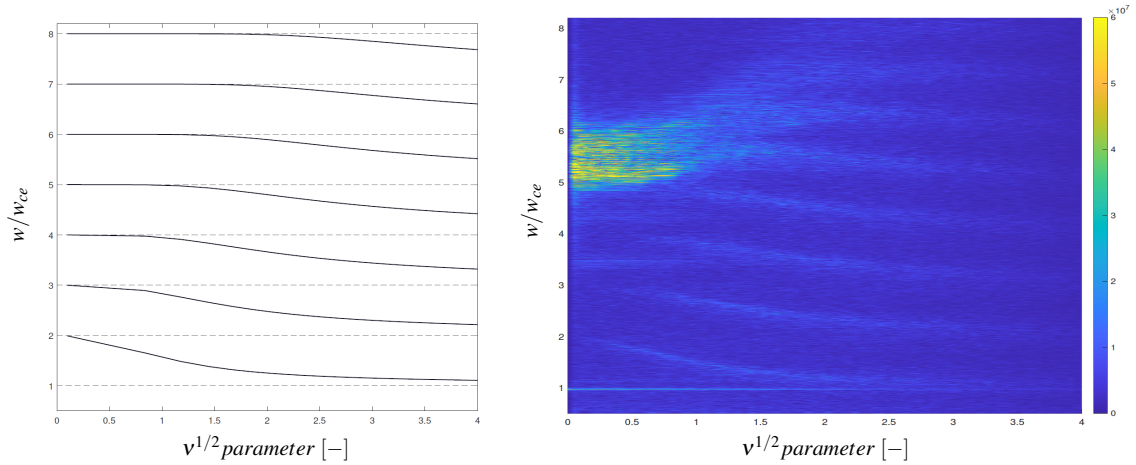
Figure 3.25: Spectrum analysis of a RF excited *SPT-100*, using a frequency of $f_{RF} = 450$ MHz and a cathode oscillating voltage of $V_{RF} = 10$ V. Peaks in power spectral density of electron temperature at different locations of the domain are represented. Results published in [1].

Dispersion Relationship

Equation 1.4 illustrates the theoretical dispersion relationship for the investigated TM quasistatic waves along a magnetostatic field (Bernstein modes). Following the spectrum analyses previously presented, the results discussed here aim to provide a deeper insight into the nature of these waves obtained with the computational model *PlasmaSim* in comparison with the theory of hot plasmas [68].

Constant Magnetic Field

Before analysing the results of the dispersion relationship for a more complicated scenario of a non-constant magnetic field such as in the *SPT-100* thruster, an example with a constant magnetic field is presented. This example uses the same inputs as the validation case (Table A.3) but changes the magnetic field topology to a constant value of $B = 0.016$ T instead of a Gaussian profile (Figure A.6c). The excitation frequency here is $f_{RF} = 478$ MHz, in order to match the exact ECR resonance throughout the longitudinal channel.



(a) Theoretical resolution of Equation 1.4 (b) Simulation results with an uniform $B = 0.016$ T

Figure 3.26: a) Theoretical dispersion relationship of TM Electrostatic waves in an uniform magnetostatic field compared with b) the results obtained in *PlasmaSim*. Simulation is excited by a quasistatic wave of $f_{RF} = 478$ MHz and $V_{RF} = 10$ V. Results published in [1].

The results are presented in Figure 3.26. On the one hand, Figure 3.26a shows the theoretical dispersion relationship of the TM quasistatic waves in a constant magnetic field by numerically solving Equation 1.4. Here, the wave frequency divided by the ECR frequency (w/w_{ce}) is represented as $\bar{\nu}^{1/2}$ (a value proportional to the wave number k). This representation is very similar to the one presented by Bittencourt [68] and shows a proportional relationship between w and k. With that, Figure 3.26a graphically represents the information collected in Table 1.2 and shows the dependency of the resonance harmonics on the values of $\bar{\nu}$. It can also be observed how the dispersion relationship flattens out as the excited harmonic increases. Specifically, for harmonics higher than 15 times the principal ECR frequency, results show that the dispersion relationship can be considered practically flat. Note that the principal resonance or frequency refers to the condition $w = Aw_{ce}$, with $A = 1$.

On the other hand, results from the simulations are presented in Figure 3.26b. Here, a 2D Fast Fourier Transform technique [193] is applied to convert a matrix of spatial/time dependent variables to the frequency/wave number domain. The electric field is displayed on this graph, but the results obtained are analogous when analysing other plasma properties, such as plasma density or electron temperature. In Figure 3.26b, a fair correlation with the theoretical evaluation of the waves (Figure 3.26a) can be observed. It can be seen that the values at ECR frequencies and

harmonics progressively rise when $\bar{\nu} \approx 2$ for the principal resonance, while going to higher $\bar{\nu}$ values and flattening out for higher resonances.

Simulations also present various observations not captured by the theoretical model. Firstly, for the principal resonance, a break-up region is observed when $\bar{\nu} = 2$, where part of the wave remains at the ECR frequency while another part goes to the second harmonic. Equation 1.4 predicts waves rising only to the second harmonic. Secondly, harmonics (from the 5th one and onwards) do not stay independent as theory predicted; instead, they accumulate at values of $\bar{\nu} < 1$.

Overall, the correlation between the theoretical evaluation and the simulation results instills confidence in the type of waves excited and the conclusions discussed so far in this thesis.

Gaussian Magnetic Field

Now, the results obtained with *PlasmaSim* using the Gaussian magnetic field of the *SPT-100* thruster are presented.

Figure 3.27 illustrates the results obtained using a wave frequency of $f_{RF} = 450$ MHz and $V_{RF} = 10$ V, as previously done with a constant magnetic field. However, in this case, the results reveal a flat dispersion relationship. This phenomenon is believed to occur because the 2D Fourier Transform considers the entire domain when representing the dispersion relationship, thus taking into account the complete set of resonance and harmonic conditions throughout the channel length. Due to the Gaussian magnetic field topology, in most parts of the domain, the excitation frequency ($f_{RF} = 450$ MHz) is a higher harmonic of the principal one, only matching at the peak magnetic field location ($B = 0.016$ T). Therefore, this scenario does not entirely represent the concept of waves being in resonance throughout the simulation domain, as was the case with the constant magnetic field topology.

As the dispersion relationship is flat, the group velocity of these waves ($v_g = \frac{dw}{dk}$) is zero, but with a finite phase velocity ($v_\varphi = \frac{v}{k}$). When these conditions are met, these waves are referred to as Zero-Group-Velocity (ZGV) waves [194]. These waves are characterised by their stationary nature and ability to locally confine energy, commonly found in most waveguide geometries.

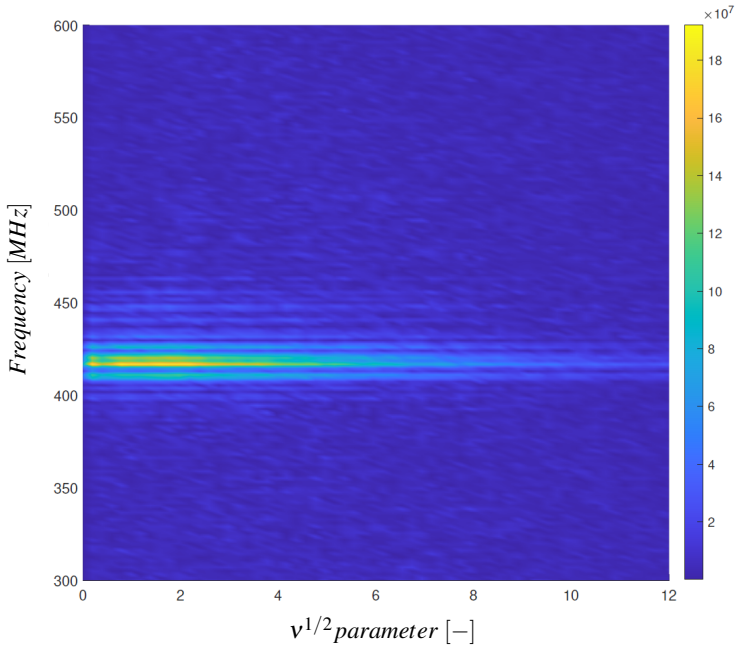


Figure 3.27: TM Electrostatic waves dispersion relationship in SPT-100 thruster. In this example a wave of frequency $f_{RF} = 450$ MHz and cathode oscillating voltage $V_{RF} = 10$ V is represented. Results published in [1].

Note that the waves captured in the dispersion relationship are slightly shifted (approximately 5%) from the excitation frequency ($f_{RF} = 450$ MHz). This phenomenon is attributed to the resolution of the 2D Fast Fourier Transform. Similar offsets are observed when exciting at different frequencies.

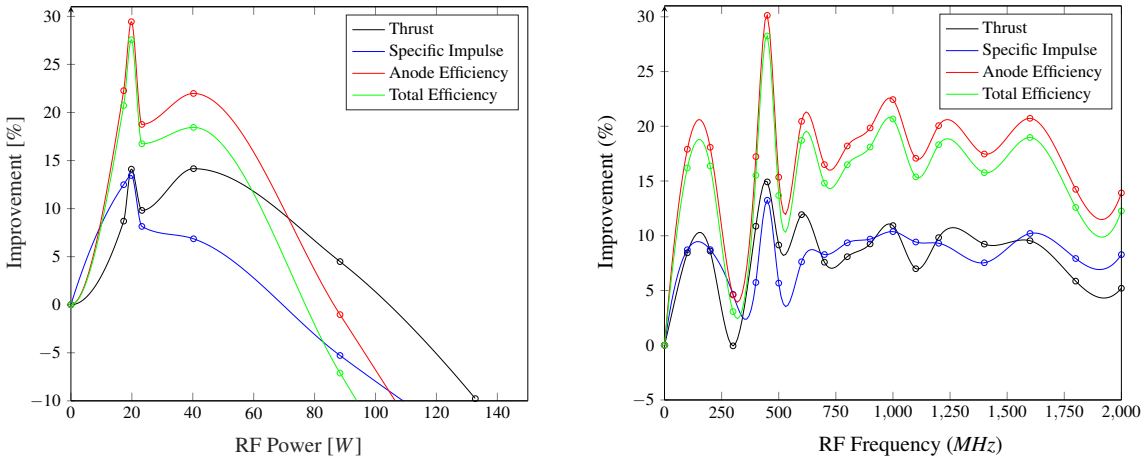
Performance Improvement in Xenon-Fuelled Hall Effect Thrusters

This section aims to quantify the potential performance enhancement of xenon-fuelled HETs using RF excitation making use of the procedures explained in Section 3.2.1.8.

Power and Frequency Sweep

First off, a power and frequency sweep was conducted to investigate the most promising combinations that might enhance the performance of xenon-fuelled HETs (specifically in this case, the *SPT-100*).

To begin, an analysis of RF power sweep is presented (Figure 3.28a), at a frequency chosen to be the most optimal one in terms of total efficiency ($f_{RF} = 450$ MHz), as will be seen subsequently.



(a) Power dependence for fixed frequency (f_{RF} = 450 MHz)

(b) Frequency dependence for fixed power (P_{RF} = 20 W, corresponding to V_{RF} = 10 V)

Figure 3.28: Performance dependence of the SPT-100 depending on RF power and frequency. Values averaged over a discharge power range between 900-1800W. Results published in [1].

From the results obtained, it is evident that the performance of the thruster might be enhanced with RF powers on the order of $P_{RF} \approx 20$ W. These RF powers correspond to voltages close to $V_{RF} = 8 - 10$ V, as previously shown in Figure 3.8b. RF powers higher than $P_{RF} = 50$ W appear to be detrimental for the augmentation of thruster performance. This is probably due to the fact the main working mechanisms of HETs could be altered if the RF power is in the order of the HET discharge power. The optimal power (around $P_{RF} \approx 20$ W) seems to be independent of the selected frequency, as other frequencies analysed also peak at similar values of RF power.

For this optimal power, a frequency sweep analysis is presented (Figure 3.28b). In this case, different peaks of anode and total efficiency are observed depending on the excitation frequency. As expected from the theoretical analysis (Section 1.2.2.2), these peaks correspond to ECR conditions and harmonics, and their accumulation at certain locations of the channel. A significant peak is obtained at frequencies closer to $f_{RF} = 450$ MHz, which matches the ECR excitation frequency at the peak of the magnetic field ($B = 0.016$ T). A weaker peak of high efficiency is found at lower frequencies ($f_{RF} \approx 200$ MHz), which corresponds to excitations of ECR at the first harmonic at $x = 0.035$ m, where the magnetic field is close to $B = 0.011$ T. Other peaks are found at higher frequencies, probably due to the accumulation of higher harmonics at particular locations of the thruster.

Table 3.11: Performance improvement of *SPT-100* average over the experimental power range ($P_d = 900 - 1800$ W) found by operating at $V_d = 300$ V. Table published in [1].

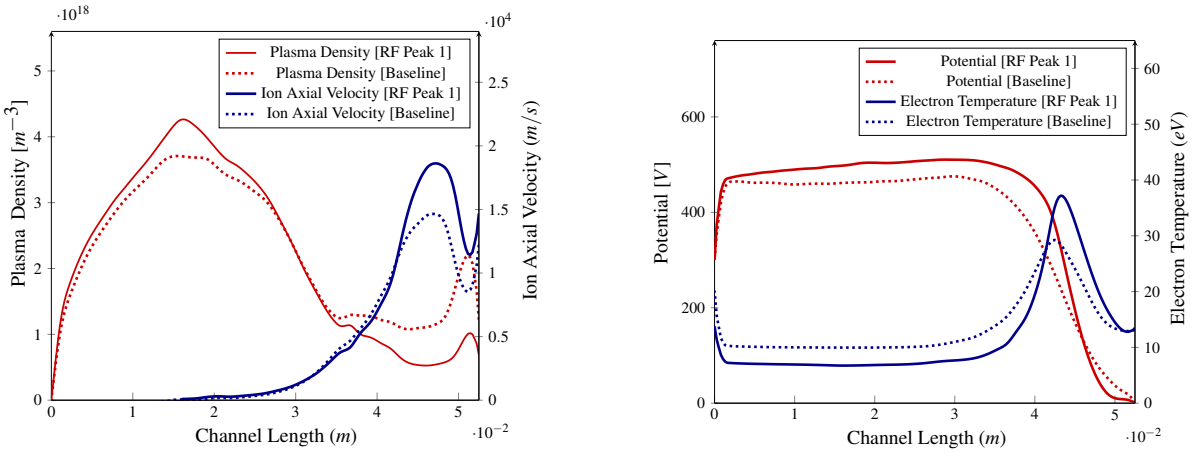
Parameters	**Baseline**	**1st Peak: 450 MHz (Absolute / % Boost)**		**2nd Peak: 600 MHz (Absolute / % Boost)**		**3rd Peak: 1000 MHz (Absolute / % Boost)**	
Voltage [V]	0	10	-	10	-	10	-
RF Power [W]	0	20	-	20	-	20	-
Thrust [mN]	94.1	108.1	+15%	105.3	+12%	104.4	+11%
Isp [s]	1192	1349	+13%	1282	+8%	1315	+10%
TTPR [mN/kW]	69.7	80.1	+15%	78.0	+12%	77.3	+11%
Anode Efficiency [%]	40.8	53.0	+30%	49.0	+20%	49.9	+22%
Total Efficiency [%]	40.8	52.2	+28%	48.3	+19%	49.2	+21%

Overall, it can be observed how waves excited at the right RF frequency and voltage could contribute to achieving higher thrust and specific impulse, resulting in higher anode and total efficiency.

Table 3.11 tabulates the performance improvement for the most optimal combinations of frequency and power for the waves. For instance, under the conditions $f_{RF} = 450$ MHz and $V_{RF} = 10$ V, a thrust and specific impulse improvement of 15% and 13%, respectively, compared to the baseline case could be obtained. The anode efficiency peaks at a 30% enhancement, corresponding to a 28% total efficiency augmentation due to the RF power utilisation at that voltage ($P_{RF} = 20$ W). Other peaks also show beneficial conditions when RF excitation is present, with an improvement close to 20% in total efficiency. These results will be experimentally checked in Section 4.7.2.1.

Plasma Properties

Figure 3.29 compares the main plasma properties at a specific discharge power condition ($P_d = 1350 \pm 10\%$ W) with the most optimal RF excitation condition ($f_{RF} = 450$ MHz, $V_{RF} = 10$ V) against the baseline case under the same operating conditions. It can be observed how RF excitation improves the plasma properties by generating a higher plasma peak while accelerating the ions further at the exit region (Figure 3.29a). Additionally, the plasma potential within the channel increases when RF excitation is present, and the electron temperature in the magnetised region exhibits a higher peak compared to the baseline case (Figure 3.29b).



(a) Plasma density and ion axial velocity

(b) Potential and electron temperature

Figure 3.29: Plasma distribution plots of the *SPT-100* with RF excitation at $P_d = 1350$ W. Plots published in [1].

A sheath affect at the cathode boundary is also present in Figure 3.29a. The enhancement of electron temperature and ion velocity was predicted by the spectral analyses (Section 3.2.2.3), where the frequency-locking phenomenon enlarges the resonance location.

Performance Improvement in Oxygen-Fuelled Hall Effect Thrusters

In a similar fashion as with xenon-fuelled HETs, the same investigation is performed with oxygen-fuelled HETs. The thruster *WET-HET* (see Section 4.1.2.1) is selected for this analysis, therefore making use of the simulation inputs detailed in Table 3.7.

Power and Frequency Sweep

Contrary to what was observed with xenon-fuelled HETs, the results obtained when using oxygen as a propellant did not lead to a noticeable performance boost.

As will be seen in Section 4.2.2.4, it was experimentally demonstrated that oxygen, as well as water vapour-fuelled HETs benefit from using a peak radial magnetic flux density along the channel centerline up to four times greater than typical xenon-fuelled HETs. Because of this, in these simulations, frequencies not just in the $f_{RF} = 450$ MHz range but also up to $f_{RF} = 2000$ MHz were tested, with a magnetic flux density resonating at that specific frequency. However, in none of these simulations was there evident proof of performance improvement. This is thought to be attributed to three factors, which can also act simultaneously.

The first factor is the amount of extra reactions that molecular propellants have (see Tables 3.5 and 3.6). These events can influence the way the wave propagates in such a way that the wave's energy is not fully captured by the electrons.

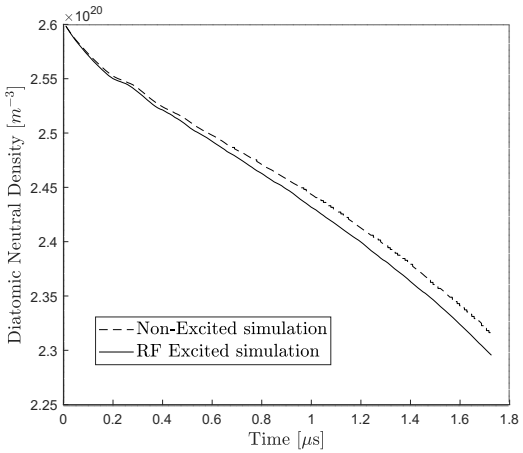
The second factor is the nature of the waves excited. The reflection of an RF wave in a plasma is determined by the plasma frequency (see Equation 1.7), which is directly proportional to the square root of the electron density. In general, when the frequency of the incident wave is lower than the plasma frequency, the wave is transmitted through the plasma. In contrast, the higher the frequency of the wave compared to the plasma frequency, the more reflection it experiences within the plasma. It is possible that, due to the fact that oxygen and water vapour-fuelled HETs need a higher magnetic flux density to operate efficiently and therefore a wave of higher frequency, these waves have a higher reflection factor and their absorption is lower compared to xenon-fuelled HETs.

Lastly, as will be demonstrated in Chapter 4, the performance of oxygen and also water vapour-fuelled HETs is lower than xenon-fuelled HETs. Therefore, the performance boost of these thrusters can be relatively lower than those fuelled by xenon and therefore not as visible.

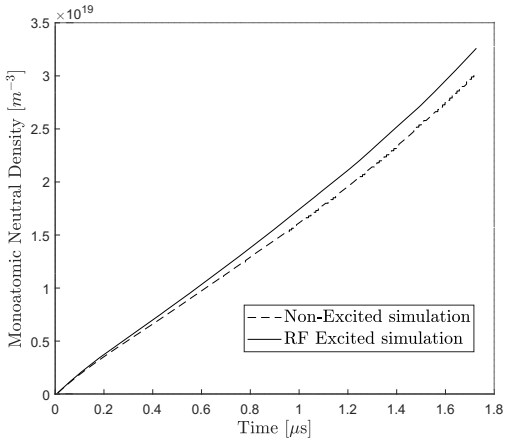
Section 4.7.2.2 will experimentally check the findings obtained with the computational model in these devices.

Plasma Properties

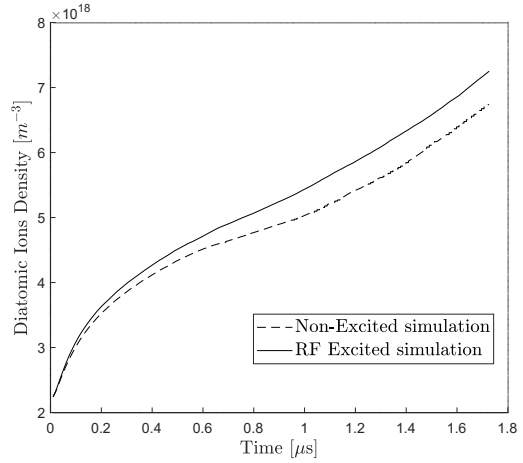
Although the plasma properties did not experience major changes with respect to the non-excited simulations, it was possible to observe that the evolution of the species led to temporally higher ionisation and dissociation rates. This is visible from the plots presented in Figure 3.30, where the density of O, O_2^+ and O^+ appears to slightly increase, whereas the propellant O_2 decreases. Based on these findings, the experimental part of this activity will aim to clarify whether or not there is a performance boost in oxygen-fuelled HETs (Section 4.7.2.2).



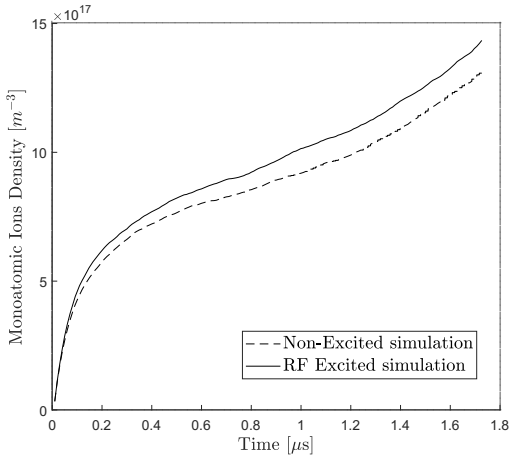
(a) O_2 neutral density evolution



(b) O neutral density evolution



(c) O_2^+ neutral density evolution



(d) O^+ neutral density evolution

Figure 3.30: Evolution of species densities over time in excited versus non-excited simulations in oxygen-fuelled HETs. Results presented in [6].

Note that Section 4.7.2.3 will compile and compare the findings obtained with this numerical model and the experimental part of this activity (available in Section 4.7) using either noble gases or oxygen as a propellant, hence validating the results shown here.

Chapter 4

EXPERIMENTAL CHARACTERISATION

4.1 Overview of Experiments

For the experimental characterisation of water-fuelled HETs, different campaigns were conducted under different set-ups, facilities and environmental conditions. This section aims to compile the shared information of all these campaigns while giving an introductory overview of the experiments conducted.

4.1.1 Technology timeline

A timeline of the technology development is presented here. This is particularly significant for comprehending the starting point of this research and the various milestones achieved in the progression towards a successful end-to-end technological validation. Part of this research was presented at the International Electric Propulsion Conference 2024 in Toulouse, France [8].

Figure 4.1 depicts the timeline documenting the evolution of water propulsion technologies for HETs, highlighting the key milestones essential for achieving the technology validation in laboratory conditions.

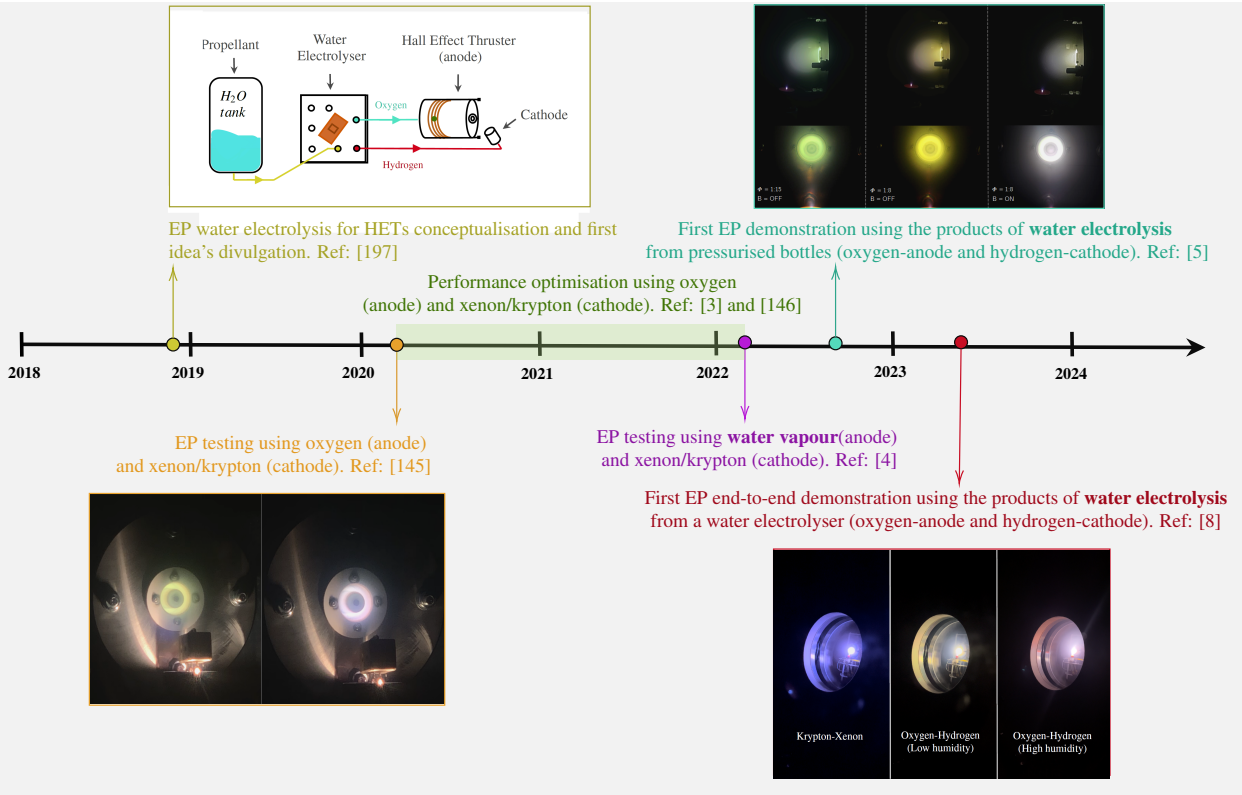


Figure 4.1: Timeline of the electric propulsion Hall Effect Thrusters technology fuelled by water (either using the products of water electrolysis -oxygen for the anode and hydrogen for the cathode- or using a direct water vapour feed).

For water propulsion, the initial milestone dates back to the end of 2018, when the conceptual framework of utilising the byproducts of water electrolysis for EP was first presented to the public (and published on January 2019 [195]). At that juncture, minimal to no prior research had been conducted regarding oxygen-fuelled thrusters and hydrogen-fuelled cathodes: on the one hand, only a Japanese publication featured the initial exploration of an oxygen-fuelled thruster, albeit with relatively lower performance (an anode efficiency of 9% and a specific impulse of $I_{sp} = 1000$ s, with no reported thrust measurements) [196]. On the other hand, hydrogen-fuelled cathodes were regarded as promising options for HETs, potentially mitigating poisoning concerns [64, 65]. However, their practical usability had yet to be demonstrated.

Recognising the need for a fundamental exploration of the physics behind oxygen-fuelled thrusters and hydrogen-fuelled cathodes, efforts were focused on this preliminary inquiry. The goal was to determine if this technology could be viable for future space missions and to identify the specific conditions that would make it work.

First off, special attention was given to understanding how oxygen could affect the thruster discharge, how its performance was compared to the state-of-the-art, and what was its impact on the surfaces exposed to the plasma. To simplify experiments focused solely on the thruster (anode), xenon and krypton were utilised to fuel the cathode in the initial set of experiments. This approach facilitated the exploration of discharge physics primarily influenced by an oxygen-fuelled HET, marking the first step in this technology exploration. These initial EP tests began in early 2020 [143], marking the start of a two-year effort to explore and improve oxygen-fuelled thrusters [3, 144]. Specifically, the investigation aimed to find the best channel length and material for optimal thruster geometry and material selection, as well as to measure the most relevant plasma physics properties of the discharge. Further details of these findings are provided in Sections 4.2 and 4.3.

Following the initial investigation into an oxygen-fuelled thruster, the subsequent research phase involved the experimental demonstration of simultaneous operation between an oxygen-fuelled thruster and a hydrogen-fuelled cathode [5]. For these next experiments, both propellants were supplied via pressurised bottles. This demonstration was achieved at the Imperial Plasma Propulsion Laboratory in late 2022, as elaborated in Section 4.4. This phase examined the impact of the hydrogen-oxygen ratio (Φ) on the discharge process and evaluated how the presence of hydrogen-oxygen plasmas affected the integrity of the hardware.

The final milestone involved the successful testing of both the thruster (anode) and cathode using the outputs of in-situ water electrolysis (oxygen and hydrogen) generated by a water electrolyser supplied with liquid water (see Section 4.5) [8]. These campaigns validated the feasibility of the technology, representing the first end-to-end demonstration of water electrolysis-fuelled HETs.

In parallel, an alternative approach to water electrolysis was conceived: direct utilisation of water vapour [4]. By using water vapour instead of the products of water electrolysis, the necessity for an onboard water electrolyser is eliminated, thereby reducing cost, mass, and system complexity. For that purpose, a water vapour feed system was designed and developed to characterise a water vapour-fuelled HET, with the aim of identifying the optimal operating conditions for this

technology (see Section 4.6).

Once the two branches of the technology (water electrolysis and water vapour) were characterised, a comparison between the two technologies was undertaken (see Section 4.6.2.3). Depending on the mission requirements, water electrolysis and water vapour propulsion in the context of HETs offer distinct advantages, holding significant promise for medium-term space missions.

The next sections describe the hardware used for these experiments and offer an in-depth description of the findings uncovered.

4.1.2 Laboratory Hardware

4.1.2.1 Hall Effect Thrusters

For these experiments, two different HETs were tested, representing the first and second generations of a water electrolysis HET.

First Generation of a Water Electrolysis Hall Effect Thruster (*WET-HET*)

The first generation of a water electrolysis HET is the so-called "Water ElecTrolysis Hall Effect Thruster" (*WET-HET*), making reference to a HET optimised to work with the products of water electrolysis [197]. The development and initial testing of this thruster using oxygen constituted the thesis topic of A. Schwertheim. Only minor modifications were implemented to the existing design to conduct the tests described in this work.

In essence, the design of the *WET-HET* affords flexibility in adjusting various parameters, such as channel length, magnetic topology and anode material to investigate their impact on thruster performance. The magnetic topology can be altered by adjusting the positioning of iron/copper rings encircling the thruster. The axial length of the channel can be customised by repositioning the anode relative to the channel exit using a series of copper extension tubes (see Section 4.2.2.6). Moreover, the anode cap, situated atop the copper extension tube, can be substituted, allowing for testing with different anode materials (see Section 4.2.2.3).

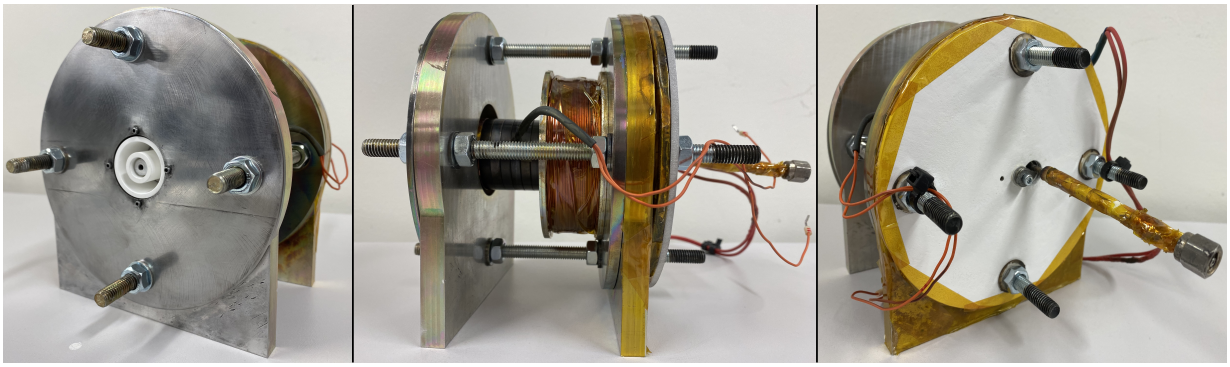


Figure 4.2: Front, side and back views of the first generation of a water electrolysis HET (the *WET-HET*). Photos published in [3].

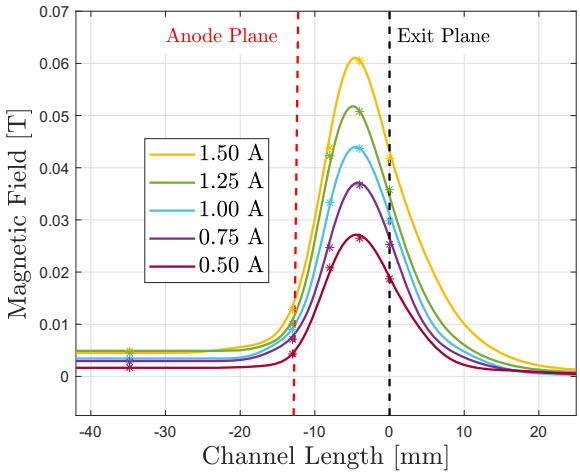


Figure 4.3: Magnetic field topology of the thruster *WET-HET* as a function of the current driven throughout the electromagnets. The dots represent experimental measurements. Plot published in [3].

Figure 4.2 displays the front, side and back views of this thruster. For a comprehensive understanding of the geometric, thermal, and magnetic design, readers are referred to previous works by A. Schwertheim [143, 144, 197].

Figure 4.3 shows the magnetic field topology and its strength, which is dependant on the current set to the electromagnets. Although, as remarked before, the magnetic field topology can be adjusted, this Gaussian magnetic field is predominantly employed for the majority of tests. The rationale behind this choice is based on the findings of previous investigations [143, 144, 197]. These studies revealed that the optimal magnetic field topology for oxygen plasmas is a narrow magnetic field situated near the channel exit. Moreover, it was observed that a magnetic flux density stronger than those typically used in xenon-fuelled HETs proved beneficial for oxygen-fuelled thrusters.

Table 4.1: Compilation of the possible experimental configurations which can be selected for the thruster *WET-HET*.

Variable	**Value**
Channel width (w), [mm]	5.0
Channel mean diameter (d_m), [mm]	20.0
Channel length (L), [mm]	5.5-59.8 (see Section 4.2.2.6)
Magnetic topology	Figure 4.3 (see Section 4.2.2.4)
Oxygen mass flow rate, [mg/s]	0.6-4.0 (see Section 4.2.2.5)
Channel walls	BN / $BNSiO_2$, Grade M26 (see Section 4.2.2.2)
Anode material	Stainless Steel / Tungsten (see Section 4.2.2.3)

For comparison, the Russian *SPT-100* features a Gaussian magnetic field topology peaking at $B = 0.016$ T in the exhaust region [198], four times weaker than the optimal case with oxygen, where the maximum magnetic field is set at $B = 0.065$ T. Alternative magnetic field configurations deviating from a Gaussian shape peaking at the end of the channel resulted in inferior overall performance in terms of thrust efficiency [144].

The different configurations available for testing the *WET-HET* are summarised in Table 4.1. Depending on the nature of the test, this configuration is adjusted to investigate the diverse performance metrics resulting from these variations.

Second Generation of a Water Electrolysis Hall Effect Thruster (*AQUAHET*)

The design of the second generation of a water electrolysis HET, referred to as the *AQUAHET*, was the result of a collaborative effort between *Imperial College London* and the company *URA Thrusters Ltd.* Figure 4.4 displays the front, side, and back views of the thruster [1]. As seen there, the thruster is mounted onto a heat sink to alleviate thermal stresses on the hardware. However, no thermal cooling was used for any of the experiments in order to explore the best possible performance without the use of active cooling. In this way, the limits of the technology could be assessed, and the performance could be compared to the first generation water electrolysis HET (the *WET-HET*), in which active cooling was not used either.

[1] Notice that the device is property of *URA Thrusters Ltd* and due to intellectual property rights, no cross-section diagram can be provided here.

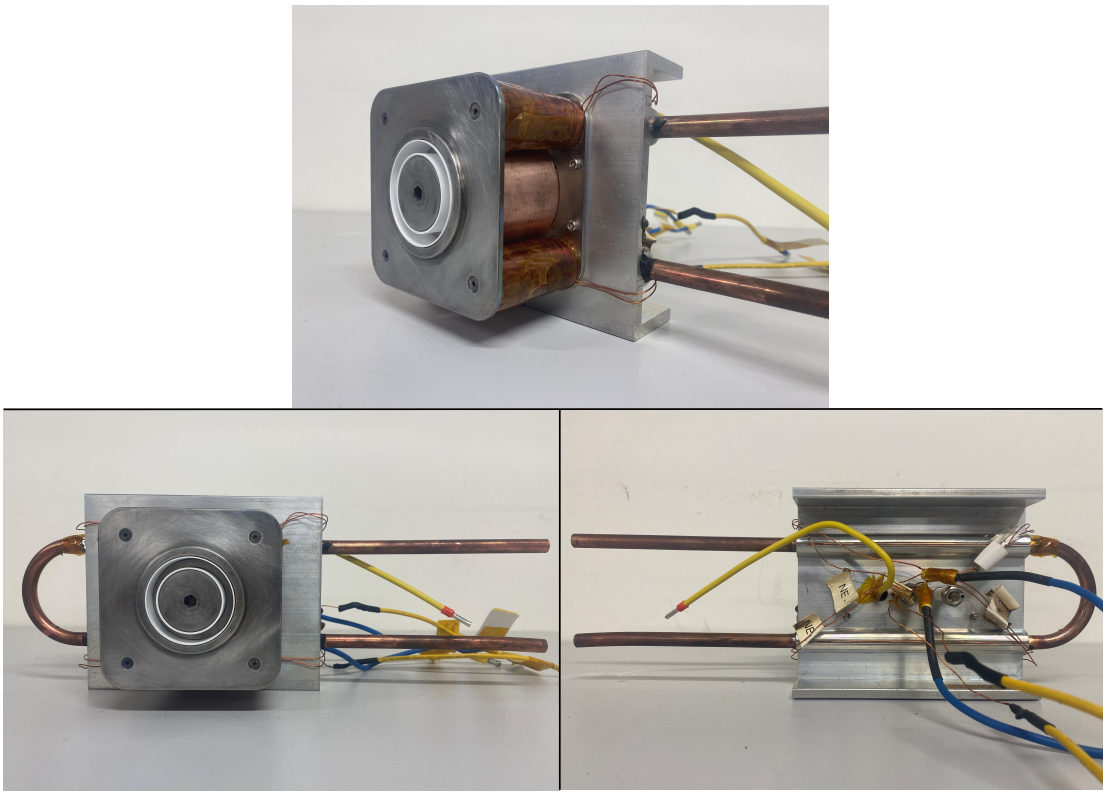


Figure 4.4: Side, front and back views of the second generation of a water electrolysis HET (*AQUAHET*).

The sizing of the *AQUAHET* thruster discharge channel is described in prior research [9] and leveraged the lessons learnt from the experimental characterisation of the *WET-HET* [197]. While performance differences in channel width could not be assessed with the *WET-HET*, such assessments were feasible with the *AQUAHET* by using thinner or thicker channel walls. The *AQUAHET* also features a larger channel mean diameter compared to the *WET-HET* [9]. As a result, the mass flow rate needed to sustain the discharge was scaled according to the anode area, resulting in a range between $\dot{m}_a = 1.0 - 2.5$ mg/s of oxygen flow for the *AQUAHET*, compared to the $\dot{m}_a = 0.7 - 1.4$ mg/s range used for the *WET-HET*. The selected channel length is $L = 13.1$ mm, for reasons that will become clear in Section 4.2.2.6.

Morevoer, due to the larger dimensions of the *AQUAHET* compared to the *WET-HET*, it was feasible to assess higher levels of operating discharge power, reaching up to $P_d = 3200$ W.

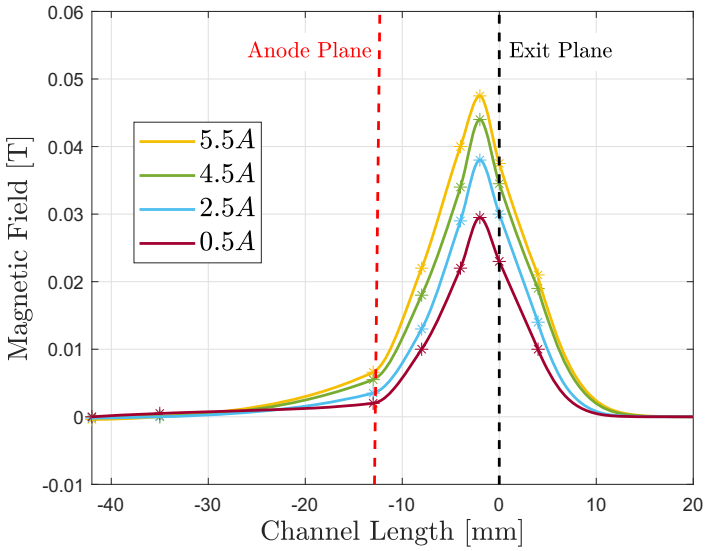


Figure 4.5: Magnetic field topology of the thruster *AQUAHET* as a function of the current driven throughout the electromagnets. The dots represent experimental measurements.

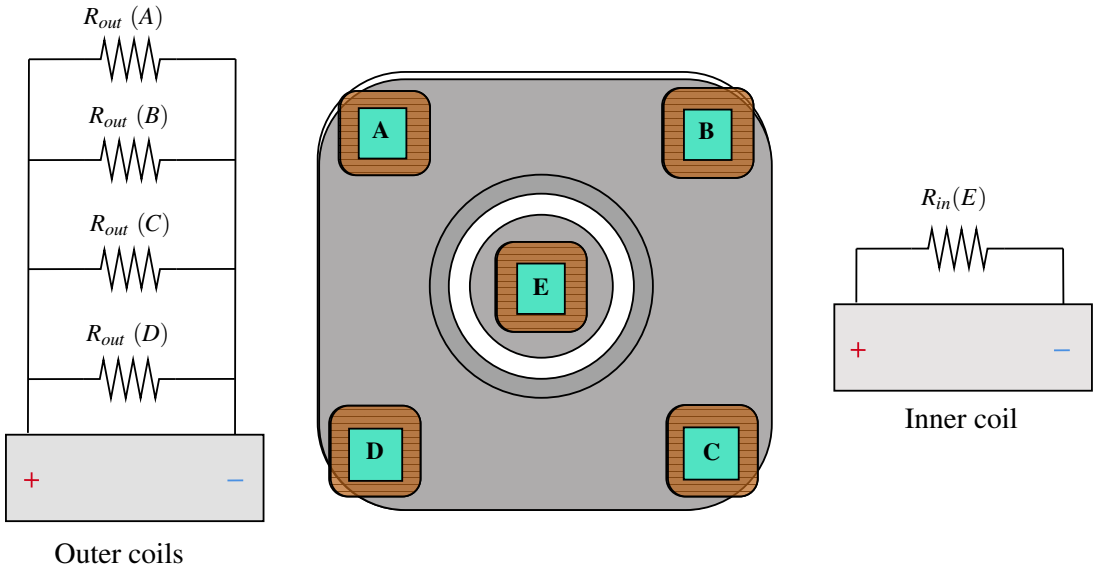


Figure 4.6: Electrical diagram of the magnetic field coils (outer and inner) of the thruster *AQUAHET*.

Similarly to the *WET-HET*, the *AQUAHET* also has a radial magnetic flux density profile with a (roughly) Gaussian shape, and a peak value along the channel centreline more than three times higher than for standard HETs (see Figure 4.5).

The *AQUAHET* also boasts a reduction of the non-radial magnetic field line components close to the thruster exit plane as compared to the *WET-HET* [9]. To achieve this objective, a configuration involving 5 coils (comprising 4 outer coils and 1 inner coil) is arranged, as illustrated in Figure 4.6. The outer coils (A, B, C, and D) possess identical resistance, denoted as R_{out}, while

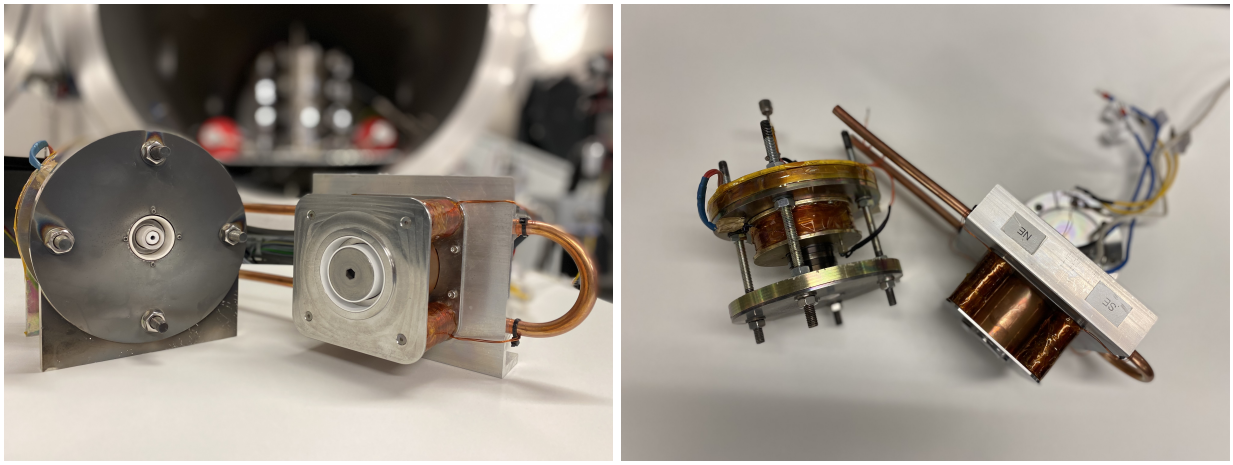
the inner coil (E) exhibits a distinct resistance, R_{in}. It is noteworthy that the resistance value is contingent upon the coil's temperature. For a current magnitude of $I_m = 5.5$ A, the resistance of the outer coil varies within the range of $R_{out} = 20 - 34\ \Omega$, whereas the inner coil's resistance ranges between $R_{in} = 7 - 12\ \Omega$. Ideally, these 5 coils can be configured in series utilising a single power supply. However, the elevated resistance of the coils, coupled with the substantial current requirement at the upper limit ($I_m = 5.5$ A), imposes stringent demands on the specifications of the power supply (requiring $V_m = 150$ V and $I_m = 5.5$ A in the worst-case scenario). As no available spare power supply with these specified requirements was accessible within the laboratory, two distinct power supplies were employed to energise the outer and inner coils, respectively (see Figure 4.6). The outer coils were interconnected in parallel using one single power supply (Figure 4.6a). In this configuration, it was imperative to verify the uniformity of resistance across each coil under all conditions to ensure equitable current distribution. Experimental assessments of the coil resistance under varied scenarios, coupled with measurements of magnetic field uniformity, substantiated the viability of this arrangement.

As anticipated, the total magnet power for the *AQUAHET* is substantially large (up to $P_m = 800$ W in the worst-case scenario, contrary to $P_m = 25$ W in the case of the thruster *WET-HET*). This is due to the sizing of the copper wires which compose the coil. By using thinner wires, the total power consumption can be substantially decreased to the standard power consumption of HETs ($P_m < 100$ W). Although this contingency penalises the performance when evaluating the total efficiency of the thruster, the main purpose of the thruster *AQUAHET* was to be a prototype that is even more optimised in terms of thrust and specific impulse as compared to the *WET-HET* when fuelled by water. Power consumption optimisation, which translates into a total efficiency optimisation, will take place next when an engineering-qualification model for a future In-Orbit-Demonstration (IOD) is designed and built.

In keeping with the lessons learnt from the *WET-HET* testing (see Sections 4.2.2.2 and 4.2.2.3), the *AQUAHET* channel walls were made of $BNSiO_2$ and the anode was made out of stainless steel.

Table 4.2: Compilation of the possible experimental configurations which can be selected for the thruster *AQUAHET*.

Variable	**Value**
Channel width (w), [mm]	4.0-5.0 (see Section 4.2.2.7)
Channel mean diameter (d_m), [mm]	40.0
Channel length (L), [mm]	13.1
Magnetic topology	Figure 4.5 (see Section 4.2.2.4)
Oxygen mass flow rate, [mg/s]	1.0-4.0 (see Section 4.2.2.5)
Channel walls	$BNSiO_2$, Grade M26
Anode material	Stainless Steel



(a) Front view of *WET-HET* (left) and *AQUAHET* (view).

(b) Top view of *WET-HET* (left) and *AQUAHET* (right).

Figure 4.7: Display of two thrusters tested, the *WET-HET* and the *AQUAHET*.

The compilation of the different experimental configurations tested for this thruster is summarised in Table 4.2. For comparison, the two thrusters side by side are shown in Figure 4.7.

4.1.2.2 Cathodes

Two different cathodes were used throughout these campaigns. This section overviews both cathodes and provide specific details about each one.

Filament Neutraliser Cathode

One of the cathodes used for the experimentation was a plasma filament bridge neutraliser [199]. The main working principles of this cathode were explained in Section 1.2.1.2. Figure 4.8 shows the main components of this cathode.

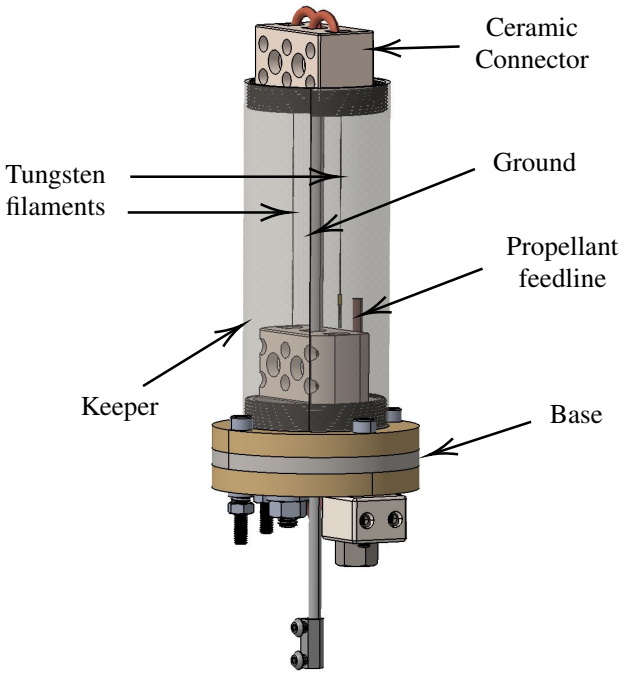


Figure 4.8: Plasma filament bridge neutraliser cathode used throughout the EP experimentation. Graph published in [3].

As seen there, this device in particular consists of two twin tungsten filaments (0.5 mm) which can be set to a high heater current ($I_h \approx 20$ A) and low heater voltage ($V_h \approx 10$ V), emitting electrons. During testing, current is set only through one of them. In case one of them breaks while operating in vacuum because of the high thermal stresses, it is possible to switch to the other one without the need of venting the chamber (which allows for experimental campaigns of longer duration). A copper tube inside of the cathode is reference to ground potential ($V_g = 0$ V), closing the circuit with the filament that is active. A tube enclosing the cathode is set to the keeper potential ($V_k \approx 300-400$ V before ignition -open circuit- and $V_k \approx 20-40$ V with $I_k \approx 1.5-2.5$ A when the plasma is active). The mass flow is provided at the base of the cathode by a Swagelok 1/8" hollow tube.

The location of the cathode with respect to the thruster was kept constant at all times, to assure that the cathode's operatibility did not have any effect on the results. As in previous experiments [144, 143], the closest edge of the cathode is set at 50 mm from the thruster's front plate. Vertically, it is set at 42 mm from the centre pole of the thruster.

As elucidated in Section 1.2.1.2, a plasma filament cathode offers a cost-effective alternative to

hollow cathodes for laboratory applications, albeit at the expense of higher power requirements for operation ($P_{fil} \approx 300$ W) [2]. Consequently, the total efficiency of a system employing such cathodes does not accurately reflect that of a flight model HET (more information in Section 4.2.2.1).

Lanthanum Hexaboride Cathode (*Hydrocat*)

Hydrocat is a hollow cathode incorporating a LaB_6 insert, designed to emulate the conditions of an in-flight cathode under realistic conditions. This cathode was specifically engineered by *ALIENA Pte Ltd*, aiming to achieve the first successful demonstration of a hydrogen-fuelled cathode in water electrolysis propulsion. Notice that the plasma filament cathode, although suitable for testing with noble gases, would encounter difficulties when used with hydrogen. This is mainly due to the hydrogen's lower mass and higher ionisation potential compared to noble gases.

Moreover, the inherent inefficiencies associated with a plasma filament cathode in sustaining plasma ignition result in significantly higher mass flows required for a krypton-fuelled plasma filament cathode (approximately $\dot{m}_c = 15$ sccm or $\dot{m}_c = 0.94$ mg/s) compared to a conventional krypton-fuelled LaB_6 cathode (approximately $\dot{m}_c = 6$ sccm or $\dot{m}_c = 0.37$ mg/s). This discrepancy becomes particularly pronounced when dealing with lightweight propellants like hydrogen, where mass flows would need to exceed stoichiometric conditions, surpassing the nominal mass flow rate of the thruster (ranging from $\dot{m}_a = 0.6 - 2.5$ mg/s, depending on the thruster). Finally, the substantial hydrogen mass flow could elevate the background pressure beyond nominal conditions for EP testing, as will be seen in Section 4.4.

Figure 4.9 shows the main components of the cathode [3]. In comparison to existing devices, this LaB_6 cathode incorporates several notable design modifications tailored to accommodate the unique characteristics of hydrogen: lower molecular weight, being approximately 65 times lighter than xenon and featuring a slightly higher ionisation potential, approximately 1.5 times higher.

[2] Throughout this thesis, the cathode power is calculated as the summation of the cathode keeper and cathode heater power: $P_c = P_k + P_h$. P_c is denoted as P_{fil} or P_{hydro} when specifically describing the plasma filament cathode power or the *Hydrocat* cathode power, respectively.

[3] Notice that the design of the device is protected by intellectual property rights by *ALIENA Pte Ltd*, and therefore no cross-section diagram can be provided here.

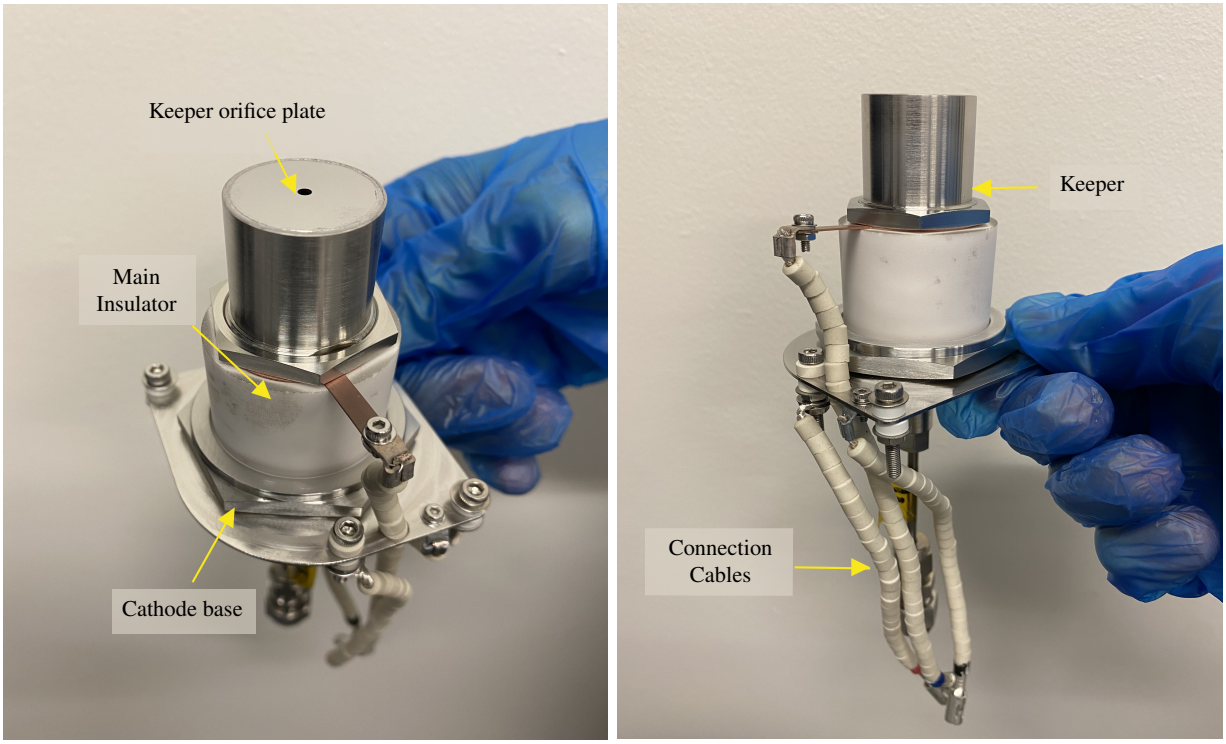
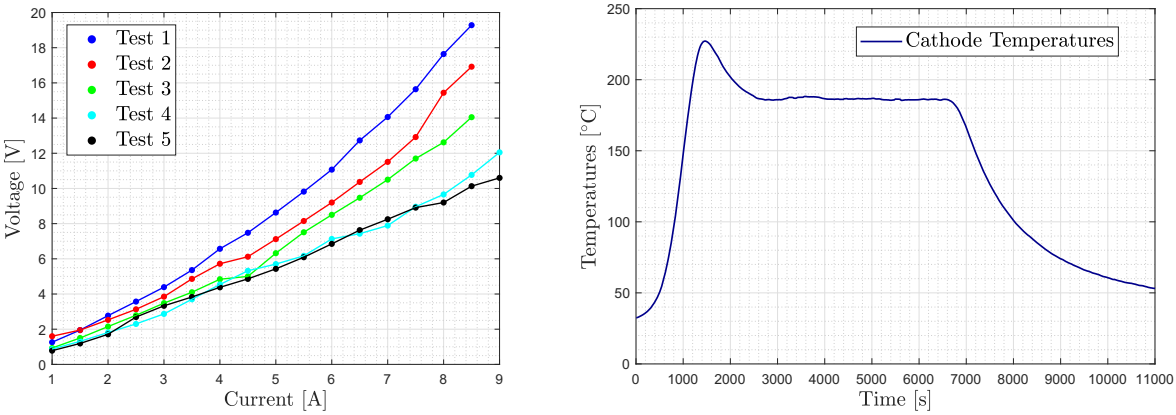


Figure 4.9: Hollow LaB_6 cathode (*Hydrocat*) used throughout the experimentation.

Regarding its design, *Hydrocat* features an emitter and cathode orifice plate fabricated from LaB_6, a material renowned for its high resistance to poisoning [12] and its ability to sustain a hydrogen plasma [200]. Sizing of the emitter and orifice was performed using a 0D self-consistent plasma model with an integrated thermal solver [201, 202].

The simulations revealed that for optimal operation with hydrogen at discharge currents ranging from I_d= 2-10 A, the emitter and cathode orifice should possess high aspect ratios to ensure low coupling potentials ($<$ 60 V) and operational temperatures ($<$ 1900 K) at flow rates up to $\dot{m}_c$ = 0.24 mg/s of H_2. For instance, the length of the emitter is $\approx$ 8 times its internal diameter. Additionally, when operating with low hydrogen flows, a high aspect ratio of the emitter is necessary to maintain a high internal neutral pressure, ideally in the range of a few torr [12].

The engineering model of *Hydrocat* also incorporates a heater composed of 3D printed ceramics (heater insulator) encapsulating a serpentine W-Re filament. The austenitic stainless steel keeper features a laser-welded molybdenum keeper orifice plate and is affixed to the austenitic stainless steel cathode base via a ceramic insulator (referred to as main insulator).



(a) Cathode's heater IV curve

(b) Cathode base temperature

Figure 4.10: Characterisation of the cathode *Hydrocat* using the data recorded during testing.

Finally, to enhance the efficiency of the heater, a thermal shield is wrapped around the heater ceramic. This component underwent testing with heavier gases, such as argon, krypton, and xenon, prior attempting hydrogen tests.

The cathode's position remained constant, at the same location as the plasma filament cathode.

Figure 4.10 depicts the current-voltage (IV) curve of the cathode heater during various tests and the cathode base (see Figure 4.9) temperature during ignition. Analysis of the IV curve reveals a decreasing cathode heater voltage for a set current for every subsequent test conducted. This decline is attributed to the reduction in heater resistance, which ultimately limits the total power of the heater and consequently, the temperature attained by the cathode. This posed a constraint on the durability of the cathode, necessitating the procurement of additional samples for subsequent testing once the total power reached was not high enough to continue testing.

The cathode base temperature gradually increases as more power is applied to the heater (increasing 0.5 A per minute until reaching $I_h = 8 - 9$ A). When the cathode base temperature surpasses 200°C, ignition is initiated. During cathode startup, the heating power can reach up to $P_h = 200$ W. Once in steady-state operation, the heater current is reduced ($I_h = 5 - 6$ A). In these conditions, the heating power is $P_h \approx 60$ W.

For the keeper, ignition is attempted at a keeper voltage of $V_k = 300 - 400$ V, with the current limit set to $I_k \approx 0.5$ A. At steady-state operation, the keeper current is increased to $I_k = 1.0 - 2.5$

A while the keeper voltage decreases to $V_k = 16 - 40$ V [4] (more information in Section 4.1.4).

In these conditions, the total power required to operate the *Hydrocat* cathode is $P_{hydro} = 70 - 150$ W (see Section 4.2.2.1). Upon completing the test, the cathode remains inside the chamber to let it gradually decrease its temperature until returning to room temperature.

4.1.2.3 Thrust Balance

A hanging pendulum thrust balance was used to obtain calibrated thrust measurements. This thrust balance was designed and developed by A. Schwertheim. Here, a small description of the instrument and the calibration system is provided. For a full overview of the device, readers are directed to A. Schwertheim work [43, 203].

In essence, the apparatus comprises a suspended and electrically isolated moving platform connected by eight thin aluminum flexures, interconnected by linkages. This moving platform is linked to both a fixed top and bottom platform by these flexures. The HET (thruster and cathode) is connected to the moving platform via an interface plate. Consequently, any force exerted by the HET induces a displacement of the suspended platform. This motion is captured by a laser directed at a suspended laser target, which is directly connected to the moving platform. This instrument was employed in numerous prior experimental investigations to this thesis [143, 144] and validated in various laboratories [203]. To establish the relationship between displacement and force, two calibration systems are employed:

The **first calibration system** is set under atmospheric conditions. It consists of a Voice Coil Actuator (VCA) connected to a high-precision sourcemeter (model: *Keysight B2901A*) that provides sensitive current inputs. The magnetic part of the VCA is connected to the moving platform whereas the coil assembly is fixed to the bottom platform. The two parts of the VCA (magnet and coil) are placed together at a distance of 2 mm ensuring there is no friction between the two of them. Once a current is set to the coil, a repulsive force is exerted on the magnet ($F_{c/m}$) which in turn moves the suspended platform.

[4] As will be seen throughout this thesis, the lower range of keeper current and voltage is typically set when testing the cathode with noble gases; whereas the higher end is employed when testing with hydrogen.

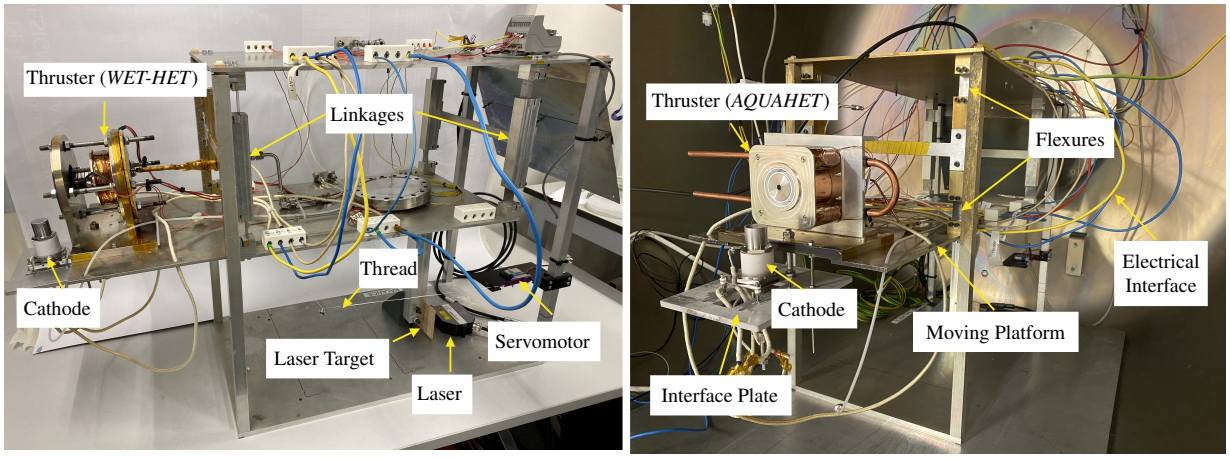
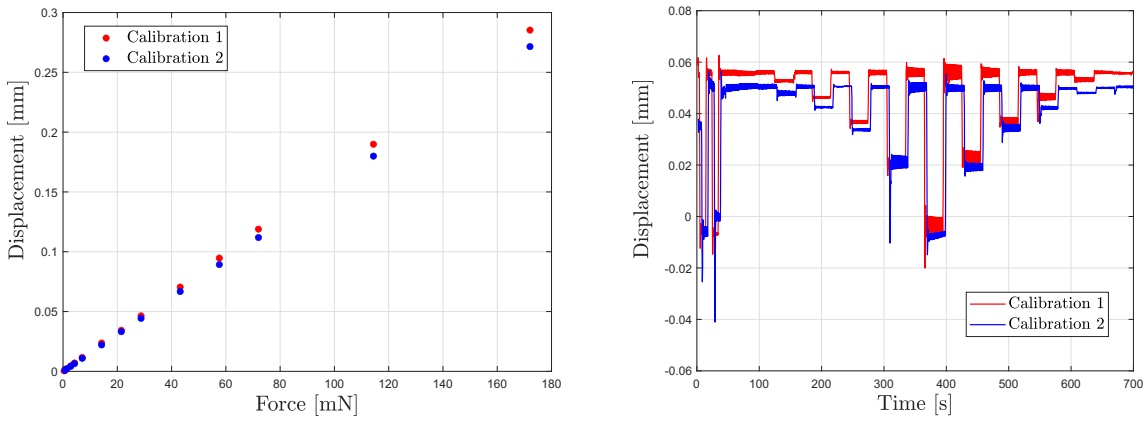


Figure 4.11: Thrust balance used for the electric propulsion testing and its main components.

In order to accurately calculate $F_{c/m}$, a high-precision calibrated scale is used to measure the weight (and in turn, the force) that the coils exert on the magnet for every set current. Although these values are fixed, it is recommended to redo this process yearly to ensure that $F_{c/m}$ has not changed due to any potential degradation of the permanent magnet within the VCA.

Once $F_{c/m}$ is known for several VCA coil currents, it is possible to record the displacement of the thrust balance when the same set of currents are applied and obtain a force-to-displacement constant (denoted as ϵ). It is anticipated that ϵ will vary depending on several factors like the weight of the suspended platform, and therefore this procedure is repeated every time the thrust balance is configured. The critical factor is ensuring that ϵ maintains linearity across different current setpoints, regardless of its absolute value. Throughout the entirety of the prepared experiments, ϵ ranged from $\epsilon = 587 - 677$ mN/mm. This correlation is subsequently utilised to correlate the displacement of the balance with the thrust exerted by the HET. Figure 4.12a illustrates two examples of VCA calibrations in distinct tests and the calibration constants derived from each.

The **second calibration system** is employed to ensure the calibration is unchanged throughout the vacuum process or before and after testing. This method involves the utilisation of a lever, capable of moving within the range of 0° to 60° owing to a servomotor, connected to the suspended plate of the thrust balance via a thread which contains a nut weighting 2.0 g (see Figure 4.11). As the lever moves, it exerts a force onto the balance, causing it to move accordingly.



(a) Voice Coil Actuator calibration

(b) In-situ calibration

Figure 4.12: Calibration of the thrust balance using the Voice Coil Actuator (VCA) method (Figure 4.12a) and the In-situ calibration method (Figure 4.12b) in two different tests. The calibration constant for test 1 and test 2 obtained were, respectively $\epsilon = 604.2$ mN/mm and $\epsilon = 634.1$ mN/mm.

By adjusting various angles, a time versus displacement curve is generated, which is used to compare multiple calibrations conducted at different instances (refer to Figure 4.12b). For these campaigns, three calibrations were conducted: 1) at atmospheric conditions, 2) before testing (under vacuum levels), and 3) after testing (also under vacuum levels). The absolute magnitude of each calibration is not critical, as it is contingent on the strength of the thread, which undergoes plastic deformation over time, resulting in reduced resistance and consequently less displacement for a given applied force. Nonetheless, ensuring the linearity of the displacement and the balance's appropriate response to the lever's movements is imperative.

An in-depth explanation of the thrust balance, calibration procedures, and error propagation is available in prior research [203].

4.1.3 Performance parameters

As explained in the previous Section 4.1.2.3, the thrust balance provides direct measurements of thrust (T). Furthermore, the readings obtained from the mass flow meters allow for the computation of the anode and cathode mass flows (m_a and m_c, respectively). The voltage and current readings from the various power supplies are directly obtained from the digital displays. Utilising this dataset, the anode specific impulse (I_{sp}), Thrust-To-Power-Ratio ($TTPR$), anode thrust efficiency

(η_{tr}), and total efficiency (η_{tot}) are calculated as follows:

$$I_{sp} = \frac{T}{\dot{m}_a g_0} \tag{4.1}$$

$$TTPR = \frac{T}{P_d} \tag{4.2}$$

$$\eta_{tr} = \frac{T^2}{2\dot{m}_a P_d} \tag{4.3}$$

$$\eta_{tot} = \frac{T^2}{2(\dot{m}_a + \dot{m}_c)(P_d + P_k + P_h + P_m)} \tag{4.4}$$

In these equations, P_h represents the heater power, P_k corresponds to the keeper power, and P_m indicates the power utilised to generate the magnetic field using electromagnets. As commented in Section 4.1.2.2, the typical heating power for the plasma filament cathode and hollow cathode *Hydrocat* are approximately $P_h \approx 300$ W and $P_h \approx 70$ W, respectively. As for P_k, the plasma filament cathode typically requires $P_k \approx 28$ W. For the hollow cathode *Hydrocat*, its magnitude varies depending on the propellant used. When krypton is utilised, a keeper power of $P_k \approx 17$ W is obtained. However, in the case of hydrogen, a higher keeper current (ranging between $I_k = 2 - 2.5$ A) results in improved discharge stabilisation, thereby increasing the keeper power to $P_k = 70 - 85$ W. Nevertheless, these values remain small compared to the discharge power of the thruster, which can reach up to $P_d = 3200$ W.

As explained in Section 4.1.2.1, the magnetic field configuration of the $AQUAHET$ necessitates two distinct power supplies, with the total power required to energise the coils contingent upon their temperature, ranging from $P_m = 500 - 800$ W when the maximum current is selected (5.5 A). In the case of the thruster *WET-HET*, only one power supply is needed, and the power requirements of the magnets are more modest, on the order of $P_m = 25$ W when $I_m = 1.5$ A are set for the electromagnets.

The uncertainty associated with thrust measurements comes from thrust balance measurements. The propagation of error arising from these measurements is assessed using the established procedures outlined in previous studies [203].

4.1.4 Electric Circuit and Ignition Process

To test and operate a HET with its respective hollow cathode, a specific arrangement of power sources needs to be set-up. This section provides a generic overview of the different power supplies needed to operate this system during laboratory testing. Figure 4.13 overviews the main electrical diagram of these devices in steady-state.

First off, the cathode heater is activated. This system functions as a closed circuit, heating the hollow cathode to initiate the thermionic emission of electrons from the insert. The heater's power requirements are significantly influenced by the design and operating conditions of the hollow cathode. For example, before igniting *Hydrocat*, the heater current is set to $I_k \approx 8 - 9$ A, with a heater voltage of $V_k \approx 20$ V.

Once the desired cathode base temperature has been obtained thanks to the heater power (in the case of *Hydrocat*, 200°C), the keeper power supply is activated. The activation is typically configured at high voltages (e.g., $V_k \approx 300 - 400$ V) and modest currents ($I_k \approx 0.5$ A). This high voltage is perceived by the electrons emanating by the emitter, which, in conjunction with the supply gas, generates a spark (the heater-keeper spark) and subsequently a plasma within the cathode. Once steady-state conditions are achieved, this plasma is stabilised at a lower voltage ($V_k \approx 20$ V) and a higher current ($I_k \approx 1$ A). At this point, it is possible to decrease the heater current to $I_h \approx 5 - 6$ A (obtaining a voltage of $V_h \approx 15 - 20$ V).

At this juncture, the cathode operates under steady-state conditions, and now the thruster is activated by switching on the anode power supply. The start-up process is executed by applying a high discharge voltage ($V_d = 500$ V) and a modest discharge current ($I_d = 1$ A). The high voltage attracts the electrons emitted by the cathode, traversing through the thruster's channel, initiating an ionisation process and generating plasma within the thruster (keeper-anode spark).

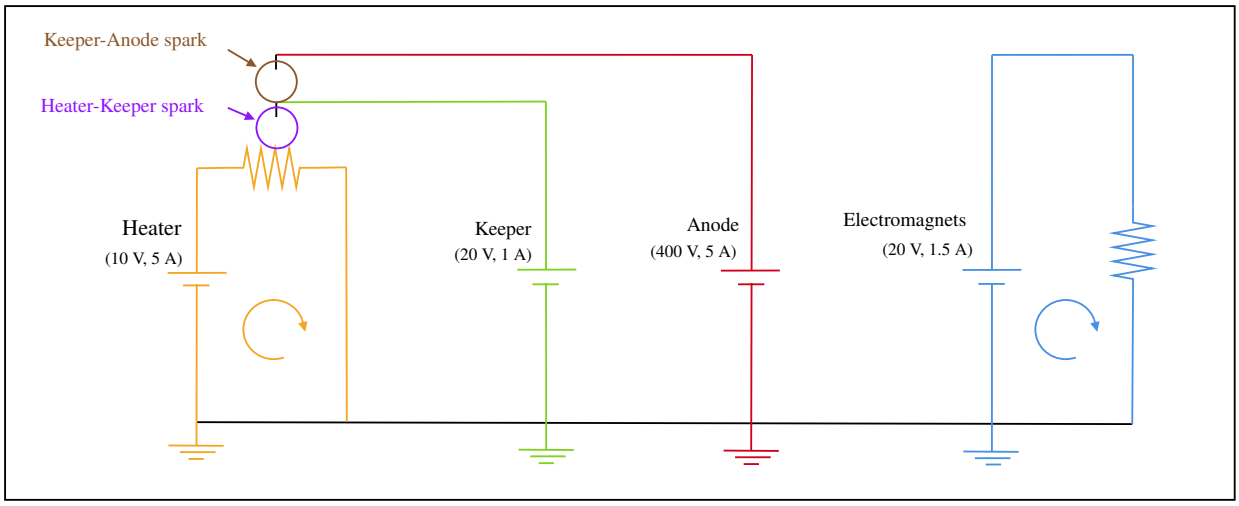


Figure 4.13: Schematic illustration of the electrical circuit of a Hall Effect Thruster suitable for laboratory experiments. The voltage and current values are taken as an example to show the order of magnitude of each one of them in steady-state ignition, and they correspond to the thruster *WET-HET* (Section 4.1.2.1) and the LaB_6 cathode *Hydrocat* (Section 4.1.2.2).

At steady-state, the voltage and current are adjusted to the thruster's desired operating point. However, it is important to note that if the thruster's magnetic field is not generated by permanent magnets, the electromagnets will need to be activated at this stage, prior to characterising the thruster's performance. In laboratory testing and space applications, generating the magnetic field using electromagnets can be advantageous, primarily due to the operational principles of these devices: by operating a HET without magnetic field (also known as "glow discharge" mode), electrons travel to the anode without resistance. Conversely, when the magnetic field is active, it acts as a resistive force to the electrons, making it more challenging for them to reach the anode. Therefore, starting without an active magnetic field allows for a gentler ignition process. Once the glow discharge is activated, the magnetic field can be progressively increased until the desired conditions are met. Notice that in some specific applications, such as low power HETs, the use of electromagnets could not be desired, as it necessitates an additional power source to operate, thereby increasing the thruster's total power requirements. Nonetheless, electromagnets offer the advantage of enabling the activation and deactivation of the magnetic field as needed, which can also be beneficial in space missions. Ultimately, the design and requirements of the space mission dictate the optimal strategy for the HET's operation. Finally, note that a different, though more

complex, setup can be achieved by allowing the system to float instead of grounding it, better representing space conditions.

4.1.5 Laboratories and Facilities

For these experiments, three different facilities were used:

- Imperial College London Boltzmann vacuum chamber facilities within the Imperial Plasma Propulsion Laboratory (in London, United Kingdom, Sections 4.2, 4.4, 4.6 and 4.7).
- Stanford University vacuum facilities within the Stanford Plasma Propulsion Laboratory (in California, United States, Section 4.3).
- ESA Propulsion Laboratory vacuum facilities within the European Space Agency (ESTEC, in Noordwijk, Netherlands, Section 4.5).

The different power supplies and hardware employed, along with the capabilities related to background pressures and setup, are contingent on the facilities utilised and are individually described in each section.

4.2 Campaigns A - Oxygen-Fuelled Hall Effect Thrusters with a Xenon/Krypton-Fuelled Cathode: Performance Characterisation

This section overviews the research on oxygen-fuelled HETs as the initial phase toward achieving and end-to-end validation of water electrolysis propulsion (see Section 4.1). Part of this work was published in ACTA Astronautica in 2023 and 2024 [3, 5].

4.2.1 Methodology

4.2.1.1 Experimental Set-Up and Vacuum Chamber Facilities

These EP experimental campaigns were carried out at the Boltzmann vacuum chamber facilities within the Imperial Plasma Propulsion Laboratory. There, two different vacuum chambers arranged in a T-shape are available for testing: a "main" vacuum chamber (1.5 x 2 m; diameter x length) and a "load-lock hatch" chamber (0.75 x 1.5 m; diameter x length). Whereas the load-lock hatch chamber is mainly used for calibration and hardware storage, the main chamber is used to obtain calibrated thrust measurements.

To reach vacuum levels suitable for EP testing, the facilities are composed of three vacuum stages:

1. Roughing pump (Leybold LV 80C): used to lower pressure levels from atmospheric conditions to $\approx 10^{-4}$ bar.

2. Turbo molecular pumps (Pfeiffer ATH 2303 M): used to further decrease the pressure levels from the roughing pump conditions ($\approx 10^{-4}$ bar) to $\approx 10^{-9} - 10^{-10}$ bar without mass flow and $\approx 10^{-8}$ bar with mass flow.

3. Cryo panel (Leybold 6000H): used to solidify gases whose freezing points are above 40K (such as oxygen, 54.36 K). This permits to keep the pressure levels of $\approx 10^{-8}$ bar during the operation of the thruster with mass flow.

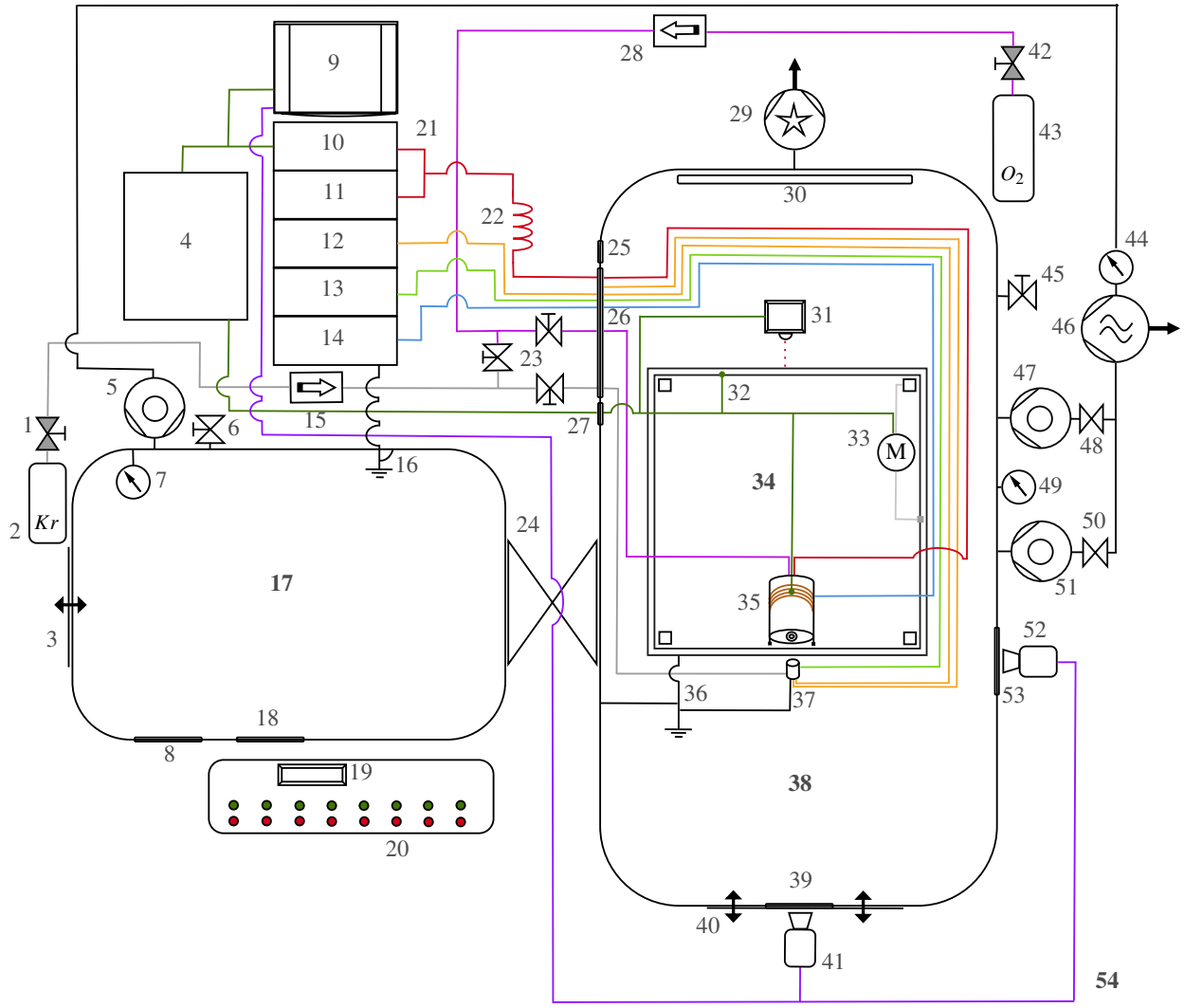


Figure 4.14: Main schematics of the Electric Space Propulsion testing at the Imperial Plasma Propulsion Laboratory. Department of aeronautics, Imperial College London. Published in [3].

The overall pumping capacity of the chamber is mainly denoted by the two turbopumps (2200 l/s of nitrogen for each one) and the cryo panel (1500 l/s of xenon).

Figure 4.14 details the experimental set-up and hardware used during this testing. The list of elements described are listed in Table 4.3.

4.2.1.2 Electronics

A rack consisting of five power supplies is utilised to supply power to both the thruster and cathode. The anode power is delivered by two parallel-connected power supplies (model *Sorenson SGA 1K0X5S-0AA*, elements 10 and 11) capable of providing up to 1000 V and 10 A each.

Table 4.3: Description of the elements depicted in Figure 4.14.

1	Pressure regulator (cathode)	**28**	Mass flow meter and controller (anode)
2	Cathode propellant bottle (Hydrogen / Krypton)	**29**	Cryohead (connected to a cryocompressor)
3	Door (vacuum load-lock hatch chamber)	**30**	Cryopanel (Stage 3)
4	Data Control and Acquisition System	**31**	Laser ILD1750
5	Turbopump (load-lock hatch chamber)	**32**	Thermocouple (to thrust balance)
6	De-pressurising valve (load-lock hatch chamber)	**33**	Servomotor (for calibration)
7	Pressure gauge (to load-lock hatch chamber)	**34**	Thrust balance
8	Vacuum feedthrough (auxiliary)	**35**	Water Electrolysis HET
9	Computer station	**36**	Grounding connection
10	Anode power supply [master] (*Sorenson SGA 1K0X5S-0AA*)	**37**	Cathode (double filament)
11	Anode power supply [slave] (*Sorenson SGA 1K0X5S-0AA R*)	**38**	Main vacuum chamber
12	Heater power supply (*Electro-Automatik EA-PSI 8080-60 DT*)	**39**	Vacuum feedthrough (window)
13	Keeper power supply (*Glassman PS/ET05R400-200*)	**40**	Door (main vacuum chamber)
14	Magnet power supply (model dependant on the thruster)	**41**	Camera Nikon D-5000 (front)
15	Mass flow meter and controller (cathode)	**42**	Pressure regulator (anode)
16	Grounding connection	**43**	Anode propellant bottle (Oxygen)
17	Vacuum load-lock hatch chamber	**44**	Pressure gauge (to roughing pump)
18	Vacuum feedthrough (window)	**45**	De-pressurising valve (main chamber)
19	Pressure readings display	**46**	Roughing pump (Stage 1)
20	Control panel of vacuum systems	**47**	Turbopump #1 (Stage 2, Leybold)
21	Parallel line connection (anode power supplies)	**48**	Pneumatic valve #1
22	Inductor	**49**	Pressure gauge (to main chamber)
23	Valves set (anode and cathode)	**50**	Pneumatic valve #2
24	Gate valve	**51**	Turbopump #2 (Stage 2, Leybold)
25	Vacuum feedthrough (auxiliary)	**52**	Camera Nikon D-5000 (side)
26	Vacuum feedthrough (power and feedlines)	**53**	Vacuum feedthrough (window)
27	Vacuum feedthrough (signals, D-Sub connector)	**54**	Imperial College London Plasma Laboratory

An inductor (element 22) is positioned between the thruster and the power supplies to enhance the stability of the thruster. The cathode operation relies on a heater (element 12) and a keeper (element 13) power supply. The maximum power available for the heater is 80 V / 60 A (used for both cathodes with the power supply *Electro-Automatik EA-PSI 8080-60 DT*). For the keeper 5000 V and 0.4 A are available using the power supply *Glassman PS/ET05R400-20*.

If additional current is required to operate the cathode, one of the anode power supplies can be repurposed to serve as the keeper power supply. Furthermore, the electromagnet power is provided by another dedicated power supply (element 14). For the *WET-HET* thruster, a single power supply suffices (utilising the *GW INSTEK SPS-3610* model, restricted to 36 V and 10 A). However, for the *AQUAHET*, two power supplies are necessary (refer to Section 4.1.2.1): the inner

coil employs the same power supply as the *WET-HET*, while the outer coils are powered by the *Electro-Automatik EA-PS 5040-40* power supply, which is constrained to 60 V and 60 A.

It should be noted that while the cathode (heater and keeper) and electromagnet power supplies are operated manually, the anode power supply is controlled by a data acquisition system (element 4).

Element 4 is also utilised to manage the two calibration systems described in Section 4.1.2.3. In Figure 4.14, only the in-situ calibration system, employing the servomotor (element 33) and laser (element 31), is depicted as it is the system in use while the thruster is operating. The temperature of this platform and the thruster are monitored using thermocouples (element 32). Additionally, two cameras (elements 41, 52) are positioned to observe the thruster and plasma discharge. The captured signals are transmitted to a monitor (element 9) situated atop the power supply rack.

4.2.1.3 Fluidics

For the anode feedline, an external oxygen tank (element 43) is positioned outside the vacuum chamber. A pressure regulator (element 42) is adjusted to maintain a pressure of 2 bar, ensuring the requisite back-pressure upstream of the anode gas mass flow controller (element 28). A similar setup is employed for the cathode feedline: a krypton tank (element 2), pressure regulator (element 1), and mass flow controller (element 15). These two lines remain separate until they converge at a set of strategically positioned valves (element 23) just before the vacuum feedthrough (see the following Section 4.2.1.4). Both connections utilise standard stainless-steel tubes and Swagelok 1/8" fittings. Note that in some tests, xenon was used as the cathode propellant instead of krypton, although the presented results in this section use krypton as a propellant. The same results and conclusions can be deducted if xenon would be used as the cathode propellant instead.

4.2.1.4 Working Procedures

In most cases, initiating the thruster with pure oxygen is feasible and this condition is maintained throughout the experimental campaign. However, on rare occasions, strong transient behaviour

and sparking may occur during thruster ignition. To address this, a krypton mass flow is initially set to the thruster to assist in starting the thruster at the beginning of the campaign. Once the thruster has operated nominally for a few minutes with krypton, the oxygen valve is opened, and the krypton valve is closed. While this procedure may not be necessary in all instances, it effectively can mitigate a possible initial sparking period of the thruster and better preserves its integrity. Following this initial procedure, the thruster is capable of initiating with pure oxygen for the remainder of the experimental tests. Valves positioned before the entrance of the feedline to the chamber are configured to actuate according to this operational procedure (element 23).

An alternative method, known as the "gas puff" technique can be utilised to reliably trigger the thruster discharge and prevent any sparking. This method entails pressurising the thruster feedline between the mass flow meter and the vacuum chamber feedline valve to 1 bar. Subsequently, the valve is opened, initiating the discharge due to the sudden release of gas at high pressure. Within one to two seconds, the mass flow rate returns to its normal set point, and the discharge stabilises.

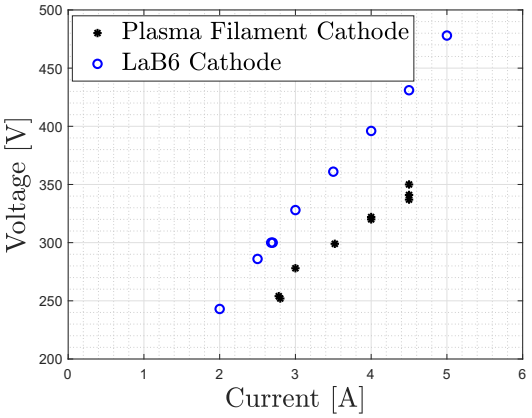
4.2.1.5 Thruster's Geometrical Configuration and Material Selection

In these experiments, the geometrical configuration and material selection for the two thrusters tested (*WET-HET* and *AQUAHET*) changed depending on the objective of the test. The specific configuration chosen is individually outlined when describing each test, based on the flexibility offered by the possible configurations of the two thrusters (Table 4.1 and Table 4.2).

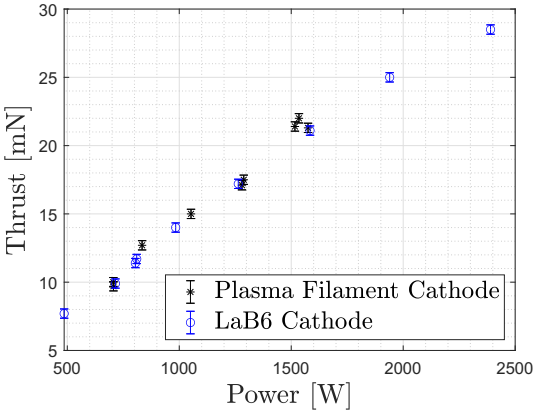
4.2.2 Results and Discussion

4.2.2.1 Influence of Cathode Selection

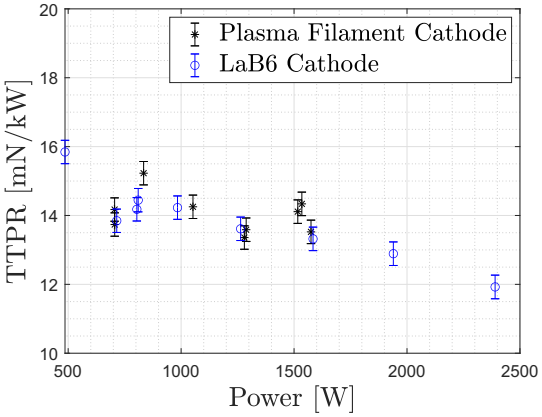
Before presenting any results, an assessment of the impact of the cathode selection is undertaken. This evaluation is necessary as two different cathodes were employed during testing (i.e., the plasma filament cathode and the hollow cathode *Hydrocat*, see Section 4.1.2.2). The motivation behind this comparison is to evaluate the extent to which the results obtained may differ when using either cathode. The results are presented in Figure 4.15.



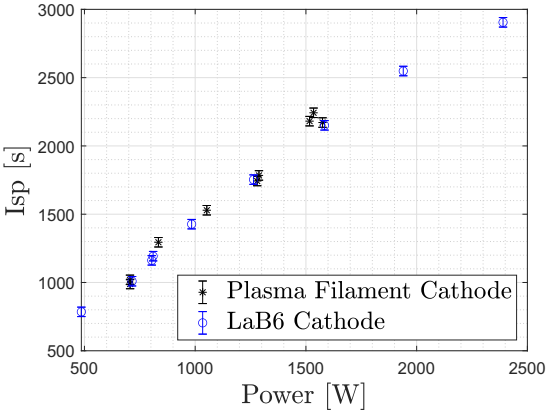
(a) IV Curve



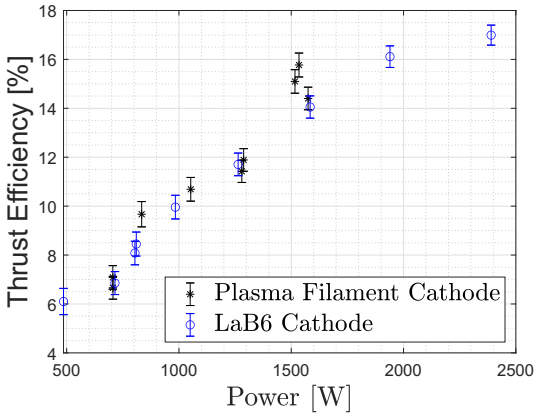
(b) Thrust (T)



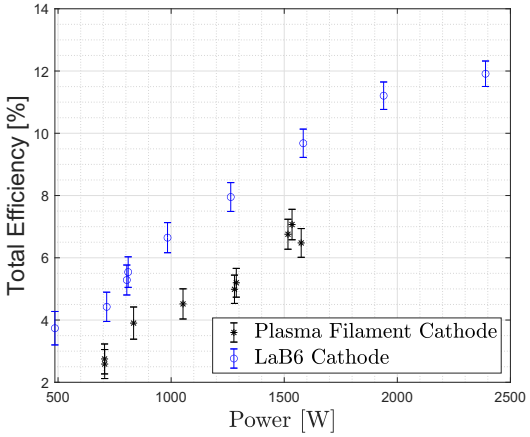
(c) Thrust-To-Power-Ratio ($TTPR$)



(d) Anode Specific Impulse (I_{sp})



(e) Anode Thrust Efficiency (η_{tr})



(f) Total Efficiency (η_{tot})

Figure 4.15: Experimental measurements of the system fuelled by oxygen (anode) in combination with two different cathodes fuelled by krypton: the plasma filament cathode and the *Hydrocat*. These values correspond to an anode mass flow of $\dot{m}_a = 1.0$ mg/s, the magnetic field topology of Figure 4.3 and the geometrical configuration of Table 4.1, using a channel length of L = 13.1 mm, an anode mass flow rate of $\dot{m}_a = 1.0$ mg/s, a stainless steel anode and ceramic walls composed of $BNSiO_2$. These results were published in [3].

The thruster employed for this experiment is the *WET-HET*, operating under the geometric and operational parameters outlined in Table 4.1. Specifically in these tests, a channel length

of L = 13.1 mm, an anode mass flow rate of $\dot{m}_a = 1.0$ mg/s, a stainless steel anode, ceramic walls composed of $BNSiO_2$ and a magnetic field topology shown in Figure 4.3 setting $I_m = 1.5$ A as the electromagnets current were used. The selection of these conditions was based on their demonstrated superior performance for the thruster, as will be detailed in subsequent sections.

The IV curve reveals that, for a given anode current, the anode voltage achieved when using the *Hydrocat* cathode exceeds that attained with the plasma filament cathode [5]. Essentially, this implies that, at a constant anode current or anode voltage, the HET will achieve a higher discharge power level when employing the *Hydrocat* cathode. It is also noteworthy that, in general, the total power consumed by the filament cathode running with krypton ($P_{fil} \approx 300$ W) exceeds that of the *Hydrocat* under the same conditions ($P_{hydro} \approx 70$ W). Additionally, as emphasised in Section 4.1.2.2, the mass flow required for the plasma filament cathode to operate (around $\dot{m}_c = 0.94$ mg/s) is more than two times greater than that needed for the *Hydrocat* (around $\dot{m}_c = 0.37$ mg/s).

Despite these differences, the performance levels from the anode perspective are quite comparable across all metrics at equivalent discharge power, as observed in Figure 4.15. Notably, the analysis of uncertainty propagation reveals no discernible disparities in the results of T, I_{sp} and η_{tr} obtained when using either of the two cathodes. This outcome was unexpected: typically, LaB_6 cathodes are more effective at achieving a lower coupling voltage (i.e., the voltage at the cathode plane). A lower coupling voltage implies that the potential difference between the anode and the cathode will be higher, thus further accelerating the ions and enhancing performance. However, this discrepancy may be attributed to the higher cathode mass flow used for the filament cathode compared to the LaB_6 cathode, as previously noted.

Consequently, it is inferred that the performance benchmarks established using a plasma filament cathode or the hollow LaB_6 cathode *Hydrocat* are mostly independent of the cathode used. Nonetheless, due to the lower mass flow and cathode power requirements of the LaB_6 cathode, the total efficiency of the system, considering all elements, is higher with the *Hydrocat*

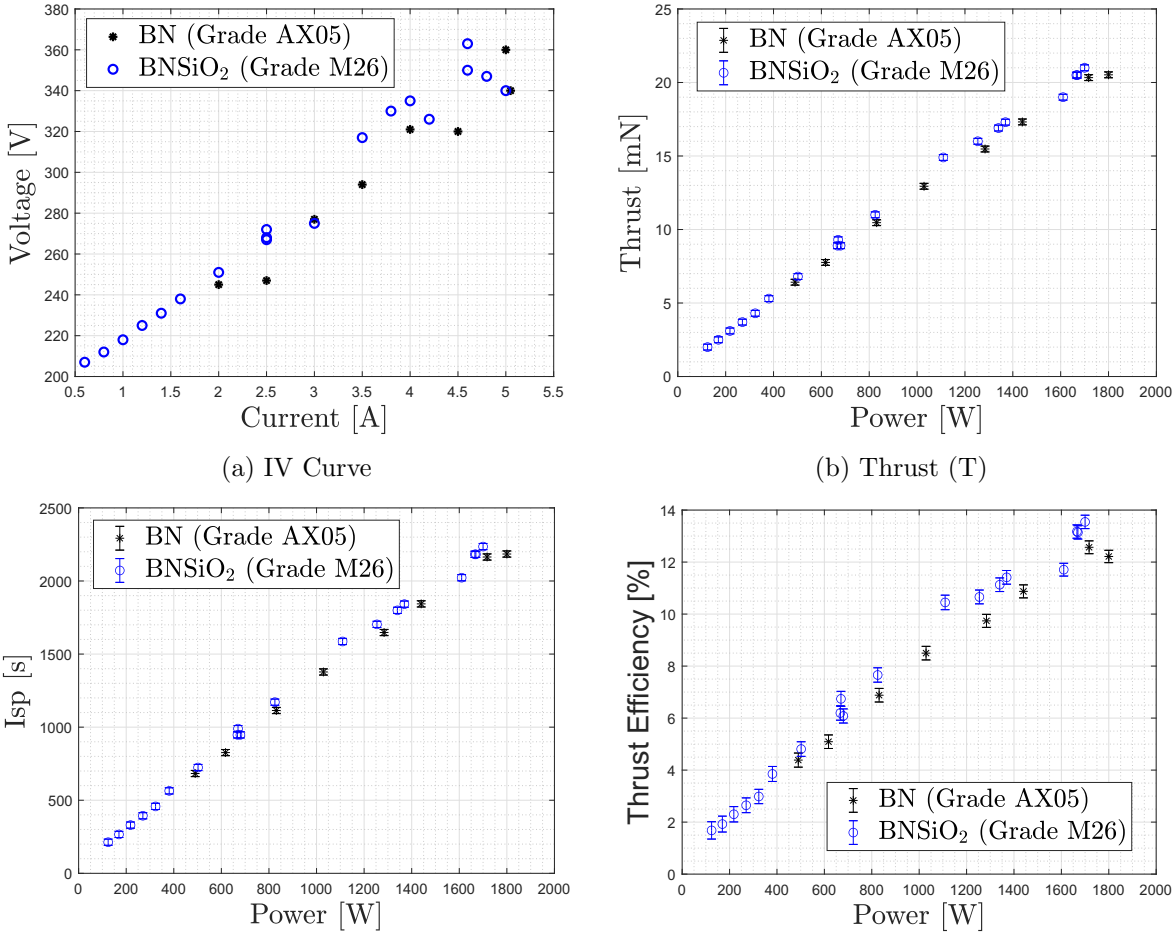
[5]Note that the IV current using oxygen or water vapour is different than the one from using xenon. In particular, the so-called "knee point" which separates the low voltage and high voltage mode with xenon [196] does not appear with these propellants. Instead, a linear relationship for voltage and current is obtained. This could be an indication of the low propellant utilisation of oxygen and water vapour compared to xenon, as can be seen in Figure 4.73.

cathode. This is observed in the total efficiency plot (Figure 4.15f), where the total efficiency of the *Hydrocat* surpasses that of the plasma filament cathode. As a result, since the performance metrics obtained with the plasma filament cathode do not accurately reflect those of an in-flight model, the total system efficiency is not depicted when this cathode is utilised. Instead, the total efficiency plots are showcased when employing the *Hydrocat* cathode, representative of a flight system device.

4.2.2.2 The Grade of the Ceramics Walls

The proper selection of the ceramics wall material is of importance as the Secondary Electron Emission (SEE) of the walls greatly depends on this choice; ultimately impacting the performance of the thruster. Although the SEE coefficient is also a function of the electron energy during operation, Boron Nitride (BN) ceramics have lower SEE compared to Al_2O_3 walls [12] for electron temperatures between $T_e = 10 - 100$ eV, resulting in superior performance among other choices [144, 204]. In fact, one of the largest improvements in previous research by A. Schwertheim when using oxygen-fuelled HETs was due to the change of the material of the ceramic walls from Al_2O_3 to BN [43].

The SEE coefficient is commonly not given by the industrial suppliers, which offer different choices of ceramic grades depending on the application. In previous work, BN Grade AX05 ceramics were selected due to its thermal properties (minimal thermal expansion, high thermal conductivity and excellent thermal shock stability), being one of the highest purity hexagonal BN solids available (> 99.7 %). In this study, BN Grade AX05 ceramic is compared against a Boron Nitride Silica compound (BNSiO_2, Grade M26, composed by 60% BN and 40% SiO_2). This new grade not only is known for its great thermal properties (high temperature strength and high thermal shock resistance) but also for its hydrophobic traits. These features are a consequence of the surface treatment with the hydrophobic silica, which made them completely resistant to moisture. In fact, this ceramic compound is tested underwater for 48 hours prior testing at elevated frequencies (a test referred to as *MIL-I-10A grade L542*).



(a) IV Curve

(b) Thrust (T)

(c) Anode Specific Impulse (I_{sp})

(d) Anode Thrust Efficiency (η_{tr})

Figure 4.16: Experimental tests on the *WET-HET* oxygen-fuelled with a krypton-fuelled plasma filament cathode over two different Boron Nitride (BN) grades: BN Grade AX05 and $BNSiO_2$ Grade M26. The configuration set for testing is the one shown in Table 4.1 using a channel length of L = 34.8 mm, an anode mass flow rate of $\dot{m}_a = 1.0$ mg/s, a stainless steel anode and the magnetic field topology shown in Figure 4.3 using $I_m = 1.5$ A to energise the electromagnets. These results were published in [3].

The hydrophobic properties can be useful when the thruster and cathode are fed directly by an electrolyser using water (where higher moist gases are expected, see Section 4.5) or when a direct water vapour feed is employed (see Section 4.6). The detailed list of thermal, electrical and mechanical properties compared to other ceramic grades can be found from the manufacturer supplier [205]. Moreover, according to the literature, BNS_iO_2 walls are claimed to exhibit lower SEE than BN, with this difference becoming more apparent when the walls' temperature exceeds $T_e = 20$ eV [12].

For this test, the *WET-HET* was used once again, operating under the geometric and operational parameters outlined in Table 4.1 using a channel length of L = 34.8 mm (in order to be able to

compare the results obtained with BN walls by A. Schwertheim [43, 144]), an anode mass flow rate of $\dot{m}_a = 1.0$ mg/s, a stainless steel anode and the magnetic field topology shown in Figure 4.3 with $I_m = 1.5$ A as the electromagnets current, in conjunction with the plasma filament cathode.

The results of this comparison are shown in Figure 4.16. From the IV curve (Figure 4.16a), it is possible to see that both ceramic walls behave very similarly. At low powers, the trend is highly linear, although the data is more scattered at higher powers. The thrust measurements (Figure 4.16b) demonstrate linearity over the investigated discharge power range (up to $P_d = 2000$ W). $BNSiO_2$ Grade M26 walls appear to perform marginally better when the discharge power exceeds $P_d > 1000$ W, although the impact on the results is not significant. This observation is also reflected on the I_{sp} (Figure 4.16c) and anode thrust efficiency (Figure 4.16d) plots.

Based on these results, it is concluded that this change in the grade of BN has negligible effects on the thruster's performance. For water electrolysis or water vapour-fuelled HETs, $BNSiO_2$ Grade M26 ceramic walls emerge as a superior choice compared to BN Grade AX05 ceramics due to their hydrophobic characteristics and absence of performance detriments compared to Grade AX05.

4.2.2.3 Anode Plate Compatibility Analyses

The suitability of the anodic material is crucial given its continuous exposure to the plasma. Unlike other metallic components that serve primarily as structural supports, the anode must maintain its integrity to sustain electrical conductivity and establish the requisite electric field characteristic of HETs. Additionally, the anode is subject to exceedingly high temperatures due to its proximity to the plasma. These temperatures are directly influenced by the thruster's discharge power and are inversely proportional to the available surface area for heat dissipation. Consequently, properties such as high electrical and thermal conductivity, elevated melting point, ease of fabrication, and resistance to oxidation from plasma interaction need to be considered when selecting an anode material.

The interaction between plasma and metals is not trivial, contingent upon factors such as the working gas, metal type, and specific application, which collectively determine the plasma's

operational characteristics. Notably, when working with gases like oxygen, inherent challenges arise concerning the oxidation of conductive metals, necessitating thorough investigation to ensure the long-term viability of this technology for space missions. Hence, experimental evaluations are necessary to assess the material's suitability for this purpose.

Tungsten was conceived as a prime candidate owing to its exceptional attributes, including a high melting point (approximately 3500°C), the highest modulus of elasticity among metals (400 GPa), robust temperature resilience, electrical conductivity, corrosion resistance, and machinability (albeit more challenging than other metals). Detailed information regarding tungsten's properties can be found in existing literature [206].

This experimental assessment involving tungsten was conducted using the *WET-HET* thruster across a range of discharge currents ($I_d = 2.0 - 4.0$ A), with the geometric parameters outlined in Table 4.1, featuring a channel depth of L = 13.1 mm, an anodic mass flow rate of $\dot{m}_a = 1.0$ mg/s, and employing the magnetic field topology depicted in Figure 4.3, with electromagnets operating at $I_m = 1.5$ A, in conjunction with a plasma filament cathode. The findings from these experiments are summarised below:

- When subjected to standard ignition and operational conditions, the tungsten anode develops a thin layer of oxidation upon contact with the plasma.
- This layer forms within approximately 20 minutes of continuous operation, although it is dependent on the operating conditions of the thruster.
- Initially, the resistance between various points on the anode measures 0.1 Ω, but once the layer forms, the resistance increases to $20 - 100$ $k\Omega$. This elevated resistance renders the layer non-conductive, thereby precluding thruster operation.
- Prior to the formation of this layer, thrust measurements can be taken, and the performance obtained is closely aligned with that of other tests conducted. However, the rapid development of the layer imposes significant limitations on test duration and the number of tests that can be performed.

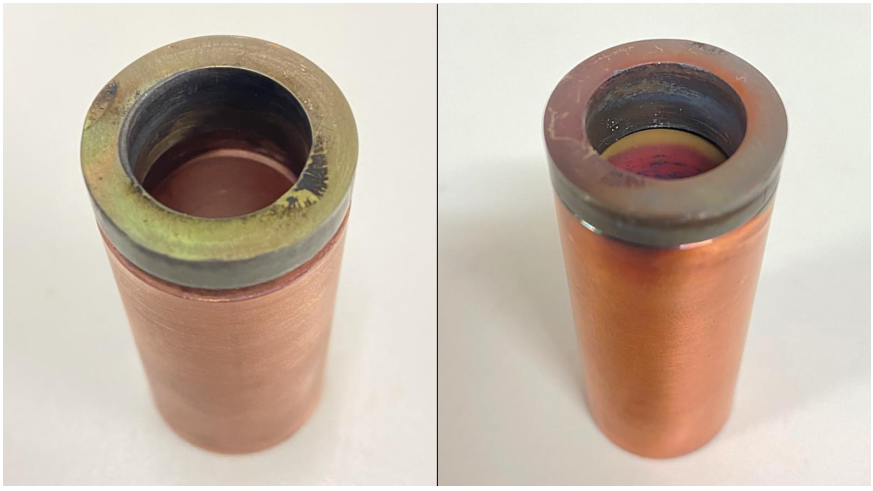


Figure 4.17: Oxidation of the anode stainless steel cap. Left: oxidation layer after low power ($P_d < 1000$ W) thrust measurements. Right: oxidation layer after high power ($P_d > 1000$ W) thrust measurements. This data was published in [3].

Based on these experiments, it was deduced that tungsten anodes are incompatible with water electrolysis propulsion in HETs. Consequently, stainless steel (316L) anodes were explored as an alternative. This decision was motivated by the stainless steel's notable attributes, including high tensile strength (621 MPa), moderate melting point (1500°C), resilience to high temperatures, ease of fabrication, resistance to oxidation, and minimal susceptibility to magnetic fields, thereby ensuring the HET's magnetic field remains unaffected. The mechanical and thermal characteristics of stainless steel are extensively documented in the literature [207]. The findings from these investigations are summarised below:

- Under typical testing conditions, the stainless steel anode also undergoes the formation of a thin oxidation layer upon contact with the plasma. It is known that this material, in the presence of air, develops a chromium oxide film, indicative of its inherent resistance to oxidation. However, investigations involving various treatments of stainless steel anodes with oxygen plasmas revealed the formation of crystals believed to be $MnFe_2O_4$ [208].

- The rate of formation closely mirrors that observed with the tungsten anode, occurring within approximately 20 minutes of continuous plasma exposure, although it is subjected to the operating conditions of the thruster.

- Compared to the tungsten anode, the newly formed oxide film on the stainless steel anode

maintains a low resistance for a longer testing time. This oxidation layer seems to be formed differently depending on the discharge power and, consequently, the anode temperature. For high power thrust measurements ($P_d > 1000$ W), the layer seems to be thicker and more detrimental to the conductivity than the one formed with lower anode temperatures ($P_d < 1000$ W). In Figure 4.17, the oxidation layer of the anode formed during these scenarios is shown.

- Thrust measurements obtained both with and without the oxidation layer exhibited negligible discrepancies, with the presence of an electrically conductive layer facilitating extended-duration tests.

Based on the findings, it was established that stainless steel anodes, despite being subjected to oxidation, are appropriate for laboratory experiments aiming to test the thruster for a couple of hours. Following the test, the oxidation layer can be removed by scraping the anode surface, thereby allowing for the resumption of testing. However, this approach is not applicable for a flight model intended to test this technology over extended periods. Section 4.4.2.3 offers additional insights into the oxidation of hardware when oxygen and hydrogen are present in the same environment (as opposed to oxygen and krypton, as discussed here). Section 6.2 explores potential solutions for this oxidation, based on the research compiled within this thesis, with the goal of identifying a suitable material combination that is not only suitable for laboratory tests but also for actual space missions.

4.2.2.4 Magnetic Field

The effects of the magnetic field are overviewed for the two thrusters, *WET-HET* and *AQUAHET*.

WET-HET

The impact of magnetic field topology and strength on the performance of the *WET-HET* fuelled by oxygen in combination with a krypton-fuelled cathode was extensively examined by A. Schwertheim [43, 144].

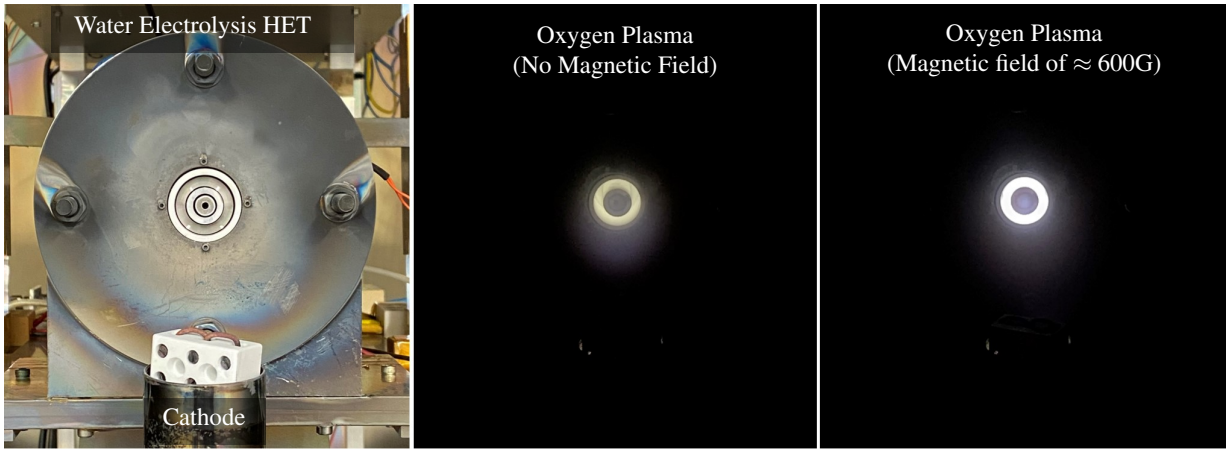


Figure 4.18: Plasma ignition of the *WET-HET* operating on oxygen (with and without magnetic field). This data was published in [3].

His results showed that a Gaussian magnetic field (the one depicted in Figure 4.3), demonstrated superior efficiency compared to other exotic topologies where the high-intensity magnetic flux density did not peak at the end of the channel but was extended further towards the anode. The influence of magnetic flux density on a fixed topology was also explored. A. Schwertheim concluded that the peak magnetic field achieved when $I_m = 1.5$ A were used to energise the electromagnets (resulting in a peak magnetic field of 600 G) provided the best efficiency [43, 144].

Consequently, these conditions were employed when the aim was to achieve the highest possible performance. Readers are directed towards these previous investigations for a more detailed overview [43, 144].

Figure 4.18 shows the thruster in operation with and without the magnetic field. In the absence of the magnetic field, the oxygen plasma appears green. However, with the magnetic field active, the plasma density increases due to the enhanced confinement and heating of the electrons throughout the magnetic field region, which increases the plasma's brightness and turns it white. Note that the decolouration of the thruster's front plate is attributed to the plasma filament cathode operation, where the use of a tungsten filament heated to high currents creates a thin tungsten deposit on the thruster.

AQUAHET

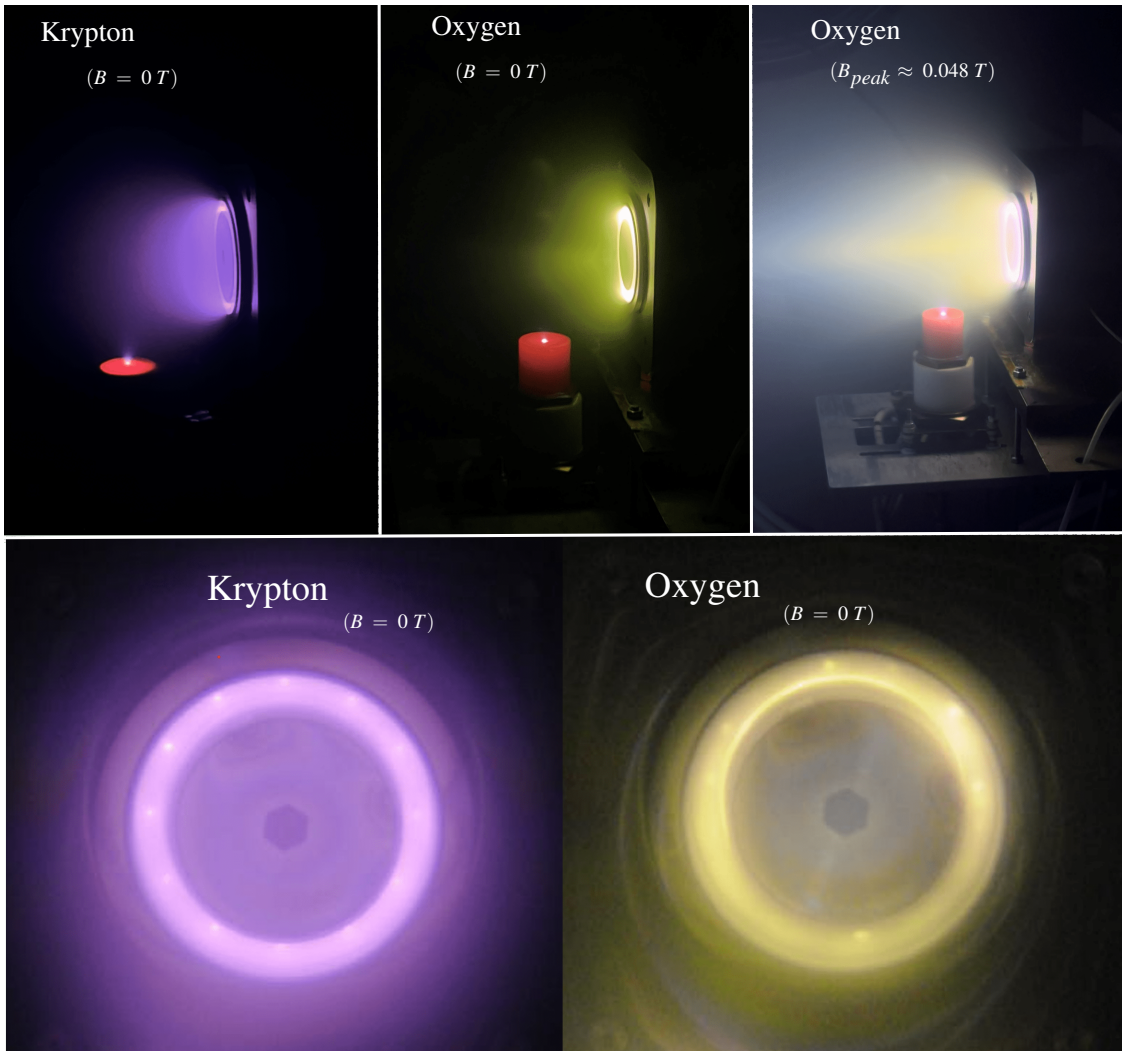
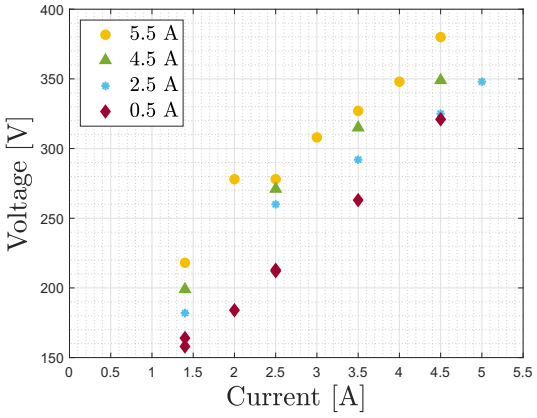
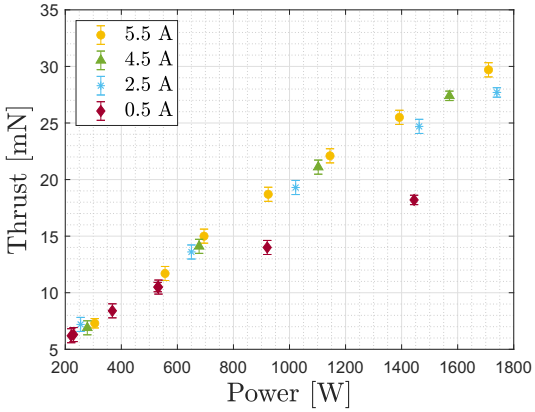


Figure 4.19: Thruster *AQUAHET* firing on krypton and oxygen, for different magnetic fields (B). The propellant injection holes are visible from the plasma discharge.

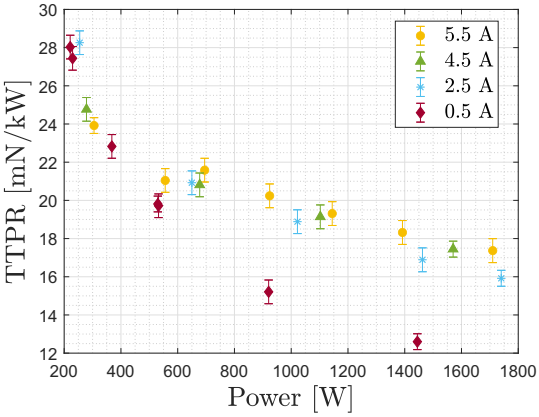
In the case of the *AQUAHET*, the impact of the magnetic flux density on the performance was yet not explored, and experimental data was gathered to evaluate its influence. Figure 4.19 shows the *AQUAHET* firing using krypton or oxygen for the anode and krypton for the cathode, for various magnetic flux densities. Figure 4.20 shows the performance obtained as a function of the magnets' current. Results for the $w = 4$ mm configuration are presented, with analogous conclusions applicable to $w = 5$ mm.



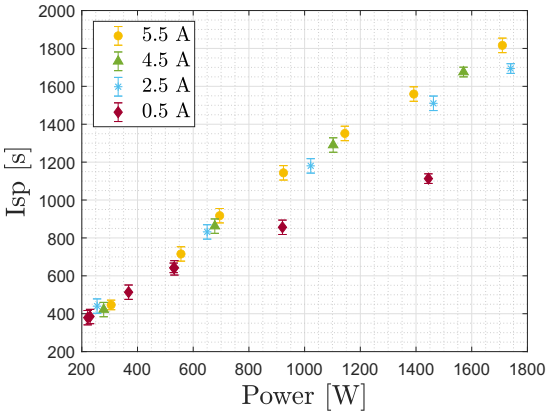
(a) IV Curve



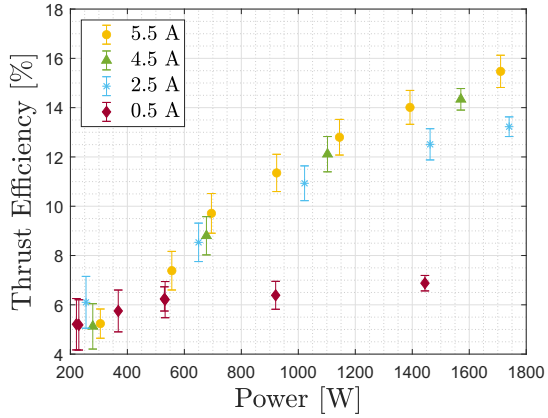
(b) Thrust (T)



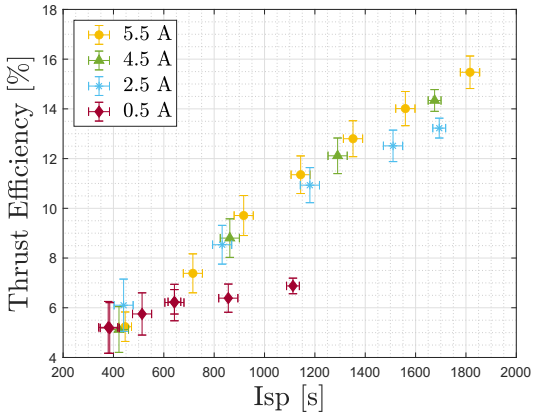
(c) $TTPR$



(d) Anode Specific Impulse (I_{sp})



(e) Anode Thrust Efficiency (η_{tr})



(f) η_{tr} vs I_{sp}

Figure 4.20: Experimental measurements of the *AQUAHET* and *Hydrocat* fuelled by oxygen (anode) and krypton (cathode) for different electromagnet currents, as in in Figure 4.5. The results correspond to an anode (oxygen) mass flow of $\dot{m}_a = 1.7$ mg/s, a cathode (krypton) mass flow of $\dot{m}_c = 0.2 - 0.4$ mg/s and a channel width of $w = 4$ mm.

The IV curve (Figure 4.20a) displays a varied trend contingent upon this parameter. Notably, for a fixed current, the attained voltage rises with the magnetic flux density. Performance, characterised by T, $TTPR$, I_{sp}, and η_{tr}, improves with an increase in magnetic flux density.

Particularly notable is the difference in performance obtained with a $I_m = 0.5$ A and $I_m = 2.5$ A magnet current (which yield peak magnetic flux densities of approximately $B \approx 0.030$ T and $B \approx 0.038$ T, respectively). Performance variation between $I_m = 2.5 - 4.5$ A ($B \approx 0.044$ T) datasets only exceeds the uncertainty margin for power levels above $P_d > 1400$ W, with a magnet current of $I_m = 4.5$ A enabling higher thrust measurements. Only small differences in thrust can be observed when comparing the $I_m = 4.5$ A and $I_m = 5.5$ A magnet current datasets, with the highest anode thrust efficiency data point collected at $I_m = 5.5$ A.

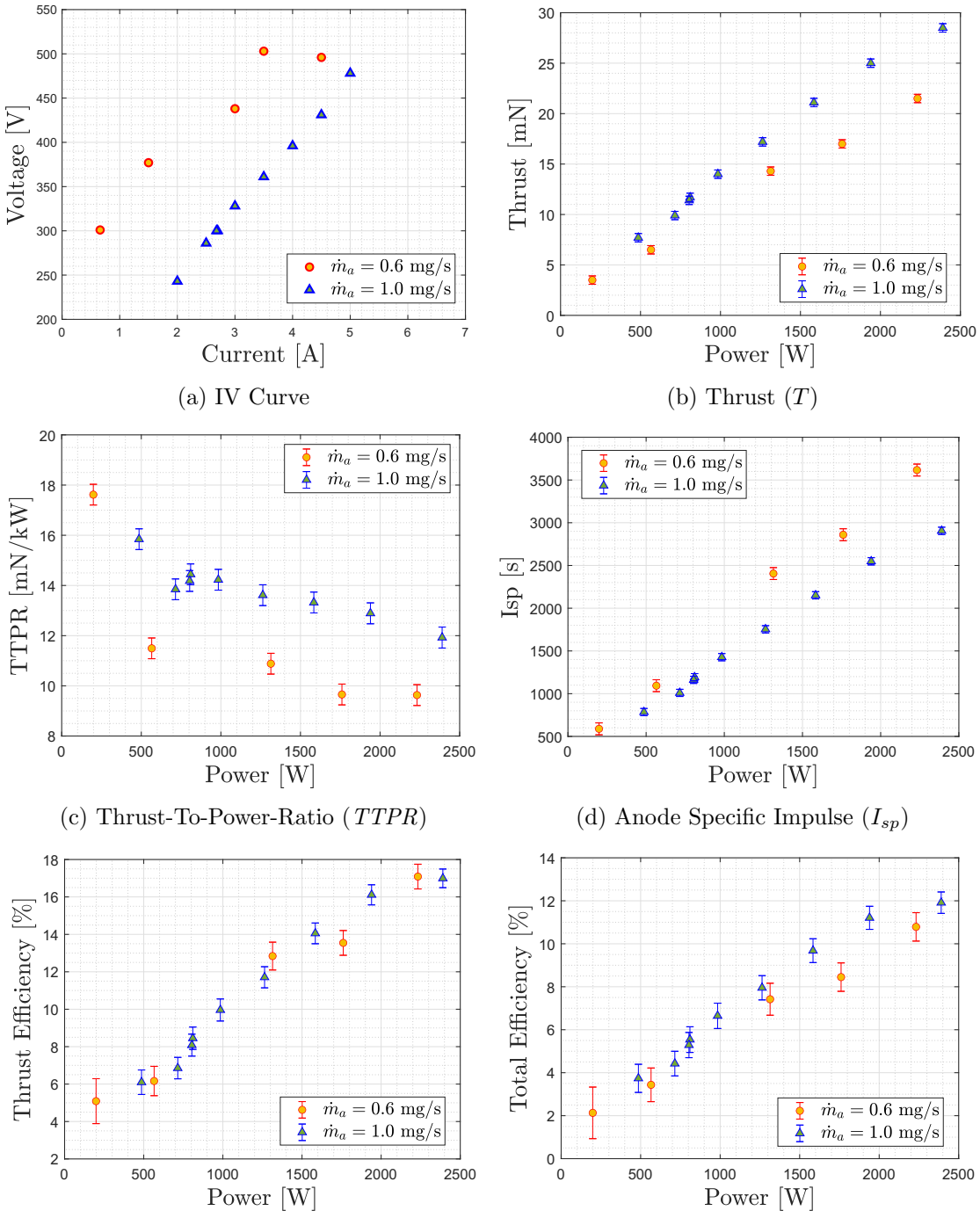
These findings are very similar to those obtained with the *WET-HET*, where a large magnetic flux density of 0.060 T was demonstrated to be the most advantageous [143].

4.2.2.5 Mass Flow

The effects of the mass flow are also overviewed for the two thrusters: *WET-HET* the *AQUAHET*.

WET-HET

The influence of anode mass flow on the performance of the oxygen-fuelled *WET-HET* thruster, in conjunction with a krypton-fuelled cathode, was initially explored by A. Schwertheim. He presented the results of thruster performance within the range of $\dot{m}_a = 1.0 - 1.8$ mg/s. These tests demonstrated that lower anode mass flows corresponded to higher I_{sp} and reduced thrust. Consequently, these two factors indicated that lower mass flows yielded superior performance. In this thesis, further studies were conducted at a reduced mass flow rate ($\dot{m}_a = 0.6$ mg/s) to assess whether or not it could further improve the performance of the system. Figure 4.21 compares the data measurements under these conditions with those obtained at $\dot{m}_a = 1.0$ mg/s at different discharge powers. For these tests, the thruster was operated in conjunction with the hollow cathode *Hydrocat* under the geometric and operational parameters detailed in Table 4.1, using a channel length of L = 13.1 mm, a stainless steel anode, ceramic walls composed of $BNSiO_2$ and the magnetic field topology depicted in Figure 4.3, with $I_m = 1.5$ A set as the electromagnets current.



(a) IV Curve

(b) Thrust (T)

(c) Thrust-To-Power-Ratio ($TTPR$)

(d) Anode Specific Impulse (I_{sp})

(e) Anode Thrust Efficiency (η_{tr})

(f) Total Efficiency (η_{tot})

Figure 4.21: Experimental measurements of the system fuelled by oxygen (anode) in combination with the hollow cathode *Hydrocat* fuelled by krypton. These values correspond to the magnetic field topology of Figure 4.3 using $I_m = 1.5$ A to energise the electromagnets and the geometrical configuration of Table 4.1, using a channel length of L = 13.1 mm, an anode mass flow rate of $\dot{m}_a = 1.0$ mg/s, a stainless steel anode and ceramic walls composed of $BNSiO_2$.

The IV curve shows that, for a constant current setting, the voltage achieved using an anode mass flow rate of $\dot{m}_a = 0.6$ mg/s consistently surpasses the one obtained with $\dot{m}_a = 1.0$ mg/s throughout the range of discharge powers examined. As anticipated, the thrust generated with

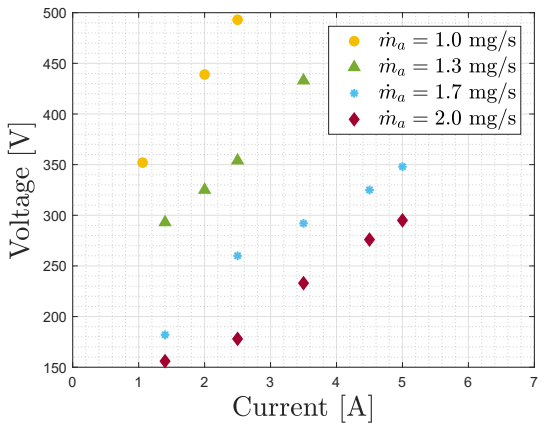
a $\dot{m}_a = 1.0$ mg/s is greater, albeit at the expense of a lower I_{sp}. Notably, thrust efficiencies for both conditions are comparable, indicating no discernible enhancement in anode performance upon reducing the mass flow rate below $\dot{m}_a = 1.0$ mg/s. However, the achieved I_{sp} levels at $\dot{m}_a = 0.6$ mg/s are attractive, yielding $I_{sp} = 3617 \pm 69$ s at the highest discharge power ($P_d = 2232 \pm 1$ W).

An evident difference observed between these two anode mass flow conditions lies in the cathode keeper voltage. At $\dot{m}_a = 0.6$ mg/s, the keeper voltage registers a higher value of $V_k = 23$ V, compared to $V_k = 15$ V at $\dot{m}_a = 1.0$ mg/s. Consequently, the total cathode power (P_{hydro}) required to sustain thruster operation at $\dot{m}_a = 0.6$ mg/s is higher, approximately $P_{hydro} \approx 77$ W in contrast to $P_{hydro} \approx 64$ W at $\dot{m}_a = 1.0$ mg/s. This disparity is reflected in the overall efficiency plot, illustrating that $\dot{m}_a = 1.0$ mg/s yields superior overall performance and greater discharge stability. Therefore, this condition is deemed as the most optimum one for this thruster.

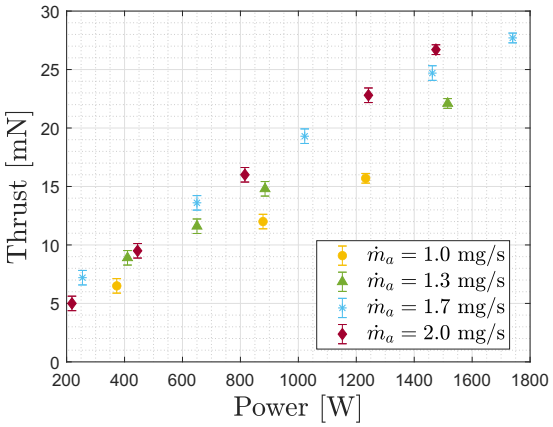
AQUAHET

The influence of the anode mass flow on performance of *AQUAHET* for its two channel width configurations ($w = 4$ mm and $w = 5$ mm) is depicted in Figure 4.22.

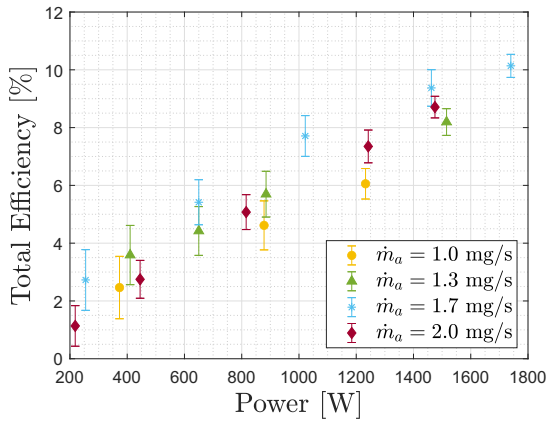
Unlike for the magnetic field, changing the channel width impacts the performance trends as a function of mass flow rate. This could be expected as changing the channel width changes the neutral pressure inside of the discharge channel, and so the in turn influences the mass flow operating envelope. Figures 4.22a, 4.22b, and 4.22c show the IV curve, T, and η_{tot} for $w = 4$ mm for mass flow rates in the range of $\dot{m}_a = 1.0 - 2.0$ mg/s. Figures 4.22d, 4.22e, and 4.22f present the same metrics for $w = 5$ mm in the range of $\dot{m}_a = 1.3 - 2.5$ mg/s. For both the $w = 4$ mm and the $w = 5$ mm testing it was independently verified that varying the magnet current between $I_m = 2.5 - 5.5$ A did not have a substantial an impact on the conclusions obtained from these tests. Therefore, data collected for a magnet current of $I_m = 2.5$ A ($B \approx 0.038$ T) for $w = 4$ mm and for $I_m = 5.5$ A ($B \approx 0.047$ T) in the case of w = 5 mm are presented here.



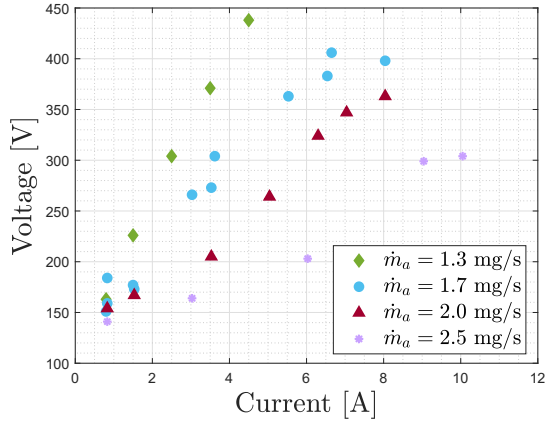
(a) IV Curve - $w = 4$ mm



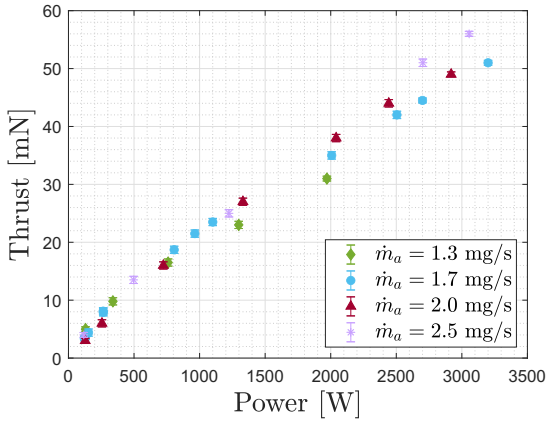
(b) Thrust (T) - $w = 4$ mm



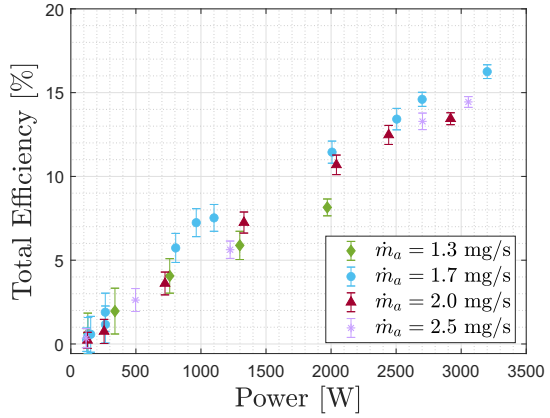
(c) Total Efficiency (η_{tot}) - $w = 4$ mm



(d) IV Curve - $w = 5$ mm



(e) Thrust (T) - $w = 5$ mm



(f) Total Efficiency (η_{tot}) - $w = 5$ mm

Figure 4.22: Experimental measurements of the *AQUAHET* and *Hydrocat* fuelled by oxygen (anode) and krypton (cathode) for two different discharge channel geometric configurations: channel width w = 4 and w = 5 mm. Measurements are taken for anode mass flow rates between $\dot{m}_a = 1.0 - 2.5$ mg/s and a cathode mass flow of $\dot{m}_c = 0.2 - 0.7$ mg/s. In this figure, the $w = 4$ mm thrust data is collected for a $I_m = 2.5$ A magnet current, while the $w = 5$ mm thrust data is collected for a $I_m = 5.5$ A magnet current (see Figure 4.5).

A distinctly different IV curve is evident when varying the mass flow. As expected, lower mass flows result in higher voltage attained for a set current (and conversely, lower current for a set

voltage). The thruster's stability was bounded by a discharge voltage of 500 V. Depending on the mass flow, this condition is reached at different power levels.

Given that the total efficiency increases with the discharge power, it is clear that operating at higher discharge power levels is beneficial in terms of efficiency. The threshold discharge voltage value at which the plasma becomes difficult to sustain is reached at lower powers for mass flows at the lower end of the ranges tested. This, in turn, means that lower total efficiency values are achieved at $\dot{m}_a = 1$ mg/s (for $w = 4$ mm) and $\dot{m}_a = 1.3$ mg/s (for $w = 5$ mm).

Comparing all the results obtained with $w = 4$ mm, it is evident that the optimum thrust performance is achieved with either $\dot{m}_a = 1.7$ mg/s or $\dot{m}_a = 2.0$ mg/s. It is difficult to discern which one of these two is the optimal one, although it could be interpreted, based on the total efficiency plot (Figure 4.22f) that $\dot{m}_a = 1.7$ mg/s is the optimum. Similar findings are observed with the configuration utilising $w = 5$ mm.

One additional set of tests were carried out to assess whether or not the thruster could work with the cathode in self-sustained mode (with no keeper and heater power). To do so, first the heater of the cathode was turned off and subsequently, the keeper current. From these tests, it was observed that stable operation was possible without the use of the heater, but a small amount of keeper current ($I_k = 0.15$ A, corresponding to a keeper voltage of $V_k = 30 - 40$ V of keeper voltage) was still necessary to stabilise the discharge.

4.2.2.6 Channel Length Dependence

While the length of the plasma discharge channel (L [6]) stands as a key aspect in a HET design, the available literature on this topic is limited [209]. Early inquiries suggested that elongated channels could decrease current utilisation but enhance propellant utilisation [210, 211]. Particularly for molecular plasmas like oxygen, whose propellant utilisation typically lags behind that of xenon-fuelled HETs [144, 196], it was hypothesised that longer channels could enhance overall performance, though this supposition lacked experimental validation. Consequently, some researchers favoured

[6]Note that, specifically for this section, the channel length (denoted in the thesis as L) has different acronyms depending on the specific length selected (see Table 4.4).

longer channels in their thruster designs utilising molecular propellants such as air [212]. Others employed computational models to evaluate the influence of channel length, such as E. Ahedo and D. Escobar, who explored the 10-40 mm range [209]. Their findings revealed a trade-off between propellant utilisation and ionisation efficiency, with peak overall thrust efficiency occurring at a channel length of L = 16.5 mm.

The following results seek to empirically demonstrate whether or not longer channels offer greater utility for molecular plasmas like oxygen, by investigating an oxygen-fuelled HET across a range of channel lengths spanning $L = 5.5 - 59.8$ mm. The conclusions drawn incorporate the previous investigations by A. Schwertheim, who examined long (L: 59.8 mm) and medium (M: 44.8 mm) channel lengths [144], and investigate in detail the short (S: 34.8 mm) and very short configurations (VS_1: 13.1 mm and VS_2: 5.5 mm) utilising the results garnered from these experimental campaigns.

The thruster *WET-HET* is used for these tests, as it is the only one of the two that permits adjustment of the channel length based on the length of the anode copper tube inserted into the channel (see Section 4.1.2.1). The geometry used is the one of Table 4.1 for various channel lengths, maintaining a constant anode mass flow rate of $\dot{m}_a = 1.0$ mg/s, and employing the magnetic field topology depicted in Figure 4.3, with electromagnets operating at $I_m = 1.5$ A. Throughout these tests, the plasma filament cathode is employed.

Table 4.4 provides an overview of the different lengths of the anode copper extension tubes alongside their corresponding chamber lengths, along with their nomenclature. Graphically, these configurations are depicted in Figure 4.23, which also showcases the tungsten and stainless steel caps that can be threaded onto the copper tubes and remain in contact with the plasma (see Section 4.2.2.3). The caps can be fully threaded or partially, depending on the desired final discharge chamber length, allowing for a clearance of up to 1 mm between them. Furthermore, these lengths are illustrated alongside the magnetic field topology in Figure 4.24. It is noteworthy that the alteration of the copper anode tube and cap is a manual process, necessitating the reconstruction of the thruster each time a new configuration is desired.

Table 4.4: Compilation of the different anode and channel lengths used for the investigation of the channel length influence on performance in the thruster *WET-HET*. Data published in [3].

Nomenclature	**Anode Length [mm]**	**Channel Length [mm]**
Long [L]	21.5	59.8
Medium [M]	36.5	44.8
Short [S]	46.5	34.8
Very Short 1 [VS_1]	68.2	13.1
Very Short 2 [VS_2]	74.2	5.5

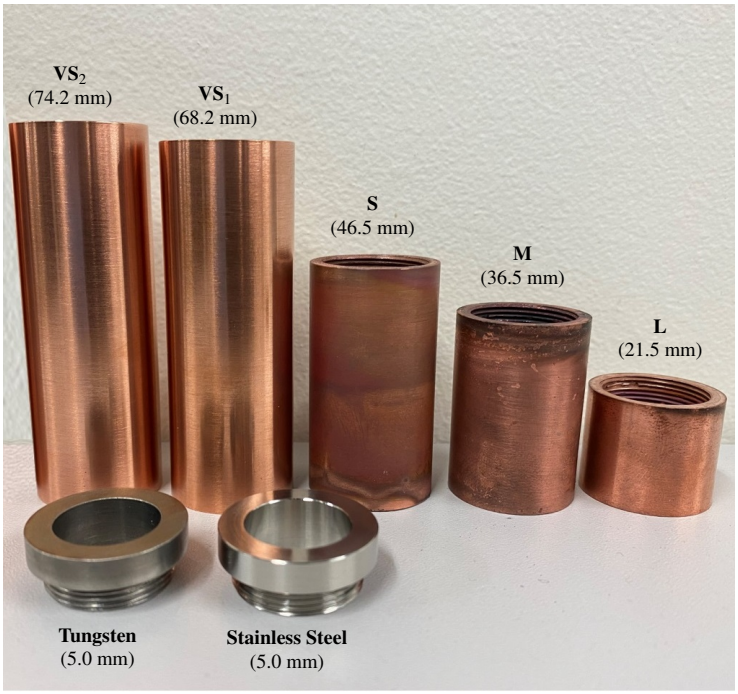


Figure 4.23: Visual description of the anode lengths and caps tested throughout the investigation of the channel length influence on performance in the thruster *WET-HET*. Graph published in [3].

Figure 4.25 illustrates the IV curve, thrust, anode I_{sp}, and thrust efficiency across channel lengths S: 34.8 mm, VS_1: 13.1 mm and VS_2: 5.5 mm. To start with, it is discernible that the shortest channel examined (VS_2: 5.5 mm) manifests a distinct IV curve compared to the other lengths (S: 34.8 mm, VS_1: 13.1 mm), across the entire discharge power range: in the low-power regime, the discharge voltage is lower than that observed with a channel depth of S: 34.8 mm. As the discharge current escalates, the discharge voltage gradually increases until approximately $P_d \approx 600$ W, reaching $V_d \approx 240$ V. At this juncture, the IV curve saturates, and the thruster fails to achieve higher voltages despite increasing the discharge current.

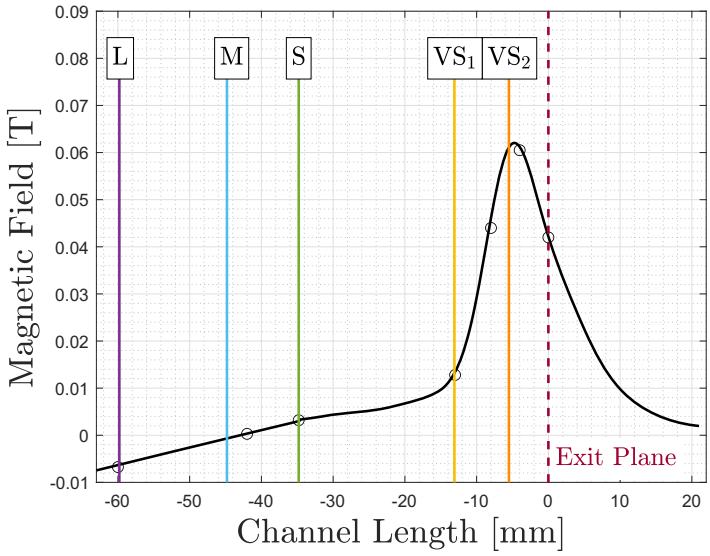


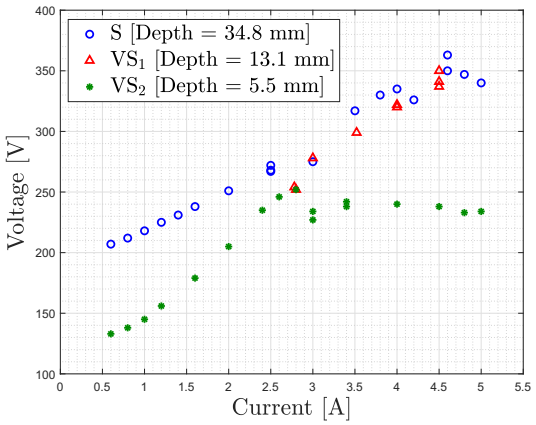
Figure 4.24: Magnetic field and channel lengths investigated in these campaigns for the *WET-HET*. The black dots represent the experimental measurements taken at the laboratory. Graph published in [3].

This behaviour corresponds to two distinct performance regions:

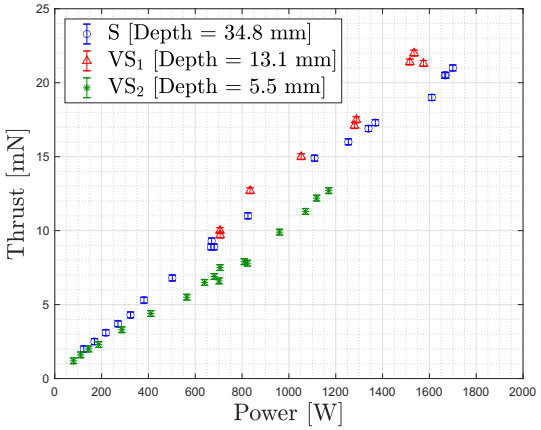
On the one hand, for very low powers ($P_d < 200$ W), the thrust, anode I_{sp} and thrust efficiency closely resemble those of the short channel (S: 34.8 mm). Nonetheless, the thruster's performance at these levels is notably deficient ($\eta_{tr} < 2\%$), as the thrust efficiency escalates with discharge power (Figure 4.25d).

On the other hand, at powers exceeding $P_d > 200$ W, encompassing the majority of the explored discharge power range, the performance of the shortest channel (VS_2: 5.5 mm) is inferior to that of the other channel lengths (S: 34.8 mm, VS_1: 13.1 mm). Ultimately, it fails to attain efficiencies exceeding 8%.

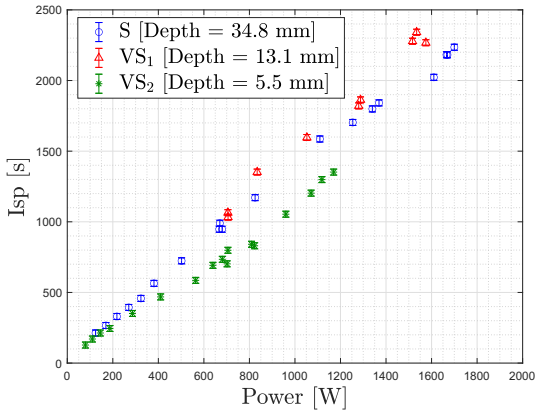
The observed behaviour is attributed to the positioning of the shortest channel length near the peak of the magnetic field (Figure 4.24). Consequently, ions fail to undergo full acceleration as they do not traverse the entire region of high electric field near the channel exit. Furthermore, despite the minimal wall losses due to the shortened channel length, the low ionisation rate outweighs these losses, resulting in a diminished overall thrust efficiency. Another drawback associated with this configuration pertains to thermal stresses: the reduced surface volume due to the shallow channel depth impedes the thruster's ability to adequately accommodate and dissipate heat.



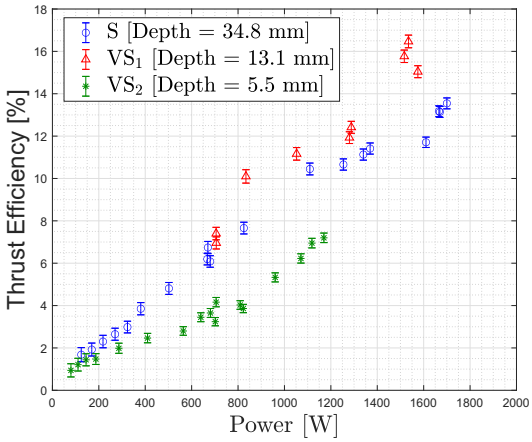
(a) IV Curve



(b) Thrust (T)



(c) Anode Specific Impulse (I_{sp})



(d) Anode Thrust Efficiency (η_{tr})

Figure 4.25: Experimental measurements of the oxygen-fuelled *WET-HET* and a krypton-fuelled plasma filament cathode, for various channel lengths (S : 34.8 mm, VS_1 : 13.1 mm and VS_2 : 5.5 mm), an anode mass flow rate of $\dot{m}_a = 1.0$ mg/s, and the magnetic field topology shown in Figure 4.3 with electromagnets operating at $I_m = 1.5$ A. Results published in [3].

Hence, it becomes impractical to attain discharge power levels surpassing $P_d > 1200$ W without compromising the thruster's integrity. One potential advantage of this setup is the ease of triggering plasma discharge owing to the short distance between the cathode and anode.

Upon comparison of configurations S: 34.8 mm and VS_1: 13.1 mm, their IV curves exhibit similar behaviour, attaining comparable voltage levels for a given current. However, the overall performance of VS_1: 13.1 mm surpasses that of S: 34.8 mm; being particularly evident at higher discharge powers. The configuration using S: 34.8 mm appears to suffer from elevated wall losses, which are not offset by the presumed increased ionisation resulting from the greater channel depth. This disparity intensifies with larger channel depths, as performance diminishes with increasing depth. Conversely, for the VS_1: 13.1 mm configuration, wall losses and ionisation rate are balanced,

yielding the most efficient scenario.

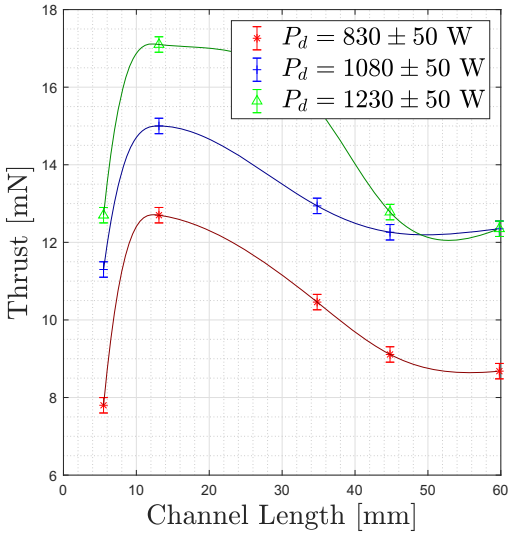
The thermal stresses within the VS_1: 13.1 mm configuration are notably better managed by the thruster in contrast to the VS2: 5.5 mm depth. Consequently, the HET can reach power levels exceeding $Pd \approx 2000$ W. Although the S: 34.8 mm configuration enables the thruster to achieve even higher power levels due to the increased surface volume for heat dissipation, a significantly greater power levels will be required to attain similar levels of thrust efficiency as with the optimal VS_1: 13.1 mm scenario.

Figure 4.26 juxtaposes the thrust, anode I_{sp}, and thrust efficiency of all investigated configurations (Table 4.4) at similar power levels ($P_d = 830 \pm 50$ W, $P_d = 1080 \pm 50$ W, and $P_d = 1230 \pm 50$ W) to ensure a fair evaluation of the results. Clearly, the superiority of the VS1: 13.1 mm configuration is evident. It should be noted that, as shown in the graphs presented in Figure 4.25, higher power levels (such as $P_d \approx 1600$ W) further highlight the advantages of selecting the optimal channel length. However, these power levels are not compared in Figure 4.26 as they cannot be reached with the VS_2: 5.5 mm configuration due to excessive thermal stresses.

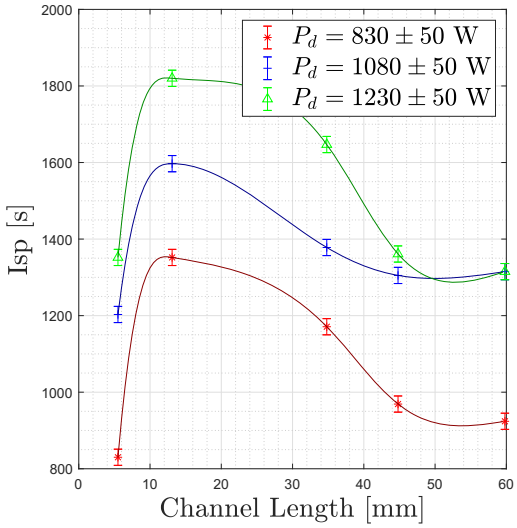
Based on these findings, it is deduced that longer channels do not yield superior performance for molecular plasmas, at least under the investigated conditions. These conclusions align closely with those anticipated by the computational model developed by E. Ahedo and D. Escobar [209].

In this performance evaluation, the highest recorded thrust measurement was achieved with a VS1: 13.1 mm channel. The recorded thrust was $T = 27.0 \pm 0.2$ mN, attained at a discharge power of $P_d = 2238 \pm 1$ W and a mass flow rate of $\dot{m}_a = 1.0$ mg/s. This corresponds to an anode specific impulse of $I_{sp} = 2874 \pm 21$ s and an anode thrust efficiency of $\eta_{tr} = 17.00 \pm 0.25$ %.

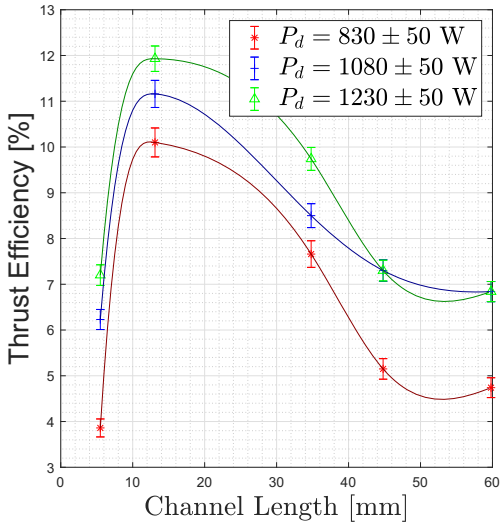
These outcomes markedly surpass those obtained in other experiments with oxygen-fuelled HETs [196]. There, the best achieved performance corresponded to a thrust efficiency of 9 % and a specific impulse of 1000 s, employing a similar mass flow rate ($\dot{m}_a = 1.16$ mg/s) but with a lower magnetic field strength ($B = 0.014$ T). Thrust measurements in that investigation were not provided.



(a) Thrust (T)



(b) Anode Specific Impulse (I_{sp})



(c) Anode Thrust Efficiency (η_{tr})

Figure 4.26: Performance of the oxygen-fuelled *WET-HET* and a krypton-fuelled plasma filament cathode as a function of the channel length for various level of power: $P_d = 830 \pm 50$ W, $P_d = 1080 \pm 50$ W and $P_d = 1230 \pm 50$ W. The rest of the geometry of the thruster is maintained fixed as in Table 4.1, using an anode mass flow rate of $\dot{m}_a = 1.0$ mg/s was set while employing the magnetic field topology depicted in Figure 4.3 with $I_m = 1.5$ A as the electromagnets current. Results published in [3].

In comparison, the thrust efficiency achieved is nearly double (1.9 times higher), and the specific impulse is nearly triple (2.9 times higher). This underscores the significance of selecting the appropriate channel length, ceramic wall material, discharge power, magnetic field strength, and mass flow rate.

4.2.2.7 Channel Width Dependence

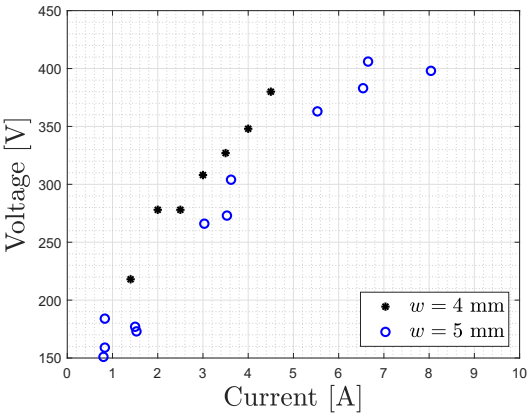
In this section, the impact of channel width on the performance of the thruster *AQUAHET* (the only thruster with the design flexibility to do so, see Section 4.1.2.1) is assessed. Two different channel widths, $w = 4$ mm and $w = 5$ mm, are examined. The findings are illustrated in Figure 4.27.

In the datasets presented, the *AQUAHET* is run at the optimal operating conditions identified in previous Sections 4.2.2.5 and 4.2.2.4: $\dot{m}_a = 1.7$ mg/s and magnet current $I_m = 5.5$ A, corresponding to $B \approx 0.047$ T.

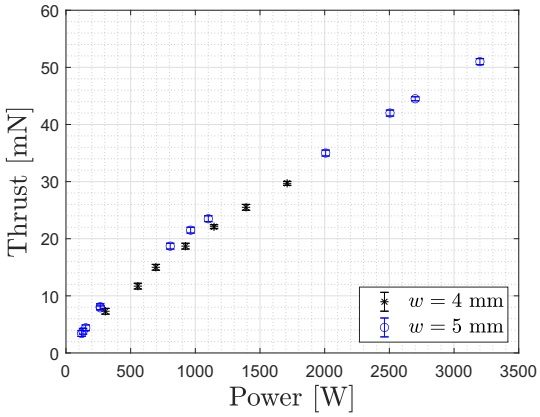
By analysing the results, it can be observed that the IV curve for both configurations displays variation. In particular, $w = 4$ mm yields a higher voltage at a given current. Lower performance, specifically in terms of thrust (T), *TTPR*, anode specific impulse (I_{sp}), anode thrust efficiency (η_{tr}), and total efficiency (η_{tot}), is measured for $w = 4$ mm. Overall, these results indicate that $w = 5$ mm presents the optimum configuration for the *AQUAHET* thruster. Notably, this channel width coincides with that of the *WET-HET*, facilitating direct comparison between the two thrusters in their most optimum conditions (see Section 4.2.2.8).

For the optimal $w = 5$ mm configuration, experimental results at high powers (up to the discharge power of $P_d = 3.2$ kW) were gathered. The best performance observed was achieved at that maximum discharge power tested $P_d = 3200 \pm 1$ W, resulting in a thrust of $T = 51.0 \pm 0.5$ mN, anode specific impulse of $I_{sp} = 3118 \pm 32$ s, $TTPR = 15.9 \pm 0.5$ mN/kW, $\eta_{tr} = 24.4 \pm 0.5$ %, and total efficiency of $\eta_{tot} = 16.3 \pm 0.5$ %. It is noteworthy that the disparity between total efficiency and anode thrust efficiency is primarily due to suboptimal magnet power consumption, an engineering issue with a straightforward solution (see Section 4.1.2.1).

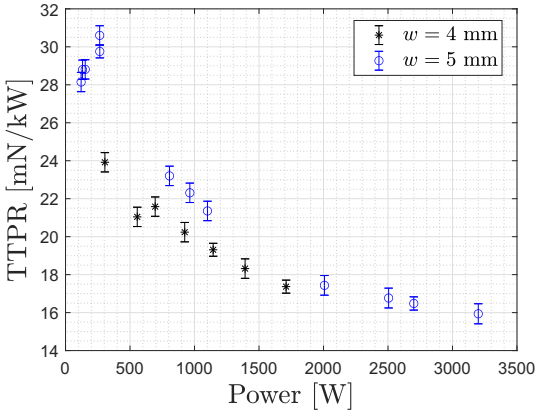
Comparing these results to the ones observed by S. Mazouffre et al. [213], the same trend was observed: a broader channel leads to enhanced thrust and specific impulse. A wider channel enables better ionisation, reduced wall loss due to a lower surface-to-volume ratio, and improved plasma confinement resulting from a stronger radial magnetic field at the walls.



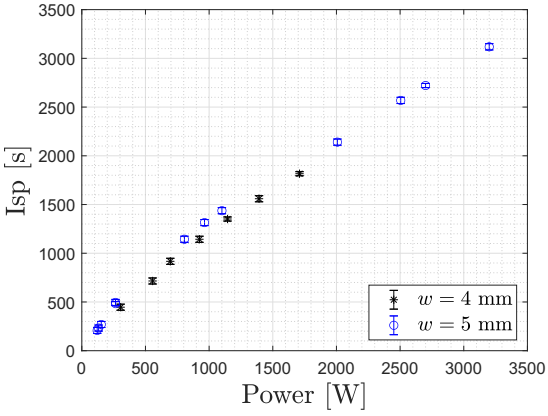
(a) IV Curve



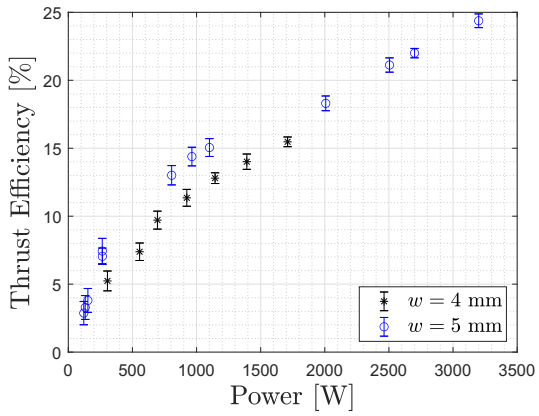
(b) Thrust (T)



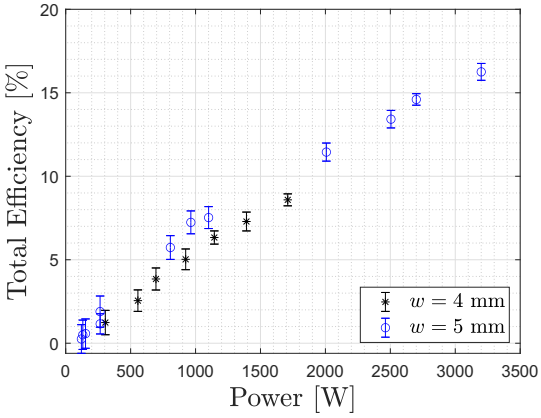
(c) Thrust-To-Power-Ratio ($TTPR$)



(d) Anode Specific Impulse (I_{sp})



(e) Anode Thrust Efficiency (η_{tr})



(f) Total Efficiency (η_{tot})

Figure 4.27: Experimental measurements of the *AQUAHET* and *Hydrocat* fuelled by oxygen (anode) and krypton (cathode) for two different discharge channel geometric configurations: channel width $w = 4$ mm and $w = 5$ mm. Measurements are taken for an anode (oxygen) mass flow rate of $\dot{m}_a = 1.7$ mg/s, a cathode mass flow rate of $\dot{m}_c = 0.3 - 0.7$ mg/s and a magnet current of $I_m = 5.5$ A (see Figure 4.5 for corresponding magnetic flux density along the channel centreline).

These factors contribute to the thruster's stability across a wider range of power settings, resulting in enhanced thrust and specific impulse. Furthermore, longer lifetimes may be anticipated due to reduced plasma-wall interactions.

4.2.2.8 Comparison Between the First (*WET-HET*) and Second (*AQUAHET*) Water Electrolysis Hall Effect Thruster Generation

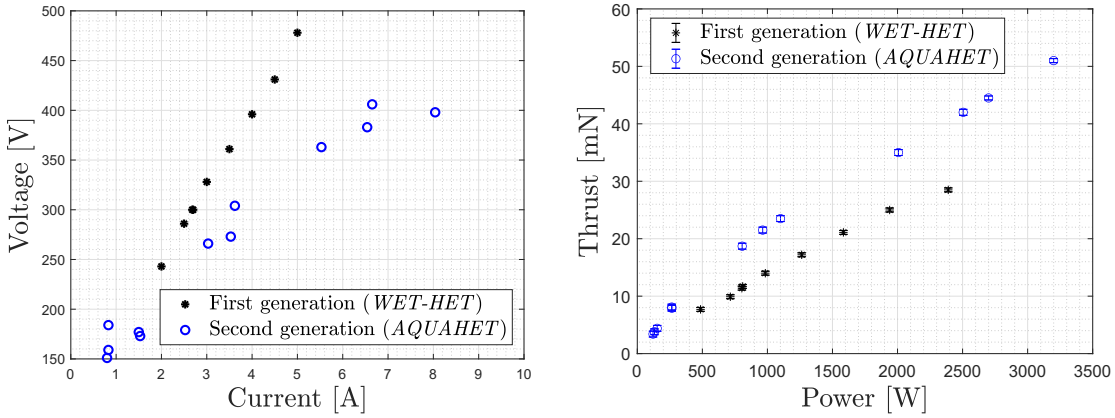
In this section, a comparative performance analysis between the first generation (*WET-HET*) and second generation (*AQUAHET*) water electrolysis-fuelled HETs is conducted.

The discharge channel configuration and key operating parameters (mass flow rate, magnet current) used for the *WET-HET* and *AQUA-HET* are selected based on the results of previous Sections 4.2.2.4, 4.2.2.5, 4.2.2.6, and 4.2.2.7 [3, 5, 144]. Following those, the *WET-HET* is tested with a mass flow rate of $\dot{m}_a = 1.0$ mg/s and a magnet current of $I_m = 1.5$ A ($B \approx 0.060$ T), whereas the *AQUAHET* features a mass flow rate of $\dot{m}_a = 1.7$ mg/s and $I_m = 5.5$ A ($B \approx 0.047$ T). For both thrusters, the channel width is $w = 5$ mm and the channel length $L = 13.1$ mm.

In these conditions, the primary distinction in geometrical configuration between the two lies in the channel mean diameter: $d_m = 40$ mm for the *AQUAHET* and $d_m = 20$ mm for the *WET-HET*.

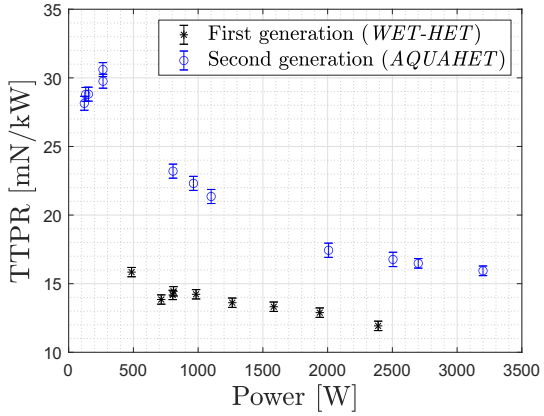
However, this comparison is not as straightforward due to the inherent differences between the two thrusters, despite their shared operating principles: notably, the *AQUAHET* magnetic field lines, particularly within the discharge channel in the zone close to the exit plane, have a reduced axial component as compared to the *WET-HET*. Additionally, other key parameters such as the magnitude of the magnetic flux density at the anode face is different between the two devices. These differences should be kept in mind when interpreting the results presented.

Figure 4.28 shows the results obtained. To start with, the IV curve from the thrusters is different. This is a result of many factors, such as the change in thruster, channel diameter, and the mass flow tested: *AQUAHET* can accommodate a larger plasma volume with a lower surface-to-volume ratio of its discharge channel. This translates to reduced wall losses and improved propellant ionisation. Larger anode currents (or lower discharge potential at constant current) are observed for a constant voltage for the *AQUAHET*, suggesting lower plasma resistivity, i.e., a denser plasma. This is mainly due to reduced wall losses but also significantly higher flow rate (70% larger than the *WET-HET*), resulting in greater thrust.

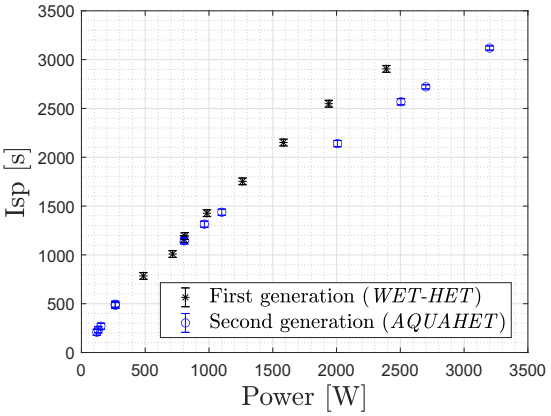


(a) IV Curve

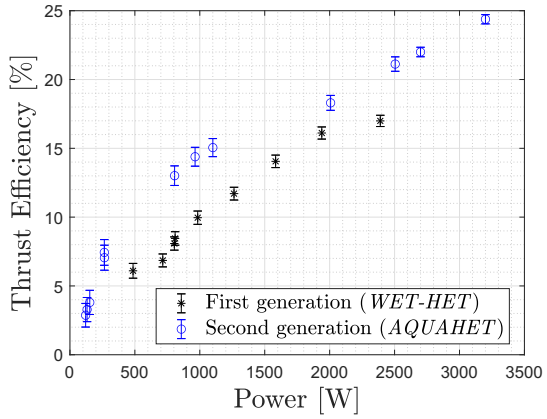
(b) Thrust (T)



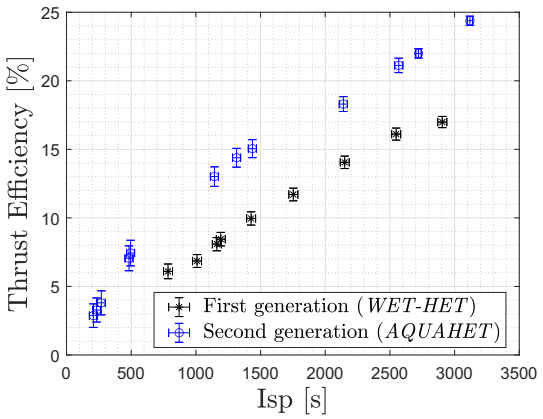
(c) Thrust-To-Power-Ratio ($TTPR$)



(d) Anode Specific Impulse (I_{sp})



(e) Anode Thrust Efficiency (η_{tr})



(f) η_{tr} vs I_{sp}

Figure 4.28: Experimental measurements of the *WET-HET* ($d_m = 20$ mm) and *AQUAHET* ($d_m = 40$ mm) for the optimum magnet current identified ($I_m = 1.5$ A and $I_m = 5.5$ A respectively, see Figure 4.5 for magnetic flux density profile as a function of channel length). Note that results are collected with oxygen flow to the thruster (anode), $\dot{m}_a = 1.0$ mg/s for the WET-HET and $\dot{m}_a = 1.7$ mg/s for the *AQUAHET*, and a krypton mass flow of $\dot{m}_c = 0.3 - 0.7$ mg/s to the cathode *Hydrocat*. Both thrusters used featured a channel width of $w = 5$ mm and a channel length of $L = 13.1$ mm.

In terms of quantitative performance, the *AQUAHET* outperforms the *WET-HET* in terms of thrust and *TTPR* for the entirety of the discharge power range investigated. However, the I_{sp}

of the *WET-HET* is higher, specifically for discharge powers from $P_d = 1200$ W onwards. These factors are jointly reflected in the anode thrust efficiency (η_{tr}), Figures 4.28e and 4.28f. In the entirety of the discharge power range, the thruster *AQUAHET* surpasses the performance of the thruster *WET-HET*, exhibiting an average of $\Delta\eta_{pr} \approx 20\%$ better performance.

Lastly, notice that the I_{sp} values obtained are approximately the same for both thrusters at powers below $P_d < 1200$ W, but increasing for the *WET-HET* at higher powers ($P_d > 1200$ W). This is also due to the higher anode flow rate required by *AQUAHET* (70% higher), as the I_{sp} is indirectly proportional to the anode flow rate. In this case, although the *WET-HET*'s thrust is 30-50% less than the *AQUAHET*, the latter consumes 70% more fuel, thus leading to the observed results.

4.2.2.9 Numerical Model and Experiments

Making use of the experimental characterisation of oxygen-fuelled HETs highlighted within this section, a preliminary estimation of the correlation between experimental results and the numerical model (Chapter 3) can be made. The results for the *WET-HET*, using the geometrical inputs from Table 4.1 with a channel length of $L = 34.8$ mm, oxygen mass flow rate of $\dot{m}_a = 1.0$ mg/s, an electromagnet current of $I_m = 0.5$ A, channel walls made of $BNSiO_2$ and a stainless steel anode (as shown in Figure 4.25), are compared to the performance estimations obtained with *PlasmaSim*, using the simulation inputs from Table 3.7. More specifically, the performance prediction from the numerical model is derived from the same simulation that was presented when showing the plasma properties in Figures 3.12, 3.13 and 3.14. Notice that, as remarked in Section 3.1.1.11, the discharge power is not a direct input in *PlasmaSim* (rather, the discharge voltage, V_d is an input and the discharge current I_d, is calculated using Equation 3.18). For that reason, it is not possible to precisely match the discharge power between experiments and simulations and compare the results at a desired power level. Consequently, the results shown (available in Table 4.5) are obtained when comparing, experimentally and computationally, an operating power discharge power window of $P_d = 520 \pm 10\%$ W.

Table 4.5: Preliminary comparison between the experimental results of *WET-HET* versus the simulation results obtained with *PlasmaSim* (Section 3.2.2.1). Values shown for the simulation inputs of Table 3.7. The geometrical and operating conditions for the simulation and experiments are kept constant as the ones shown Table 4.1 with a channel length of $L = 34.8$ mm, oxygen mass flow rate of $\dot{m}_a = 1.0$ mg/s, an electromagnet current of $I_m = 0.5$ A, channel walls made of $BNSiO_2$ and a stainless steel anode and an operating power discharge power window of $P_d = 520 \pm 10\%$ W.

	Thrust [mN] (Value / Rel Diff %)		**Anode Specific Impulse [s]** (Value / Rel Diff %)		**Anode Thrust Efficiency [%]** (Value / Rel Diff %)	
Experiments	7.6	-	774	-	4.78	-
PlasmaSim	7.8	2.63%	720	7.50%	5.85	22.38%

From these results, it is observed a strong correlation in terms of thrust (2.6% discrepancy with the values of *PlasmaSim* marginally overestimating the performance) and anode specific impulse (discrepancy of 7.5%, with the values of *PlasmaSim* slightly underestimating the performance). As these two factors come together when computing the anode thrust efficiency, the predictions of *PlasmaSim* in relative terms show a worse correlation for this factor; although in absolute terms, the difference is 1%.

Note, that similarly to other PIC codes, *PlasmaSim* does not currently account for certain factors such as the cathode propellant, grade of the ceramic walls, anode material, or gas humidity. These factors can influence the performance of the HET, as discussed within this thesis. The purpose of this comparative study is to obtain preliminary results that can be further examined and implemented in future work. For that matter, running multiple simulations (at the expense of weeks/months of simulation time) under different geometrical and operating conditions are encouraged.

4.3 Campaigns B - Oxygen-Fuelled Hall Effect Thrusters with a Xenon/Krypton-Fuelled Cathode: Physics Characterisation

In this investigation, the physics of oxygen-fuelled HETs were explored using various diagnostic instruments to measure the principal plasma characteristics of the discharge under varying operational parameters. This research was part of a Visiting Research Programme at Stanford University during 2023. The results presented here were disseminated at the Space Propulsion Conference in 2024 [7], being awarded as best PhD paper of the conference.

4.3.1 Methodology

4.3.1.1 Experimental Set-Up and Vacuum Chamber Facilities

This study was conducted at the vacuum chamber facilities of the Stanford Plasma Propulsion Laboratory, property of Stanford University. A single vacuum chamber measuring 1.5 meters in diameter and 3 meters in length was utilised to set-up the HET and the necessary hardware for conducting the experiments. Similar to the setup at the Imperial Plasma Propulsion Laboratory, vacuum levels were achieved through a three-stage process: the initial vacuum system uses a roughing pump (*General Electric 5K4254A21* model) to reach approximately 10^{-4} bar. For the second stage, a single turbo pump is activated (*Varian 951-5218* model), capable of reducing the background pressure to around 10^{-9} bar without mass flow and approximately 10^{-8} bar with mass flow into the chamber. Finally, these pressure levels were maintained using two cryo pumps (*CVi-CBST 6.0 W-2* model) to counteract any pressure increases when mass flow entered the chamber, operating within the range of approximately 10^{-8} bar. It is noteworthy, however, that these pumps are not optimised for evacuating alternative propellants such as oxygen. Therefore, testing in this environment presents additional challenges in achieving stable thruster ignition.

Figure 4.29 illustrates the principal components and layout employed during testing, while Table 4.6 enumerates these elements.

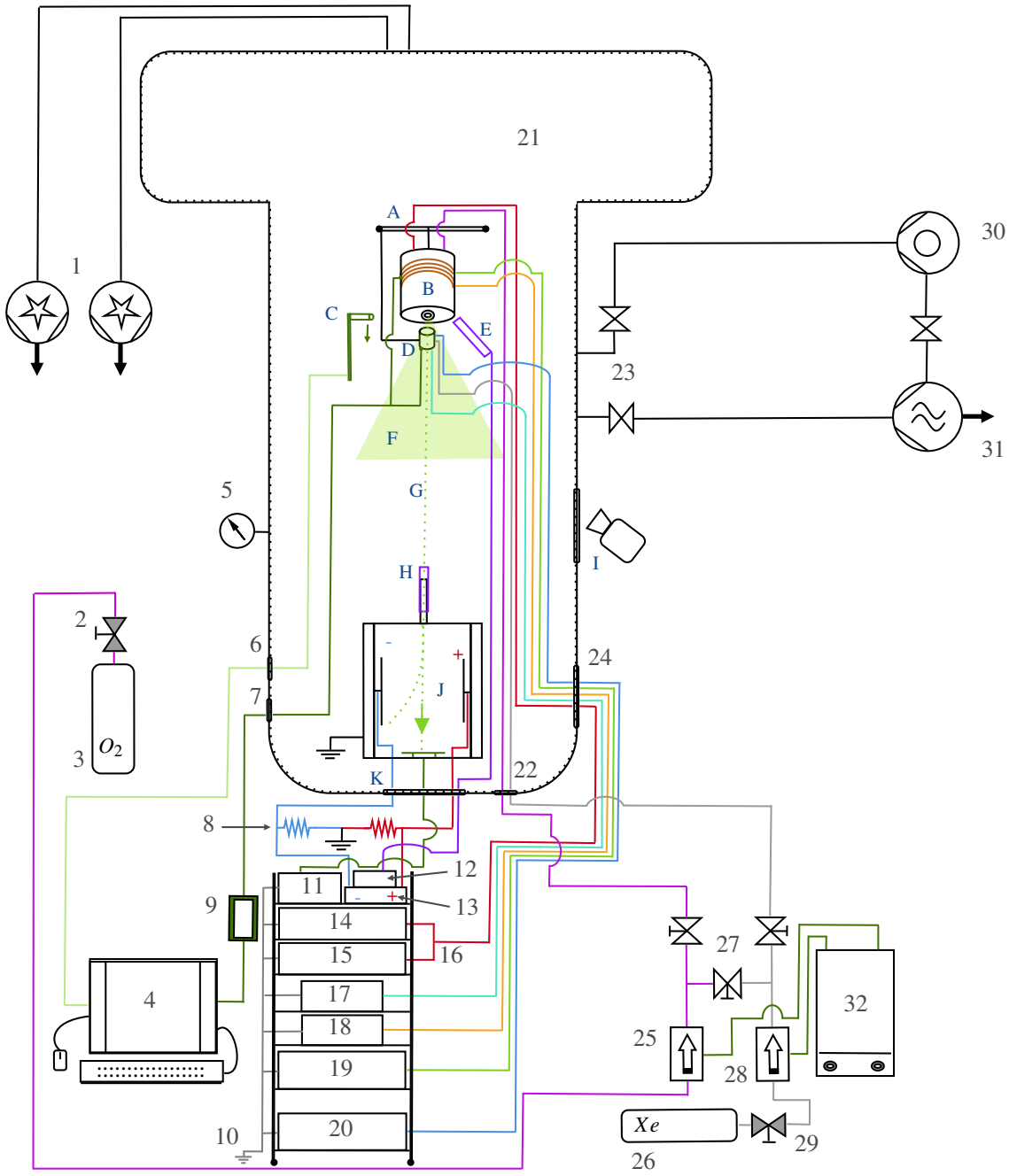


Figure 4.29: Main schematics of the Electric Space Propulsion testing at the Stanford Plasma Propulsion Laboratory. Department of mechanical engineering, Stanford University. Diagram presented in [7].

This is complemented with Figure 4.30 and Table 4.7, which specifically show the instruments used to characterise the plasma plume of the thruster. A summary of the electronics, fluidics and procedures followed in this experiment is presented below.

Table 4.6: Description of the elements depicted in Figure 4.29. Table presented in [7].

1	Cryo pumps (*CVi-CBST 6.0 W-2*)	**17**	Heater power supply (*Sorensen DLM 40-15*)
2	Pressure regulator (anode)	**18**	Magnet (inner) power supply (*Sorensen DLM 40-15*)
3	Anode propellant bottle (oxygen)	**19**	Magnet (outer) power supply (*Xantrex XFR60-20*)
4	Computer station	**20**	Keeper power supply (*Power Ten Inc P62B-3006.6*)
5	Pressure gauge	**21**	Stanford Plasma Propulsion Laboratory
6	Vacuum feedthrough (Spectrometer)	**22**	Vacuum feedthrough (fluidics)
7	Vacuum feedthrough (Thermocouples)	**23**	Pneumatic valve
8	Circuitry of the ExB probe (Figure 3)	**24**	Vacuum feedthrough (power supplies)
9	Thermocouple - Electronics (Arduino)	**25**	Mass flow meter (anode)
10	Ground return of power supplies	**26**	Cathode propellant bottle (xenon)
11	Picoammeter (*Keithley model 485*)	**27**	Manual valves set
12	Langmuir probe power supply (*SPS-H1203*)	**28**	Mass flow meter (cathode)
13	ExB probe power supply (*Sorensen XG 600-1.4*)	**29**	Pressure regulator (cathode)
14	Anode power supply [master] (*Sorensen DCS 600-1.7*)	**30**	Turbopump (*Varian 951-5218*)
15	Anode power supply [slave] (*Sorensen DCS 600-1.7*)	**31**	Roughing pump (*General Electric 5K4254A21*)
16	Parallel line connection (anode power supplies)	**32**	Multichannel mass flow controller (*URS-100*)

4.3.1.2 Electronics

Two anode power supplies (elements 14, 15) were set in parallel (model *Sorensen DCS 600-1.7*, each one limited to 600 V and 1.7 A). Compared to the experimentation at the Imperial Plasma Propulsion Laboratory, these power supplies limited the total amount of available discharge current to $I_d = 3.4$ A (compared to $I_d = 10.0$ A, as in the previous investigation).

The cathode (either the plasma filament cathode or *Hydrocat*) was powered using a heater (element 17, model *Sorensen DLM 40-15*, limited to 40 V and 15 A) and a keeper (element 20, model *Power Ten Inc P62B-3006.6*, limited to 300 V and 6.6 A). Notice that the keeper power supply imposes a strong restriction on the keeper voltage. Typically, a higher voltage (around $V_k = 500$ V) would favour triggering the plasma on the cathode. However this was the best option available at the laboratory. The magnetic field is powered using one power supply for the *WET-HET* (element 18, model *Sorensen DLM 40-15* providing up to 40 A and 15 V). The *AQUAHET* uses this power supply for the inner magnets and an additional one for the outer magnets (element 19, model *Xantrex XFR60-20*, up to 60 V and 20 A). In reality, in order to achieve the maximum magnetic field (Figure 4.5), $I_m = 22$ A will be needed ($I_m = 5.5$ A per one of four outer coils).

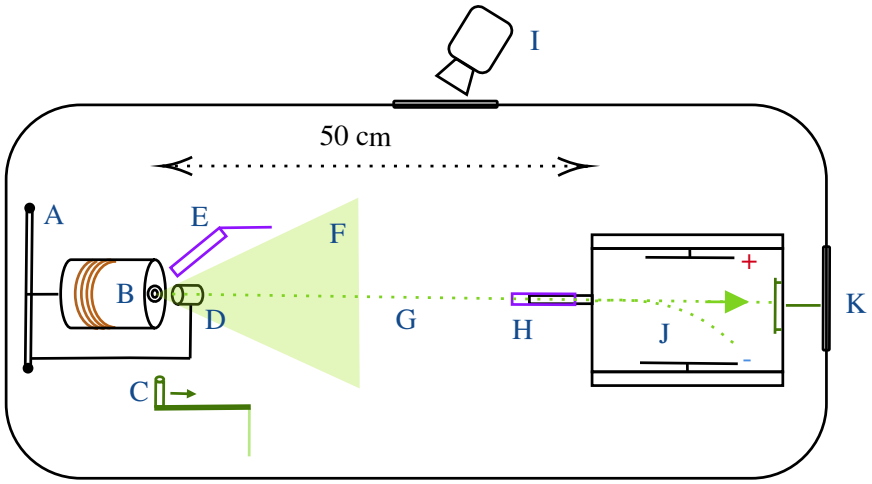


Figure 4.30: High-level schematics of the Hall Effect Thruster in combination with the diagnostic tools at the Stanford Plasma Propulsion Laboratory facilities. Diagram presented in [7].

Table 4.7: Description of the elements highlighted in Figure 4.30. Table presented in [7].

Index	Element
A	Structural support
B	Hall Effect Thruster
C	Spectrometer
D	Cathode
E	Langmuir probe
F	Oxygen plasma
G	Oxygen particle's path
H	QLP / Langmuir probe
I	Camera
J	ExB probe (Wein filter)
K	Front door / feedthrough

However no power supply at the laboratory could reach this current limit and a slightly lower magnetic field intensity was used instead. The electronics set-up used for the diagnostic tools will be explained in detailed in the following sections.

4.3.1.3 Fluidics

In a similar manner to the experiments undertaken at Imperial College London, an oxygen tank (element 3) alongside its corresponding pressure regulator (element 2) were situated external to the vacuum chamber. A xenon tank (element 26) and its pressure regulator (element 29) were arranged to supply the cathode. However, within this laboratory, flow regulation was not conducted directly

via mass flow controllers. Instead, a mass flow meter (elements 25 and 28 for the anode and cathode, respectively) and a multichannel mass flow controller (32) were employed. The lines for the anode and cathode remained unconnected until converging at a series of strategically positioned valves (element 27) immediately prior to the vacuum feedthrough. This set-up was prepared in case the anode wants to be fuelled with xenon instead of oxygen. Both connections utilised standard stainless-steel tubing and a mix between Swagelok 1/8" and 1/4" fittings. Notice that, although some tests were conducted using krypton instead of xenon, the results presented here were taken when using xenon as a propellant. Parallel conclusions and results can be deducted in case krypton would be used as the cathode propellant instead.

4.3.1.4 Working Procedures

The same procedures as the ones explained in Section 4.2.1 were followed to guarantee a secure and consistent ignition and testing of the thruster.

4.3.1.5 Thrusters Set-Up

The experimental configurations of the tested thrusters (*WET-HET* and *AQUAHET*) during these campaigns are summarised in Table 4.8. The *WET-HET* utilised the best-performing channel length (L = 13.1 mm, as detailed in Section 4.2.2.6). Similarly, the *AQUAHET* employed the same channel length along with the optimal channel width (w = 5.0 mm, see Section 4.2.2.7). The magnetic field topology used is the one depicted in Figures 4.3 and 4.5, with a strength which varied depending on the test and that will be specified throughout this section. Regarding the oxygen mass flow, the most optimum ones, as described in Section 4.2.2.5, were challenging due to difficulties in maintaining stable ignition, particularly because the facilities were not optimised for lightweight propellants such as oxygen, posing additional testing challenges. Therefore, larger mass flows were used (between $\dot{m}_a = 2.5 - 4.0$ mg/s for the *WET-HET* and $\dot{m}_a = 4.0$ mg/s for the *AQUAHET*). The $BNSiO_2$ (Grade M26) thruster ceramic walls were chosen because of their performance and hydrophobic properties.

Table 4.8: Experimental configuration of the HETs (*WET-HET* and *AQUAHET*) used during testing.

Variable	**WET-HET**	**AQUAHET**
Channel width (w), [mm]	5.0	5.0 (see Section 4.2.2.7)
Channel mean diameter (d_m), [mm]	20.0	40.0
Channel length (L), [mm]	13.1 (see Section 4.2.2.6)	13.1
Magnetic topology	Figure 4.3	Figure 4.5 (see Section 4.2.2.4)
Oxygen Mass flow rate [mg/s]	2.5-4.0	4.0
Channel walls	$BNSiO_2$ (Grade M26, see Section 4.2.2.2)	$BNSiO_2$ (Grade M26)
Anode material	Stainless steel (see Section 4.2.2.3)	Stainless steel

Lastly, stainless steel anodes were employed for both thrusters due to their resistance to oxidation compared to tungsten (refer to Section 4.2.2.3).

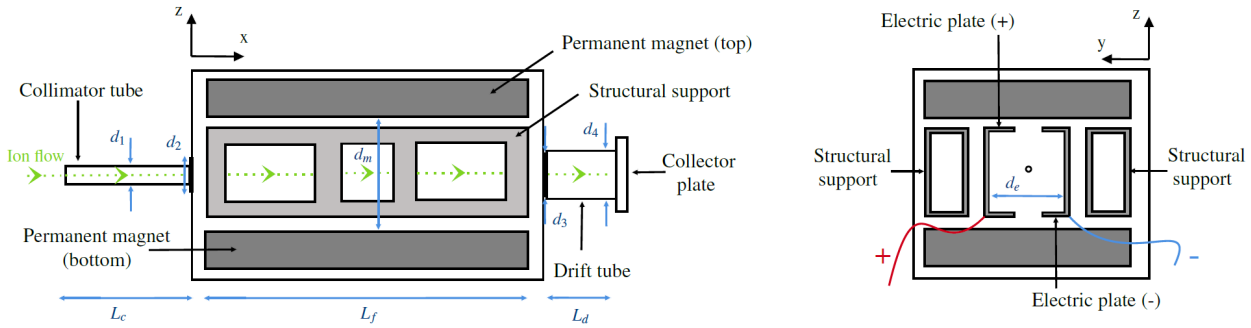
The next subsections describe the instruments used to measure the properties of the oxygen plasma discharge and the results obtained from them.

4.3.1.6 ExB Probe

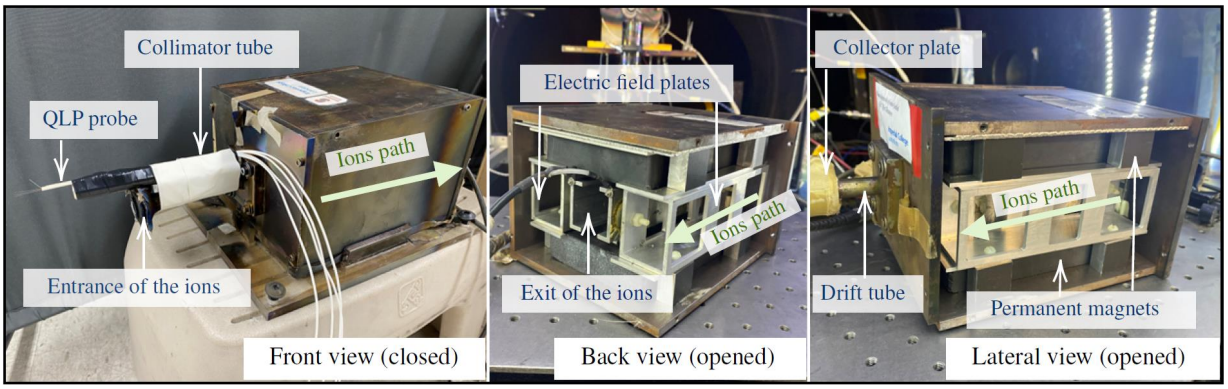
Probe Description

An ExB probe, also known as a Wein filter, was employed to selectively filter various particle species based on their electric charge and mass. This probe was also used by A. Gurciullo to investigate ion plumes in Xe/N_2 and Xe/air mixtures [214]. The design and constituent components of the ExB probe, depicted in Figure 4.30 and outlined in Table 4.7 alongside other utilised instruments, are expounded upon in greater detail in Figure 4.31 and Table 4.9. This final geometrical configuration is the result of an iterative experimental process aimed at selecting the appropriate parameters for the probe's functionality.

The probe comprises primarily three distinct regions. Firstly, there is the collimator tube (L_c), which serves as the entry point for ions into the filter. Next, there is the ExB fields region (L_f), wherein ions with incorrect mass-to-charge ratios undergo deflection. Lastly, there is the drift tube (L_d). Both the collimator and the drift tube play pivotal roles in determining the efficacy of the instrument as they physically obstruct ions travelling in undesired directions.



a) Lateral view (left) and back view (right) diagrams of the ExB probe (Wein filter)



b) Front view (left), back view (middle) and left view (right) of the ExB probe (Wein filter)

Figure 4.31: Design and different components of the ExB probe used for the characterisation of the HETs plasma plumes. Diagrams presented in [7].

Table 4.9: Main design variables of the ExB probe. Data taken from [215].

Design variable	**Value**
Collimator diameter (d_1) [mm]	0.8
Collimator length (L_c) [mm]	113.1
Collimator exit diameter (d_2) [mm]	2.1
ExB region length (L_f) [mm]	150.0
Electric field plates distance (d_e) [mm]	36.5
Drift tube input diameter (d_3) [mm]	4.0
Drift tube length (L_d) [mm]	66.8
Drift tube exit diameter (d_4) [mm]	11.5
HET - ExB probe distance [mm]	500.0
Magnets distance (d_m) [mm]	53.6
Magnetic field strength [T]	0.134
Plates voltage [V]	0 - 250

The selection of appropriate diameters for both, the collimator and the drift tube, is critical in achieving a balance between signal strength and background noise levels. Optimal diameter

sizes must be chosen to ensure adequate signal strength without introducing excessive noise. For instance, an excessively small collimator diameter may result in a weak signal, whereas an overly large diameter can lead to a noisy signal due to an excessive number of particles passing through.

It is important to note that these factors do not operate independently but interact with other variables, such as the distance between the HET and the ExB probe. The proximity of the HET and the probe significantly influences both the signal strength and the background noise level. A closer proximity enhances the signal strength but concurrently increases the level of background noise. Conversely, increasing the distance between them attenuates the signal while reducing the noise level. Furthermore, the presence of other objects in close proximity to the plasma plume can influence the discharge process. Placing the probe too near the thruster can induce instability in the discharge, making it challenging to sustain.

Ultimately, the ions that successfully traverse these three stages collide with a tungsten plate. At this juncture, they undergo neutralisation by acquiring electrons from the collector plate. This component is linked to a device for current measurement, specifically a picoammeter (element 11).

The outer casing of the filter is fabricated from iron, serving to reinforce its structural integrity and confine the magnetic field while preventing interference with the plasma plume. To create this magnetic field, permanent magnets are used, measuring 150 mm in length, 100 mm in width, and 25.5 mm in thickness.

C-shaped electrode design is implemented to enhance the uniformity of the electric field [216]. Lastly, the probe incorporates two apertures designed to equalise its internal pressure with that of the vacuum chamber's interior.

In general, it is advisable to maintain flexibility in design variables post-initial experimentation to facilitate the identification of the most optimal parameters.

Probe Working Principles

In an ExB probe, particles are filtered within the ExB region, where their trajectories are influenced by their mass (m) and charge (qZ). By using Lorentz's equation:

$$F = qZ(E + v \times B) \tag{4.5}$$

(where F represents the total force, q denotes the elementary charge, Z signifies the charge number, and v stands for the particle velocity affected by the electric (E) and magnetic (B) fields), one can set $F = 0$ (indicating no deviation in the particle's trajectory). This condition corresponds to a specific velocity known as the Wein velocity ($v = v_w$):

$$v_w = \frac{E}{B} = \frac{\Delta V}{d_e B} \tag{4.6}$$

being ΔV the voltage difference between the two plates and d_e the distance between the two plates (see Table 4.9). Essentially, if a particle possesses the specific velocity v_w, it will remain undeviated while traversing the ExB region. Notice that, in practical terms, the B field of the ExB probe remains constant (determined by the magnetic field generated by the permanent magnets), while E can vary based on the voltage difference applied between the probe's two plates. Consequently, by sweeping through a range of E while maintaining B constant, the probe can identify different signal peaks correspondent to a specific particle type being detected (as its path is not bent and therefore goes straight to the collector plate).

In parallel, by equating two forms of kinetic energy of the ions (K_i):

$$K_i = \frac{1}{2} m \left(v^*\right)^2 = \text{ q Z } \Delta V_a \tag{4.7}$$

$$v^* = \sqrt{\frac{2\text{qZ}\Delta V_a}{m}} \tag{4.8}$$

where ΔV_a is the acceleration potential of the ion, v^* (the velocity of the ion) can be calculated.

As an initial approximation, it can be stated that $\Delta V_a = \Delta V_d - \Delta V_c$, indicating that the acceleration potential equals the discharge potential (ΔV_d, as perceived by the anode power supply) minus the potential measured at the cathode location (ΔV_c). This assertion, however, is not entirely accurate, as it presupposes that the ions are generated at the anode plate and hence undergo the entire potential acceleration of the discharge. As elucidated later in this section, depending on the species, they will exhibit distinct acceleration potentials. Nonetheless, this approximation enables the derivation of preliminary results regarding the potential locations of these peaks by setting $v^* = v_w$ (that is, assuming that the velocity of the ion from Equation 4.8 indeed corresponds to the Wein velocity, thus experiencing no deviation within the ExB region, as per Equation 4.6). Introducing the constant magnetic field (B) of the ExB probe and d_e (refer to Table 4.9), the potential difference of the ExB plates corresponding to that specific combination of mass and charge (ΔV) can be determined from Equation 4.6 in this way:

$$\Delta V = E d_e = v_w B d_e = \sqrt{\frac{2\mathrm{qZ}\Delta V_a}{m}} B d_e \tag{4.9}$$

Table 4.10 presents the expected voltage difference between the two plates of the ExB probe, indicating where the propellant species are anticipated to be detected. These predictions are based on a discharge voltage of 125 V and a plasma potential at the cathode location of 36 V, resulting in $\Delta V_a = 89$ V.

As it can be seen, the peaks exhibit sufficient voltage dispersion, (for example, the gap between O_2^+ and O^+ is 46.8 V). This is a consequence of the potent magnetic field induced by the permanent magnets ($B = 0.134$ T, detailed in Table 4.9), necessitating stronger electric fields for a given velocity (as per Equation 4.6). Conversely, employing electromagnets configured in a Helmholtz coil configuration could yield to a markedly weaker magnetic field, (such as $B = 0.006$ T generated by a $I_m = 3$ A current, as in the case of the Imperial College London ExB probe [217]). Under this scenario, one would expect the peaks corresponding to O_2^+ and O^+ species to manifest at 5.05 V and 7.15 V, respectively.

Table 4.10: Voltage difference between the ExB plates where the presence of plasma species is anticipated to be detected. Data presented in [7].

Specie	**Mass [u]**	**Charge number (Z)**	**Voltage Prediction [V]**
Xe^{+}	131.3	1	55.78
Xe^{++}	131.3	2	78.88
O_2^{+}	32.0	1	112.98
O_2^{++}	32.0	2	159.78
O^{+}	16.0	1	159.78
O^{++}	16.0	2	225.96

This narrow spacing between these peaks complicates their individual discernment, primarily due to their tendency to assume a Gaussian profile encompassing their theoretical maxima. If this is the case, one will struggle to identify the contribution to each species to the plasma discharge (condition which was observed when testing the Imperial College London ExB probe using electromagnets).

In general, in ExB probes, it is advisable to opt for permanent magnets with their inherently robust magnetic fields to ensure the optimal functionality of the filter, such as the ones used in the Stanford University probe (150 mm in length, 100 mm in width, and 25.5 mm in thickness).

Not only the design but also the electrical configuration of the ExB circuitry is crucial for achieving successful outcomes. In Figure 4.32, an electrical schematic outlines the connection between the power supply, responsible for creating the potential difference across the two plates of the probe, and the ExB probe itself. This procedural approach follows the precedent set by previous studies conducted at the Stanford Plasma Propulsion Laboratory [214, 218].

Two resistors, each with a resistance of $R = 9$ MΩ, are integrated into the plate circuit to adjust the voltage along the central axis of the ExB probe to the system's reference potential.

This alignment is achieved by solving the equation of charge conservation within loop G [215], as follows:

$$V_{\text{axis}} = \frac{V^{+} - V^{-}}{2} = V_g \tag{4.10}$$

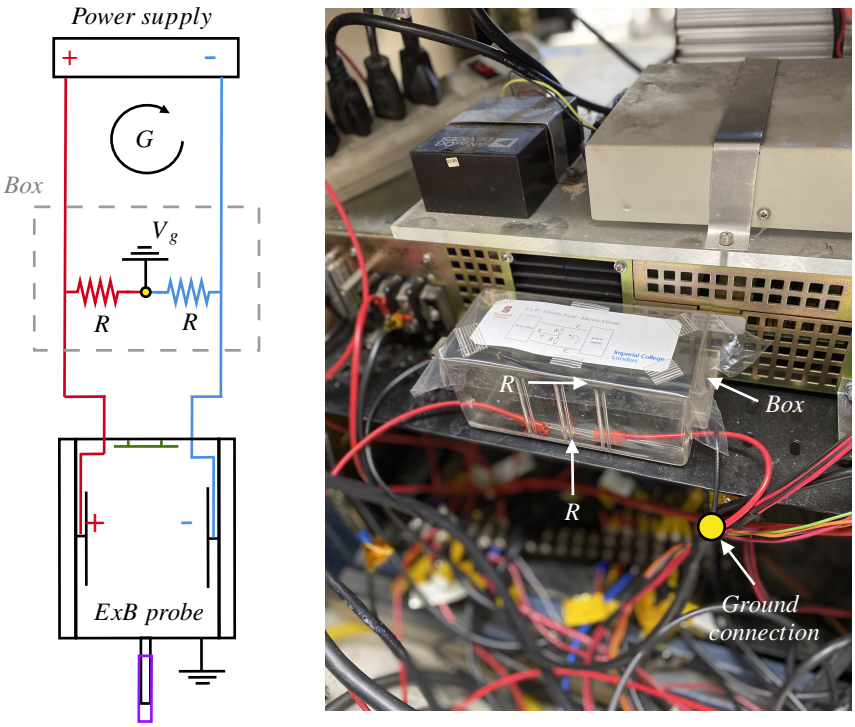


Figure 4.32: Circuitry of the ExB probe. Sketch and photo presented in [7].

where V_{axis} is the voltage value at the middle longitudinal axis of the ExB probe, V^+ and V^- correspond to the positive and negative values of voltage set by the power supply and V_g is the ground voltage.

The purpose of this voltage divider is to mitigate potential sources of error stemming from the voltage fluctuations along the ExB probe axis. Consequently, the voltage divider plays a crucial role in maintaining, along the longitudinal axis of the ExB probe (referred to as the "Ion flow" in Figure 4.31), a specified and constant voltage (V_{axis}) which ideally corresponds to the system's ground ($V_g = 0$).

Any inconsistency in V_{axis} would lead to variations in the voltage across the plates (V_{plates}), resulting in the acceleration of ions entering the filter from the plasma potential to a voltage that fluctuates over time. These fluctuations in ion velocity within the filter would introduce significant errors in the amplitudes and positions of the peaks identified by the probe [215].

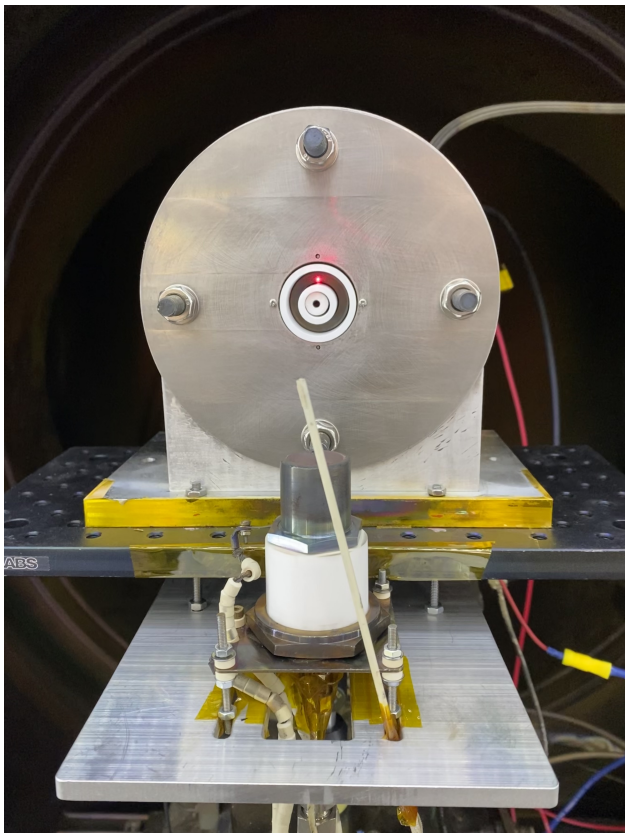


Figure 4.33: Alignment of the ExB probe with the WET-HET thruster before testing. Picture presented in [7].

Although these procedures are effective in reducing potential errors during the data acquisition process, errors may still occur. This is primarily attributed to any ion drift caused by inherent discrepancies in the resistances, which are nominally set at $R = 9$ MΩ but may not be precisely matched to that value. The error-handling techniques employed in this study closely align with the established approaches documented in previous research utilising the same filter [214, 215].

To collect data accurately, it is important to ensure the correct positioning of the ExB collimator tube entrance relative to the HET channel. In this specific experimental setup, the collimator tube was aligned with the middle portion of the discharge channel, as illustrated in Figure 4.33 for the WET-HET configuration. Note that, in practice, an alignment with any part of the channel, whether upper, lower, right, or left, is equally feasible.

Once the thruster is operating under nominal conditions, the ExB voltage plate range is swept every 2 V within the range of $0 - 250$ V (see Table 4.9). Under these conditions, the acquisition time needs to be at least 10 minutes.

After identifying the peaks through Gaussian fitting [216, 218], the subsequent step involves computing the acceleration voltages (V_{acc}) for the distinct ion species present in the plasma. Determining V_{acc} relies on the prior calculation of v_w. However, there is no need to estimate v_w using Equation 4.8 since the actual ΔV at which the peak occurs is now known. Therefore, the calculation of the actual v_w can be performed directly using Equation 4.6.

However, it becomes necessary to adjust the Wein velocity v_w due to the fact that V_{axis} accelerates the ions from their plasma potential (φ_p) at the entrance of the filter, causing a shift in the ExB probe spectra towards higher plate voltage values. As a result, it could happen that $V_{axis} \neq \varphi_p \neq V_g = 0$. The computation of the corrected ion velocity is based on the principle of conserving ion energy at the filter's entrance:

$$v_{ion} = \sqrt{v_w^2 - \frac{2qZ}{m}(\varphi_p - V_{axis})} \tag{4.11}$$

Where v_{ion} is the corrected ion velocity. Once v_{ion} is known, V_{acc} is calculated as:

$$V_{acc} = \frac{m v_{\text{ion}}^2}{2qZ} \tag{4.12}$$

Notice that these acceleration voltages are inherently associated with ion energy (E_{ion}):

$$E_{ion} = qZV_{acc} \tag{4.13}$$

Sections 4.3.2.1 and 4.3.2.2 discusses the results obtained using the methodologies here described.

4.3.1.7 Langmuir Probes

This section explains the instruments employed, the methodology applied, and the results obtained from the measurement of plasma properties using Langmuir probes.

Probe Description

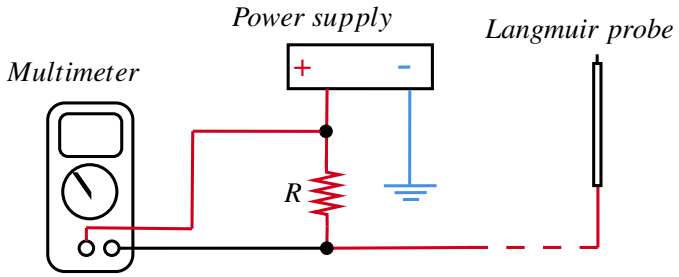


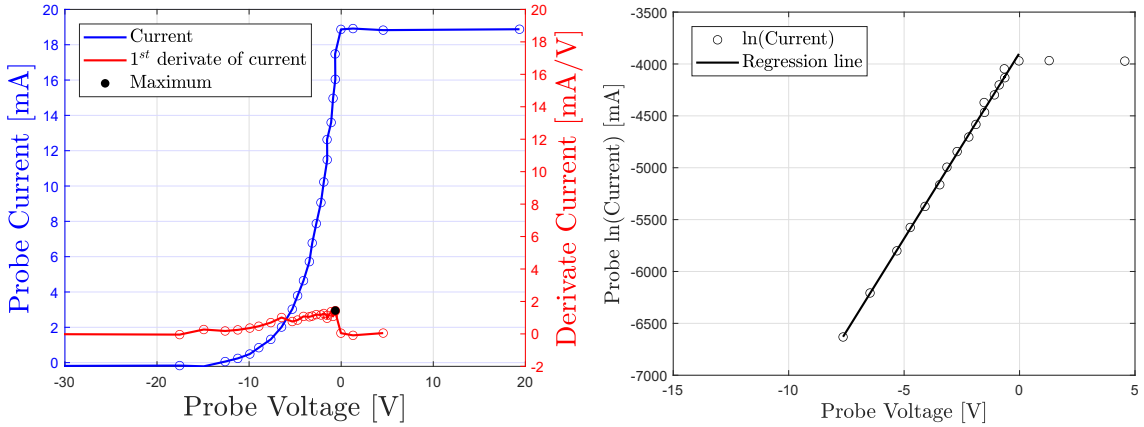
Figure 4.34: Circuitry of the Langmuir probe. Sketch presented in [7].

A series of Langmuir probes were positioned at various distances from the channel exit: 480 mm, 90 mm, and at the channel exit, facilitating the measurement of plasma potential, floating potential, electron temperature, and plasma density. These Langmuir probes are custom-made, constructed from tungsten wire encased in an alumina tube, with only the tip of the wire (length of 7 mm and diameter of 0.37 mm) exposed to the plasma. Additionally, a set of four Quadrupole Langmuir probes (QLP) were deployed to capture time-dependent plasma properties.

Probe Working Principles

The electrical schematic of the Langmuir probe is illustrated in Figure 4.34. Generally, the current collected by the Langmuir probe falls below the resolution of a power supply (in the milliampere range or less). Hence, a multimeter is interposed between the two terminals of a resistance ($R = 1.1$ $k\Omega$) to measure the voltage. The use of this high resistance ensures that the voltage is amplified and accurately registered by the multimeter.

Then, by applying Ohm's law, the current sensed by the Langmuir probe is calculated as $I = V/R$. Once the IV curve is obtained for a particular operating condition, the data can be postprocessed to determine the plasma properties corresponding to that operating condition at the specified location.



(a) Ideal IV curve, data taken from [219].

(b) ln vs probe voltage.

Figure 4.35: Representation of the ideal IV curve and Natural logarithm of a Langmuir probe. Plots presented in [7].

For accomplishing this, the methodology applied is explained herein using an ideal IV curve of a single Langmuir probe (Figure 4.35a), utilising data extracted from [219].

To begin, the floating potential (φ_f) is computed as the voltage at which the current sensed by the Langmuir probe equals zero. In Figure 4.35a, this condition is attained at $\varphi_f = -12.6$ V.

The plasma potential (φ_p) is identified just before entering the electron saturation region. To determine the specific point at which this occurs, it is necessary to calculate the maximum of the first derivative of the current sensed by the Langmuir probe. The point where the maximum is situated corresponds to φ_p. In this instance, $\varphi_p = 0.6$ V.

It can also be demonstrated that assuming a planar probe tip (i.e., the electron drift speed travels along one direction), the electron temperature can be computed from the slope of the curve between $\ln(I_e)$ (where I_e represents the electron current) and the voltage in between φ_f and φ_p [67, 219]:

$$\ln\left(I_e\right) = \frac{e}{k_B T_e} V + C \tag{4.14}$$

where C is a constant. Figure 4.35b shows $\ln(I_e)$ versus the probe voltage and a regression line from which the slope is calculated. Using the data from Figure 4.35a, the electron temperature results in $T_e = 2.8$ eV.

Finally, for calculating the plasma density n_o [7], it is first needed to compute the ion saturation current (I_{si}), which is defined as the steady current sensed by the probe in the ion saturation region (see Figure 4.35a). In this example, $I_{si} = 2.8694 \times 10^{-4}$ A. From I_{si}, it can be demonstrated that the plasma density is equal to

$$n_o = \frac{2I_{si}}{Ae} \left(\frac{m_i}{k_B T_e} \right)^{\frac{1}{2}} \tag{4.15}$$

In this example, $n_o = 7.14 \times 10^{16}\ m^{-3}$. Utilising this methodology, the plasma properties at various locations from the channel exit are presented in Section 4.3.2.3.

4.3.1.8 Spectrometer

Device Description

A spectrometer was employed to measure the transmission, reflection, scattering, or absorption of various species coming from the thrusters' plume. Specifically, the spectrometer utilised was the *HR2000+ES* by *Ocean Optics*. This apparatus was coupled with a stepping motor and a VXM stepping motor controller (from *Velmex Inc*), facilitating the acquisition of the oxygen plasma spectrum at distinct locations from the channel exit.

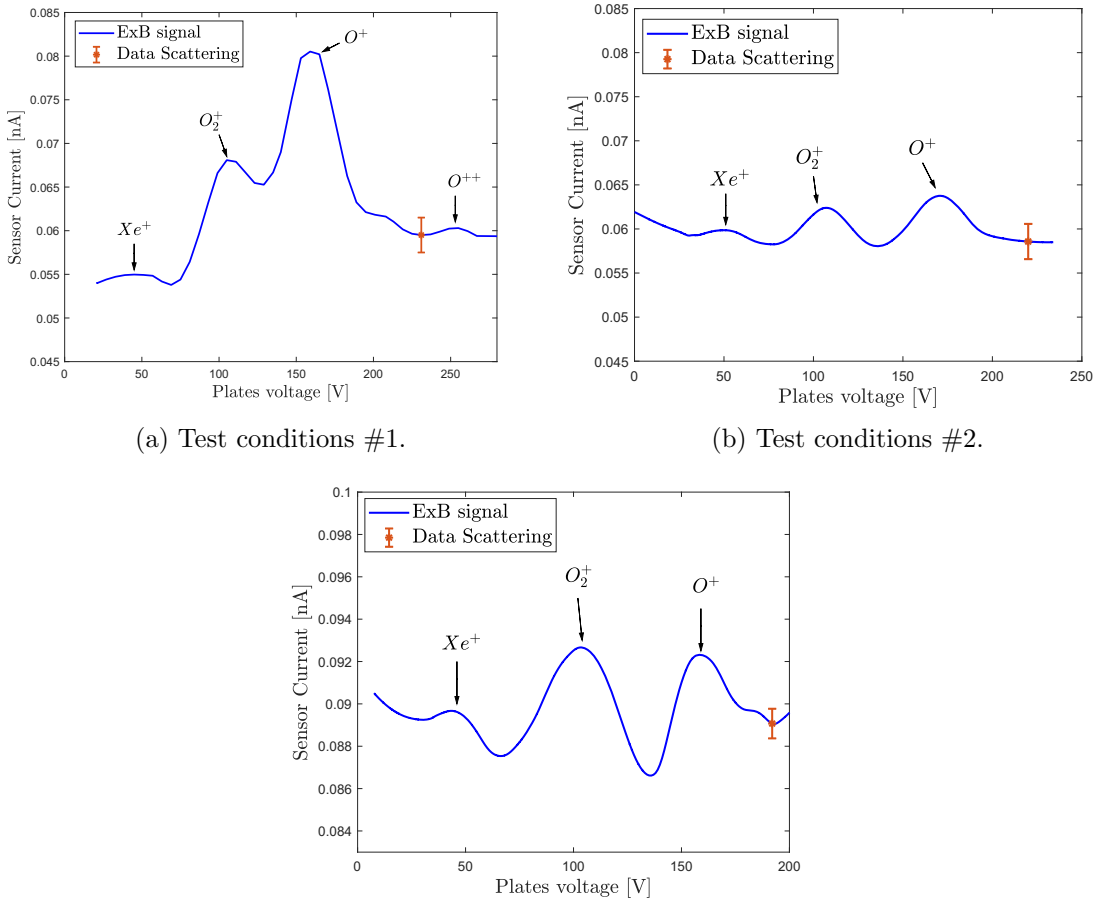
Device Working Principles

The data acquired by the spectrometer is directly processed by the in-house software *HR2000+* provided by *Ocean Optics*. For each wavelength (measured in nanometers, *nm*), this software yields the intensity of the spectrum (expressed in adimensional units, *a.u.*). The data is recorded at intervals of 5 milliseconds, ensuring a total exposure time of around 2.5 seconds. It is important to note that the spectrometer is positioned transversely to the discharge (as illustrated in Figure 4.30, element C), with its nominal position situated at the channel exit plate. Subsequently, the spectrometer position is automatically adjusted using a stepper motor in 4 mm intervals from the channel exit.

[7] Notice that, assuming quasineutrality, the electron density will be equal to the ion density and referred here to as n_o.

4.3.2 Results and Discussion

4.3.2.1 Plasma Particles' Composition



(a) Test conditions #1.

(b) Test conditions #2.

(c) Test conditions #3.

Figure 4.36: ExB oxygen plasma composition of the thruster *AQUAHET* under different testing conditions. Refer to Table 4.11 for a description of the testing conditions. Data presented in [7].

Table 4.11: Oxygen plasma composition for different conditions of discharge power and magnetic field strengths, all for a constant mass flow of $\dot{m}_a \approx 4$ mg/s. Data presented in [7].

Test	Discharge Conditions		Density Fractions					
	Power [W]	Peak Bfield [Gauss]	Xe^+	O_2^+	O+	O^{++}	O_2^{++}	Ratio O_2^+/O^+
#1	$\approx$ 400	295	5%	33%	59%	3%	-	-82%
#2	$\approx$ 250	380	14%	37%	49%	-	-	-33%
#3	$\approx$ 400	380	11%	50%	39%	-	-	22%

The data from the ExB probe unveils the particles' composition of the oxygen plume. Figure 4.36 provides an illustrative representation of the plasma composition observed during Test #1, Test

#2, and Test #3 with the *AQUAHET* thruster (refer to Table 4.11 for a summary of the results). As the contribution of double ions is negligible or not discernible, the density fraction of each ion "i" is directly computed from its current measurement as: $\frac{I_{\text{ion i}}}{I_{\text{total}}}$.

The primary constituents of the plasma consist of O_2^+ and O^+ particles, with their ratio being influenced by both discharge power and magnetic field strength. It is important to understand that, as explained in Section 3.2, to enhance efficiency levels in an oxygen-fuelled HET, it is essential to maximise the O_2^+/O^+ ratio. This is because O^+ particles are the result of a dissociation process ($O_2 + e \rightarrow O + O + e$), which does not directly contribute to thrust generation (it does not create ions), thus representing an energy loss within the system.

These experimental findings suggest that an increase in discharge power results in a higher O_2^+/O^+ ratio. However, the magnetic field's influence is even more significant, as a stronger magnetic field strength yields a higher O_2^+/O^+ ratio compared to that achieved solely through an increase in discharge power.

These results are consistent with the performance assessments of the thruster in Section 4.2, where higher powers and magnetic field strengths optimised the system's overall performance.

Figure 4.37 examines the cross sections of molecular O_2 for varying electron temperatures (data sourced from [166]). Within the range $T_e = 10 - 30$ eV, it becomes evident that increasing the electron temperature, achievable by operating at higher discharge power or applying a stronger magnetic field, notably enhances the ionisation cross section (red curve in Figure 4.37) while maintaining a stable dissociation rate (blue curve). Essentially, this leads to an increased O_2^+/O^+ ratio, a phenomenon supported by the experimental tests depicted in Figure 4.36 and Table 4.11. This enhancement proves advantageous for the plasma, resulting in an intensified ionisation rate with relatively constant dissociation losses. However, it is important to note that, as electron temperatures exceed $T_e = 30$ eV, the ion dissociation reaction (green curve) begins to exhibit an upward trend, potentially introducing losses into the system. The ionisation reaction however, keeps increasing until reaching approximately $T_e = 50$ eV, with the dissociation curve going down as the electron temperature increases.

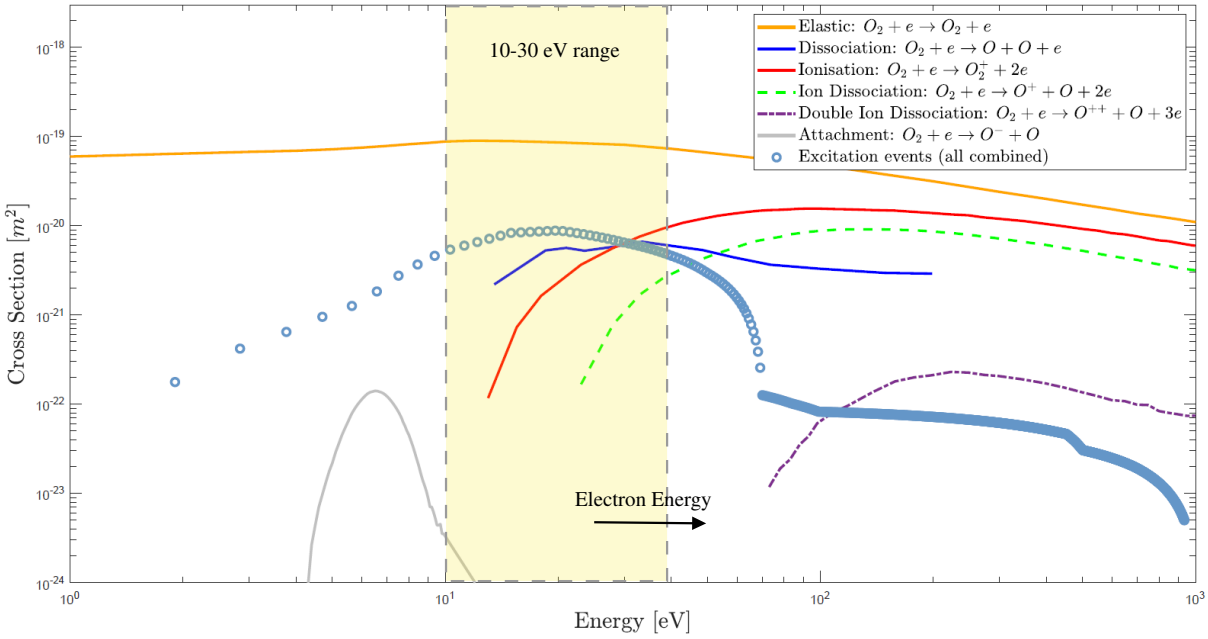


Figure 4.37: Cross sections of molecular O_2 as a function of the electron energy, with the energy range highlighted within a light yellow frame. Data taken from Y. Itikawa's work [166], and results presented in [7].

Based on this analysis, the optimal operational parameters for the thruster could lie around electron temperatures of approximately $T_e = 50$ eV, where the ionisation cross section (plotted in red) is way above the dissociation cross section (blue labelled) and the ion dissociation curve (in green) still has not reached its peak. Notice that, within this range of $T_e = 10 - 50$ eV, the contribution of negative ions to the discharge is also negligible.

Nonetheless, notice that the improved performance resulting from these factors such as increased discharge power or magnetic field strength cannot solely be attributed to an optimised O_2^+/O^+ ratio. Other factors, such as the heightened electron temperature within the channel, also play a role in fostering superior propellant utilisation efficiency.

The results of the oxygen plasma composition for the *WET-HET* thruster are also shown (Figure 4.38). Based on this, a comparison can be drawn between the data obtained from the *WET-HET* (Figure 4.38) and Test #2 of the *AQUAHET* (Figure 4.36b): in this comparative analysis, the discharge power levels are closely matched, with the sole distinction lying in the magnetic field strength: $B = 500$ G for the *WET-HET* and $B = 380$ G for the *AQUAHET*.

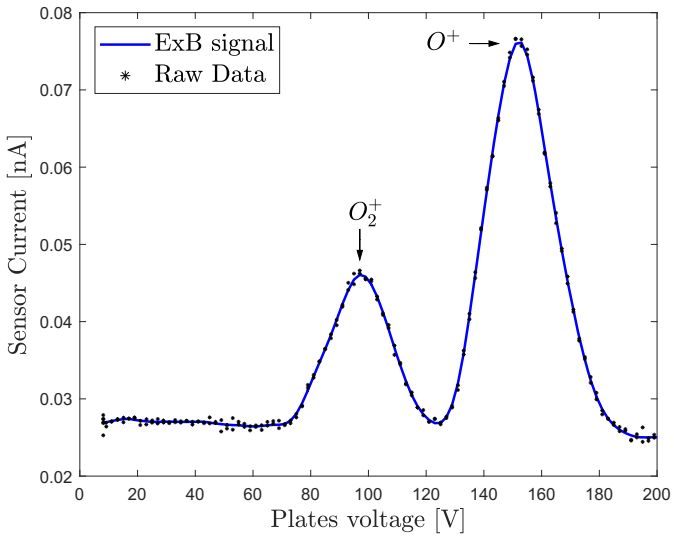


Figure 4.38: ExB oxygen plasma composition of the thruster *WET-HET* for a discharge power of $P_d \approx 250$ W, a peak magnetic field strength of $B = 500$ G and a mass flow of $\dot{m}_a \approx 4$ mg/s. Data presented in [7].

If these conditions were applied to the same thruster, it would be reasonable to anticipate a higher O_2^+/O^+ ratio for the greater magnetic field strength. However, in this instance, it is noted that the O_2^+/O^+ ratio in the *WET-HET* is lower than that in the *AQUAHET*.

From a performance perspective, this would imply that the thrust efficiency of the *WET-HET* is lower than that of the *AQUAHET*. Nevertheless, owing to the generation of more lightweight ions, the specific impulse of the *WET-HET* is expected to surpass that of the *AQUAHET*. Both aspects have been validated experimentally (see Section 4.2.2.8), bolstering confidence in the obtained findings. This variation in plasma species composition could be predominantly attributed to the distinctive geometrical configurations of both thrusters and/or the improved radial directionality of the *AQUAHET* compared to the *WET-HET*, as these factors constitute the primary differentiators between the two designs.

An important aspect to consider in this analysis is the ability to differentiate between double-charged ions, namely O_2^{++} and O^{++} ions. As outlined in Table 4.10, O_2^{++} ions appear at the same plate voltage as O^+ ions (see Equation 4.9). In practical terms, this implies that the ExB probe lacks the capability to discern whether it is O_2^{++} or O^+ ions entering the probe. However, insights from computational simulations, as presented in Sections 3.2.2.1 and 3.2.2.2, indicate that

the presence of double-charged species is relatively insignificant compared to singly ionised species, at least in these operating conditions. Assuming this to be the case, the prevailing composition of the plasma primarily consists of O_2^+ and O^+ particles.

Regarding O^{++} ions, they would emerge at ExB plate voltages above 200 V, which could not be achieved for all tests due to operational constraints in maintaining thruster stability throughout the entire electric field sweep of the ExB probe. The technical limitation encountered here stemmed from the suboptimal configuration of the Stanford Plasma Propulsion Laboratory facilities for conducting experiments involving molecular propellants such as oxygen. It is highly recommended to integrate a specialised pumping system and mass flow meters optimised for oxygen to alleviate the inherent complexities associated with the experimental setup.

In any case, as depicted in Figure 4.37, the double ion dissociation cross section only begins to rise for electron temperatures exceeding $T_e > 100$ eV. This scenario is not expected unless very high powers are utilised; however, these double-ionised species may originate from other sources, such as an ionisation event occurring twice.

Overall, further testing in more operating conditions than the ones described here is encouraged to assess in which scenarios double ions could become relevant in the discharge. These additional campaigns could potentially give more insights into how this technology works.

4.3.2.2 Acceleration Voltages

The acceleration voltages for distinct species are graphically depicted in Figure 4.39.

A close examination of these results reveals that monoatomic species and double-ionised species demonstrate higher acceleration voltages than single-ionised species. This observation can be attributed to two distinct factors. Firstly, temporal oscillations in the plasma properties within the channel may play an important role here. These fluctuations in electron temperature, electric field, and other plasma properties can cause dynamic shifts in their profiles and associated peaks, potentially influencing ion production locally [183].

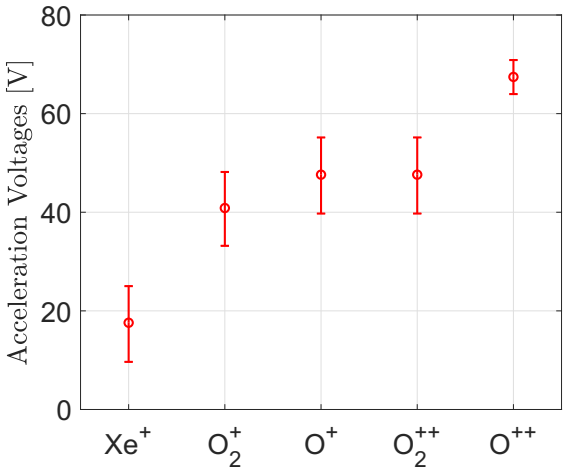


Figure 4.39: Main acceleration voltages of the species coming from the plume of the oxygen-fuelled *WET-HET* in combination with a xenon-fuelled cathode. Data presented in [7].

To gain a deeper understanding of this phenomenon, one could measure species production over the breathing mode cycle to assess its impact on the obtained results.

Secondly, the location of species generation may also contribute. Monoatomic species appear to originate upstream of the channel exit compared to diatomic species, given their higher acceleration voltage. This observation may shed light on why shorter channels have demonstrated superior performance, as previously reported in Section 4.2.2.6: prolonged channels tend to promote a reduced O_2^+/O^+ ratio by generating an increased population of O^+ ions near the anode, where the electron temperature is lower compared to the peak electron temperature located near the apex of the magnetic field [220]. Consequently, extending the channel results in a broader segment characterised by lower electron temperature, typically around $T_e = 5$ eV, thereby enhancing the production of O^+ ions and decreasing the thruster's performance.

It is also conceivable that certain O^+ ions generated upstream may undergo further ionisation while traversing the high electron temperature region near the anode exit, transforming into O^{++} ions. This dynamic provides a plausible explanation for the elevated acceleration voltage observed in double-charged ions, predominantly originating from singly ionised ions generated near the anode and subsequently longitudinally traversing towards the channel exit, evolving into O^{++} ions (or O_2^{++} ions if the precursor species is O_2^+).

4.3.2.3 Plasma Properties at Different Locations

Table 4.12: Plasma properties measurement of the thruster *WET-HET* oxygen-fuelled with a xenon-fuelled cathode. Data presented in [7].

Test	**Power** $[W]$	**Peak Magnetic Field** $[G]$	**Mass Flow** $[mg/s]$	**Location from channel exit** $[mm]$	**Floating Potential** $[V]$	**Plasma Potential** $[V]$	**Electron Temperature** $[eV]$	**Plasma Density** $[m^{-3}]$
# 1	192	450	4.0	0	32.0	-	9	1.67×10^{17}
# 2	208	600	4.0	0	32.0	-	11.7	2.04×10^{17}
# 3	799	600	4.0	0	29.5	-	13.9	1.84×10^{17}
# 4	1005	600	2.5	0	25.6	-	15.3	1.07×10^{17}
# 5	181	600	4.0	90	18.0	30	8.4	3.90×10^{15}
# 6	236	600	4.0	480	14.0	38	3.2	1.60×10^{15}

Measurements were carried out using Langmuir probes positioned at distinct locations: 480 mm from the channel exit (near the entrance of the ExB probe), 90 mm, and one at the channel exit. The results are summarised in Table 4.12. These measurements corresponded to two sweeps: from zero voltage to the upper voltage bound, and viceversa, ensuring both results are consistent. For negative voltages, the polarity of the power supply was reversed, and the same procedure is applied.

Upon comparing Test #1 and #2, with the most notable difference being the magnetic field strength, it becomes apparent that a stronger magnetic field correlates with a higher electron temperature at the channel exit. Additionally, there is an increase in plasma density with an elevation in magnetic field strength.

Conversely, in the case of Tests #2 and #3, where only the discharge power is altered, the electron temperature shows corresponding fluctuations with changes in discharge power. However, in this scenario, a subtle reduction in plasma density is noted. It is important to note that, in the context of xenon-fuelled HETs, the electron temperature peak conventionally resides at the channel exit, while the plasma density peak is typically situated within the channel itself. Therefore, a decrease in discharge power does not inherently indicate a diminished peak plasma density within the channel, which is presumably the primary location for the peak density.

Test #4 corresponds to the highest discharge power analysed, where the electron temperature

reaches $T_e = 15.3$ eV. This discharge power was attained through the reduction in mass flow in this test. Notice though that, as mentioned throughout this section, the facilities are not optimised to test with oxygen, and therefore the mass flow meters used are not calibrated for oxygen flows, thus introducing an uncertainty associated with the provided numbers. Nevertheless, the obtained values serve as an approximation of the plasma properties under various conditions and serve as a valuable tool for correlating numerical models.

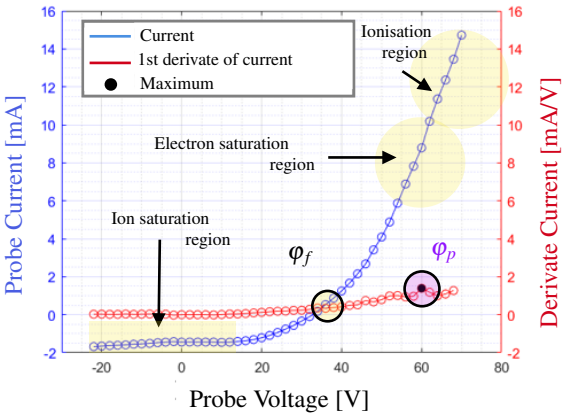
Finally, it is observed that, starting from the anode plate, the plasma potential decreases until it reaches the cathode (from 100 V to 30 V). Subsequently, the potential increases again as it traverses through the vacuum chamber (38 V). These findings align with observations made by other researchers investigating the plasma properties of an HET in a location far from the channel exit [220], where an increase in plasma potential was noted before reaching saturation.

Figure 4.40 illustrates the IV characteristics of the Langmuir probes at various spatial positions along the channel exit, specifically corresponding to Tests #2, #5, and #6.

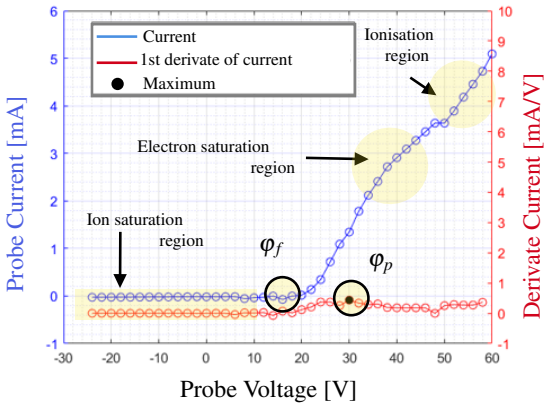
In comparison to the theoretical Langmuir probe IV curve depicted in Figure 4.35a, it is seen that the start of the electron saturation region is less pronounced: instead of appearing as a sharp corner, the electron saturation gradually emerges with increasing voltage. This phenomenon is particularly evident in Figure 4.40c, where the probe is positioned 480 mm away from the thruster.

When the probe is situated near the thruster, as shown in Figure 4.40b, an additional region, referred to as the "ionisation region," appears after the electron saturation region. This region arises under conditions of elevated voltage and sufficient plasma density, causing the Langmuir probe to create a plasma envelope around itself, as illustrated in Figure 4.41.

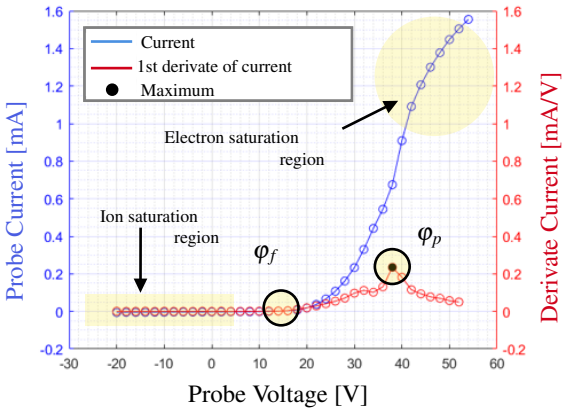
Finally, when the probe is placed at the channel exit (Figure 4.40a), it becomes more challenging to accurately distinguish the end of the electron saturation region and the beginning of the ionisation region. Consequently, the precise value of φ_p in these conditions cannot be ascertained with full certainty and is thus omitted from Table 4.12. However, employing the methodology expounded before, an estimated value of $\varphi_p \approx 60$ V could be derived. Utilising a regression analysis between φ_f and φ_p, the electron temperature and the plasma density values are deduced.



(a) Exit plane (test #2).



(b) Distance: 90 mm (test #5).



(c) Distance: 480 mm (test #6).

Figure 4.40: IV curves of the Langmuir probes taken at different distances from the oxygen-fuelled thruster WET-HET with a xenon-fuelled cathode. The test conditions are summarised in Table 4.12. Data presented in [7].

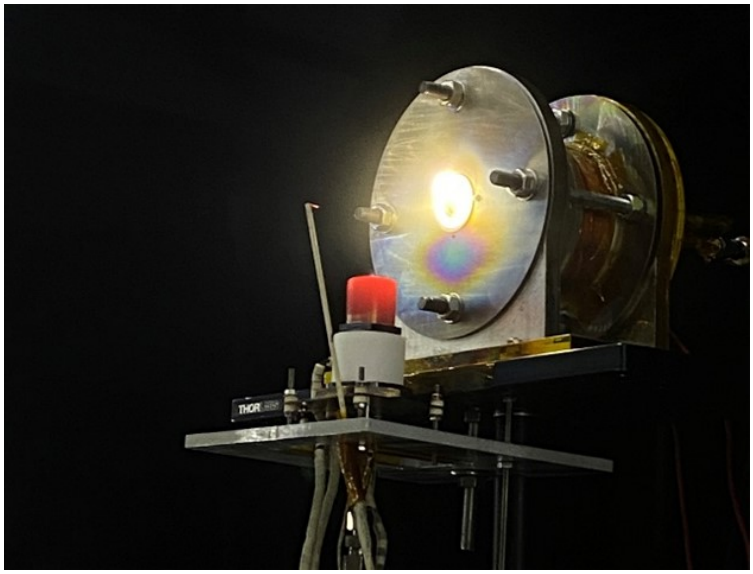


Figure 4.41: The oxygen-fuelled *WET-HET* with a xenon-fuelled cathode firing in combination with a Langmuir probe placed at 90 mm from the channel exit. The Langmuir probe region found during the snapshot is the ionisation region (as seen in Figure 4.40b). Picture presented in [7].

4.3.2.4 Oxygen Plasma Spectrum

Figure 4.42 illustrates the spectral lines obtained with the spectrometer within the $400 - 1000$ nm range at three distinct distances from the exit plane (8 mm, 4 mm, and at the exit plane itself). Throughout all tests, the operational parameters remain consistent, with a peak magnetic field strength of approximately $B = 100$ G, a mass flow rate of approximately $\dot{m}_a = 4$ mg/s, and a discharge power of approximately $P_d = 200$ W. The spectral lines and their corresponding species are identified based on prior studies [221] and the NIST database [222].

The major peak is identified at 777.3 nm, corresponding to atomic oxygen (O). The remaining spectral lines comprise a combination of O_2^+, O^+, and O. Upon relocating the spectrometer to distances of 4 mm and 8 mm from the exit plane, the differentiation of spectral lines becomes more intricate, with only the most significant lines discernible within the spectrum.

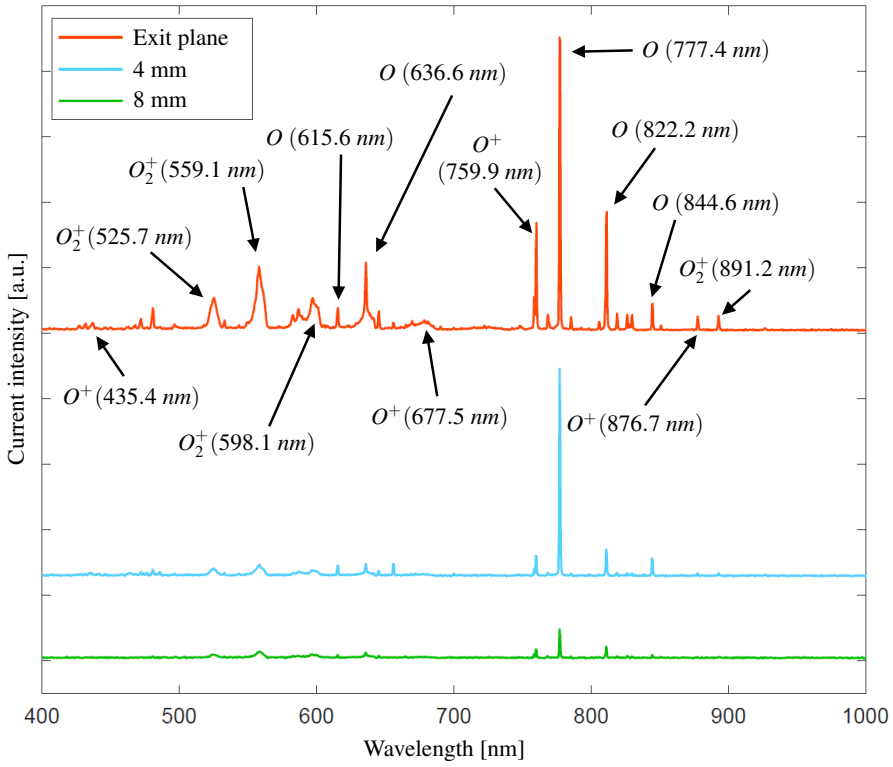


Figure 4.42: Spectral lines taken by the spectrometer for the thruster *WET-HET*. For this test, the peak magnetic field strength is set to $B \approx 100$ G, the mass flow of $\dot{m}_a \approx 4$ mg/s and a discharge power of $P_d \approx 200$ W. Graph presented in [7].

4.3.2.5 Numerical Model and Experiments

Table 4.13: Preliminary comparison of the oxygen plume's composition of *WET-HET* between experimental and simulation results obtained with *PlasmaSim* (Section 3.2.2.1).

	Discharge Conditions		**Density Fractions [%]**			
	Power [W]	Peak Magnetic Field [G]	O_2^+	O^+	O^{++}	O_2^{++}
Experiment	400	295	39	61	-	-
PlasmaSim	520	250	43	55	1	1

As seen within this section, the correlation between the experiments conducted here and the results from the numerical model presented in Section 3.2.2.1 is promising. Firstly, the numerical model indicated that the production of O_2^+/O^+ ions increases with the electron energy (Table 3.9). Similarly, the experimental results exhibit the same trend (Table 4.11).

Secondly, as shown in Table 4.13, the oxygen plume composition of the thruster is consistent between simulations and experiments. This is observed, not only in the O_2^+/O^+ proportion but also on the numerical model's indication that double ions and negative ions are negligible compared to the production of other species existing within the plume. However, it should be noted that, as shown in Figure 3.6a, the production of these particles depends on the energy of the electrons. Variations in operating conditions can influence the electron energy (as seen in Table 4.12) and, consequently, the relative proportion of these ions within the thruster's discharge.

4.4 Campaigns C - Water Electrolysis-Fuelled Hall Effect Thrusters: Oxygen and Hydrogen from Pressurised Cylinders

In contrast to previous sections examining water electrolysis propulsion using oxygen for the thruster (anode) and a noble gas for the cathode (xenon/krypton), this section presents, to the author's knowledge, the first experimental results showcasing an oxygen-fuelled HET in combination with a hydrogen-fuelled cathode (the two byproducts of water electrolysis), both supplied from pressurised cylinders. The results presented here were published in [5].

4.4.1 Methodology

4.4.1.1 Experimental Set-Up and Vacuum Chamber Facilities

The entirety of this research was conducted in the Boltzmann vacuum facility within the the Imperial Plasma Propulsion Laboratory. A schematic illustration of the experimental set-up employed for conducting oxygen and hydrogen testing is depicted in Figure 4.43. The description of the elements used is summarised in Table 4.14. In terms of hardware, electronics, fluidics and procedures, a very similar set-up to the one explained in Section 4.2.1 was implemented for this set of experiments. Here, the main novelties of the set-up are highlighted.

4.4.1.2 Electronics, Fluidics and Working Procedures

In contrast to the previous experimental setup, the current configuration required a more elaborate system to safely manage both pressurised oxygen and hydrogen within the same controlled environment. This precaution is essential as oxygen and hydrogen mixed at stoichiometric ratios can potentially lead to explosions unless adequate safety measures are in place. To mitigate these risks, the oxygen cylinder [element 48] is maintained at atmospheric pressure within the laboratory premises, while the hydrogen tanks are securely stored within the load-lock hatch chamber [element 26]. This deliberate separation of the oxygen and hydrogen tanks serves as a safety precaution to prevent any potential explosive interactions in case of emergencies.

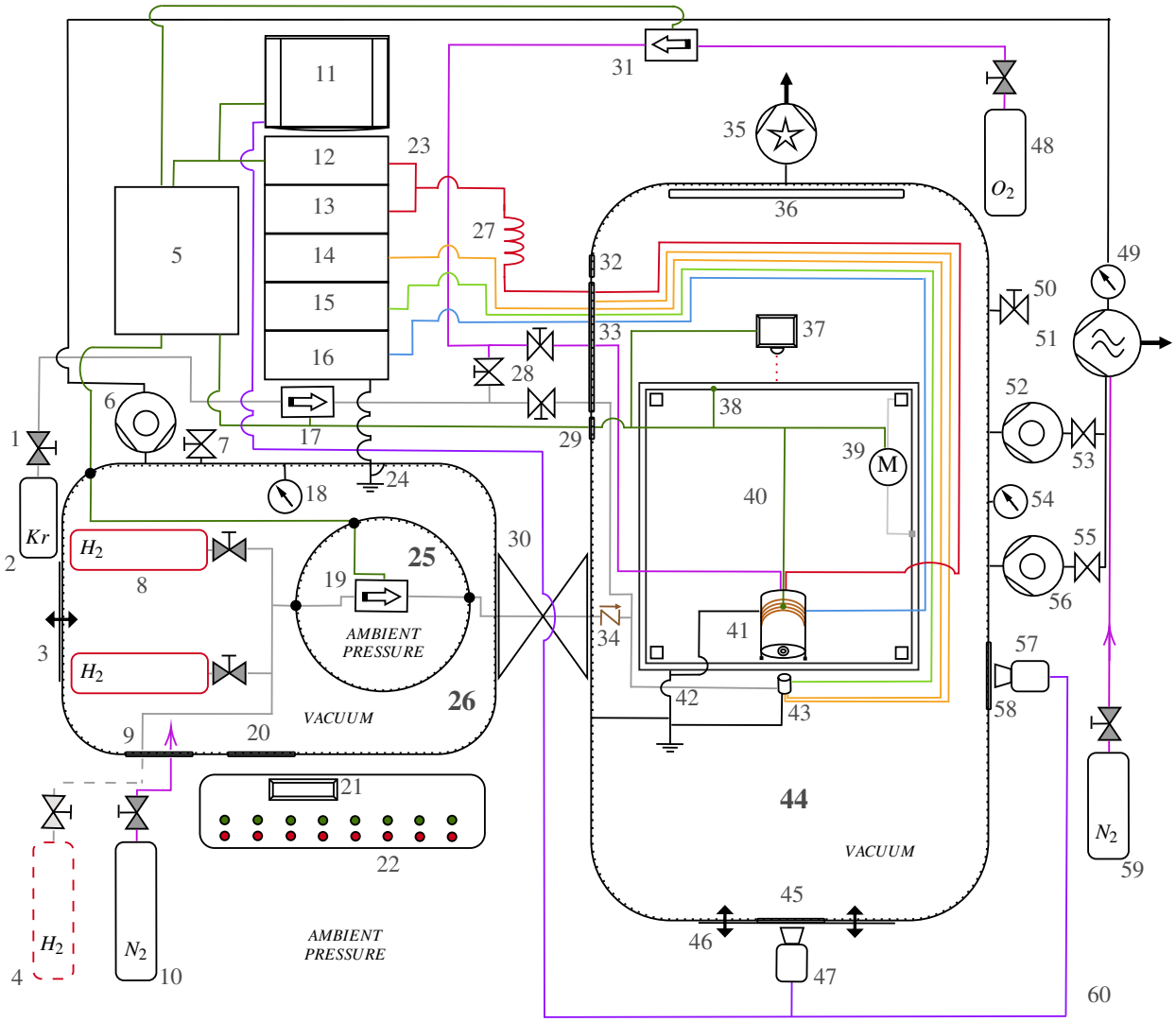


Figure 4.43: Main schematics of the water electrolysis (oxygen and hydrogen) electric space propulsion testing at the Imperial Plasma Propulsion Laboratory. Diagram published in [5].

Consequently, only oxygen and hydrogen can come into contact at the low mass flows required for the thruster and cathode (see Table 4.15).

Furthermore, a non-return valve [element 34] is installed at the end of the hydrogen line to prevent any backflow of oxygen down the hydrogen line.

Despite the low mass flow rates for both the thruster and cathode, compressed gas cylinders are necessary to maintain the back pressure of the mass flow controllers in line with the manufacturer's specifications. Specifically, the oxygen mass flow controller [element 31] requires a back pressure of 2 bar, while the hydrogen mass flow controller [element 19] necessitates 11 bar.

Table 4.14: Description of the elements illustrated in Figure 4.43, composing the set-up for the oxygen/hydrogen testing at the Imperial Plasma Propulsion facilities. Table published in [5].

1	Pressure regulator (cathode)	**31**	Massflowmeter anode [oxygen] (*F-201CV-200-AAD-22-V*)
2	Cathode auxiliary propellant bottle (krypton)	**32**	Vacuum feedthrough (auxiliary)
3	Door (vacuum load-lock hatch chamber)	**33**	Vacuum feedthrough (power and feedlines)
4	Removable hydrogen tank to refill #8 cylinders	**34**	Non-Return Valve
5	Electronics box	**35**	Cryohead (connected to a cryocompressor)
6	Turbopump (load-lock hatch chamber)	**36**	Cryopanel (Stage 3: *Leyvac 6000H*)
7	De-pressurising valve (load-lock hatch chamber)	**37**	Laser optoNCDT 1750
8	Cathode propellant bottles (hydrogen)	**38**	Thermocouple (to thrust balance)
9	Vacuum feedthrough	**39**	Servomotor (for calibration)
10	Nitrogen tank to de-pressurise the chambers	**40**	Thrust balance
11	Computer station	**41**	The Water Electrolysis Hall Effect Thruster (anode)
12	Anode power supply [master] (*Sorenson SGA 1K0X5S-0AA*)	**42**	Grounding connection
13	Anode power supply [slave] (*Sorenson SGA 1K0X5S-0AA R*)	**43**	LaB6 cathode (*Hydrocat*, by *ALIENA Pte Ltd*)
14	Heater power supply (*Electro-Automatik EA-PSI 8080-60*)	**44**	Main vacuum chamber
15	Keeper power supply (*Glassman PS/ET05R400-200*)	**45**	Vacuum feedthrough (window)
16	Magnet power supply (*GW INSTEK SPS-3610*)	**46**	Door (main vacuum chamber)
17	Massflowmeter cathode [krypton] (*F-201CV-100-AAD-22-V*)	**47**	Camera Nikon D-5000 (front)
18	Pressure gauge (load-lock hatch chamber)	**48**	Anode propellant bottle (oxygen)
19	Massflowmeter cathode [hydrogen] (*FG-201CV-AAD-22-V*)	**49**	Pressure gauge (to roughing pump)
20	Vacuum feedthrough (window)	**50**	De-pressurising valve (main chamber)
21	Pressure readings display	**51**	Roughing pump (Stage 1: *Leyvac LV 80C*)
22	Control panel of vacuum systems	**52**	Turbopump #1 (Stage 2: *Pfeiffer ATH 2303 M*)
23	Parallelising line (anode power supplies)	**53**	Pneumatic valve #1
24	Grounding connection of all power supplies	**54**	Pressure gauge (to main chamber)
25	Vacuum chamber (at atmospheric pressure)	**55**	Pneumatic valve #2
26	Vacuum chamber (at atmospheric pressure)	**56**	Turbopump #2 (Stage 2: *Pfeiffer ATH 2303 M*)
27	Inductor	**57**	Camera Nikon D-5000 (side)
28	Valves set (anode and cathode)	**58**	Vacuum feedthrough (window)
29	Vacuum feedthrough (signals, D-Sub connector)	**59**	Roughing pump purging system (nitrogen tank)
30	Gate valve (kept open)	**60**	Imperial Plasma Propulsion Laboratory

The hydrogen cylinders are filled before testing by temporarily placing an auxiliary hydrogen cylinder outside the facility [element 4]. Once the hydrogen cylinders inside the load-lock hatch chamber [element 8] have been replenished, the auxiliary cylinder is removed.

Regarding the mass flow meters, they should operate under atmospheric conditions according to the manufacturer [223]. Hence, a small pressure vessel at atmospheric pressure is placed within the load-lock hatch chamber (under vacuum during testing) to accommodate the hydrogen mass flow meter, which is controlled remotely from outside the chambers.

During the venting process, the pressurised hydrogen sourced from the cylinders stored within the load-lock hatch chamber should be effectively purged into the chamber and diluted with nitrogen (and not atmospheric air) before evacuation.

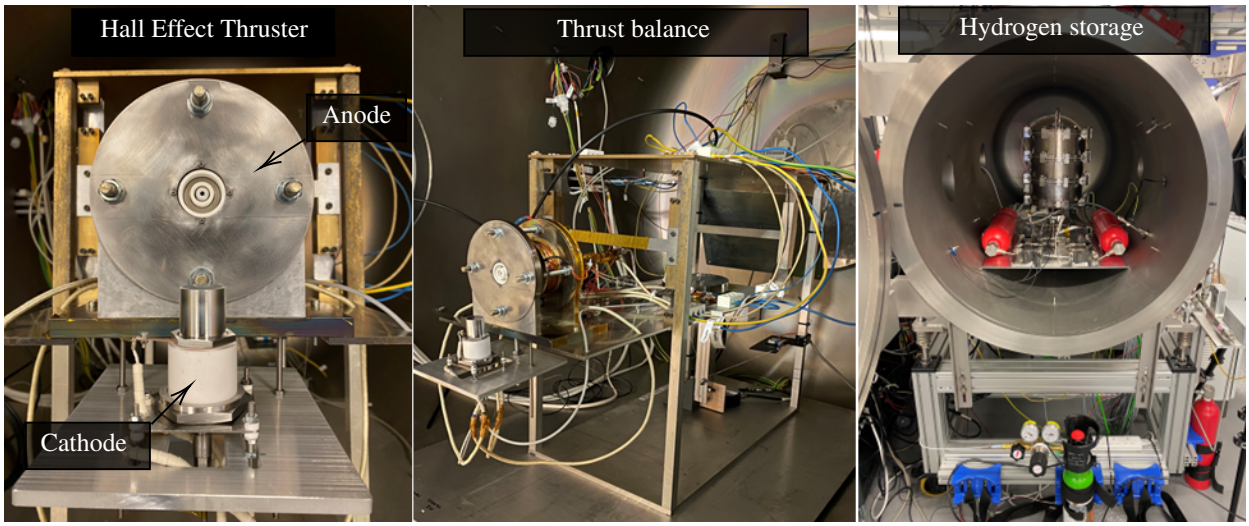


Figure 4.44: Set-up of the experiment using oxygen and hydrogen from pressurised bottles. Left: the thruster *WET-HET* and cathode *Hydrocat* (from *ALIENA Pte Ltd*). Middle: thrust balance in the main vacuum chamber. Right: hydrogen flowline disposition in the load-lock hatch chamber. Pictures published in [5].

This precaution ensures that oxygen is not inadvertently introduced into the chamber while evacuating the hydrogen cylinders.

The same set of pumping stages outlined in Section 4.2.1 is utilised here. The main distinction is that the roughing pump now features a purging system with a continuous nitrogen flow of 80 normal air litres per minute (80 NI/min) [224]. This feature is essential for simultaneously evacuating both hydrogen and oxygen, ensuring the safety of the set-up. It is also important to note that the third and final stage, incorporating the cryo panel (*Leyvac 6000H* for the cryo compressor and *COOLpower-CP140T* for the cryo head), maintains a nominal temperature of approximately 20 K. This low temperature solidifies oxygen molecules, which undergo a phase transition at approximately 54 K. However, the cryo panel does not contribute to freezing hydrogen molecules, as the freezing point of hydrogen is around 14 K. Consequently, most of the hydrogen will be vented through the roughing and turbomolecular pumps (first and second stages). As will be explained in Section 4.4.2.1, this scenario is suboptimal for maintaining low pressures in all situations. To achieve the best testing conditions, all pumping stages should be capable of evacuating hydrogen and oxygen simultaneously, particularly the second and third stages.

Figure 4.44 shows the a photo of the set-up used for this experimentation (thruster, cathode,

thrust balance and hydrogen storage), based on the indications presented here and further described in Figure 4.43 and Table 4.14.

4.4.1.3 Thrusters' Geometrical and Material Configuration

The findings delineated in Sections 4.2 and 4.3, which focused on the thruster's operation with oxygen, identified the optimal operational conditions and explored the underlying physical phenomena. To ensure optimal performance and facilitate comparison with the utilisation of a hydrogen-fuelled cathode instead of a noble gas, these best-performing operating conditions were maintained whenever feasible. It is noteworthy that the cathode utilised in these experiments is the *Hydrocat*, not the plasma filament cathode. This selection was made due to the challenges associated with operating a plasma filament cathode in a hydrogen plasma, as elaborated in Section 4.1.2.2.

The geometric and material composition of the thrusters *WET-HET* and *AQUAHET* is summarised in Table 4.15. This configuration is very similar to the one described in Section 4.3 (Table 4.8) with three changes which are highlighted hereafter. First, the channel width of the thruster *AQUAHET* is w = 4 mm, instead of the best performing length (w = 5 mm, see Section 4.2.2.7). This is because no hardware was available with a w = 5 mm channel width when performing these tests.

Second, as these tests were conducted at the Imperial Plasma Propulsion Laboratory, optimised to work with lightweight propellants, the mass flows that could be used are the most optimum ones for both thrusters (see Section 4.2.2.5) instead of using larger mass flows to increase their stability as in Section 4.3.

Third, the magnetic field strength of the thruster *AQUA-HET* is obtained using $I_m = 2.5$ A to energise the electromagnets (corresponding to a peak magnetic field of B = 0.038 T, as seen in Figure 4.5). As demonstrated in Section 4.2.2.4, enhancing the magnetic field strength further slightly augments the thruster's performance at the expense of heightened thermal loads on the electrocoils. However, as the primary objective of these tests was to establish a baseline of oxygen/hydrogen results to later compare to the results of Section 4.2, priority was accorded to ensuring the integrity of the thruster *AQUAHET* during the hydrogen tests.

Table 4.15: Experimental configuration of the thrusters *WET-HET* and *AQUAHET* used during testing with the byproducts of water electrolysis (oxygen and hydrogen from pressurised bottles). Table published in [5].

Variable	**WET-HET**	**AQUAHET**
Channel width (w), [mm]	5.0	4.0 (see Section 4.2.2.7)
Channel mean diameter (d_m), [mm]	20.0	40.0
Channel length (L), [mm]	13.1 (see Section 4.2.2.6)	13.1
Magnetic field topology	Figure 4.3, $I_m = 1.5$ A (see Section 4.2.2.4)	Figure 4.5, $I_m = 2.5$ A (see Section 4.2.2.4)
Oxygen mass flow rate, [mg/s]	0.6 - 1.0 (see Section 4.2.2.5)	1.7 (see Section 4.2.2.5)
Hydrogen mass flow rate, [mg/s]	0.04 - 0.17	0.05 - 0.20
Hydrogen-oxygen ratios (Φ)	1:6 - 1:25 (see Section 4.4.2.1)	1:8 - 1:35 (see Section 4.4.2.1)
Channel walls	$BNSiO_2$ (Grade M26, see Section 4.2.2.2)	$BNSiO_2$ (Grade M26)
Anode material	Stainless steel (see Section 4.2.2.3)	Stainless steel

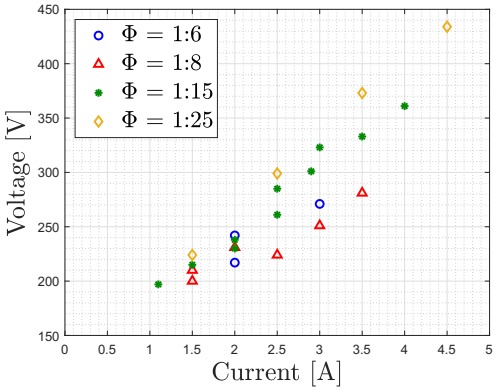
4.4.2 Results and Discussion

4.4.2.1 Hydrogen-To-Oxygen Ratios (Φ)

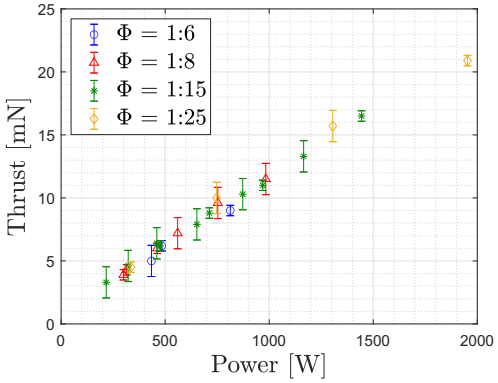
This section presents a summary of the results obtained using the byproducts of water electrolysis at various hydrogen-to-oxygen ratios (Φ). For instance, Φ = 1:15 indicates that the oxygen mass flow is 15 times greater than the hydrogen mass flow. The rationale behind altering Φ is to evaluate whether there exists a preferred condition wherein: a) the system achieves maximum stability, b) the system demonstrates superior overall performance, and c) any surplus hydrogen mass flow could be repurposed for other applications, as discussed in the multi-functional architecture outlined in Section 2.2. Notice that the stoichiometric ratio is achieved when Φ = 1:8. This is due to the differences in molecular weight between oxygen (O_2 = 16 amu) and hydrogen (H_2 = 2 amu).

WET-HET

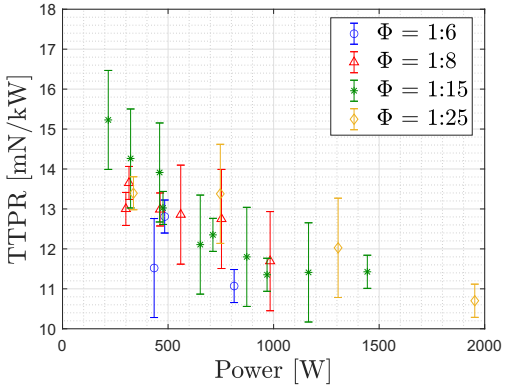
These results correspond to the thruster *WET-HET* employing a constant oxygen mass flow of $\dot{m}_a = 1.0$ mg/s while varying the hydrogen mass flow within the range of $\dot{m}_c = 0.04 - 0.17$ mg/s with the most optimum magnetic field topology (Figure 4.3) using I_m = 1.5 A to energise the electrocoils. This enabled assessments across different hydrogen-to-oxygen ratios spanning from Φ = 1:6 to 1:25. Figure 4.45 illustrates the IV curve, T, $TTPR$, I_{sp}, η_{tr}, and η_{tot} for various discharge powers.



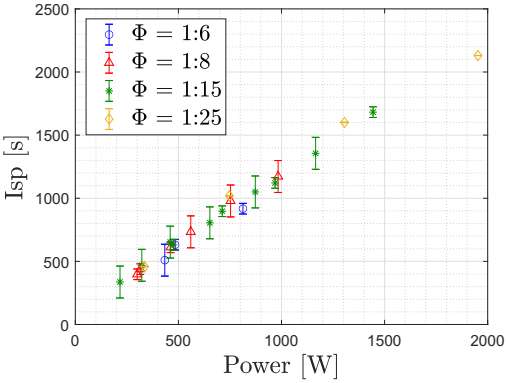
(a) IV Curve



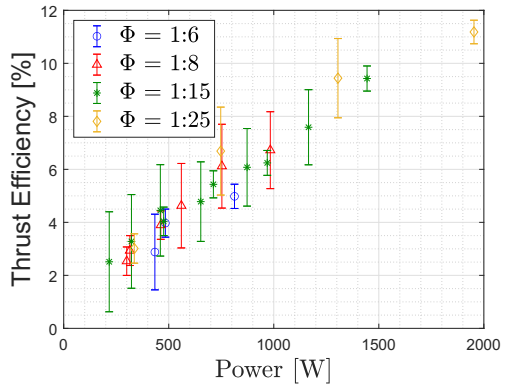
(b) Thrust (T)



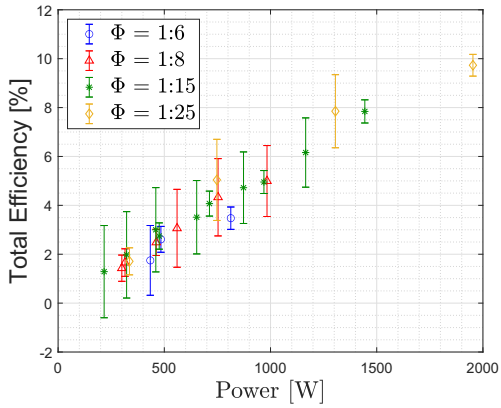
(c) Thrust-To-Power-Ratio ($TTPR$)



(d) Anode Specific Impulse (I_{sp})



(e) Anode Thrust Efficiency (η_{tr})



(f) Total Efficiency (η_{tot})

Figure 4.45: Experimental measurements of the thruster *WET-HET* fuelled by the products of water electrolysis (oxygen for the anode and hydrogen for the cathode, both from pressurised bottles) for various hydrogen-oxygen ratios (Φ). These values correspond to an anode mass flow of $\dot{m}_a = 1.0$ mg/s and the geometrical and material configuration of Table 4.15. Graphs published in [5].

From the observations depicted in Figure 4.45, it can be inferred that the system's performance remains consistent regardless of operating under, at, or beyond the stoichiometric ratio. However, while performance consistency prevails, the IV curve displays variations contingent upon the parameter Φ. Several factors could contribute to this variation.

Firstly, hydrogen emanating from the cathode might undergo back-ingestion into the thruster discharge channel, potentially generating additional current due to back-ingested particles.

Secondly, fluctuations in hydrogen mass flow and the timing of measurements during the test campaign (owing to pressure accumulation) may influence the background pressure within the chamber. As remarked in Section 4.4.1.1, the roughing and turbomolecular pumps play a pivotal role in evacuating both oxygen and hydrogen from vacuum facilities, whereas the cryo panel solely aids in oxygen removal. With this configuration, the chamber's background pressure typically resides in the 10^{-6} mbar range in the absence of mass flow into the chamber. Upon system activation, the background pressure elevates to a range between 10^{-5} to 10^{-4} mbar, contingent upon the operational mass flows. Nevertheless, should a continuous hydrogen mass flow persist for over approximately 30 minutes, especially when testing near the upper limit of hydrogen mass (approximately $\dot{m}_c = 0.17$ mg/s), there exists a potential scenario wherein the background pressure might rise to as high as 10^{-3} mbar. The pressure accumulation resulting from this setup may impact the stabilisation of the thruster's discharge, particularly at higher discharge power settings. Consequently, achieving higher discharge powers, synonymous with enhanced efficiency performance, is only feasible in this setup when operating below the stoichiometric ratio (e.g., Φ = 1:15 or Φ = 1:25). In instances where background pressures of 10^{-4} mbar (or even 10^{-3} mbar) are attained and the thruster fails to stabilise under these conditions, the experimentation is temporarily halted until the pumps successfully restore the pressure to acceptable levels (at least 10^{-6} mbar with no mass flow). Note however, that the pressure gauges are not calibrated for the use of hydrogen but nitrogen, so these values could be overestimated.

According to literature, differences in performance of HETs under varying pressure conditions primarily stem from the stability of the thruster itself [225]. However, as previously noted, the thruster exhibited visual stability during the conducted tests, with consistent discharge readings from the power supplies and demonstrating very similar performance across different background pressures. Performance measurements on the *SPT-140* at $P_d = 2$ kW of discharge power showcased remarkably similar thrust performance across the pressure range around 10^{-5} mbar [226]. Other

researchers investigating the same thruster analysed thrust sensitivity values up to 1.3×10^{-5} mbar, reporting akin values at constant power within an uncertainty range of 2-4% [227].

In conclusion, despite potential variations in discharge evidenced by the IV curve due to differing background pressures and/or hydrogen flow re-ingestion, such discrepancies do not manifest in discernible differences in performance when utilising this thrust balance (see Section 4.1.2.3).

Given the consistency of performance across various values of Φ, a multifunctional approach at the system level is conceivable: typically, a water electrolyser operating in a steady-state mode produces hydrogen and oxygen at a stoichiometric ratio (Φ = 1:8). This ratio can be directly employed as propellant for the thruster system, or alternatively, a portion of the cathode's hydrogen can be allocated to other spacecraft functions, such as powering a cold gas system while the system operates under the stoichoimetric ratio (e.g., Φ = 1:15) [2]. This strategic allocation facilitates a more versatile system where onboard propellant serves multiple purposes. However, it is worth noting that excessively low flow rates fuelling the cathode could lead to different setbacks, such as cathode overheating, increased wear, and a diminished ability to sustain discharge autonomously (necessitating greater power requirements from the keeper or heater circuits). A longevity test would be imperative to evaluate the feasibility of reduced hydrogen mass flow to the cathode.

Within these tests presented, the most optimal performance was obtained at the highest discharge power tested ($P_d = 1953 \pm 1$ W), using a hydrogen-to-oxygen ratio of Φ = 1:25. This operating point corresponded to a thrust of $T = 20.9 \pm 0.2$ mN, anode specific impulse of $I_{sp} = 2130 \pm 20$ s, thrust-to-power ratio of $TTPR = 10.7 \pm 0.5$ mN/kW, anode thrust efficiency of $\eta_{tr} = 11.2 \pm 0.3$ %, and total efficiency of $\eta_{tot} = 10.1 \pm 0.3$ %.

The thruster *WET-HET* firing on the byproducts of water electrolysis for different Φ ratios is also shown in Figure 4.46. A variation in the plasma plume's colour was observed with changes in Φ when the magnetic field was deactivated (although, as previously noted, it had no impact on system performance). Conversely, when the magnetic field is active, the plume appears brighter (whiter), with no discernible difference in plume colour irrespective of Φ.

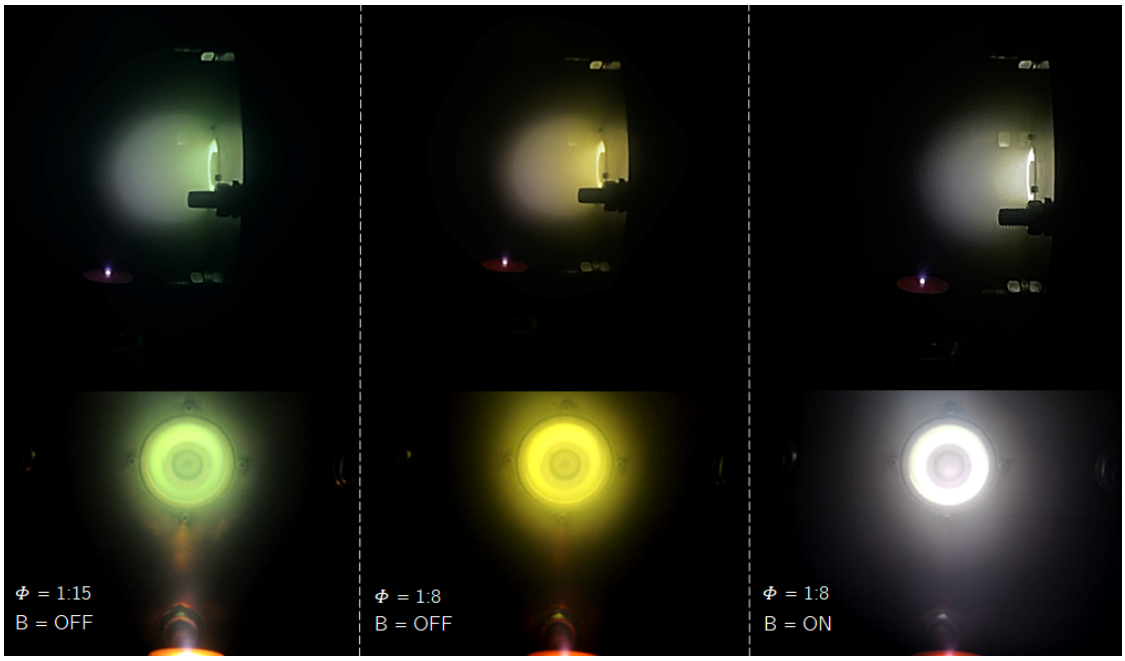
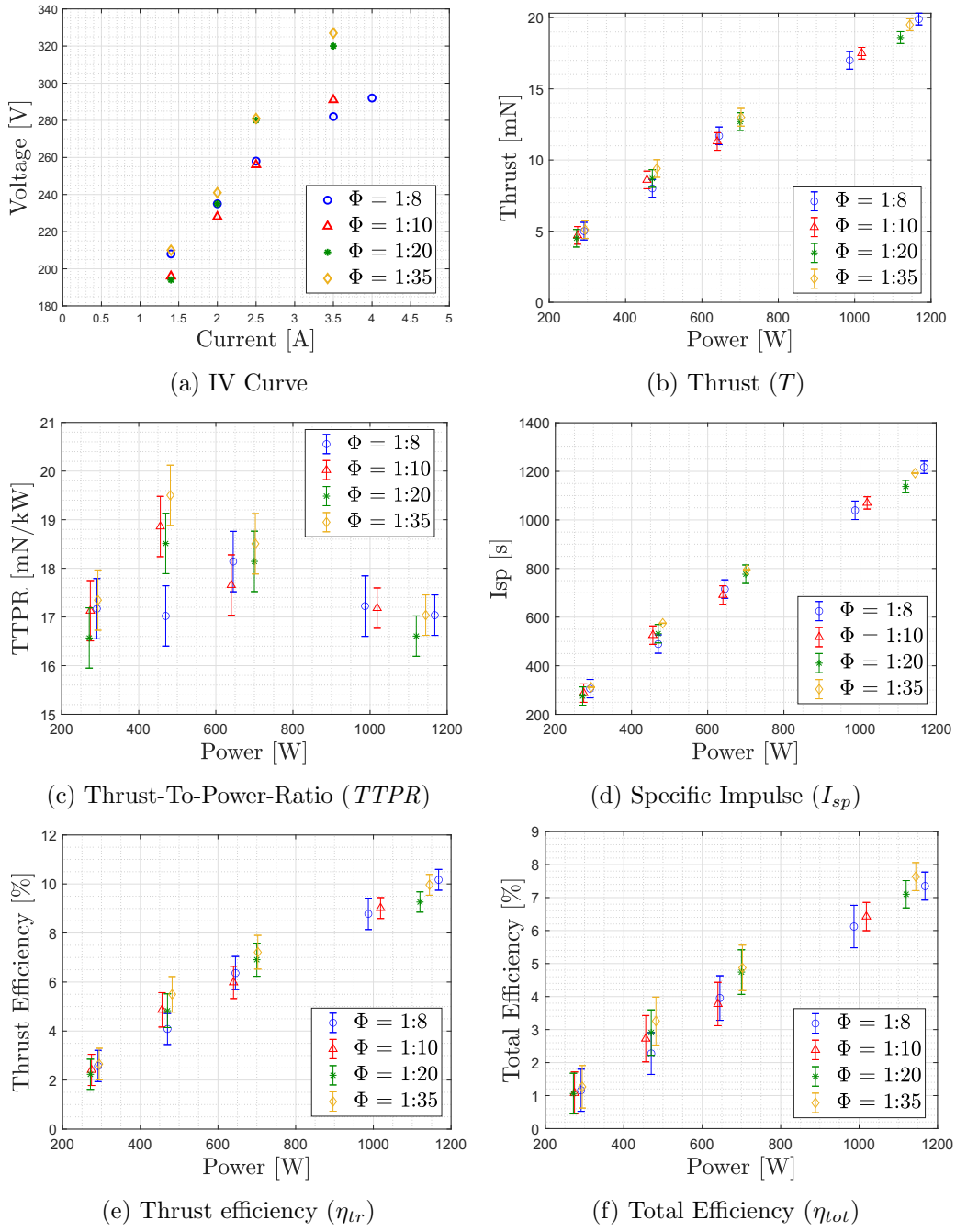


Figure 4.46: Plasma plume of the WET-HET under different conditions. Left: no magnetic field, hydrogen-oxygen (Φ) = 1:15. Middle: no magnetic field, hydrogen-oxygen (Φ) = 1:8. Right: magnetic field peak value of B = 600 G (see Figure 4.3), hydrogen-oxygen (Φ) = 1:8. Notice that the there is no colour change in the plume independently of Φ when the magnetic field is on. Picture published in [5].

AQUAHET

Figure 4.47 shows the performance of the *AQUAHET* thruster utilising the optimal mass flow rate ($\dot{m}_a$ = 1.7 mg/s) and a magnetic flux density of $B \approx 0.038$ T (I_m = 2.5 A). The discharge characteristics were explored across hydrogen-oxygen ratios from Φ = 1:8 to 1:35 (i.e., a hydrogen mass flow range of $\dot{m}_c = 0.20 - 0.05$ mg/s for a fixed oxygen mass flow of $\dot{m}_a = 1.7$ mg/s).

The IV curve exhibits similar trends at lower power levels with different Φ, although differing voltages for the same current are observed for some measurements. The previous investigation utilising the *WET-HET* thruster indicated that the IV characteristics of the thruster and stability were influenced by the local background pressure during measurements. Overall, the pressure conditions recorded during these tests surpassed those reported with the *WET-HET* thruster owing to the fact that the optimal mass flow rate for the *AQUAHET* exceeds that of the *WET-HET* ($\dot{m}_a$ = 1.7 mg/s versus $\dot{m}_a$ = 1.0 mg/s, see Section 4.2.2.5). This also explains why the discharge power achieved for *AQUAHET* in this specified case was lower than for *WET-HET*.



(a) IV Curve

(b) Thrust (T)

(c) Thrust-To-Power-Ratio ($TTPR$)

(d) Specific Impulse (I_{sp})

(e) Thrust efficiency (η_{tr})

(f) Total Efficiency (η_{tot})

Figure 4.47: Experimental measurements of the *AQUAHET* fuelled by the products of water electrolysis (oxygen for the anode and hydrogen for the cathode) for various hydrogen-to-oxygen ratios (Φ = 1:8 to 1:35, i.e., a hydrogen mass flow range of $\dot{m}_c = 0.20 - 0.05$ mg/s for a constant anode (oxygen) mass flow of $\dot{m}_a = 1.7$ mg/s). These values correspond to a magnet current of $I_m = 2.5$ A (Figure 4.5) and $w = 4$ mm.

Despite the differences obtained in the IV curve for some measurements, the performance measured across Φ = 1:8 to 1:35 remains very similar. These findings correlate with those obtained with the *WET-HET*, where thrust measurements in the range of Φ = 1:6 to 1:25 also exhibited non discernable differences in performance. The optimal thrust measurement under these conditions

was attained at the highest tested discharge power $P_d = 1168 \pm 1$ W, yielding a thrust of $T = 20.0 \pm 0.4$ mN, anode specific impulse of $I_{sp} = 1216 \pm 25$ s, $TTPR = 17.0 \pm 0.4$ mN/kW, $\eta_{tr} = 10.2 \pm 0.4$ %, and total efficiency of $\eta_{tot} = 7.4 \pm 0.5$ %.

4.4.2.2 Water Electrolysis (Oxygen/Hydrogen) vs Oxygen/Krypton

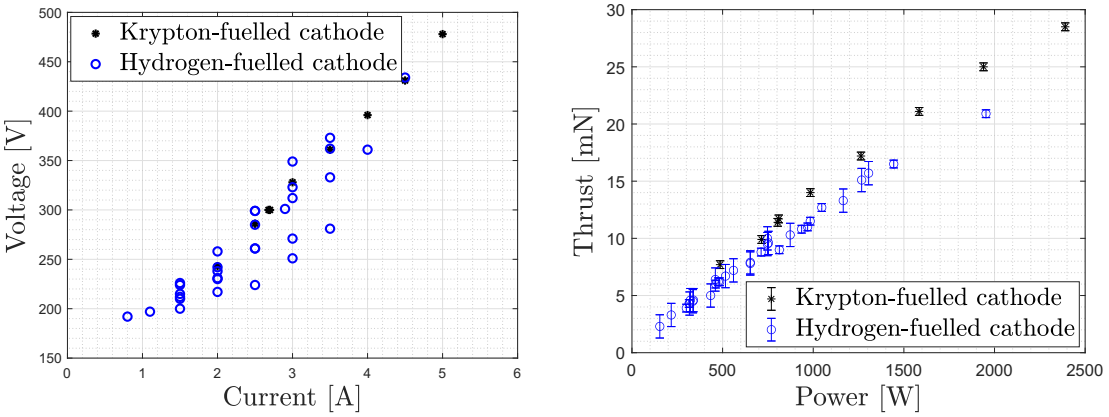
In this section, a comparative analysis of the performance achieved by a HET operating with water electrolysis products (oxygen for the anode and hydrogen for the cathode sourced from pressurised bottles) versus oxygen (anode) and krypton (cathode) is presented. When presenting these results, it is assumed, as deduced in Section 4.4.2.1, that Φ does not exert a significant influence on performance. Hence, the outcomes of the system operating at different Φ are juxtaposed with those using oxygen/krypton. To ensure a fair comparison, the geometric and material configurations (Table 4.15), magnetic field topology and strength (Figure 4.3 with $I_m = 1.5$ A energising the electromagnetic coils for the *WET-HET* thruster and Figure 4.5 setting $I_m = 2.5$ A for the *AQUAHET* thruster), and oxygen operating point ($\dot{m}_a = 1.0$ mg/s for the *WET-HET* thruster and $\dot{m}_a = 1.7$ mg/s for the *AQUAHET* thruster) have been upheld to ensure a comparison under identical conditions, with the only variation being the propellant the cathode operates on.

WET-HET

Figure 4.48 displays the results obtained from the operation of the *WET-HET* thruster.

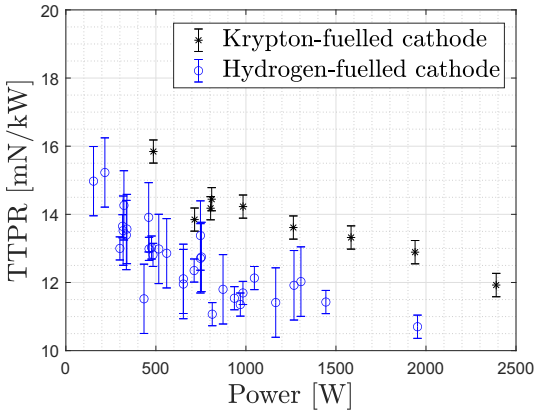
The comparison drawn from this analysis indicates that the IV curves of the thruster when utilising either hydrogen or krypton align approximately at the same values, although disparities emerge in the IV curve when employing different hydrogen mass flow rates. As expounded in Section 4.4.2.1, the chamber's background pressure does influence the attained voltage, although it does not affect the performance results at equal discharge power.

From a performance standpoint, as depicted in Figure 4.48, it becomes evident that the anode's performance when operating with the products of water electrolysis marginally lags behind that achieved when employing oxygen-krypton, particularly at high power levels ($\Delta\eta_{pr} \approx 10$ %).

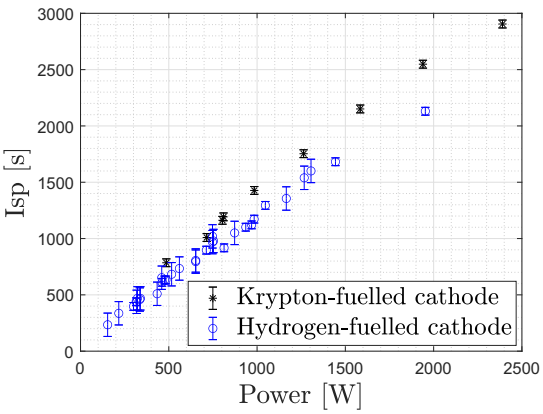


(a) IV Curve

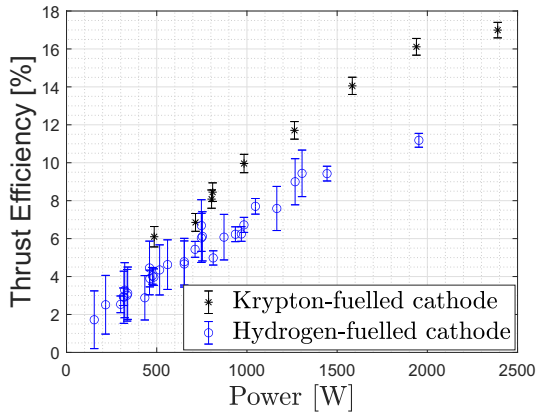
(b) Thrust (T)



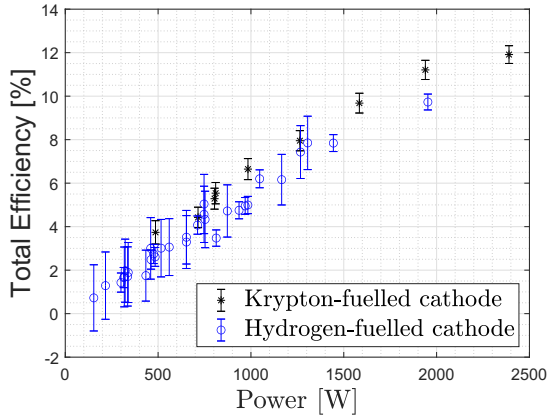
(c) Thrust-To-Power-Ratio ($TTPR$)



(d) Anode Specific Impulse (I_{sp})



(e) Anode Thrust Efficiency (η_{tr})



(f) Total Efficiency (η_{tot})

Figure 4.48: Experimental measurements of the thruster *WET-HET* fuelled by the products of water electrolysis (oxygen for the anode and hydrogen for the cathode, both from pressurised bottles) at all hydrogen-to-oxygen ratios (Φ), juxtaposed with the thruster running with oxygen and the cathode with krypton (at $\dot{m}_c = 6$ sccm, $\dot{m}_c = 0.37$ mg/s), both represented across an anode discharge power of $P_d = 0 - 2500$ W. These values correspond to an anode (oxygen) mass flow of $\dot{m}_a = 1.0$ mg/s, the magnetic field topology of Figure 4.3 using $I_m = 1.5$ A to energise the electrocoils and the geometrical and material configuration of Table 4.15. Plots published in [5].

This disparity can be attributed to two factors:

1. The cathode, functioning on a lighter mass propellant (H_2), inherently exhibits lower efficiency

in neutralising the beam and establishing a low coupling voltage compared to a noble gas such as xenon or krypton. This discrepancy arises because hydrogen possesses a larger ionisation potential (including dissociation losses), leading to a larger voltage drop at the cathode sheath. Consequently, the ions generated by the thruster experience a reduced acceleration potential, potentially resulting in slightly diminished thrust and specific impulse.

2. When utilising noble gases such as xenon-krypton, a portion of the gas can undergo ionisation and acceleration within the thruster's plume, contributing to thrust generation. Conversely, when hydrogen is employed, this phenomenon holds less significance due to the significantly smaller size of hydrogen molecules relative to krypton, (with hydrogen molecules being approximately 42 times smaller). Consequently, the contribution of hydrogen to thrust generation is deemed negligible compared to the use of krypton as a cathode propellant.

To comprehensively investigate phenomenon 2, a standalone test is conducted. The same operating conditions and geometrical configuration are maintained, with the sole deviation being the absence of oxygen mass flow and the exclusive use of the cathode propellant. It is worth noting that, in these tests, despite the absence of anode mass flow, the anode discharge voltage remains active throughout the experiments, alongside the magnetic field. Subsequently, various krypton mass flows flowing from the cathode are set. Figure 4.49 presents the thrust measurements obtained from this experiment.

From the presented data, it becomes apparent that a marginal level of thrust is generated by the cathode propellant, propelled by the applied discharge voltage between the anode and cathode. It is noteworthy that this thrust primarily stems from the ionisation of the krypton ions and their subsequent acceleration by the voltage difference between the anode and cathode, rather than from the cold gas flow: the cathode orifice plate's location, where the propellant exits, is perpendicular to the thrust direction, resulting in negligible contribution from the flow, as experimentally verified.

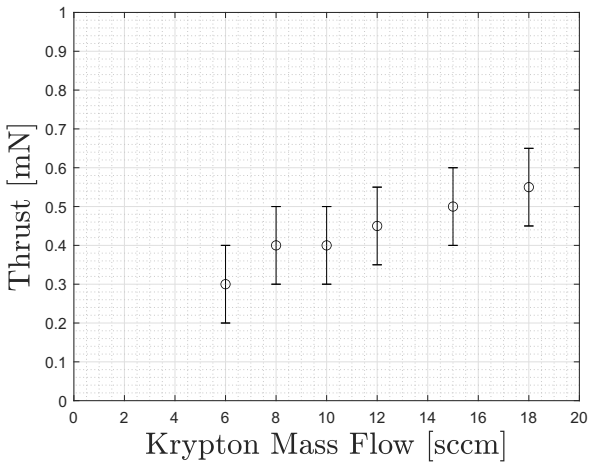
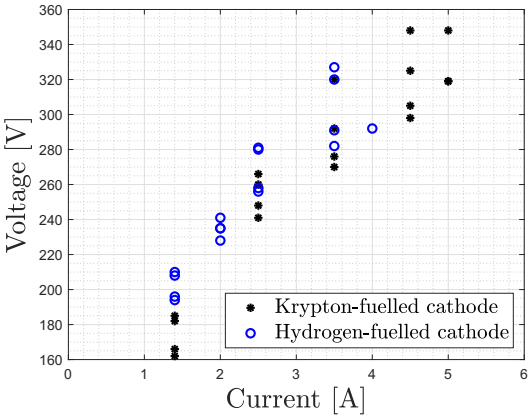


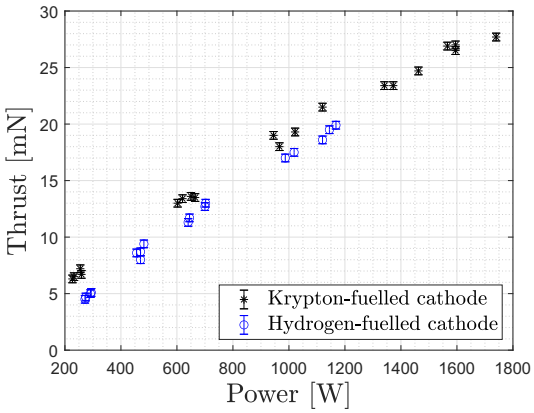
Figure 4.49: Thrust obtained from the acceleration of krypton ions coming from the cathode, in a standalone test on the thruster *WET-HET* where no anode mass flow is set. Plot published in [5].

The magnitude of the thrust appears to increase proportionally with higher krypton mass flow rates. In contrast, no such thrust is observed when hydrogen is employed as the cathode propellant. In reality, during nominal thruster operation, the cathode propellant undergoes ionisation and subsequently recombines with the oxygen plasma to establish a stable plasma beam, thereby generating thrust. These intricate particle interactions occurring during the thruster's nominal operation are not captured in the standalone test. Consequently, the thrust measured in this isolated test does not precisely reflect the exact performance difference observed between the use of krypton and hydrogen, as this assessment should also consider the contributions of phenomenon (1) to fully elucidate the disparity. Nevertheless, this test substantiates the assertion that the cathode propellant contributes to thrust, particularly when utilising krypton.

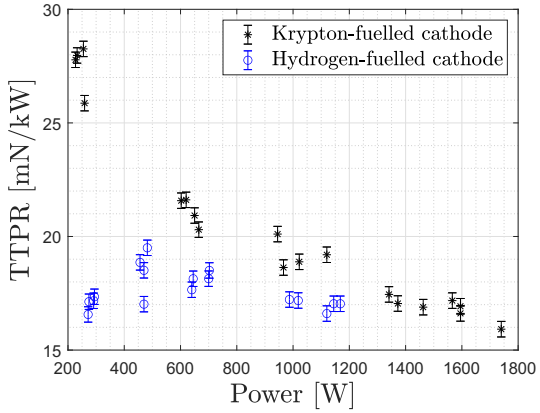
Collectively, these factors make the anode operation with the products of water electrolysis less efficient compared to operation with oxygen-krypton, although the reduction in performance is not substantial. However, it is worth noting that this reduction in performance is mitigated when calculating the total efficiency. Typically, the hydrogen mass flow rate utilised (ranging from $\dot{m}_c = 0.04 - 0.018$ mg/s) is lower than that employed with krypton under nominal conditions ($\dot{m}_c = 0.37$ mg/s). Hence, when comparing total efficiency, the results with krypton or hydrogen employed in the cathode converge closely.



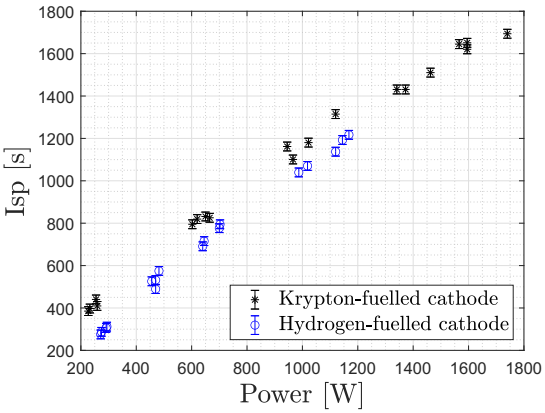
(a) IV Curve



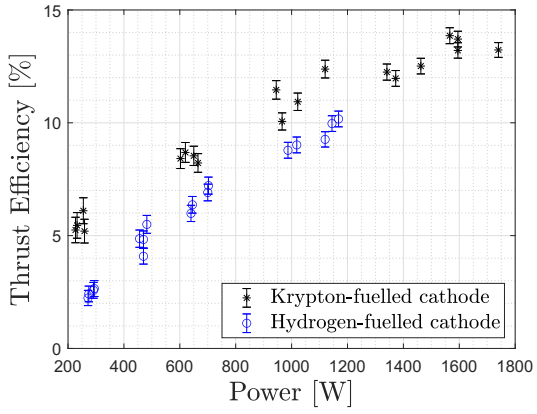
(b) Thrust (T)



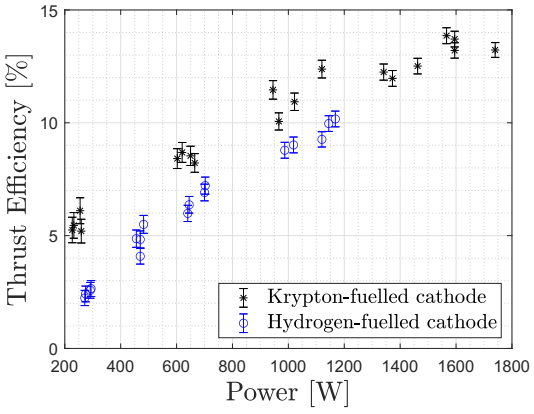
(c) Thrust-To-Power-Ratio ($TTPR$)



(d) Specific Impulse (I_{sp})



(e) Thrust efficiency (η_{tr})



(f) Thrust efficiency (η_{tr}) vs I_{sp}

Figure 4.50: Experimental measurements of the *AQUAHET* and *Hydrocat* fuelled by the products of water electrolysis (oxygen for the anode and hydrogen for the cathode, both from pressurised gas bottles) at various hydrogen-to-oxygen ratios (Φ = 1:8 to 1:35, i.e. for a cathode (hydrogen) mass flow range of $\dot{m}_c = 0.05-0.20$ mg/s and for a constant anode (oxygen) mass flow of $\dot{m}_a = 1.7$ mg/s). Also plotted are performance measurements with the thruster running on oxygen ($\dot{m}_a = 1.7$ mg/s) for the anode and krypton ($\dot{m}_c = 0.2 - 0.9$ mg/s) for the cathode. The magnet current used was 2.5 A (see Figure 4.5), with $w = 4$ mm.

In a similar fashion as presented with the thruster *WET-HET*, Figure 4.50 compares the metrics of the thruster using oxygen for the anode and krypton or hydrogen for the cathode when using the thruster *AQUAHET*. The cathode mass flow rate during these tests varied from $m_c = 0.25 - 0.90$ mg/s in the case of krypton, and $m_c = 0.05 - 0.20$ mg/s when hydrogen was used.

The same conclusions as obtained previously can be derived by looking at this data: while the results obtained with oxygen and hydrogen indicated a slight decline in performance, this change did not reach statistical significance ($\Delta\eta_{pr} \approx 10$ %). It can be expected that similar performance metrics for high-power ($P_d = 3.2$ kW) applications could be achieved when employing oxygen and hydrogen as anode and cathode propellants, respectively.

4.4.2.3 Oxidation of the Hardware Using Oxygen and Hydrogen

The presence of oxygen plasma and its potential interactions on the hardware has been a central concern since the conceptualisation of this technology. Unlike the use of noble gases such as xenon or krypton, oxygen plasmas have a tendency to react with certain surfaces, including iron (Fe), aluminium (Al), copper (Cu), magnesium (Mg), and alloys containing these metals, such as stainless steel [228]. Upon interaction, they form an oxidation layer, which can be of paramount importance if the layer displays non-conductive properties (see Section 4.2.2.3).

Section 4.2.2.3 evaluated the implications on the hardware when using oxygen to the anode (thruster) and krypton to the cathode. There, it was observed that the stainless steel anode suffered from oxidation when in contact with the oxygen plasma, although this situation was manageable for laboratory purposes without implicating any major drawback than limiting the testing time. In this campaign, where oxygen and hydrogen were employed, the observed oxidation on the hardware appeared to be more severe compared to when oxygen and krypton were used. According to several studies involving oxygen and hydrogen plasmas [229, 230], hydrogen demonstrates the capability to pre-oxidise metallic components, including but not limited to chromium (Cr), nickel (Ni), and iron (Fe). Consequently, this phenomenon holds the potential to facilitate the inward diffusion of oxygen and, thereby, enhance the oxidation rate at the interface.

Figures 4.51 and 4.52 present a visual representation of the cathode's and thurster's condition following hours of testing under this specific environmental context. A distinctive discoloration, characterised as "bluing" or "blueing", is observed. This terminology is employed to describe a surface modification phenomenon induced by the interaction of oxygen at elevated temperatures with specific metals. In this scenario, the term describes the interaction of the oxygen plasma with the stainless steel components of the cathode and front plate of the thruster [231]. Under these specific conditions, the metal undergoes a transformation in both its surface characteristics and coloration.

The particular oxide layer formed depends on factors such as the steel's chromium content (chromium resists oxidation), surface condition (rough surfaces oxidise more rapidly), presence of surface contaminants, and the temperature of the oxygen at the relevant location [232]. Progressing from lower to higher temperatures, a range of surface colourations can be observed: light yellow to yellow ($\approx$ 290-370$^{\circ}C$), brown to purple-brown ($\approx$ 390-420$^{\circ}C$), dark purple ($\approx$ 450$^{\circ}C$), and finally blue to dark blue ($\approx$ 540-600$^{\circ}C$). The cathode's temperature was monitored using an infrared (IR) camera (model *FLIR 29395-261 A6261sc*) positioned outside the vacuum chamber. The data was post-processed using the *FLIR ResearchIR Max 4* software, as illustrated in Figure 4.51. Although this camera is constrained to measure temperatures within the range of $490 - 700^{\circ}C$, a significant correlation emerges among the observed colors in the hardware following testing, the recorded temperatures, and the expected theoretical range wherein these distinct colors should manifest.

This bluing process is, in fact, a conventional technique long employed in the watch industry to convey the impression of high quality on a mass-produced scale [233]. Beyond aesthetic considerations, this method serves a practical purpose by safeguarding metals against rust formation due to the oxide layer formed [233]. In this practical scenario, although the oxidation of the cathode and thrusters' external components is evident, no discernible impact on the overall operation and performance of the device throughout these experimental campaigns was observed, aside from further reducing the time these devices could be tested in the laboratory (see Section 4.2.2.3).

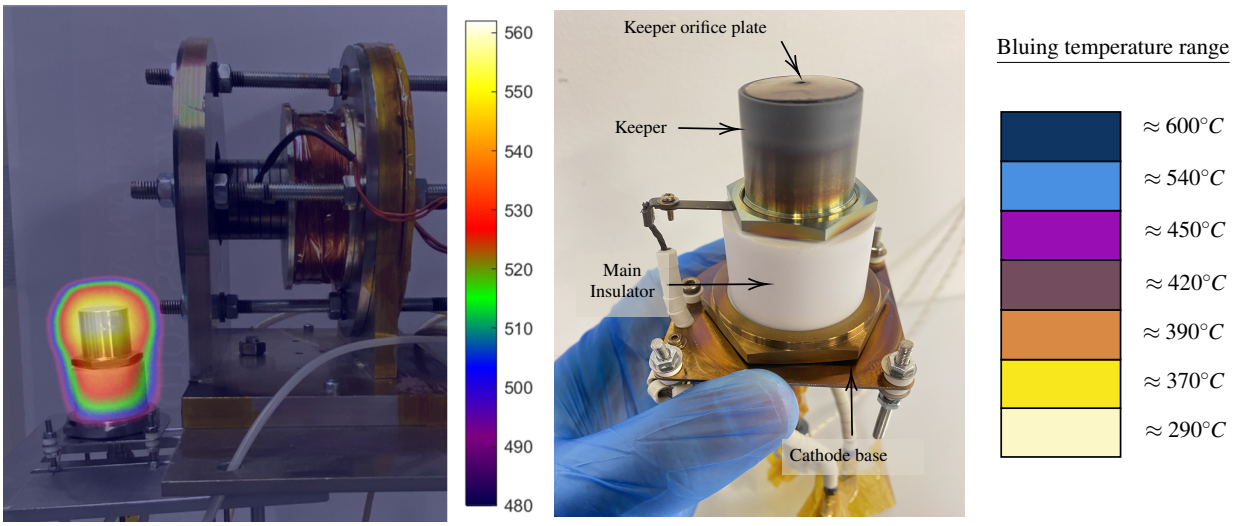


Figure 4.51: Temperatures and associated bluing oxidation process observed in the cathode *Hydrocat* while being in the presence of a hydrogen-oxygen plasma. Left: temperature measured by the infrared camera. Middle: bluing oxidation process after testing. Right: temperature range of the bluing oxidation process. Graphs published in [5].

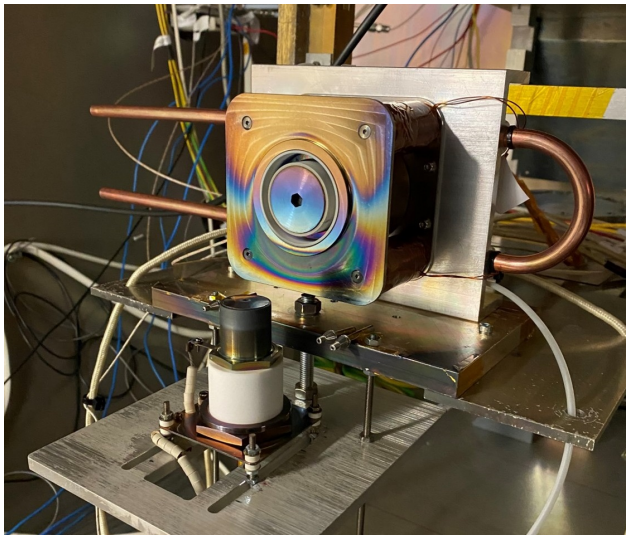


Figure 4.52: Bluing oxidation process observed in the thruster *AQUAHET* and cathode *Hydrocat* after the exposure to the oxygen and hydrogen plasma.

Nevertheless, this could potentially impact the structural integrity of the HET during prolonged firing over thousands of hours and further investigation in a lifetime test is required.

4.4.2.4 Performance Comparison

Table 4.16: Comparison of the Hall Effect Thrusters *WET-HET* and *AQUAHET* and the cathode *Hydrocat* using oxygen and krypton or oxygen and hydrogen (products of water electrolysis) in comparison with xenon-fuelled HETs: *Sitael HT5k* [234], *BHT-1500-C* [235] and *SPT-100* [147, 148]) for various discharge powers, used as reference (denoted as "Ref").

Thruster	Anode Propellant	Cathode Propellant	Power [W]	Mass Flow [mg/s]	Thrust [mN]	Specific Impulse [s]	Anode Efficiency [%]
Sitael HT5k	**Xenon**	**Xenon**	**3350**	**12.00**	**206.0 (Ref)**	**1740 (Ref)**	**53.0% (Ref)**
AQUAHET	Oxygen	Krypton	3200	2.00	51.0 (-75.2%)	3119 (+79.3%)	24.4% (-53.9%)
Sitael HT5k	**Xenon**	**Xenon**	**2310**	**8.00**	**135.0 (Ref)**	**1720 (Ref)**	**49.0% (Ref)**
WET-HET	Oxygen	Krypton	2232	0.60	21.5 (-84%)	3617 (+110.3%)	17.1% (-65.1%)
AQUAHET	Oxygen	Krypton	2443	2.00	44.0 (-67.4%)	2220 (+29.1%)	19.6% (-60.0%)
BHT-1500-C	**Xenon**	**Xenon**	**1900**	**6.88**	**114.7 (Ref)**	**1700 (Ref)**	**53.1% (Ref)**
WET-HET	Oxygen	Krypton	1940	1.00	25.0 (-78.2%)	2548 (+48%)	16.1% (-69.7%)
WET-HET	Oxygen	Hydrogen	1953	1.00	20.9 (-81.7%)	2130 (+25.3%)	11.2% (-78.9%)
SPT-100	**Xenon**	**Xenon**	**1430**	**5.23**	**92.0 (Ref)**	**1500 (Ref)**	**47.4% (Ref)**
WET-HET	Oxygen	Krypton	1440	1.00	17.3 (-81.2%)	1765 (+17.7%)	10.4% (-78.1%)
WET-HET	Oxygen	Hydrogen	1444	1.00	16.7 (-81.8%)	1702 (+13.5%)	9.7% (-79.5%)

Table 4.16 provides a comparative performance examination using as a baseline three different xenon-fuelled HETs: the *Sitael HT5k* manufactured by *Sitael* [234], the *SPT-100* developed by *ODB Fakel* (and evaluated by *NASA* [147, 148]), and the *BHT-1500-C* produced by *Busek* [235]. This comparison is juxtaposed with the HETs assessed in this thesis: the *WET-HET* and the *AQUAHET*, in conjunction with the *Hydrocat* cathode, utilising either oxygen/krypton or oxygen/hydrogen (products of water electrolysis). It is noteworthy that the data collected in Table 4.16 uses the 42 mm channel length version of the thruster *SPT-100* due to the abundance of available literature for this particular model [147, 148, 198, 236].

The comparison is delineated at four distinct discharge power levels: $P_d \approx 3300$ W, $P_d \approx 2300$ W, $P_d \approx 1900$ W and $P_d \approx 1400$ W), using the results gathered in Section 4.2 and Section 4.4.

From the comparison, xenon-fuelled HETs demonstrate superior thrust and anode efficiency, while oxygen-fuelled HETs show enhanced anode specific impulse. This was expected, as discussed in Section 1.2.1.3. Nevertheless, it is important to highlight that oxygen-fuelled HETs tend to perform better as discharge power increases, a trend demonstrated throughout this thesis. Table

4.16 further supports this observation by illustrating the relative performance difference between xenon and oxygen-fuelled HETs at various power levels.

In summary, while oxygen-fuelled and water electrolysis-fuelled HETs may not match the anode efficiency of xenon-fuelled counterparts, their additional benefits, such as increased specific impulse, potential for ISRU, cost efficiency, and environmental sustainability (refer to Table 1.1 and Section 2.2.2.1), could make them very interesting candidates for medium-term space missions. Furthermore, in line with the trends discussed herein, the prospects for water electrolysis-fuelled HETs at higher powers are very promising, indicating improved performance with increasing discharge power.

4.5 Campaigns D - Water Electrolysis-Fuelled Hall Effect Thrusters: End-to-End Testing with a Water Electrolyser

The final stage in water electrolysis propulsion for HETs involves the development of an end-to-end test test wherein the byproducts of water electrolysis (oxygen and hydrogen), instead of being supplied by pressurised bottles as described in Section 4.4, are directly generated by a water electrolyser. These tests present additional challenges, such as managing potential humidity in the oxygen and hydrogen lines and ensuring a continuous mass flow production from the water electrolyser, which introduces another potential point of failure. These test campaigns were conducted in collaboration with the European Space Agency at their ESTEC facilities located in Noordwijk, Netherlands. This work was presented at the 38^{th} International Electric Propulsion Conference in Toulouse, France [8].

4.5.1 Methodology

4.5.1.1 Experimental Set-Up and Vacuum Chamber Facilities

The experiments were conducted within the Small Plasma Facility (SPF) situated at the ESA Propulsion Laboratory (EPL), owned by the European Space Agency. Unlike previous experiments at this facility involving noble gases, this test necessitated modifications to the vacuum chamber setup to safely handle and provide, for the first time, oxygen and hydrogen at stoichiometric ratios. The configuration of the facilities and various components is depicted in Figure 4.53. The different elements depicted in this diagram are outlined in Table 4.17. This final setup integrates all the insights gleaned from previous experiments conducted at the Imperial Plasma Propulsion Laboratory, as detailed in Sections 4.2 and 4.4.

The SPF consists of two distinct vacuum chambers arranged linearly: a “main” vacuum chamber (dimensions: 2.0 x 3.4 m; diameter x length) and a “hatch” chamber (dimensions: 1.0 x 1.0 m; diameter x length), where the thrust balance, thruster, and cathode are situated.

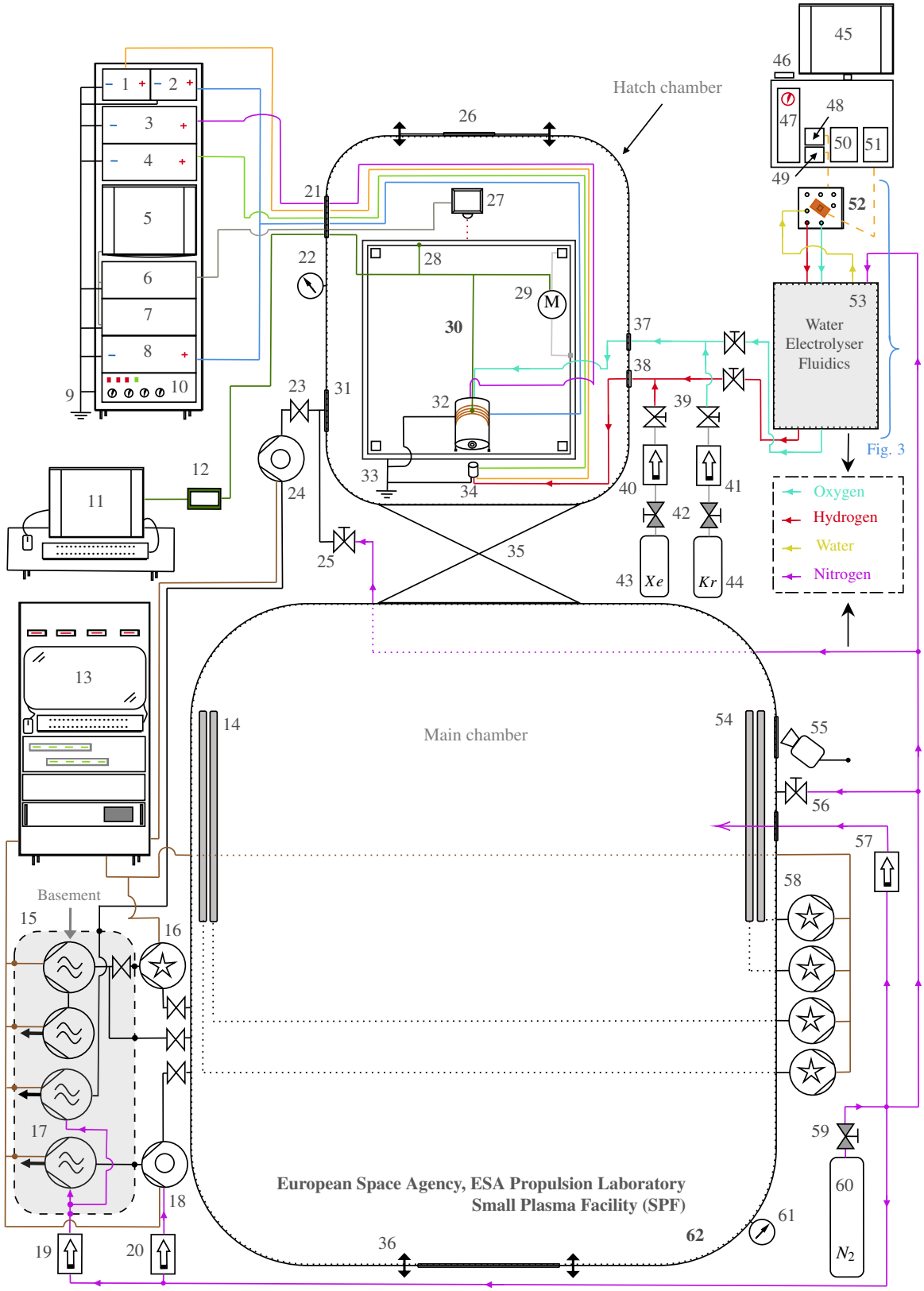


Figure 4.53: Main schematics of the water electrolysis electric space propulsion testing at the ESA Propulsion Laboratory of the European Space Agency. The Small Plasma Facility vacuum chamber was used for the experimentation. Diagram presented in [8].

Table 4.17: Description of the elements depicted in Figure 4.53. Table presented in [8].

1	Heater power supply (*Agilent 6038A*)	**32**	Water Electrolysis Hall Effect Thruster (anode)
2	Inner electromagnet power supply (*Agilent 6038A*)	**33**	Grounding connection
3	Anode power supply (*FUG MCP 4200-650*)	**34**	Cathode (Hydrocat)
4	Keeper power supply (*Glassman LPD 600-10*)	**35**	Main gate valve (hatch to main chamber)
5	Thrust balance monitor	**36**	Door (main chamber)
6	Thrust balance electronics box	**37**	Vacuum feedline (oxygen)
7	Thrust balance computer	**38**	Vacuum feedline (hydrogen)
8	Outer electromagnet power supply (*Delta SM120-25D*)	**39**	Manual valves set
9	Power supplies ground connection	**40**	Mass flow controller (xenon)
10	Auxiliary power outlet	**41**	Mass flow controller (krypton)
11	External computer station and monitor	**42**	Pressure regulators (xenon and krypton)
12	Thermocouples electronics	**43**	Cathode propellant bottle (xenon)
13	Pumping system control station	**44**	Anode propellant bottle (krypton)
14	Cryo panel (x2, not used)	**45**	Monitor (electrolyser control station)
15	Basement	**46**	Analog to digital converter (ADC, SCB-68A)
16	Cryo pump, with compressor (*COOLVAC 10 000* CL)	**47**	Switchbox
17	Roughing pump (*Varian TriScroll 300 Dry Scroll Pump*)	**48**	Electrolysis membrane power supply
18	Turbopump (*Varian Turbo-V 3K-G ISO 250 F*)	**49**	Water feed barrier power supply
19	Mass flow controller, roughing pump purging (nitrogen)	**50**	PXI controller
20	Mass flow controller, turbopump purging (nitrogen)	**51**	Pressure transducers power supply
21	Vacuum feedthrough (power)	**52**	Water electrolyser
22	Pressure gauge (hatch chamber)	**53**	Water Electrolyser fluidics (refer to Figure 4.55)
23	Gate valve	**54**	Cryo panel (x2, not used)
24	Turbopump (*Leybold, TURBOVAC 1000 C*)	**55**	Camera
25	Venting valve (hatch chamber)	**56**	Venting valve (main chamber)
26	Door (hatch)	**57**	Mass flow controller, chamber purging (nitrogen)
27	Laser ILD1750	**58**	Cryo heads (x4, Leybold COOLPOWER 140T)
28	Thermocouple (to thrust balance)	**59**	Pressure regulator (nitrogen)
29	Servomotor (for calibration)	**60**	Purging and venting propellant bottle (nitrogen)
30	Thrust balance	**61**	Pressure gauge (main chamber)
31	Vacuum feedthrough	**62**	Small Plasma Facility (European Space Agency)

The thrust balance (element 30) is strategically positioned within the hatch chamber, placing the system's thruster and cathode at the periphery of the main gate valve (element 35) between the hatch and main chamber. This arrangement allows the plasma to expand freely into the main chamber, minimising reflection of plasma and neutrals due to the larger vacuum area.

The first pumping stage consisted of two roughing pumps (model *Varian TriScroll 300 Dry Scroll Pump*, element 17): one dedicated to the main chamber and an additional pump allocated to the hatch chamber. It is noted that two extra roughing pumps, positioned at the exit of the

cryo pump, were available. However, as will be elaborated later, due to the non-operation of the cryo pump, its associated primary pumps remained inactive. The two primary pumps utilised were equipped with a nitrogen purging system, recommended for diluting the oxygen and hydrogen flow to mitigate any risk of ignition. This system necessitated a continuous nitrogen flow of 10 l/min.

However, these pumps were situated within the unvented basement of the facility, as illustrated in Figure 4.53 (element 15). Venting the gases from the facility into the unvented basement raised safety concerns due to the potential reduction of oxygen levels below the safety threshold (19% or below). Following this concern, it was calculated that, due to the large volumetric area of the basement, even after 20 hours of testing with the purging system active and the two pumps in operation, the oxygen level in the basement would remain higher (20.2%) than the minimum required level (19%) mandated by the health and safety department of the European Space Agency. Consequently, the purging system was activated, which permitted the use of these pumps.

The second evacuation stage comprised two turbopumps: a *Leybold, TURBOVAC 1000 C* for the hatch chamber (element 24) and a *VARIAN Turbo-V 3K-G ISO 250 F* for the main chamber (element 24). However, only the turbopump connected to the main chamber had a nitrogen purging capability (with a recommended flow of 20 sccm of nitrogen). Therefore, the turbopump for the hatch chamber was solely employed for the initial evacuation of the facility and remained disconnected thereafter, while the turbopump for the main chamber and its purging system were utilised throughout all experimentation.

The third stage included a cryo pump (element 16) and four cryo panels (elements 14 and 54). However, for this initial test, the third stage could not be utilised as the equipment had never been tested under these conditions, nor had the facilities previously operated with both oxygen and hydrogen simultaneously. Concerns arose regarding potential oxygen and hydrogen accumulation at the cryo pump, posing considerable risks during its venting process if both gases were released simultaneously. Furthermore, there were concerns that the cryo panels might be compromised upon contact with oxygen. Therefore, they were covered and not used throughout the test.

Lastly, to further mitigate any potential risk of ignition, nitrogen was introduced into the

chamber during testing. The aim was to maintain the same ratios of oxygen and nitrogen as found in atmospheric air ($N_2 \approx 78\%$, $O_2 \approx 21\%$). For instance, if 1.6 mg/s of oxygen was introduced, 5.9 mg/s of nitrogen was concurrently fed into the chamber.

Notice that, in contrast to the previous experimental setup [5], there are no pressurised cylinders: the gases are produced by the water electrolyser. Therefore, the safety concerns regarding the presence of oxygen and hydrogen in proximity are not applicable and both gases can coexist outside and inside the vacuum chambers.

4.5.1.2 Electronics, Fluidics and Working Procedures

This experimentation, marking the European Space Agency's first-ever test involving the mixing of oxygen and hydrogen for EP, necessitated a careful safety assessment to ensure maximum safety.

For this reason, within the setup, krypton and xenon bottles (elements 43 and 44) with their respective mass flow meters (elements 40 and 41) were also positioned to initially supply the thruster (anode) and cathode. This approach allows for the gradual reduction of noble gases in the system once ignition is successful, while simultaneously increasing the flow of oxygen and hydrogen until only oxygen and hydrogen propel the system. This gradual transition enhances safety by enabling continuous monitoring of the setup's safety with incremental increases of oxygen and hydrogen, thus avoiding any potential initial sparking of the thruster and cathode, thereby preserving the system's integrity for a longer duration. It is noteworthy that while this transition was implemented in this laboratory test, it is not necessary for an in-orbit space demonstration.

Regarding electronics, the anode power supply *FUG MCP 4200-650*, limited to 650 V and 6 A, powered the anode (element 3). For the cathode, the power supply *Glassman LPD 600-10* (limited to 600 V and 10 A) was used for the keeper (element 4), and *Agilent 6038A* (limited to 60 V and 10 A) for the heater (element 1). The electromagnets of the thruster *WET-HET* were powered by another *Agilent 6038A* power supply (element 2). In the case of the *AQUAHET*, this power supply was employed to energise the inner electromagnet, whereas the power supply *Delta SM120-25D* (limited to 120 V and 25 A) was used for the outer magnets (element 8).

The thrust balance, along with its respective electronics, are a replica of the ones existing at Imperial College London. For further insights, Sections 4.2 and 4.4 expound on the strategies employed, which were consistent with these tests.

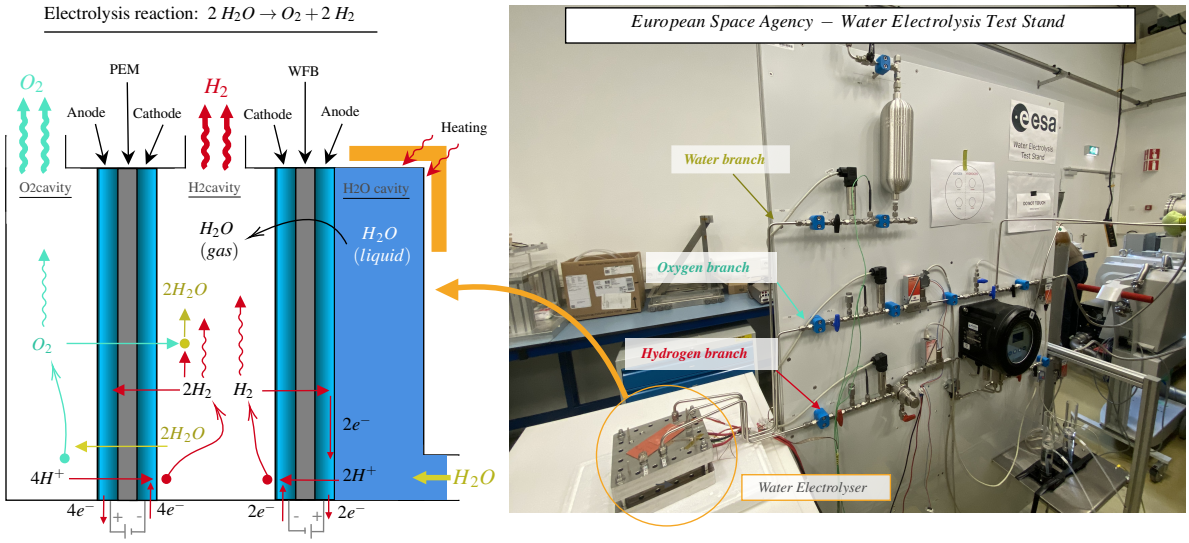
4.5.1.3 Thrusters' Geometrical and Material Configuration

The geometrical and material configuration of the two thrusters tested (*WET-HET* and *AQUAHET*) is the same as the one described in the previous Section 4.4.1.1 (summarised in Table 4.15)

4.5.1.4 Water Electrolyser Hardware

The water electrolyser [237] and its associated fluidic setup [238] were developed by the European Space Agency. For a detailed explanation of these systems, readers are referred to the literature and previous work [237, 238, 239]. A summary is provided here.

The water electrolyser design is based on the "Cathode Vapour Feed" (CVF) topology depicted in Figure 4.54. In this model, the water electrolyser consists of two membranes: the Water-Feed Barrier (WFB) and the Proton-Exchange-Membrane (PEM), each connected to an independent power supply, both connected to the same ground. This setup effectively divides the apparatus into three distinct cavities: the H_2O cavity (primarily containing liquid H_2O), the H_2 cavity (mainly comprising gaseous H_2), and the O_2 cavity (mostly composed of gaseous O_2). Upon system initiation, liquid H_2O, heated to a certain temperature (e.g., 70 °C), permeates the WFB, transitioning into gaseous H_2O. Subsequently, gaseous H_2O diffuses through the PEM, undergoing decomposition in accordance with the fundamental water electrolysis reaction: $2H_2O \rightarrow O_2 + 2H_2$. Notice that this reaction is the result of the Oxygen Evolution Reaction (OER), and its complementary half, the Hydrogen Evolution Reaction (HER), which occur simultaneously to complete the electrical circuit. The polymeric membrane acts as an electrolyser, facilitating the migration of protons through the electric field. Notably, these reactions are enabled by a catalyst applied to the membrane, comprising iridium oxide on the oxygen side and platinum on the hydrogen side.



a) Water electrolyser working principle

b) Water electrolyser fluidics

Figure 4.54: Main schematic of the Cathode Vapour Feed (CVF) water electrolyser designed by the European Space Agency. Diagram presented in [8].

The different reactions ocurring within CVF electrolysers are also shown in Figure 4.54. For instance, within the H_2 cavity, H_2 may diffuse through the WFB, transforming into $2H^+$, which then diffuses back to the H_2 cavity. Additionally, H_2 can permeate through the PEM towards the O_2 cavity, where $4H^+$ can traverse back through the PEM, neutralised by the electrons in the circuit, and reform into $2H_2$ in the H_2 cavity. Moreover, O_2 has the capability to diffuse through the PEM, subsequently recombining with the $2H_2$ in the H_2 cavity to generate $2H_2O$. This resultant compound can once again permeate through the PEM, restarting the primary electrolysis reaction. Ultimately, the permeability of water across both membranes dictates that both the hydrogen and oxygen produced contain varying amounts of water vapour. Understanding the impact of water vapour on thruster and cathode operation is crucial for the proposed application. The inclusion of these effects separates this study from the previous experiments (Section 4.4), which all used high purity dry gases supplied from cylinders.

CVF electrolysers outperform other concepts such as the Liquid-Anode-Feed (LAF) electrolyser thanks to its improved behaviour in microgravity conditions. This is because LAF electrolysers rely on the density contrast between fluids for their separation from liquid water.

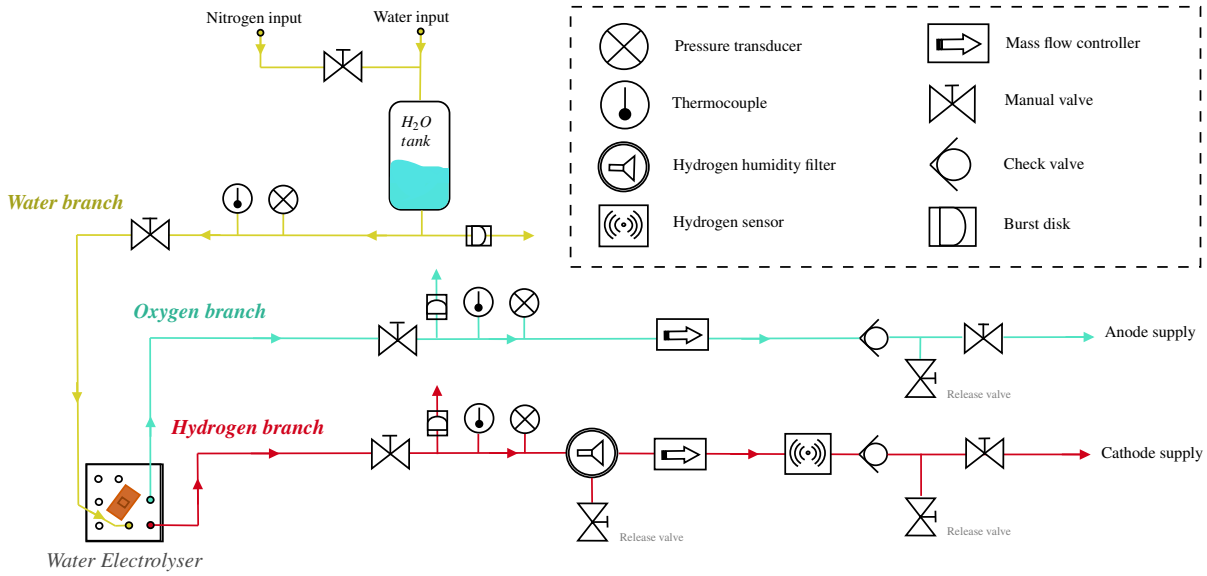


Figure 4.55: Water electrolyser fluidics schematic set-up for testing at the ESA Propulsion Laboratory of the European Space Agency. Diagram presented in [8].

Moreover, although LAF electrolysers produce greater current density than CVF electrolyser because it is fed with liquid water instead of vapour, in the absence of gravity to facilitate this separation, LAF electrolysers encounter operational challenges [237].

The water electrolyser is integrated with the fluidics as depicted in Figure 4.54. A more detailed schematic of the components comprising the water electrolyser fluidics is shown in Figure 4.55.

The propellant feed system comprises three branches: 1) the water branch, providing liquid water to the electrolyser, and the 2) oxygen and 3) hydrogen branches, outputs from the water electrolyser. A description of the system is provided hereafter.

To start with, liquid water is introduced into the system. A nitrogen feed is also available to pressurise the water within the tank, replicating conditions typical of a space mission. The temperature and pressure of the tank's output feed are monitored using pressure transducers and thermocouples. A burst disk is incorporated to release fluid in case the pressure exceeds the allowable maximum within the line (between 40-50 bars at 20 °C). A manual valve controls the flow of liquid water into the water electrolyser, where it is converted into gaseous oxygen and hydrogen, as described earlier.

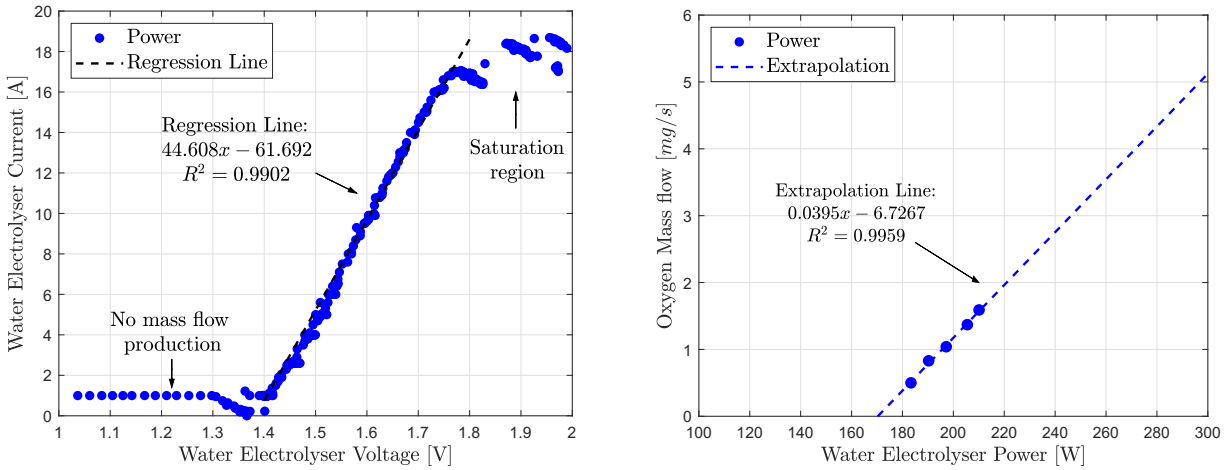
Manual valves are positioned at the beginning of both the oxygen and hydrogen lines. Temperature

and pressure sensors, along with a burst disk, are subsequently installed for each line. The hydrogen line is further equipped with a hydrogen humidity filter designed to partially capture moisture present within the line. Any water content within the hydrogen can be released via a manual valve. To regulate the mass flow of oxygen and hydrogen, a mass flow controller is employed. Following this, a hydrogen sensor is integrated to assess the purity of hydrogen within the pipeline. A check valve is also installed to ensure unidirectional fluid flow for both lines. Additionally, two manual valves are configured to purge oxygen and hydrogen if necessary (refer to Figure 4.55). Finally, two manual valves control the flow into the thruster (anode) and the cathode.

4.5.2 Results and Discussion

4.5.2.1 Water Electrolyser Validation

The operational characteristics of the water electrolyser are significantly influenced by its temperature. Previous research on this device has revealed the correlation between the water electrolyser's mass flow production rate, as characterised by the IV curve, and temperature [237]. Maximum oxygen continuous mass flow production ($\dot{m}_a \approx 1.3$ mg/s), without compromising membrane integrity, is achieved at 70 °C. Notice that up to $\dot{m}_a = 1.6$ mg/s of oxygen flow can be produced, although for a shorter time duration. To attain this temperature, two heaters positioned at the top and bottom of the water electrolyser are employed, consuming a combined maximum power of 175 W. This substantial heating capacity is incorporated to expedite the heating process of the electrolyser. It is noteworthy that the current design, featuring two large clamping plates with significant heat capacity, has not been fine-tuned to minimise power requirements [237]. Modifying materials or redesigning the electrolyser could significantly reduce the necessary heating power. Additionally, it is important to note that this heating capacity of 175 W is utilised to elevate the temperature of the electrolyser to its nominal level. Upon reaching this temperature, the heating power required to maintain it decreases. However, to ensure a conservative estimate, this heating power is utilised for calculating the overall power demands of the system.



(a) IV curve

(b) Power versus mass flow

Figure 4.56: Water Electrolyser characterisation. a) Current-voltage (IV) curve. b) Power versus oxygen mass flow. Results presented in [8].

As will be observed in Section 4.5.2.3, even with a suboptimal design and being conservative, it is expected that the water electrolyser's total power consumption would represent a fraction (8%) of the system's overall power, primarily dictated by the thruster's discharge power (83%).

Figure 4.56a illustrates the IV curve corresponding to the water electrolyser at 70 °C. Three distinct regions are discernible. Below 1.4 V, the water electrolyser exhibits negligible to no mass flow production, with currents measuring below 1 A. Within the range of 1.4-1.8 V, a linear relationship is observed, resulting in varying mass flow rates contingent upon the IV curve's positioning before reaching saturation (third region). Each point on the IV curve corresponds to a different power setting, with higher power correlating to increased mass flow production. Figure 4.56b describes the total power consumption by the water electrolyser against the oxygen mass flow. The maximum hydrogen and oxygen mass flow rates that this water electrolyser can produce are $\dot{m}_c = 0.2$ mg/s and $\dot{m}_a = 1.6$ mg/s, respectively. The power required to achieve this condition is 211 W. As explained in Section 4.5.1.4 and shown in Figure 4.54, power is needed for the two membranes and to heat up the device. Specifically, 35 W are needed to power the PEM (first membrane) and 1 W for the WFB (second membrane). The rest of the power (175 W) is required for achieving a temperature of 70 °C. Consequently, in the current configuration, heating constitutes the majority of the total power prerequisite for the water electrolyser to operate.

A linear projection of the power/mass flow relationship suggests that an HET requiring approximately $\dot{m}_a = 5.0$ mg/s of oxygen (anode) and $\dot{m}_c = 0.6$ mg/s of hydrogen (cathode) would necessitate a water electrolyser consuming approximately 300 W of power, being conservative.

4.5.2.2 Hydrogen Cathode Validation

This section consolidates the findings from the standalone validation of the cathode *Hydrocat*, supplied by *Aliena Pte Ltd*, and fuelled by the hydrogen in-situ generated by the water electrolyser.

The ignition of the cathode is accomplished with a noble gas (in this case xenon) and subsequently, hydrogen is gradually introduced into the system. The transition from pure xenon to pure hydrogen and the resulting change in plume colour are visually depicted in Figure 4.57. Figure 4.58a illustrates the set and measured mass flows of xenon and hydrogen during the validation test and Figure 4.58b the IV characteristics of the cathode keeper when being fuelled by xenon and hydrogen.

As seen in Figure 4.58a, stable ignition with pure hydrogen supplied by the water electrolyser was achieved, enabling successful testing across a range of hydrogen mass flows spanning $\dot{m}_c = 0.07 - 0.16$ mg/s, with uninterrupted operation of the cathode for over 15 minutes before the conclusion of the test.

The results shown in Figure 4.58b indicate that the mass flow rates using hydrogen are lower than those used during the xenon tests. This is due to the inherent limitation of the water electrolyser to produce larger mass flows, with hydrogen production being limited to the stoichiometric mass ratio ($\Phi = 1{:}8$). Consequently, due to the lower mass flow rates, the recorded keeper voltage with hydrogen exceeded that with xenon, thereby increasing the total power consumption by the cathode. However, even with these varying mass flow rates of hydrogen and xenon, the difference in keeper power is minimal ($P_k \approx 96$ W for hydrogen at $\dot{m}_c = 0.16$ mg/s and $P_k \approx 56$ W for xenon at $\dot{m}_c = 0.6$ mg/s). A visual examination of the trend in Figure 4.58b indicates that the power consumption considering equal mass flow rates would be comparable.

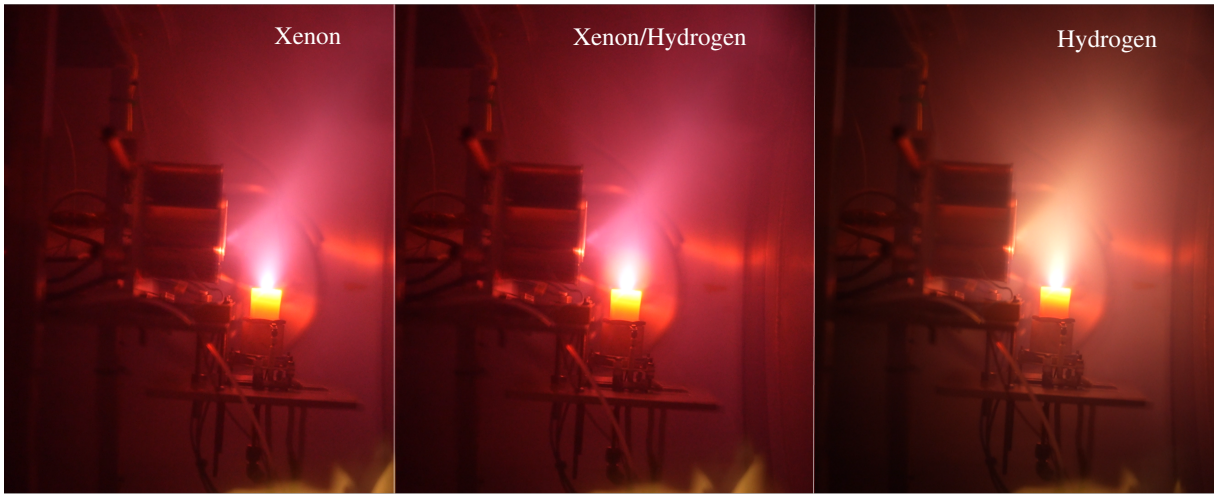
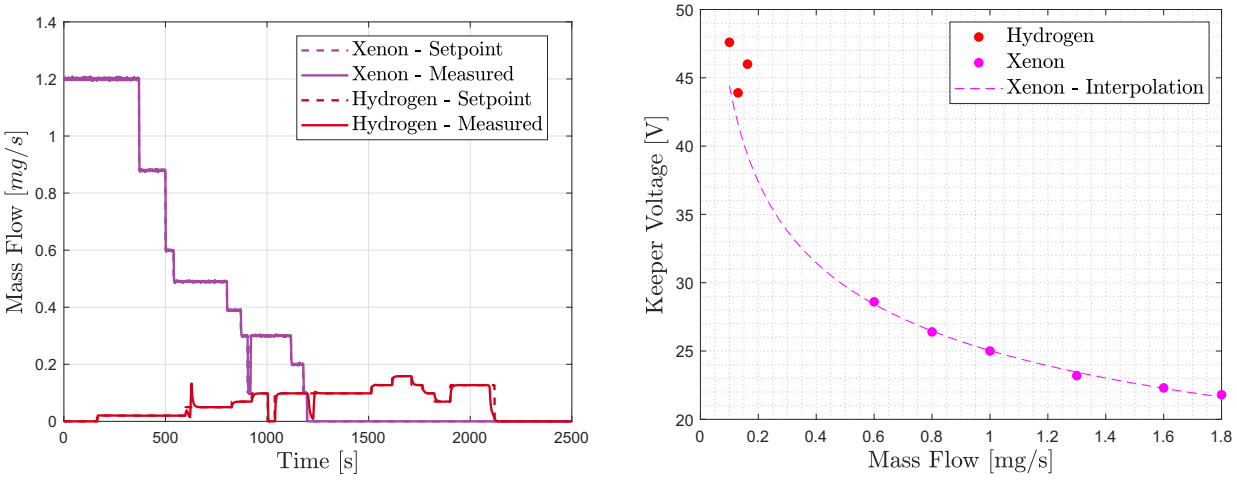


Figure 4.57: Transition from pure xenon to pure hydrogen (produced by a water electrolyser) in the standalone experimental validation of the cathode *Hydrocat*. Pictures presented in [8].



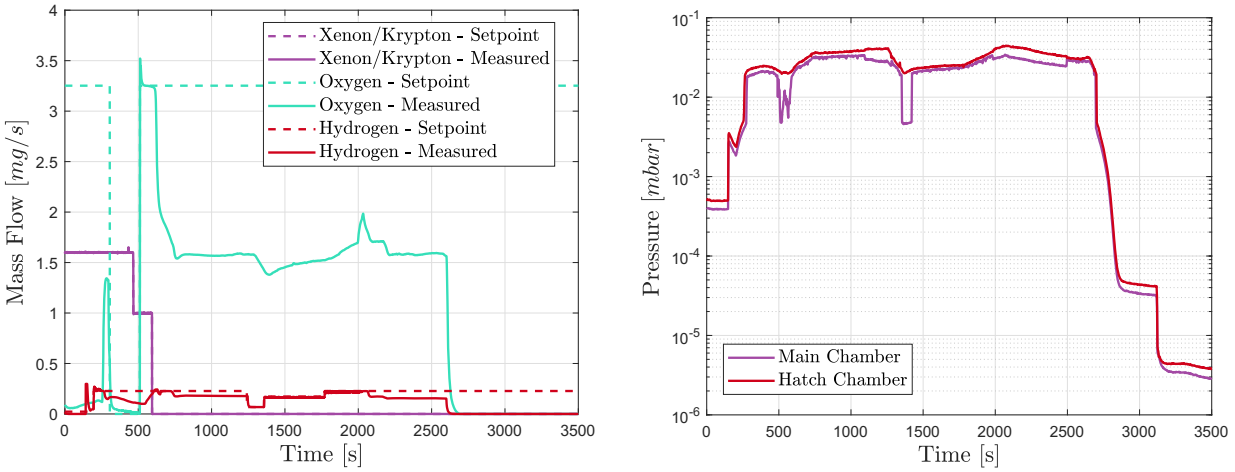
(a) *Hydrocat* mass flows

(b) Keeper voltage

Figure 4.58: Hydrogen cathode validation. a) Mass flows used during the experimental validation of the hydrogen-fuelled cathode *Hydrocat*. b) Keeper voltage reached when using either xenon or hydrogen. Results presented in [8].

4.5.2.3 End-to-End Water Electrolysis Hall Effect Thruster Validation

Finally, the results of the end-to-end testing involving the HET and cathode, fuelled by oxygen and hydrogen respectively, produced by the water electrolyser fed by liquid water, are presented. Figure 4.59a illustrates the set and measured flows of the system during the test, while Figure 4.59b depicts the pressures recorded simultaneously with the introduction of these mass flows into the system. These figures correspond to the thruster *WET-HET* and cathode *Hydrocat*, which successfully achieved stable ignition in these conditions.



(a) *WET-HET* and *Hydrocat* mass flows

(b) Facility pressures

Figure 4.59: End-to-end water electrolysis validation. a) Mass flows used by the *WET-HET* oxygen-fuelled in combination with *Hydrocat*, hydrogen-fuelled. b) Pressure of the vacuum chamber facilities during the test. Results presented in [8].

Similarly to the standalone cathode test (Section 4.5.2.2), the integration of the system's thruster and cathode (illustrated in Figure 4.59) began by using a noble gas: xenon for the cathode and krypton for the thruster, anode. It is important to note that this initial choice of propellant is simply due to the higher cost of xenon compared to krypton (the cathode requires lower mass flow rates than krypton so it is cheaper to operate in this way).

Once stability with xenon/krypton was established (at time $T_{ime} = 0$ s in Figure 4.59a), the gradual introduction of oxygen and hydrogen into the system commenced. During the test, the facilities and hardware were continuously monitored to ensure safety and a stable discharge. Notably, during the initial transition phase, the thruster operated at a higher mass flow rate ($\dot{m}_a \approx$ 3.2 mg/s) than the steady-state capacity of the electrolyser. This was achieved by pressurising a small section of the line with the oxygen produced by the water electrolyser before releasing the flow to the thruster. This methodology ensured the initial stability of the thruster (anode) before reaching the steady-state conditions of pure water electrolysis feed ($\dot{m}_a \approx 1.6$ mg/s of oxygen for the anode and $\dot{m}_c \approx 0.2$ mg/s for the cathode) at time $T_{ime} = 750$ s.

At that point, various oxygen and hydrogen mass flows were introduced into the thruster (anode) and cathode to evaluate the system's stability range.

The *WET-HET* successfully operated on oxygen within the range of $\dot{m}_a = 1.3 - 3.2$ mg/s, while the *Hydrocat* functioned optimally with hydrogen in the range of $\dot{m}_c = 0.07 - 0.22$ mg/s. The total duration of this test was approximately 34 minutes. During steady firing, the mass flow setpoints of oxygen and hydrogen were set to the highest value (fully open valve configuration) so that the flow was not restricted by the mass flow meters and the entire gas production of the water electrolyser was fed into the system.

Throughout this period, the pressures of the main and hatch chambers were concurrently recorded (Figure 4.59b). Notice however that the pressures observed during the test were unusually high. As delineated in Section 4.5.1.1, part of the pumping system remained inactive during this technological validation test due to concerns regarding the combination of oxygen and hydrogen at stoichiometric ratios.

As a reminder, the vacuum facility's pumping capabilities were limited to the utilisation of the two main chamber roughing pumps (model *Varian TriScroll 300 Dry Scroll Pump*), which employed the nitrogen purging system, and the main chamber turbopump (model *VARIAN Turbo-V 3K-G ISO 250 F*), accompanied by another associated purging system. It is important to remark that the pressure gauges were not calibrated for measuring vacuum environments with hydrogen, potentially leading to slightly overestimated pressure readings.

Another significant factor impacting the system discharge pertains to the humidity levels within the feedline. As detailed in Section 4.5.1.4, CVF water electrolysers produce a humid compound of oxygen and hydrogen rather than pure gases. In general, desiccants are typically employed to dehydrate gases from water electrolysers. However, this initial test aimed to evaluate the system's response without desiccants to assess their importance for future advancements in water electrolysers. As visually shown in Figure 4.60, the line's humidity caused a variation in the thruster plume's color, deviating from the typical green-yellowish plasma [3] to a more pinkish plume, characteristic of water vapour plasmas, as will be seen in the next Section 4.6.

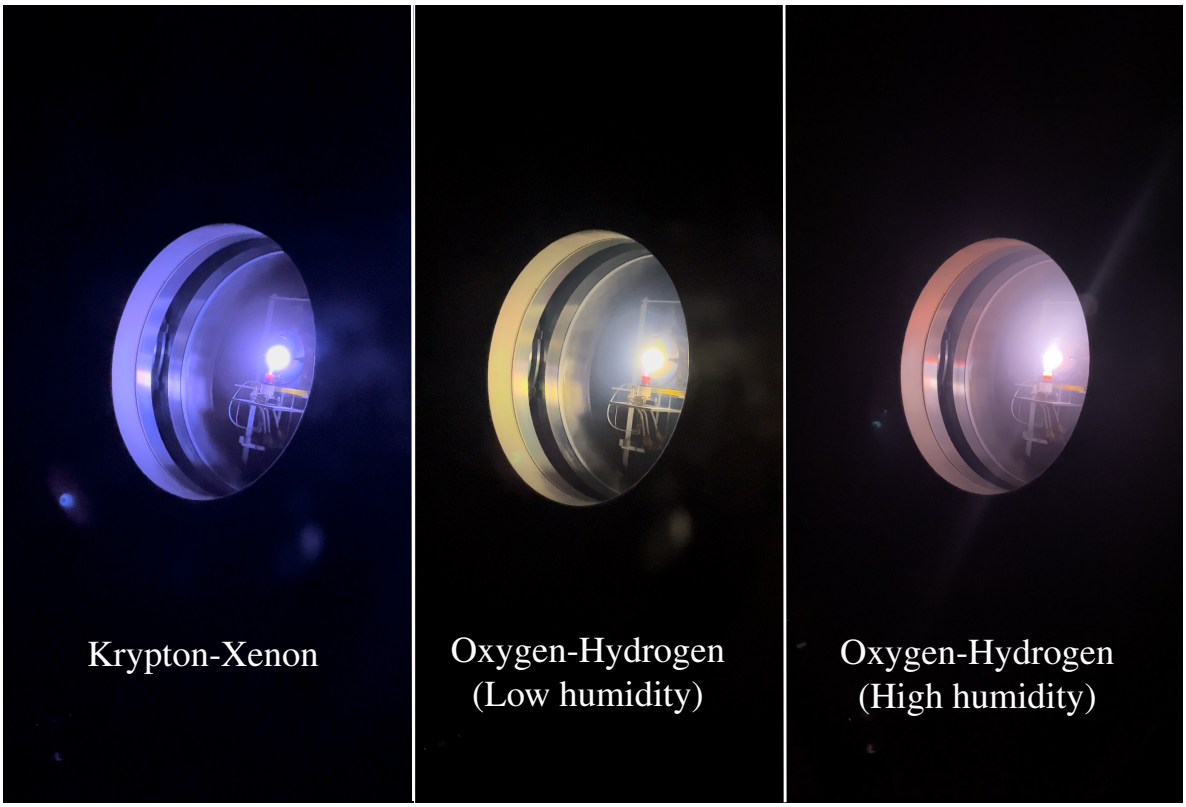
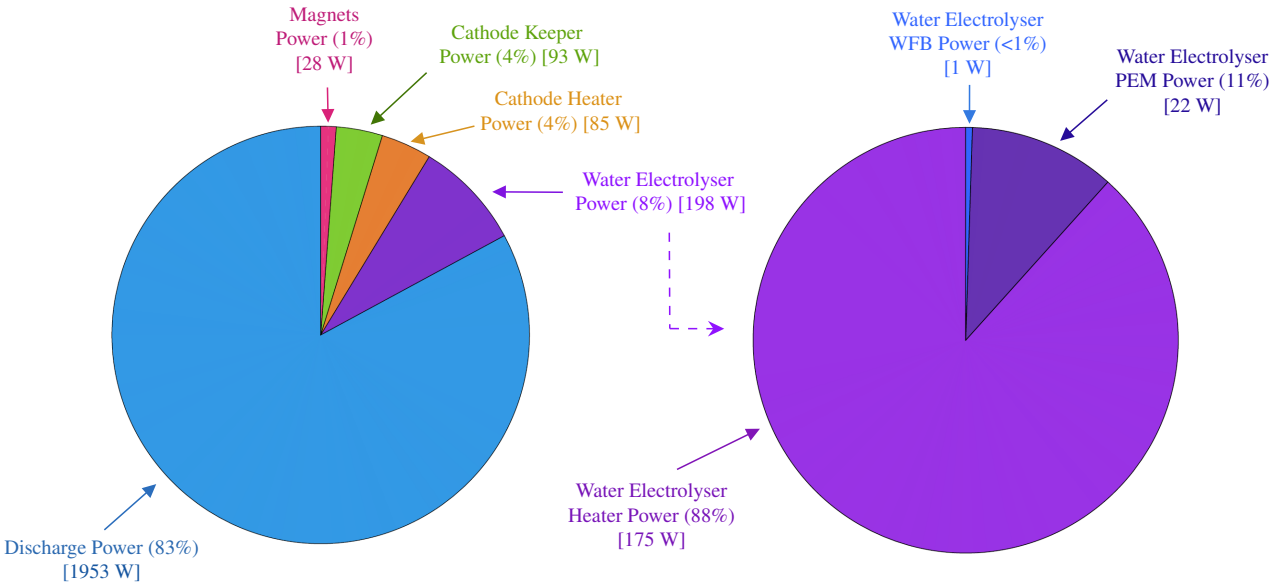


Figure 4.60: Transition from pure xenon to water electrolysis (oxygen for the anode and hydrogen for the cathode, in-situ produced by a water electrolyser) of the end-to-end experimental validation of the thruster *WET-HET* with the cathode *Hydrocat*. Pictures presented in [8].

The combination of high pressures and humidity in the line sometimes caused the thruster to flicker and become more unstable with increasing magnetic field strength. Another constraint within the system was the maximum mass flow rate achievable by the water electrolyser, capped at $\dot{m}_a = 1.6$ mg/s of oxygen. While this limitation was not a significant constraint for the *WET-HET* thruster (which worked successfully, as explained before), it posed a challenge for the *AQUAHET* thruster due to its larger geometry, which demanded higher mass flows for stable operation. This limitation hindered its stability with pure oxygen and hydrogen, although partial success with this thruster was also achieved by introducing a small fraction of xenon/krypton to sustain ignition in the discharge. In Section 5, various modifications to the facilities and water electrolyser fluidics are proposed to address these issues in subsequent tests involving this space technology.

By combining all the power requirements of the system in this test, alongside those recorded in previous experimentation using oxygen and hydrogen from pressurised bottles (Section 4.4), the total power demands of the technology are calculated (Figure 4.61).



a) Total power distribution [2356 W]

b) Water electrolyser power distribution [198W]

Figure 4.61: Power distribution of the complete water electrolysis EP system. Results presented in [8].

More specifically, reference values for the magnet, cathode keeper, cathode heater, and anode discharge power were obtained from a firing test of the *WET-HET* and *Hydrocat* (Section 4.2). In this test, the anode current and voltage were 4.5 A and 434 V, respectively. The cathode keeper current and voltage were $I_k = 2.5$ A and $V_k = 37$ V, respectively, while the cathode heater current and voltage were $I_h = 6.5$ A and $V_h = 13$ V, respectively. The magnet current and voltage were $I_m = 1.5$ A and $V_m = 18.7$ V, respectively. The anode and cathode were supplied with $\dot{m}_a = 1.0$ mg/s and $\dot{m}_c = 0.125$ mg/s of oxygen and hydrogen from compressed gas cylinders. It is important to note that while the thruster's performance is anticipated to be consistent whether using oxygen and hydrogen from pressurised cylinders or from a water electrolyser, this comparison is planned for further experimentation.

Within the framework of the water electrolyser, the predominant share of power (88%) is allocated to heating it to the operational temperature of 70°C, which corresponds to the temperature yielding maximum mass flow production. As explained in Section 4.5.2.1, this assessment is conservative: firstly, the heating capacity of 175 W is used to elevate the electrolyser's temperature to its operational threshold. Upon attainment of this temperature, the requisite heating power

for maintenance is anticipated to decrease. Secondly, the design of the water electrolysis system does not prioritise minimising power requirements, particularly concerning heating. Hence, there exists potential to substantially reduce the total heating power. For example, by designing a water electrolyser using thinner plates with diminished heat capacity a significant decrease in the total heating requirements will be obtained [237]. Nonetheless, even under this suboptimal scenario, the prospects for water electrolysis EP systems remains highly encouraging, as the adoption of this technology, which inherently necessitates an onboard water electrolyser, does not entail substantial penalties in terms of additional power requirements. As illustrated in Figure 4.61, a mere 8% of the overall power is necessitated by the water electrolyser.

These campaigns, constituting the first experimental demonstration of a HET operating with the in-situ generation of the byproducts of water electrolysis (oxygen and hydrogen) produced by a water electrolyser, underscore the feasibility of adopting this technology and highlights the potential environmental, multi-functional, and cost benefits that a space mission could benefit from if water electrolysis is selected as the principal propellant for their propulsion system.

Note that an additional set of campaigns was conducted at the end of this PhD (May-June 2024) to perform the first end-to-end thrust measurements under these conditions. For this purpose, desiccants were included in the setup, and the entire pumping system was active. The results showed that, without desiccants, the humidity in the oxygen and hydrogen lines is higher than 80%, also depending on the operating mode of the water electrolyser: when it starts running, the humidity is typically lower (low humidity mode) than after a few hours of operation (high humidity mode), as seen in Figure 4.60. This is due to water permeating through the membranes and increasing humidity over time. However, with desiccants, the humidity content is reduced to less than 1% for the whole operation of the system. The combination of low humidity and low background pressures (approximately $\approx 10^4 - 10^5$ mbar) made the thruster more stable. The thrust measurements conducted showed no discernible differences from those presented in Section 4.4, although further experiments are encouraged to better validate this finding.

4.6 Campaigns E - Water Vapour-Fuelled Hall Effect Thrusters: Performance Characterisation

As explained in Section 2.1, feeding a HET with a direct water vapour feed presents an alternative concept for utilising water as a propellant in spacecraft. This section provides an overview of the facility setup, feed system, pressure and temperature monitoring apparatus, and the system's performance when operating with water vapour.

The results shown here were published in [4].

4.6.1 Methodology

4.6.1.1 Experimental Set-Up and Vacuum Chamber Facilities

As in Sections 4.2 and 4.4, the experimental campaigns were conducted at the Boltzmann vacuum chamber facilities of the Imperial Plasma Propulsion Laboratory. For a comprehensive understanding of the facilities, electronics, and operational procedures, readers are directed to Section 4.2.1. Throughout this section, the most notable changes made in the set-up (mainly on the fluidics' side) to accommodate the facilities for water vapour propulsion are highlighted. Figure 4.62 shows the whole schematic setup of the laboratory when using water vapour. The different elements comprising this set-up are enumerated in Table 4.18.

4.6.1.2 Electronics, Fluidics and Working Procedures

In contrast to previous experiments utilising oxygen as the thruster's propellant, these tests employ liquid water, which is subsequently converted to gaseous water to supply the thruster. Subsequent sections, namely Sections 4.6.1.4 and 4.6.1.5, provide detailed explanations of the feed system and the pressure and temperature monitoring setup employed to ensure that water remains in the gaseous phase before reaching the thruster. Similar to Section 4.2, krypton was utilised as the cathode propellant, employing the same electronics, procedures, and pressure systems.

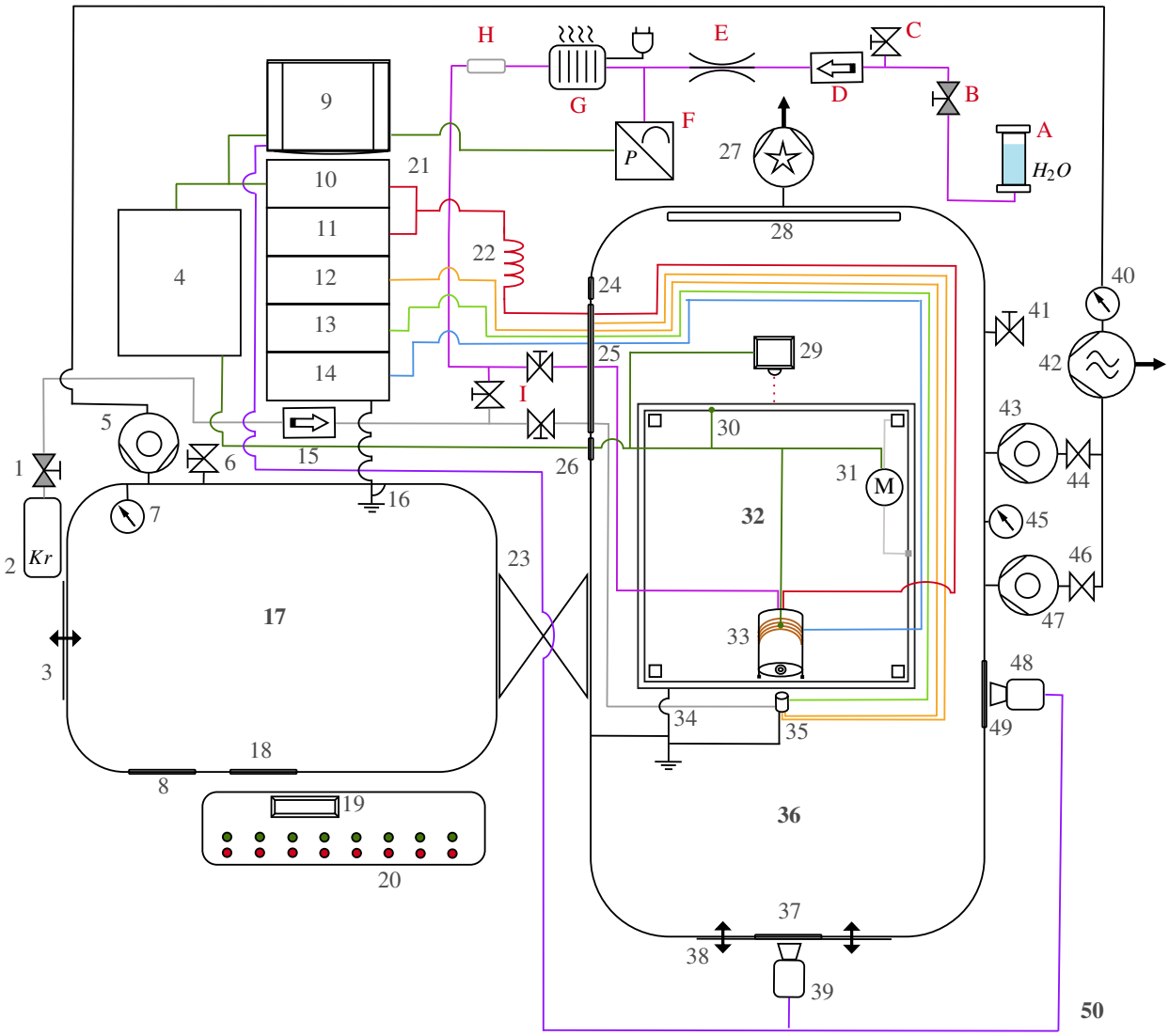


Figure 4.62: Main schematics of the water vapour electric space propulsion testing at the Imperial Plasma Propulsion Laboratory. Diagram published in [4].

4.6.1.3 Thrusters' Geometrical and Material Configuration

Section 4.2 evaluated the optimal performance configurations of oxygen-fuelled HETs concerning mass flow and magnetic field strength. However, these operating conditions may not be the most suitable for water vapour propulsion, thus necessitating further analysis. In this context, the thruster *WET-HET* and the plasma filament cathode are employed throughout these experiments.

Regarding the geometrical configuration of the *WET-HET* thruster, a similar analysis to that presented in Section 4.2.2.6 suggested that a channel length of L = 13.1 mm is likely the most optimal for water vapour propulsion, although additional research is necessary to confirm this assertion.

Table 4.18: Description of the elements depicted in Figure 4.62. Table published in [4].

1	Pressure regulator (cathode)	**26**	Vacuum feedthrough (signals, D-Sub connector)
2	Cathode propellant bottle (Krypton)	**27**	Cryohead (connected to a cryocompressor)
3	Door (vacuum load-lock hatch chamber)	**28**	Cryohead (connected to a cryocompressor)
4	Electronics box	**29**	Laser ILD1750
5	Turbopump (load-lock hatch chamber)	**30**	Thermocouple (to thrust balance)
6	De-pressurising valve (load-lock hatch chamber)	**31**	Servomotor (for calibration)
7	Pressure gauge (to load-lock hatch chamber)	**32**	Thrust balance
8	Vacuum feedthrough (auxiliary)	**33**	Water Electrolysis HET
9	Computer station	**34**	Grounding connection
10	Anode power supply [master] (*Sorenson SGA 1K0X5S-0AA*)	**35**	Cathode (double filament)
11	Anode power supply [slave] (*Sorenson SGA 1K0X5S-0AA R*)	**36**	Main vacuum chamber
12	Heater power supply (*Electro-Automatik EA-PSI 8080-60*)	**37**	Vacuum feedthrough (window)
13	Keeper power supply (*Glassman PS/ET05R400-200*)	**38**	Door (main vacuum chamber)
14	Magnet power supply (*GW INSTEK SPS-3610*)	**39**	Camera Nikon D-5000 (front)
15	Mass flow controller (cathode)	**40**	Pressure gauge (to roughing pump)
16	Grounding connection	**41**	De-pressurising valve (main chamber)
17	Vacuum load-lock hatch chamber	**42**	Roughing pump (Stage 1)
18	Vacuum feedthrough (window)	**43**	Turbopump #1 (Stage 2, Leybold)
19	Pressure readings display	**44**	Pneumatic valve #1
20	Control panel of vacuum systems	**45**	Pressure gauge (to main chamber)
21	Parallel line connection (anode power supplies)	**46**	Pneumatic valve #2
22	Inductor	**47**	Turbopump #2 (Stage 2, Leybold)
23	Gate valve	**48**	Camera Nikon D-5000 (side)
24	Vacuum feedthrough (auxiliary)	**49**	Vacuum feedthrough (window)
25	Vacuum feedthrough (power and feedlines)	**50**	Imperial College London Plasma Laboratory

In these tests, the geometrical configuration outlined in Table 4.1, featuring a channel length of L = 13.1 mm, is selected. The mass flow rates range from $\dot{m}_a = 1.0 - 2.0$ mg/s (refer to Section 4.6.2.1). The magnetic field topology employed is the Gaussian profile illustrated in Figure 4.3, with varying strengths being analysed (see Section 4.6.2.2), ranging from $B = 200 - 600$ G as the peak magnetic field strength. The ceramic walls are constructed of $BNSiO_2$ Grade M26 (see Section 4.2.2.2), and the anode plate is composed of stainless steel (see Section 4.2.2.3).

4.6.1.4 Water Vapour Feed System

Figure 4.63 shows the components of the water vapour feed system. The actual representation during testing is displayed in Figure 4.64. These elements are listed in Table 4.19. Lastly, Figure 4.65 shows the HET with the water vapour feed system in an open-out configuration (FlatSat).

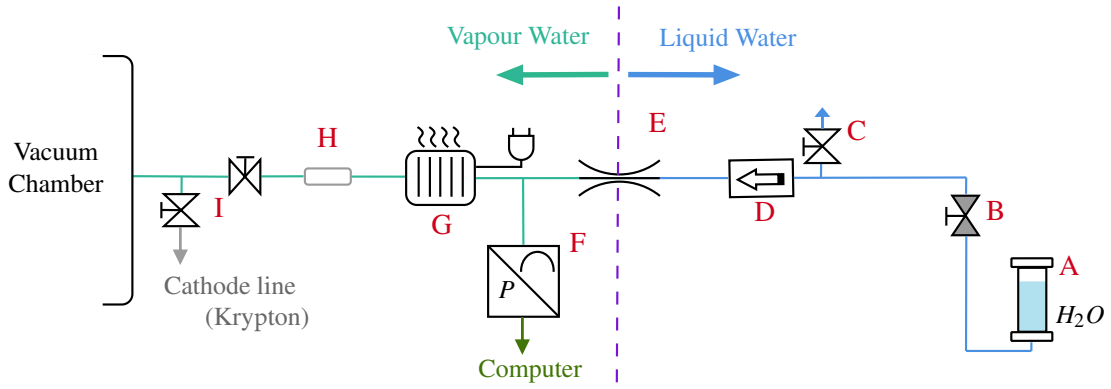


Figure 4.63: Diagram of the water feed system used for the HET electric propulsion testing at the Imperial Plasma Propulsion Laboratory facilities. Published in [4].

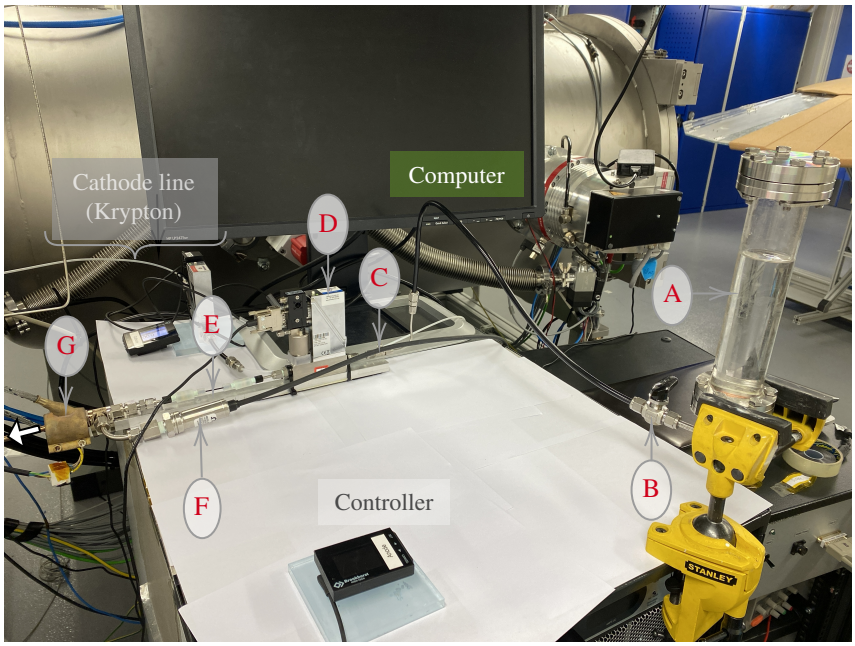


Figure 4.64: Water feed system disposition during testing at the Imperial Plasma Propulsion Laboratory facilities. Diagram published in [4].

Table 4.19: Description of the water feed system elements used to test the HET with water vapour. Table published in [4].

A	H_20 bottle container
B	Manual Valve (to control water flow)
C	Manual Valve (to evacuate bubbles)
D	Liquid Mass Flow Meter (Bronkhorst L13V12)
E	Flow restrictor (liquid to vapour water transition)
F	Pressure transducer
G	Heating system
H	Transparent feedline (to check condensation)
I	Manual Valves set

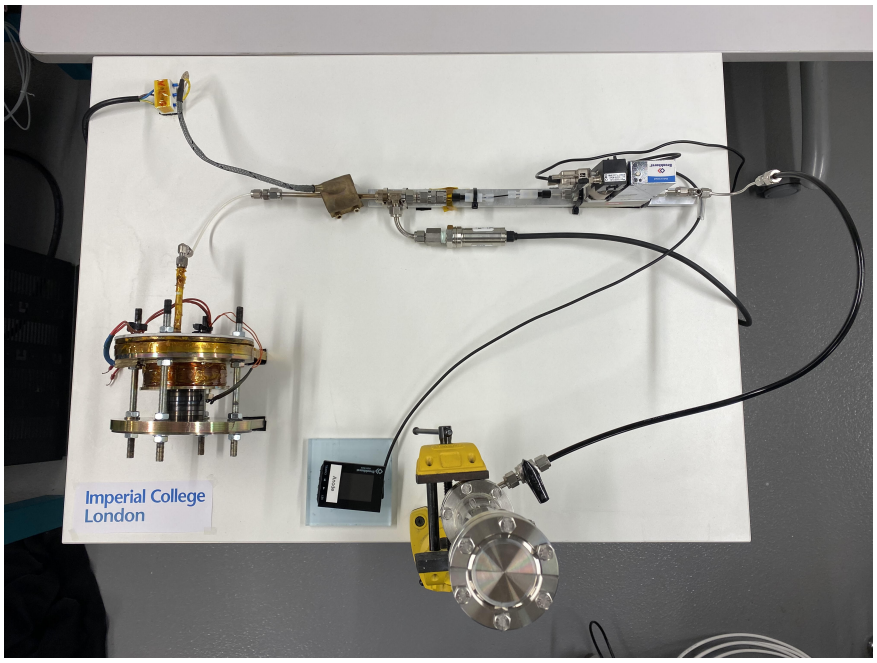


Figure 4.65: Water feed system and HET in Opened-out 'FlatSat' configuration. Picture published in [4].

The water vapour feed system commences with a water tank [A], where distilled water is stored under atmospheric pressure. This tank is designed to prevent water leakage while permitting air ingress. Consequently, the air aids in pushing the water downward, facilitating its movement along the line. A manual valve [B] regulates the flow of water from the container. Moving along the line, another valve [C] is positioned to evacuate any trapped bubbles in the feedline. Once the feedline between valves B and C is free of bubbles, valve C is closed. Adjacent to valve C, a liquid mass flow meter [D] (model *Bronkhorst L13V12 model*) is installed. The choice of a liquid mass flow controller, as opposed to a gas flow controller, is driven by the need for higher flow precision into the thruster.

Up to this point (from [A] to [D]), the water remains in the liquid phase. The transition to the gaseous phase occurs just before the flow restrictor [E]. In a space application it is recommended to incorporate a particle filter at this point to prevent any clogging in the line during operation. For the laboratory experiments, it was not necessary to implement one. The flow restrictor itself comprises a polyetheretherketone (PEEK) capillary tube with a very thin orifice (100 μm) and an outer diameter of 1/16", along with a set of perfluoroalkoxy (PFA) fittings, 1/4-28 unions, and

ethylene tetrafluoroethylene (TFE) flangeless ferrules. This configuration ensures compatibility between the capillary tube and a standard Swagelok 1/8" tube. These components were procured from Darwin Microfluidics [240].

The phase transition from liquid to water vapour unfolds as follows: upon encountering the entrance of the flow restrictor, the water encounters significant resistance as it attempts to flow through the thin orifice (the resistance is directly proportional to the size of the orifice). Upon traversing the 100 μm orifice tube, the water, still in the liquid phase, suddenly expands back into the feedline tube (1/8"). This abrupt expansion triggers a subsequent phase change. The pressure at this juncture is regulated by a pressure transducer [F], which is monitored by computer software. As will be explained in Section 4.6.1.5, this segment of the line experiences the highest pressure, thus posing a greater likelihood of water condensation. Therefore, a pressure transducer is placed here to monitor the water pressure.

To maintain the water in its gaseous state, a heating system warms the feedline [G]. A transparent tube section [H] follows the heating line, allowing visual inspection for any occurrence of water condensation. Lastly, a strategic arrangement of valves [I] is positioned to enable the use of krypton to initiate the thruster plasma discharge before transitioning to water vapour (similarly to the previous sections). Krypton was also used as the cathode's propellant.

4.6.1.5 Water Condensation Control System

The water condensation control system includes a pressure [F] and temperature [G] monitor system, along with a transparent feedline tube [H] for visual inspection of water condensation. The pressure transducer readings over time for two different mass flows ($\dot{m}_a = 1$ mg/s and $\dot{m}_a = 3$ mg/s) are depicted in Figure 4.66. Notably, during these readings, the heating system is activated to warm the feedline and mitigate water condensation. Theoretical values for water condensation at specific pressures and temperatures (300K, 302K, and 304K) are also provided, obtained using the open-source program *CoolProp* [241].

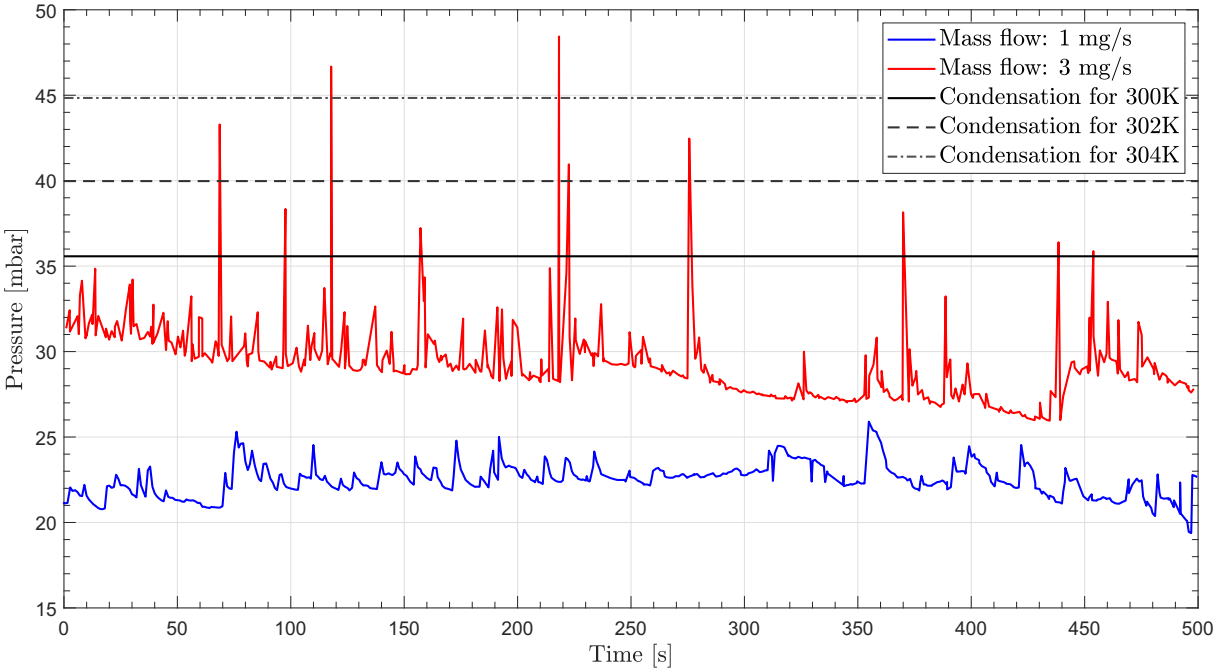


Figure 4.66: Water pressure in the feedline just after the flow restrictor, for various mass flow rates and a heating system activated. The experimental data is compared with the theoretical condensation pressures for water condensation at 300 K, 302 K and 300 K. Results published in [4].

For a mass flow of $\dot{m}_a = 1$ mg/s of water vapour, the pressure transducer readings remain constant between 20 to 25 mbar, well below any water condensation threshold for temperatures above 300K. However, for mass flows of $\dot{m}_a = 3$ mg/s or higher, pressure peaks emerge after some time of operation, indicating sudden pressure losses due to water condensation in the line. As a result, these large mass flows experience water condensation and cannot be used for thruster testing with the current setup. Mass flows of $\dot{m}_a = 2$ mg/s or below are deemed suitable for use since no condensation was detected during operation. This limitation in mass flow does not affect the investigation, as the most optimum operation of the investigated thruster, the *WET-HET*, is $\dot{m}_a = 1$ mg/s (see Section 4.2.2.5).

These results were achieved after several iterations of the feedline design to minimise pressure losses during operation. Initially, condensation was observed at $\dot{m}_a = 1$ mg/s and below, necessitating a redesign of the feedline. Feedline optimisation was guided by the Darcy-Weisbach equation, commonly used for calculating pressure losses in pipes [242]. Figure 4.67 presents the pressures of water from the flow restrictor to the vacuum chamber.

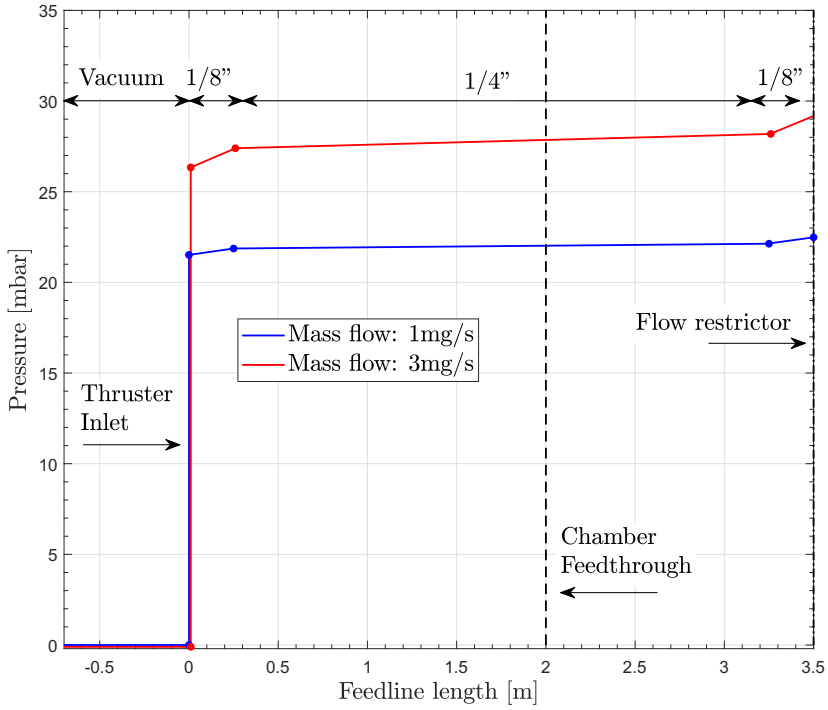


Figure 4.67: Calculated pressure as a function of the feedline length. From vacuum conditions, the pressure rises at the thruster inlet and throughout the 1/4” and 1/8” sections due to pressure losses, until the water vapour reaches the flow restrictor (point of maximum pressure). Results published in [4].

Notice that, when referring to the path from the flow restrictor to the chamber (from right to left in Figure 4.67), the pipelines are described as creating “pressure losses.” Conversely, when considering the path from the chamber to the flow restrictor (from left to right in Figure 4.67), the feedline is described as introducing “pressure surges” or “a pressure rise.” The primary objective remains to reduce the pressure at the flow restrictor (the point of the feedline with the highest pressure, see Figure 4.67) to prevent water condensation during tests.

In Figure 4.67, the initial pressure value at the flow restrictor (at $x = 3.5$ m) and the pressure value in the vacuum (at $x = 0$ m and $x = -0.5$ m) are derived from experimental measurements taken by the pressure monitoring system of the feedline and the vacuum facilities pressure readings, respectively. The intermediate points are computed numerically using the Darcy-Weisbach equation. For laminar flow, it can be expressed as: [242, 243, 244]:

$$\Delta p = L_p \frac{128 \mu_v Q}{\pi D_c^4} \tag{4.16}$$

Here, Δp represents the pressure loss in the pipe, L_p is the pipe length, μ_v is the dynamic viscosity of the water vapour, Q is the volumetric mass flow rate (derived from the propellant mass flow rate), and D_c is the pipe diameter. Equation 4.16 demonstrates that, given a mass flow rate, pressure losses can be reduced by using shorter pipes (decreasing L_p) and/or thicker pipe diameters (increasing D_c). As D_c is a fourth-order term, increasing pipe diameter has a more significant impact on pressure than reducing the feedline length, although both are important for minimising pressure losses.

In the latest iteration of the feedline, the pipe diameter was increased from 1/8" to 1/4" for most of the line (see Figure 4.67), and the total feedline length was reduced from 5.0 m to 3.5 m (see again Figure 4.67). These changes enabled testing of mass flows up to $\dot{m}_a = 2$ mg/s without inducing water condensation.

At the thruster's inlet, the pressure surge arises from the method of propellant introduction into the thruster: in the *WET-HET*, propellant injection involves a 1/8" tube terminating in a reservoir (the bottom part of the copper anode tube, see Figure 4.23), from which the gas flows into the discharge chamber through a narrow gap (0.5 mm) between the inner ceramic wall and the anode [3, 144]. While this strategy is suitable for water electrolysis testing since the gases are naturally in vapour form, it may not be optimal for water vapour experimentation, as it results in a significant pressure increase (Figure 4.67), potentially leading to water condensation if the flow rate exceeds a certain threshold ($\dot{m}_a = 3$ mg/s or higher in this experiment). Alternative strategies, such as propellant injection through relatively large-diameter holes, may result in a lower pressure increase and allow testing at higher mass flow rates. However, even with such strategies, a pressure increase at the thruster inlet is inevitable due to the small diameter of the propellant holes typically used for flow distribution in HETs (typically, on the order of mm).

Finally, notice that, due to the incompressibility of liquid water and the small pressure drop across the liquid mass flow meter (1 mbar according to the manufacturer [223]), liquid water is expected to be at atmospheric conditions upstream of the flow restrictor.

4.6.2 Results and Discussion

4.6.2.1 Mass Flow Dependence

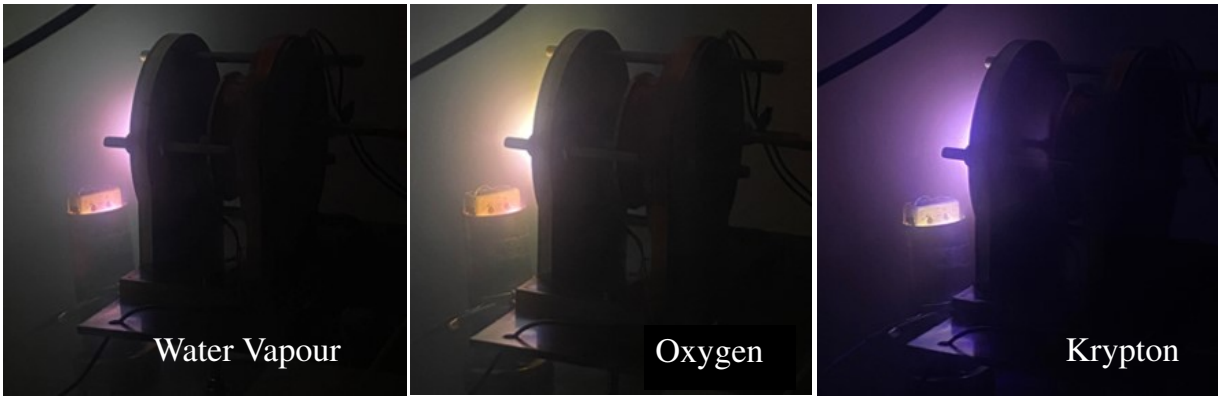
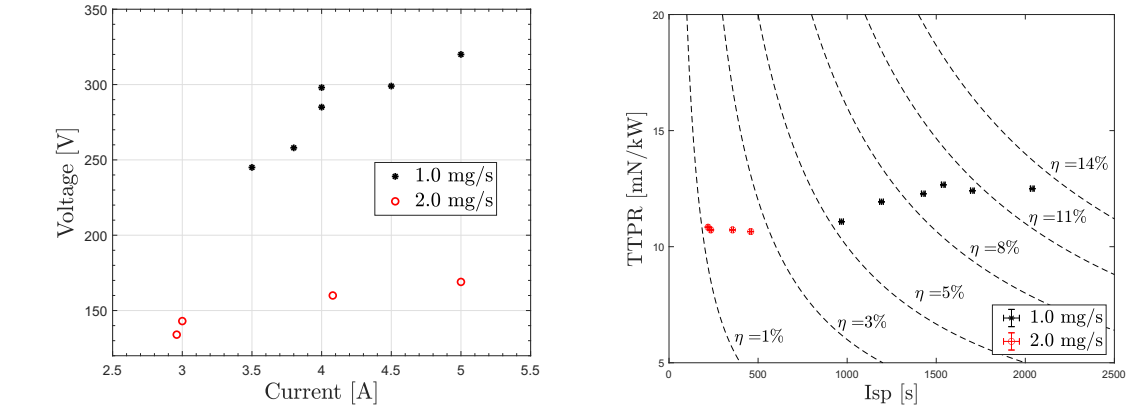


Figure 4.68: Plasma plumes of the thruster *WET-HET* operating with water vapour, oxygen and krypton.

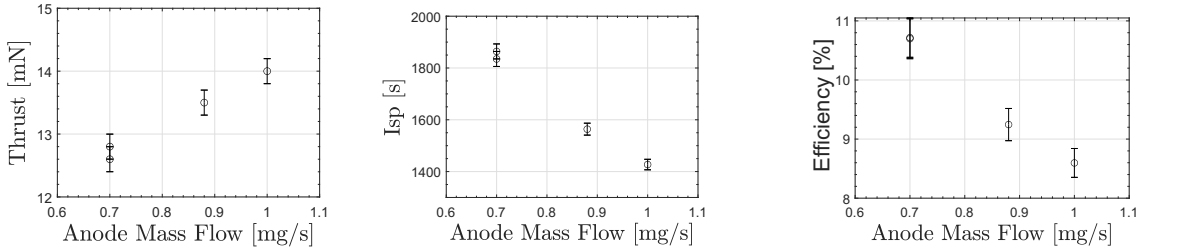
In this section, the dependence of the HET's mass flow performance when operating with water vapour is investigated. Figure 4.68 illustrates the *WET-HET* fuelled by water vapour alongside oxygen and krypton to facilitate a comparison of the plume colour change. Water vapour plasmas exhibit a distinctive pink colour (similar to the one found when working with humid oxygen, see Figure 4.60), contrasting with the greenish-yellowish colour of the oxygen discharge.

The experimental results are depicted in Figure 4.69. Specifically, Figure 4.69a presents the IV curve for two different mass flow rates: $\dot{m}_a = 1.0$ mg/s and $\dot{m}_a = 2.0$ mg/s. *TTPR* as a function of anode specific impulse is calculated in Figure 4.69b. Thrust (Figure 4.69c), anode specific impulse (Figure 4.69d), and anode thrust efficiency (Figure 4.69e) of the thruster over the mass flow range of $\dot{m}_a = 0.7 - 1.0$ mg/s are also presented. These measurements were conducted at a discharge power of $P_d = 1100 \pm 50$ W, with a magnetic field topology corresponding to an electromagnet current strength of $I_m = 1.5$ A, for reasons that will be explained in Section 4.6.2.2. It is noteworthy that the discharge power achieved when running $\dot{m}_a = 2.0$ mg/s does not meet the target ($P_d = 1100 \pm 50$ W) due to the low discharge voltage recorded in these measurements, thus these data points are not included in Figures 4.69c, 4.69d, nor 4.69e.



(a) IV Curve

(b) *TTPR* vs Anode specific impulse



(c) Thrust - T

(d) Anode specific impulse - I_{sp}

(e) Anode thrust efficiency - η_{tr}

Figure 4.69: Experimental measurements of the water vapour-fuelled *WET-HET* over different mass flow rates. Thrust (T), anode specific impulse (I_{sp}), Thrust-To-Power-Ratio ($TTPR$) and anode thrust efficiency (η_{tr}) values are presented for a discharge power of $P_d = 1100 \pm 50$ W, a maximum magnetic field strength of $B = 0.06$ T (corresponding to an electromagnet current strength of $I_m = 1.5$ A, Figure 4.3). Results published in [4].

From the obtained results, it is evident that lower mass flow rates, while generating less thrust (Figure 4.69c), yield higher anode specific impulse (Figure 4.69d), ultimately resulting in higher anode thrust efficiency (Figure 4.69e). As will be elaborated in Section 4.6.2.3, this could be attributed to dissociation and ion dissociation reactions undergone by water vapour, with the energy used in these reactions resulting in losses compared to single ionisation events.

When testing the *WET-HET* under the same conditions using oxygen, a similar trend was observed: higher thrust with higher mass flow, and better anode specific impulse at lower mass flow rates (see Figure 4.21). However, when testing with oxygen, the anode thrust efficiency with mass flows in the range of $\dot{m}_a = 0.6 - 1.0$ mg/s was similar. With water vapour, it is observed that the anode thrust efficiency is higher at $\dot{m}_a = 0.7$ mg/s is higher than at $\dot{m}_a = 1.0$ mg/s. This trend may indicate slightly lower propellant utilisation for water vapour than for oxygen, as the thruster does not effectively utilise the additional mass flow provided at higher water vapour

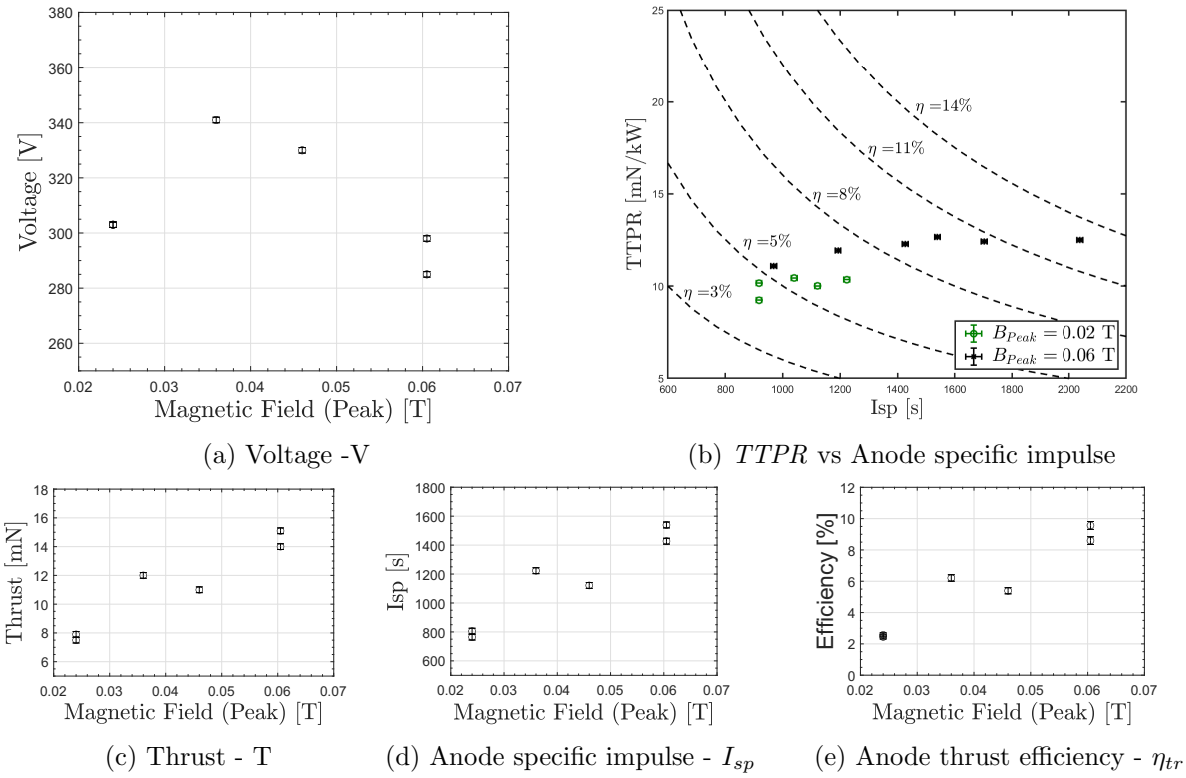
flow rates. More information about the comparison between water vapour and oxygen will be provided in Section 4.6.2.3 Additionally, it is observed that $TTPR$ is higher for the mass flow rate of $\dot{m}_a = 1.0$ mg/s compared to $\dot{m}_a = 2.0$ mg/s, with $TTPR$ showing relative stability within the investigated anode specific impulse range.

However, another important factor to consider is the stability of the plasma during operation. Across these mass flow rates, experimental tests indicated that $\dot{m}_a = 1.0$ mg/s offered the best balance between anode thrust efficiency and discharge stability. Consequently, this set-point is deemed as the most optimal one, coinciding with the optimal configuration of the *WET-HET* when operating with oxygen.

4.6.2.2 Magnetic Field Strength Dependence

Now that the preferred mass flow condition has been determined ($\dot{m}_a = 1.0$ mg/s), the thruster's performance is tested under various magnetic field strengths. Figure 4.70 compiles the results from these experiments, presenting voltage (Figure 4.70a), $TTPR$ versus anode specific impulse (Figure 4.70b), thrust (Figure 4.70c), I_{sp} (Figure 4.70d), and thrust efficiency (Figure 4.70e). The performance plots are represented as a function of the peak magnetic field, within the range of $B = 0.024 - 0.061$ T, according to Figure 4.3. Higher magnetic field strengths could not be tested due to difficulties in maintaining stable thruster operation. This is attributed to the increased electron resistance towards the anode as the magnetic field strength rises. The discharge power used for comparing these thrust measurements was $P_d = 1170 \pm 50$ W, consistent with the previous Section 4.2.2.5.

The results indicate that higher magnetic field strengths correspond to increased thrust (Figure 4.70c), anode specific impulse (Figure 4.70d), and thrust efficiency (Figure 4.70e). Maximum performance was achieved with a peak magnetic field strength of $B = 0.061$ T. This behaviour mirrors the findings from testing with oxygen (Section 4.2.2.4), where strong magnetic fields were also preferred. Finally, Figure 4.70b complements this discussion by showing that a higher anode specific impulse and anode thrust efficiency are attained with stronger magnetic fields.



(a) Voltage -V

(b) *TTPR* vs Anode specific impulse

(c) Thrust - T

(d) Anode specific impulse - I_{sp}

(e) Anode thrust efficiency - η_{tr}

Figure 4.70: Experimental measurements of a water vapour-fuelled *WET-HET* over a maximum magnetic field strength of $B = 0.024 - 0.061$ T, corresponding to the Gaussian magnetic topologies of Figure 4.3. Values presented for a discharge power of $P_d = 1170 \pm 50$ W, mass flow of $\dot{m}_a = 1.0$ mg/s and geometrical configuration of Table 4.1 with a channel length of L = 13.1 mm. Results published in [4].

The most optimum thrust measurement recorded with water vapour was $T = 20.0 \pm 0.2$ mN; with a specific impulse of $I_{sp} = 2039 \pm 20$ s and an anode efficiency of $\eta_{tr} = 12.5 \pm 0.3$ % at the largest discharge power of investigation ($P_d = 1600 \pm 1$ W).

In summary, the most optimal operating conditions of the *WET-HET* thruster, in terms of mass flow and magnetic field strength, considering performance and stability, coincide with those determined when using oxygen. This alignment facilitates the comparison of oxygen (water electrolysis) and water vapour under the same optimal conditions for both propellants as will be analysed in the next section.

4.6.2.3 Water Electrolysis vs Water Vapour-Fuelled Hall Effect Thrusters

Based on the findings collected throughout this thesis, water electrolysis and water vapour propulsion technologies are evaluated and compared against. To start this analysis, the most relevant physical considerations of using oxygen (the intended thruster propellant of water electrolysis) and water vapour are underscored. Subsequently, the performance of these systems at the same discharge power is assessed. Finally, a trade-off analysis of the two ideas is presented. The results and discussions included in this section were published in [4].

Physical Considerations

The primary objective of this study is to enhance the overall understanding of how the performance of HET fuelled by oxygen (from water electrolysis) or water vapour might be influenced just by looking at the primary characteristics of these two propellants relative to each other.

To begin, the mass and Van der Waals radius of these molecules are presented in Table 4.20. The mass of the particle plays a critical role for two primary reasons: first, a higher mass expelled results in greater thrust of the HET. Second, a lighter molecule undergoes greater acceleration, leading to an expected increase in specific impulse. Notice that the ion mass is nearly identical to the mass of the neutral particle, owing to the negligible mass of the electron (9.109×10^{-31} kg). From these data, it is observed that the mass of oxygen is 44% greater than that of water vapour. Therefore, under equivalent ionisation conditions, a higher specific impulse is anticipated for water vapour, albeit with lower thrust. The Van der Waals radius also influences the collision rate of the particles. For water vapour, data is directly sourced from the literature [245]. For the oxygen molecule, an average between the transverse ($1.88\mathring{A}$) and longitudinal Van der Waals radius ($1.66\mathring{A}$) is utilised, yielding a value of $1.77\mathring{A}$ (equivalent to 1.77×10^{-10} m) [246]. Notably, these values exhibit close similarity to each other.

Table 4.20: Mass and Van der Waals radius of the water vapour and oxygen molecules. The ratio is obtained using the molecule of oxygen as a baseline to compare against. Table published in [4].

	Water vapour $[H_2O]$	**Oxygen (water electrolysis)** $[O_2]$	**Ratio**
Molecular mass [u]	18	32	56%
Van der Waals radius [m]	1.70×10^{-10}	1.77×10^{-10}	96%

Another crucial consideration pertains to the intrinsic reactive model of these two molecules, as it was discussed in Section 3.2.1.2. Unlike xenon, water vapour and oxygen molecules not only undergo ionisation but also dissociation, double ionisation, and attachment events. As a reminder, from the thruster's perspective, ionising the plasma is the most efficient process for generating thrust. This is because the energy expended in dissociating the particle (or ionising it more than once) does not directly contribute to thrust. Attachment processes generate negative ions, which are accelerated inward toward the channel and should be avoided. Moreover, the higher the ionisation potential, the lower the propellant utilisation, as more energy will be needed to ionise a neutral particle.

In Figure 4.71, the reactive model of water vapour is compared to that of oxygen, utilising data collected once again by Y. Itikawa [166, 169]. As a brief summary, for the water vapour model, various dissociation, ion dissociation, and attachment events exist. For instance, an electron collision can dissociate the water molecule to produce OH and H, or O and H_2. Ion dissociation events can yield ions such as OH^+, O^+, H_2^+, or H^+. Attachment can lead to negative ions such as OH^-, O^-, or even a dissociative attachment process creating H^- and H. The sum of these cross-sections is depicted in Figure 4.71. This contrasts with the oxygen molecule, where the products are unique for each type of reaction. Detailed information about each individual water vapour and oxygen reaction can be found in Section 3.2.1.2.

For a HET, the electron temperature varies within the channel, typically peaking at the end [1] and being a function of discharge power, geometry, and operating mass flow [12].

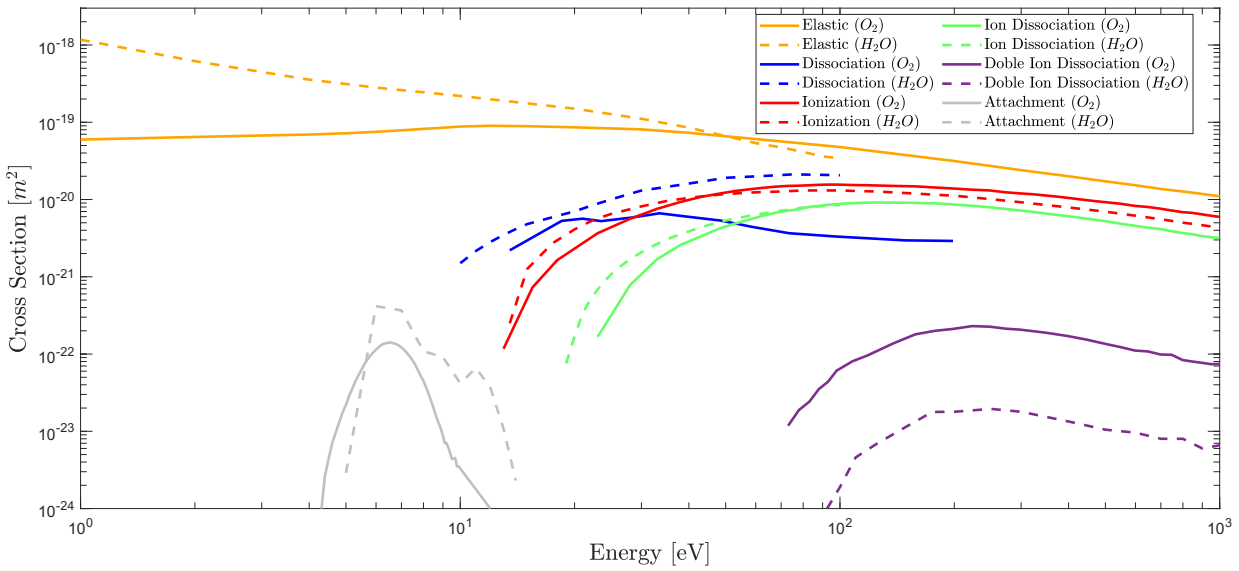


Figure 4.71: Comparison of the cross-sections of water vapour and oxygen molecules, as a function of the electron energy (i.e., the electron temperature). Data taken from experimental results coming from diverse studies. This data is compiled and analysed by Y. Itikawa in [166, 169]. Diagram published in [4].

The plasma temperature within the channel is often estimated as one-tenth of the discharge voltage, a prediction supported by experimental observations [12, 247, 196]. With a discharge voltage of $V_d \approx 300$ V, the electron temperature range of interest would centre around $T_e = 30$ eV following a Maxwellian distribution. Figure 4.71 indicates that for water vapour, the dissociation cross-section surpasses the ionisation cross-section regardless of electron energy. Conversely, the ionisation cross-section of oxygen exceeds the dissociation cross-section for electron temperatures above $T_e \approx 15$ eV. This implies that for water vapour, a larger portion of energy is consumed to dissociate the molecule rather than directly ionising it, potentially leading to inefficiencies compared to oxygen. Attachment reactions occur within the range of electron temperatures between $T_e = 4 - 10$ eV, although their cross-section is generally an order of magnitude lower than ionisation and dissociation events. A similar trend is observed with double ionisation processes, primarily significant above $T_e > 100$ eV and an order of magnitude less prevalent than ionisation and dissociation events.

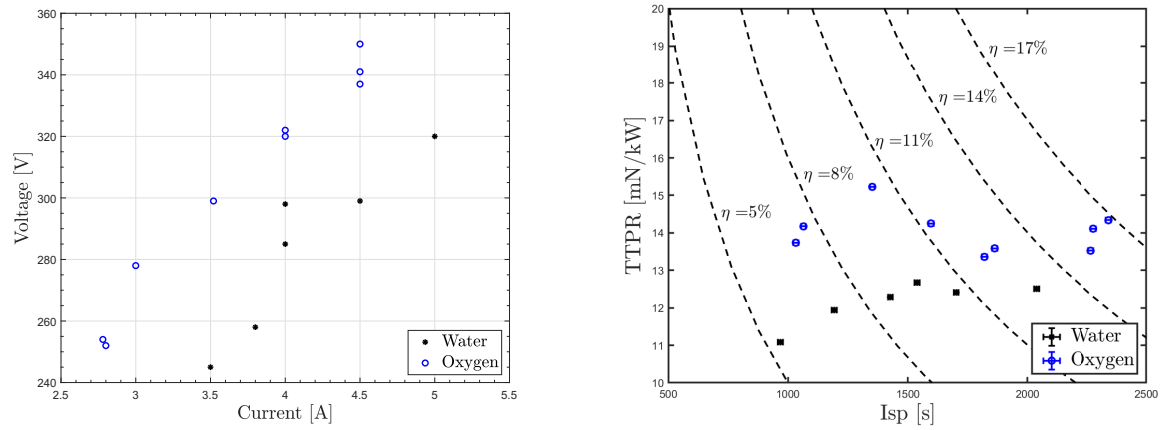
Performance Comparison

This section compares the performance of water electrolysis and water vapour propulsion using the same thruster (*WET-HET*) and cathode (plasma filament cathode). The cathode propellant for both anode propellants is set as krypton to ensure a direct comparison without introducing additional uncertainty sources. The most optimal operating conditions for both thrusters were determined to be the same ($\dot{m}_a$ = 1 mg/s of anode mass flow and a peak magnetic field of B = 0.061 T, as seen in Figure 4.3). Therefore, these conditions are used in this analysis for both propellants. The geometrical and material configuration of the thruster used in these tests (*WET-HET*) is the one presented in Table 4.1 using a channel length of L = 13.1 mm, ceramic walls made of $BNSiO_2$ Grade M26, and a stainless steel anode plate.

Figure 4.72 presents the IV curve (Figure 4.72a), *TTPR* versus anode I_{sp} (Figure 4.72b), thrust (Figure 4.72c), anode specific impulse (Figure 4.69d), and anode thrust efficiency (Figure 4.72e) of the HET working with oxygen (propellant of water electrolysis) and water vapour, across a discharge power range of $P_d = 600 - 1600$ W.

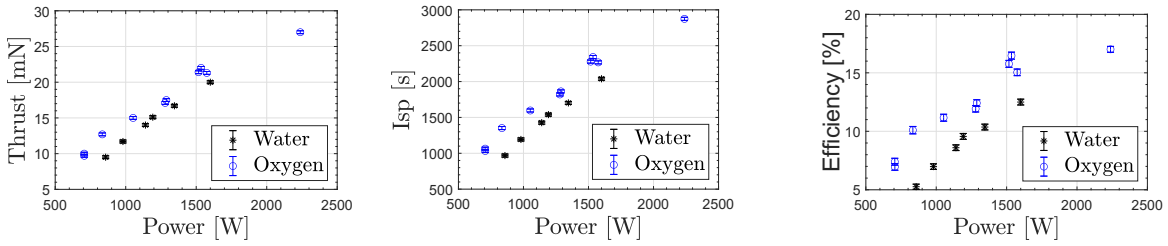
By examining Figure 4.72a, it is observed that the discharge voltage of the thruster when operating with water vapour is lower than when working with oxygen. This finding suggests a potentially lower ionisation rate of water vapour compared to oxygen, as seen in Figure 4.71. For both propellants and throughout the entire power range investigated, the voltage increases linearly with the current for both cases, indicative of the "low voltage mode" typical of HETs working with xenon. However, unlike xenon, where an abrupt increase in the IV curve slope occurs at a certain discharge current (observed at 1.6 A in other studies [196]), no such behaviour is observed in water vapour or oxygen. Only one operating regime appears for both gases, without a distinct transition to the "high voltage mode" seen in xenon-fuelled thrusters.

In the *TTPR* versus anode specific impulse analysis (Figure 4.72b), *TTPR* remains relatively stable as a function of the anode specific impulse. However, there appears to be an indication of a peak in *TTPR*, observed at efficiencies around $\eta_{tr} = 11\%$, for both oxygen and water vapour.



(a) IV Curve

(b) $TTPR$ vs I_{sp}



(c) Thrust

(d) I_{sp}

(e) Thrust Efficiency

Figure 4.72: Experimental measurements of the water vapour-fuelled *WET-HET*, for a discharge power range of $P_d = 600 - 1600$ W. Values presented for a mass flow of $\dot{m}_a = 1.0$ mg/s, peak magnetic flux density of $B \approx 0.06$ T (correspondent to an electromagnet current of $I_m = 1.5$ A, Figure 4.3). Values compared with oxygen [3] under the same conditions. Results published in [4].

The thrust (Figure 4.72c) increases linearly with the discharge power, as does the anode specific impulse. In both cases, water vapour demonstrates inferior performance compared to oxygen, as reflected in the anode thrust efficiency (Figure 4.72e). On average across all discharge powers, oxygen proves to be approximately $\Delta\eta_{pr} \approx 20$ % more efficient than water vapour under the same testing conditions.

To contextualise the performance, Table 4.21 presents the metrics of the *WET-HET* with water electrolysis (i.e., oxygen) and water vapour compared to the *SPT-100* using xenon [147, 148]. Notice that the *WET-HET* running with xenon is not included in the comparison due to being optimised solely for lightweight propellants. Therefore, using this thruster as a reference for comparison with heavy traditional propellants might not provide a realistic assessment of the full potential of these thrusters operating with krypton and xenon. The experimental results demonstrate how the *WET-HET* can achieve a better anode specific impulse at the expense of significantly lower thrust (similar findings as the ones presented in Table 4.16).

Table 4.21: Comparison of the *WET-HET* operating with oxygen and water vapour propellants and krypton as the cathode propellant versus the *SPT-100* [147, 148], running with xenon. The relative performance difference considers the *SPT-100* as the baseline. Results published in [4].

	Propellant	**Power [W]**	**Mass Flow [mg/s]**	**Thrust [mN]**	**Anode Specific Impulse [s]**	**Anode Efficiency [%]**
SPT-100	Xenon	1520	4.93	87.6 (Ref)	1720 (Ref)	51.2% (Ref)
WET-HET	Water Vapour	1600	1.00	20.0 (-77%)	2039 (+19%)	12.5% (-76%)
WET-HET	Oxygen	1534	1.00	22.0 (-75%)	2243 (+30%)	15.8% (-69%)

This trend was also observed when presenting the performance comparison of water electrolysis and oxygen/krypton versus other xenon-fuelled thrusters (Table 4.16). As remarked there, although the anode thrust efficiency of the thruster with alternative propellants is notably lower than with xenon, testing at a larger discharge power, can make this technology even more competitive.

Additionally, Figure 4.73 illustrates the propellant utilisation efficiency of the thruster when operating with water vapour and oxygen, compared to the *SPT-100* using xenon, using data obtained from the literature [144, 147, 148, 248]. The propellant utilisation efficiency (α) is derived from an analytical formulation, as follows [144, 248]:

$$\alpha = \frac{I_i}{I_{\dot{m}}} = \frac{T}{\dot{m}_a \sqrt{V_d(1-\delta)2q/m_n}} \tag{4.17}$$

where I_i represents the ion current, $I_{\dot{m}}$ is the equivalent current for the injected mass flow ($I_{\dot{m}} = q\ \dot{m}_a/m_n$), with m_n the neutral mass. The parameter δ relates to discharge efficiency and typically ranges from 0.1 to 0.3 [249]. Being conservative, δ is assumed to vary between $0 < \delta < 0.5$ [144]. Consequently, the error bars are calculated using $\delta = 0$ (lower error bar) or $\delta = 0.5$ (upper error bar). As expected, the propellant utilisation efficiency for xenon thrusters like the *SPT-100* exceeds that of any other HET working with alternative propellants (see Figure 4.73). Due to uncertainty in the parameter δ, and the analytical nature of the calculation, it is not feasible to determine whether water vapour or oxygen exhibits higher propellant utilisation. Nonetheless, it could be inferred from the findings of this analysis that the propellant utilisation of water vapour would be lower than that achieved with oxygen.

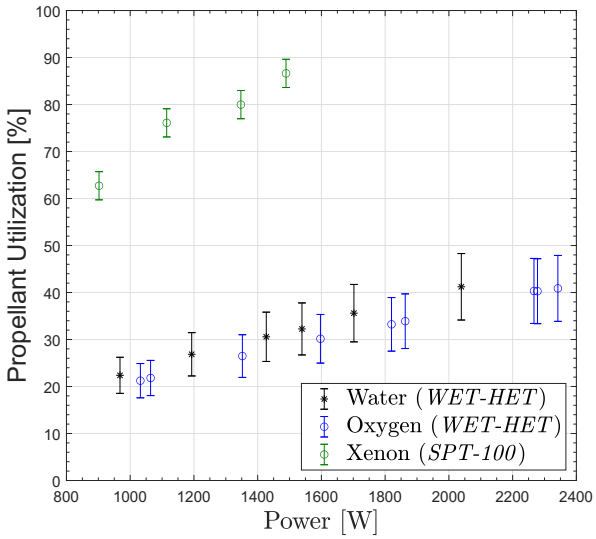


Figure 4.73: Analytical calculation of the propellant utilisation of the thruster *WET-HET* with water vapour and oxygen, in comparison with the xenon-fuelled *SPT-100*. Graph published in [4].

Technology Trade Off

This dissertation has extensively examined the performance of water electrolysis and water vapour propulsion systems under various operational parameters. The results have indicated that oxygen (i.e., water electrolysis) is roughly 20% greater efficiency than water vapour in HETs under the same operating conditions (which resulted to be the same for both propellants). However, the comparison between these technologies extends beyond thruster performance to factors like cathode compatibility, as well as mass, volume, and power requirements.

Table 4.22 compares water vapour and water electrolysis HET propulsion based on the insights gathered throughout this thesis. It assesses these technologies across performance, cathode compatibility, mass and volume budgets, and power consumption. As it can be seen, water electrolysis outperforms water vapour in terms of performance and cathode compatibility, the two most important factors to consider. Conversely, water vapour HETs are advantageous in terms of mass, volume, and power budgets due to their independence from a water electrolyser. Notice that these technologies are still evolving, and future findings may alter the conclusions presented in Table 4.22. For example, further exploration could involve evaluating potential satellite contamination from water contact, particularly ice formation around critical components during space missions.

Table 4.22: Representative trade-off table between water electrolysis and water vapour HET propulsion systems. A part of these outcomes was published in [4].

	Factor Weight	*Water Vapour*	*Water Electrolysis*	*Description*
Performance	High	Low	Medium	According to the research presented in this thesis, the performance of water electrolysis surpasses the one of water vapour. On average, water electrolysis is 20% more efficient considering the most optimal conditions (which resulted to be the same for both propellants).
Cathode Compatibility	High	Medium	High	For water electrolysis, the selection of the propellant for the cathode is straightforward: the electrolyser separates water into oxygen (for the thruster) and hydrogen (for the cathode). Section 4.4 and 4.5 showed the suitability and potential of a cathode working with hydrogen. For water vapour propulsion however, the right choice of propellant for the cathode is not that clear: a separate tank of krypton or xenon can be used to feed the cathode or a microwave cathode can be used to include water vapour [250], among other options.
Mass and Volume budget	Medium	Medium	High	Water vapour does not need an electrolyser on board of the spacecraft, which lessens the amount of mass on board, overall cost and the technical difficulties of qualifying extra hardware. However, water electrolysis propulsion depends on the use of the electrolyser and that increases the mass and volume onboard.
Power budget	Medium	Low	Low	Water electrolysis needs heating systems to keep the electrolysers under the operating temperature range (around 70°C, according to the system tested in Section 4.5). Water vapour propulsion also needs heating systems to keep the gas in vapour form. However, these amounts of power ($\approx$ 200 W) are relatively low compared to the discharge power of the thruster ($\approx$ 2000 W).

In summary, water electrolysis propulsion holds superior prospects compared to water vapour due to its enhanced performance and its superior cathode compatibility, making it a preferable choice for in-space applications. In any case, despite the higher mass and volume requirements coming from the need for a water electrolyser onboard the spacecraft or the needs of a specific feeding system for water vapour, water presents opportunities for ISRU, synergies with other subsystems, potential for a combined EP and CP system utilising oxygen and hydrogen, environmental advantages, and overall cost-effectiveness compared to other alternatives (see Section 2.2). Ultimately, the selection of the optimal propellant depends on the specific needs of the space mission, with both water electrolysis and water vapour presenting competitive options for medium-term space missions.

Table 4.23: Preliminary comparison between the experimental results of *WET-HET* versus the simulation results obtained with *PlasmaSim* (Section 3.2.2.2). Values shown for the simulation inputs of Table 3.7. The geometrical and operating conditions for the simulation and experiments are kept constant as the ones shown Table 4.1 with a channel length of $L = 34.8$ mm, water mass flow rate of $\dot{m}_a = 1.0$ mg/s, an electromagnet current of $I_m = 0.5$ A, channel walls made of $BNSiO_2$, a stainless steel anode and an operating power discharge power window of $P_d = 1200 \pm 10\%$ W.

	Thrust [mN] (Value / Rel Diff %)		**Anode Specific Impulse [s]** (Value / Rel Diff %)		**Anode Thrust Efficiency [%]** (Value / Rel Diff %)	
Experiments	11.2	-	1142	-	5.46	-
PlasmaSim	12.4	10.71%	933	18.30%	6.41	15.34%

4.6.2.4 Numerical Model and Experiments

Similarly to Section 4.2.2.9, a preliminary correlation of the performance of a HET fuelled by water, comparing the numerical results obtained from the simulation shown in Section 3.2.2.2 and the experimental results, is addressed. For this comparison, the thruster *WET-HET* with the experimental configuration of Table 4.1 using a channel length of $L = 34.8$ mm, a water mass flow rate of $\dot{m}_a = 1.0$ mg/s, an electromagnet current of $I_m = 0.5$ A, channel walls made of $BNSiO_2$, and a stainless steel anode is employed. For the discharge power, an operating power discharge power window of $P_d = 1200 \pm 10\%$ W is used as this is the one derived from the simulations using *PlasmaSim*.

From the results shown in Table 4.23, a correlation in thrust of 10% is obtained. For the anode specific impulse and anode thrust efficiency, the comparison shows a discrepancy of about 18% and 15%. Note that these results are coming from self-consistent formulations where no parameters are altered in order to get a better match between simulation and experiments. As such, the main goal of this comparison is to show how the results of self-consistent simulations correlate with experiments. This comparison is encouraging as the software shows promising results when replicating the performance of water-fueled HETs albeit with room for improvement. In order to increase the confidence in the code to replicate the performance of these complex devices, more simulations are encouraged under other geometrical and operating conditions as part of the future work of this activity (see Section 6).

4.7 Campaigns F - Radiofrequency (RF) Excitation

This section experimentally evaluates the implications in performance of a HET when being excited with RF waves in accordance with the theoretical framework described in Section 1.2.2.2 and guided by the insights derived from the computational model outlined in Section 3.2.2.3.

Prior to commencing, it is pertinent to acknowledge that the frequency of the waves selected, falling within the RF spectrum, is utilised by other radio enthusiasts and communication systems. To ensure responsible use of this frequency band, an amateur radio examination was undertaken, resulting in the issuance of a licence for conducting these experiments (licence number 50864, issued by the *Radio Society of Great Britain* on the 18^{th} of December 2021).

4.7.1 Methodology

4.7.1.1 Experimental Set-Up and Vacuum Chamber Facilities

Similarly to Sections 4.2, 4.4 and 4.6, the experimental campaigns were conducted at the Boltzmann vacuum chamber facilities of the Imperial Plasma Propulsion Laboratory. Figure 4.74 shows the whole schematic setup of the laboratory used to excite a HET with radiofrequency waves. The different elements comprising this set-up are enumerated in Table 4.24.

4.7.1.2 Electronics, Fluidics and Working Procedures

In these experiments, noble gases (xenon and krypton) and oxygen are used to characterise the performance of a HET using RF excitation. Still, the electronics, operational principles, and pressure systems adhere to the descriptions provided in Section 4.2, with a few novelties related to the RF excitation which are highlighted in detail in Section 4.7.1.4.

4.7.1.3 Thrusters' Geometrical and Material Configuration

The two thrusters described in Section 4.1.2.1 (*WET-HET* and *AQUAHET*), in combination with the cathode *Hydrocat* (Section 4.1.2.2) were tested with RF excitation.

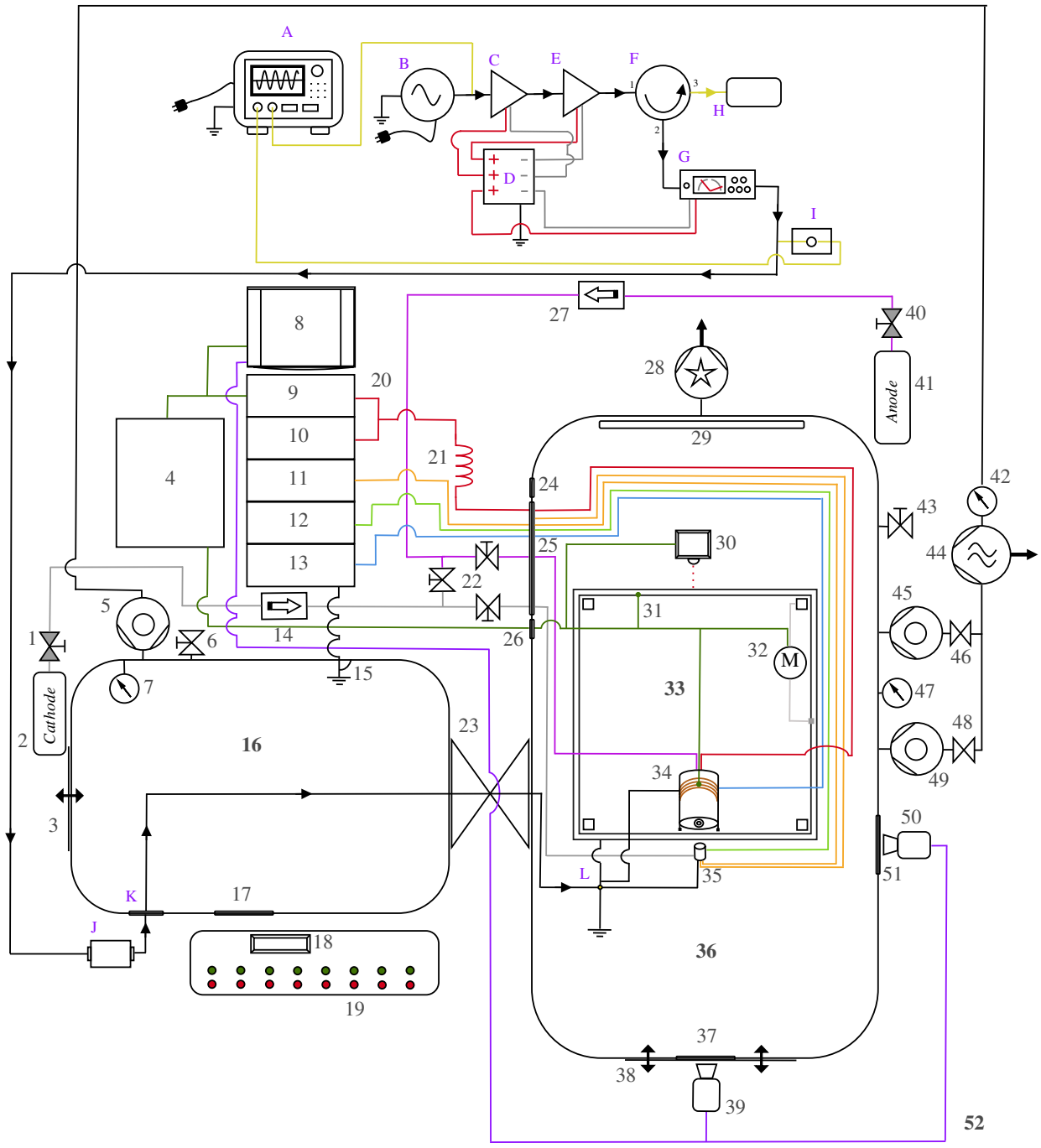


Figure 4.74: Main schematics of Hall Effect Thrusters with radiofrequency excitation testing at the Imperial Plasma Propulsion Laboratory.

Regarding the geometrical configuration of the *WET-HET* thruster, the set-up outlined in Table 4.1, featuring a channel length of L = 13.1 mm (the best performing one, see Section 4.2.2.6) was selected. The mass flow rates ranged from $\dot{m}_a = 2.0 - 6.0$ mg/s when using noble gases and $\dot{m}_a = 2.0$ mg/s when using oxygen. The ceramic walls are constructed of $BNSiO_2$ Grade M26, and the anode plate is composed of stainless steel.

Table 4.24: Description of the elements depicted in Figure 4.74.

1	Pressure regulator (cathode)	**27**	Massflowmeter (anode)
2	Propellant bottle (cathode)	**28**	Vacuum feedthrough (signals, D-Sub connector)
3	Door (vacuum load-lock hatch chamber)	**29**	Cryohead (connected to a cryocompressor)
4	Electronics box	**30**	Laser ILD1750
5	Turbopump (load-lock hatch chamber)	**31**	Thermocouple (to thrust balance)
6	De-pressurising valve (load-lock hatch chamber)	**32**	Servomotor (for calibration)
7	Pressure gauge (to load-lock hatch chamber)	**33**	Thrust balance
8	Computer station	**34**	Water Electrolysis HET
9	Anode power supply (master)	**35**	Cathode
10	Anode power supply (slave)	**36**	Main vacuum chamber
11	Cathode power supply	**37**	Vacuum feedthrough (window)
12	Heater power supply	**38**	Door (main vacuum chamber)
13	Magnet power supply	**39**	Camera Nikon D-5000 (front)
14	Massflowmeter (cathode)	**40**	Pressure regulator (anode, thruster)
15	Grounding connection	**41**	Propellant bottle (anode, thruster)
16	Vacuum load-lock hatch chamber	**42**	Pressure gauge (to roughing pump)
17	Vacuum feedthrough (window)	**43**	De-pressurising valve (main chamber)
18	Pressure readings display	**44**	Roughing pump (Stage 1)
19	Control panel of vacuum systems	**45**	Turbopump #1 (Stage 2, Leybold)
20	Parallelising line (anode power supplies)	**46**	Pneumatic valve #1
21	Inductor	**47**	Pressure gauge (to main chamber)
22	Manual valves	**48**	Pneumatic valve #2
23	Gate valve	**49**	Turbopump #2 (Stage 2, Leybold)
24	Vacuum feedthrough (auxiliary)	**50**	Camera Nikon D-5000 (side)
25	Vacuum feedthrough (power and feedlines)	**51**	Vacuum feedthrough (window)
26	Vacuum feedthrough (power and feedlines)	**52**	Imperial College London Plasma Laboratory

For the thruster *AQUAHET*, the configuration presented in Table 4.2 using a channel width of w = 5 mm (the most optimum one, see Section 4.2.2.7) was chosen. The mass flow rate using noble gases was $\dot{m}_a = 2.5$ mg/s and from $\dot{m}_a = 1.0 - 2.5$ mg/s when using oxygen.

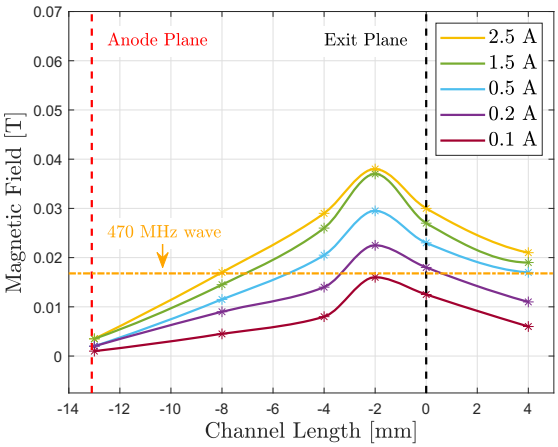
It should be noted that the mass flow rates used for both thrusters are higher than the optimum ones found (see Section 4.2.2.5). This choice is made to reduce the discharge voltage and characterise the thruster under low-power conditions, potentially resulting in thrust measurements below $T < 10$ mN. This decision is based on the capabilities of the thrust balance, which has a resolution range spanning in the range of $T = 0.5 - 100$ mN with an accuracy contingent upon the thrust measurement range. For thrust measurements falling within the $T = 0.5 - 10$ mN range, it has been experimentally checked that the thrust balance can detect changes in thrust of $T = 0.1$

mN or greater. However, for measurements well beyond this range, the typical accuracy of the balance is on the order of $T = 0.3$ mN (refer to Section 4.2). As will become apparent during the evaluation of the obtained results, the enhancement in performance facilitated by RF excitation is marginal (less than T = 0.5 mN). Therefore, it was necessary to conduct tests in the low-power regime, where thrust measurements are small, to accurately detect the changes introduced by RF excitation.

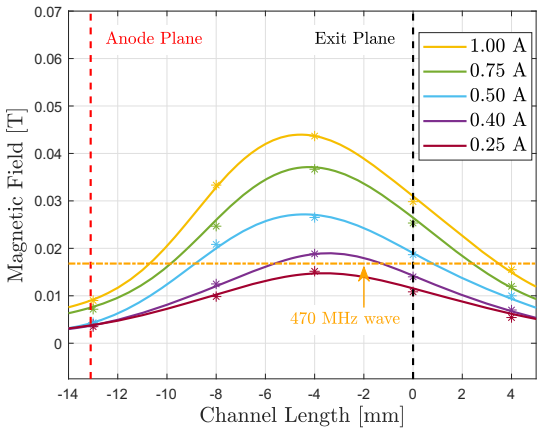
As the RF excitation is highly influenced by the magnetic field topology and strength (as seen in Sections 1.2.2.2 and 3.2.2.3), a detailed discussion is addressed below:

The magnetic field of HETs, typically on the order of $B = 10^{-2}$ T, necessitates a wave in the RF range to achieve resonance within the channel. For instance, in the case of the *SPT-100* thruster whose peak magnetic field strength is B = 0.016 T [147, 148], a wave with a frequency of $f_{\mathrm{RF}} = 448$ MHz will resonate at that peak magnetic field location, as derived from Equation 1.6. The computational findings from this investigation (Section 3.2.2.3) demonstrated optimal performance when resonance coincides with the magnetic field's peak. Consequently, waves of this magnitude resonating at the peak magnetic field strength are experimentally investigated. It is important to remember that, as remarked in Section 1.2.2.2, due to the typical Gaussian nature of the magnetic field in HETs, resonance is only locally achieved. Nonetheless, these specific waves exhibit resonances not only at the ECR condition but also at higher harmonics [1, 67, 68] (see Table 1.2), suggesting the potential for resonance at other locations within the channel as well.

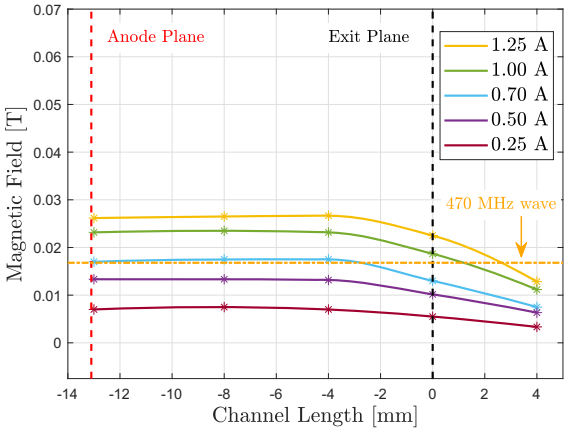
To explore a range of diverse ECR conditions, adjustments can be made to either the frequency or the magnetic field of the thruster (refer to Equation 1.6). As will seen throughout the section, changing the frequency can result in high reflected power even with the best possible impedance matching configuration. However, modifying the magnetic field strength is significantly more straightforward: the magnetic field's intensity can be adjusted based on the current flowing through the thrusters' electromagnets. Consequently, during the experiment, the frequency will be kept fixed, and variations in magnetic field strength will be employed to explore different ECR conditions.



(a) *AQUAHET*



(b) *WET-HET*, Gaussian



(c) *WET-HET*, constant

Figure 4.75: Magnetic field topologies of the thrusters tested (*AQUAHET* and *WET-HET*) for the radiofrequency excitation experiment. The dots represent experimental measurements. The magnetic field strength that resonates with a wave of frequency $f_{RF} = 470$ MHz is also shown.

As will be detailed in Section 4.7.1.4, a wave with a frequency of $f_{\mathrm{RF}} = 470$ MHz is chosen for the experiment due to the setup's capability to adjust and project a wave at this specific frequency. Consequently, the peak magnetic field strength is adjusted to resonate at $f_{\mathrm{RF}} = 470$ MHz (approximately $B = 0.0168$ T).

The magnetic field of the *AQUAHET* thruster is depicted in Figure 4.75a for various investigated strengths. Furthermore, in the case of the *WET-HET*, not only can the magnetic field strength be adjusted, but also the topology by employing different configurations of the metallic coils surrounding the channel [43] (see Section 4.1.2.1). This allows for the attainment of either a Gaussian or a constant magnetic field strength in the channel. The rationale for altering the field is to augment the region where resonance conditions may occur at the principal ECR frequency. The

constant magnetic field topology is not typical of HETs, but it is studied to further understand how the performance changes when using RF excitation. Figure 4.75b illustrates the Gaussian magnetic field topology investigated for various strengths, while Figure 4.75c presents the same for the constant magnetic field strength at different levels. Note that all the profiles shown in Figure 4.75 represent experimental measurements of the magnetic field using a magnetometer.

4.7.1.4 Radiofrequency (RF) Hardware

As seen in the main facility diagram (Figure 4.74), this set-up needed to incorporate a system which can excite RF waves in a HET. Figure 4.76 illustrates a schematic of the electronics employed and the various components through which the wave must traverse before reaching the thruster. The physical arrangement of the hardware for the experiment is depicted in Figure 4.77. The components presented therein are itemised in Table 4.25.

It is also noteworthy that the frequency bandwidth of the components becomes more specific along the path of the wave. The bandwidth limit comes from the fact that the signal generation covers a wide range of frequencies, while amplification and tuning are focused on a narrower bandwidth. The frequency bandwidth and power amplification of the wave on its journey from the signal generator to the thruster are shown in Figure 4.78.

To commence, the RF wave is generated by a signal generator (element B). The signal generator can produce a weak signal (with a maximum power of $P_{\text{sg}} = 0.02$ W) in the frequency range of $f_{\text{sg}} = 150$ MHz to 3.0 GHz. To amplify this wave, a double-stage power amplifier is employed. The initial component is a power pre-amplifier (element C), with an amplification capability up to $P_{\text{PA1}} = 2$ W in a bandwidth of waves from $f_{\text{PA1}} = 10$ MHz to 1.0 GHz. However, this amplification is insufficient, as the targeted power should be approximately $P_{RF} = 20$ W according to the computational studies (Section 3.2.2.3, [1]). Therefore, a second power amplifier is integrated into the setup. This post-power amplifier (element D) elevates the power of waves between $f_{\text{PA2}} = 400$-470 MHz up to $P_{\text{PA2}} = 80$ W.

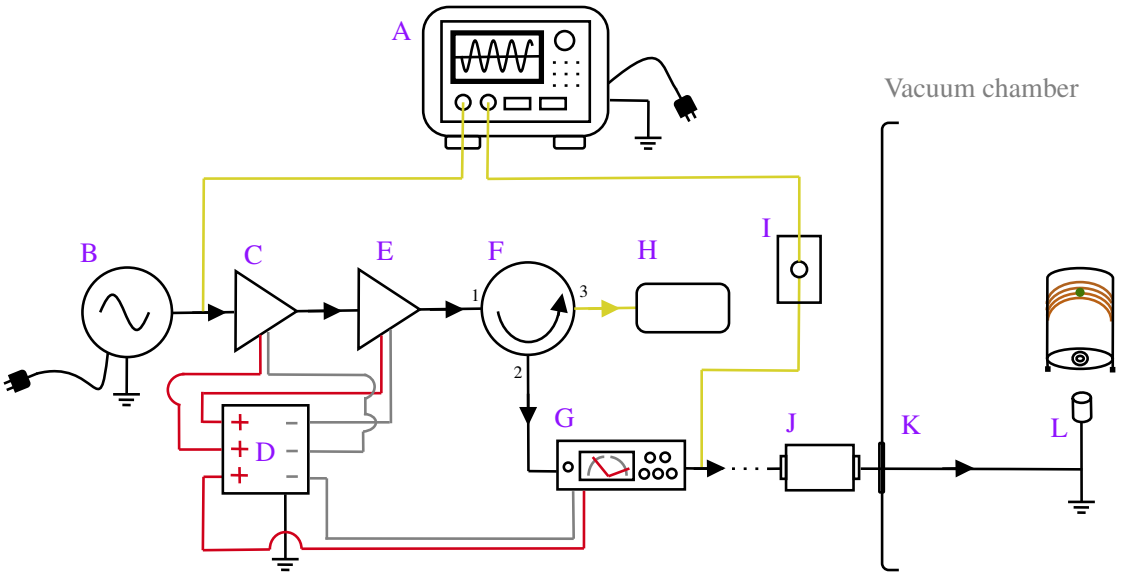


Figure 4.76: Diagram of the set-up used for the excitation of a Hall Effect Thruster with radiofrequency waves.

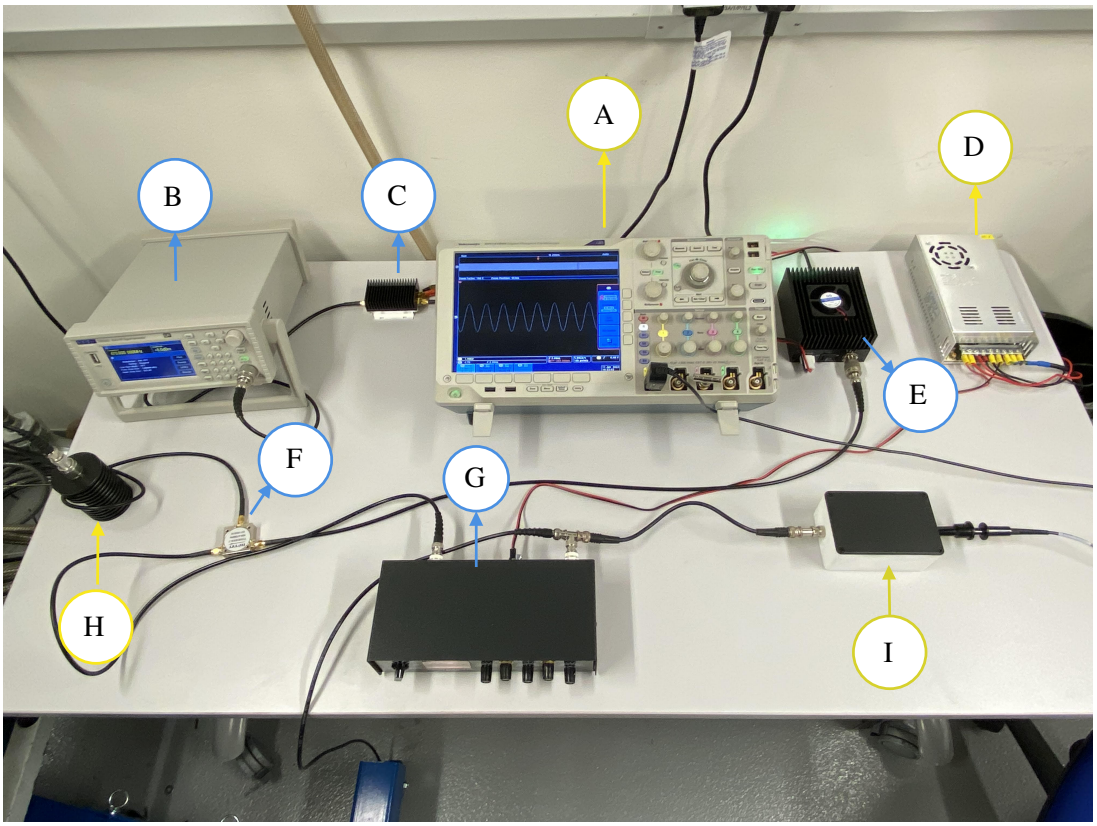


Figure 4.77: Radiofrequency electronics set-up for the excitation of a Hall Effect Thruster. Blue-circled elements denote the primary path of the wave, while yellow-circled elements represent additional components in the setup.

Table 4.25: Description of the elements shown in Figure 4.76 and Figure 4.77.

A	Oscilloscope (Tektronix DPO-4104B)	**G**	Antenna matching unit (MFJ-923)
B	Signal generator (Aim-Tti TGR2053)	**H**	Dummy load (Surecom, 100 W)
C	Power pre-amplifier (Aliexpress)	**I**	High voltage differential probe (Fluke VPS410)
D	Power supply (12V DC - 400 W)	**J**	RF surge protector (IS-B50LU-C0)
E	Power post-amplifier (GeekStyl TZT)	**K**	Coaxial vacuum feedthrough
F	RF isolator (TH3538XS-1)	**L**	Ground connection

Although the output power from the post-amplifier ($P_{\mathrm{PA2}} = 80$ W) surpasses the target RF power ($P_{\mathrm{RF}} = 20$ W), it is anticipated that a portion of the power will be dissipated in the coaxial connections between components and along the coaxial cables. Moreover, some will be reflected back due to the impedance mismatch between the thruster and the RF connection.

To safeguard the integrity of the signal generator and power amplifiers, a RF isolator (element F) is employed. This device enables the transmission of forward power from the post-RF generator while redirecting reflected power to an alternate route, terminating in a dummy load (element H). This strategy ensures that no reflected power traverses through components E to B, which could potentially damage the equipment. The forward power of the post-amplifier is directed towards an Antenna Matching Unit (AMU). This device, commonly used by radio amateurs, minimises reflected power and maximises forward power. This is done by tuning three different knobs, which control an antenna capacitance, transmitter capacitance, and inductance. The capacitors are fully unmeshed when turned clockwise and meshed when turned counterclockwise. Notice that it is crucial to position the AMU after all preceding components for two reasons. Firstly, it is the sole element in the line capable of rectifying any possible impedance mismatch in line. Secondly, it provides direct measurements of forward and reflected power, essential for characterising the wave. According to the manufacturer, the frequency range where this device can tune the signal spans in the range of $f_{\mathrm{AMU}} = 420$-460 MHz, although as will be explained later, experimentally it was tested that it can actuate in a broader span ($f_{\mathrm{AMU}} = 410$-510 MHz).

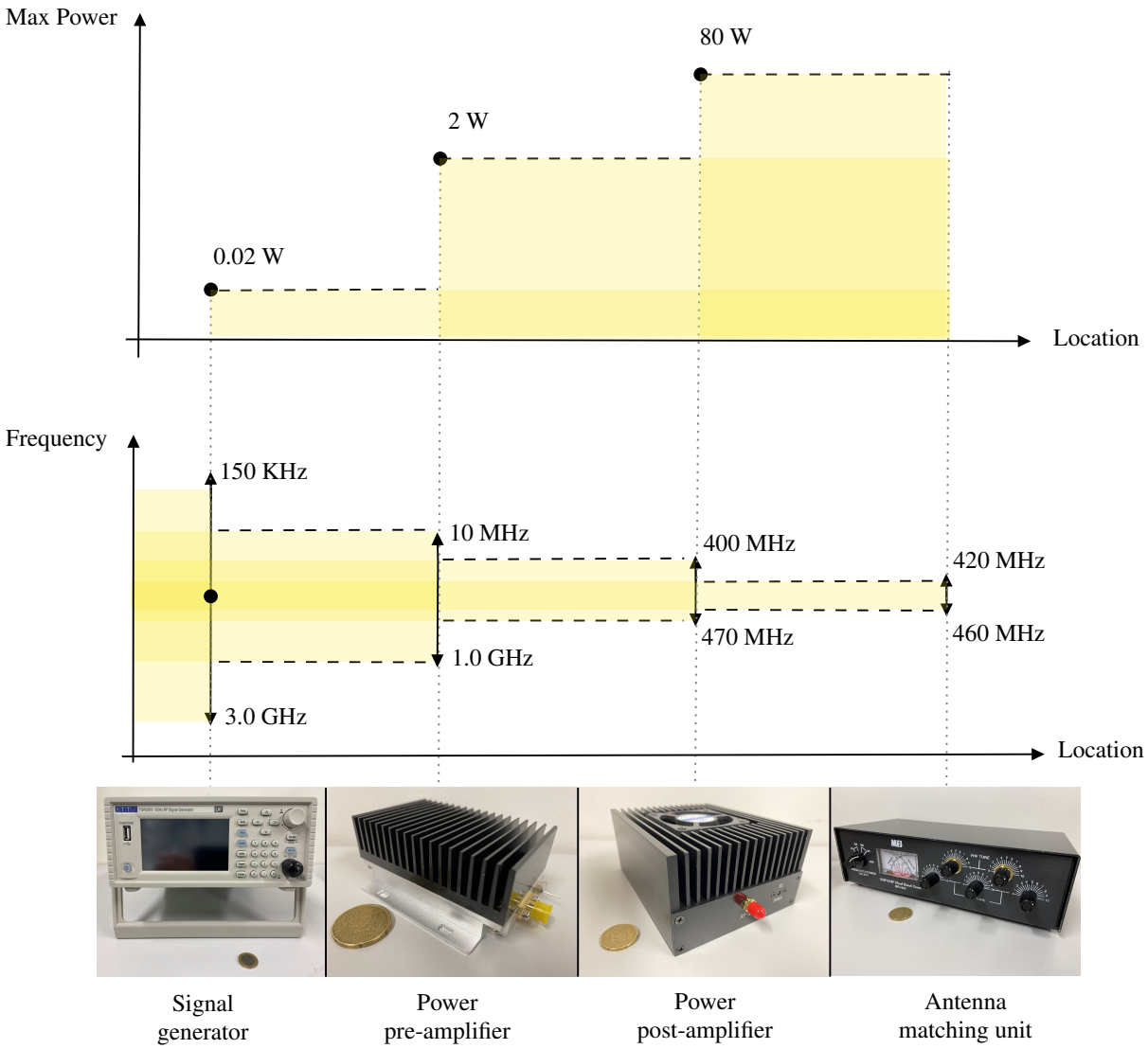


Figure 4.78: Frequency and power limits of the initial radiofrequency signal when it goes through the different components in the radiofrequency set-up, according to the manufacturer. A coin is used to show the relative size of the hardware.

After passing through the AMU and before entering the chamber's interior, a RF surge protector (element J) is integrated into the setup. This device does not correct any impedance mismatch but absorbs high-frequency peaks emanating from the thruster, which could cause substantial damage if they reached any device. In practice, the RF surge protector is utilised to safeguard antennas situated outside buildings from rays, a function that well aligns with the purposes of this experiment. It is important to note that not just the RF surge protector but none of this equipment is specifically designed for testing a plasma thruster. Most of it is used by radio amateurs in controlled environments. Hence, preserving their integrity is paramount to ensure the experiment's safety.

To power the components C, E and G, a 12 V DC power supply with a total power output of 400 W is employed (element D). Signal diagnostics are collected using an oscilloscope (element A), capable of simultaneously measuring up to four waves and characterising them in terms of RF voltage and frequency, but not power. One channel is dedicated to measuring the signal directly from the signal generator, while the second channel is utilised to measure the signal from the AMU using a high voltage differential probe, enclosed in a non-conductive bespoke metallic box (element I). This enclosure is essential to prevent any RF power leakage, which could pose a danger to individuals near the setup due to any potential mismatch between the probe connection and the wave.

A coaxial feedthrough from the RF surge protector establishes a connection between the interior of the vacuum chamber and the RF wave. Subsequently, the RF wave is directed into the thruster. Previous investigations (Section 3.2.1.8) suggested that applying an oscillating RF voltage at the cathode ground was the most practical choice in terms of simplicity and efficiency. Consequently, the computational studies (Section 3.2.2.3) focused on varying the cathode ground potential at the appropriate frequency. Therefore, this is the approach implemented in the experimental part of this activity (see Figure 4.79a). To excite the thruster using this technique, a T-junction is established between the RF signal, the cathode ground, and the chamber ground (Figure 4.79b). Using this configuration, the characteristics of the wave without plasma were measured. The AMU adjusts the wave to optimise forward power (Figure 4.79c), while the oscilloscope and high voltage differential probe are temporarily connected inside the chamber to gather information about the wave directly from the cathode ground return (Figure 4.79d). The comparison of the signals measured at the exit of the AMU and at the cathode ground is illustrated in Figure 4.80.

From these measurements, it is observed that the signal is attenuated from the AMU to the cathode ground, decreasing from an initial voltage of 38 V to 9 V. This attenuation is due to various factors, including inherent losses when an RF signal travels through a coaxial cable, losses during the connection of the RF surge protector, the coaxial vacuum feedthrough, and the connection to the cathode itself. This underscores the necessity of the post-amplifier in the setup.

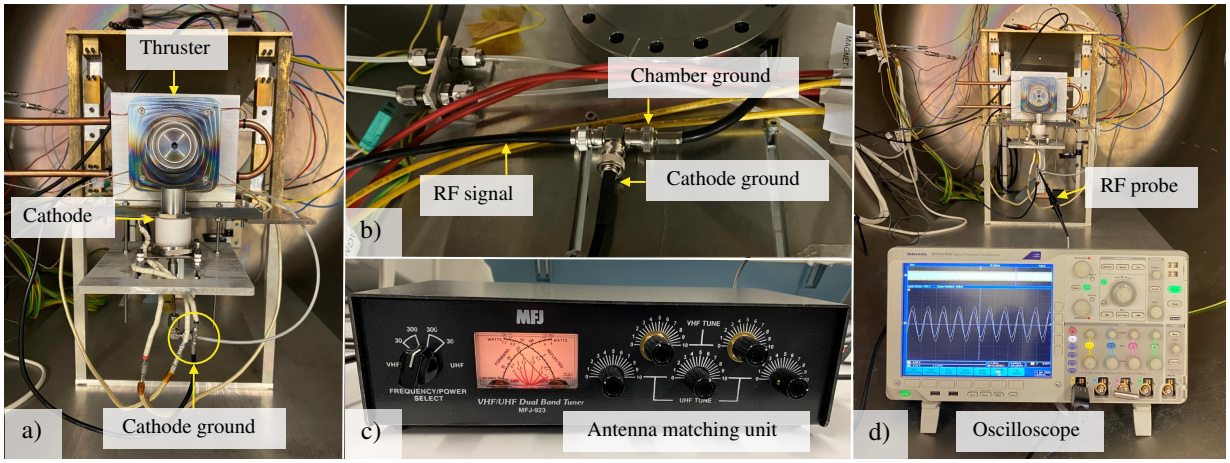


Figure 4.79: Details of the connection between the cathode and the radiofrequency equipment.

The measurements of power and voltage at the AMU exit (both being direct measurements), and voltage and power at the cathode ground (direct and estimated measurements, respectively) for different initial power levels of a signal with a frequency of $f_{\mathrm{RF}} = 470$ MHz are compiled in Table 4.26.

The power at the cathode ground is derived by extrapolating the relationship between RF voltage and power at the AMU exit. The computational studies of these waves also crosschecked this trend, which provided confidence in the reported values (see Figure 3.8b). Notice that, in this data collection, the plasma is inactive as the chamber must be open to position the oscilloscope and high voltage RF differential probe at the cathode. Routing these components outside the chamber and taking measurements there is unsuitable as they would not accurately capture the real signal but an attenuated version of it, as demonstrated in the attenuation seen in Figure 4.80.

Once all the setup is prepared, the thruster is ignited. Prior to excitation, stable ignition is ensured. Then, a small amount of RF power is applied to the system. This is achieved by setting the minimum power of the wave from the signal generator. This approach allows for tuning the signal using the AMU without encountering excessive reflected power. Only after the signal is tuned, the optimum power is applied. Table 4.27 compiles the forward and reflected power for various frequencies at the optimal tuning configuration achieved with the thruster running.

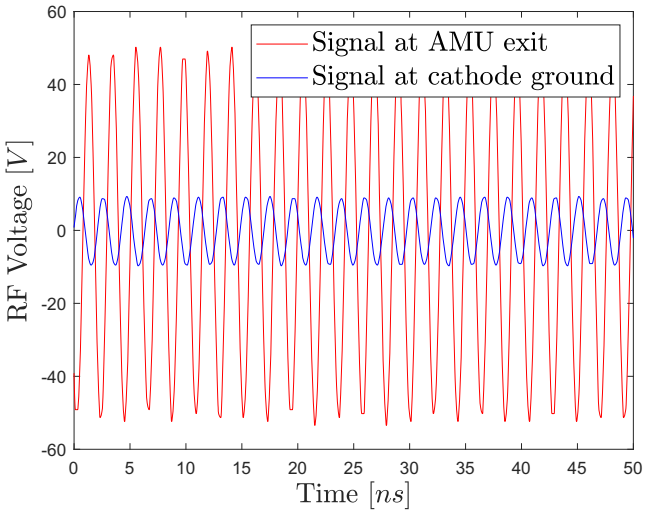


Figure 4.80: Measured radiofrequency signal at the exit of the Antenna Matching Unit (AMU) and at the cathode ground. The frequency of the signal excited was $f_{RF} = 470$ MHz. The thruster was not in operation during this data gathering.

Table 4.26: Measured radiofrequency power and radiofrequency voltage for the best tuned frequency ($f_{RF} = 470$ MHz) at two different locations of the circuit: exit of the Antenna Matching Unit (AMU) and at the cathode ground (plasma off).

Frequency [MHz]	**Measured Voltage at AMU Exit [V]**	**Measured Power at AMU Exit [W]**	**Measured Voltage at Cathode Ground [V]**	**Estimated Power at Cathode Ground [W]**
470	38	50	9	12
470	30	30	6	6
470	25	15	4	2

Table 4.27: Forward and reflected power depending on the frequency using the best tuning setting with the Antenna Matching Unit, AMU (plasma on).

Frequency [MHz]	**Max Power - Forward [W]**	**Max Power - Reflected [W]**
410	40.0	10.0
420	50.0	4.0
430	55.0	5.0
440	52.0	1.0
450	20.0	2.0
460	40.0	1.0
470	**60.0**	**0.5**
480	60.0	1.0
490	55.0	0.0
500	55.0	1.5
510	30.0	20.0

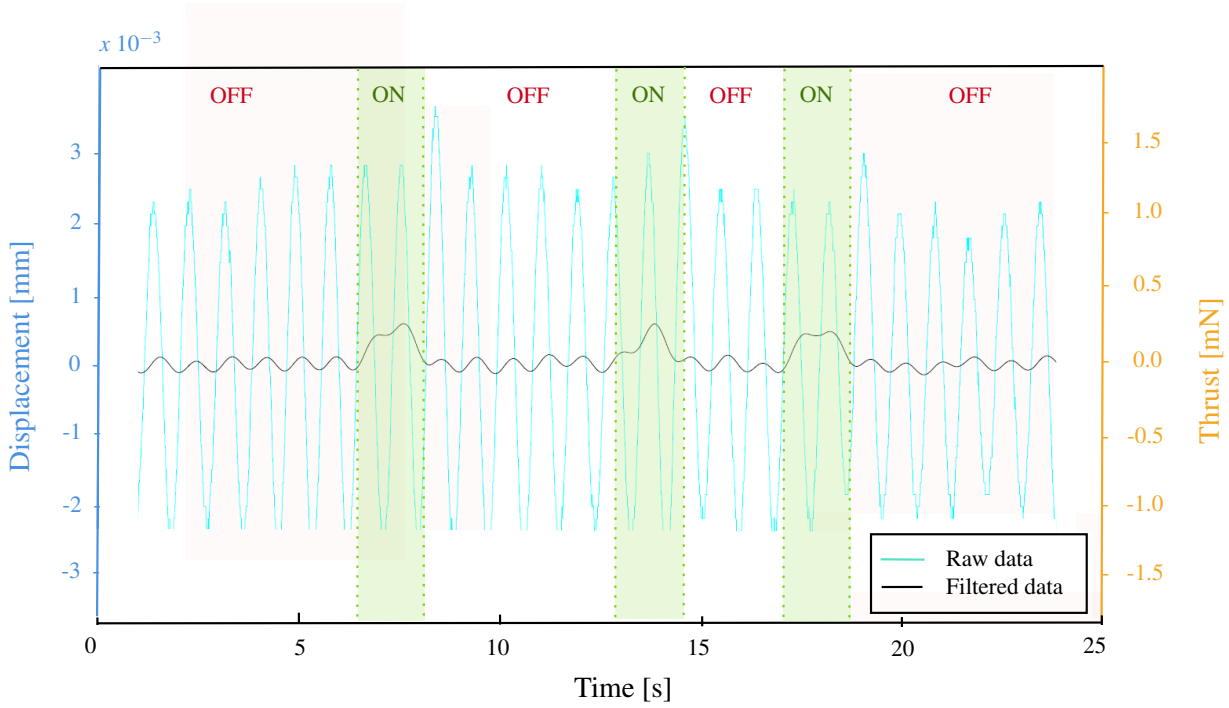


Figure 4.81: Measurements of the displacement of the thrust balance as recorded by the laser when the system is excited using radiofrequency waves versus no excitation. Example shown with the thruster *AQUAHET* propelled by krypton using a wave of frequency $f_{RF} = 470$ MHz with a power at the cathode ground of $P_{RF} = 12$ W. Radiofrequency interference between the equipment and the sensor was assessed and cross-checked to ensure it did not affect the results.

These results indicate that frequencies ranging between $f_{\mathrm{RF}} = 410$-510 MHz can be excited. Beyond the boundaries of that range, the reflected power becomes more pronounced. Therefore, no testing over these limits was performed. Based on the outcomes of this tuning procedure, a frequency of $f_{\mathrm{RF}} = 470$ MHz exhibited the best ratio of forward to reflected power and thus, was chosen for the experiments. Bearing this in mind, the magnetic field of the thrusters was adjusted, with the aid of the electromagnets, to attain a magnetic field capable of resonating at this frequency ($B = 0.0168$ T). Weaker and stronger magnetic fields were also configured to examine the relationship between the performance obtained and the resonance condition.

During the measurements, the laser displacement over time was recorded. Upon achieving stable ignition, the thruster underwent excitation with the RF wave, and the variations in the thrust balance displacement between the non-excited and excited states were measured. The absolute value of the measurement was also documented to provide comprehensive performance metrics. Figure 4.81 depicts an example of the thrust balance displacement with and without

RF excitation. These measurements pertain to the thruster *AQUAHET*, employing a wave of frequency $f_{RF} = 470$ MHz with a power at the cathode ground of $P_{RF} = 12$ W.

The results obtained are categorised into two sections based on the propellant utilised: its selection, whether noble gases (xenon/krypton) or oxygen, appeared to influence the thruster's performance differences with RF excitation. Section 4.7.2.1 presents the results using noble gases (xenon and krypton) for both Gaussian and constant magnetic fields, while Section 4.7.2.2 explores the same for oxygen. In all of these experiments, krypton served as the cathode propellant.

4.7.2 Results and Discussion

4.7.2.1 Noble Gases-fuelled HETs: Xenon and Krypton

Figure 4.82 shows the thruster *AQUAHET* firing with and without RF excitation using krypton as a propellant. When excited, the plume was more luminous and discernible to the naked eye. Note that the striped patterns are merely a camera artifact. Figure 4.83 presents the thruster *WET-HET* operating with xenon, showing both side and front views. Note that the investigation of RF excitation in a HET is divided into two different parts. First, the performance evaluation with and without RF excitation using a Gaussian magnetic field (Figures 4.75a and 4.75b) is presented. Secondly, it is investigated how these waves affect the performance of a HET when using a constant magnetic field (Figure 4.75c).

Gaussian Magnetic Field

The results provided here correspond to the thruster *AQUAHET* propelled by krypton using the Gaussian magnetic field topology depicted in Figure 4.75a. Notice however, that akin conclusions can be inferred using xenon as a propellant or when evaluating the thruster *WET-HET* in the same descriptions as commented here. Due to the previous analysis on the system's capability to induce a wave with the maximum forward power and minimal reflected power, a frequency of $f_{RF} = 470$ MHz is employed. Correspondingly, a magnetic field with a peak strength of $B = 0.0168$ T is selected to instigate an ECR phenomenon.

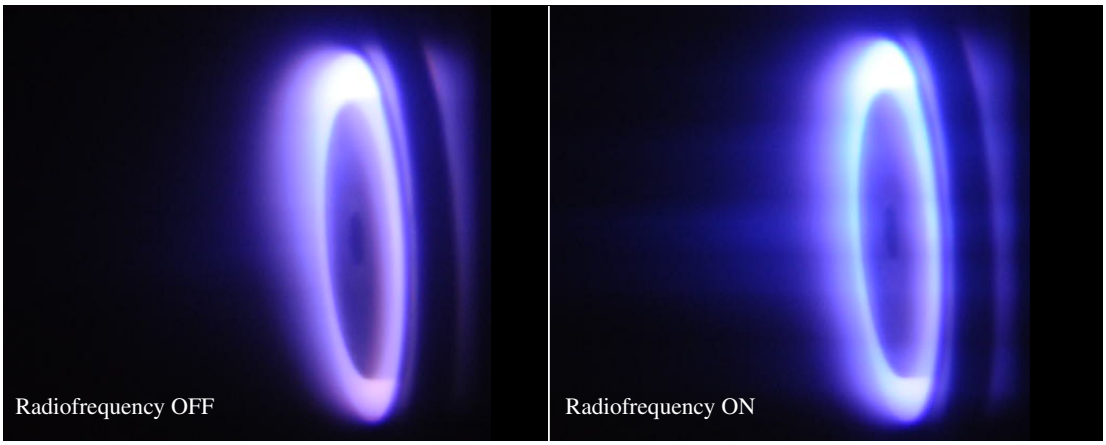


Figure 4.82: Thruster *AQUAHET* propelled by xenon with and without radiofrequency excitation.

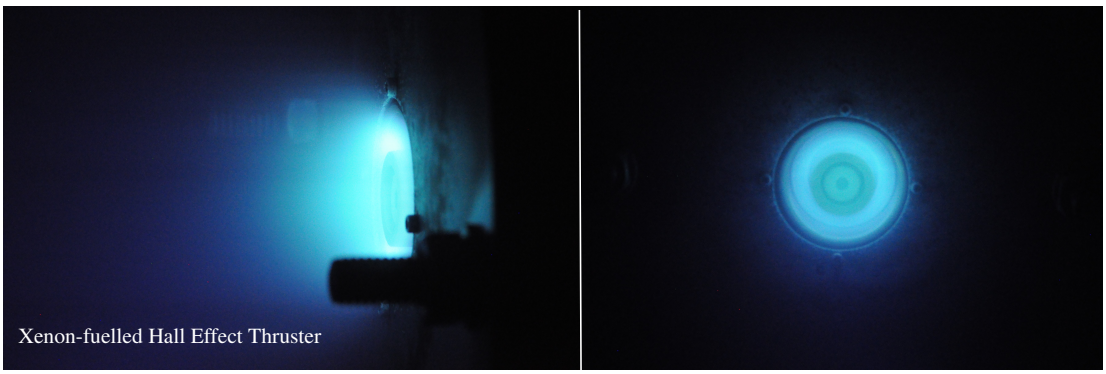
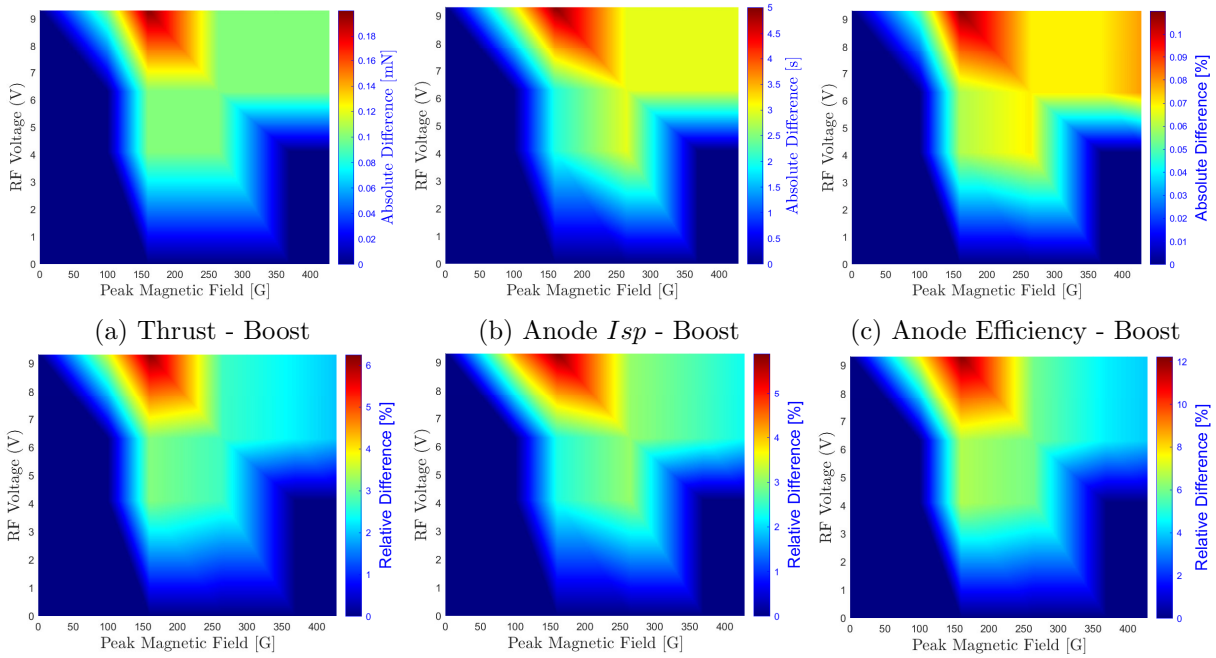


Figure 4.83: Thruster *WET-HET* propelled by xenon with radiofrequency excitation.

Various voltages and powers of the wave were assessed according to Table 4.26 to evaluate the system's performance under different configurations. Similarly, alterations in magnetic field strength below and above the resonance condition of $B = 0.0168$ T were made to mimic frequency adjustments of the wave.

As previously mentioned, the displacements of the thrust balance laser were recorded (as depicted in Figure 4.81) to ascertain the difference in performance and absolute values.

Figure 4.84 examines the absolute and relative difference in thrust, anode specific impulse, and anode thrust efficiency of the thruster across various conditions of RF voltage and peak magnetic field. The results without RF excitation are taken as the baseline for comparison. The results for various RF voltages at the magnetic field strength peaking at B = 0.0168 T with a wave frequency of $f_{RF} = 470$ MHz are tabulated in Table 4.28. The outcomes demonstrate an efficiency enhancement contingent upon two factors: the strength of the wave and magnetic flux density.



(a) Thrust - Boost (b) Anode Isp - Boost (c) Anode Efficiency - Boost

(d) Thrust - Rel. Diff. (e) Anode Isp - Rel. Diff. (f) Anode Efficiency - Rel. Diff.

Figure 4.84: Experimental measurements of the thruster *AQUAHET* fuelled by krypton and the cathode using krypton as well, under radiofrequency excitation ($f_{RF} = 470$ MHz) and employing a Gaussian magnetic field topology (Figure 4.75a).

Table 4.28: Performance comparison of the thruster *AQUAHET* with a Gaussian magnetic field peaking at B = 0.0168 T (Figure 4.75a) with and without radiofrequency excitation. These measurements correspond to a discharge voltage of $V_d = 58$ V, an anode mass flow of $\dot{m}_a = 3.8$ mg/s of krypton and $f_{RF} = 470$ MHz. A detailed analysis is graphically shown in Figure 4.84.

Excitation	**RF Voltage [V]**	**RF Power [W]**	**Discharge Power [W]**	**Thrust [mN]**
OFF	-	-	146	3.2 [Ref]
ON	4.1	2.5	146	3.3 [+3.1%]
ON	6.3	6.3	146	3.3[+3.1%]
ON	9.4	12.3	146	3.4 [+4.3%]

More in detail, it can be observed that for lower RF powers (approximately below $P_{RF} <$ 2.5 W), there is no discernible difference in the usage or not of RF excitation. However, as the power of the RF wave escalates, so does the performance boost obtained.

The computational studies indicated that waves with an RF voltage of $V_{RF} = 10$ V produced the most optimum results (see Section 3.2.2.3). Here, the maximum voltage tested was $V_{RF} =$ 9.35 V, closely aligned with computational suggestions. Higher voltages could not be tested due to the power constraints of the setup (see Section 4.77).

Looking closely at the magnetic field strength, the most optimal configuration is achieved

when the peak magnetic field aligns with the ECR condition (in this instance, B= 0.0168 T). Lower-intensity magnetic fields did not enhance the system's performance. Conversely, for stronger magnetic field intensities, there is an incremental performance improvement, albeit not as pronounced as with B = 0.0168 T. This is postulated to be attributed to the resonances of the Bernstein modes at the ECR condition and upper harmonics [68]. Consequently, although to a lesser extent, they still contribute to performance enhancement.

Overall, the performance using RF excitation demonstrates an improvement in the thrust total. Moreover, due to the fact that the power of the RF wave is relatively modest (up to $P_{RF} = 12.3$ W) compared to the discharge power ($P_d = 146$ W), and also the performance difference in thrust when the wave is active, an improvement in the total thrust efficiency is obtained. In the best scenario found, the relative improvement in thrust is around $\Delta T = 4\%$ (corresponding to an increase of $\Delta T = 0.2$ mN, see Figure 4.81), in anode specific impulse around $\Delta I_{sp} = 6\%$, in anode thrust efficiency $\Delta\eta_{tr} = 12\%$ and in total thrust efficiency around $\Delta\eta_{tot} = 11\%$. This is also a consequence coming from the fact that, when the RF wave is active, the changes in the discharge power are not significant. At the most, it is possible to see in increase up to $\Delta V_d = +3$ V in the anode power supply. That means that the total discharge power remains practically unaltered. This test case correspond to the firing of Figure 4.82 where it could be observed that the discharge gets brighter when the excitation is active in the most optimum excitation conditions.

Nevertheless, it should be noted that the relative performance depends on the absolute value of the thrust obtained. In these tests, the absolute performance of the thruster is very small ($\Delta\eta_{tot} \approx 1$ %). This is due to different factors: the two thrusters tested (*AQUAHET* and *WET-HET*) are optimised to operate with water as a propellant and not noble gases. HETs operating on gases which they have not being designed for is not ideal as they offer low efficiency values [44]. During these tests, the discharge voltage obtained ($V_d = 58$ V) is very small, and so is the ionisation efficiency. It is feasible to augment the discharge voltage by employing a reduced mass flow rate (in these tests, $\dot{m}_a = 3.8$ mg/s). Previous research on these thrusters fuelled by oxygen (Sections 4.2 and 4.4) has demonstrated that their performance scales with discharge power, but

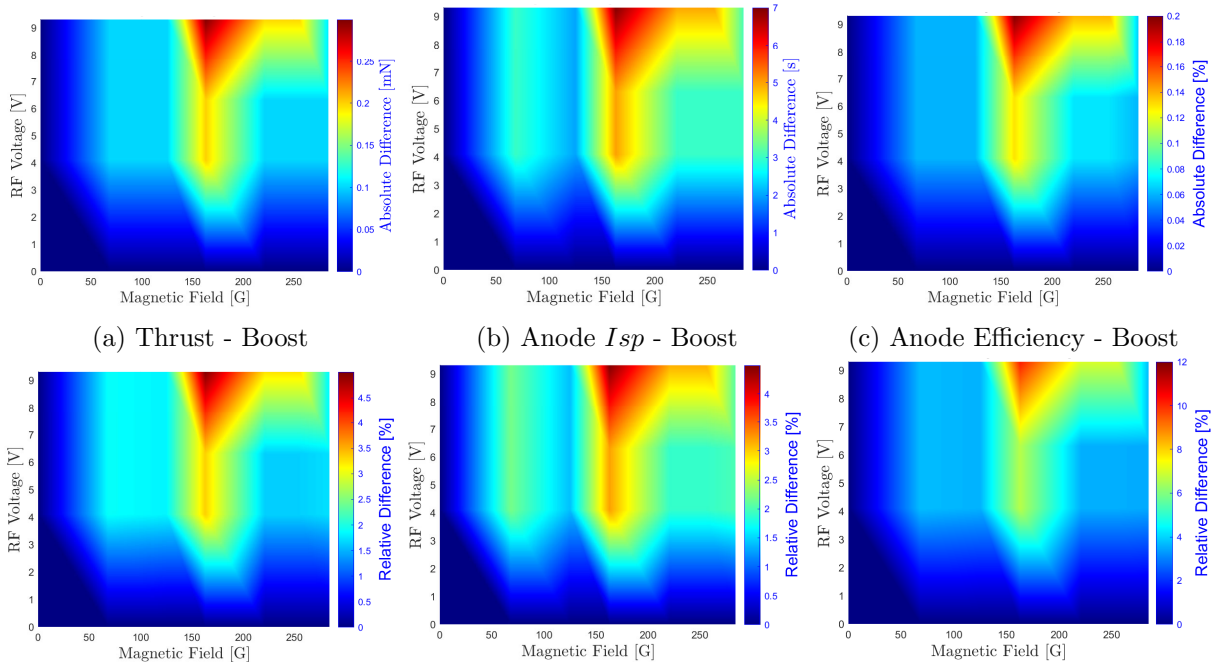
they exhibit suboptimal performance at low discharge powers ($P_d < 500$ W) [5, 4]. Nevertheless, as explained in Section 4.7.1.1, it was essential to conduct testing at these low power levels to discern the performance variations when employing the RF wave. As a consequence, the performance enhancement with RF excitation could not be evaluated for larger thrust measurements, where the total efficiency of the system could be representative of the state-of-the-art of these devices.

Constant Magnetic Field

This section evaluates the performance of the system with and without RF excitation under a constant magnetic field (Figure 4.75c). The findings herein pertain to the thruster *WET-HET* using xenon as a propellant (Figure 4.83), which is the only one of the two thrusters whose magnetic field topology can be customised. The results are shown in Figure 4.85 and tabulated in Table 4.29.

Similarly as when using a Gaussian magnetic field, the results reveal variations in performance enhancement concerning RF voltage and the constant magnetic field strength. For low RF powers (roughly below $P_{RF} < 2.5$ W) and magnetic field strengths lower than the resonance condition ($B < 0.0168$ T), no noticeable performance variation is evident. Conversely, at the resonance condition, a discernible performance enhancement is observed. Compared to using a Gaussian magnetic field topology, employing a constant profile localises the enhancement more prominently at the resonance location. Nevertheless, higher harmonics of the ECR still induce a performance boost, albeit less pronounced.

In absolute terms, the thrust variation is higher, $\Delta T = 0.3$ mN in the optimal scenario (compared to the previous $\Delta T = 0.2$ mN enhancement). Notice however, that the relative percentage increase depends on the absolute thrust measurement values. For these tests utilising a different engine and propellant (xenon), thrust values ranged around T = 7 mN (compared to the previous T = 3 mN overall thrust). Hence, while the relative performance increment remains positive, it is not as substantial as before ($\Delta T = 4\%$, $\Delta I_{sp} = 4\%$, $\Delta \eta_{tr} = 9\%$, and $\Delta \eta_{tot} = 8\%$).



(a) Thrust - Boost (b) Anode Isp - Boost (c) Anode Efficiency - Boost

(d) Thrust - Rel. Diff. (e) Anode Isp - Rel. Diff. (f) Anode Efficiency - Rel. Diff.

Figure 4.85: Experimental measurements of the thruster *WET-HET* fuelled by xenon and cathode fuelled by krypton, under radiofrequency excitation (f_{RF} = 470 MHz) and using a constant magnetic field (Figure 4.75c).

Table 4.29: Performance comparison of the thruster *WET-HET* with a constant magnetic field of strength B = 0.0168 T (Figure 4.75c) with and without radiofrequency excitation. These measurements correspond to a discharge voltage of $V_d = 51$ V, an anode mass flow of $\dot{m}_a = 3.9$ mg/s of xenon and $f_{RF} = 470$ MHz. A detailed analysis is graphically shown in Figure 4.85.

Excitation	**RF Voltage [V]**	**RF Power [W]**	**Discharge Power [W]**	**Thrust [mN]**
OFF	-	-	320	7.0 [Ref]
ON	4.1	2.5	320	7.1 [+1.4%]
ON	6.3	6.3	320	7.2 [+2.9%]
ON	9.4	12.3	320	7.3 [+4.3%]

In general, these experiments using noble gases demonstrate an increase in performance with RF excitation, also observable in the thruster discharge (Figure 4.82) and in thrust balance displacement (Figure 4.81). Power supply readings remained largely unchanged, with minor variations of $\Delta V_d = +1 - 3$ V under optimal excitation conditions. Thrust variation ranged from $\Delta T = 0.1 - 0.3$ mN, which may not be significant for larger thrusters with thrust levels exceeding T = 50 mN but becomes meaningful if unexcited thrust falls below T = 10 mN. Measuring thrust within this range was also essential to accurately discern differences between excited and non-excited conditions using the thrust balance apparatus available in the laboratory.

The performance difference with a constant magnetic field is more pronounced at the resonance condition, accompanied by a slight improvement in overall thrust (ΔT = 0.3 mN versus ΔT = 0.2 mN). Higher RF power correlates with increased performance enhancement, with the best outcomes achieved at the maximum RF power tested (P_{RF} = 12.3 W). Further power escalation may yield even better performance, but constraints on system power capped the maximum total power at that value.

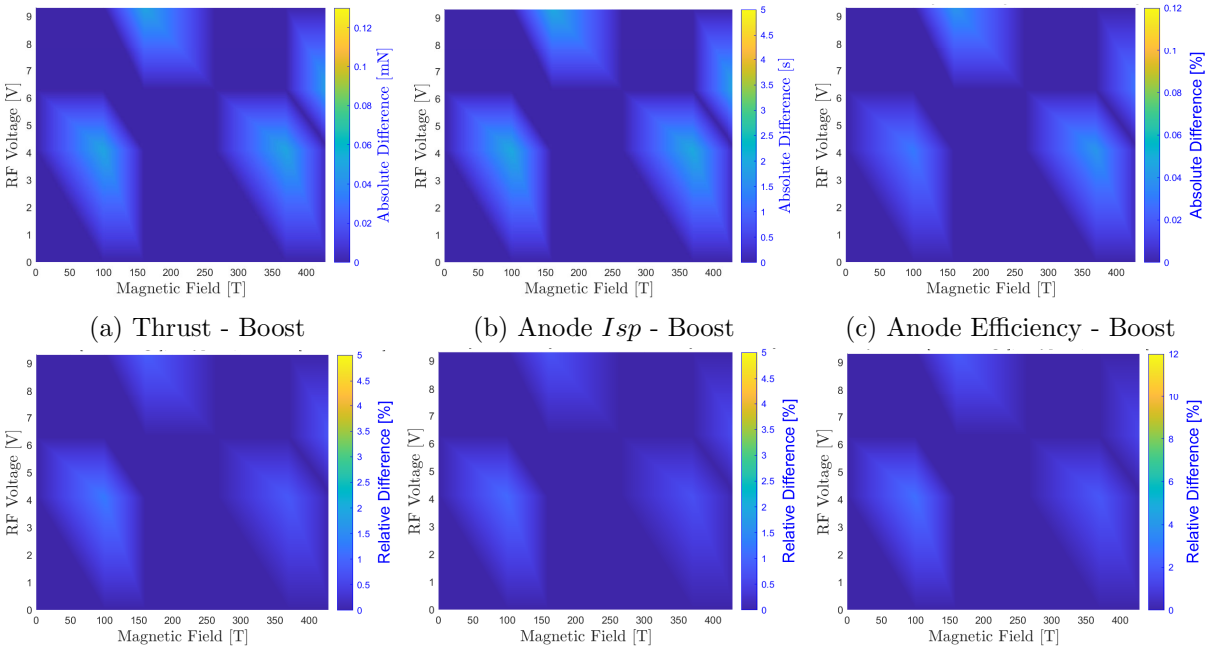
4.7.2.2 Oxygen-Fuelled HETs

This section endeavours to elaborate a quantitative analysis of the performance augmentation of the system employing oxygen as a propellant (intended to be the thruster propellant in water electrolysis propulsion) in a similar fashion as done before with the noble gases. The ensuing discussion elaborates on the findings obtained under both, Gaussian and constant magnetic field configurations, as the conclusions derived from both instances are congruent.

The outcomes are illustrated in Figure 4.86, showcasing the application of a constant magnetic field in the *WET-HET* thruster. From these results, it is seen that, irrespective of the RF voltage and magnetic field employed, no discernible variation in performance is observed. This trend mirrors the findings observed under a Gaussian magnetic field or with the *AQUAHET* thruster. To elucidate these outcomes further, the subsequent points are underscored:

As demonstrated in Section 4.2.2.4, when employing propellants such as oxygen or water vapour, the optimal magnetic field strength is notably higher (fourfold) than conventionally employed. For instance, in the case of the *WET-HET* thruster, the best performing magnetic field exhibits a Gaussian profile peaking at B = 0.06 T. To achieve a resonance condition at this level of magnetic field strength (B = 0.06 T), a corresponding wave of frequency f_{RF} = 1.68 GHz needs to be excited.

However, limitations in the bandwidth of the experimental setup preclude testing at this frequency (refer to Figure 4.78). Notably, the advantage of operating within the RF range of $f_{RF} = 400 - 500$ MHz lies in the availability of commercial equipment for testing:



(a) Thrust - Boost (b) Anode Isp - Boost (c) Anode Efficiency - Boost

(d) Thrust - Rel. Diff. (e) Anode Isp - Rel. Diff. (f) Anode Efficiency - Rel. Diff.

Figure 4.86: Experimental measurements of the thruster *WET-HET* fuelled by oxygen and krypton for the cathode, under radiofrequency excitation and employing a constant magnetic field (Figure 4.75c).

Radio amateurs utilise this frequency band for communication, facilitating access to commercially available equipment without necessitating bespoke hardware, thus mitigating costs.

Furthermore, it is imperative to note that the characteristics of waves are contingent upon frequency. Waves with higher frequencies could exhibit greater reflectivity and lower penetration depth compared to their lower frequency counterparts. Thus, an increase in frequency could potentially alter the propagation characteristics of the wave and subsequently its absorption by the plasma.

Notice however that it is plausible that performance differences exist when employing oxygen as a propellant but they are too subtle for the thrust balance to discern. As previously mentioned, the thrust balance is only capable of detecting thrust variations of $\Delta T = 0.1$ mN or higher within this range of thrust measurement.

Another point to remark is that, as this thesis has demonstrated, oxygen exhibits lower system performance compared to xenon or krypton. The lower performance could indicate that the potential performance enhancement of these systems is also constrained.

Finally, notice that the findings of the computational model utilising oxygen (Section 3.2.2.3) also indicated that the anticipated performance enhancement when employing oxygen was considerably smaller [6], thereby corroborating the findings delineated herein.

In summary, it is hypothesised that disparities in the optimal magnetic field strength with oxygen (approximately B = 0.06 T) and the corresponding resonance frequency (f_{RF} = 1.68 GHz), coupled with the frequency-dependent wave characteristics (higher potential reflectivity), lower overall performance of oxygen-fuelled HETs compared to xenon or krypton, and the additional reactions inherent to molecular propellants (dissociation, ion dissociation, and additional vibrational and excitation modes of species) could collectively have contributed to this scenario where the performance enhancements resulting from RF excitation under these conditions elude detection by the thrust balance.

4.7.2.3 Numerical Model and Experiments

As demonstrated throughout this section, the agreement between the numerical model elaborated in Section 3.2 and the experimental part of the activity is encouraging.

For noble gases, the results from *PlasmaSim* indicated that RF voltages of V_{RF} = 20 W, coupled with RF frequencies matching the ECR condition at the peak magnetic field strength of a Gaussian magnetic topology (f_{RF} = 450 MHz for B = 0.016 T), show a performance improvement in the overall efficiency of the system. The experimental results corroborated this trend, with excitations at a RF voltage of V_{RF} = 9.35 W and a frequency also matching the ECR condition at the peak magnetic field strength (f_{RF} = 470 MHz for B = 0.0168 T) demonstrating the best performance. This analysis also confirmed that higher harmonics of the ECR frequency, though to a lesser extent, still show a performance improvement, aligning with the computational model.

For oxygen tests, both the computational model and the experimental data agreed that there is a noticeable enhancement in performance when RF excitation is applied under the same conditions as with noble gases. The most plausible explanations for this phenomenon were discussed in Section 4.7.2.2.

Chapter 5

CONCLUSIONS

The field of EP is undergoing a transformative phase, marked by a notable uptick in the utilisation of alternative propellants. While the EP market has been historically dominated by xenon, the escalating cost and limited availability of this propellant have prompted a shift towards exploring alternative options within the community [2, 12]. This transition is further fuelled by the substantial growth in the number of satellites launched with EP systems, particularly HETs.

Amidst the quest for alternative propellants, water is conceived as a promising candidate owing to its cost-effectiveness, abundance within the solar system, and compatibility with other spacecraft subsystems such as life support and thermal cooling [2].

In this thesis, a computational and experimental characterisation of water-fuelled HETs in its two branches (water electrolysis and water vapour) has been addressed.

5.1 Computational Characterisation

Based on the baseline established by A. Schwertheim and A.Knoll, a computational code combining a 0D and 2D PIC formulation (referred to as *PlasmaSim*) was developed. The code demonstrated the capability to simulate both branches of water propulsion methods for HETs (specifically, the production of oxygen through water electrolysis and the utilisation of water vapour). To achieve this, reactions involving the primary diatomic species, namely O_2 and H_2O, as well as

reactions involving neutral products resulting from dissociation reactions (O, OH, H_2, H), were incorporated, together with its most relevant excitation events. The 0D model provided initial estimates to expedite the time advancement of the 2D model, facilitating the efficient resolution of plasma properties within the thruster channel. The combined use of these two models permitted the analysis of the plasma properties within the channel.

In the case of the simulated cases for water electrolysis propulsion, both the 0D and 2D models indicated that neutral (O_2 and O) and ion species (O_2^+ and O^+) were present in similar proportions, with double ions and negative ions being less significant. The 2D model corroborated the findings of the 0D model. Monoatomic O neutrals peaked in the channel centre due to reactive events occurring near the peak magnetic field. Conversely, O_2 neutrals peaked near the anode and decreased along the channel. O^+ ions had a higher velocity due to their lower mass compared to O_2^+ ions. Electron temperature peaked near the peak magnetic field. Excitation losses of O were significant, but the main power losses came from O_2 and O ionisation events.

For water vapour, the 0D model indicated that the neutral population was primarily composed of H particles, with OH, H, and O also significant, albeit to a lesser extent. However, H_2 particles had a much lower neutral density and, therefore, were not considered to accelerate convergence in the 2D model. For the simulated cases, the neutral and ion densities of double and negative ions were deemed negligible compared to the rest of species. The 2D model largely confirmed these findings, although it suggested that H^+ ions were more significant compared to the results predicted by the 0D model. Similar to water electrolysis, the neutral population peaked in the channel centre, alongside the associated ion number density. The propellant, H_2O, decreased along the channel from its maximum at the injection plane. Electron density distribution mirrored that of ions, with H^+ ions peaking near the channel exit, leading to a corresponding peak in electron density.

RF excitation was also studied with the developed computational code *PlasmaSim* to assess its influence on the performance of HETs. This investigation proposed a new performance enhancement method based on frequencies that were near to the ECR frequency and its harmonics up to

$f_{RF} \approx 2$ GHz. To excite them, the ground reference voltage of the neutralising cathode was varied sinusoidally, centred at 0 V, with an optimal amplitude of $V_{RF} = 10$ V corresponding to a RF power of approximately $P_{RF} = 20$ W. Results coming from *PlasmaSim* gave a deeper insight of the nature of these waves and the mechanisms in which energy is deposited into the plasma.

Firstly, unexcited simulations showed intrinsic resonances at the ECR frequency. Then, when excitation was introduced, a frequency-locking phenomenon in the magnetic field region was observed, which enlarged the absorptance region of the plasma wave. When comparing the dispersion relationship obtained from hot plasmas' theory against simulations, a very similar trend was obtained. There, an accumulation of interdependent harmonics was found, which was not predicted by theoretical models. From these results, the waves were classified as Zero-Velocity-Waves because of the flat dispersion relationship with finite phase velocity.

By introducing these waves into a xenon-fuelled HET (the *SPT-100*), a clear performance improvement of the thruster, particularly at the ECR frequency corresponding to the peak magnetic field strength within the channel ($f_{RF} = 450$ MHz with B = 0.016 T), was found. For this particular combination, thrust and specific impulse enhancement was shown to be $\Delta T = 15\%$ and $\Delta I_{sp} = 13\%$ respectively. Anode and total efficiency were reported to substantially increase, being $\Delta\eta_{tr} = 30\%$ and $\Delta\eta_{tot} = 28\%$ higher than the non-RF excited simulation results, respectively. However, such performance improvement was not observed in oxygen-fuelled HETs and experimental campaigns were established to further confirm these predictions.

5.2 Experimental Characterisation

The computational phase of the thesis followed multiple experimental campaigns over HETs. For that matter, a timeline was established to achieve the world's first successful end-to-end technological demonstration of HET directly fuelled by the byproducts of a water electrolyser (oxygen and hydrogen). Two different thrusters were tested: the first (*WET-HET*) and second (*AQUAHET*) generation of water electrolysis-fuelled HETs. The main difference between these

two thrusters relied on the mean channel diameter (20 mm for the *WET-HET* and 40 mm for the *AQUAHET*). The *AQUAHET* also featured a reduction of the non-radial magnetic field line components close to the thruster exit plane as compared to the *WET-HET*. Finally, while the *WET-HET* permitted studies with different channel lengths, the *AQUAHET* allowed changes between two different channel widths, in order to investigate the best possible geometry for these devices.

The first experiments were focused on the thruster fuelled by oxygen, while the cathode propellant selected was a noble gas (xenon or krypton), instead of hydrogen. This strategy permitted the initial exploration of the physics of the the thruster while alleviating the complexity of the experiment, as tests involving oxygen and hydrogen necessitated much more elaborate safety procedures. In this context, anode and ceramic walls material analysis, magnetic flux density, mass flow, changes in channel length and in channel width were investigated.

Anodes made out of different materials were tested when in contact with an oxygen plasma, for a power range up to $P_d = 2000$ W. Tungsten anodes, although thought to be a good choice due to its excellent thermal properties, were not compatible with this technology because of the non-conductive oxidation film formed after short duration tests. Stainless steel anodes however, developed a thinner oxidation layer which did not affect the functionality of the thruster and just limiting the duration of every experimental test.

Subsequent tests with different BN Grades: 1) Grade AX05, pure BN and 2) Grade M26, a compound of $BNSiO_2$: 60% BN and 40% SiO_2, ceramic walls concluded that these grades behave similarly with minor effects on the thruster performance. $BNSiO_2$ Grade M26 ceramic walls were then preferred because of their hydrophobic properties, which favour the use of moist gases coming from a water electrolyser.

Analyses over different magnetic currents in the *WET-HET* and *AQUAHET* indicated that a Gaussian magnetic field topology with a magnetic flux density stronger (between 3-4 times) than conventional xenon-fuelled HETs (such as the *SPT-100*) was optimum to achieve the best possible anode thrust efficiency. From a physical point of view, this is thought to be due to the fact

that stronger magnetic flux densities increase the energy of the electrons and increase the ratio of O_2^+/O^+ ions (hence, fostering ionisation reactions and diminishing dissociation reactions).

The most optimum oxygen mass flow determined for the thruster *WET-HET* was $\dot{m}_a$ = 1.0 mg/s. For the *AQUA-HET*, $\dot{m}_a$ = 1.7 mg/s showed the best results in terms of performance and plasma stability.

An extensive study on the most suitable channel length for oxygen in the thruster *WET-HET* concluded the most optimum length in terms of thrust efficiency: L = 13.1 mm. Longer channels did not increase the performance of the thruster, as previously theorised by other researchers [212]. Although the ionisation rate and propellant utilisation could augment with longer channels, the wall losses and current utilisation decrease. Studies on a shorter channel length (L = 5.5 mm), placed within the raising magnetic field location, showed differences in the IV curve and a worse overall performance compared to the best performing condition found (L = 13.1 mm). It is theorised that, with this shortest length, ions were produced within or downstream of the peak electric field region of the thruster, being not fully accelerated and therefore lowering the overall performance of the system. This depth also struggled with the thermal loads, as the surface volume is not large enough to accommodate and dissipate them properly. With the channel length of L = 13.1 mm the ionisation rate and wall losses seemed to be balanced with each other, ending up in the best thrust efficiency of all the others tested (ranging from $L = 5.5 - 59.8$ mm).

The second generation of water electrolysis-fuelled HETs (*AQUAHET*) offered the added flexibility to modify the channel width from w = 4 mm to w = 5 mm. For these studies, the most optimum channel length found (L = 13.1 mm) was used. The results demonstrated that a channel width of $w = 5$ mm outperformed $w = 4$ mm across the range of tested discharge powers (up to 3.2 kW). This observation aligns with previous findings [213] suggesting that a wider channel enables better ionisation, reduced wall losses due to a lower surface-to-volume ratio, and improved plasma confinement resulting from a stronger radial magnetic field at the walls.

When comparing both generations of water electrolysis HETs, although the *WET-HET* demonstrated higher anode specific impulse for powers $P_d > 1200$ W, the *AQUAHET* exhibited superior thrust

in the entirety of the power range investigated (up to $P_d = 3200$ W). Considering both factors, the *AQUAHET* boasted an average of $\Delta\eta_{tr} = 20\%$ better anode thrust efficiency than its predecessor. Because of its larger anode area, *AQUAHET* can accommodate a larger plasma volume with a lower surface-to-volume ratio of its discharge channel. This translates to reduced wall losses and improved propellant ionisation.

Finally, by using langmuir probes, ExB probes and a spectrometer, the plasma properties of these devices were measured (floating potential, plasma potential, electron temperature, plasma density and ions' plume composition) under different operating conditions.

Overall, the best performance obtained for the *WET-HET* was achieved at a discharge power of $P_d = 2232 \pm 1$ W, corresponding to a thrust of $T = 21.5 \pm 0.4$ mN, anode specific impulse of $I_{sp} = 3617 \pm 69$ s, and anode thrust efficiency of $\eta_{tr} = 17.1 \pm 0.7$ %. For the *AQUAHET*, the most optimum metrics were achieved at $P_d = 3200 \pm 1$ W, reporting a thrust of $T = 51.0 \pm 0.3$ mN, anode specific impulse of $I_{sp} = 3119 \pm 27$ s, and anode thrust efficiency of $\eta_{tr} = 24.4 \pm 0.3$ %.

The next set of tests corresponded to the first experimental demonstration of a HET running with the byproducts of water electrolysis (oxygen and hydrogen) from pressurised bottles. When comparing the system running with the products of water electrolysis (oxygen for the anode and hydrogen for the cathode both from pressurised bottles) versus using oxygen (anode) and krypton (cathode), the analyses reveled a marginal reduction in performance, approximately $\Delta\eta_{tr} = 10\%$, for a fixed operating point of power and mass flow. The reduction in performance can be attributed to several factors. Firstly, it can be due to the decreased efficiency of the cathode when operating with hydrogen as the propellant: since hydrogen has a larger ionisation potential (including dissociation losses), the voltage drop at the cathode sheath can be larger. Therefore, the ions produced by the thruster see a lower acceleration potential, which may translate into slightly less thrust and specific impulse. Secondly, when heavier propellants like xenon or krypton are used, a portion of the gas is emitted from the cathode and undergoes ionisation. This ionised plasma is then accelerated within the thruster's plume, leading to increased thrust. In contrast, when hydrogen, a significantly lighter molecule, is used, the contribution to thrust from this process

becomes less significant, resulting in only a marginal improvement in performance due to the cathode propellant.

To assess the potential impact of deviations from the stoichiometric hydrogen-oxygen ratio (Φ = 1:8), various mixtures were examined, with the findings suggesting that alterations in Φ do not influence the thruster performance. Consequently, it becomes plausible to consider ratios such as Φ = 1:25, allocating the surplus hydrogen for alternative applications within the spacecraft, such as a cold gas system. However, it is important to note that these low mass flow rates can have implications on the cathode lifetime, and longer duration tests should be carried out to check the real viability of these cathode mass flow rates.

Lastly, an important observation pertained to the susceptibility of hardware to oxidation in the presence of an oxygen-hydrogen plasma, which was found to be more pronounced when compared to the presence of an oxygen-krypton plasma. This discrepancy was attributed to the catalytic effect of hydrogen on the oxidation process, particularly on stainless steel surfaces.

Finally, an end-to-end technological validation of water electrolysis fuelled by products of water electrolysis (oxygen and hydrogen) directly produced by a water electrolyser was conducted at the European Space Agency facilities. In these tests, it was demonstrated that the technology can successfully function under these conditions.

During this technology's validation, the water electrolyser operated under varied power conditions, allowing for diverse mass flows to the thruster and cathode, achieving up to $\dot{m}_a$ = 1.6 mg/s of oxygen and $\dot{m}_c$ = 0.2 mg/s of hydrogen under steady-state conditions. The predominant power consumption by the water electrolyser was directed towards heating, essential to maintain a temperature of 70 °C for optimal mass flow output. Despite the design of the water electrolyser not being optimised to minimise the power consumption, the total power needed for the water electrolyser to run was calculated to correspond to just 8% of the total system power. The most significant portion of the total system power (83%) was attributed to the anode discharge power. Overall, this bodes well for the technology, as the power overheads for incorporating a water electrolyser onboard spacecraft constitute only a fraction of the overall power requirement.

This consideration, together with other distinctive attributes of water, such as its potential for integrating both a CP and EP system, prospects for ISRU, synergies with astronaut life support systems, thermal cooling capabilities, cost-effectiveness, and environmental friendliness, position water as a highly promising candidate to fuel HETs for medium to long-duration space missions.

In parallel of these activities, water vapour-fuelled HETs were tested and compared to water electrolysis-fuelled HETs.

For that purpose, a bespoke water feed system was used to allow for a liquid-vapour phase change and subsequently fuel the thruster. A liquid mass flow meter set the operating point, and, downstream, a capillary tube was used to increase the fluidic resistance of water and create a sudden expansion at the end of the tube; which ultimately caused the evaporation of water. A heating system was employed to raise the temperature of the pipelines and prevent water condensation. By means of a pressure transducer, the pressure of the line was monitored to determine if water condensation had occurred. Following an analysis of the pipe losses using the Darcy-Weisbach equation, the total length of the line was reduced and the diameter of the pipe thickened, reducing pressure losses throughout the line from the thruster exit to the flow restrictor. After these iterations on the water feedline, mass flows below $\dot{m}_a < 2$ mg/s could be used without condensation.

The experimental campaigns investigated the *WET-HET* under the mass flow range of $\dot{m}_a = 0.7 - 1.0$ mg/s. From these results, it is observed that although by using a lower mass flow the thrust is reduced, the thrust efficiency is higher. However, when conducting a trade-off between performance and stability, a mass flow of $\dot{m}_a = 1.0$ mg/s was preferable, coinciding with the results obtained with water electrolysis. Experimental results in this operating point analysed the performance of the thruster under different magnetic fields strengths up to four times stronger than typical HETs. A Gaussian magnetic field topology peaking at $B = 0.061$ T was the most beneficial one in terms of thrust efficiency, once again matching the best operating conditions for water electrolysis propulsion.

By looking at the reactive model of these two molecules, a poorer performance for water vapour was predicted. This was thought to be because, in the case of water vapour, the cross-

section of the OH dissociative reaction (H_2O + e $\rightarrow$ OH + H + e) is higher than any ionisation process. The energy used when dissociating the molecule does not contribute to the thrust as it does not generate ions, and therefore, it is an energy loss in the system. In the case of oxygen, the opposite situation is found: for most of the electron energies, the ionising reaction O_2^+ is more statistically more probable than the dissociating one. The experiments conducted with both propellants under the same thruster and operating conditions ratified this prediction, showing the oxygen is approximately $\Delta\eta_{tr} = 20\%$ more efficient than water vapour.

On the basis of these results, a representative trade-off analysis between water vapour and water electrolysis propulsion was conducted. Performance, cathode compatibility, mass, volume and power budgets were the factors selected to make this comparison. The mass and volume budgets of water vapour are less than those with water electrolysis, merely because of the lack of an electrolyser onboard of the spacecraft. In terms of the power requirements, although both technologies need extra power to accommodate a heating system and/or an electrolyser, these requirements are not significant compared to the discharge power of the thruster. All in all, the type of space mission and its requirements will ultimately decide which propulsion technology is the most favorable.

Finally, campaigns involving RF-excited HETs were conducted. A RF set-up was designed, implemented, tuned, and tested in conjunction with two HETs to delineate differences in performance ensuing from the introduction of the excited wave into the system. The setup comprised a signal generator, two power amplifiers, a RF isolator, an AMU, a RF surge protector, and various diagnostic apparatuses to assess the frequency and power of the induced waves.

The resonance condition for these waves was identified at the ECR frequency and upper harmonics [67, 68]. Consequently, to achieve resonance, either the magnetic field intensity or the frequency could be adjusted, or both. The magnetic field strength of the tested thrusters (*AQUAHET* and *WET-HET*) could be easily modified by selecting a different current to energise the electromagnets. However, regarding frequency, there are more stringent constraints due to the bandwidth limitations of the hardware. Thus, various ECR conditions were explored by altering

the magnetic field intensity while keeping the frequency constant.

To determine the optimal frequency for excitation, computational studies suggested that a frequency matching the peak magnetic field intensity (f_{RF} = 450 MHz and B = 0.016 T for the *SPT-100* thruster) with a cathode ground oscillating voltage of V_{RF} = 10 V yielded the most advantageous results in terms of overall performance enhancement. Following this research, and considering the wave frequency that enabled the maximum forward power (60.0 W) with minimal reflection (0.5 W) with the optimal tuning configuration provided by the AMU, a frequency of f_{RF} = 470 MHz and V_{RF} = 9.35 V, corresponding to a magnetic field intensity of B = 0.0168 T, was employed for experimentation.

Under these conditions, various RF powers and magnetic field strengths around the theorised ECR condition were investigated using noble gases (xenon and krypton) as well as oxygen. For the noble gas tests, wave excitation was observed to enhance thrust up to ΔT = 0.3 mN, thereby improving the total system efficiency up to $\Delta\eta_{tot}$ = 12%. The results either using a Gaussian magnetic field or a constant one were very similar. However, the measurements were conducted at a very low discharge power level ($P_d < 320$ W) to precisely measure the influence of RF excitation on the system using the thrust balance instrumentation of the Imperial Plasma Propulsion Laboratory.

Conversely, the results with oxygen showed no discernible effect on thrust, irrespective of the magnetic field strength or the RF wave intensity. This phenomenon was attributed to the nature of oxygen-fuelled HETs, wherein the optimal magnetic fields are four times stronger than standard HETs (B = 0.016 T for the *SPT-100*) [4, 143, 144]. To achieve wave matching under these conditions, the frequency would need to be on the order of f_{RF} = 1.68 GHz. Such frequencies were beyond the scope of this research, as they necessitate a separate bespoke setup to manage this frequency range. Notice however, that the characteristics of the waves are frequency-dependent, and it is plausible that due to the higher frequency of these waves, absorption may not be as pronounced as with the f_{RF} = 470 MHz wave. Additionally, the different dissociation processes and more intricate excitation and vibration modes could have influenced wave absorption to the extent that the thrust balance was unable to detect changes in thrust when using oxygen.

Chapter 6

FUTURE WORK

This chapter reflects and discusses the future work of this technology, leveraging the lessons learnt from this PhD thesis.

6.1 Computational Characterisation

From a computational perspective, a new model (*PlasmaSim*) combining 0D and 2D PIC code formulations has been developed. Although the code in its current state is, to the author's knowledge, the most advanced for simulating the behaviour of water-fuelled HETs, there are modifications and improvements that can further enhance its fidelity:

- **Pseudo 3D formulation**. Thanks to the previously described pseudo-technique for solving Poisson's equation, a pseudo-3D formulation is conceivable. This would allow the complete resolution of the HET physics in axial, radial, and azimuthal directions. Currently, full-3D simulations are not feasible due to the extensive computational resources required.

- **Experimental data correlation**. This thesis aimed to gather experimental data on water-fuelled HETs under various conditions of magnetic field, mass flow, discharge power, cathode propellant, geometry and RF excitation. Sections 4.2.2.9, 4.3.2.5, 4.6.2.4 and 4.7.2.3 demonstrated a strong correlation between the numerical code *PlasmaSim* and these experimental results. To further enhance confidence in the code, additional experiments and simulations

under various conditions should be performed, particularly for the case of water vapour propulsion. Through these efforts, it would be feasible to continue validating the code and refine its current formulation if necessary.

- **Parametric analyses**. In its current formulation, *PlasmaSim* can be a powerful tool for conducting systematic studies under various operating conditions. Specifically, these simulations can provide valuable insights before developing the "third generation of a water electrolysis-fuelled HET". Specifically, it is recommended to run simulations at high power with thrusters featuring larger channel mean diameters and widths than those tested here, while keeping the channel length fixed at the most optimal value found ($L = 13.1$ mm). In other words, simulating HETs with $w > 4$ mm, $d_m > 40$ mm, and $L = 13.1$ mm would be of high interest to further understand the performance limits of this technology.

- **Cylindrical coordinates formulation**. in the current state of *PlasmaSim*, the annular domain of a HET is unwrapped into a cubic domain, facilitating the use of Cartesian coordinates. One of the steps envisioned in the code is the use of cylindrical coordinates. This improvement can enhance the fidelity of the code by accelerating the electrons along a circular trajectory instead of in a straight domain, implying, for example, an intrinsic centrifugal acceleration.

- **RF excitation on water-fuelled HETs**. The computational code can also be used to enhance the current understanding of RF excitation in water-fuelled HETs. This thesis observed that RF excitation was beneficial for noble gas-fuelled HETs (xenon and krypton) but not for oxygen. Although different reasons on why this is the case were presented, it is possible to further improve the current understanding of this problem. For example, by running multiple simulations deactivating and activating reactions and physical properties while varying the RF frequency and voltage, more information could be obtained to understand why this is the case. To do so, the current formulation of the code should be expedited to enable these simulations to be run within a reasonable timescale.

6.2 Experimental Characterisation

Multiple experimental campaigns were conducted as part of this thesis to advance the state-of-the-art in water-fuelled HETs in both water electrolysis and water vapour formulations to the point that now this technology has been validated in laboratory conditions. The subsequent experimental campaigns are encouraged to achieve the ultimate goal: bringing this technology into orbit.

- **Development of "The Third Generation of a Water-Electrolysis-Fuelled HET"**.
  - **Design improvements**: Future thruster designs should address thermal management for longer duration tests. As shown in Figure 6.1, most heat is concentrated in the anode walls, especially during high power testing. By designing, constructing, and testing HETs with larger channel widths and mean diameters, thermal dissipation can be improved. Additionally, these geometrical changes could enhance the overall performance of the thruster, as discussed in Sections 4.2.2.7 and 4.2.2.8.
  - **Magnetic shielding**: According to the literature, this technique can significantly reduce the erosion of the acceleration channel (by at least a few orders of magnitude) in xenon-fuelled HETs [251, 252]. This could be of particular interest in oxygen-fuelled HETs, where not only the efficiency could be increased by reducing the electron impact on the walls but also the wall erosion when in contact with oxygen could be reduced. This is fundamental for space missions aiming to operate these thrusters continuously for hundreds of hours.
  - **Anode material**: While stainless steel anodes are suitable for laboratory testing (see Section 4.2.2.3), improvements are needed for in-orbit hardware. A coating layer made of chromium and rhodium is recommended due to their low oxidation rate at high temperatures [228, 253], which could solve the material compatibility issues of water-fuelled HETs.
  - **Life tests**: After addressing the aforementioned points, life tests should determine if

the hardware is ready for space deployment. These tests should aim to: check ceramic wall erosion, oxidation of metallic surfaces, control hardware temperature, and assess the potential use of hydrogen under stoichiometric ratios for other purposes (e.g., a cold gas system).

- **Water Vapour Propulsion**:
  - **Cathode Propellant for Water Vapour Propulsion**. While hydrogen as the cathode propellant for water electrolysis propulsion has been validated within this thesis, the choice for water vapour propulsion is less clear. Future tests should aim to identify the best cathode propellant for water vapour propulsion. For instance, water vapour could be used in cathodes that do not rely on emitters prone to oxidation (such as RF cathodes). Alternatively, other gases already onboard the spacecraft could be used for the cathode.
  - **Plasma Properties Characterisation of Water Vapour-Fuelled HETs**. Section 4.3 investigated the physics of oxygen-fuelled HETs. Similarly, research on the physics of water vapour-fuelled HETs would be highly beneficial to further understand this technology and correlate the data obtained with numerical models.
- **In-Orbit Demonstration**. This is the ultimate goal for this technology. If the investigations previously highlighted are successfully conducted, this technology should be ready to achieve a Technology Readiness Level (TRL) of 8-9 and serve as a commercial product for satellite manufacturers. For the industry, maturity, performance, and cost are crucial factors. If green propulsion and other significant issues such as space debris management are priorities, public funding is essential to support these activities. Only with sufficient public support can these products achieve the competitiveness needed to be considered for commercial satellite platforms.
- **RF Excitation**. Additional campaigns using higher RF excitation powers and frequencies are encouraged to better understand the absorption and potential benefits of this technique

in water-fuelled HETs. Concurrently, the use of diagnostic tools such as Langmuir probes could enhance the current understanding of this technique and further evaluate its suitability for space applications.

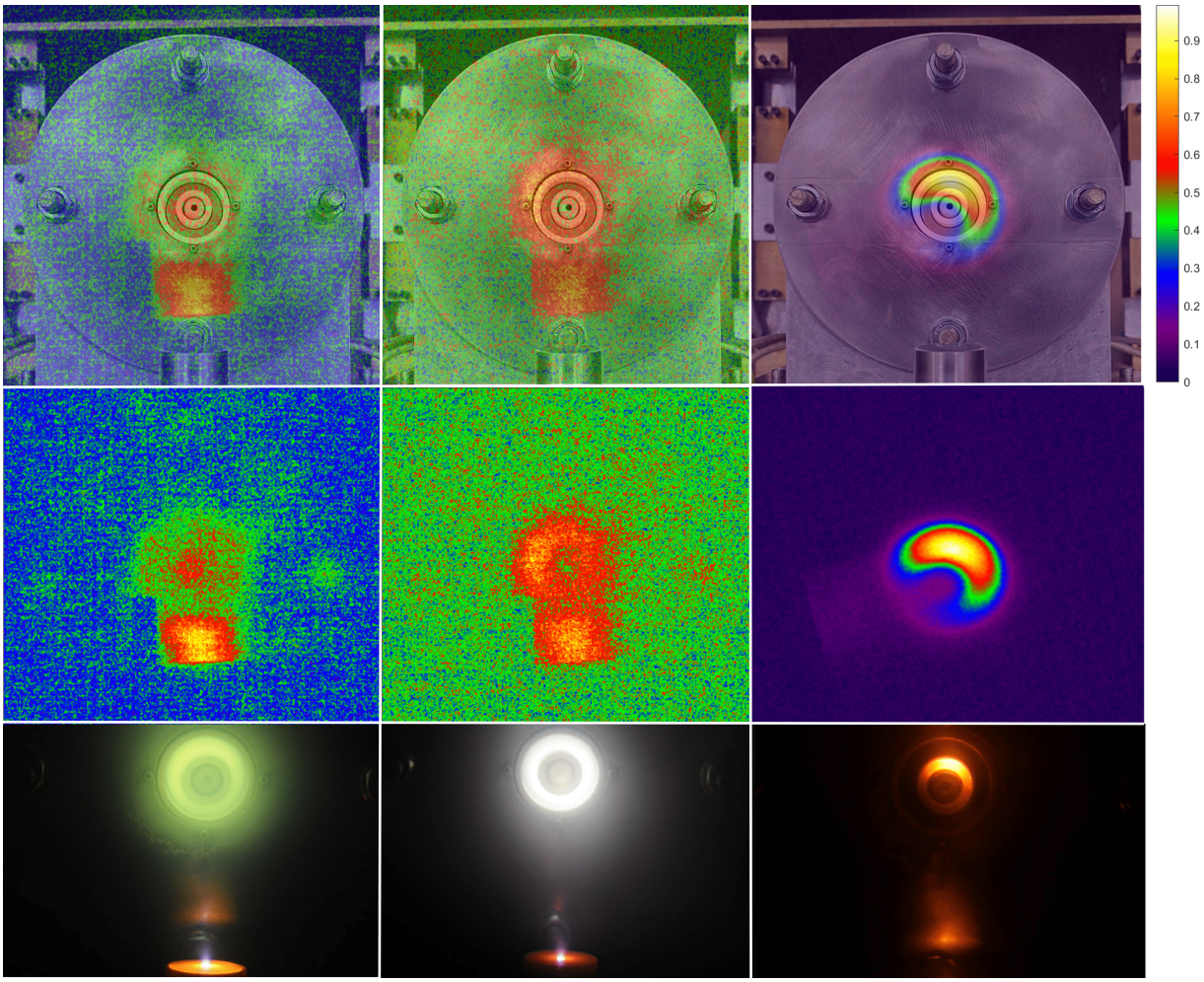


Figure 6.1: Adimensional temperature distribution of the thruster *WET-HET* under diverse operating points of power and magnetic field.

Appendix A

APPENDIX

A.1 Analysis of Strengths, Weaknesses, Opportunities and Threats (SWOT)

The Strengths, Weaknesses, Opportunities and Threats (SWOT) that a water electrolysis-based propulsion system presents are assessed. It is analysed how internal and external factors may be helpful or harmful to a spacecraft a water propulsion system. The SWOT analysis is graphically summarised in Table A.1.

Table A.1: SWOT matrix summarising the strengths, weaknesses, opportunities and threats one should consider when implementing a water propulsion system.

	Helpful	**Harmful**
Internal Origin	STRENGTHS: • Reduction of carbon footprint. • No dependence on toxic chemicals. • Multimodal propulsion capabilities. • System is highly modular. • Low cost.	WEAKNESSES: • Higher system complexity and single points of failure. • Possible reliance on other raw material. • Low thrust efficiency compared to xenon.
External Origin	OPPORTUNITIES: • Future ISRU potential. • Hyper flexible multi-modal missions. • Not vulnerable to xenon price volatility.	THREATS: • Not considering the environmental impact of today's space propulsion technologies (xenon, hydrazine). • Propulsion technology developed towards short-term applicability and revenue share rather than a sustainable and environmentally-friendly long-term vision.

A.1.1 Strengths

One of the strongest driving forces for a multi-mode water propulsion system is the ability to offer a more sustainable alternative to traditional hydrazine and xenon propellants. When switching to water as a propellant, less hydrazine and xenon needs to be manufactured, reducing the environmental impact of the spacecraft. Moreover, enabling multi-mode propulsion unlocks a new class of trajectories not possible with either subsystem alone. Also, replacing traditional batteries with regenerative fuel cells has been shown to reduce system mass greatly [254]. Different synergies can be achieved as explained in Section 2.2.2 by, for example, combing the electrolyser with a fuel cell system, such that hardware is shared between propulsion and energy storage subsystems and overall system mass is reduced. Although the greatest benefits arise when two propulsion systems and energy storage systems are combined, the systems themselves can be tested and qualified independently, opening up the potential for a range of different modular technologies.

A.1.2 Weaknesses

The more subsystems that are added to the unified water architecture (e.g., propulsion systems, energy storage systems, thermal management systems...), the more vulnerable the system becomes to a single point of failure. This means that a highly unified system such as this one must be designed with several redundancies to eliminate single point failure modes.

Moreover, the catalyst coated membranes required for electrolyser production depend on precious Platinum Group Metals (PGMs) such as platinum, ruthenium and iridium [255]. These metals are already very rare, and their price is expected to increase as investment in electrolysers for green hydrogen production increases [255]. However, it is important to note that the quantity of PGMs required to build even a high-power space electrolyser is on the order of grams. This cost is offset by no longer needing to purchase tens if not hundreds of kilograms of xenon or hydrazine. Xenon prices are highly volatile and increased by a factor of ten in less than eight years, to now costing upwards several thousand pounds per kilogram [133]. This volatility is in part due to the very

small volumes of xenon produced each year. The rate of this production cannot simply be increased with demand, due to being bottle-necked by the number of air separation units producing PKCs [256]. This means that the utilisation of xenon in other industries such as medicine [257] can have a huge impact on cost. Such volatility is not foreseen in the PGM market, where an increase in demand is met with an increase in supply [255].

Finally, although the specific impulse of water-fuelled HETs has been shown to be higher to the state-of-the-art xenon systems, the thrust efficiency is considerably lower, as has been shown throughout this thesis.

A.1.3 Opportunities

Water has long been identified as one of the most suitable minerals for ISRU, due to being both, a precursor for chemical propellants, and a necessity for life (see Section 2.2.4). Water is found ubiquitously throughout space: on the Moon, on Mars and on many asteroids. Space mining of water is already at a surprisingly high TRL, meaning that a water propulsion system will be well suited to refuel in space in the future [258]. As discussed previously the ability for a propulsion system to utilise water in a multi-mode propulsion system provides flexibility to spacecraft providers, even after launch. Being able to choose between such drastically different propulsion systems mid-flight will allow new multi-adaptable mission profiles.

Finally, water propulsion is currently gaining much international attention. *Tethers Unlimited* has recently demonstrated the viability of water electrolysis for chemical propulsion [259]. Japanese researchers have also demonstrated both water-gridded ion engines and water magneto plasma dynamic electric propulsion systems [260, 261].

A.1.4 Threats

The motivation for finding hydrazine replacements has been driven by the regulation on Registration, Evaluation, Authorisation and Restriction of Chemicals (REACH) [104]. No such regulation yet exists for xenon production. As mentioned previously, the production of xenon requires

an enormous amount of energy (see Figure 2.1), and therefore produces a very large carbon footprint. This fact can be overlooked by many key electric propulsion players by not considering the environmental and commercial benefits to adopt alternative propellants such as water.

A.2 Verification Studies of *PlasmaSim*

This section aims to verify the software *PlasmaSim* by comparing the plasma properties' time evolution and time-averaged profiles obtained in different case studies. Part of this section was published in [1] and presented in [6].

A.2.1 Benchmark of Axial-Radial Particle-In-Cell Codes

In the current state of the art, benchmark cases are available for several PIC codes, including 1D azimuthal PIC , 2D azimuthal-axial PIC , and 2D azimuthal-radial PIC. These benchmarks are evaluated, compiled, and tested by the *LANDMARK* (Low Temperature Magnetized Plasma Benchmarks) community. However, there is no existing benchmark for 2D axial-radial PIC codes.

This section proposes a 2D axial-radial benchmark case using various state-of-the-art hybrid and kinetic PIC codes. The primary goal of this effort is to assess the validity of the assumptions used in the development of *PlasmaSim* (described in Chapter 3) by comparing its results with other axial-radial codes in the literature for the same case study (*SPT-100* operating at 300V). The short-channel version of the *SPT-100* is taken as the study case due to the large amount of 2D axial-radial literature studies for this thruster [262, 263, 264, 265, 266, 267], mainly performed by European EP groups. Because of that, this version will be referred to as the "European version" of the *SPT-100* throughout the appendix.

This benchmark is constructed similarly to the work done by Mario Panelli et al. [263], who evaluated the physics of the *SPT-100* using a hybrid plasma code. They compared the plasma properties of the channel with those obtained by Hofer et al. [262], Kawashima et al. [264], and experimental results from MacDonald-Tenenbaum et al [267]. The data presented here is extended with the fully kinetic PIC model by JAXA [265] and the results obtained with *PlasmaSim*.

A.2.1.1 Simulation Inputs

Table A.2: *PlasmaSim* simulation inputs for European *SPT-100* benchmark validation case. Table published in [1].

Parameter	Input	Units	Reference
Discharge voltage (V_d)	300	V	[265]
Cathode location (X_C)	31	mm	Section 3.1.1.2
Channel mean diameter (d_m)	84	mm	[265]
Channel length (L)	25	mm	[265]
Channel width (w)	16	mm	[265]
Magnetic field (B)	Figure A.1	T	[262]
Number density of neutrals (n_n)	Figure A.1	m^{-3}	-
Number density of plasma (n_e)	2.0×10^{17}	m^{-3}	-
Number of superparticles per cell	> 25	-	-
Temperature of electrons (T_e)	5	eV	-
Temperature of ions (T_i)	≈ 0.1	eV	-
Temperature of neutrals (T_n)	300	K	-

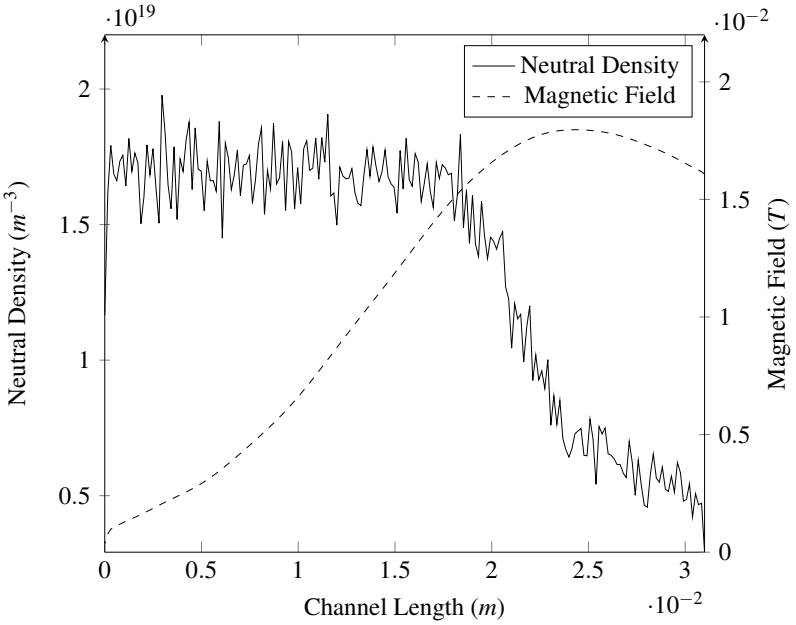


Figure A.1: Inputs of neutral density and magnetic field profiles for the *SPT-100* (European version). Graph published in [1].

Table A.2 summarises the input variables utilised in the *PlasmaSim* benchmark case for the European version of the *SPT-100*. Figure A.1 illustrates the neutral density profile (see Section 3.1.1.4) and the magnetic field distribution used in the simulation. The neutral density profile

is derived from prior pseudo-2D simulations conducted under the same conditions which have advanced over time. Using this input accelerates the attainment of the steady-state condition in the simulation.

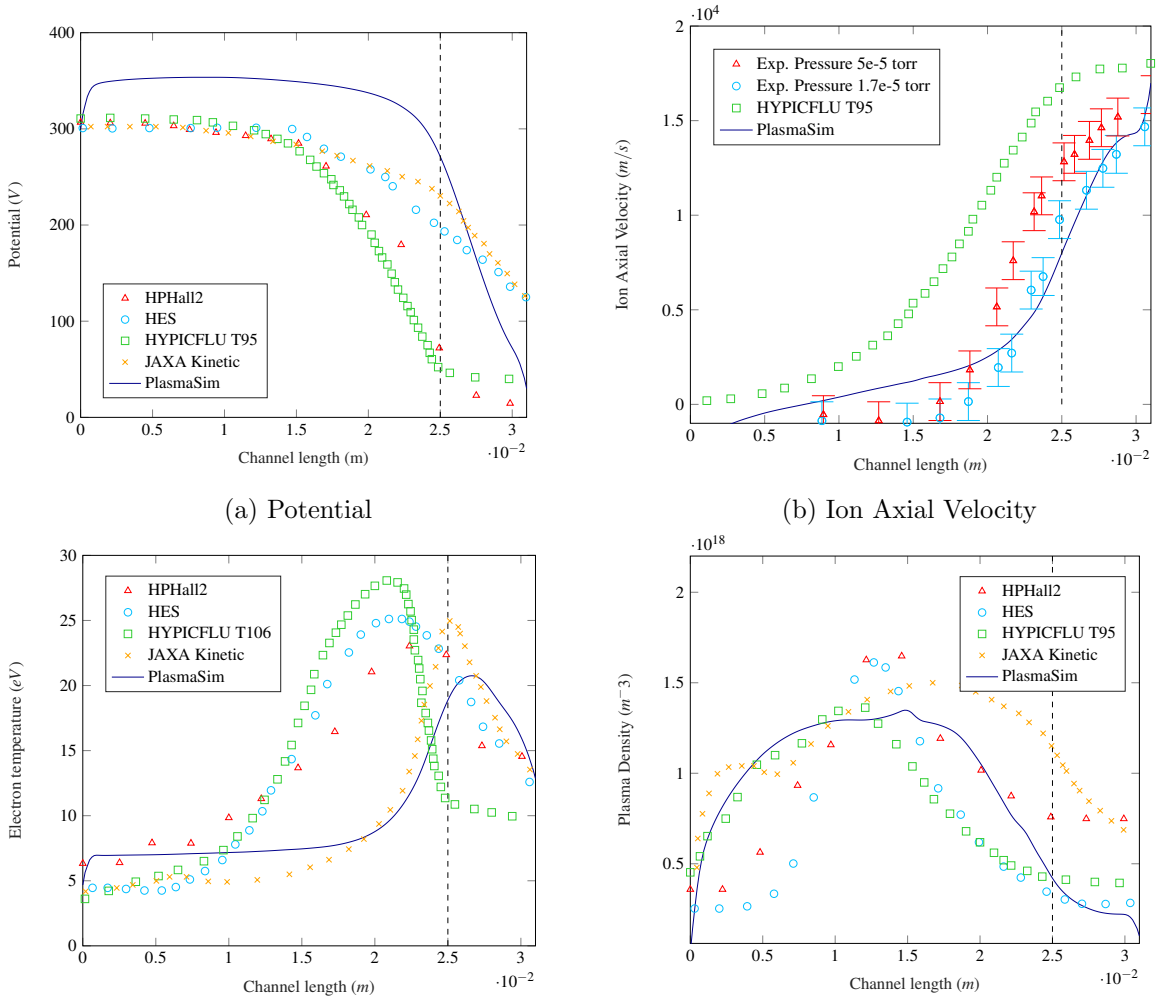
A.2.1.2 Verification Results

This benchmark analysis compares the profiles of electric potential (ϕ, Figure A.2a), ion axial velocity ($v_{i,x}$, Figure A.2b), electron temperature (T_e, Figure A.2c), and plasma density (n_e, Figure A.2d) across the various 2D axial-radial codes previously highlighted and the experimental data from [267].

Starting with the electric potential, *PlasmaSim* shows a decrease in the peak magnetic field region due to the increased resistance to electron movement. The values are generally overestimated along most of the channel length compared to other codes, likely due to an enhanced Near Wall Conductivity (NWC). This increases the rate of electron cross-field transport towards the anode due to interactions with the sheaths near the lateral walls. Despite the higher potential, the model seems to correctly capture the main physical behaviour without affecting other plasma parameters. The ion axial velocity aligns well with experimental results throughout the domain. The electron temperature profile is similar to that of the *JAXA* PIC code, with the maximum temperature at the exit plane. Hybrid codes predict this peak closer to the exit plane.

The plasma density profile varies within the community; *PlasmaSim* and most other codes indicate a peak near the middle of the channel. In PIC codes like *PlasmaSim* and *JAXA*, the plasma profile is less steep compared to hybrid codes, where it is more pronounced.

Despite some noted shortcomings of the *PlasmaSim* model, the general physical processes within HETs appear to be well represented. The next section discusses the incorporation of the reactive model used to simulate water-fuelled HETs.



(a) Potential

(b) Ion Axial Velocity

(c) Electron Temperature

(d) Plasma Density

Figure A.2: PIC Axial-Radial Benchmark analysis using the case study of the *SPT-100* European version at 300 V. Experimental data is also included in Figure A.2b. Graphs published in [1].

A.2.2 Reactive Model Against an Analytical Solution

The development of the governing equations for the verification of the reactions of diatomic species is presented here. Notice that the verification model assumes the following:

- Constant electron temperature ($T_e = constant$)
- Stationary and uniform plasma ($v_e = 0$)
- Particles reflected in the walls such that the wall loss rate ($\dot{R}_w$) is zero ($\dot{R}_w = 0$).

This simplified scenario, where the electron temperature remains constant and the reactive model is only considered as a source and sink of particles, allow one to compare the results of *PlasmaSim* against an analytical solution.

A.2.2.1 Analytical Diatomic Model

To verify the suitability of this approach for representing a reactive propellant such as oxygen, dissociative, ion-dissociative, and ionising reactions were independently verified before being integrated into the complete model. The verification technique involves setting up a model with an analytical solution using the simplifications previously highlighted. Specifically, this particular problem has an analytical solution derived from the conservation of mass for the five species: electrons, diatomic ions, monoatomic ions, diatomic neutrals, and monoatomic neutrals, which reads as follows:

$$\frac{dn_e}{dt} = \dot{R}_{ion} + \dot{R}_{dion} \qquad \longrightarrow \qquad \frac{dn_e}{dt} = n_{O_2} n_e \sqrt{\frac{8k_B T_e}{\pi m_e}} \left(\sigma_{O_2 ion} + \sigma_{O_2 dion}\right) \tag{A.1a}$$

$$\frac{dn_{O_2^+}}{dt} = \dot{R}_{ion} \qquad \longrightarrow \qquad \frac{dn_{O_2^+}}{dt} = n_{O_2} n_e \sqrt{\frac{8k_B T_e}{\pi m_e}} \sigma_{O_2 ion} \tag{A.1b}$$

$$\frac{dn_{O^+}}{dt} = \dot{R}_{dion} \qquad \longrightarrow \qquad \frac{dn_{O^+}}{dt} = n_{O_2} n_e \sqrt{\frac{8k_B T_e}{\pi m_e}} \sigma_{O_2 dion} \tag{A.1c}$$

$$\frac{dn_{O_2}}{dt} = -\dot{R}_{ion} - \dot{R}_{dion} - \dot{R}_{di} \qquad \longrightarrow \qquad \frac{dn_{O_2}}{dt} = -n_{O_2} n_e \sqrt{\frac{8k_B T_e}{\pi m_e}} \left(\sigma_{O_2 ion} + \sigma_{O_2 dion} + 2\sigma_{O_2 di}\right) \tag{A.1d}$$

$$\frac{dn_O}{dt} = \dot{R}_{dion} + \dot{R}_{di} \qquad \longrightarrow \qquad \frac{dn_O}{dt} = n_{O_2} n_e \sqrt{\frac{8k_B T_e}{\pi m_e}} \left(\sigma_{O_2 dion} + 2\sigma_{O_2 dion}\right) \tag{A.1e}$$

where R_x is the loss rate of the reaction x. As will be seen in the next subsections, this set of equations can be simplified depending on which reaction is analytically crosschecked (ionisation, dissociation or ion dissociation).

A.2.2.2 Analytical Solutions for the Dissociative Reaction

When only the dissociation reaction ($O_2+e \rightarrow 2O+e$) takes place, the set of equations A.1 simplifies by setting the ionisation and ion dissociation cross sections to zero ($\sigma_{O_2dion} = \sigma_{O_2ion} = 0$) and just considering the dissociation cross section (σ_{O_2di}) (see Figure 3.6a [166]). The analytical solution in this case is as follows:

$$\frac{dn_e}{dt} = 0 \qquad \longrightarrow \qquad n_e = n_e^0 \tag{A.2a}$$

$$\frac{dn_{O_2^+}}{dt} = 0 \qquad \longrightarrow \qquad n_{O_2^+} = n_{O_2^+}^0 \tag{A.2b}$$

$$\frac{dn_{O^+}}{dt} = 0 \qquad \longrightarrow \qquad n_{O^+} = n_{O^+}^0 \tag{A.2c}$$

$$\frac{dn_{O_2}}{dt} = -n_{O_2} n_e \sqrt{\frac{8k_B T_e}{\pi m_e}} \sigma_{O_2di} \qquad \longrightarrow \qquad n_{O_2} = n_{O_2}^0 \exp\left(-t\sqrt{\frac{8k_B T_e}{\pi m_e}}\right) \tag{A.2d}$$

$$\frac{dn_O}{dt} = 2n_{O_2} n_e \sqrt{\frac{8k_B T_e}{\pi m_e}} \sigma_{O_2di} \qquad \longrightarrow \qquad n_{O_2} = 2n_{O_2}^0 \left[1 - \exp\left(-t\sqrt{\frac{8k_B T_e}{\pi m_e}}\right)\right] \tag{A.2e}$$

Which in practice represents a system of two coupled differential equations of unknowns x and y of the kind: $\frac{dx}{dt} = -Kx$; $\frac{dy}{dt} = 2Kx$ with K being a constant.

A.2.2.3 Analytical Solutions for the Ionising Reaction

Similarly, by setting the dissociative and ion dissociative cross sections to zero ($\sigma_{O_2di} = \sigma_{O_2dion} = 0$) and just considering the ionising reaction ($O_2+e \rightarrow O_2^+ +2e$) and its relative cross section (σ_{O_2ion}),

the solution can be analytically resolved. In this formulation, two constants related to the initial conditions of the density of the particles are introduced: $C_1 = n_e^0 + n_{O_2}^0$ and $C_2 = \frac{n_e^0}{n_{O_2}^0}$. The set of equations can be resolved as:

$$\frac{dn_e}{dt} = n_{O_2} n_e \sqrt{\frac{8k_B T_e}{\pi m_e}} \sigma_{O_2 ion} \qquad \longrightarrow \qquad n_e = \frac{C_1 C_2 \exp\left(tC_1\sqrt{\frac{8k_B T_e}{\pi m_e}}\right)}{1 + C_2 \exp\left(tC_1\sqrt{\frac{8k_B T_e}{\pi m_e}}\right)} \tag{A.3a}$$

$$\frac{dn_{O_2^+}}{dt} = n_{O_2} n_e \sqrt{\frac{8k_B T_e}{\pi m_e}} \sigma_{O_2 ion} \qquad \longrightarrow \qquad n_{O_2^+} = n_{O_2^+}^0 - \frac{C_1}{C_2 \exp\left(tC_1\sqrt{\frac{8k_B T_e}{\pi m_e}}\right) + 1} + \frac{C_1}{C_2 + 1} \tag{A.3b}$$

$$\frac{dn_{O^+}}{dt} = 0 \qquad \longrightarrow \qquad n_{O^+} = n_{O^+}^0 \tag{A.3c}$$

$$\frac{dn_{O_2}}{dt} = -n_{O_2} n_e \sqrt{\frac{8k_B T_e}{\pi m_e}} \sigma_{O_2 ion} \qquad \longrightarrow \qquad n_{O_2} = C_1 - \frac{C_1 C_2 \exp\left(tC_1\sqrt{\frac{8k_B T_e}{\pi m_e}}\right)}{1 + C_2 \exp\left(tC_1\sqrt{\frac{8k_B T_e}{\pi m_e}}\right)} \tag{A.3d}$$

$$\frac{dn_O}{dt} = 0 \qquad \longrightarrow \qquad n_{O_2} = n_{O_2}^0 \tag{A.3e}$$

Which in practice represents a system of three differential equations of unknowns x, y and z; being x and y coupled together in the form: $\frac{dx}{dt} = Kxy$; $\frac{dy}{dt} = -Kxy$ and $\frac{dz}{dt} = Kxy$ with K being a constant.

A.2.2.4 Analytical Solutions for the Dissociative-Ionising Reaction

Finally, by setting the dissociative and ionising cross sections to zero ($\sigma_{O_2di} = \sigma_{O_2ion} = 0$) and just considering the dissociative-ionising reaction ($O_2 + e \rightarrow O^+ + O + 2e$) and its respective cross section (σ_{O_2dion}), the problem has an analytical solution as follows:

$$\frac{dn_e}{dt} = n_{O_2} n_e \sqrt{\frac{8k_B T_e}{\pi m_e}} \sigma_{O_2dion} \qquad \longrightarrow \qquad n_e = \frac{C_1 C_2 \exp\left(tC_1\sqrt{\frac{8k_B T_e}{\pi m_e}}\right)}{1 + C_2 \exp\left(tC_1\sqrt{\frac{8k_B T_e}{\pi m_e}}\right)} \tag{A.4a}$$

$$\frac{dn_{O_2^+}}{dt} = 0 \qquad \longrightarrow \qquad n_{O_2^+} = n^0_{O_2^+} \tag{A.4b}$$

$$\frac{dn_{O^+}}{dt} = n_{O_2} n_e \sqrt{\frac{8k_B T_e}{\pi m_e}} \sigma_{O_2dion} \qquad \longrightarrow \qquad n_{O^+} = n^0_{O^+} - \frac{C_1}{C_2 \exp\left(tC_1\sqrt{\frac{8k_B T_e}{\pi m_e}}\right) + 1} + \frac{C_1}{C_2 + 1} \tag{A.4c}$$

$$\frac{dn_{O_2}}{dt} = -n_{O_2} n_e \sqrt{\frac{8k_B T_e}{\pi m_e}} \sigma_{O_2dion} \qquad \longrightarrow \qquad n_{O_2} = C_1 - \frac{C_1 C_2 \exp\left(tC_1\sqrt{\frac{8k_B T_e}{\pi m_e}}\right)}{1 + C_2 \exp\left(tC_1\sqrt{\frac{8k_B T_e}{\pi m_e}}\right)} \tag{A.4d}$$

$$\frac{dn_O}{dt} = n_{O_2} n_e \sqrt{\frac{8k_B T_e}{\pi m_e}} \sigma_{O_2dion} \qquad \longrightarrow \qquad n_O = n^0_O - \frac{C_1}{C_2 \exp\left(tC_1\sqrt{\frac{8k_B T_e}{\pi m_e}}\right) + 1} + \frac{C_1}{C_2 + 1} \tag{A.4e}$$

Which in practice represents a system of four differential equations of unknowns x, y, z and γ; being x and y coupled together in the form: $\frac{dx}{dt} = Axy$; $\frac{dy}{dt} = -Axy$ and with $\frac{dz}{dt} = Axy$ and

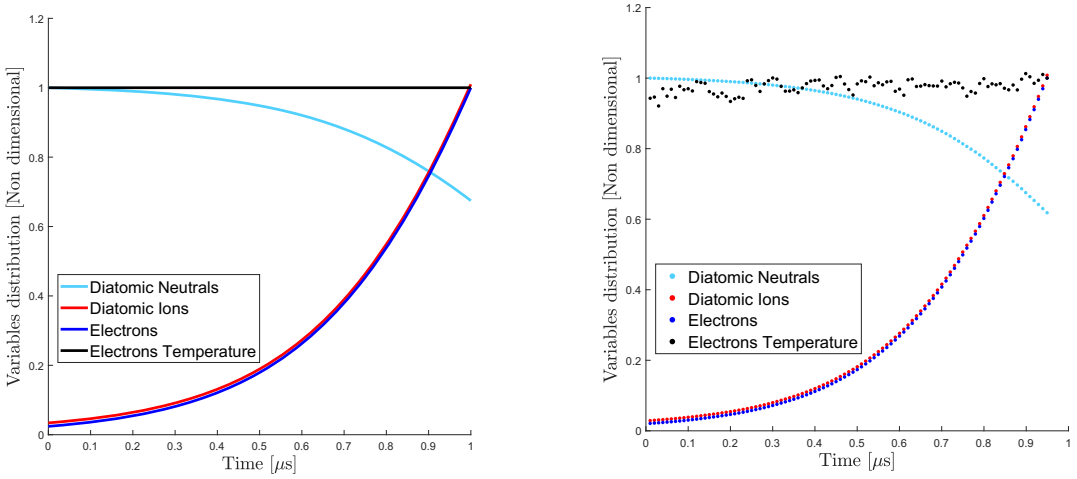
$\frac{d\gamma}{dt} = Axy$; with A being a constant.

In *PlasmaSim*, the scenario of Sections A.2.2.2, A.2.2.3 and A.2.2.4 is simulated by confining the plasma within a fixed domain ($1.0 \times 1.0 \times 1.0$ mm in this case) where all particles are specularly reflected at the walls at an initial temperature set by the user. Due to this small domain and the correspondingly high wall collision rate, the computational code maintains an approximately constant temperature throughout the simulation, allowing the particles to react and collide. Consequently, the solution is comparable to the proposed analytical solution, enabling verification of the model using this methodology.

However, this strategy leads to an exponential increase in the number of particles the program needs to track over time as there are no loss mechanisms for the particles (they are merely reflected). Particle creation is directly proportional to the cross-section, meaning that reactions with a large cross-section (such as ionisation, compared to those with a smaller cross-section like dissociation or ion dissociation) will create more species, limiting the maximum computational time achievable. Despite this limitation, the model can represent the correlation between the analytical and computational models for a reasonable amount of time, highlighting any discrepancies in their behaviour.

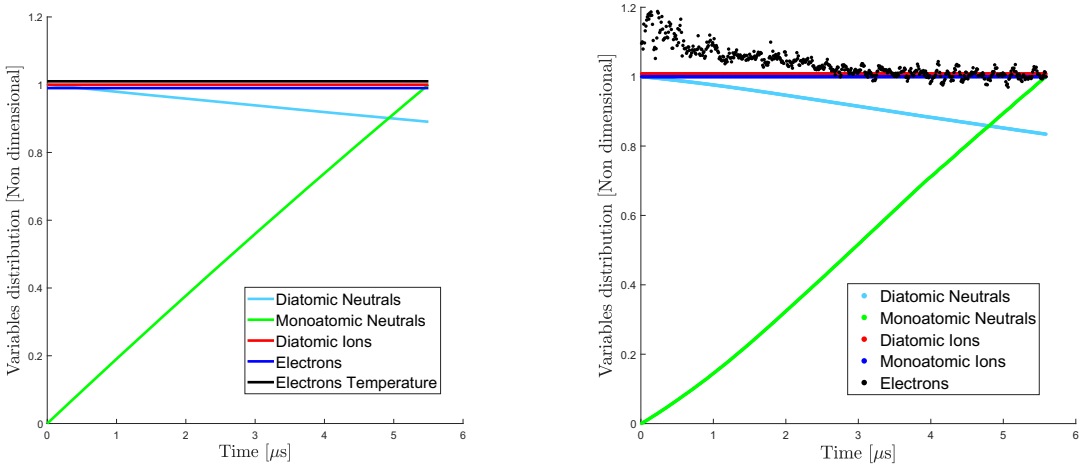
The results of this verification exercise are shown in the following figures: Figure A.3 (ionisation), Figure A.4 (dissociation), and Figure A.5 (ion dissociation). Generally, it can be observed that at the start of the simulation, although the electron temperature is not entirely constant due to initial fluctuations in particle properties, it quickly stabilises and remains practically unchanged.

The correlation between the analytical model and *PlasmaSim* is highly promising for the three models verified (ionisation, dissociation, and ion dissociation), with *PlasmaSim* slightly overestimating the reaction rate compared to the analytical model. This confirms the suitability of the reactive model to the fully incorporated in *PlasmaSim*.



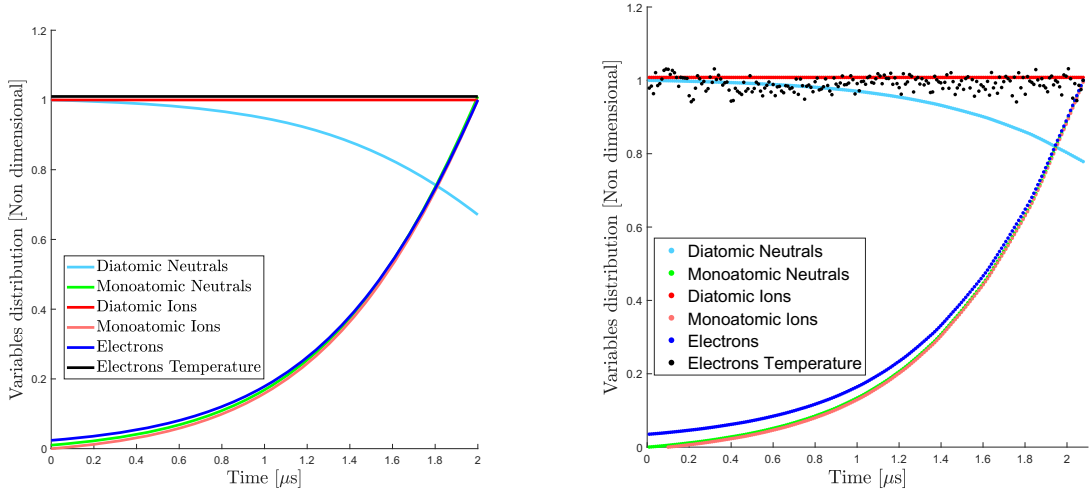
(a) Analytical solution. (b) Computational (*PlasmaSim*) solution.

Figure A.3: Verification of the ionisation model. Plots presented in [6].



(a) Analytical solution. (b) Computational (*PlasmaSim*) solution.

Figure A.4: Verification of the dissociation model. Plots presented in [6].



(a) Analytical solution. (b) Computational (*PlasmaSim*) solution.

Figure A.5: Verification of the ion dissociation model. Plots presented in [6].

A.3 Validation Studies of *PlasmaSim*

Table A.3: *PlasmaSim* simulation inputs for the American *SPT-100* performance validation case.

Parameter	Input	Units	Reference
Discharge voltage (V_d)	300	V	[147, 148]
Cathode location (X_C)	53	mm	Section 3.1.1.2
Channel mean diameter (d_m)	84	mm	[198, 236]
Channel length (L)	42	mm	[198, 236]
Channel width (w)	16	mm	[198, 236]
Magnetic field (B)	Figure A.6c	T	[198]
Number density of neutrals (n_n)	Figure A.6d	m^{-3}	-
Number density of plasma (n_e)	2.0×10^{17}	m^{-3}	-
Number of superparticles per cell	> 25	-	-
Temperature of electrons (T_e)	5	eV	-
Temperature of ions (T_i)	≈ 0.1	eV	-
Temperature of neutrals (T_n)	300	K	-

The performance results of *PlasmaSim* have been compared against experimental data from the *SPT-100* and other plasma simulation codes in the literature for the same study case. The long channel version of the *SPT-100* is used here due to the extensive NASA experimental studies conducted across a wide power range operating at $V_d = 300$ V [147, 148]. This version is referred to as the "American version" due to its extensive study by NASA and other American electric propulsion groups [198, 268]. As shown in Tables A.2 and A.3, the two main differences between these *SPT-100* thruster models are the channel length (L = 25 mm for the European version versus L = 42 mm for the American version) and the magnetic field topology (compare Figures A.1 and A.6c).

As in Section A.2.1, the initial conditions and input variables are described (Section A.3.1). Using that, the simulation outcomes and performance characteristics are discussed in Section A.3.2.

A.3.1 Simulation Inputs

Table A.3 summarises the input variables used to validate *PlasmaSim* against the *SPT-100* (American version).

A.3.2 Validation Results

Parameter	**Units**	**[Experiments] Average / Range**		***PlasmaSim* Average / Rel. Error**		**Hybrid 1D Method [198] Average / Rel. Error**		**Fluid 1D Method [268] Average / Rel. Error**	
Thrust	mN	83.3	69.2-86.9	93.9	13%	90.2	8%	82.0	-2%
Isp	s	1584	1380-1660	1424	-10%	1500	-5%	1728	9%
Power Input	kW	1.35	1.34-1.36	1.47	9%	1.11	-18%	1.43	6%
TTPR	mN/Kw	61.7	52.0-63.9	64.0	4%	81.3	32%	57.3	-7%
Efficiency	%	48	46-51	41	-14%	60	25%	49	2%

Table A.4: *PlasmaSim* SPT-100 simulation-averaged results, compared to experimental results and other plasma simulation codes from Refs. [198, 268].

Using the performance estimations described in Section 3.1.1.11, the characteristics of the *SPT-100* in terms of thrust (T, Equation 3.14), discharge power (P_d, Equation 3.15), anode specific impulse (I_{sp}, Equation 3.16) and anode thrust efficiency (η_{tr}, Equation 3.17) are evaluated using the results from *PlasmaSim* in comparison with previous works from other plasma simulation models and experimental data.

For that matter, Table A.4 compares *PlasmaSim*'s average simulation results against other plasma simulation codes using hybrid [198] and fluid plasma simulation codes [268], where the condition of $P_d = 1350 \pm 10$ W and $\dot{m}_a = 4.9 \pm 0.1$ mg/s is used as a reference for comparison against experimental results. A discharge power range of $P_d = 900 - 1800$ W is analysed, based on experimentally reported conditions for the SPT-100 [147, 148]. Note that most operating conditions at 300 V fall within $P_d = 900 - 1500$ W. However, according to the NASA experimental report in [148], this thruster can reach up to $P_d = 1788$ W at this operating voltage.

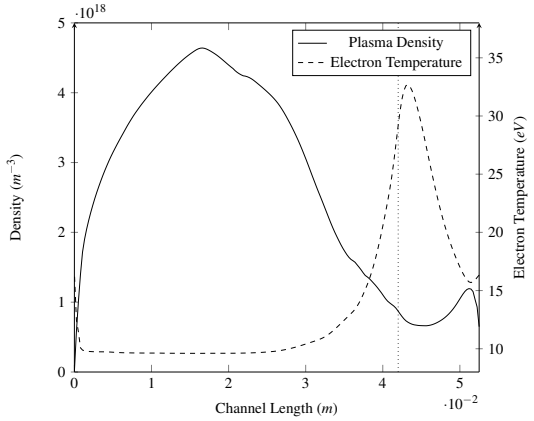
The following discussion aims to quantitatively summarise the discrepancies observed between the simulation and experimental results at each power level. For this analysis, average results in *PlasmaSim* are taken when the simulation reaches the discharge power of interest, using a ±10%

discharge power window to minimise possible data scattering within a specific discharge power range. It should be noted that experimental results for the *SPT-100* show an uncertainty window of 18%, influenced by vacuum chamber pressure, cathode location, and cathode mass flow. For example, at $P_d = 1300$ W, specific impulse measurements vary from $I_{sp} = 1340 - 1600$ s, thrust between $T = 63.8 - 81.4$ mN, and anode efficiency between $\eta_{tr} = 32 - 49\%$ [147, 148]. To assess these discrepancies, an experimental average is taken, representing the most common values of the performance parameters reported in these experiments.

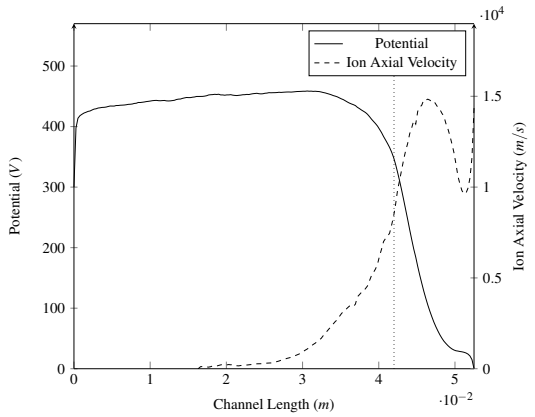
Overall, *PlasmaSim* shows relatively good agreement at all power levels. The I_{sp} values are underestimated by 10% for the upper limit of the discharge power and slightly more for lower power levels. The uncertainty levels are similar to those observed in the experimental data measurements. Thrust and TTPR closely follow experimental results within a 7% discrepancy. Relative errors increase when the discharge power reaches the upper range ($P_d = 1500 - 1800$ W). However, as previously mentioned, there is insufficient experimental data at these discharge powers for proper comparison. Anode efficiency, on average across all discharge powers, correlates with around a 10% discrepancy. No power level exhibited fundamentally different errors than the overall trend observed in the simulations.

In the literature, no other plasma simulation code has been found to correlate the performance of the *SPT-100* across all power levels, as demonstrated here. In contrast, average results from simulations are typically compared to experimental results at a single power level, such as in [198, 268].

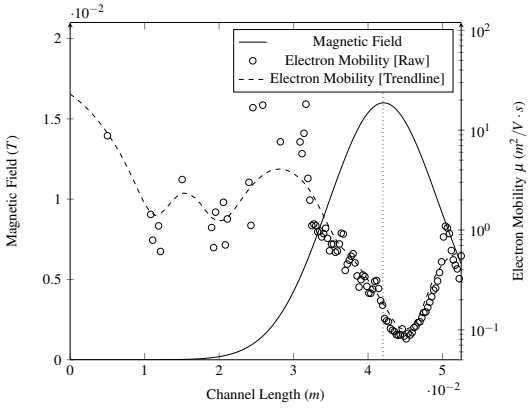
Figure A.6 illustrates the evolution of the main plasma parameters: plasma density and electron temperature in Figure A.6a; potential and ion axial velocity in Figure A.6b; magnetic field and electron mobility in Figure A.6c; and initial and final neutral density distribution in Figure A.6d, over the longitudinal channel ($\vec{x}$ axis) of the *SPT-100* for the discharge power range of $P_d = 900 - 1800$ W.



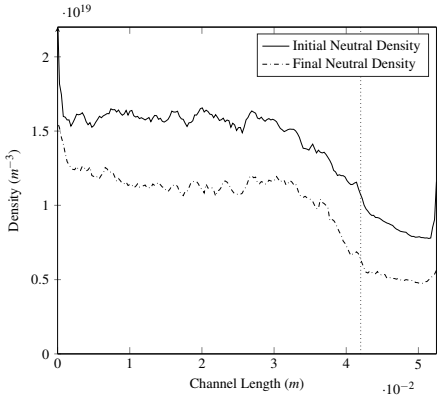
(a) Plasma density, n_e and electron temperature, T_e



(b) Potential, ϕ and ion axial velocity, $v_{i,x}$



(c) Magnetic field, B and electron mobility, μ



(d) Initial and final neutral densities, n_n

Figure A.6: Plasma properties profiles for the *SPT-100* validation case, data averaged over the discharge power range $P_d = 900 - 1800$ W.

Starting with the plasma density profile, the distribution peaks near the middle of the channel, decreasing towards the cathode boundary. The electron temperature increases and peaks close to the maximum electron axial velocity, as observed in the literature [12, 236]. The potential profile within the channel appears to be overestimated, as previously discussed in the benchmark analysis (Section A.2.1).

With respect to the electron mobility, it is observed that it reaches a minimum value near the peak magnetic field, which is consistent with experimental and numerical model results, such as the PPSX000®ML [269] and the UM/AFRL P5 [270]. Greater uncertainty is present outside the magnetic field region, where data points are more dispersed due to large unsteady fluctuations.

At the cathode side ($X_c = 0.053$ m), a sheath region can be observed in both ion and electron densities, velocities, and temperatures, which is believed to be non-physical. In particular, the

drop and rise of ion velocity (Figure A.6b) correspond to the bump in plasma density (Figure A.6a) in that region. This is likely a consequence of the boundary conditions imposed in Section 3.1.1.9. Overall, the relative agreement in the thruster's performance compared to experimental observations is encouraging.

A.3.3 Error Accumulation

When solving Poisson's Equation 3.7, the pseudo 2D axial-radial approach computes the electric field in a grid of finite size cells of N_{cells} per direction, using a second order convergent scheme (Equations 3.10 and 3.11). Numerical solvers used in real simulations operate with a finite cell size, which introduces an error that accumulates for successive time steps in convergent schemes. By either refining the grid (i.e., reducing the length scale of the cells) and/or reducing the number of time steps, the accumulated error decreases [271]. This section puts forward an evaluation of the numerical error's accumulation and the numerical precision of the numerical solver used (Equations 3.10 and 3.11). To do so, the precision estimation technique of N. Smirnov [271, 272] is applied. The allowable error for the total duration of the simulation is set to be 1%.

Table A.5 compiles the error estimation results when simulating the *SPT-100* European and American versions. Notice that all time steps, together with the number of cells and spatial steps, are dynamically updated in every single iteration step based on the simulation constraints (Section 3.1.1.6). Results in Table A.5 are the most conservative ones which lead to the worst case scenario of error accumulation (i.e., the widest grid and smaller time step found). The number of cells in the American version is greater due to the larger channel length compared to the European version. This is due to the fact that the computational domain of the *SPT-100* European version is 31×16 mm (channel length including cathode location and width, respectively), in comparison with 53×16 mm for the *SPT-100* American version (as seen in Tables A.2 and A.3).

Table A.5: Error accumulation in the resolution of the Poisson's equation.

Test Case	**Number of cells**	**Simulation time**	**Number of time steps**	**Accumulated error**	**Allowable number of time steps**	**Reliability**
SPT-100 European	> 4000	$\approx 15\ \mu s$	$< 15 \times 10^6$	1.21×10^{-7}	1.02×10^{17}	6.83×10^9
SPT-100 American	> 7000	$\approx 15\ \mu s$	$< 15 \times 10^6$	2.26×10^{-8}	2.94×10^{18}	1.96×10^{11}

In the implemented approach, the Poisson's equation is solved twice per time step (axially and radially) in a discretised domain of N_{cells}. Therefore, these two error's contributions is added together to calculate the total accumulated error. Simulations with and without RF excitation present the same results. Reliability is defined as the ratio of the maximum allowed error (1%) by the accumulated error. The higher this number is, the lower the error [271]. Following the formulation of Refs. [271, 272], it is found that, very reliably, the accumulated error throughout the whole duration of the simulation is very small ($\mathcal{O}(10^{-7})$). This is a consequence of the length scale of the physical problem (mm) and the refined grid used, which allows to run the simulation for seconds before reaching the 1% accumulated error threshold despite the very small time step ($\Delta t \approx 1 \times 10^{-12}$ s).

Judging the error estimation, together with the verification and validation analyses described in Appendixes A.2 and A.3, it is concluded that this model can be used as a tool in order to discuss the most relevant physics phenomena of HETs.

Bibliography

[1] JM. Tejeda, M. Reza, F. Faraji and A. Knoll. Performance enhancement of Hall Effect Thruster using radiofrequency excitation. *Acta Astronautica*, 194:145–161, 2022.

[2] JM. Tejeda, A. Schwertheim and A. Knoll. Water as an environmentally friendly propellant for a multi-functional spacecraft architecture. *International Journal of Energetic Materials and Chemical Propulsion*, 22(2), 2023.

[3] JM. Tejeda and A. Knoll. An oxygen-fuelled Hall Effect Thruster: Channel length, ceramic walls and anode material experimental analyses. *Acta Astronautica*, 203:2, 2022.

[4] JM. Tejeda and A. Knoll. A water vapour fuelled Hall Effect Thruster: Characterization and comparison with oxygen. *Acta Astronautica*, 211:702–715, 2023.

[5] JM. Tejeda et al. Experimental demonstration of a water electrolysis Hall Effect Thruster operating with a hydrogen cathode. *Acta Astronautica*, 2019:542–554, 2023.

[6] JM. Tejeda and A.Knoll. A water electrolysis Hall Effect Thruster computational model with radiofrequency excitation. In *37th International Electric Propulsion Conference, IEPC-2022-313, Massachusetts Institute of Technology, Cambridge, MA, USA*, 2022.

[7] JM. Tejeda, A. Knoll, F. Marchioni and M. Cappelli. Plasma properties characterization of oxygen-fuelled Hall Effect Thruster for water electrolysis propulsion. In *Space Propulsion Conference*, number 0015, 05 2024.

[8] JM. Tejeda et al. First end-to-end technological demonstration of a water electrolysis Hall Effect Thruster operating with a water electrolyser. In *International Electric Propulsion Conference*, number 00175, 05 2024.

[9] E. Rosati et al. Sizing and preliminary design of a 2-kW water propelled Hall Effect Thruster. In *International Electric Propulsion Conference*, Boston, US, 2022-317.

[10] M. Abbi et al. Investigation on the wall interactions of a Hall Effect Thruster using water vapor as a propellant. In *37th International Electric Propulsion Conference, IEPC-2022-346, Massachusetts Institute of Technology, Cambridge, MA, USA*, 2022.

[11] W. Ley. *Rockets, Missiles, and Men in Space*. The Viking Press, 1958.

[12] D. Goebel and I. Katz. *Fundamentals of Electric Propulsion*. John Wiley Sons, Ltd, 2008.

[13] D. Huzel and D. Huang. *History of Liquid Propellant Rocket Engines*. American Institute of Aeronautics and Astronautics, 1971.

[14] M. Neufeld. *The Rocket and the Reich: Peenemünde and the Coming of the Ballistic Missile Era*. Harvard University Press, 1995.

[15] G. Sutton and O. Biblarz. *Rocket Propulsion Elements*. John Wiley & Sons, 2010.

[16] E. Ezell and L. Ezell. *The Partnership: A History of the Apollo-Soyuz Test Project*. NASA History Office, 1978.

[17] K. E. Tsiolkovsky. The exploration of cosmic space by means of reaction devices. *Popular Mechanics*, 11(10):132–133, 1911.

[18] R. E. Bilstein. *Stages to Saturn: A Technological History of the Apollo/Saturn Launch Vehicles*. DIANE Publishing, 1996.

[19] J. Harford. *Korolev: How One Man Masterminded the Soviet Drive to Beat America to the Moon*. John Wiley & Sons, 1997.

[20] R. Gabrielliand G. Herdrich. Review of nuclear thermal propulsion systems. *Progress in Aerospace Sciences*, 79:92–113, 2015.

[21] D. O'Reilly, G. Herdrich and D. Kavanagh. Electric propulsion methods for small satellites: A review. *Aerospace*, 8(1):22, 2021.

[22] C. Mitchell et al. Ignition and combustion characteristics of solid propellants. *Technical report for 1 Oct 62-30 Sep 63,*, page 70, 1963.

[23] D. Huzel and D. Huang. NASA SP-125: Design of liquid propellant rocket engines. Technical report, NASA, 1992.

[24] R. Ranjan, S. Chou, F. Riazand and K. Karthikeyan. Cold gas micro propulsion development for satellite application. *Energy Procedia*, 143:754–761, 2017.

[25] J. Tomei, J. Nichols and The Aerospace Corporation. Explosive equivalence of hypergolic propellants. Technical report, 2019.

[26] M. Sorgenfrei, T. Stevenson and G. Lightsey. Performance characterization of a cold gas propulsion system for a deep space cubesat. In *40th Annual AAS Guidance and Control Conference*, page 47, Breckenridge, CO, February 2017.

[27] B. Frongello et al. Spacecraft electric propulsion at an inflection point. In *Advanced Space Propulsion and Energy Systems*, page 4151. 2021.

[28] JG. del Amo. European space agency (ESA) electric propulsion activities. In *37th International Electric Propulsion Conference, Kobe*, pages 4–10, 2015.

[29] J. González del Amo. Activities on electric propulsion at ESA. In *5th Space Propulsion Conference, Rome, Italy*, pages 1–10, 2016.

[30] A. Cervone et al. Green micro-resistojet research at Delft University of Technology: new options for cubesat propulsion. *CEAS Space Journal*, 9:111–125, 2017.

[31] NASA Lewis Research Center and Rocket Research Company. Arcjet thruster research and technology. Phase II final report. NAS 3-24631, 1991.

[32] D. Jovel, M. Walker and D. Herman. Review of high-power electrostatic and electrothermal electric propulsion. *Journal of Propulsion and Power*, 38(6):1051–1081, 2022.

[33] M. Sangregorio, X. Kan, W. Ningfei, G. Ning, and Z. Zhang. Ion engine grids: Function, main parameters, issues, configurations, geometries, materials and fabrication methods. *Chinese Journal of Aeronautics*, 31(8):1635–1649, 2018.

[34] M. Bharti and S. Chalia. Literature study of field emission electric propulsion microthruster. *Int. Res. J. Eng. Tech*, 4:2777–2781, 2017.

[35] R. Myers. Electromagnetic propulsion for spacecraft. In *1993 Aerospace Design Conference*, number NASA-CR-191186. NASA, 1993.

[36] A. Bapat, P. Salunkhe and A. Patil. Hall Effect Thrusters for deep-space missions: A review. *IEEE Transactions on Plasma Science*, 50(2):189–202, 2022.

[37] Z. Zhang et al. A review of the characterization and optimization of ablative pulsed plasma thrusters. *Reviews of Modern Plasma Physics*, 3:1–41, 2019.

[38] J. Balkenhohl, J. Glowacki, N. Rattenbury, and J. Cater. A review of low-power applied-field magnetoplasmadynamic thruster research and the development of an improved performance model. *Journal of Electric Propulsion*, 2(1):1, 2023.

[39] R. Gabrielli and G. Herdrich. Review of nuclear thermal propulsion systems. *Progress in Aerospace Sciences*, 79:92–113, 2015.

[40] R. Cassady et al. Recent advances in nuclear powered electric propulsion for space exploration. *Energy Conversion and Management*, 49(3):412–435, 2008.

[41] D. Burns and S. Johnson. *Nuclear Thermal Propulsion Reactor Materials*. IntechOpen, 2020.

[42] K. Polzin, Y. Raitses, J. Gayoso and N. Fisch. Comparisons in performance of electromagnet and permanent-magnet cylindrical Hall-Effect Thrusters.

[43] A. Schwertheim. *The Water Electrolysis Hall Effect Thruster*. PhD thesis, Imperial College London, 2022.

[44] V. Tirila, A. Demairé and C. Ryan. Review of alternative propellants in Hall thrusters. *Acta Astronautica*, 212:284–306, 2023.

[45] T. Morishita, R. Tsukizaki, N. Yamamoto, K. Kinefuchi and K. Nishiyama, Kazutaka. Application of a microwave cathode to a 200-w Hall thruster with comparison to a hollow cathode. *Acta Astronautica*, 176:413–423, 2020.

[46] P. Zheng, J. Wu, Y. Zhang, and B. Wu. A comprehensive review of atmosphere-breathing electric propulsion systems. *International Journal of Aerospace Engineering*, 2020:1–21, 2020.

[47] M. Tisaev et al. Air-breathing electric propulsion: Flight envelope identification and development of control for long-term orbital stability. *Acta Astronautica*, 191:374–393, 2022.

[48] F. Marchioni and M. Cappelli. Extended channel Hall thruster for air-breathing electric propulsion. *Journal of Applied Physics*, 130(5), 2021.

[49] Nist atomic spectra database, 2023. Accessed: 2023-12-05.

[50] Space Exploration Technologies Corp. Spacex. https://www.spacex.com/, 2023. Accessed: April 17, 2023.

[51] J.A. Linnell and A.D. Gallimore. Efficiency analysis of a Hall thruster operating with krypton and xenon. *Journal of Propulsion and Power*, 22(6):1402–1412, 2006.

[52] G. Xia, H. Li, Y. Ding, L. Wei and S. Chen, and D. Yu. Performance optimization of a krypton Hall thruster with a rotating propellant supply. *Acta Astronautica*, 171:290–299, 2020.

[53] G. Xia et al. Performance optimization of a krypton Hall thruster with a rotating propellant supply. *Acta Astronautica*, 171:290–299, 2020.

[54] SpaceX. SpaceX on Twitter: "Argon Hall thruster tech specs". https://twitter.com/SpaceX/status/1629948869239873538?lang=en, February 2023. Online, accessed: March 8, 2024.

[55] D. Rafalskyi et al. In-orbit demonstration of an iodine electric propulsion system. *Nature*, 599:411–415, 2021.

[56] J. Szabo, M. Robin and V. Hruby. Bismuth vapor Hall Effect Thruster performance and plume experiments. In *35th International Electric Propulsion Conference, IEPC-2017-25, Georgia Institute of Technology, Georgia, USA*, 2019.

[57] C. Marrese et al. The vhital program to demonstrate the performance and lifetime of a bismuth-fueled very high isp Hall thruster. In *41st AIAA/ASME/SAE/ASEE Joint Propulsion Conference & Exhibit*, page 4564, 2005.

[58] M.A. Hopkins and L.B. King. Performance comparison between a magnesium-and xenon-fueled 2 kilowatt Hall thruster. *Journal of Propulsion and Power*, 32(4):1015–1021, 2016.

[59] J.M. Makela, R.L. Washeleski, D.R. Massey, L.B. King, and M.A. Hopkins. Development of a magnesium and zinc Hall Effect Thruster. *Journal of Propulsion and Power*, 26(5):1029–1035, 2010.

[60] S. Dworski, J. Martin, C. Ryan and E. Dyer. The operation of a low-power cylindrical Hall thruster with zinc as the propellant. In *36th International Electric Propulsion Conference, IEPC-2019-A920, University of Vienna, Vienna, Austria*, 2019.

[61] M.A. Bretti. Progress and developments of ultra-compact 10 watt class adamantane fueled Hall thrusters for picosatellites. In *37th International Electric Propulsion Conference, IEPC-2022-349, Massachusetts Institute of Technology, Cambridge, MA, USA*, 2022.

[62] A.C. Scharlemann. Theoretical and experimental investigation of c60-propellant for ion propulsion. *Acta Astronautica*, 51(12):865–872, 2002.

[63] A. Kieckhafer and L. King. Energetics of propellant options for high-power Hall thrusters. *Journal of propulsion and power*, 23(1):21–26, 2007.

[64] H.E. Gallagher. Poisoning of lab6 cathodes. *Journal of Applied Physics*, 40(1):44–51, 1969.

[65] D.M. Goebel, J.T. Crow, J.T and A.T. Forrester. Lanthanum hexaboride hollow cathode for dense plasma production. *Review of Scientific Instruments*, 49(4):469–472, 1978.

[66] G-C. Potrivitu. *On the low-current hollow cathodes for electric propulsion for small satellites.* PhD thesis, 07 2022.

[67] F. Chen. *Introduction to plasma physics and controlled fusion. Vol 1. Plasma physics.* Plemum Pr, Springer, 2ed. edition, 2006.

[68] J.A. Bittencourt. *Fundamentals of Plasma Physics.* Springer New York, 2013.

[69] JP. Boeuf. Tutorial: Physics and modeling of Hall thrusters. *Journal of Applied Physics*, 121(1):011101, 01 2017.

[70] D. Pavarin et al. Low power RF plasma thruster experimental characterization. In *48th AIAA/ASME/SAE/ASEE Joint Propulsion Conference & Exhibit*, page 4191, 2012.

[71] Y. Yamagiwa, Yoshiki and K. Kuriki. Performance of double-stage-discharge Hall ion thruster. *Journal of Propulsion and Power*, 7(1):65–70, 1991.

[72] R. Hofer, P. Peterson and A. Gallimore and R. Jankovsky. A high specific impulse two-stage Hall thruster with plasma lens focusing. pages 15–19, 11 2001.

[73] P. Rossetti, M. Capacci and G. Noci. *Preliminary Experimental Results on a Double Stage Hall-Effect Thruster.*

[74] D. Escobar, A. Antón and E. Ahedo. Simulation of high-specific-impulse and double-stage Hall thrusters. In *29th International Electric Propulsion Conference, Princeton, USA*, 2005.

[75] Hirohisa Kuwano, A. Ohno, and Hideki Nakashima. Development and thrust performance of a microwave discharge Hall thruster. In *30th International Electric Propulsion Conference, Florence, Italy*, 2007.

[76] B. Brian, A. Gallimore, D. Morris, C. Davis, K. Lemmer. *Development of an Annular Helicon Source for Electric Propulsion Applications.*

[77] A. Shabshelowitz, A. Gallimore and P. Peterson. Performance of a helicon Hall thruster operating with xenon, argon, and nitrogen. *Journal of Propulsion and Power*, 30(3):664–671, 2014.

[78] P. Peterson, D. Massey, A. Shabshelowitz. R. Shastry and R. Liang. Performance and plume characterization of a helicon Hall thruster. In *32nd International Electric Propulsion Conference, Wiesbaden, Germany*, 2011.

[79] Ira B. Bernstein. Waves in a Plasma in a Magnetic Field. *Phys. Rev.*, 109:10–21, Jan 1958.

[80] Richard Haberman. *Applied Partial Differential Equations: With Fourier series and boundary value problems.* China Machine Press, 4th edition edition, 2005.

[81] F. Cichocki. *Analysis of the expansion of a plasma thruster plume into vacuum.* PhD thesis, Universidad Carlos III de Madrid, Leganés, Spain, 2017.

[82] A.B Birdsall, C.K; Langdon. *Plasma Physics via Computer Simulation.* Series in Plasma Physics and Fluid Dynamics. CRC Press, 2004.

[83] F. Taccogna and Laurent Garrigues. Latest progress in Hall thrusters plasma modelling. *Reviews of Modern Plasma Physics*, 3(1), 2019.

[84] Mario Merino, Aurélien Proux, Pablo Fajardo, and Eduardo Ahedo. Collisionless electron cooling in unmagnetized plasma thruster plumes. In 52^{nd} *AIAA/ASME/SAE/ASEE Joint Propulsion Conference & Exhibit*, 2016.

[85] Manuel Martínez-Sánchez, Jaume Navarro-Cavallé, and Eduardo Ahedo. Electron cooling and finite potential drop in a magnetized plasma expansion. *Physics of Plasmas*, 22(5):053501, 2015.

[86] T. Lafleur and R. W. Boswell. Particle-In-Cell simulations of hollow cathode enhanced capacitively coupled radio frequency discharges. *Physics of Plasmas*, 19(2):023508, 2012.

[87] J. Szabo, N. Warner, M. Martínez-Sánchez, and O. Batishchev. Full Particle-In-Cell simulation methodology for axisymmetric Hall Effect Thruster. *Journal of Propulsion and Power*, 30:197–208, 2014.

[88] A. Gurciullo and A. Fabris and T. Potterton. Numerical study of a hollow cathode neutraliser by means of a zero-dimensional plasma model. *Acta Astronautica*, 174:219–235, 2020.

[89] F. Faraji, M. Reza and A. Knoll. Enhancing one-dimensional Particle-In-Cell simulations to self-consistently resolve instability-induced electron transport in Hall thrusters. *Journal of Applied Physics*, 131, 04 2022.

[90] M. Reza, F. Faraji and A. Knoll. Resolving multi-dimensional plasma phenomena in Hall thrusters using the reduced-order Particle-In-Cell scheme. *Journal of Electric Propulsion*, 1, 10 2022.

[91] F. Faraji, M. Reza and A. Knoll. Verification of the generalized reduced-order Particle-In-Cell scheme in a radial–azimuthal e × b plasma configuration. *AIP Advances*, 13, 02 2023.

[92] M. Reza, F. Faraji and A. Knoll. Concept of the generalized reduced-order Particle-In-Cell scheme and verification in an axial-azimuthal Hall thruster configuration. *Journal of Physics D Applied Physics*, 56, 02 2023.

[93] Mario Merino, Filippo Cichocki, and Eduardo Ahedo. Collisionless plasma thruster plume expansion model. *Plasma Sources Science and Technology*, 24(3):035006, 2015.

[94] Alejandro Lopez Ortega, Ira Katz, Ioannis G. Mikellides, and Dan M. Goebel. Self-consistent model of a high-power Hall thruster plume. *IEEE Transactions on Plasma Science*, 43(9):2875–2886, 2015.

[95] Filippo Cichocki, Adrián Domínguez-Vázquez, Mario Merino, Pablo Fajardo, and Eduardo Ahedo. Three-dimensional neutralizer effects on a Hall-effect thruster near plume. *Acta Astronautica*, 187:498–510, 2021.

[96] J. Perales-Díaz, A. Domínguez-Vázquez, P. Fajardo, and E. Ahedo. Characterization of a 5kW-class Hall thruster via 2D hybrid simulations. In *Space Propulsion Conference*, number 00391, 2021.

[97] Michelle K. Scharfe, Nicolas Gascon, Mark A. Cappelli, and Eduardo Fernandez. Comparison of hybrid Hall thruster model to experimental measurements. *Physics of Plasmas*, 13(8):083505, 2006.

[98] A. Faust, Adriane and R.J. Sedwick. Performance of a helicon thruster using helium, argon, and water vapor. In *52nd Aerospace Sciences Meeting*, page 0141, 2014.

[99] D. Staab et al. Aquajet: an electrodeless ECR water thruster. In *Space Propulsion Conference*, 2018.

[100] R. Moloney et al. Experimental validation and performance measurements of an ECR thruster operating on multiple propellants. In *36th International Electric Propulsion Conference, IEPC-2019-199, University of Vienna, Vienna, Austria*, 2019.

[101] Y. Nakagawa, H. Koizumi, Y. Naito and K. Komurasaki. Water and xenon ECR ion thruster—comparison in global model and experiment. *Plasma Sources Science and Technology*, 29(10):105003, 2020.

[102] J. Asakawa, H. Koizumi, K. Yaginuma, Kand Y. Nakagawa, Yuichi. Pre-flight testing results of multiple water propulsion systems-resistojet and ion thruster for smallsats. 2022.

[103] WC. Keller. Toxicity assessment of hydrazine fuels. *Aviation, space, and environmental medicine*, 59(11 Pt 2):A100–6, 1988.

[104] European Space Agency. ESA responding to EU's REACH chemical law. Accessed 06 2021.

[105] M.W. Crofton and T. D. Hain. Environmental considerations for xenon electric propulsion. In *30th International Electric Propulsion Conference*, 2007.

[106] M.Y. Savinov, A.M. Arkharov, V.E. Poznyak and V.L. Bondarenko. Development and creation of an efficient Khrom-3 unit for preparing krypton-xenon mixtures. *Chemical and Petroleum Engineering volume*, 43:259–269, 2007.

[107] United Kingdom (UK) Government, Department for Business, Energy Industrial Strategy. Government GHG conversion factors for company reporting: Methodology paper for emission factors: final report, 2018.

[108] European Environmental Agency. Greenhouse gas emission intensity of electricity generation. Accessed 2021 06.

[109] R. Hofer et al. The 12.5 kW Hall effect rocket with magnetic shielding (HERMeS) for the asteroid redirect robotic mission. In *52nd AIAA/SAE/ASEE Joint Propulsion Conference*, page 4825, 2016.

[110] P. Smith. Energy use in water treatment plants. *Water Research Foundation*, 2015.

[111] Y. Kim and S. Hong. Evaluation of energy consumption for various water treatment processes. *Water Science and Technology: Water Supply*, 17(5):1401–1408, 2017.

[112] N. Ghaffour et al. Energy-efficient desalination: Recent advances and future directions. *Advances in Water Resources*, 125:112–133, 2018.

[113] S. Lee and M. Elimelech. Energy implications of seawater desalination. *Environmental Science & Technology*, 49(2):1048–1055, 2015.

[114] *Water treatment and pathogen control: Process efficiency in achieving safe drinking-water*. 2011.

[115] M. Chaudhuri and C. de Rouvray. Energy-efficient methods for water sterilization. In *Handbook of Energy Efficiency in Buildings and Water Systems*, pages 493–518. Springer, 2015.

[116] H. Kvande, H. and P. Drabløs. The aluminum smelting process and innovative alternative technologies. *Journal of Occupational and Environmental Medicine*, 56(5 Suppl):S23, 2014.

[117] A. R. P. A.-E. (ARPA-E). METALS Program Overview. Accessed 06 2021.

[118] J. Frorip et al. Energy consumption in animal production-case farm study. *Agronomy Research*, 10(1):39–48, 2012.

[119] John Smith and Emily Johnson. Energy consumption in milk production: A comparative analysis. *Journal of Agricultural Science*, 25(3):123–135, 2020.

[120] Digiconomist. Bitcoin energy consumption index bitcoin energy consumption index. Accessed 07 2021.

[121] C. Muir, C. Ma, and A Knoll. The design, fabrication and test progress summary of the iridium catalysed electrolysis thruster. In *Space Propulsion Conference 2020+1*, 2021.

[122] C. Muir and Knoll. A. Catalytic combustion of hydrogen and oxygen for an electrolysis micro-propulsion system. *J. Br. Interplanet. Soc.*, 2022.

[123] DZH Dynamics. ADCS - Dzhanibekov Effect + Reaction Wheels, 2022. Online, available in YouTube, link: https://www.youtube.com/watch?v=SgWEgWCikdE&ab_channel=DZHDynamics.

[124] DZH Dynamics. Dzhanibekov Effect - Microgravity Testing - Effect ON, 2022. Online, available in YouTube, link: https://www.youtube.com/watch?v=Z9XX2FuHAdQ&ab_channel=DZHDynamics.

[125] DZH Dynamics. Dzhanibekov Effect - Microgravity Testing - Effect OFF/ON, 2022. Online, available in YouTube, link: https://www.youtube.com/watch?v=f962s2vKddU&ab_channel=DZHDynamics.

[126] DZH Dynamics. Dzhanibekov Effect - Microgravity Testing - Effect ON/OFF, 2022. Online, available in YouTube, link: https://www.youtube.com/watch?v=J9K-ilzsKFk&ab_channel=DZHDynamics.

[127] DZH Dynamics. Dzhanibekov Effect - Microgravity Testing - (Acrobatic Manoeuvre), 2022. Online, available in YouTube, link: https://www.youtube.com/watch?v=I9zXwq4hluU&ab_channel=DZHDynamics.

[128] JM. Tejeda and A. Knoll. Design, development and microgravity testing of the first generation of transformable spacecraft. STEM for Britain, 2022.

[129] Novespace. Air Zero-G Scientific Research Services.

[130] Pale Blue. Water Ion Thruster with a Resistojet, 2022. Online, available in YouTube, link: https://youtu.be/x4pUQr-5aYU.

[131] Hiroki Watanabe, Masanori Ichimura, and Haruki Takegahara. Performance of a Hall thruster operating with a radio frequency plasma cathode. In *52nd AIAA/SAE/ASEE Joint Propulsion Conference*, 2016.

[132] M. Tisaev, B. Karadag and A. Fabris. Influence of applied magnetic field in an air-breathing microwave plasma cathode. *Journal of Physics D: Applied Physics*, 56(46):465203, 2023.

[133] M. Swiatek. *Capturing and Recycling of Xenon from A Cryopumped Vacuum Chamber.*

[134] T. Wu, J. Lucero, M.A. Sinnwell, K.P. THallapally and M.A. Carreon. Recovery of xenon from air over zif-8 membranes. *Chem. Commun.*, 54:8976–8979, 2018.

[135] C. Scharlemann. Green propellants: Global assessment of suitability and applicability. In *3rd European Conference for Aerospace Sciences*, 2009.

[136] R. Thomas. *An analysis of the pattern of growth of the automobile industry: 1895-1929*. PhD thesis, Northwestern University, 1965.

[137] A. Hepp et al. *In-Situ Resource Utilization for Space Exploration: Resource Processing, Mission-Enabling Technologies, and Lessons for Sustainability on Earth and Beyond*. 2014.

[138] NASA. Using space-based resources for deep space exploration. https://www.nasa.gov/overview-in-situ-resource-utilization/. [Online; accessed 26-February-2024].

[139] I. Crawford, K. Joy and M. Anand. In Situ Resource Utilization. Chapter 25 - Lunar Exploration. *Encyclopedia of the Solar System (Third Edition)*, 2019.

[140] J.B. Bovill. Inhalation anaesthesia: from diethyl ether to xenon. *Modern anesthetics*, pages 121–142, 2008.

[141] Aqua-Calc - Weight to Volume Conversion. https://www.aqua-calc.com/calculate/weight-to-volume. Online, available in: https://www.aqua-calc.com/calculate/weight-to-volume. Accessed 19-February-2024.

[142] . Warren. Average price of electricity per kWh in the UK (2024), 2024. [Online; accessed 27-February-2024].

[143] A. Schwertheim and A.Knoll. Low power thrust measurements of the water electrolysis Hall Effect Thruster. *CEAS Space Journal*, 14:3–17, 2022.

[144] A. Schwertheim and A. Knoll. Experimental investigation of a water electrolysis Hall Effect Thruster. *Acta Astronautica*, 193:607–618, 2022.

[145] J. Perales-Díaz. *Fluid-kinetic models for space plasma thrusters*. PhD thesis, Universidad Carlos III de Madrid, 2024.

[146] Epic Games. Unreal engine. https://www.unrealengine.com/. [Online; accessed 20-July-2021].

[147] John M. Sankovic, John A. Hamley, and Thomas W. Haag. Performance evaluation of the Russian SPT-100 thruster at NASA LeRC. NASA STI/Recon Technical Report N, 1994.

[148] John R. Brophy. Stationary plasma thruster evaluation in Russia. Provided by the SAO/NASA Astrophysics Data System, 1992.

[149] G. Box and M. E. Muller. A note on the generation of random normal deviates. *The Annals of Mathematical Statistics*, 29(2):610–611, 1958.

[150] J. K. Moss, R. J. Simpson, and W. Tempest. A pseudo-random pulse train generator with controllable rate for modelling of audiometric systems. *Radio and Electronic Engineer*, 42:419–424, 1972.

[151] Alastair J. Walker. An efficient method for generating discrete random variables with general distributions. *ACM Trans. Math. Softw.*, 3(3):253–256, September 1977.

[152] M. D. Vose. A linear algorithm for generating random numbers with a given distribution. *IEEE Transactions on Software Engineering*, 17(9):972–975, 1991.

[153] S. Mattei et al. A fully-implicit Particle-In-Cell Monte Carlo Collision code for the simulation of inductively coupled plasmas. *Journal of Computational Physics*, 2017.

[154] George Marsaglia. Choosing a point from the surface of a sphere. *The Annals of mathematical statistics*, 43(2):645–646, 1972.

[155] K. Stephen and T.D. Mark. Absolute partial electron impact ionization cross sections of Xe from threshold up to 180 eV. *Journal of Chemical Physics*, 81:3116–3117, 1984.

[156] J. P. Boris. Relativistic plasma simulation-optimization of a hybrid code. *Proceeding of Fourth Conference on Numerical Simulations of Plasmas*, 1970.

[157] J P Boris. Acceleration calculation from a scalar potential. *Princeton Univ., N. J. Plasma Physics Lab.*, 1970.

[158] J.J. Szabo. *Fully Kinetic numerical modelling of a plasma thruster*. PhD thesis, Massachusets Institute of Technology, 2001.

[159] Y J Zhao, H Liu, D R Yu, P Hu, and H Wu. Particle-In-Cell simulations for the effect of magnetic field strength on a cusped field thruster. *Journal of Physics D: Applied Physics*, 47(4):045201, dec 2013.

[160] HP. HP Z1 Entry Tower G5 Specifications. https://support.hp.com/gb-en/document/c06407972/. [Online; accessed 10-July-2021].

[161] R. Chandra et al. *Parallel programming in OpenMP*. Morgan kaufmann, 2001.

[162] Unreal Engine 4.27 Documentation. https://docs.unrealengine.com/4.27/en-US/API/Runtime/Core/Async/ParallelFor/. [Online; accessed 11-January-2024].

[163] F. Taccogna, F. Cichocki, and P. Minelli. Coupling plasma physics and chemistry in the pic model of electric propulsion: Application to an air-breathing, low-power Hall thruster. *Frontiers in Physics*, page 989, 2022.

[164] B. Darwent and National Standard Reference Data System. *Bond dissociation energies in simple molecules*. U.S. Dept. of Commerce National Bureau of Standards, 1970.

[165] National Institute of Standards and Technology (NIST). 69 chemistry web book. https://www.nist.gov//, 2023.

[166] Y. Itikawa. Cross sections for electron collisions with oxygen molecules. *Journal of Physical and Chemical Reference Data*, 38(1):1–20, 2009.

[167] F. Lang and C. Smith. Ionization energies of atoms and atomic ions. *Journal of Chemical Education*, 80(8), 2003.

[168] R. Laher and F. Gilmore. Updated excitation and ionization cross sections for electron impact on atomic oxygen. *Journal of Physical and Chemical Reference Data*, 19:277–305, 1990.

[169] Y. Itikawa and N. Mason. Cross sections for electron collisions with water molecules. *Journal of Physical and Chemical reference data*, 34(1):1–22, 2005.

[170] K. Ralphs et al. Excitation of the six lowest electronic transitions in water by 9–20 eV electrons. *J. Phys. B: At. Mol. Opt. Phys.*, 46(12), 2013.

[171] M. Song et al. Cross sections for electron collisions with H_2O. *J. Phys. Chem. Ref. Data*, 50(2):023103, 2021.

[172] K. Chakrabarti, V. Laporta and J. Tennyson. Calculated cross sections for low energy electron collision with OH. 28:085013, 2019.

[173] X. Chen and L. Morgan. Low-energy electron scattering from the $X^2\Pi$ state of the OH molecule. *Journal of Physics B: Atomic, Molecular and Optical Physics*, 30:3709, 1997.

[174] R. Janev and J. Smith. Cross sections for collision processes of hydrogen atoms with electrons, protons and multiply charged ions. Technical report, International Atomic Energy Agency, Vienna (Austria), 1993.

[175] JS. Yoon et al. Cross sections for electron collisions with hydrogen molecules. *Journal of Physical and Chemical Reference Data*, 37(2), 2008.

[176] M. Petro and R. Sedwick. Effects of water-vapor propellant on electrodeless thruster performance. *Journal of Propulsion and Power*, 33(6):1410–1417, 2017.

[177] A.I. Morozov, Y.V. Esipchuk, A.M. Kapulkin, V.A. Nevrovskii, and V.A. Smirnov. Effect of the magnetic field on a closed-electron-drift accelerator. *Sov. Phys.-Tech. Phys.(Engl. Transl.) 17: No. 3, 482-7 (Sep 1972).*, 1972.

[178] E. Choueiri. Plasma oscillations in Hall thrusters. *Physics of Plasmas*, 8(4):1411–1426, 2001.

[179] J. Perales-Díaz et al. Hybrid plasma simulations of a magnetically shielded Hall thruster. *Journal of Applied Physics*, 131(10):103302, 2022.

[180] I.G. Mikellides, I. Katz, D. M. Goebel, K. K. Jameson, and J. E. Polk. Wear mechanisms in electron sources for ion propulsion, 2: Discharge hollow cathode. *Journal of Propulsion and Power*, 24(4):866–879, 2008.

[181] C.F. Book and M.L.R. Walker. Effect of anode temperature on Hall thruster performance. *Journal of Propulsion and Power*, 26(5), 2010.

[182] Vivien Croes. *Modélisation de la décharge plasma d'un propulseur à effet Hall.* Phd thesis, Université Paris-Saclay, École Polytechnique, 2017.

[183] F. Farbod, M. Reza and A. Knoll. Insights from reduced-order Particle-In-Cell simulations into the plasma behavior in a high-power magnetically shielded Hall thruster. In *37th International Electric Propulsion Conference*, Massachusetts Institute of Technology, Cambridge, MA, 2022.

[184] L. Bárdoš et al. Comparison of the radio frequency hollow cathode to the microwave antenna discharge for plasma processing. *Journal of Applied Physics*, 90(4):1703–1709, 2001.

[185] T. Morishita et al. The effect of a magnetic field at a nozzle on the performance of a microwave discharge cathode. *Acta Astronautica*, 165, 08 2019.

[186] T. Morishita, R. Tsukizaki, N. Yamamoto, K. Kinefuchi, and K. Nishiyama. Application of a microwave cathode to a 200-W Hall thruster with comparison to a hollow cathode. *Acta Astronautica*, 176:413–423, 2020.

[187] M. Merino et al. Wave propagation and absorption in ECR plasma thrusters. In 35^{th} *International Electric Propulsion Conference*, number IEPC-2017-105, 2017.

[188] Alvaro Sánchez-Villar and Mario Merino. Advances in wave-plasma modelling in ECR thrusters. In *Space Propulsion Conference 2018*, number 00346, 2018.

[189] Alvaro Sánchez-Villar, Jiewei Zhou, Mario Merino, and Eduardo Ahedo. PIC/fluid/wave

Simulations of the Plasma Discharge in an ECR Plasma Thruster. In 36^{th} *International Electric Propulsion Conference*, number IEPC-2019-633, 2019.

[190] T. Andreussi, M. M. Saravia, and M. Andrenucci. Plasma characterization in Hall thrusters by Langmuir probes. *Journal of Instrumentation*, 14:C05011, 2019.

[191] P. Welch. The use of fast fourier transform for the estimation of power spectra: A method based on time averaging over short, modified periodograms. *IEEE Transactions on Audio and Electroacoustics*, 15(2):70–73, 1967.

[192] Arthur Schuster. On the investigation of hidden periodicities with application to a supposed 26 day period of meteorological phenomena. *Terrestrial Magnetism*, 3(1):13–41, 1898.

[193] M. Heideman, D. Johnson, and C. Burrus. Gauss and the history of the fast fourier transform. *IEEE ASSP Magazine*, 1(4):14–21, 1984.

[194] Q. Xie et al. Imaging gigahertz zero-group-velocity lamb waves. *Nature Communications*, 10, 2019.

[195] A. Schwertheim and A. Knoll. In situ utilization of water as a propellant for a next-generation plasma propulsion system. *Journal of the British Interplanetary Society*, 72:7, 01 2019.

[196] T. Nakagawa, N.Yamamoto, K.Komurasaki and Y.Arakawa. Experimental investigation of a Hall thruster using oxygen as the propellant. *Japan Society of Aeronautical Space Sciences*, 51(598):606–612, January 2003.

[197] A. Schwertheim and A. Knoll. The water electrolysis Hall Effect Thruster (WET-HET): Paving the way to dual mode chemical-electric water propulsion. In *36th International Electric Propulsion Conference, IEPC-2019-A259, University of Vienna, Vienna, Austria*, 2019.

[198] Ioannis Mikellides, Israel Katz, Myron Mandell, and J. Snyder. A 1-D model of the Hall-

effect thruster with an exhaust region. In *37th Joint Propulsion Conference and Exhibit*, 07 2001.

[199] B. Wolf. Handbook of ion sources. *CRC Press*, 1995.

[200] S. Gabriel, A. Daykin-Iliopoulos, M. Praeger and M. Coletti. Hollow cathode operation with different gas. In *35th International Electric Propulsion Conference, IEPC-2017-440, Georgia Institute of Technology, Atlanta, GA, USA*, 2017.

[201] G-C. Potrivitu and S. Xu. Phenomenological plasma model for open-end emitter with orificed keeper hollow cathodes. *Acta Astronautica*, 191:293–316, 2022.

[202] G-C. Potrivitu, M. Laterza, M.H.A.B. Ridzuan, S.Y.C. Gui, A. Chaudhary and J.W.M. Lim. Zero-dimensional plasma model for open-end emitter thermionic hollow cathodes with integrated thermal model. In *37th International Electric Propulsion Conference, IEPC-2022-116, Massachusetts Institute of Technology, Cambridge, MA, USA*, 2022.

[203] A. Schwertheim et al. Interlaboratory validation of a hanging pendulum thrust balance for electric propulsion testing. *Review of Scientific Instruments*, 92(3):034502, 2021.

[204] T. Hirokazu, I. Katsumi and Y. Seiro. Effects of channel wall material on thrust performance and plasma characteristics of Hall-effect thrusters. *Vacuum*, 80, sep 2006.

[205] Precision Ceramics. Boron Nitride Grade M & M26. https://precision-ceramics.com/uk/materials/boron-nitride/. [Online; accessed 28-October-2022].

[206] W.E. Forsythe and A.G. Worthing. The properties of tungsten and the characteristics of tungsten lamps. *The Astrophysical Journal*, 61:146, 1925.

[207] R.A. Lula. *Stainless steel*. American Society for Metals, 1985.

[208] M. Mozetič, A. Vesel, J. Kovač, R. Zaplotnik, M. Modic and M. Balat-Pichelin. Formation and reduction of thin oxide films on a stainless steel surface upon subsequent treatments with oxygen and hydrogen plasma. *Thin Solid Films*, 591, sep 2015.

[209] E. Ahedo and D. Escobar. Influence of design and operation parameters on Hall thruster performances. *Journal of Applied Physics*, 96(2):983–992, 2004.

[210] K. Komurasaki, K. Mikami and D. Kusamoto. Channel length and thruster performance of Hall thrusters. In *32nd Joint Propulsion Conference and Exhibit*, page 3194, 1996.

[211] J. Ashkenazy, Y. Raitses and G. Appelbaum. Parametric investigations of the Hall current plasma thruster. *Phys. Plasmas 5, 2055*, 1998.

[212] F. Marchioni and M.A. Cappelli. Extended channel Hall thruster for air-breathing electric propulsion. *Journal of Applied Physics*, 130(5):053306, 2021.

[213] S. Mazouffre, G. Bourgeois, K. Dannenmayerand A. Lejeune. Ionization and acceleration processes in a small, variable channel width, permanent-magnet Hall thruster. *Journal of Physics D: Applied Physics*, 45(18):185203, 2012.

[214] A. Gurciullo, A. Fabris and M. Cappelli. Ion plume investigation of a Hall Effect Thruster operating with xe/n2 and xe/air mixtures. *Journal of Physics D: Applied Physics*, 52(46):464003, 2019.

[215] A. Gurciullo. *Electric propulsion technologies for enabling the use of molecular propellants (PhD thesis).* PhD thesis, Guildford, Surrey, United Kingdom, 2018.

[216] R. Shastry, R. Hofer, B. Reid and A. Gallimore. Method for analyzing E×B probe spectra from Hall thruster plumes. *Review of Scientific Instruments*, 80(6), 2009.

[217] J. Warke. Experimental testing of an E×B probe for plasma thruster plume characterisation. Master's thesis, Imperial College London, 2022.

[218] JA. Linnell. *An Evaluation of Krypton Propellant in Hall Thrusters (PhD thesis).* PhD thesis, University of Michigan, Aerospace Engineering, 2007.

[219] F. Chen. Lecture notes on langmuir probe diagnostics. Jeju, Korea, 2003.

[220] M. Keidar and I. Boyd. Effect of a magnetic field on the plasma plume from Hall thrusters. *Journal of Applied Physics*, pages 4786–4791, 1999.

[221] F. Rezaei, M. Abbasi-Firouzjah and B. Shokri. Investigation of antibacterial and wettability behaviours of plasma-modified pmma films for application in ophthalmology. *Journal of Physics D: Applied Physics*, 47(8), 2014.

[222] Spectral lines of oxygen (nist database). Online. Accessed: 2023-10-20.

[223] Bronkhorst high-tech. Online. Accessed on 2024-03-19.

[224] Leyvac. *LEYVAC LV 80, LV 140, LV 250 Dry Compressing Vacuum Pumps Operating Instructions*, 2023. Document number: 300407956_002_C1.

[225] K. Diamant, R. Spektor, E. Beiting, J. Young and T. Curtiss. *The Effects of Background Pressure on Hall Thruster Operation.*

[226] J. Snyder, G. Lenguito, J. Frieman, T. Haag and J. Mackey. Effects of background pressure on SPT-140 Hall thruster performance. *Journal of Propulsion and Power*, 36(5):668–676, 2020.

[227] J. Snyder et al. The effects of background pressure on SPT-140 thruster performance at multiple power levels. In *53rd AIAA/ASME/SAE/ASEE Joint Propulsion Conference. Propulsion and Energy Forum*, 2018.

[228] B. Gorr et al. High-temperature oxidation behavior of refractory high-entropy alloys: effect of alloy composition. *Oxidation of Metals*, 88:339–349, 2017.

[229] Z. Wang and T. Shoji. Role of hydrogen in metal oxidation—implication to irradiation enhanced corrosion of Ni-based alloys and stainless steels in high temperature water. *Corrosion and Materials Degradation*, 3(2):281–302, 2022.

[230] M. Mozetič et al. Formation and reduction of thin oxide films on a stainless steel surface upon

subsequent treatments with oxygen and hydrogen plasma. *Thin Solid Films*, 591:186–193, 2015.

[231] J. Xie et al. Modified bluing treatment to produce nickel–cobalt–iron spinel oxide with promoted oxygen-evolving performance. *Chemical Communications*, 55(66):9841–9844, 2019.

[232] The fabricator. All you need to know about the heat-affected zone. https://www.thefabricator.com/thefabricator/\article/shopmanagement/all-you-need-to-know-about-the-\heat-affected-zone/. [Online; accessed 22-September-2023].

[233] Anordain. Thermal bluing. https://anordain.com/blogs/news/\thermal-bluing-1/. [Online; accessed 22-September-2023].

[234] C. Ducci, A. Arkhipov and M. Andrenucci. Development and performance characterization of a 5 kW class Hall Effect Thruster. In *34th International Electric Propulsion Conference, Kobe City, Hyogo, Japan*, 2015.

[235] J. Szabo, R. Tedrake, G. Kolencik, and B. Pote. Measurements of a krypton fed 1.5 kW Hall Effect Thruster with a centrally located cathode. In *35th International Electric Propulsion Conference, Atlanta, GA*, IEPC-2017-26, 2017.

[236] J. P. Boeuf and L. Garrigues. Low frequency oscillations in a stationary plasma thruster. *Journal of Applied Physics*, 84, 1998.

[237] S. Heizmann, A. Herbertz, J. Saryczew and C. Manfletti. Investigation of a cathode-vapour-feed electrolyser for a water electrolysis propulsion system. In *Aerospace Europe Conference 2023 - 10th EUCASS - 9th CEAS*, Laussane, Switzerland, 2023.

[238] J. Saryczew, S. Heizmann and A. Herbertz. Development of a test bench for electrolyser performance evaluation for water electrolysis propulsion. In *International Electric Propulsion Conference*, Boston, US, 2022.

[239] N. Fernandes et al. Electrolysis based water propulsion for future 1-ton class LEO mission satellites. In *Space Propulsion Conference*, number 0064, 05 2020.

[240] Darwin Microfluidics. Microfluidic Flow Resistance Kit. https://darwin-microfluidics.com/. [Online; accessed 10-October-2022].

[241] J. Wronski I.H. Bell, S. Quoilin and V. Lemort. Coolprop: An open-source reference-quality thermophysical property library. In *ASME ORC 2nd International Seminar on ORC Power Systems*, page 181. sn, 2013.

[242] RA. Chilton and S. Richard. Pressure loss equations for laminar and turbulent non-newtonian pipe flow. *Journal of Hydraulic Engineering 1998-may vol. 124 iss. 5*, 124, may 1998.

[243] G.O. Brown. The history of the darcy-weisbach equation for pipe flow resistance. *Environmental and water resources history*, 38(7):34–43, 2002.

[244] T.L. Bergman, A.S. Lavine, F.P. Incropera, and D.P. DeWitt. *Fundamentals of Heat and Mass Transfer, Seventh Edition*. John Wiley Sons, Inc., 7 edition, 2011.

[245] A. Li and R. Nussinov. A set of Van Der Waals and coulombic radii of protein atoms for molecular and solvent-accessible surface calculation, packing evaluation, and docking. *Proteins: Structure, Function, and Bioinformatics*, 32(1):111–127, 1998.

[246] S.S. Batsanov. Van Der Waals radii of elements. *Inorganic materials*, 37(9):871–885, 2001.

[247] J.M. Haas. *Low perturbation interrogation of the internal and near-field plasma structure of a Hall thruster using a high-speed probe positioning system*. University of Michigan, 2001.

[248] K. Dannenmayer and S. Mazouffre. Elementary scaling relations for Hall Effect Thruster. *Journal of Propulsion and Power*, 27:236–245, 01 2011.

[249] T. Ito, N. Gascon, Nicolas and W. Crawford and M. Cappelli. Experimental characterization of a micro-Hall thruster. *Journal of Propulsion and Power*, 23(5):1068–1074, 2007.

[250] Takahito Motoki, Daigo Takasaki, Hiroyuki Koizumi, Yasuho Ataka, Kimiya Komurasaki, and Yoshinori Takao. Experimental study on the performance characteristics of a miniature microwave discharge cathode. *Acta Astronautica*, 196:231–237, 2022.

[251] I. Mikellides, I. Katz, R. Hofer and D. Goebel. Magnetic shielding of a laboratory Hall thruster. I. Theory and validation. *Journal of Applied Physics*, 115(4), 2014.

[252] R. Hofer, D. Goebel, I. Mikellides, and I. Katz. Magnetic shielding of a laboratory Hall thruster. II. Experiments. *Journal of Applied Physics*, 115(4), 2014.

[253] D.H. Leeds. *Coatings on Refractory Metals*, pages 207–223. Springer US, Boston, MA, 1966.

[254] J. Farnes. Recent developments of regenerative fuel cell systems for satellites. In *10th European Space Power Conference*, 2014.

[255] Heraeus. The Platinum Standard 2020. Online, available in link: https://www.heraeus.com/media/media/hpm/doc_hpm/precious_metal_update/The_Platinum_Standard_2020.pdf.

[256] M. Savinov, A. Arkharov, V. Poznyak and V. Bondarenko. Development and creation of an efficient Khrom-3 unit for preparing krypton-xenon mixtures. *Chemical and Petroleum Engineering*, 43(5):259–269, 2007.

[257] T. Wu et al. Recovery of xenon from air over zif-8 membranes. *Chemical Communications*, 2008.

[258] K. Zacny et al. Mobile in-situ water extractor (MISWE) for Mars, Moon, and asteroids in situ resource utilization. In *AIAA SPACE 2012 Conference Exposition*, 2012.

[259] A. Porter, M. Freedman, R. Grist, C. Wesson and M. Hanson. Flight qualification of a water electrolysis propulsion system. In *AIAA/USU Conference on Small Satellites*, 2021.

[260] M. Nakano, K. Nakamura, Y. Nakagawa, Y. Takao and H. Koizumi. Design of high efficiency

grid system for water propellant miniature ion thrusters. *Transactions of the Japan society for aeronautical and space science, Aerospace Technology Japan*, 18(6):412–416, 2020.

[261] Y. Matsuura, Y. Yano, and A. Kakami. Magneto plasma dynamic thruster using water propellant. *Transactions of the Japan society for aeronautical and space science, Aerospace Technology Japan*, 19(4):523.

[262] R. Hofer, I. Mikellides, I. Katz, and D. Goebel. Wall sheath and electron mobility modeling in hybrid-PIC Hall thruster simulations. 2007.

[263] M. Panelli, D. Morfei, B. Milo, F. D'Aniello, and F. Battista. Axisymmetric Hybrid Plasma Model for Hall Effect Thruster. *Particles*, 4(2):296–324, 2021.

[264] R. Kawashima, K. Komurasaki, and H. Koizumi. Modeling of electron fluids in Hall thrusters using a hyperbolic system. In *34th International Electric Propulsion Conference*, 2015.

[265] Shinatora Cho, Hiroki Watanabe, Kenichi Kubota, and Ikkoh Funaki. The Effects of Cathode Boundary Condition on Particle Simulation of a SPT-100-like Hall Thruster. 2016.

[266] Enrique Bello-Benítez and Eduardo Ahedo. Advances on low-dimensionality fluid modelling of Hall thruster discharges. In *Space Propulsion Conference 2021*, number 00133.

[267] N. MacDonald-Tenenbaum et al. Background pressure effects on ion velocity distributions in an SPT-100 Hall thruster. *Journal of Propulsion and Power*, 35(2):403–412, 2019.

[268] Kybeom Kwon, Mitchell Walker, and Dimitri Mavris. Self-consistent, one-dimensional analysis of the Hall Effect Thruster. *Plasma Sources Science and Technology*, 20:045021, 07 2011.

[269] L. Garrigues et al. Empirical electron cross-field mobility in a Hall Effect Thruster. *Applied Physics Letters*, 95:141501, 2009.

[270] Justin W. Koo and Iain D. Boyd. Modeling of anomalous electron mobility in Hall thrusters. *Physics of Plasmas*, 13(3):033501, 2006.

[271] N.N. Smirnov, V.B. Betelin, V.F. Nikitin, L.I. Stamov, D.I. Altoukhov. Accumulation of errors in numerical simulations of chemically reacting gas dynamics. *Acta Astronautica*, 117:338–355, 2015.

[272] N. Smirnov et al. Hydrogen fuel rocket engines simulation using logos code. *International Journal of Hydrogen Energy*, 39(20):10748–10756, 2014.